Development of Non-Prestressed UHP-FRC Girders for Long-Span Bridges with DCSR Design Concept
and
Collapse Assessment of SMFs with Calibrated RC and UHP-FRC Columns Based on Full-Scale Experiments

By

Seyed Missagh Shamshiri Guilvayi

Dissertation

Submitted in partial fulfillment of the requirements

for the degree of Doctor of Philosophy at

The University of Texas at Arlington

August 2021

Supervising Committee:

Dr. Shih-Ho Chao

Dr. Suyun Ham

Dr. Himan Hojat Jalali

Dr. Haiying Huang

ACKNOWLEDGEMENTS

I am extremely grateful to my advisor Dr. Shih-Ho Chao for his support and invaluable contribution during my PhD Study. I would also like to express my appreciation to my dissertation committee: Dr. Jalali, Dr. Ham, and Dr. Huang.

I am deeply indebted to my family. My mother for her invaluable support and positive thoughts and my brothers for always encouraging me to move forward and believing in me. I would also like to extend my gratitude to my dear wife who stood by me every day through my study and helped me with his insightful suggestions.

July 2021

Abstract

Development of Non-Prestressed UHP-FRC Girders for Long-Span Bridges with DCSR Design Concept
and
Collapse Assessment of SMFs with Calibrated RC and UHP-FRC Columns Based on Full-Scale Experiments

By

Seyed Missagh Shamshiri Guilvayi

University of Texas at Arlington, 2021

Supervising Professor: Shih-Ho Chao

The work presented here is divided in two parts. This summary includes two paragraphs, each summarizing the topics presented in this dissertation.

Ultra-high-performance fiber-reinforced concrete (UHP-FRC) is an emerging material and revolutionarily utilize its mechanical properties can offer a new way to design conventional precast prestressed concrete girders. Its ultra-high compressive strength (> 20 ksi) accompanying by exceptional compressive ductility with a maximum useable compressive strain of 0.015–0.03 allow designers to use higher amount of reinforcement. Current design codes (ACI 318 Building Code and AASHTO LRFD Bridge Design Specifications), limits the maximum useable compressive strain, ε_{cu}, to 0.003 for conventional plain concrete to assure the ductile failure of the member. This limitation leads to a section with smaller

amount of reinforcement and more vulnerable to cracking and corrosion. Part one of this study investigates an innovative design concept – ductile-concrete strong-reinforcement (DCSR) for designing long-span UHP-FRC bridge girders without prestressing. This new design concept eliminates the use of prestress through enhancing the flexural first cracking strength by using high amount of non-prestressed corrosion and fatigue resistance ASTM A1035 rebars. This allows the elimination of prestressing. The uncracked section maintains the stiffness of the section under service loading and consequently the well-controls the deflection. Even after cracks occur, the combination of high amount of reinforcement with fiber bridging considerably prevents the crack development and propagation. This keeps the section stiffness nearly unchanged up to very high loads. The high amount of reinforcement not only considerably increases the flexural capacity of the girder, the small stresses in rebars also help close the cracks if overload occurs. Experimental testing shows beams design by DCSR concept showing high ductility due to UHP-FRC's exceptional compressive ductility. UHP-FRC's high shear strength also allow the shear reinforcement to be minimized or eliminated. Long-span bridges with different lengths were designed and illustrated using DCSR concept with optimized sections.

In the second part of this dissertation, a commonly used energy-based degradation model for reinforced concrete (RC) columns were examined against recent full-scale column testing results. The experimental tests consisted of five identical full-scale ACI 318 compliant RC columns subjected to various loading protocols up to collapse. The results indicate that currently used energy-based deterioration hysteretic models cannot accurately predict the behavior of RC columns subjected to different loading protocols. The test result analysis shows that when the P-Delta effect is removed, there is no evidence of negative

stiffness due to in-cycle degradation resulting from material nonlinearities in the response even up to large drift ratios (DR > 10%). Another drawback of current model is that it needs to be recalibrated for different loading protocols. A new dual degrading model (DDM) is proposed for modeling the nonlinear behavior of RC columns subjected to collapse level displacement reversals. This model features a dual degrading system at the plastic hinge for predicting the behavior of an RC column under different loading histories. DDM can be calibrated by multiple loading protocols simultaneously with only one set of parameters. This increases the accuracy and confidence of the model for predicting a structure's seismic behavior. The new dual degrading model is shown capable of matching the behavior of the full-scale test results up to collapse level drift ratios. Then, the new model is applied to prototype four-story and 20-story RC buildings analyzed by nonlinear time-history analyses. For the four-story building, results indicate an appreciable difference in the seismic response in term of maximum drift ratio as compared to the analysis using the conventional energy-based degradation model. These effects become significant where the ground motion intensity is scaled up for collapse simulations. Incremental dynamic analyses (IDA) indicate that the predicted collapse resistance for low rise frames can have a 10% difference between the seismic force resisting system (SFRS) with DDM and conventional energy-based degradation model. This difference becomes insignificant for high-rise buildings as the collapse drift ratio level for them is generally in smaller levels where the plastic hinge models exhibit similar behavior.

Table of Contents

List of Illustrations

List of Tables

Chapter 1

Organization of Dissertation

This dissertation is comprised of two main topics, and it is organized into two major parts. The organization of the dissertation is discussed in this chapter (Chapter 1).

Part 1 of this dissertation discusses the development and implementation of a new design concept called ductile-concrete strong-reinforcement (DCSR) that uses the high strength and enlarged compressive ductility of ultra-high performance fiber reinforced concrete (UHP-FRC). Part 1 is covered in chapter 2 through chapter 5. Chapter 2 presents a literature review on the materials and the methods currently are in practice. Chapter 3 discusses a series of experimental tests that are performed to investigate the synergy between the UHP-FRC and the reinforcement amount, which affects the tensile behavior of the UHP-FRC material. Chapter 4 discusses the fundamental of the DCSR design concept including enhanced ductility of a component design with DCSR design concept, difference in crack pattern for different matrix materials (RC, SFRC and UHP-FRC), as well as the experimental tests performed in prior studies. This chapter includes a series of numerically analyzed sections that compares the effect of geometry and reinforcement amount in DCSR design concept. Chapter 5 addresses the implementation of DCSR design concept in building and bridges. In this chapter, a series of non-prestress girders designed with DCSR design concept are presented. Also, the use of DCSR design concept columns in buildings are assessed through an incremental dynamic analysis (IDA) approach.

Part 2 is covered in chapter 6 through chapter 9. This part introduces a new dual-degradation model (DDM) for column plastic hinges in special moment frames (SMFs). Chapter 6 presents a literature review on the methodology on collapse assessment, plastic hinge models, and importance of loading protocol. The results of an experimental test for five large-scale nominally identical columns subjected to different types of loadings are

presented in this chapter. Chapter 7 discusses the fundamental of the dual degrading model (DDM) and elaborate the differences of this new model with the currently used plastic hinge models. In this chapter, the non-linear time history (TH) analysis result for a 4-story building with DDM plastic hinge is compared against a frame model in which the column plastic hinges are modeled with a current model. Chapter 8 expands the discussion on the new model with the IDA approach. In this chapter, the record-to-record analysis of the DDM plastic hinge is assessed as well as the collapse resistance of a frame modeled with this method. Chapter 9 discussed an improved plastic hinge using UHP-FRC material at the plastic hinge zone of the columns. Chapter 10 contains a summary and conclusion of both part 1 and part 2 of this dissertation.

Chapter 2
Part I

Introduction to

Non-Prestressed Girders with UHP-FRC

2.1 Introduction

This research introduces an innovative precast non-prestressed ultra-high-performance fiber-reinforced concrete (UHP-FRC or UHPC) decked bulb-tee (DBT) or box bridge girder reinforced with high-strength corrosion-resistant rebars. A new ductile-concrete strong-reinforcement (DCSR) design concept is introduced and used to design this innovative bridge girder. Eliminating prestressing allows UHP-FRC bridge girders to be built onsite for long-span bridges. It also allows any precast plant to produce bridge girders even it has no prestressing facilities. This new precast bridge girder has the following unique features: (1) It requires no prestressing, thereby eliminating expensive facilities, labor cost, prestress losses, end zone cracking, and camber issues associated with prestressing, (2) It has high corrosion-resistance and long-term durability, (3) It allows very long span and/or curved profile that can hardly be achieved by traditional precast prestressed concrete girders, (4) The girder design is straightforward with a simpler shear design and does not require cracking control reinforcement and complicated computation regarding long-term prestress loss and camber, (5) DBT or box UHP-FRC girders do not need cast-in-place decks; hence, they can considerably accelerate the construction process of bridges, (6) It provides safety benefits due to the accelerated bridge construction and lower maintenance demand. These features provide greater durability, high damage tolerance, life-cycle cost savings, simplified and accelerated construction, and structural efficiency when compared to competing conventional precast prestressed concrete and steel girders. The DCSR design concept utilizes the exceptional compressive ductility of UHP-FRC to increase the amount of reinforcement, which in turn fully utilizes the capacity of UHP-FRC in compression and reduces the stress in steel. The new girders provide

equivalent or greater stiffness and first-cracking resistance and a much higher ultimate strength than conventional precast, prestressed concrete girders. Prototype single-span 95-ft and 250-ft long non-prestressed UHP-FRC box girders were designed using DCSR concept. Finite element analysis using AASHTO live load indicates both girders satisfy code requirements. The experimental and analytical results indicate that conventional precast prestressed concrete girders can be replaced by the new non-prestressed decked or box UHP-FRC girders.

2.2 Literature review

2.2.1 Ultra-High-Performance Fiber-Reinforced Concrete (UHP-FRC)

Ultra-high-performance fiber-reinforced concrete (UHP-FRC) is a new generation of fiber-reinforced concrete, which has ultra-high compressive ductility and strength (124 to 207 MPa for ultimate compressive strength and 69 to 83 MPa after 24 hours). Concrete with only ultra-high compressive strength is not suitable for earthquake resistant applications, even when reinforced with mild reinforcing steel, as the very brittle nature can cause potential issues such as abrupt, unpredictable failures and a minimum capability of stress redistribution. UHP-FRC was developed by changing the porous nature of conventional concrete through reducing dimensions of microcracking (or defects) in the concrete. This is achieved in UHP-FRC through a very low water to cementitious materials ratio (0.18 to 0.25) and a dense particle packing. The consequences of a very dense microstructure and low-water ratio result in enhanced compressive strength (Horii and Nemat-Nasser, 1985) and delayed liquid ingress (FHWA, 2011). Furthermore, the addition of high-strength steel

or synthetic fibers improves the brittle nature of concrete by increasing the tensile cracking resistance, post-cracking strength, ductility, and energy absorption capacity. In terms of corrosion resistance, research has indicated that UHP-FRC has a much greater durability than conventional concrete due to its very dense microstructure (Ahlborn et al., 2011). This dense microstructure impedes the conductive chloride ions from coming into direct contact with the steel reinforcing bars, which protects the reinforcing bars from corrosion. Table 2-1 provides a comparison between typical conventional concrete and UHP-FRC.

Table 2-1 Comparison of typical conventional concrete and UHP-FRC
(All data from UT Arlington research except rapid chloride penetration test)

Properties of Concrete	Conventional Concrete	UHP-FRC
Ultimate Compressive Strength	< 55 MPa	124 to 207 MPa
24-hour compressive strength	< 21 MPa	69 to 83 MPa
Flexural Strength	< 4.6 MPa	17 to 41 MPa
Shear strength	< 1.2 MPa	> 4.1 MPa
Direct Tension	< 3 MPa	up to 10 MPa
Rapid Chloride Penetration Test*	2000-4000 Coulombs passed	Negligible (< 100 Coulombs passed)
Ductility	Negligible	High ductility
Ultimate Compressive Strain, ε_{cu}	0.003	0.015 to 0.03
Confining	Negligible	High confining capability

* (Ahlborn et al., 2011)

Fiber-reinforced concrete (FRC) has been used for many decades; however, conventional FRC only enhances post-cracking ductility, and its compressive strength is close to that of plain concrete (35 to 55 MPa). In other words, conventional FRC does not fundamentally change the micro-structure of concrete, but it has a greater residual tensile capacity and

ductility after cracking. Research shows that even a high-performance FRC column (an FRC with tensile strain-hardening behavior) has essentially the same failure mode as that of an RC column after FRC is crushed, which leads to rebar buckling and fracture (Aviram, 2010). Typically, UHPC mix without fibers has a characteristic compressive strength of higher than 150 MPa, with a high modulus of elasticity in the range of 45 GPa to 55 GPa, and a tendency to exhibit extreme brittle failure after peak strength. Similar to conventional and high strength concretes, an increase in compressive strength leads to an increase in brittleness in UHPC. The increased density of the hardened paste results in a higher modulus of the elasticity. The explosive nature of UHPC prevents the recording of the post-peak curve. However, the addition of fibers to the UHP-FRC matrix decreases the brittleness and increases the maximum usable compressive strain. Also, the presence of fibers slightly increases the compressive strength. The UHP-FRC shows more distinct nonlinear behavior before the peak compressive strength as compared to regular concrete and UHPC without fibers. The UHP-FRC mix (Aghdasi et al., 2016) used in this study shows a maximum useable strain of approximately 1.2-1.4% as shown in Figure 2-1.

2.2.2 Fiber-Reinforced Polymer (FRP) reinforcement

Corrosion is an issue of concern when steel reinforcement is used for concrete structures exposed to aggressive environments. Composite materials such as fiber-reinforced polymer (FRP) are a suitable alternative to steel reinforcing bars when RC structures are exposed to deicing salts, seawater, or other corrosive environments. Fiber-reinforced polymers use a polymeric resin system reinforced with fibers. Fibers are typically aramid, basalt, carbon, or glass, and the polymer is usually an epoxy, phenol formaldehyde resin, polyester

thermosetting plastic or vinyl ester. In this study, basalt fiber-reinforced polymer (BFRP) reinforcement was used. Basalt fibers are a mineral-based inorganic product and were recently introduced to the structural engineering community (NCHRP, 2017).

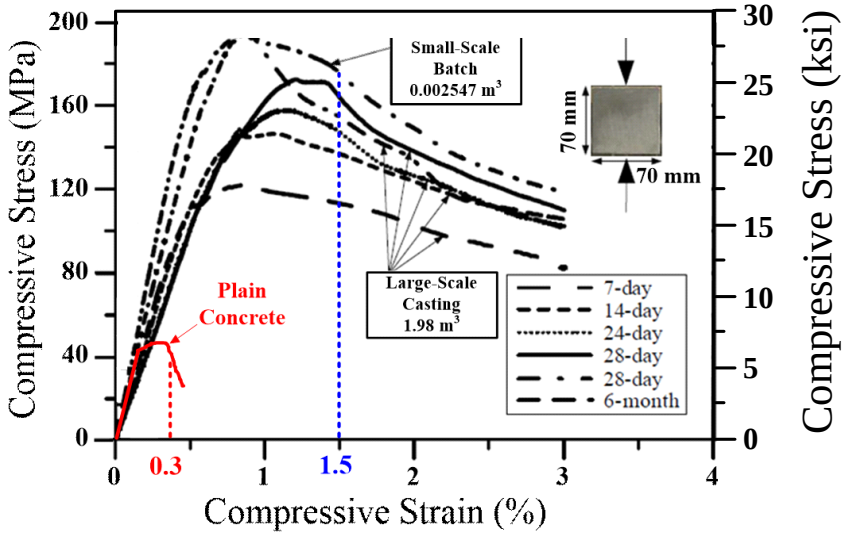

Figure 2-1 Comparison between compressive stress-strain behavior of UHP-FRC (Aghdasi et al., 2016) and regular concrete

The tensile behavior of FRP bars is controlled by fiber and resin properties, fiber volume fraction, as well as fiber geometry and orientation within the matrix (Nanni et al., 2014). FRP materials are anisotropic in nature and show purely elastic behavior until failure. This lack of ductility should be taken into considerations while designing concrete structures reinforced with FRP bars. FRP bars have much higher tensile strength than steel bars but the tensile modulus of FRP bars is significantly lower than their steel counterparts, as small as 20% (ACI, 2015). BFRP bars used in this study have an ultimate tensile strength of approximately 1014 MPa and an ultimate tensile strain of 0.017 to 0.025.

2.2.3 Brittle flexural failure of conventional concrete reinforced with FRP bars

Design of reinforced concrete members with FRP reinforcement is similar to the design of steel-reinforced concrete members. However, unlike steel, the FRP bars do not exhibit ductility. Hence, the failure of reinforced concrete due to rupture of FRP bars before concrete crushes is sudden, destructive and not desirable. In addition, the low axial stiffness of FRP bars typically causes large crack width and significantly smaller shear capacity due to the loss of aggregate interlock for widened crack widths. Consequently, it is preferable for FRP-reinforced concrete members to fail in compression rather than by the rupture of FRP bars (Nanni, 1993). However, for FRP-reinforced structural members, neither tension-controlled nor compression-controlled failure mode can provide sufficient ductility to the structure. Therefore, ACI 440.1R (ACI, 2015) suggests a more conservative design for FRP-reinforced members than for the steel-reinforced members. If high-strength concrete is used with the FRP reinforcement bars, stiffness of the cracked section is increased but it reduces the deformability of the flexural member compared to normal strength concrete (ACI, 2015).

2.2.4 Conventional RC design concept

An ideal structural member would simultaneously have both high flexural and shear strength as well as high stiffness, high ductility, high durability (high corrosion resistance), and high resilience (ability to recover from overloading). Notably, these characteristics cannot happen simultaneously in conventional reinforced concrete (RC) members due to their current code design constraints, which require a tension-controlled behavior for flexural members (AASHTO, 2017; ACI, 2019). That is, the longitudinal reinforcement

ratio of a flexural member should be kept low so the steel reinforcement can develop significant yield strain before the concrete reaches its maximum useable strain – typically at 0.003. The purpose is to ensure sufficient deformation, i.e., a warning, before failure occurs. Because concrete's compressive failure is naturally brittle, the large deformation relies on the inelastic elongation of steel rebars. While this approach provides deformation capacity to the structural members, it also leads to the following consequences:

1. A lower reinforcement ratio leads to a smaller compression zone and a limited ultimate flexural strength, which does not fully utilize the cross-section.
2. A lower reinforcement ratio causes greater elongation of the rebars after cracking, which in turn leads to a larger crack width. A wider crack width reduces the flexural stiffness, resulting in greater deflection. A larger crack width (thus, a deeper crack and smaller compression zone) reduces the shear transfer capacity due to the smaller compression zone, as well as the diminished aggregate interlock and dowel capacity (Wight, 2016).
3. A lower reinforcement ratio causes high stresses in steel rebars, which deteriorates the bond strength. The yielding of steel rebars provides ductility but also cause unrecoverable permanent deformation. The permanent deformation along with concrete crushing will reduce the resilience of a structure after overloading.

Cracks present a critical vulnerability to any concrete structure, allowing harmful ions and gases to penetrate the structure's interior. In many cases, these harmful substances come in contact with the reinforcing steel used in most concrete structures. Corrosion of the steel rebars via the permeation of either water, air, and/or chloride (such as found in marine environments, common deicing salts, or brackish water) can result in a 12–27% reduction

in the usable life expectancy of concrete structures (Jones et al., 2015). In fact, the overwhelming majority of concrete durability problems, about 90%, are related to steel reinforcement corrosion (Mehta and Monteiro, 2014; Scrivener et al., 2018). Notably, the magnitude and consequences of corrosion in prestressing steels are much more severe than in rebars. This is not only because high-grade steel is more susceptible to corrosion but also because the diameter of prestressing tendons is relatively small. Thus, even a small uniform corrosive layer or a corroded spot can substantially reduce the cross-sectional area of the steel, induce stress concentrations, and eventually lead to premature failure. (Naaman, 2012).

2.2.5 Prestressed concrete

Freyssinet (Freyssinet, 1936) summarized the advantages of using prestressed concrete as compared to conventional reinforced concrete as: 1) a considerable reduction of deformation (deflection), 2) complete suppression of cracks, 3) a decrease of the maximum compression stress in bending, 4) a decrease of tension produced in the concrete by the shear stresses, and 5) considerable resistance against repeated stressing. Since prestressed concrete does not crack under service loads, the entire section is generally active in resisting the load and provides effective deflection control, while in reinforced concrete only the uncracked part of the section is active (Naaman, 2012). Together with the use of high-strength prestressing steel and concrete, prestressed concrete members are generally lighter. Also, it is often claimed that prestressed concrete has high resilience because the considerable elastic restoring force from the reinforcement can close the cracks temporarily developed due to overloading (Leonhardt, 1964; Lin, 1981).

On the other hand, prestressed concrete also has its disadvantages. The consequences of corrosion in prestressing steel are more severe than in mild steel reinforcement because of the presence of high-stress in the steel and the diameter of prestressing steel is relatively small (Naaman, 2012). The production of precast, prestressed concrete members involves the use of special prestressing equipment, requiring a prestressing bed and skilled labor. Additionally, the prediction of long-term prestress losses is usually cumbersome and by no means accurate. The initial high stress in concrete can also require additional longitudinal mild steel reinforcement and debonding of strands at the ends of girders to control the cracking. Delivery of large prestressed structures and the cost of transportation usually eliminates the possibilities of a very long span and/or curved profile to be precast. Camber-related issues often pose challenges to designers, fabricators and contractors. One example is the prefabricated deck bulb-tee (DBT) girders. Many state DOTs and the Federal Highway Administration (FHWA) are promoting accelerated bridge construction (ABC). Using a prefabricated DBT eliminates the need for constructing cast-in-place decks and, hence, provides the benefits of rapid construction, improved safety for construction personnel and the public, and improved structural performance and durability (NCHRP, 2017); however, the use of DBT girders has been limited to relatively short-span and low-traffic bridges. One of the reasons is the large prestress-induced cambers, which require considerable on-site effort to line up skewed DBT girders to eliminate the deck profile problems.

Chapter 3
Part I

Experimental Program

3.1 Introduction

Prior research has shown that the presence of reinforcing bars in structural members enhances the cracking distribution and tensile ductility of steel fiber-reinforced concrete (SFRC) due to the tension-stiffening effect (Chao et al., 2007; Aghdasi et al., 2016). Therefore, adding a large amount of longitudinal reinforcement not only increases the flexural strength of UHP-FRC beams, but also enhances the mechanical behavior of UHP-FRC on the tensile side of the beam. In this research study the effect of reinforcement ratio at bottom layer of the reinforcements is investigated.

In this section test design, preparation, analyses, and result of a series of small beams are presented. The intention of this tests is to investigate the effect of reinforcement ratio on the behavior of a section fabricated by UHP-FRC as the matrix. More specifically, the tensile strength of UHP-FRC is studied with the variation of the reinforcement ratio in the tension zone.

3.2 Design of the specimens

In a series of experimental tests, eight number of small specimens was casted. In this experiment it was intended to investigate the effect of reinforcement ratio on the flexural cracking strength, f_r, in Ultra-High-Performance Fiber-Reinforced Concrete (UHP-FRC). In these specimens A706 reinforcement steel rebars were used. A longitudinal reinforcement ratio, ρ_{TA}, is defined as the area of the longitudinal reinforcement to the concrete tributary area which is the product of the width of the beam by twice the cover (bottom concrete fiber to the centroid of the reinforcement). For one of the specimens the

beam was fabricated with no reinforcement for comparison purposes. The rest of the specimens were designed to have different reinforcement ratio amount. The designed reinforcement ratio was increased up to ρ_{TA} =17%. Each specimen has a square cross section with a width of 4 in. To provide a pure bending zone in the specimen and minimize the effect of shear in the critical section for cracking, a four-point loading test was considered. Figure 3-1 illustrates the typical dimensions and loading points for all the specimens. The two loading points equally spaced from the midspan of the beam creates the 10 in. pure bending zone for the specimens. The supports at each end are free to rotate and does not apply rotational resistance. The center of the loading for all the loading points including the center of the supports is distanced 10 in. from the adjacent loading point(s). A 1 in. thick steel plate was located at the loading points and a thin layer of grout was fabricated between the steel plates and the beam. Due to slenderness of the beams and high shear capacity of UHP-FRC, shear stirrups were not used in the specimens.

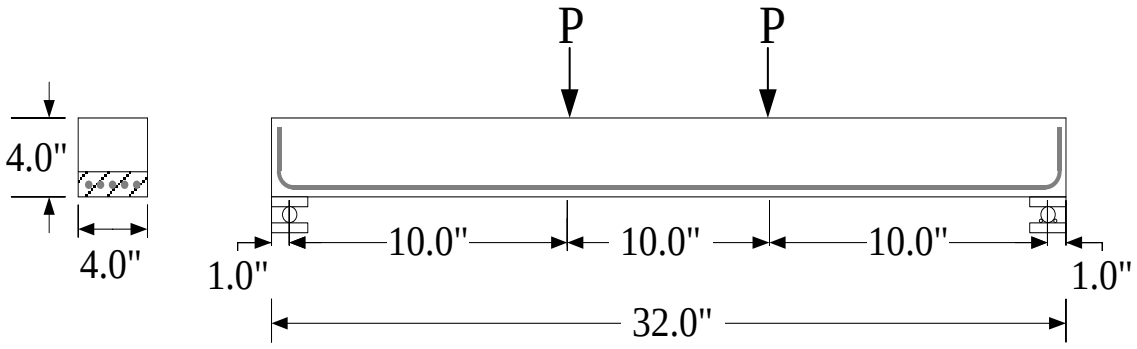

Figure 3-1 typical dimension and loading points for all the specimens

Figure 3-2 shows the reinforcement arrangement used for the specimens. Typically, the increase of the reinforcement will increase the tributary reinforcement ratio. However, this ratio does not increase proportional to the production of number and the area of the rebars. This ratio is reduced if the number of the layers increase or the need for the clear cover increases as the size of the rebar increases.

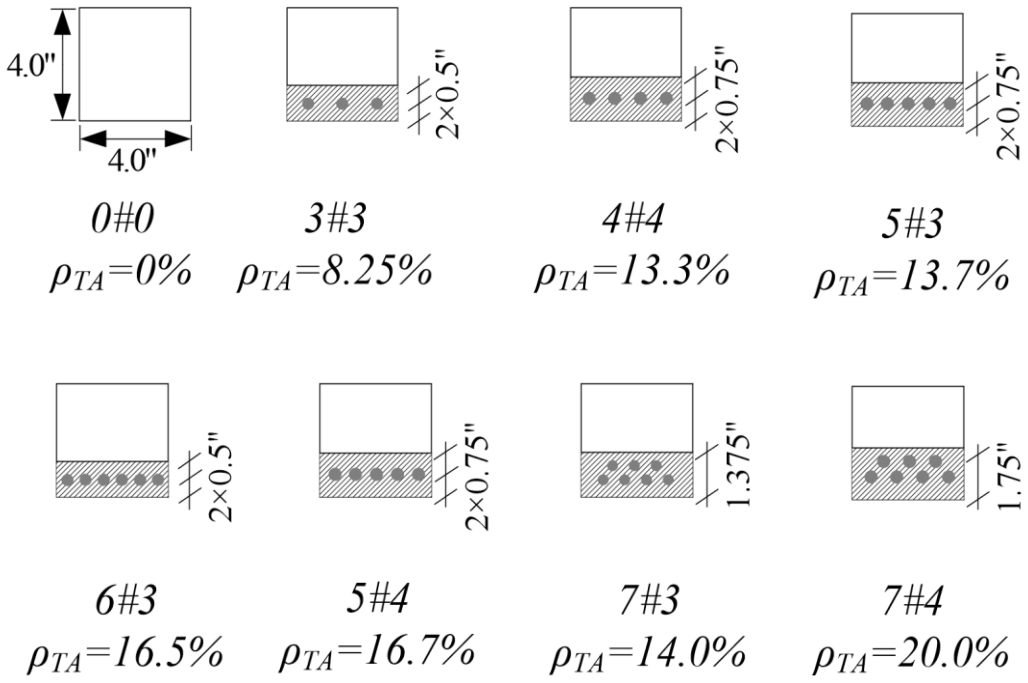

Figure 3-2 reinforcement arrangement for specimens

3.3 Preparation

The specimens were prepared and tested in the Civil Engineering Lab Building (CELB) of the University of Texas at Arlington. Specimen preparation started with building the formworks. Thereafter, the longitudinal reinforcement rebars were casted and placed in the formwork. Since the scale of the specimens were small, the fabrication precision of the specimens and location of the rebars play important roles in the result. Hence, the

dimensions of the rebars and the cover (bottom layer to the center of the rebars) were checked many times after casting and placing in the formworks. Figure 3-3 represents the fabrication of the specimens.

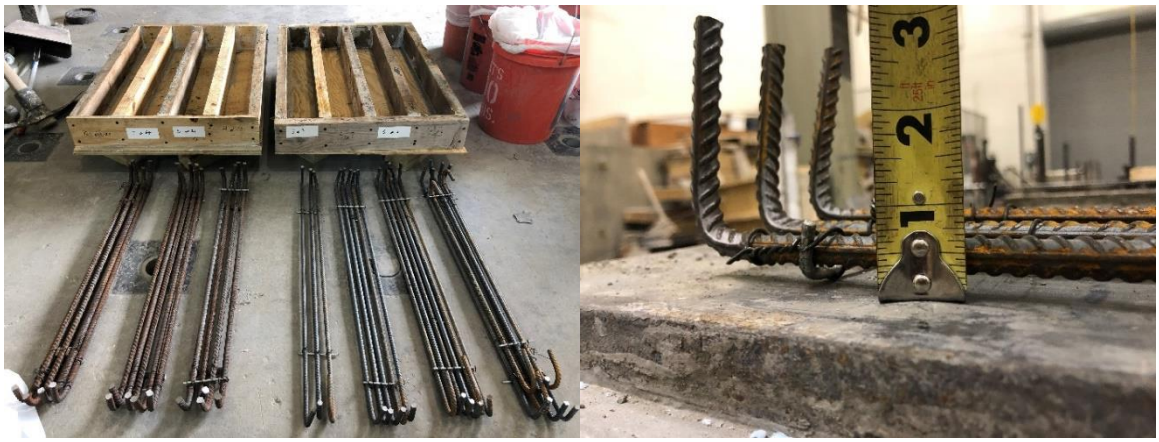

Figure 3-3 specimen preparation

Since in some of the specimens the reinforcement configuration was very congested, it was important to keep the gap between the rebars for the concrete to flow through and coat the reinforcement rebars. In Figure 3-4 (a) the congestion of the reinforcement for a beam with two layer of steel rebars is shown. The need for vibrating the specimens was eliminated due to the high workability of the UHP-FRC. Figure 3-4 (b) Shows the workability of the UHP-FRC. After pouring the concrete, the specimens were cured in a humid curing chamber in CELB with 90% humidity.

(a) (b)

Figure 3-4 a) congested reinforcement with two layers of steel rebars and b) the high-workability of UHP-FRC

3.4 Test setup

All the specimens were loaded under a four-point loading test. The applied force from the 400K machine was transferred through a loading platen with two loading pins which divided the applied load to two equal loads. The loading was monotonically increased with the rate of 0.01 in/min. To record the settlement of the supports, two Linear Variable Differential Transformers (LVDT) were used. Also, two LVDTs were installed at both sides of the specimen at the midspan to record the deflection of the beams under during the test. The net deflection for the midspan o the beam would be calculated from the difference of the total midspan deflection subtracted by the average of the settlements read from the two LVDTs installed at the supports. Figure 3-5 represents the test setup for the specimens.

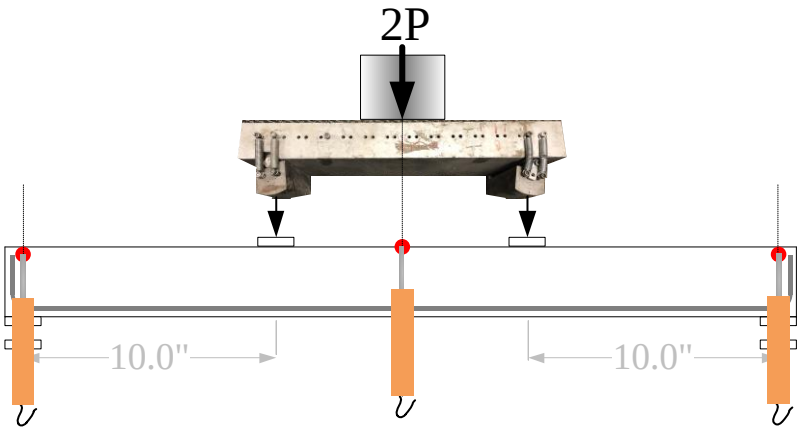

Figure 3-5 test setup for the specimens

3.5 Result

In this section, the test results of specimens is provided. The first six specimens experienced a flexural cracking occurred prior to shear cracking. However, in the last two specimens that had two rows of reinforcement shear cracking was observed first. For analyses purposes, only the first six specimens -that experienced flexural cracking prior to shear cracking- was considered.

Specimen with no reinforcement (0#0)

In this specimen no reinforcement was used. Figure 3-6 shows the response plot of this specimen and its test setup. This specimen reached to a maximum loading point of 6.4 kips at a deflection of 0.1 in. at the midspan. The first cracking occurred at a loading of 3.2 kips. With a moment of inertia of 21.33 in^4, the tensile strength of the UHP-FRC at the bottom layer of the specimen is 1.44 ksi. Figure 3-7 shows the flexural cracking in the specimen 0#0. As represented, unlike the conventional concrete with no reinforcement, at the onset stage the size of the crack is very small which is very difficult to see with naked eyes. Also,

the crack does not propagate suddenly, and the width of the crack remains small even in higher loadings.

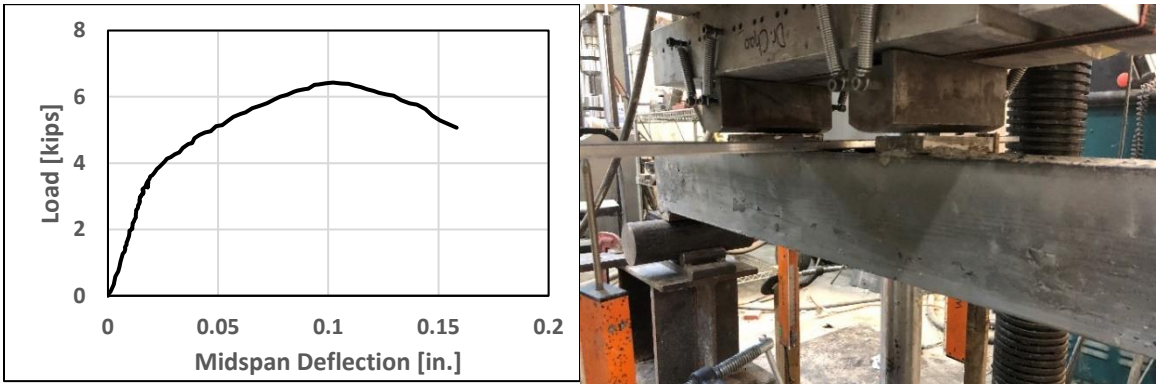

(a) (b)

Figure 3-6 a) Load-Midspan deflection and b) test setup for specimen 0#0

(a)

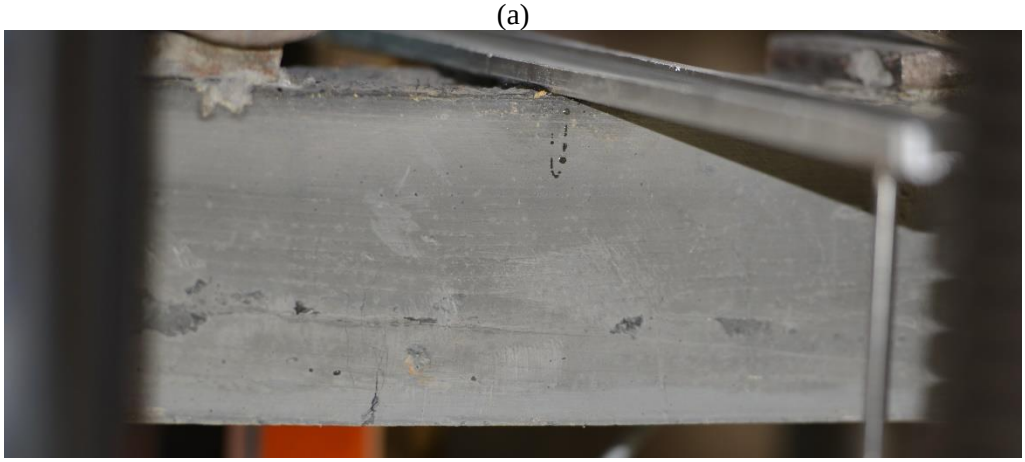

(b)

Figure 3-7 Cracking of specimen 0#0: a) initiation and b) at the end of the test

Specimen 3#3

In this specimen 3 steel reinforcement of size #3 was used. All the rebars were located in one layer. Figure 3-8 shows the response plot of this specimen and the bending zone of the specimen at the beginning of the test. This specimen reached to a maximum loading point of 25.6 kips at a deflection of 0.35 in. at the midspan. The first cracking occurred at a loading of 6.6 kips. With a moment of inertia of 24.2 in^4, the tensile strength of the UHP-FRC at the bottom layer of the specimen is 2.49 ksi. In this specimen, the stiffness of the beam was kept the same even after first cracking. This is because the reinforcement was able to keep the stiffness and prevent further crack opening. Figure 3-9 (a) and Figure 3-9 (b) show the cracking pattern in the specimen 3#3. As represented, unlike the conventional concrete with no fiber, at the onset stage the size of the crack is very small which is very difficult to see with naked eyes. Also, the crack does not propagate suddenly, and the width of the crack remains small even in higher loadings. In this specimen, there are more number of cracks comparing with the specimen with no rebars. This is because of the contribution of rebars in taking the force in the cracked section and transferring the stresses through the beam. Additionally, by increasing the flexural strength of the beam, as the loading increases, some cracks that were initiated due to bending stresses (vertically at the onset), became more inclined which shows the effect of shear stresses in the beam (Figure 3-9 (c)).

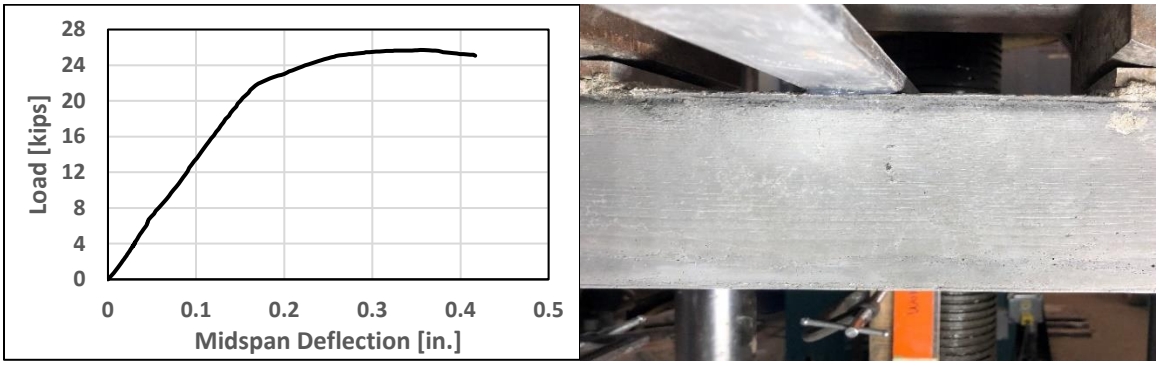

(a) (b)

Figure 3-8 a) Load-Midspan deflection and b) test setup for specimen 3#3

(a)

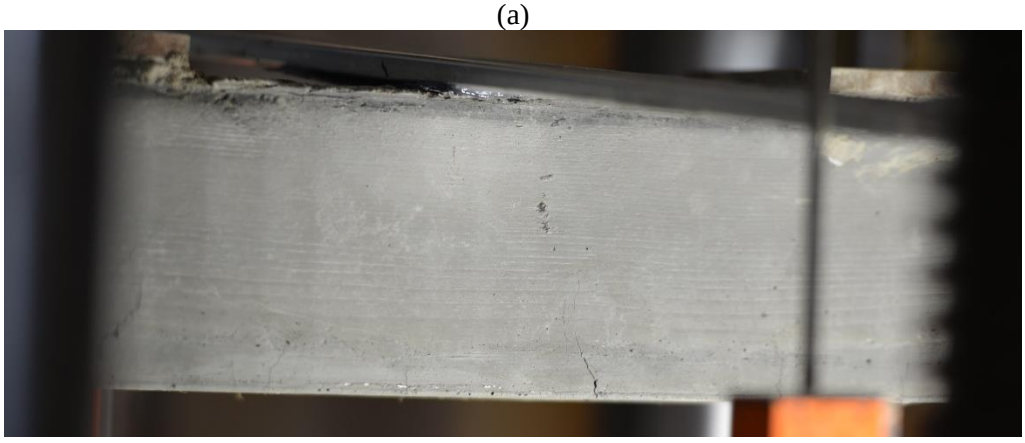

(b)

(c)

Figure 3-9 Cracking of specimen 3#3: a) initiation, b) at the end of the test c) shear cracking

Specimen 4#4

In this specimen 4 steel reinforcement of size #4 was used. All the rebars were located in one layer. Figure 3-10 shows the response plot of this specimen and the bending zone of the specimen at the beginning of the test. This specimen reached to a maximum loading point of 31.9 kips at a deflection of 0.34 in. at the midspan. The first cracking occurred at a loading of 12.8 kips. With a moment of inertia of 27.1 in^4, the tensile strength of the UHP-FRC at the bottom layer of the specimen is 4.13 ksi. In this specimen, the stiffness of the beam was kept the same even after first cracking. This is because the reinforcement was able to keep the stiffness and prevent further crack opening. Figure 3-11 shows the cracking pattern in the specimen 4#4. Compared with the specimen with no rebars, this specimen benefits having more number of cracks. This is because of the contribution of rebars in taking the force in the cracked section and transferring the stresses through the beam. Additionally, in this specimen, as the loading increases, shear cracks with inclined angles occurs that shows the effect of shear stresses in the beam (Figure 3-11 (b)).

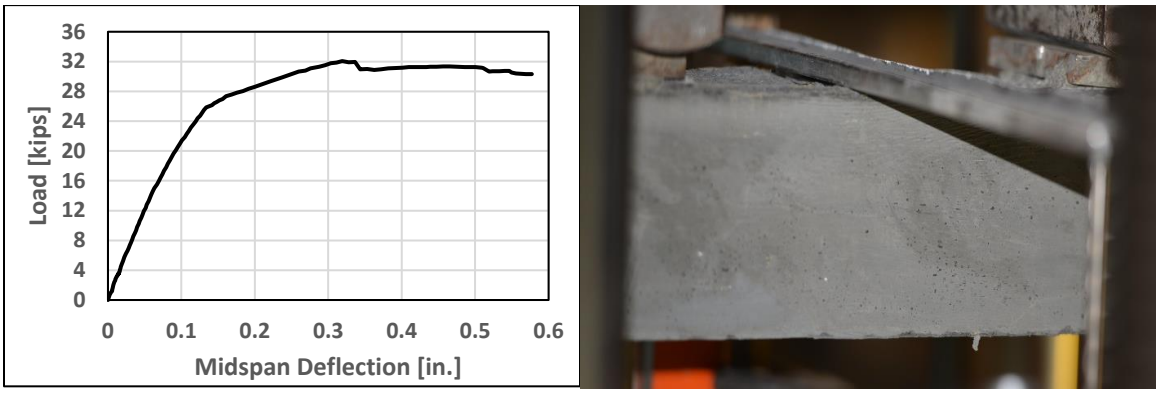

(a) (b)

Figure 3-10 a) Load-Midspan deflection and b) test setup for specimen 3#3

(a)

(b)

Figure 3-11 Cracking of specimen 4#4: a) in the pure bending zone b) shear cracking under a loading point

Specimen 5#3

In this specimen 5 steel reinforcement of size #3 was used. All the rebars were located in one layer. Figure 3-12 shows the response plot of this specimen and the bending zone of the specimen at the beginning of the test. This specimen reached to a maximum loading point of 27 kips at a deflection of 0.24 in. at the midspan. The first cracking occurred at a loading of 11.7 kips. With a moment of inertia of 26.6 in^4, the tensile strength of the UHP-FRC at the bottom layer of the specimen is 3.9 ksi. In this specimen, the stiffness of the beam was kept the same even after first cracking. This is because the reinforcement was able to keep the stiffness and prevent further crack opening. Figure 3-13 shows the cracking pattern in the specimen 5#3. Although the loading was increasing the test was stopped because of misreading of the LVDTs. Since the amount of reinforcement is largely increased in this specimen, the compression side off the section starts crushing in higher loads (Figure 3-13 (b)).

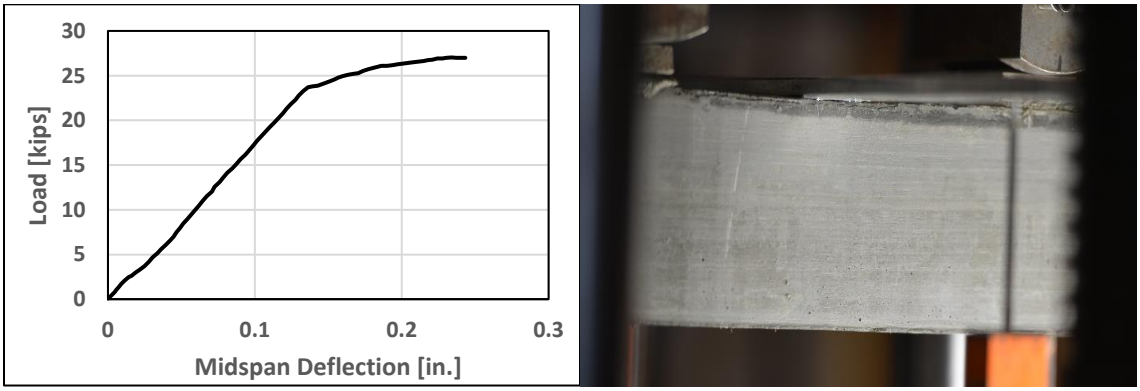

(a) (b)

Figure 3-12 a) Load-Midspan deflection and b) test setup for specimen 5#3

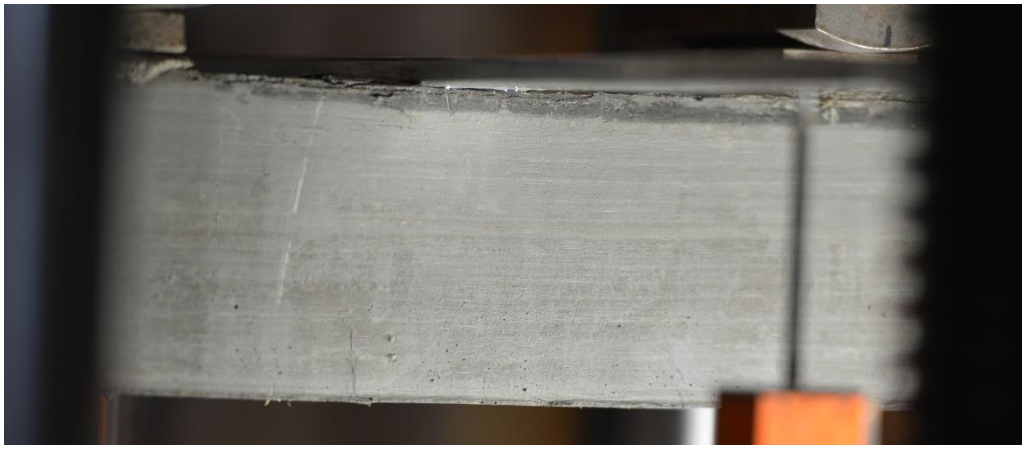

(a)

(b)

Figure 3-13 Cracking of specimen 5#3: a) tensile cracking in the pure bending zone b) concrete crushing in larger loadings

Specimen 6#3

In this specimen 6 steel reinforcement of size #3 was used. All the rebars were located in one layer. Figure 3-14 shows the response plot of this specimen and the bending zone of the specimen at the beginning of the test. This specimen reached to a maximum loading point of 37.4 kips at a deflection of 0.34 in. at the midspan. The first cracking occurred at a loading of 12.2 kips. With a moment of inertia of 27.87 in^4, the tensile strength of the UHP-FRC at the bottom layer of the specimen is 3.8 ksi. Like previous specimen, the

stiffness of the beam was kept the same even after first cracking due to the reinforcement's contribution in the stiffness and preventing further crack opening. Figure 3-15 shows the cracking pattern in the specimen 6#3. Although the loading was increasing the test was stopped because of misreading of the LVDTs. Since the amount of reinforcement is largely increased in this specimen, the compression side off the section starts crushing in higher loads (Figure 3-15 (b)). Comparing the response plot of specimen 6#3 and 3#3, it clearly shows that the post-cracking/post-yielding behavior of the section changes with the ratio of the reinforcement used in the section. For example, in specimen 6#3, the stiffness gradually reduces which is similar to the behavior of the UHP-FRC in compression prior to crushing. However, in the specimen 3#3, the behavior of the specimen after cracking is similar to the yielding behavior of steel rebars used as the reinforcement for the section. In conventional concrete higher amount of reinforcement results in a brittle failure of the section starting from the sudden crushing of the concrete in the top layer of the compression zone of the section. However, unlike the conventional concrete with limited strain at the crushing point, UHP-FRC benefits a very high usable compression strain at peak strength. The combination of high strength and larger compression strain prior to crushing in UHP-FRC, allows the use of higher amount of reinforcement in the tensile zone which also leads to a smaller stress and strain in rebars. Consequently, the tensile crack width will not grow, and the uncracked part of the section will be maintained. Hence, the stiffness of the section will not drop significantly.

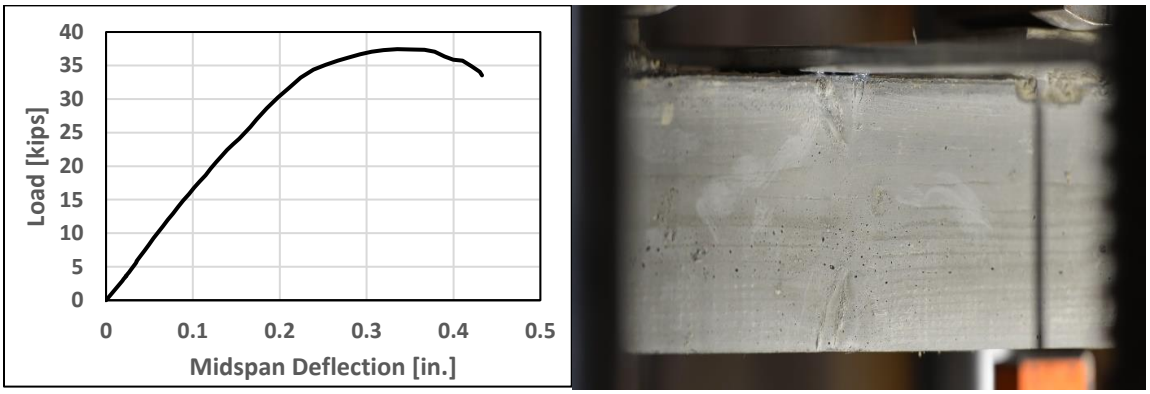

(a) (b)

Figure 3-14 a) Load-Midspan deflection and b) test setup for specimen 5#3

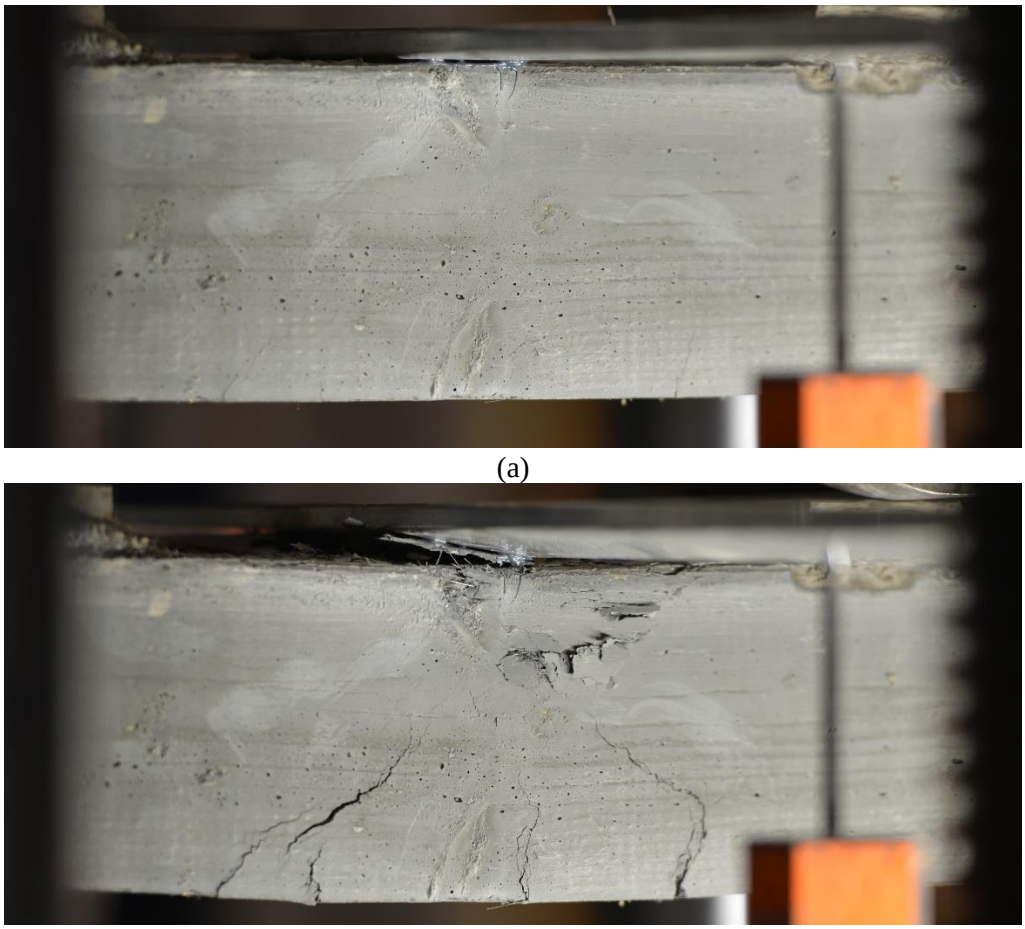

(a)

(b)

Figure 3-15 Cracking of specimen 6#3: a) tensile cracking in the pure bending zone b) concrete crushing in larger loadings

Specimen 5#4

In this specimen 5 steel reinforcement of size #4 was used. All the rebars were located in one layer. Figure 3-16 shows the response plot of this specimen and the bending zone of the specimen at the beginning of the test. This specimen reached to a maximum loading point of 39.0 kips at a deflection of 0.28 in. at the midspan. The first cracking occurred at a loading of 13.5 kips. With a moment of inertia of 28.98 in^4, the tensile strength of the UHP-FRC at the bottom layer of the specimen is 4.0 ksi. Like previous specimen, the stiffness of the beam was kept the same even after first cracking due to the reinforcement's contribution in the stiffness and preventing further crack opening. Figure 3-17 shows the cracking pattern in the specimen 5#4. Although the loading was increasing the test was stopped because of misreading of the LVDTs. Since the amount of reinforcement is largely increased in this specimen, the compression side off the section starts crushing in higher loads (Figure 3-17 (b)).

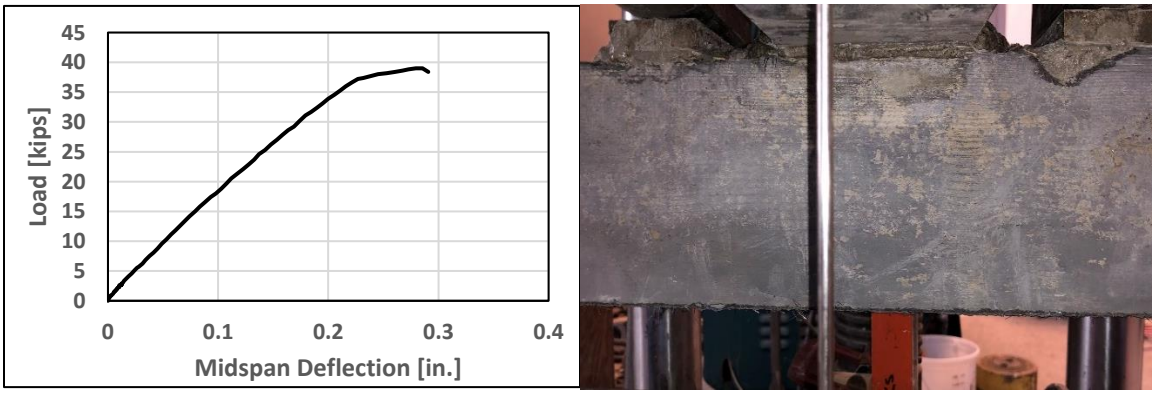

(a) (b)

Figure 3-16 a) Load-Midspan deflection and b) test setup for specimen 5#3

(a)

(b)

Figure 3-17 Cracking of specimen 6#3: a) tensile cracking in the pure bending zone b) concrete crushing in larger loadings

3.6 Discussion

Figure 3-18 summarizes results for four-point loading testing of a series of small UHP-FRC beams for investigating the effect of reinforcement ratio on the flexural cracking strength, f_r. The constant bending moment region between the two loading points is 10 in. One of the specimens, 0#0, has no reinforcement and rest of them are reinforced (Table 3-1). The longitudinal reinforcement ratio, ρ_{TA}, is defined as the area of the longitudinal reinforcement to the concrete tributary area which is the product of the width of the beam

by twice the cover (bottom concrete fiber to the centroid of the reinforcement). In all specimens, the flexural cracking occurred prior to shear cracks. Conservatively, the flexural cracking strength was calculated based on the minimum of 1) the loading when the first crack was observed and 2) the first deviation point in the load-deflection diagram. The first cracking load for each specimen is listed in Table 3-1 and highlighted in Figure 3-18 (b). Test results show that when ρ_{TA} approaches to approximately 13%, the first flexural cracking strength increases by 270%, from 1.4 ksi (9.9 MPa) to 3.8 ksi (26.2 MPa). This high cracking strength provides an effect similar to prestressing, which increases the first cracking strength of plain concrete (ranges approximately from 0.5 ksi to 0.75 ksi [3.4 MPa to 5.2 MPa]). While concrete's cracking strength can hardly be considerably increased in a typical RC member because the longitudinal reinforcement ratio is kept low to maintain a tension-controlled behavior, this study shows that a high amount of reinforcement ratio can significantly increase the cracking strength of concrete. A similar finding was reported by Shah (1992) who showed that a very high cracking strength of concrete can be obtained if a high volume fraction of fibers (about 15%) is used. This is because when the fiber amount reaches a certain critical threshold, they can effectively carry the force and prevent concrete's microcracks from growing and interconnecting to form a percolation crack (Balaguru and Shah, 1992). It is believed that a high reinforcing bar ratio provides the same effect. Allowing a higher amount of reinforcing bars leads to smaller stress in tensile reinforcement even at a higher load. Because crack widths in concrete beams are roughly proportional to the stress in steel reinforcement, the low stress will allow better control of the crack width and, hence, stiffness of the member. When the steel stresses are kept low under the service load, the accompanying low strains in the

concrete and steel will produce only small rotations of the cross sections along the member, which translates into a small deflection (Nilson, 1987).

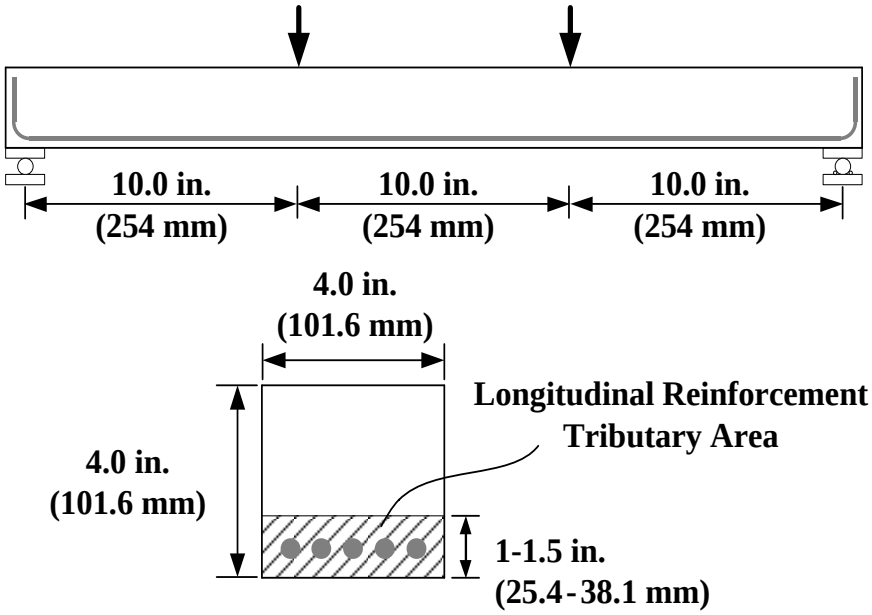

(a)

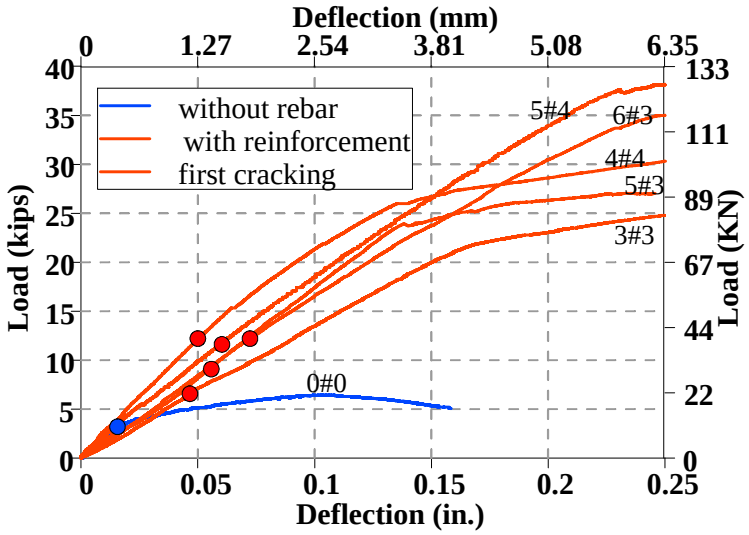

(b)

Figure 3-18 a) Specimens for flexural cracking strength study, b) Testing results

Table 3-1 Information of specimens subjected to four-point loading

No rebars (0#0)	3#3 rebars	4#4 rebars	5#3 rebars	6#3 rebars	5#4 rebars
ρ_{TA}=0.00%	ρ_{TA}=8.25%	ρ_{TA}=13.33%	ρ_{TA}=13.75%	ρ_{TA}=16.50%	ρ_{TA}=16.67%
P_{cr} = 3.0 kips (13.4 KN)	P_{cr} = 6.3 kips (28.0 KN)	P_{cr} = 12.3 kips (54.7 KN)	P_{cr} = 11.2 kips (49.8 KN)	P_{cr} = 11.7 kips (52.0 KN)	P_{cr} = 12.9 kips (57.4 KN)
f_r = 1.4 ksi (9.9 MPa)	f_r = 2.5 ksi (17.2 MPa)	f_r = 4.1 ksi (28.3 MPa)	f_r = 3.9 ksi (26.9 MPa)	f_r = 3.8 ksi (26.2 MPa)	f_r = 4.0 ksi (27.6 MPa)

Figure 3-19 illustrates that UHP-FRC's crack strength significantly increases by using high amount of longitudinal rebars. It shows that the effect of reinforcement of the cracking strength reduces when the reinforcement ratio is 12% or more.

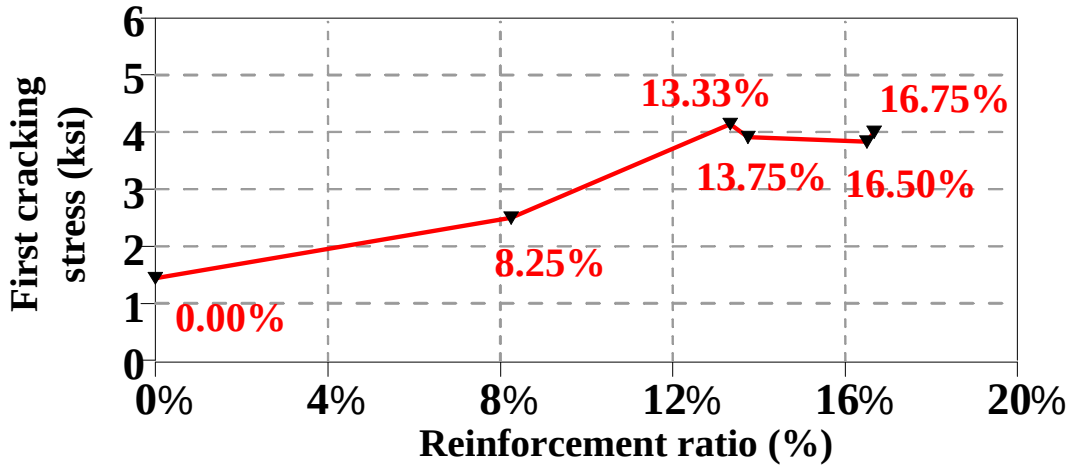

Figure 3-19 Effect of reinforcement ratio on UHP-FRC's crack strength

Chapter 4
Part I

Ductile-Concrete Strong-Reinforcement

(DCSR) Design Concept

4.1 Introduction

The Ductile-Concrete Strong-Reinforcement (DCSR) design concept, is achieved by utilizing the unique mechanical characteristics of UHP-FRC in combination with high amount of Reinforcement. Unlike regular concrete, tensile strength of UHP-FRC is considerable; therefore, the DCSR designed section remains uncracked up to a certain loading. Furthermore, due to contribution of tension zone to the stiffness of the section, rebars' stress remains smaller, as well as the deflection of the beam. However, in RC when the load exceeds the cracking load, the crack will quickly reach up to neutral axis and a major portion of the section will not contribute to the stiffness of the section. With no fiber in the RC cracked section, all the tension would be resisted by the reinforcement at the cracked section (Figure 4-1 (a)). This increases the stress and subsequently, the rebar's strain at the cracked section, which leads to further crack widening. If steel fibers are added to the concrete (SFRC), the fibers bridge the crack and incorporate to load transfer at the cracked section. In this case, the rebar's strain is less, and the crack width would be smaller (Figure 4-1 (b)). Toward a higher level, using UHP-FRC with high amount of reinforcement - DCSR concept - (Figure 4-1 (c)), the rebar strain is limited to considerably lower values in two ways: first, the bridging effect in the UHP-FRC is higher than SFRC; therefore, the strain in the rebar would remain smaller effectively. Second, the higher amount of steel leads to smaller stress in the reinforcement under the same external loading. Moreover, in general, when the crack is smaller the bridging is more effective. Additionally, since the small cracks are generally shallow, the section's moment of inertia does not drop, and the stiffness of the section would be maintained. This synergy results in well controlled deflection and prevention of major cracking formation under larger

loadings as shown in the experimental tests. This is a desirable feature where fatigue is a design issue, such as bridge girders under service loading.

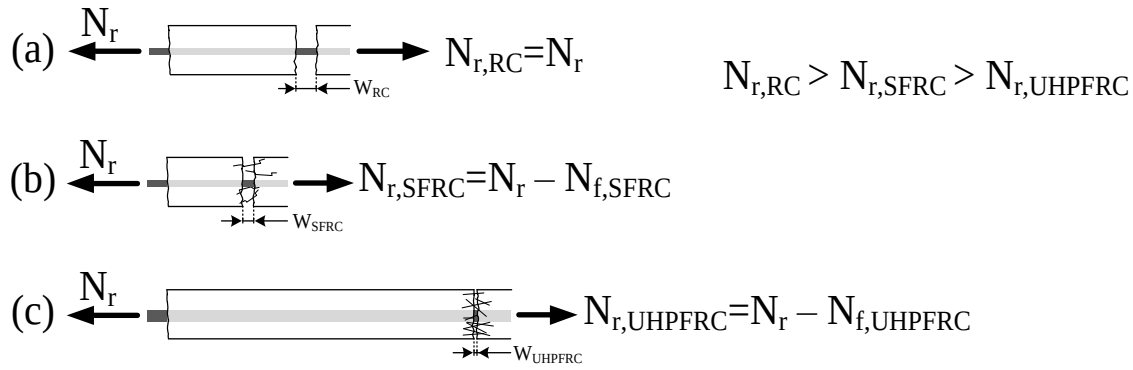

Figure 4-1 Composite contribution in tension zone of a cracked section in: a) RC, b) SFRC and c) UHP-FRC

In conventional concrete design methods for RC with steel reinforcement, the design is accepted if the ductility of the section is sufficient. This criterion is controlled by specifying a minimum amount of strain in the bottom layer of the steel reinforcement ($\varepsilon_t \geq \varepsilon_{yt} + 0.003$), while the strain in the top layer of the concrete in compression is less than 0.003 (ACI, 2019). This type of design which is called tension-controlled design is achievable by limiting the amount of longitudinal reinforcement used in the tensile part of the section. When the amount of tensile reinforcement is limited, the strain in the reinforcement in the tensile part of this section increases. In result, the curvature that this section is experiencing increases. Consequently, the depth of the neutral axis reduces. This reduction in compression zone occurs with many numbers of large flexural cracks quickly propagated to the neutral axis in the tensile zone. This will result in a reduced resisting shear area at the ultimate loading. If mild steel reinforcements are used, and the section is designed to

have a tension-controlled failure, the reinforcements will yield, and the failure will be preceded by an enlarged curvature due to high strain in the reinforcement. If the steel reinforcement is replaced by FRP rebars, a sudden failure is expected due to the combination of the brittle nature of plain concrete in compression and the elastic behavior of the FRP in tension up to rupture. A sudden and abrupt failure of conventional concrete reinforced with FRP rebars has been experimentally shown (Ovitigala et al., 2016; Wang and Belarbi, 2005). For plain concrete with FRP reinforcement, the maximum curvature is determined by maximum usable compressive strain for concrete and the allowable rupture strain of the FRP reinforcement bars. Figure 4-2 demonstrates the curvature at the ultimate loading for a plain concrete reinforced with steel reinforcing rebars and FRP reinforcement bars, parametrically. On the other hand, the design of reinforced concrete members with FRP reinforcement is similar to the design of steel-reinforced concrete members. However, unlike steel, FRP rebars do not exhibit ductility. Hence, the failure of reinforced concrete due to the rupture of FRP bars before the concrete crushes can be sudden and destructive. In addition, the low axial stiffness of FRP rebars (a product of the rebar area and elastic modulus) typically causes a large crack width and significantly smaller shear capacity due to the smaller compression zone and loss of aggregate interlock for widened crack widths (Stratford and Burgoyne, 2003; ACI, 2015). Consequently, it is preferable for FRP-reinforced concrete members to fail in compression first (that is, a compression-controlled design) rather than by the rupture of FRP bars (Nanni, 1993; ACI, 2015). However, for FRP-reinforced structural members, neither a tension-controlled nor compression-controlled failure mode can provide sufficient ductility to the structure. Therefore, ACI 440.1R (ACI, 2015) suggests a more conservative design using a low strength reduction

factor of 0.65 for FRP-reinforced members, which is 28% lower than that required for the steel-reinforced members. If high-strength concrete is used with the FRP rebars, stiffness of the cracked section is increased but the deformability of the flexural member reduces compared to normal strength concrete (ACI, 2015).

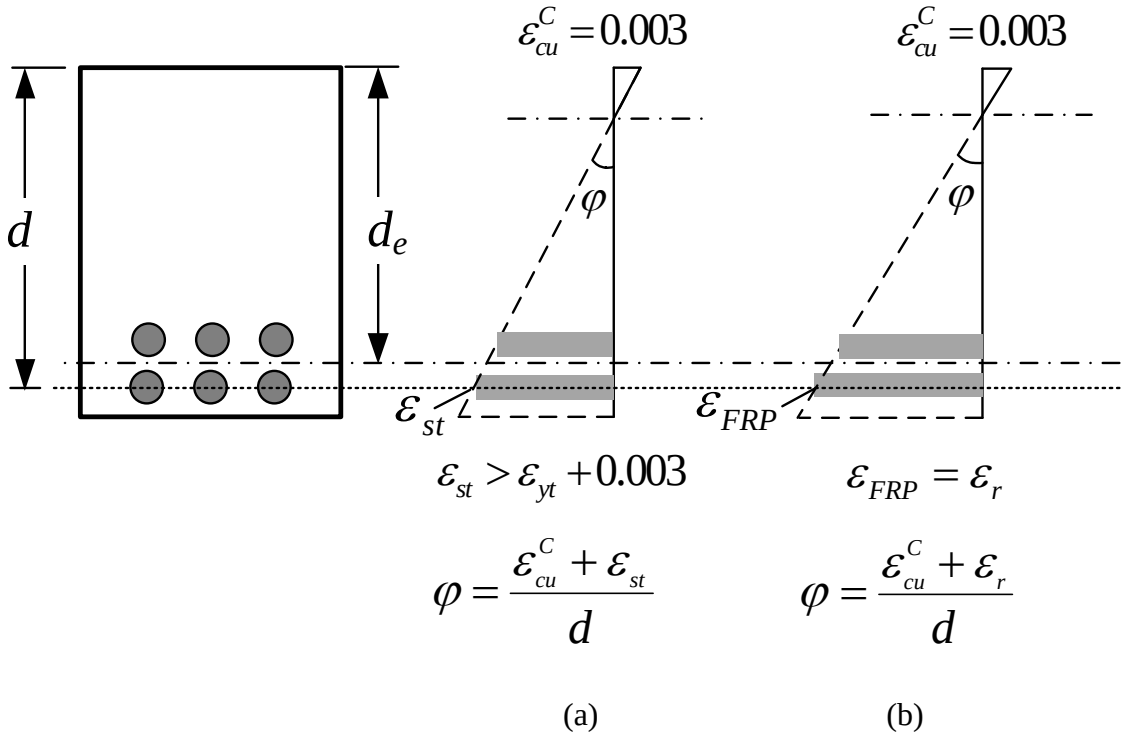

Figure 4-2 Strain distribution and curvature calculation at the ultimate load for: (a) RC reinforced with steel rebars and (b) RC reinforced with FRP rebars

While the maximum usable concrete strain for plain concrete is limited to ε_{cu} = 0.003 in commonly used standards such as AASHTO LRFD Specifications (AASHTO, 2017) and ACI 318 (ACI, 2019), the maximum usable compressive strain in much larger for UHP-

FRC and even conservatively can be taken as 0.015. Figure 4-3 compares the stress-strain plot for UHP-FRC and plain concrete.

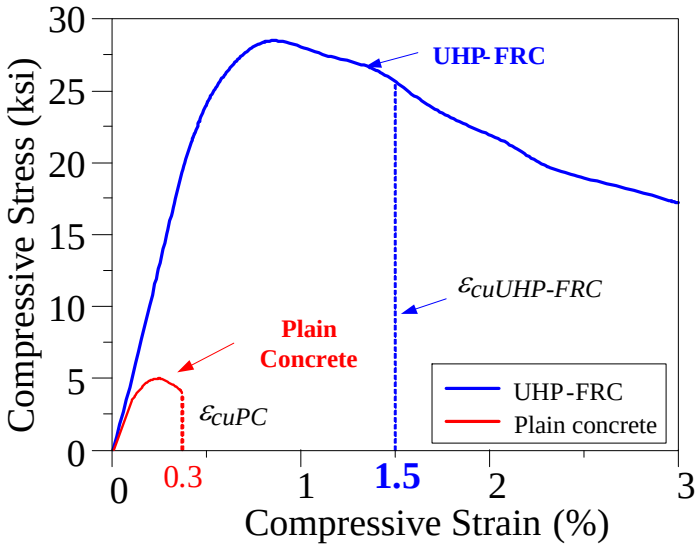

Figure 4-3 Comparison between compressive stress-strain behavior of UHP-FRC (Aghdasi et al., 2016)

With a matrix like UHP-FRC benefiting a much larger maximum usable concrete strain (more than five times), the section is capable to include much higher amount of reinforcement. This leads to a new design concept called Ductile-Concrete Strong-Reinforcement. Since both the strength and the maximum usable concrete strain is larger, the compressive part of the section becomes much stronger and allows the section to have much larger amount of reinforcement.

On the other hand, if FRP is used as reinforcement, the ductile behavior of the UHP-FRC in compression, can provide a relatively more ductile failure for the section. Figure 4-4 demonstrates the curvature at the ultimate loading for a plain concrete reinforced with FRP reinforcing rebars and UHP-FRC with FRP reinforcement bars, parametrically.

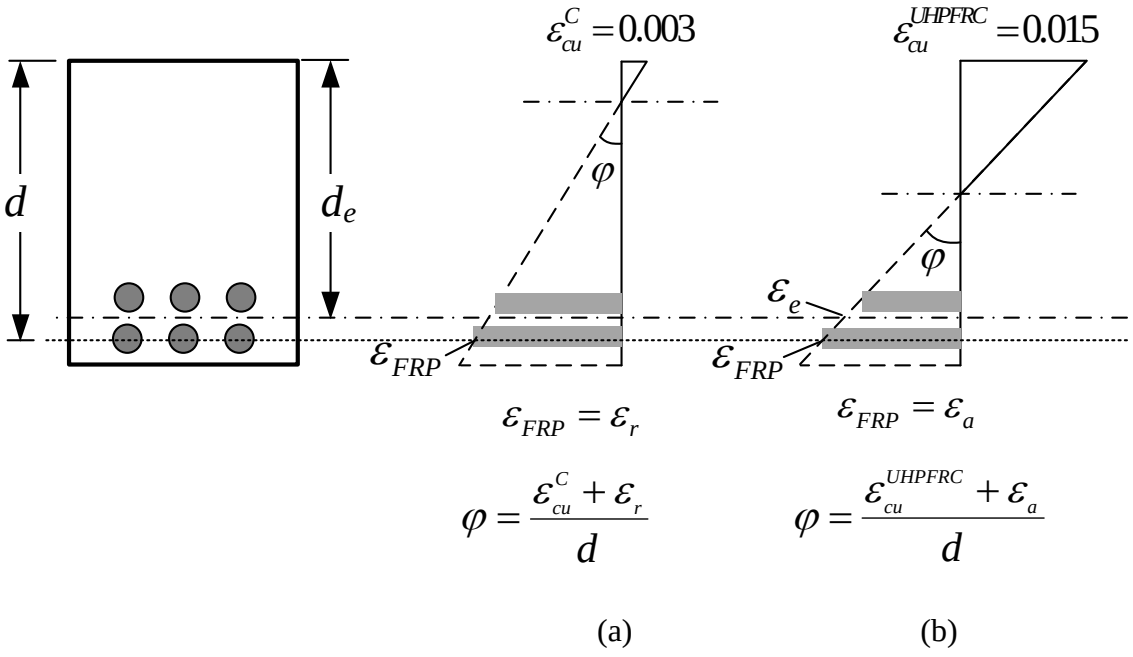

Figure 4-4 Strain distribution and curvature calculation at the ultimate load for: (a) RC and (b) UHP-FRC reinforced with FRP rebars

4.2 Enhanced ductility in DCSR design concept

Ductile failure at ultimate loading in RC sections can be only achieved through yielding of rebars followed by excessive strain at the bottom reinforcement layer. This coincides with many numbers of cracks along the member because of the very limited tensile strain capacity of concrete. Since the bond strength between regular concrete and the rebars cannot resist the post-yielding strains of reinforcements, a certain length of rebars adjacent to sides of the cracks becomes debonded (Figure 4-5 (a)). Due to strain hardening behavior of steel reinforcement, the total debonded length can yield. This phenomenon, added to member flexural stiffness reduction due to many numbers of cracks, allow the section to undergo a certain deflection prior to failure. However, in UHP-FRC, the bond strength is strong enough to prevent the debonding. Should UHP-FRC used with conventional tension

control design concept, the rebar length that can stretch due to yielding, is limited to the crack width. When the crack width widens slightly, the bridging effect of the fibers decreases and the carried force by the fibers, will be majorly transferred to the rebars (Figure 4-5 (b)). At this moment, a very small additional deflection will increase the rebar's strain considerably at the cracked section, resulting in bar fracture and a premature brittle failure of the member (Figure 4-6).

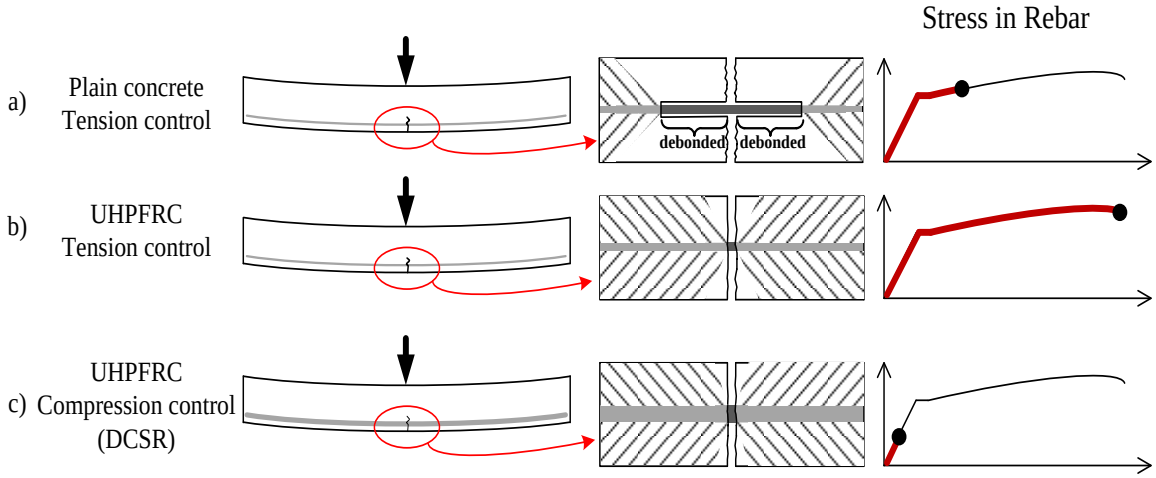

Figure 4-5 Stress in steel reinforcement adjacent to a cracked section in: a) RC, b) SFRC and c) UHP-FRC

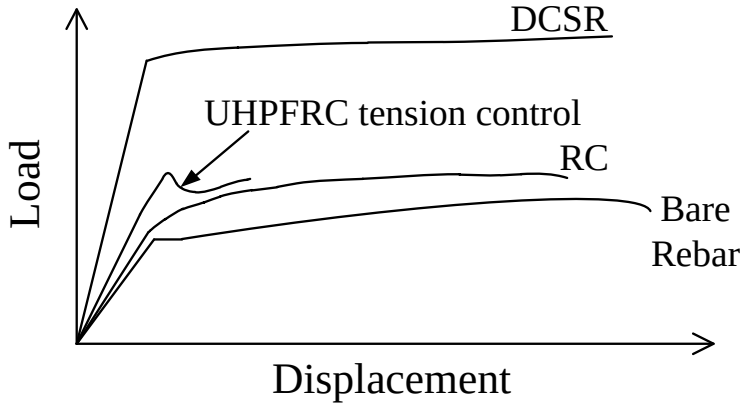

Figure 4-6 Schematic behavior of sections designed with different concepts: RC, UHP-FRC tension control and DCSR

In DCSR design concept, benefitting the high maximum usable compressive strain of UHP-FRC, the enlarged compression zone allows the section to have a high amount of reinforcement. When the crack occurs, unlike tension controlled UHP-FRC section, a sudden strain increase is prevented due to high amount of reinforcement (Figure 4-5 (c)) and the crack width will be efficiently controlled. Smaller width of the crack allows the fibers to contribute to resisting tension force as well (Figure 4-1). Due to small cracks and high amount of steel, the stiffness of the section is well maintained even after cracking onset. At the ultimate loading, the ductile failure of the section is improved by the high maximum usable compressive strain of UHP-FRC. Although the neutral axis would be deeper, the high compressive strain capacity of UHP-FRC allows the reinforcements to yield up to desired extents. Figure 4-6 compares the behavior of different sections schematically. In oppose to conventional RC design where the ductility is solely provided through yielding of the rebars, DSCR design method improves the ductility by utilizing the high usable compressive strain of UHP-FRC.

4.3 Crack Pattern in RC, SFRC and UHP-FRC

At a cracked section, the majority of the tensile force is being transferred through the reinforcement. Adjacent to a cracked section, part of the force would be transferred to the composite (concrete + fibers) along a transition distance. Based on equilibrium for an infinitesimal bar in transition length, the stress transfer (to the composite) equation is (Naaman, 2012):

$$\sigma_m = \frac{P\tau}{A_m} x$$ Equation 4.1

Where is the tensile stress in the composite at a distance of x, P is the perimeter of the reinforcement, is the bond stress between the bar and the composite and A_m is cross sectional area of the composite.

The experimental tests showed that the cracking distances in RC is more than what was observed in SFRC. This happens because of two reasons: first, in the absence of fibers, at the cracked section the stress in the composite drops to zero. However, in the presence of fiber, some part of the force will be transferred through fiber bridging and the stress in the composite (fiber + concrete) does not drop to zero (Fantilli et al., 2009). This is schematically presented in Figure 4-7. Since the composite stress is maintained to some level at the cracked section, it reaches the cracking strength of the composite in smaller distances. Secondly, assuming similar geometry, due to stronger bond stress between steel reinforcement and composite, the stress transfer coefficient ($= \frac{P\tau}{A_m}$) in fiber concrete is larger. Although, the cracking strength of fiber concrete is higher, based on two aforementioned reasons, the stress in composite reaches the cracking strength in smaller distances. Figure 4-8 elaborates the smaller crack distances in SFRC.

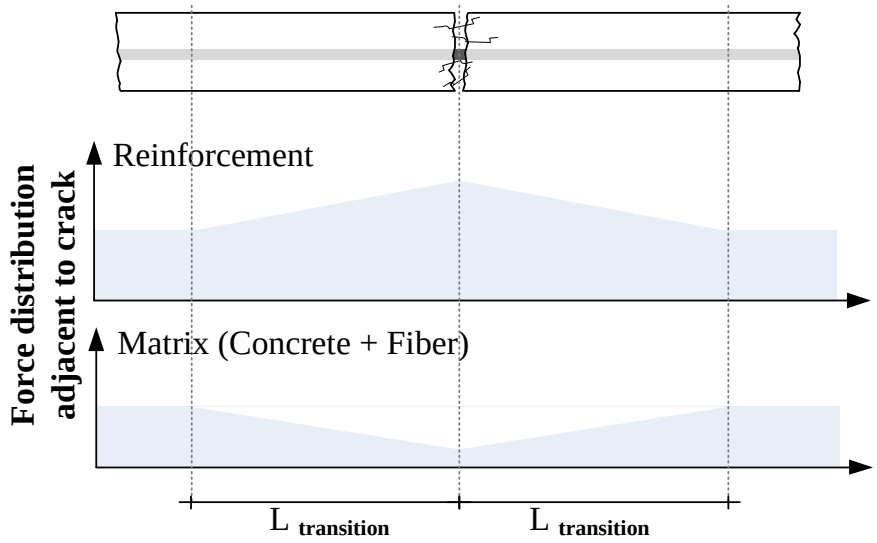

Figure 4-7 Schematic behavior of force distribution adjacent to crack in the presence of fiber

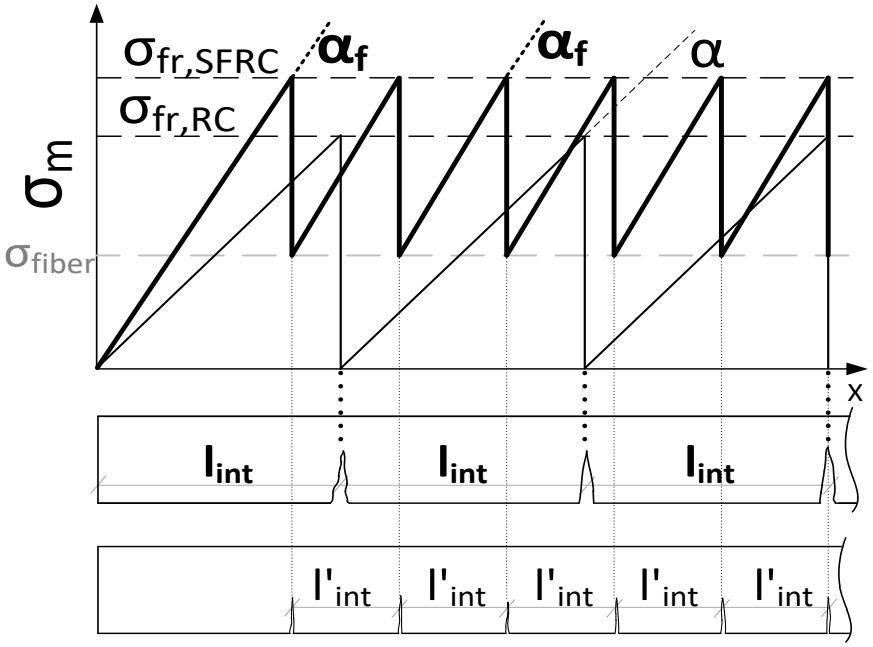

Figure 4-8 Higher stress transfer coefficient in SFRC

For a UHP-FRC section, the larger stress transfer coefficient due to larger amount of P and stronger bonding strength, tends to reduce the cracking distances along the element.

However, in a member designed with DCSR concept, higher amount of reinforcement largely reinvigorates the cracking strength of the matrix (discussed in Chapter 3) such that even with a larger stress transfer coefficient, the distance between cracks will be enlarged to a great extent (Figure 4-9). A comparison between cracking distances in RC, SFRC and UHP-FRC designed with DCSR concept is illustrated in Figure 4-9.

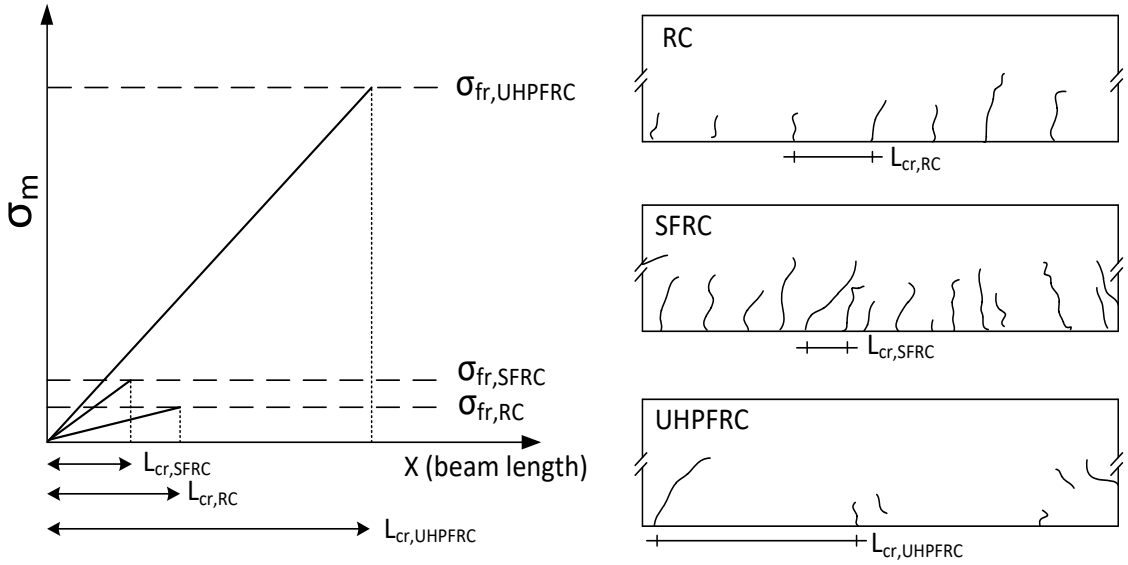

Figure 4-9 Crack distance in RC, SFRC and UHP-FRC

4.4 Effect of Reinforcement on First Cracking Strength

This effect is elaborated in detail in the experimental program of this dissertation.

4.5 Large scale experimental study

4.5.1 UHP-FRC with steel reinforcement

Four simply supported beams, one made of reinforced concrete (RC) and three made of UHP-FRC were monotonically loaded to failure. All beam specimens had a width of 9 in.

(229 mm), a height of 16 in. (406 mm), and a span length of 134 in. (3404 mm). A 20-in. (508 mm) constant moment region was at the mid-span of all specimens. Table 4-1 lists the design parameters of beams used in this experimental program. Specimens RC and UHP-FRC #1 used ASTM A615 reinforcing bars, while Specimens UHP-FRC #2 and UHP-FRC #3 used ASTM A1035 high-strength corrosion-resistant low-carbon chromium reinforcing bars to reduce the reinforcement congestion. To investigate the shear capacity of UHP-FRC in flexural members no shear reinforcement was used in Specimens UHP-FRC #2 and UHP-FRC #3.

Table 4-1 Design parameters of RC and UHP-FRC specimens

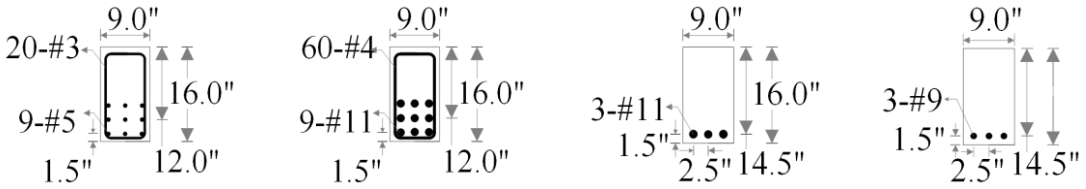

RC #1 UHP-FRC #1 UHP-FRC #2 UHP-FRC #3

Specimen	Effective depth (d), in. (mm)	*a/d*	ρ (%)	V_f (%)	Targeted, f'c (ksi) (MPa)	Measured, f'c (ksi) (MPa)
RC1	12.0 (305)	4.75	2.58 (60S)	0	5 (35)	5 (35)
UHP-FRC #1	12.0 (305)	4.75	13.0 (60S)	3.0	22 (152)	21 (145)
UHP-FRC #2	14.5 (368)	3.93	3.59 (100S)	3.0	22 (152)	20.8 (143)
UHP-FRC #3	14.5 (368)	3.93	2.30 (100S)	3.0	22 (152)	20.8 (143)

The RC beam was designed to have the highest amount of longitudinal reinforcement while still maintaining tension-controlled behavior based on ACI 318 (ACI, 2019) and AASHTO LRFD (AASHTO, 2017) provisions. In other words, the extreme tensile reinforcement reaches a 0.005 strain when the maximum concrete strain is 0.003. This led to the use of nine No. 5 reinforcing bars, corresponding to a flexural reinforcement ratio of $\rho = 2.58\%$ (Table 4-1). Shear reinforcement was provided outside of the constant moment region to ensure that failure was not governed by shear before reaching the ultimate flexural strength. Design compressive strength of the RC beam was 5,000 psi (34.5 MPa). The design compressive strength of UHP-FRC was 22 ksi (152 MPa) and the maximum usable compressive strain, ε_{cu}, was taken as 0.015. The flexural reinforcement ratio for specimen UHP-FRC #1 with Gr. 60 reinforcing bars was five times that of the RC beam which resulted in a ratio of $\rho = 13\%$, corresponding to nine No. 11 reinforcing bars (Table 4-1). The reinforcement areas were considerably reduced in specimens UHP-FRC #2 and UHP-FRC #3 with Grade 100 reinforcing bars. To simplify the design, the β_1 factor was assumed the same for plain concrete as recommended by ACI 318 and AASHTO LRFD. Neglecting the contribution of UHP-FRC on the tension side, which is a conservative assumption for design, it was calculated that the tensile strain of the extreme reinforcing bars in the UHP-FRC #1 beam was much larger (0.013) than the tension-controlled limit (0.005), even with a considerably higher reinforcement ratio.

Experimental results

In the RC beam, the first flexural crack was observed at a stress on the tension side nearly equal to the modulus of rupture of the concrete (load: 12.0 kips or 53 kN). However, in

UHP-FRC #1, the first visible flexural crack was not traced until 120 kips loading. The load versus deflection curve in Figure 4-10 (a) shows that the slope changed very slightly at about 60 kips (267 kN), which is conservatively considered the first cracking load. Nevertheless, UHP-FRC #1 exhibits a nearly linear uncracked behavior up to 250 kips (1112 kN), thereby maintaining a very high stiffness up to 80% of the peak strength. The average concrete's compressive strains in the RC and UHP-FRC #1 beams at their peak strength were measured by a DIC system as 0.003 and 0.015, respectively. The maximum measured strains were 0.006 and 0.025, respectively, for RC and UHP-FRC #1. This indicates that using a strain (ε_{cu} = 0.015) to design a UHP-FRC beam provides a sufficient safety margin. The ultimate strength of the UHP-FRC #1 beam is 318 kips (1415 kN), which is 4.4 times that of an RC beam (72 kips or 320 kN). Figure 4-10 (a) also shows that the UHP-FRC #1 beam had ample ductility, even with a reinforcement ratio five times greater than that of the RC beam. This indicates that using UHP-FRC in flexural members can largely increase the strength and stiffness while maintaining a small self-weight. In fact, because the overstrength of the UHP-FRC beam beyond the design load (approximately 60 kips [267 kN]) is very large, the ductility capacity becomes less critical. Figure 4-10 (b) and Figure 4-10 (c) show that the visible cracks in the UHP-FRC #1 beam are very small even at a very high load of 300 kips (1,334 kN).

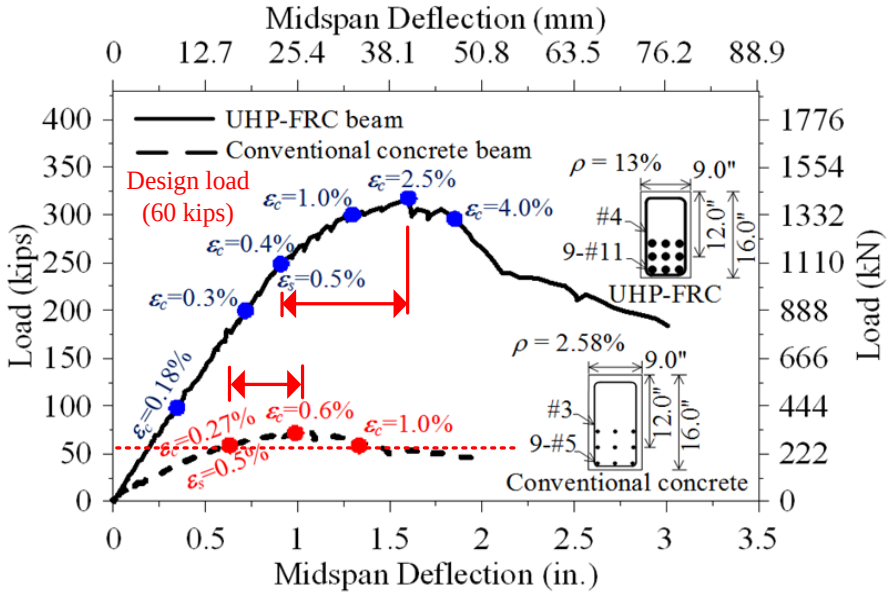

(a)

(b)

(c)

Figure 4-10 (a) Load vs. mid-span deflection responses of RC and UHP-FRC #1 beams, (b) observed cracks in UHP-FRC #1 beam at 300-kip (1334 kN) load, and(c) observed cracks in RC beam at 70-kip (311 kN) load

Strain gauge data indicates that the strains in the bottom reinforcing bars in the UHP-FRC #1 beam all reached 0.013, which is well beyond the tension-control limit of 0.005. At the 0.005 strain in longitudinal reinforcing bars, the concrete compressive strain observed in the UHP-FRC #1 beam was 0.004, which was much less than the design compressive strain of ε_{cu} = 0.015. At the assumed first cracking of 60 kips (267 kN), the strains in the reinforcing bars were approximately 0.0005, corresponding to a stress of 14.5 ksi (100 MPa). Since conventional ASTM A615 reinforcing bars typically exhibit a fatigue

endurance limit (1×106 cycles) at a stress range of approximately 24 ksi (166 MPa) (Wight, 2016), it indicates that UHP-FRC #1 can carry a full service live load of up to about 100 kips (445 kN) without fatigue concern. This loading is greater than the RC beam's ultimate load. On the other hand, in the RC beam, all reinforcing bars reached 60 ksi (414 MPa) at a load of approximately 50 kips (222 kN). Specimen UHP-FRC #1 remained at nearly a "pseudo" uncracked state up to nearly 90% of the peak load. The beam showed a very large deflection with a few small flexural cracks. This behavior is very different from the conventional RC beams, and indicates a significant synergetic action and tension-stiffening effect between the reinforcing bars and UHP-FRC in carrying the tensile stresses.

UHP-FRC #2 and UHP-FRC #3 were designed to intentionally fail in shear. For UHP-FRC #2, the first visible flexural crack was observed at 60 kips (267 kN). This approximately matches the point where the stiffness of the load vs. deflection curve starts decreasing (Figure 4-11 (b)). A critical web shear crack was developed at 150 kips (667 kN) (shear stress: 4.0√f'c (577 psi)). At an ultimate load of 163 kips (725 kN) (shear stress: 4.5√f'c (650 psi)), the web shear crack quickly propagated toward the loading point and support, eventually causing dowel failure along the bars. For UHP-FRC #3, the first visible flexural crack was observed at 50 kips (222 kN). This approximately agrees with the point where the stiffness of the load vs. deflection curve started decreasing (Figure 4-11 (b)). A critical web shear crack also appeared at 150 kips (667 kN) (shear stress: 4.0√f'c (577 psi)), and the beam failed at an ultimate failure load of 179 kips (796 kN) (shear stress: 4.9√f'c (710 psi)) due to the loss of shear and dowel capacity. Load deflection and cracking behavior of UHP-FRC #3 is very similar to UHP-FRC #2 except for the fact that UHP-FRC #3 had a

slightly better bond strength and dowel performance due to the smaller diameter of the bars.

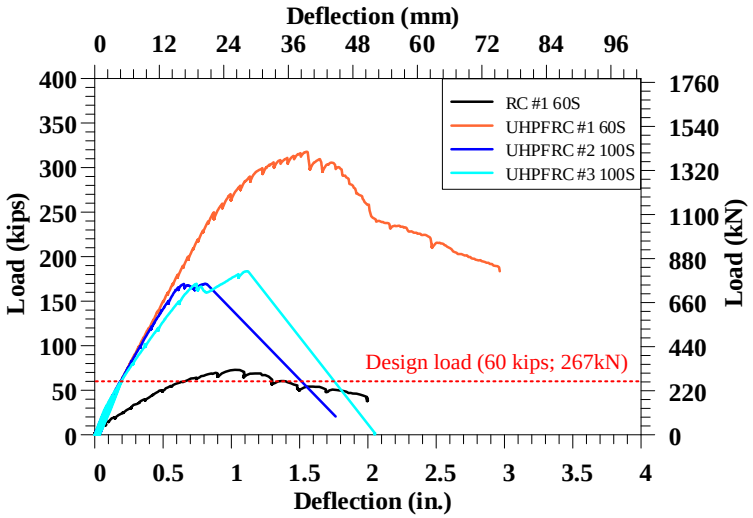

(a)

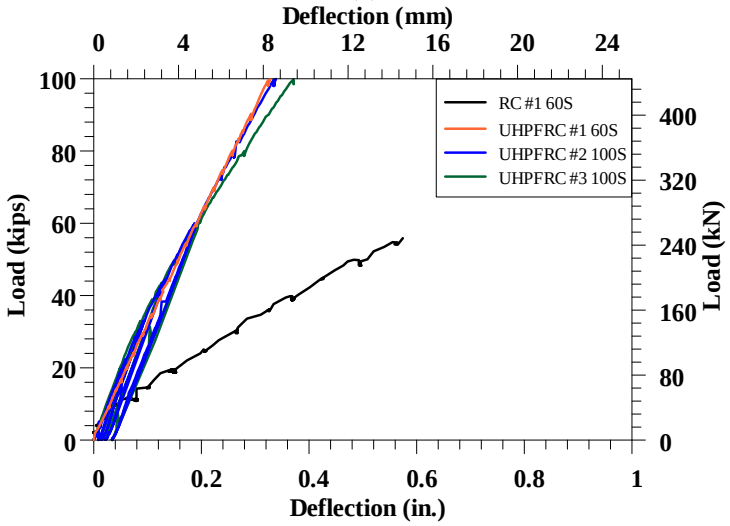

(b)

Figure 4-11 Load vs. deflection: (a) entire curves and (b) up to 100 kips (445 kN)

Strain gauge data indicates that the steel stress after cracking (about 60 kips or 267 kN) in Specimens UHP-FRC #2 and UHP-FRC #3 was approximately 24 ksi (166 MPa). Experiment results reported by DeJong and MacDougall (2006) indicated that ASTM A1035 high-strength corrosion-resistant low-carbon chromium reinforcing bars exhibit a

fatigue endurance limit (1×10^6 cycles) at a stress range of approximately 45 ksi (310 MPa). Thus, the ASTM A1035 reinforcing bars' superior fatigue resistance can allow a full-service load up to approximately 120 kips (534 MPa) which is 10 times that of the RC beams' cracking load.

4.5.2 UHP-FRC with FRP

In this section, the result of three beams and two columns are presented. Also, the results are compared to a steel reinforced RC section (RC1 in the previous section). The concrete in all the specimens is UHP-FRC and they are reinforced with FRP reinforcement bars. In the following the design process and the result of the tests are presented.

For comparison purposes, one beam is designed with the use of plain concrete reinforced with FRP reinforcement rebars. ACI 440 (2015) design criteria is used to design a compression-controlled beam section reinforced with FRP rebars. Based on ACI 440, for the first step, the balanced reinforcement ratio, ρ_{bf}, needs to be calculated. Then a safety factor is applied to ensure that the concrete crushes prior to rebar rupture. Figure 4-12 shows the considered beam section with one layer of reinforcement. Based on equilibrium at the ultimate loading:

$$T = C \Rightarrow A_{FRP} E_{FRP} \varepsilon_r = 0.85 f_c' \beta_1 c b \qquad \textit{Equation 4.2}$$

where ε_r is the rupture strain of FRP rebars.

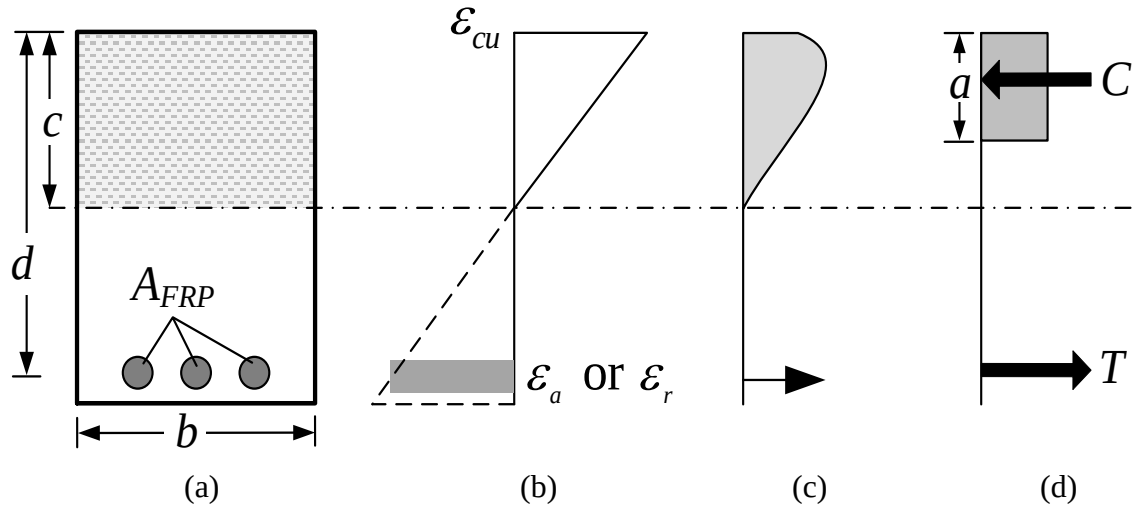

Figure 4-12 (a) Typical beam cross section with an effective depth of *d*, (b) strain distribution at the ultimate load, (c) actual stress distribution, and (d) equivalent rectangular stress block

Using the strain distribution diagram shown in Figure 4-4:

$$c = \frac{\varepsilon_{cu}}{\varepsilon_{cu} + \varepsilon_r} d \Rightarrow A_{FRP} = 0.85\beta_1 bd \left(\frac{\varepsilon_{cu}}{\varepsilon_{cu} + \varepsilon_r} \right) \left(\frac{f'_c}{E_{FRP}\varepsilon_r} \right) \qquad \textit{Equation 4.3}$$

The balanced reinforcement ratio can be computed as:

$$\rho_{fb} = \frac{A_{FRP}}{bd} \quad \Rightarrow \rho_{\min} = 0.85\beta_1 \left(\frac{\varepsilon_{cu}}{\varepsilon_{cu} + \varepsilon_r} \right) \left(\frac{f'_c}{E_{FRP}\varepsilon_r} \right) \qquad \textit{Equation 4.4}$$

For a concrete beam reinforced with FRP rebars to be qualified as a compression-controlled section, ACI 440 requires the design reinforcement ratio be at least 40% more than ρ_{fb}; that is, $\rho \geq 1.4\rho_{fb}$.

Since FRP rebars cannot provide the ductility for the section, in DCSR design method, to ensure that UHP-FRC reaches ε_{cu} prior to the rupture of FRP rebars, the strain in FRP rebars is limited to an allowable rupture strain, ε_a, which is smaller than the FRP rupture strain (ε_r). Using the strain distribution diagram in Figure 4-4 and equilibrium equations, a minimum reinforcement area can be found. Below some calculation examples are provided on the design process of the UHP-frc section reinforced with FRP rebars. To simplify the design, the stress block coefficient, β_1 = 0.65 corresponding high-strength concrete was used for UHP-FRC. This value is the smallest value for β_1 given in AASHTO and ACI codes. Since UHP-FRC has a more gradual descending behavior in compression in comparison to plain concrete, this value can be slightly higher because the slope descending branch of the stress-strain curve is gradual.

Below design calculation for ductile concrete strong reinforcement with UHP-FRC and FRP is given.

Design of a section with one row of reinforcement:

Assumptions:

- Whitney block
- one row of reinforcement
- $\varepsilon_{cu} = 0.015$
- $\varepsilon_r = 0.014$

Whitney block ➔ $C = 0.85\, abf_c'$; $UHPFRC \Rightarrow a = 0.65\, c$

And: $T = A_{FRP}\, \sigma = A_{FRP}\, E_{FRP}\, \varepsilon_{FRP}$

limiting ε_{FRP} to $\varepsilon_r = 0.014$ and using UHP-FRC's ductility for ductile behavior at ultimate loading:

$\varepsilon_{cu} = 0.015$

To make sure that concrete failure occurs first:

$$T > C \Rightarrow A_{FRP}\, E_{FRP}\, \varepsilon_{FRP} > (0.85)(0.65c) b f_c' \qquad \textit{Equation 4.5}$$

From the similar triangles and at ultimate: $c = \frac{\varepsilon_{cu}}{\varepsilon_{cu}+\varepsilon_r} d$

$$\Rightarrow A_{FRP}\, E_{FRP}\, \varepsilon_r > (0.85)\left(0.65\left(\frac{\varepsilon_{cu}}{\varepsilon_{cu}+\varepsilon_r} d\right)\right) b f_c' \qquad \textit{Equation 4.6}$$

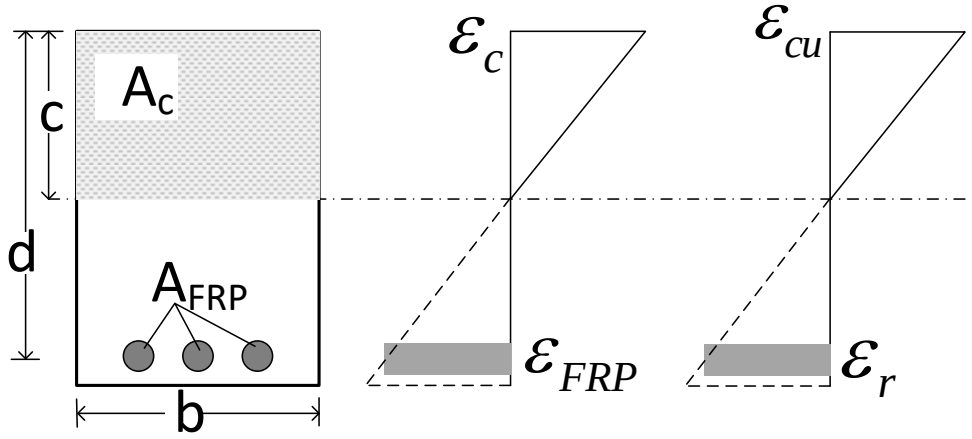

Figure 4-13 UHP-FRC with FRP reinforcement in one row

Rewrite the equation:

$$\frac{A_{FRP}}{bd} > (0.85)(0.65)\left(\frac{\varepsilon_{cu}}{\varepsilon_{cu}+\varepsilon_r}\right) f_c' \left(\frac{1}{E_{FRP}\, \varepsilon_r}\right) \qquad \textit{Equation 4.7}$$

By definition: $\rho = \frac{A_{FRP}}{bd}$

$$\Rightarrow \rho_{min} = (0.85)(0.65)\left(\frac{\varepsilon_{cu}}{\varepsilon_{cu}+\varepsilon_r}\right)\left(\frac{f_c'}{E_{FRP}\ \varepsilon_r}\right) \qquad \textit{Equation 4.8}$$

For this case: $\frac{\varepsilon_{cu}}{\varepsilon_{cu}+\varepsilon_r} = \frac{0.015}{0.015+0.014} = \frac{15}{29}$

$$\Rightarrow \rho_{min} = (0.85)(0.65)\left(\frac{15}{29}\right)\left(\frac{f_c'}{E_{FRP}\ \varepsilon_r}\right) = 0.2858\left(\frac{f_c'}{E_{FRP}\ \varepsilon_r}\right)$$

Substituting: $f_c' = 22\ ksi$; $E_{FRP} = 6141\ ksi$; $\varepsilon_r = 0.014$

$$\Rightarrow \rho_{min} = 0.2858\left(\frac{22}{6141 \times 0.014}\right) = 0.0731 = 7.31\%$$

Substituting: $f_c' = 22\ ksi$; $E_{FRP} = 6141\ ksi$; $\varepsilon_r = 0.017$

$$\Rightarrow \rho_{min} = (0.85)(0.65)\left(\frac{15}{32}\right)\left(\frac{f_c'}{E_{FRP}\ \varepsilon_r}\right) = 0.2589\left(\frac{22}{6141 \times 0.017}\right) = 0.0546$$

$$= 5.46\%$$

Substituting: $f_c' = 22\ ksi$; $E_{FRP} = 6141\ ksi$; $\varepsilon_r = 0.02$

$$\Rightarrow \rho_{min} = (0.85)(0.65)\left(\frac{15}{35}\right)\left(\frac{f_c'}{E_{FRP}\ \varepsilon_r}\right) = 0.2368\left(\frac{22}{6141 \times 0.02}\right) = 0.0424 = 4.24\%$$

Substituting: $f_c' = 20\ ksi$; $E_{FRP} = 6141\ ksi$; $\varepsilon_r = 0.017$

$$\Rightarrow \rho_{min} = 0.2589\left(\frac{20}{6141 \times 0.017}\right) = 0.0496 = 4.96\%$$

Substituting: $f_c' = 20\ ksi$; $E_{FRP} = 6141\ ksi$; $\varepsilon_r = 0.02$

$$\Rightarrow \rho_{min} = 0.2368\left(\frac{20}{6141 \times 0.02}\right) = 0.0386 = 3.86\%$$

Substituting: $f_c' = 18.5\ ksi$; $E_{FRP} = 6141\ ksi$; $\varepsilon_r = 0.020$

$$\Rightarrow \rho_{min} = 0.2368\left(\frac{18.5}{6141 \times 0.02}\right) = 0.0357 = 3.57\%$$

This means that to have a ductile failure for the section based on the initial assumptions, and with using the ductility of the UHP-FRC, $\rho_{min} = 7.31\%$ needs to be provided. However, this amount of reinforcement is not practical for one row of reinforcements. For example, for b=9 in and d=14.5 in, the minimum amount of reinforcement is:

$\rho_{min} = 0.0731$

$\Rightarrow A_{min} = 0.0731 \times 9 \times 14.5 = 9.534\ in^2$

This amount of reinforcement cannot be provided even with using #14 bars.

Considering *two rows* of reinforcement we will redo the calculation:

Assumptions:

- Whitney block
- two rows of reinforcement with equal amount in each row
- $\varepsilon_{cu} = 0.015$
- $\varepsilon_r = 0.014$ which occurs at the bottom row of reinforcement

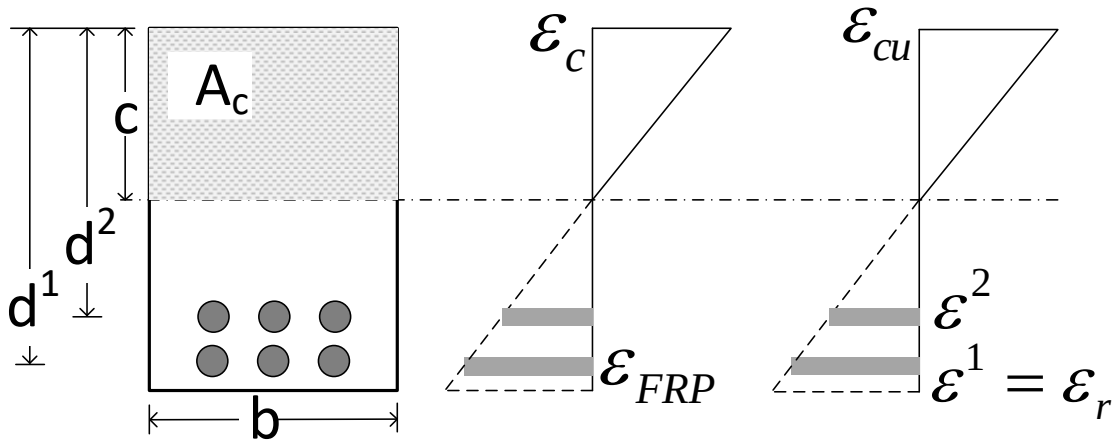

Figure 4-14 UHP-FRC with FRP reinforcement in two rows

To make sure that concrete failure occurs first:

$$T > C \Rightarrow T_1 + T_2 > C \qquad \textit{Equation 4.9}$$

$$\Rightarrow A^1_{FRP} E_{FRP}\, \varepsilon^1_{FRP} + A^2_{FRP} E_{FRP}\, \varepsilon^2_{FRP} > (0.85)(0.65c) b f'_c \qquad \textit{Equation 4.10}$$

Based on assumption: $A^1_{FRP} = A^2_{FRP} = 0.5A_{FRP}$; and at the failure: $\varepsilon^1_{FRP} = \varepsilon_r$

From the similar triangles and at ultimate: $c = \frac{\varepsilon_{cu}}{\varepsilon_{cu}+\varepsilon_r} d_1$ and:

$$\varepsilon^2_{FRP} = (\varepsilon^1_{FRP} + \varepsilon_{cu})\left({}^{d_2}/_{d_1}\right) - \varepsilon_{cu} = (\varepsilon_r + \varepsilon_{cu})\left({}^{d_2}/_{d_1}\right) - \varepsilon_{cu} \qquad \text{Equation 4.11}$$

Substituting the given terms, the equation is rewritten as:

$$\Rightarrow \; E_{FRP}\,(0.5A_{FRP})\left((\varepsilon_r+\varepsilon_{cu})\left({}^{d_2}/_{d_1}\right)-\varepsilon_{cu}+\varepsilon_r\right) > (0.85)(0.65(\frac{\varepsilon_{cu}}{\varepsilon_{cu}+\varepsilon_r}d_1))\; bf_c'$$

$$\Rightarrow \; E_{FRP}\,(0.5A_{FRP})\left(\frac{(d_1+d_2)(\varepsilon_r)+(d_1-d_2)(\varepsilon_{cu})}{d_1}\right) > (0.85)(0.65(\frac{\varepsilon_{cu}}{\varepsilon_{cu}+\varepsilon_r}d_1))\; bf_c'$$

$$\Rightarrow \; E_{FRP}\,A_{FRP}\left(\frac{1}{d_1}\right) > (\frac{1}{0.5})(0.85)(\frac{1}{(d_1+d_2)(\varepsilon_r)+(d_1-d_2)(\varepsilon_{cu})})(0.65(\frac{\varepsilon_{cu}}{\varepsilon_{cu}+\varepsilon_r}d_1))\; bf_c'$$

Equation 4.12

To find the ρ_{min}:

$$\Rightarrow \; \frac{A_{FRP}}{bd_1} > \left(\frac{0.85\times0.65}{0.5}\right)\left(\frac{d_1}{(d_1+d_2)(\varepsilon_r)+(d_1-d_2)(\varepsilon_{cu})}\right)\left(\frac{\varepsilon_{cu}}{\varepsilon_{cu}+\varepsilon_r}\right)\left(\frac{f_c'}{E_{FRP}}\right)$$

$$\Rightarrow \; \rho_{min} = 1.105\left(\frac{d_1}{(d_1+d_2)(\varepsilon_r)+(d_1-d_2)(\varepsilon_{cu})}\right)\left(\frac{\varepsilon_{cu}}{\varepsilon_{cu}+\varepsilon_r}\right)\left(\frac{f_c'}{E_{FRP}}\right) \qquad \textit{Equation 4.13}$$

To simplify the equation, we define $\propto = \varepsilon_{cu}/\varepsilon_r$:

$$\Rightarrow \; \rho_{min} = 1.105\left(\frac{d_1}{(d_1+d_2)+(d_1-d_2)(\propto)}\right)\left(\frac{\propto}{\propto+1}\right)\left(\frac{f_c'}{E_{FRP}\varepsilon_r}\right) \qquad \textit{Equation 4.14}$$

For a given set of values as bellow:

$d_1 = 14.5\; in\;;\; d_1 = 12.0\; in\;;\; \varepsilon_r = 0.014\;;\; \varepsilon_{cu} = 0.015$

$$\Rightarrow \quad \rho_{min} = 1.105(0.4969)(0.5172)\left(\frac{f_c'}{E_{FRP}\,\varepsilon_r}\right) = 0.284\left(\frac{f_c'}{E_{FRP}\,\varepsilon_r}\right)$$

if $\varepsilon_r = 0.020$

$$\Rightarrow \quad \rho_{min} = 1.105(0.5110)(0.2420)\left(\frac{f_c'}{E_{FRP}\,\varepsilon_r}\right) = 0.242\left(\frac{f_c'}{E_{FRP}\,\varepsilon_r}\right)$$

Substituting: $f_c' = 22\ ksi$; $E_{FRP} = 6141\ ksi$; $\varepsilon_r = 0.014$

$$\Rightarrow \rho_{min} = 0.284\left(\frac{22}{6141\times0.014}\right) = 0.0726 = 7.26\%$$

Half of this amount needs to be provided for each row of reinforcement. For example, for b=9 in and d=14.5 in, the minimum amount of reinforcement is:

$\rho_{min} = 0.0726$

$$\Rightarrow A_{min} = 0.0726 \times 9 \times 14.5 = 9.48\ in^2$$

A minimum of half of this amount, 4.74 in^2, is needed for one row. Three number of #11 bars can provide this amount.

Substituting: $f_c' = 18.5\ ksi$; $E_{FRP} = 6141\ ksi$; $\varepsilon_r = 0.020$

$$\Rightarrow \rho_{min} = 0.242\left(\frac{18.5}{6141\times0.020}\right) = 0.0365 = 3.65\%$$

$\Rightarrow A_{min} = 0.0365 \times 9 \times 14.5 = 4.76\ in^2$

A minimum of half of this amount, $2.38\ in^2$, is needed for one row. Three number of #8 bars can provide this amount.

In this study another beam with three rows (3 rebar at the two bottom row and two at the top row) is tested. The related calculation is as follows:

Considering *three rows* of reinforcement we will redo the calculation:

Assumptions:

- Whitney block
- three rows of reinforcement with equal amount in two bottom rows
- $\varepsilon_{cu} = 0.015$
- $\varepsilon_r = 0.020$ which occurs at the bottom row of reinforcement

To make sure that concrete failure occurs first:

$T > C \ \Rightarrow T_1 + T_2 + T_3 > C$ *Equation 4.15*

$$\Rightarrow A^1_{FRP} E_{FRP}\ \varepsilon^1_{FRP} + A^2_{FRP} E_{FRP}\ \varepsilon^2_{FRP} + A^3_{FRP} E_{FRP}\ \varepsilon^3_{FRP} > (0.85)(0.65c) b f'_c$$

Equation 4.16

Based on assumption: $A^1_{FRP} = A^2_{FRP} = 3A_{bar}$ and $A^3_{FRP} = 2A_{bar}$; and at the failure: $\varepsilon^1_{FRP} = \varepsilon_r$

From the similar triangles and at ultimate: $c = \frac{\varepsilon_{cu}}{\varepsilon_{cu} + \varepsilon_r} d_1$ and

$$\varepsilon_{FRP}^{2} = (\varepsilon_{FRP}^{1} + \varepsilon_{cu})\left({}^{d_2}/_{d_1}\right) - \varepsilon_{cu} = (\varepsilon_r + \varepsilon_{cu})\left({}^{d_2}/_{d_1}\right) - \varepsilon_{cu}$$ *Equation 4.17*

$$\varepsilon_{FRP}^{3} = (\varepsilon_{FRP}^{1} + \varepsilon_{cu})\left({}^{d_3}/_{d_1}\right) - \varepsilon_{cu} = (\varepsilon_r + \varepsilon_{cu})\left({}^{d_3}/_{d_1}\right) - \varepsilon_{cu}$$

To ease the calculations, will forward the solution with the assumptions and the beam section:

$$\varepsilon_{FRP}^{2} = (\varepsilon_{FRP}^{1} + \varepsilon_{cu})\left({}^{d_2}/_{d_1}\right) - \varepsilon_{cu} = (\varepsilon_r + \varepsilon_{cu})\left({}^{d_2}/_{d_1}\right) - \varepsilon_{cu} = (0.02 + 0.015)\left({}^{12}/_{14.5}\right) - 0.015 = 0.0140$$

$$\varepsilon_{FRP}^{3} = (\varepsilon_{FRP}^{1} + \varepsilon_{cu})\left({}^{d_3}/_{d_1}\right) - \varepsilon_{cu} = (\varepsilon_r + \varepsilon_{cu})\left({}^{d_3}/_{d_1}\right) - \varepsilon_{cu} = (0.02 + 0.015)\left({}^{9.5}/_{14.5}\right) - 0.015 = 0.0079$$

$$\Rightarrow T = (3A_{bar})(6141)(0.020) + (3A_{bar})(6141)(0.014) + (2A_{bar})(6141)(0.008) = 724.638 \times A_{bar}$$

$$C = (0.85)(0.65)\left(\frac{0.015}{0.015+0.020}d_1\right)bf_c' = 0.237 \times (d_1 b) \times f_c'$$

$$T > C \;\Rightarrow\; 724.638 \times A_{bar} > \; 0.237 \times (d_1 b) \times f_c'$$

$$\Rightarrow \rho_{min} = \frac{A_{FRP}}{bd_1} = \frac{n\,A_{bar}}{bd_1} = n\,\frac{0.237 \times f_c'}{724.638}$$

A summary of the designed beam specimens is tabulated in Table 4-2. Figure 4-15 shows the figuration of the designed specimens.

Table 4-2 Design summary of beam specimens

Specimen	**Matrix**	**Reinforcement**	**Effective depth (*d*)**	**ρ (%)**	**Targeted f_c' (ksi)**	**Measured f_c' (ksi)**
RC/ST	RC	9 # 5 - Steel	12.00 in	2.58	5	5
RC/FRP	RC	3 # 7 - BFRP	14.50 in	1.38	5	5
UHP-FRC/FRP1	UHP-FRC	8 # 8 - BFRP	12.28 in	5.71	22	18.5
UHP-FRC/FRP2*	UHP-FRC	6 # 7 - BFRP	13.25 in	3.02	22	18.5

*No shear reinforcement was used in UHP-FRC/FRP2

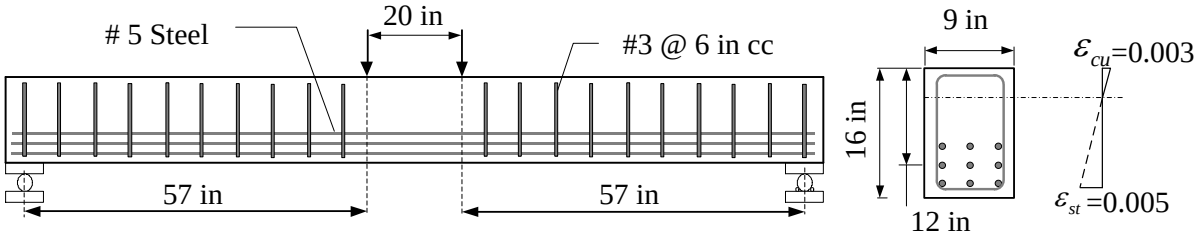

(a)

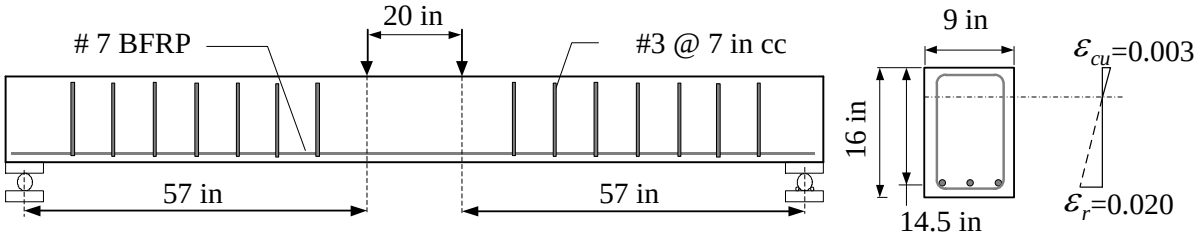

(b)

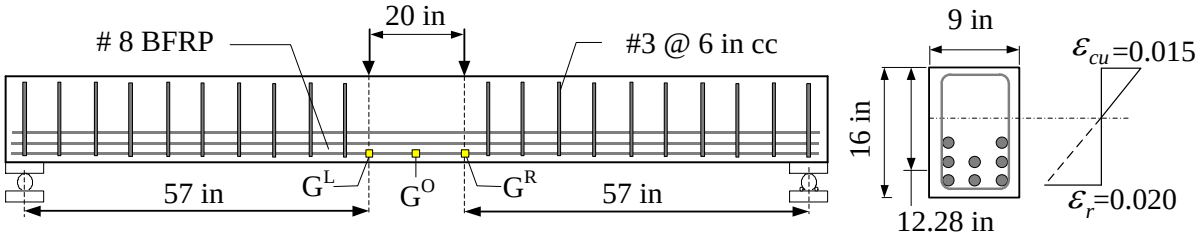

(c)

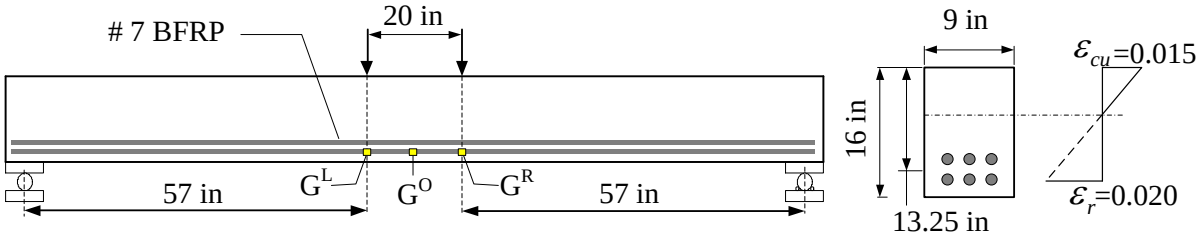

(d)

Figure 4-15 Reinforcement details and strain distribution of each specimen: (a) RC/ST, (b) RC/FRP, (c) UHP-FRC/FRP1, and (d) UHP-FRC/FRP2; also, GL, GO, and GR indicate the location of rebar gauges
(1 in= 25.4 mm)

Experimental results

In this study, basalt fiber-reinforced polymer (BFRP) reinforcement was used. Basalt fibers are a mineral-based inorganic product, which represent a fairly recent addition to the structural engineering community's reinforcement options (NCHRP, 2017). In this study, BFRP bars (#7 and #8), according to the manufacturer, had an ultimate tensile strength of 147 ksi, an ultimate tensile strain of 0.024 to 0.031, and an elastic modulus of 6090 ksi. All the beam specimens were subjected to a four-point loading test with a pure bending region in the middle 1/7 span (Figure 4-15). The shear span had an average a/d ratio of 4.4 to prevent a direct load transfer from the loading point to the support (a = 57 in. Figure 4-15). The beam specimens were monotonically loaded up to failure. To evaluate the results of DCSR design concept, two of the beam specimens were designed with conventional design methods using plain concrete: one reinforced with Gr. 60 steel rebars and one with BFRP rebars. In the other two beam specimens, UHP-FRC was used with the BFRP rebars. The design concrete compressive strength of the RC beams was 5 ksi. For the UHP-FRC beams, the design concrete compressive strength of UHP-FRC was 22 ksi. The UHP-FRC used in all specimens contained micro high-strength steel fibers (3% by volume) which were 0.5in (13 mm) in length and 0.2 mm in diameter with a tensile strength of 399 ksi (Aghdasi et al., 2016). During the tests, DIC was used to monitor strains of the beams' pure bending region. Linear variable differential transformers (LVDTs) and strain gauges were used to measure the specimen deflections and rebar strains, respectively. Figure 4-15 shows the specimen dimensions and reinforcement details.

The RC/ST beam is the same as RC1 in Table 4-1. It was designed to have the highest amount of longitudinal reinforcement while still maintaining a tension-controlled behavior according to ACI 318 (ACI, 2019) or AASHTO LRFD Specifications (AASHTO, 2017). In other words, the bottom tensile reinforcement reaches a strain of 0.005 when the maximum concrete compressive strain is 0.003. For the first beam specimen, the predicted peak load was P_n = 57 kips.

For the RC specimen with BFRP rebars (RC/FRP), the section was designed to experience concrete crushing prior to the rupture of the BFRP rebars according to ACI 440 (2015). Three #7 BFRP bars (Figure 4-15 (b)) were used to provide a reinforcement ratio of 1.38% which is more than the minimum requirement for compression-control failure per ACI 440 ($1.4\rho_{fb} = 0.42\%$). As shown in Figure 4-15 (b), when concrete reaches the maximum useable strain, the BFRP rebars have a strain of 0.0095, which is smaller than their rupture strain. The predicted peak load was P_n = 48 kips.

The third beam specimen (UHP-FRC/FRP1) was designed based on the DCSR design concept. In this specimen UHP-FRC was reinforced with high amount of BFRP rebars. While the ultimate tensile strain of 0.024 to 0.031 was suggested by the manufacturer, an ultimate tensile allowable strain at rupture of $\varepsilon_a = 0.02$ was conservatively selected for the BFRP rebars. $\varepsilon_a = 0.02$ was also reported for #3 to #8 BFRP rebars by Ovitigala et al. (2016). In a prior study, a maximum value of ε_{cu} = 0.025 across a gauge length of 10 in was measured at peak load in UHP-FRC beams by DIC while the average ε_{cu} of UHP-FRC within the gauge length was 0.015 (Kaka et al., 2016). In this study $\varepsilon_{cu} = 0.015$ was used for the design. To meet the requirements of $\varepsilon_{cu} = 0.015$ and $\varepsilon_a = 0.02$, after a few trials,

eight #8 BFRP rebars were provided as shown in Figure 4-15 (c), which gave a reinforcement ratio of 5.71%. In this specimen, #3 Gr. 60 steel rebars at a spacing of 6 in were used as shear reinforcement to avoid the shear failure Figure 4-15 (c).

For the fourth beam specimen (UHP-FRC/FRP2), however, no shear reinforcement was used to investigate the shear capacity of the UHP-FRC beam reinforced with BFRP rebars. The design was carried out to ensure that a shear failure would precede the flexural failure. By using the shear strength of UHP-FRC obtained from beams with steel rebars (Kaka and Chao, 2018) and assuming $\varepsilon_a = 0.02$ for BFRP rebars, it was calculated that the beam would fail in shear at a load of 162 kips and fail in flexure at a load of 184 kips if six #7 BFRPs were used. It provided a reinforcement ratio of $\rho = 3.02\%$. Notably, even though using eight #8 BFRP rebars (as in UHP-FRC/FRP1) could further increase the flexural capacity to ensure a shear failure, this was avoided in the design because increasing the longitudinal reinforcement ratio has been shown to increase the shear strength of concrete beams without shear reinforcement (Khaja and Sherwood, 2013; ACI 440, 2015).

Test results of beam specimens are presented in Figure 4-16.

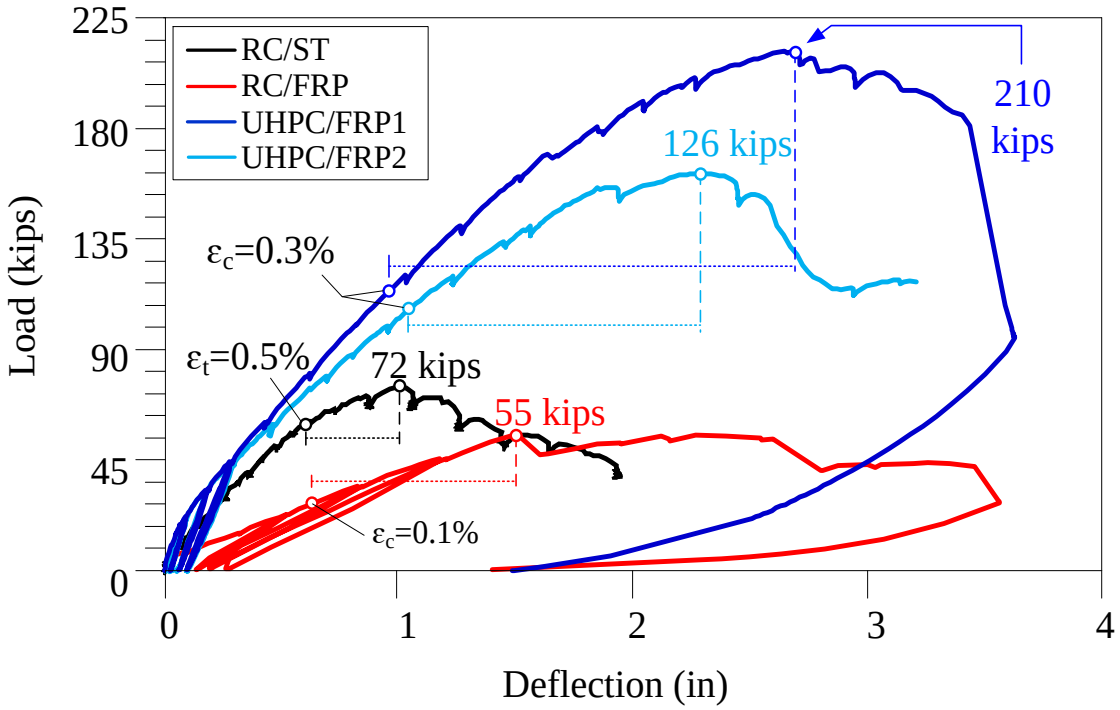

Figure 4-16 Load deflection response of the beam specimens

For specimen RC/ST, the first noticeable flexural crack occurred at a load of 11.9 kips, and the maximum load recorded during the test was 72 kips at a deflection of 1in. The steel rebars in the bottom layer reached the strain value of $\varepsilon_t = 0.5\%$ at a deflection of 0.55 in. The peak load is much larger than the predicted peak load (= 57 kips), which can be attributed to rebar's overstrength due to the strain-hardening. Severe crushing and spalling of concrete at the compression zone was observed during the test. The RC/FRP beam had a peak load of P_u = 55 kips. The corresponding deflection at the peak loading was 1.5 in. The first flexural crack was observed at 6.1 kips and the first shear crack appeared as a flexural-shear crack in the shear span close to the loading point at a load of 22 kips. A critical flexural-shear crack eventually occurred in the constant moment region along with the initiation of splitting cracks at the rebar level. The compression zone was reduced due

to the wide and deep flexural-shear crack. Very severe concrete damage was observed in the RC beam reinforced with BFRP rebars. Due to the deeper and wider cracks, the RC/FRP beam showed a much smaller flexural stiffness than that of the RC/ST beam.

The UHP-FRC/FRP1 was designed based on the DCSR concept. Therefore, the stronger concrete and better utilization of the UHP-FRC's compressive behavior, in combination with high reinforcement ratio, led to a peak load of P_u = 210 kips, which is nearly a 300% improvement compared to the peak load of RC/ST specimen. UHP-FRC/FRP1 had a much greater flexural stiffness compared to that of the RC/FRP and RC/ST beams due to the high reinforcement ratio used by the DCSR design. Thus, the DCSR design limits the deformation of rebars and reduces crack width. The beam also exhibited a great ductility and deformation capability. The measured peak load was less than the predicted load (=233 kips) because the compressive strength of UHP-FRC was lower (18.5 ksi) than the design strength (22 ksi). Figure 4-17 shows only very fine flexural cracks occurring at a load of 80 kips; the RC/ST beam failed in a lessor loading.

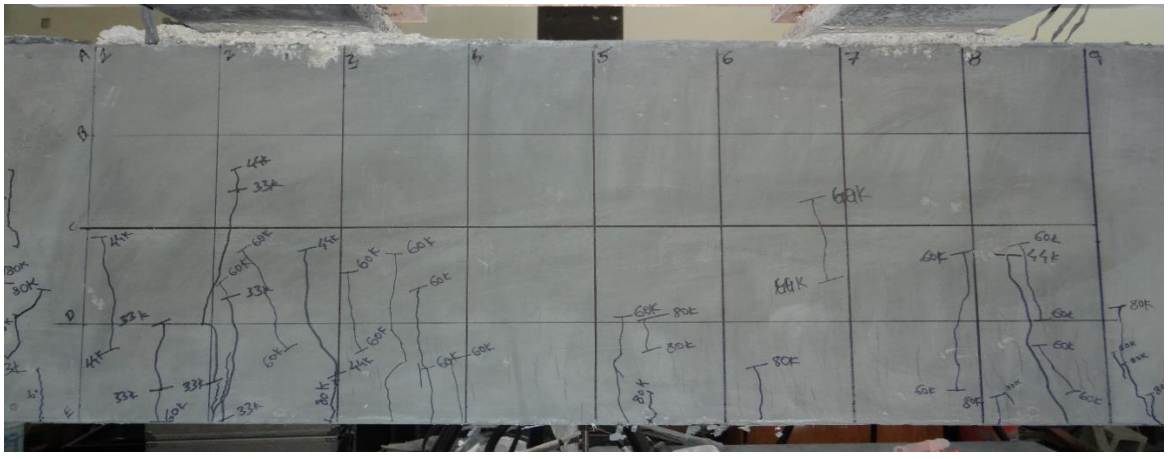

Figure 4-17 Cracking patterns for beam specimens UHP-FRC/FRP1 at 82 kips

The compression zone had a distributed crushing zone, with no spalling. The first flexural crack was observed at 33 kips. The primary visible shear crack was initiated in the shear span as the flexural cracks turned into diagonal cracks at 120 kips. After 160 kips, minor crushing of concrete was observed in the shear span near the loading point, followed by a minor crushing in the constant moment region. Crushing of concrete in the compression zone extended to a greater length of the constant moment region. No rebar slip was observed, indicating that UHP-FRC provided a strong bond strength.

The UHP-FRC/FRP2 beam specimen's strength was controlled by a shear failure. The first flexural crack appeared at 20 kips. The initial visible shear crack originated in the shear span area as the flexural crack began to slant at a load of 120 kips. A critical flexural-shear crack formed in the shear span near the loading point and extended towards the loading point. From there, the crack began to widen after a load of 142 kips. This critical shear crack eventually led to the load drop after attaining a peak load of 162 kips, which corresponds to a concrete shear capacity of 81 kips. At the same time, splitting cracks began to appear along the bottom rebars because no shear reinforcement was provided. Unlike UHP-FRC/FRP1, except some concrete damage at the beam's side faces, no concrete crushing occurred at the beam's top compressive surface.

Because DCSR design is inherently a compression-controlled design, it naturally provides much higher strength than the required design load. In other words, a UHP-FRC flexural member designed by DSCR will always meet the factored load's design requirement for a conventional RC beam having the same dimensions. In addition, the ductile behavior of UHP-FRC material in compression enhances the ductility of the section (Figure 4-16). Both UHP-FRC/FRP specimens showed greater ductility in comparison with conventional RC

beams. Contrary to conventional steel reinforced sections in which ductility originates from rebar yielding, the ductility of the DCSR section originates from nonlinear behavior of UHP-FRC in compression. In Figure 4-16, since BFRP rebars behave elastically up to rupture, the starting point of nonlinearity of the beams reinforced by BFRP rebars can be defined from the point where the nonlinear behavior of the concrete starts. For plain concrete, this point can be defined when the strain at the top surface of the concrete reaches $\varepsilon_c = 0.1\%$ (Wang and Belarbi, 2005). For the two UHP-FRC beam specimens, the strain at which the nonlinear behavior of the concrete starts is considered as $\varepsilon_c = 0.3\%$ based on Figure 4-3. According to the DIC, when the maximum strains reached $\varepsilon_c = 0.3\%$. The load-deflection responses of these specimens also show a deviation point at the corresponding points (Figure 4-16).

Figure 4-18 shows the measured strains in the longitudinal BFRP rebars in the UHP-FRC/FRP specimens. The strain gauges' locations are provided in Figure 4-15. The results indicate that the maximum strains were close to but smaller than the allowable tensile strain $\varepsilon_a = 0.02$.

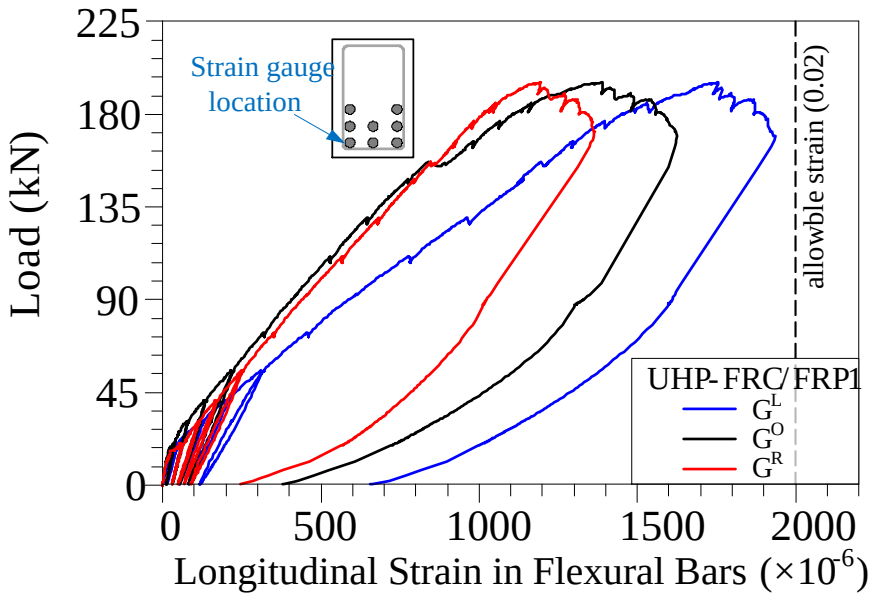

(a)

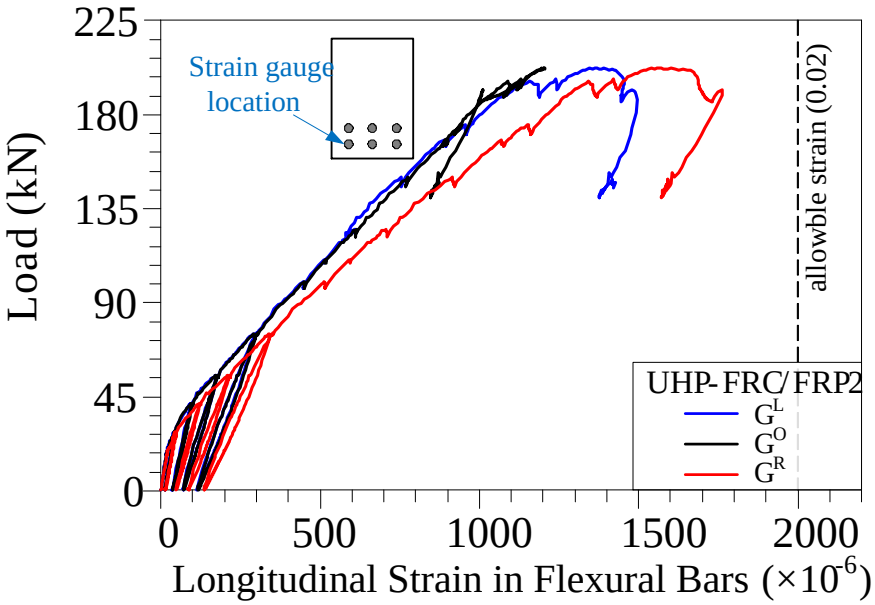

(b)

Figure 4-18 Measured strains in BFRP rebars: (a) UHP-FRC/FRP1 and (b) UHP-FRC/FRP2

4.6 Numerical analyses for response comparison between RC section and DCSR sections with different section properties

In this section, a series of numerical study is presented to compare the stress and strain distribution along the section for different members that are designed with DCSR design concept with different section properties and plain concrete reinforced with steel rebars. In these analyses, the neutral axis height, the flexural capacity and the strain at the rebars are calculated vs the increment in the curvature. During the analysis, the curvature increases and the strain at each height is calculated based on the equilibrium equation in horizontal direction (i.e., the horizontal tensile and compressive components generated in steel and concrete). Then after, an iteration is used to find the neutral axis where at the same time the equilibrium equation is satisfied. The stress at each height is found from the strain distributed along the height of the section and the stress strain behavior of the materials. In all the calculations, is assume that plane section remain plane during the loading.

4.6.1 Material properties

Reinforcement steel

In these analyses grade 60 reinforcing steel is used. Figure 4-19 represents the Stress-Strain plot for Grade 60 reinforcement steel. Although the rupture strain exceeds 0.1, in these analyses a maximum usable rupture strain of 0.1 is considered, conservatively.

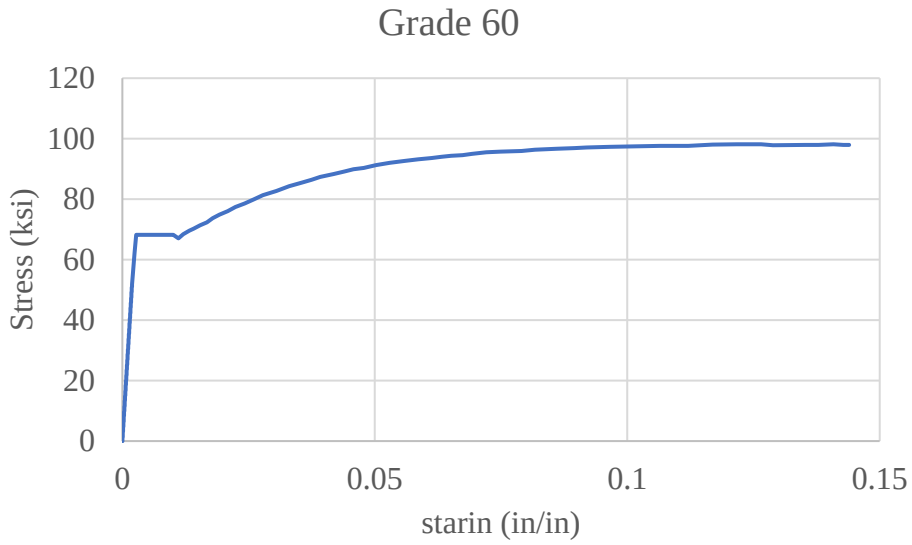

Figure 4-19 Stress-Strain plot for Grade 60 reinforcement steel

UHP-FRC

Although the in the design process the equivalent rectangular stress block method presented in the current AASHTO LRFD and ACI codes are commonly used to design the section, here the actual behavior of the UHP-FRC derived from the experimental test is used (Aghdasi et al., 2016) (Aghdasi et al., 2016). Figure 4-20 shows the compressive stress strain behavior of UHP-FRC used here. Although the maximum compressive strain recorded in the experimental test reaches a value of 0.03, the maximum compressive strain used in these analyses are limited to 0.015. Also, since in all the UHP-FRC sections the minimum tributary area (ρ_{TA}) is more than 11%, the tensile strength of the ultra-high performance fiber reinforced concrete is 3 ksi (see Figure 3-19). Since the strain at the compressive peak strength and maximum usable strain is a considerable value for UHP-

FRC, a strain value of 0.003 is assigned as a point in which the compressive nonlinearity initiates in UHP-FRC.

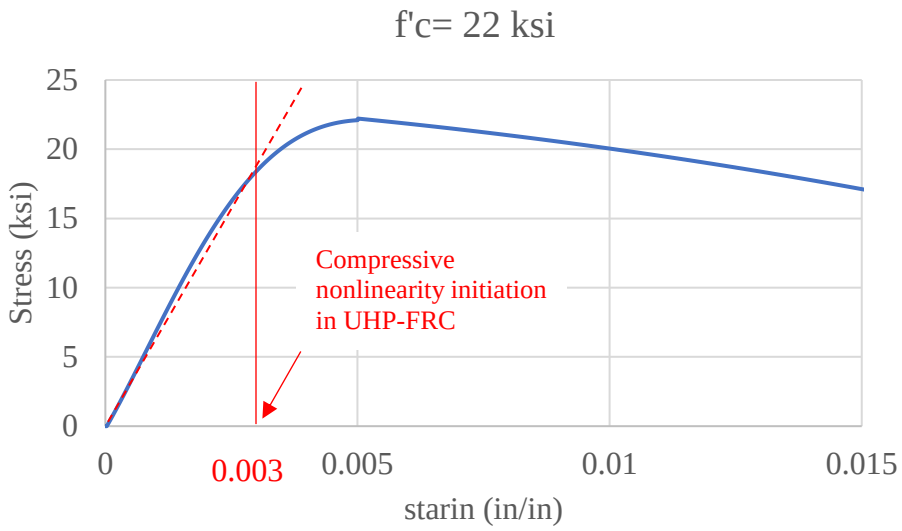

Figure 4-20 compressive stress strain behavior of UHP-FRC (Aghdasi et al., 2016)

4.6.2 Section property and reinforcement arrangement (Rectangular section)

RC/St60 16R-1

For comparison purposes, and as a baseline, an RC section is modeled and analyzed with the same method. This section is equal to the section that has been presented in the experimental test result before (RC specimen in Table 4-1). Figure 4-21 section dimension and arrangement of longitudinal reinforcement steel rebars for RC/St60 16R-1.

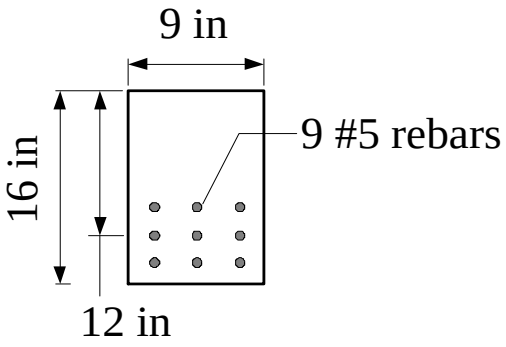

Figure 4-21 Section dimension and arrangement of longitudinal reinforcement steel rebars for section RC/St60 16R-1

Although the numerical analyses are targeting only one section, the result from the Digital Image Correlation (DIC) system verifies the accuracy of neutral access position calculated from the numerical analysis.

Figure 4-22 represents the full-field concrete longitudinal strain (ε_x) along moment region for RC#1 at an applied load of 72 kips (peak load). Figure 4-23 (a) shows the calculated neutral axis with respect to curvature in section RC/St60 16R-1. For both the numerical analysis and the experimental test result the value are in the range of 5-5.5 in.

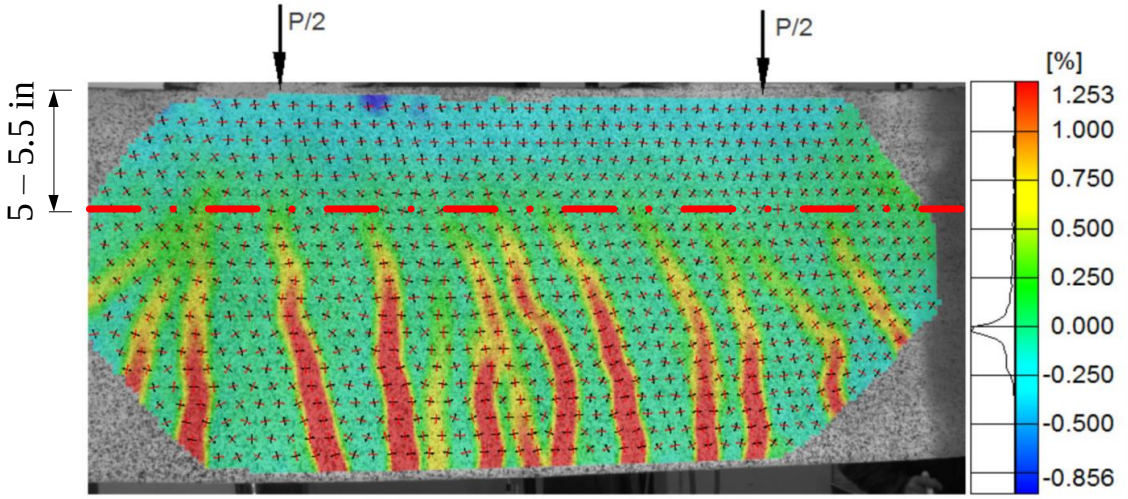

Figure 4-22 Full-field concrete longitudinal strain (ε_x) along moment region for RC#1 at an applied load of 72 kips (peak load) (Kaka, 2017)

Table 4-3 design and section parameters for section RC/St60 16R-1

f 'c =	**5 ksi**	reinf. Type=	**Grade 60**	ρ =	**2.14%**
e_{cu}=	**0.003**	max strain=	**0.004**	ρ TA=	**3.44%**

Beam Width, b =	**9 in**
Total Beam Depth, h=	**16 in**
β1=	**0.8**

H.M.bars?	bar size	A_{st}	d
	#	[in^2]	[in]
3	**5**	**0.93**	**14.5**
3	**5**	**0.93**	**12**
3	**5**	**0.93**	**9.5**

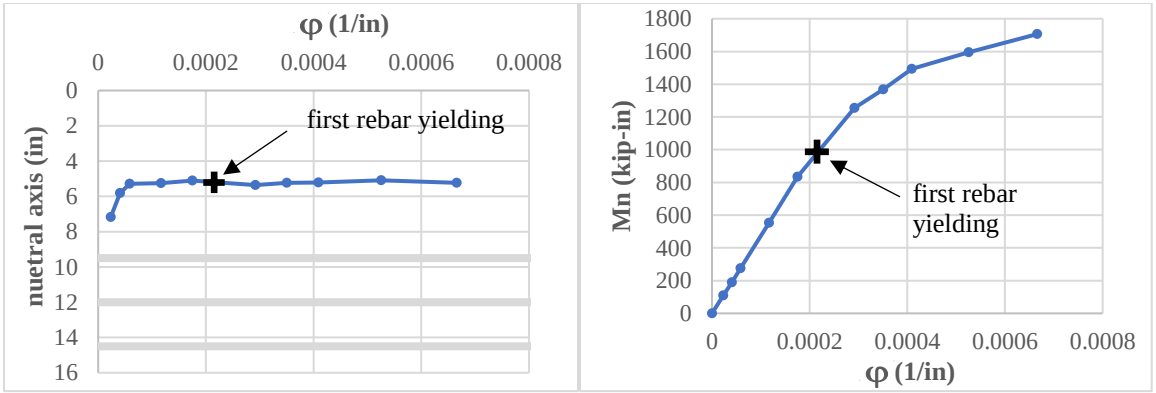

(a) (b)

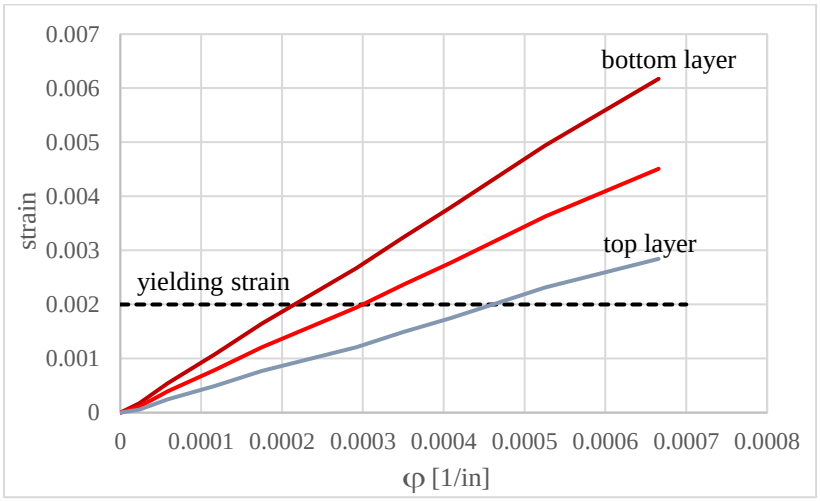

(c)

Figure 4-23 The changes of a) neutral axis, b) moment capacity and c) strain in rebars in section RC/St60 16R-1

UHP/St60 16R-2

This section is ultra-high performance fiber reinforced concrete as the matrix for the section along with grade 60 steel reinforcements. Figure 4-24 shows the section dimension and arrangement of longitudinal reinforcement steel rebars for section UHP/St60 16R-2.

Table 4-4 summarizes the design and section parameters for section UHP/St60 16R-2.

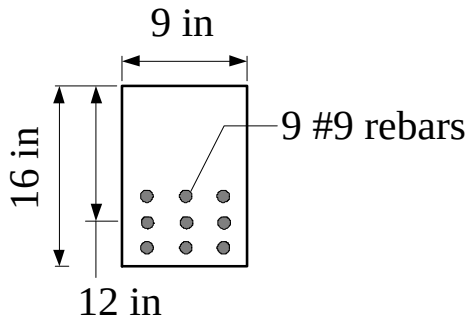

Figure 4-24 Section dimension and arrangement of longitudinal reinforcement steel rebars for section UHP/St60 16R-2

Table 4-4 design and section parameters for section UHP/St60 16R-2

f 'c =	**22 ksi**	reinf. Type=	**Grade 60**	ρ =	**6.90%**
e_{cu}=	**0.015**	max strain=	**0.034**	ρ_{TA}=	**11.11%**

Beam Width, b =	**9 in**
Total Beam Depth, h=	**16 in**
β1=	**0.65**

H.M.bars?	bar size	A_{st}	d
	#	[in^2]	[in]
3	**9**	**3**	**14.5**
3	**9**	**3**	**12**
3	**9**	**3**	**9.5**

The results of the numerical analysis for this section is presented in Figure 4-25. The curvature is increased until the strain at the top layer in the compressive part of the section reaches 0.015 (the last point in the plots). In this section the concrete crushing occurs when

the maximum strain in the bottom layer of the reinforcement is almost 0.028. In this section the rebar yielding in the bottom layer of the reinforcements, occurs prior to the UHP-FRC compressive nonlinearity initiation.

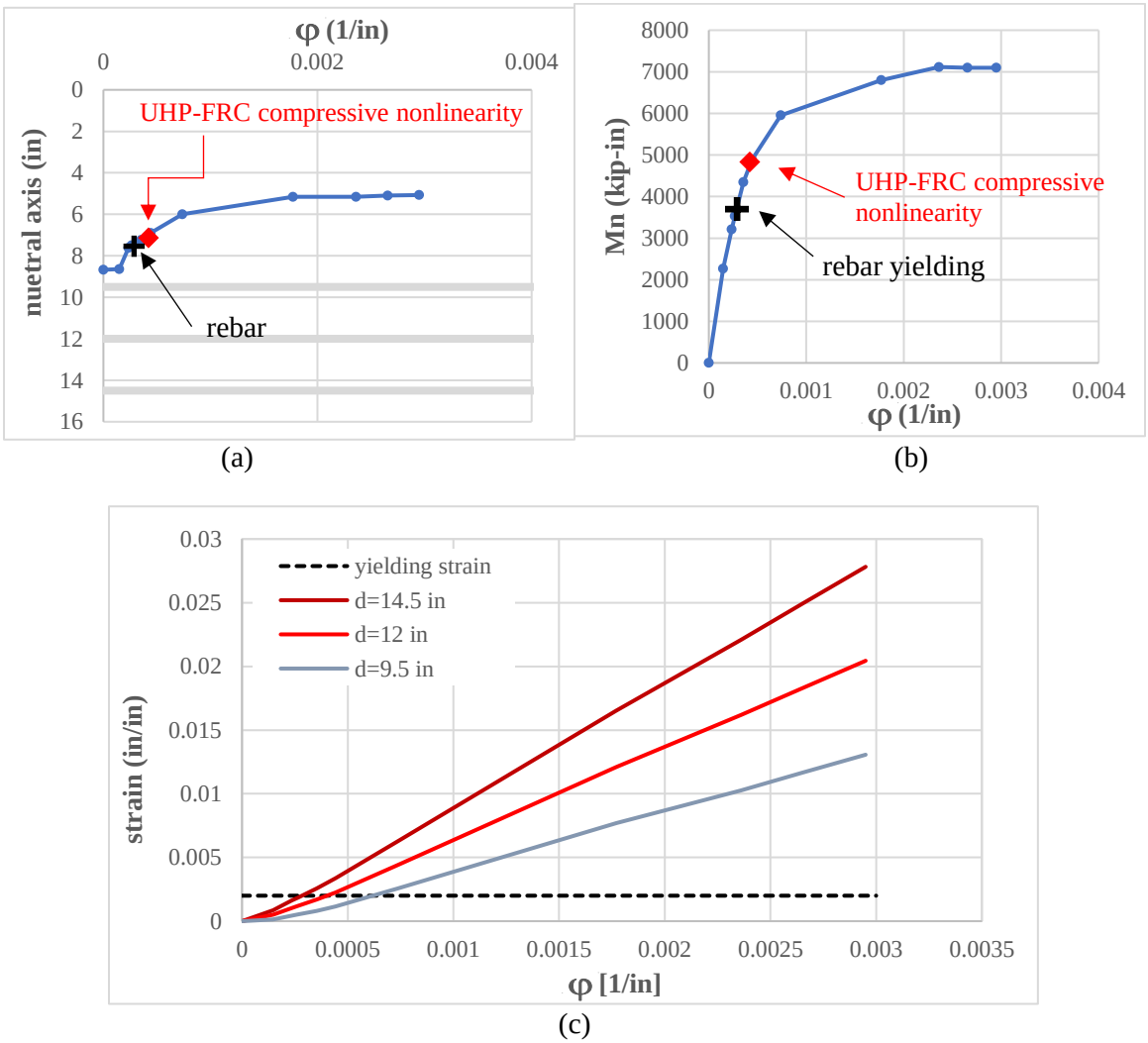

Figure 4-25 The changes of a) neutral axis, b) moment capacity and c) strain in rebars in section UHP/St60 16R-2

Figure 4-26 compares the moment curvature diagrams for RC/St60 16R-1 and UHP/St60 16R-2. This comparison shows that not only the strength of the section with ultra-high performance fiber reinforced concrete is increased, it also shows a great post yielding ductility.

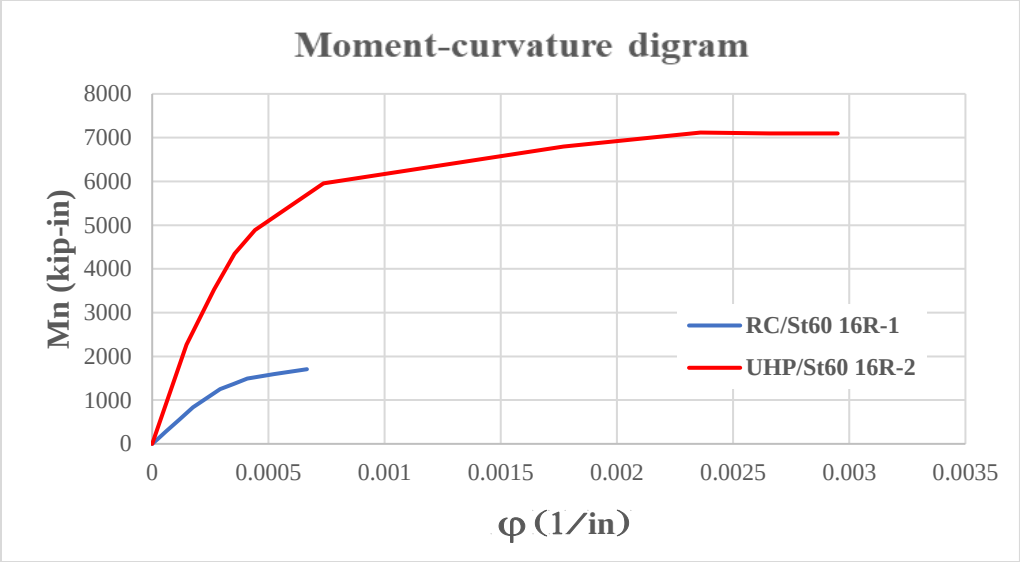

Figure 4-26 comparison between moment curvature diagram of RC/St60 16R-1 and UHP/St60 16R-2

UHP/St60 16R-3

This section is ultra-high performance fiber reinforced concrete as the matrix for the section along with grade 60 steel reinforcements. Figure 4-27 shows the section dimension and arrangement of longitudinal reinforcement steel rebars for section UHP/St60 16R-3. Table 4-5 summarizes the design and section parameters for section UHP/St60 16R-3.

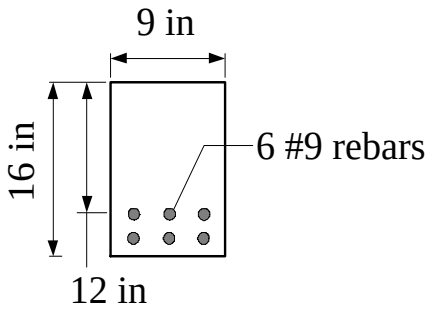

Figure 4-27 Section dimension and arrangement of longitudinal reinforcement steel rebars for section UHP/St60 16R-3

Table 4-5 design and section parameters for section UHP/St60 16R-3

f 'c =	22 ksi	reinf. Type=	Grade 60	ρ =	4.60%
e_{cu}=	0.015	max strain=	0.049	ρ_{TA}=	11.11%

Beam Width, b = 9 in

Total Beam Depth, h= 16 in

β1= 0.65

H.M.bars?	bar size #	A_{st} [in^2]	d [in]
3	9	3	14.5
3	9	3	12

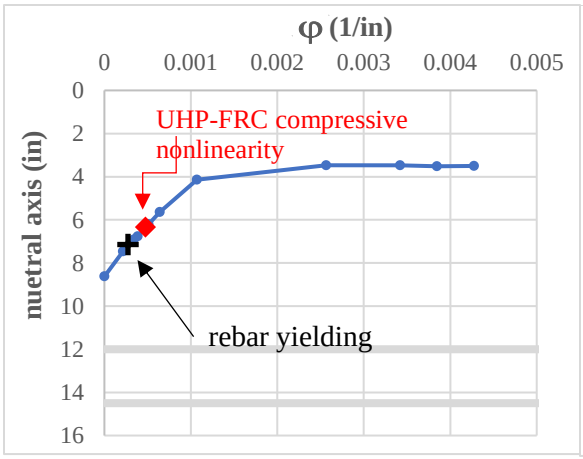

(a)

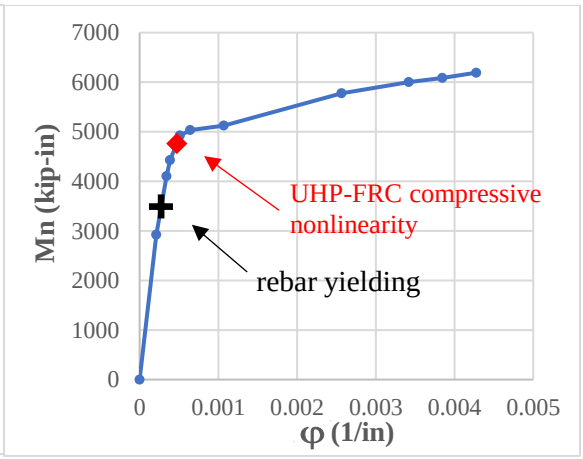

(b)

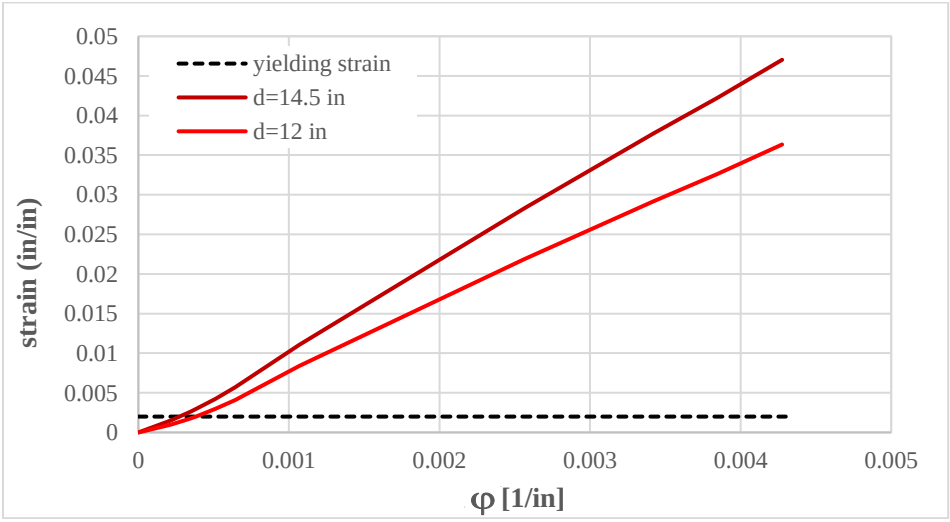

(c)

Figure 4-28 The changes of a) neutral axis, b) moment capacity and c) strain in rebars in section UHP/St60 16R-3

The results of the numerical analysis for this section is presented in Figure 4-28. Same as the previous section, the curvature increment is stopped when the top layer in the compressive part of the section reaches 0.015 (the last point in the plots). In this section the concrete crushing occurs when the maximum strain in the bottom layer of the reinforcement is almost 0.047. Due to lesser amount of reinforcement in this section comparing with the previous one, the maximum strain in the rebars, which occurs in the bottom layer, is higher than section UHP/St60 16R-2. Same as the section with three layers of rebar, the rebar yielding in the bottom layer of the reinforcements, occurs prior to the UHP-FRC compressive nonlinearity initiation. In both UHP/St60 16R-2 and UHP/St60 16R-3 sections, after flexural cracking initiation and yielding at the bottom layer of the reinforcements, the neutral axis in each of the sections shifts upward. At the same time, the rate of increasing a strain with respect to curvature increment increases. Toward to the maximum experienced curvature, the compressive depth of the UHP/St60 16R-2 section converges to value of more than 4 inches. However, this value is less than 4 inches for UHP/St60 16R-3. This shows the benefit of implementing more reinforcement if ultra-high performance fiber reinforcement concrete is used as matrix.

UHP/St60 16R-4

In this section, three reinforcement rebars of #9 are used in one row. Figure 4-29 shows the section dimension and arrangement of longitudinal reinforcement steel rebars for section UHP/St60 16R-4. Table 4-6 summarizes the design and section parameters for section UHP/St60 16R-4.

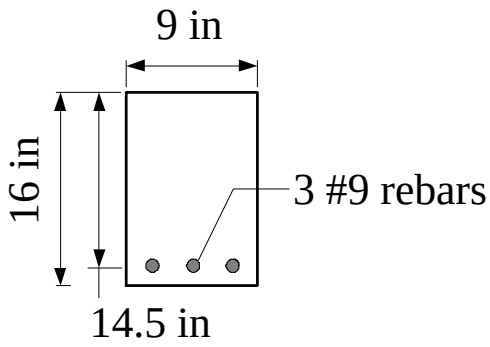

Figure 4-29 Section dimension and arrangement of longitudinal reinforcement steel rebars for section UHP/St60 16R-3

Table 4-6 design and section parameters for section UHP/St60 16R-3

f 'c =	**22 ksi**	reinf. Type=	**Grade 60**	ρ =	**2.30%**
e_{cu}=	**0.015**	max strain=	**0.1**	ρ_{TA}=	**11.11%**

Beam Width, b =	**9 in**
Total Beam Depth, h=	**16 in**
β1=	**0.65**

H.M.bars?	bar size #	A_{st} [in^2]	d [in]
3	**9**	**3**	**14.5**

The results of the numerical analysis for this section is presented in Figure 4-30. In this section, unlike the two previous sections, the maximum compressive strain at the top layer of the UHP-FRC occurs at the same time with the bottom layer of the reinforcement reaches the strain value of 0.1 (which is considered a maximum rupture usable strain). This shows than, when ultra-high performance fiber reinforced concrete, with enlarged compressive ductility is used, a minimum limit amount of tensile reinforcement is required. Same as the section with three and two layers of rebar, the first rebar yielding of the reinforcements,

occurs prior to the UHP-FRC compressive nonlinearity initiation. It is noteworthy that the lag between first yielding and first flexural cracking in the bottom layer of the UHP-FRC is increased when the total number of rebars or reduced. In both UHP/St60 16R-2 and UHP/St60 16R-3 sections, the final value for the neutral axis (compression depth) of this section, converges to around 4 inches. However, for the UHP/St60 16R-4 section, with only three rebars of #9, the neutral axis converges to 2 inches.

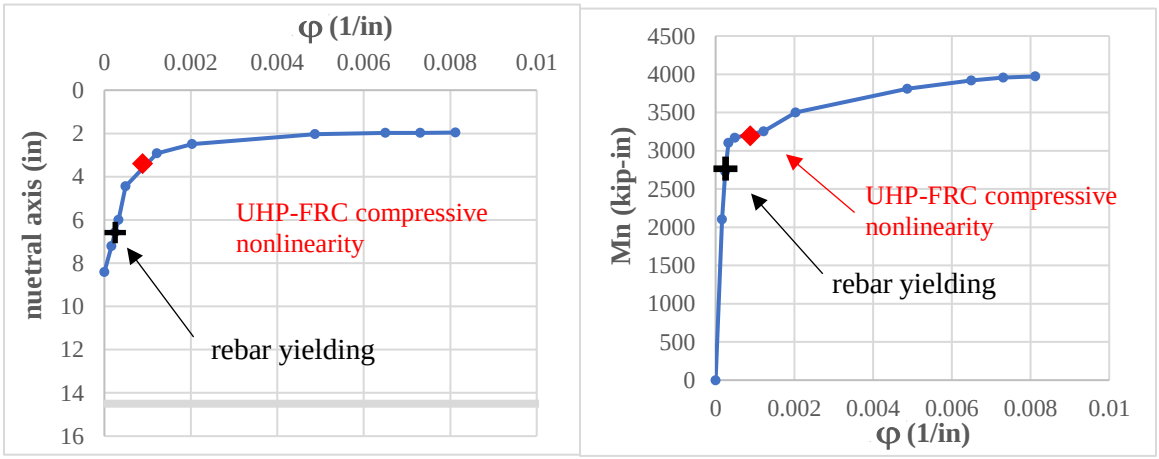

(a) (b)

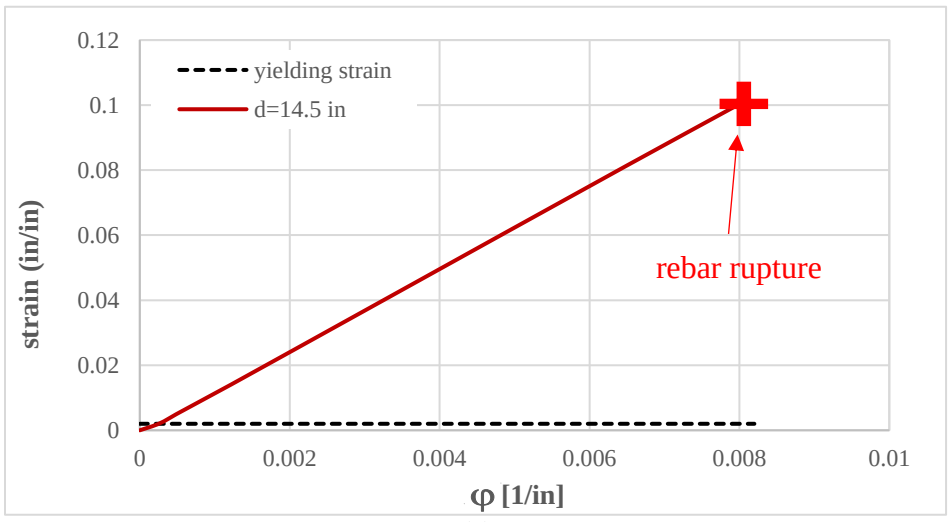

(c)

Figure 4-30 The changes of a) neutral axis, b) moment capacity and c) strain in rebars in section UHP/St60 16R-4

Figure 4-31 compares the moment curvature diagrams of UHP/St60 16R-2, UHP/St60 16R-3 and UHP/St60 16R-4. This comparison illustrates that when the total amount of the tensile reinforcement is reduced, the ductility tends to increase. However, this may cost the brittle rupture of the reinforcement. Also, the maximum flexural capacity of the section is smaller when the total amount of reinforcement is reduced. It is noteworthy to mention that when larger amount of total reinforcement is used, generally the neutral axis locates a lower position which means the larger area of the section is working in compression. In other words, a better utilization of the ultra-high performance fiber reinforced concrete is achieved. It should be noted that, in all the three sections with ultra-high performance fiber reinforced concrete, the tributary reinforcement ratio was the same.

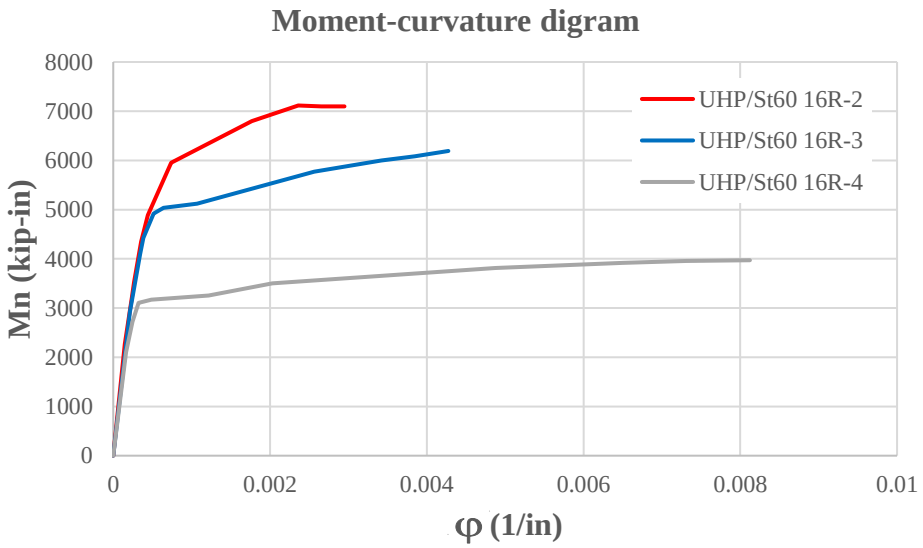

Figure 4-31 Comparison between moment curvature diagram of UHP/St60 16R-2, UHP/St60 16R-3 and UHP/St60 16R-4

In the next step, four other sections with the same width but larger height or analyzed. Same as above, the total amount of tensile reinforcement is variable among those sections.

UHP/St60 40R-1

This section is ultra-high performance fiber reinforced concrete as the matrix for the section along with grade 60 steel reinforcements. Figure 4-32 shows the section dimension and arrangement of longitudinal reinforcement steel rebars for section UHP/St60 40R-1. Table 4-7 summarizes the design and section parameters for section UHP/St60 40R-1.

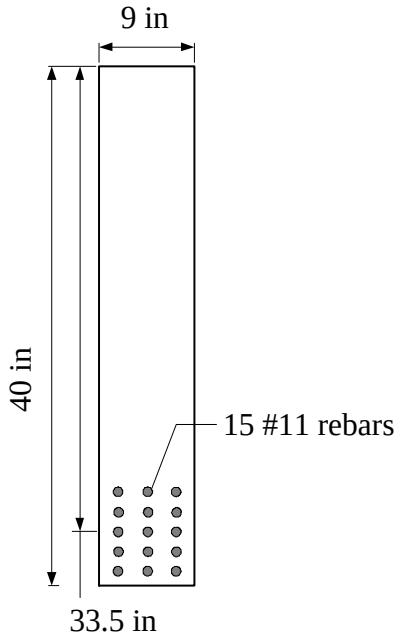

Figure 4-32 Section dimension and arrangement of longitudinal reinforcement steel rebars for section UHP/St60 40R-1

The results of the numerical analysis for this section are presented in Figure 4-33. The curvature is increased until the strain at the top layer in the compressive part of the section reaches 0.015 (the last point in the plots). In this section the concrete crushing occurs when the maximum strain in the bottom layer of the reinforcement is almost 0.034. In this section the rebar yielding in the bottom layer of the reinforcements, occurs prior to the UHP-FRC compressive nonlinearity initiation.

Table 4-7 design and section parameters for section UHP/St60 40R-1

f 'c =	22 ksi	reinf. Type=	Grade 60	ρ =	6.75%
e_{cu}=	0.015	max strain=	0.033	ρ TA=	17.33%

Beam Width, b = 9 in

Total Beam Depth, h= 40 in

β1= 0.65

H.M.bars?	bar size	A_{st}	d
	#	[in^2]	[in]
3	11	4.68	38.5
3	11	4.68	36
3	11	4.68	33.5
3	11	4.68	31
3	11	4.68	28.5

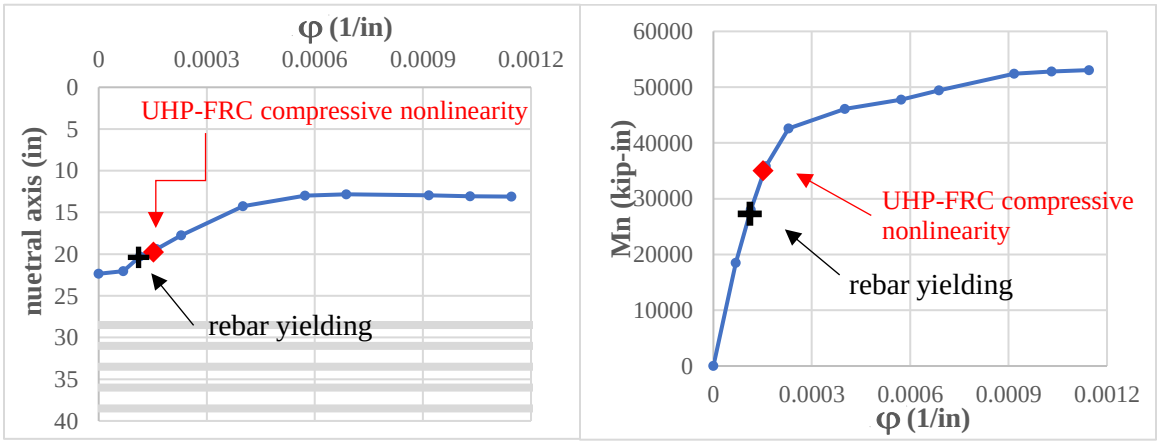

(a) (b)

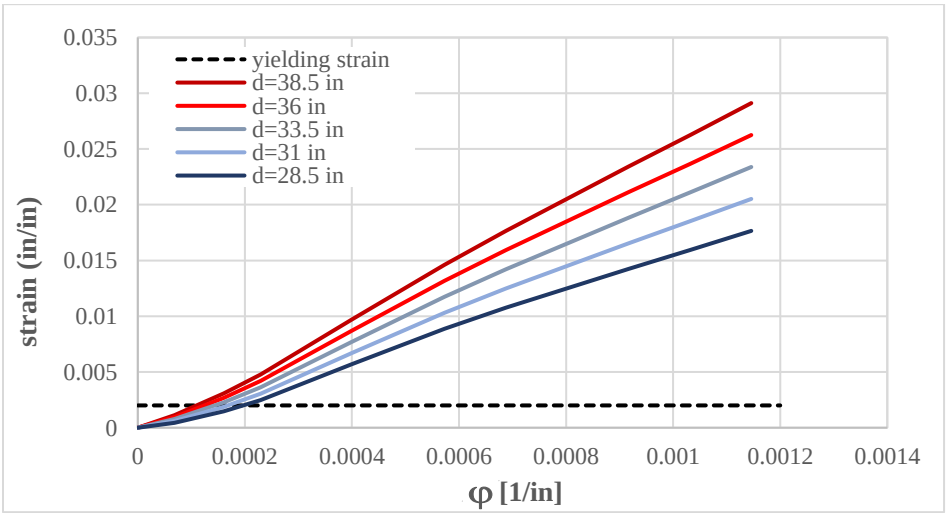

(c)

Figure 4-33 The changes of a) neutral axis, b) moment capacity and c) strain in rebars in section UHP/St60 40R-1

UHP/St60 40R-2

Figure 4-34 shows the section dimension and arrangement of longitudinal reinforcement steel rebars for section UHP/St60 40R-2. Table 4-8 summarizes the design and section parameters for section UHP/St60 40R-2. The results of the numerical analysis for this section is presented in Figure 4-35. Same as the previous section, the curvature increment is stopped when the top layer in the compressive part of the section reaches 0.015 (the last point in the plots). In this section the concrete crushing occurs when the maximum strain in the bottom layer of the reinforcement is almost 0.05. The general trends in the change of behavior from UHP/St60 40R-1 to UHP/St60 40R-2 are same as the first two UHP-FRC sections with 16 inches height including the changes in the neutral axis position and strain changes in the reinforcement rebars.

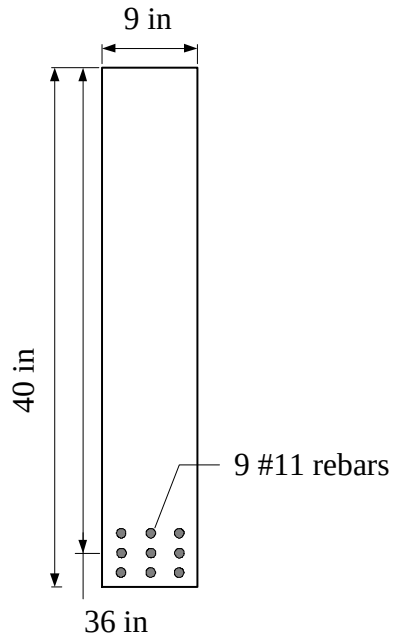

Figure 4-34 Section dimension and arrangement of longitudinal reinforcement steel rebars for section UHP/St60 40R-2

Table 4-8 design and section parameters for section UHP/St60 40R-2

f 'c =	22 ksi	reinf. Type=	Grade 60	ρ =	4.05%
e_{cu}=	0.015	max strain=	0.055	ρ_{TA}=	17.33%

Beam Width, b = 9 in

Total Beam Depth, h= 40 in

β1= 0.65

H.M.bars?	bar size #	A_{st} [in^2]	d [in]
3	11	4.68	38.5
3	11	4.68	36
3	11	4.68	33.5

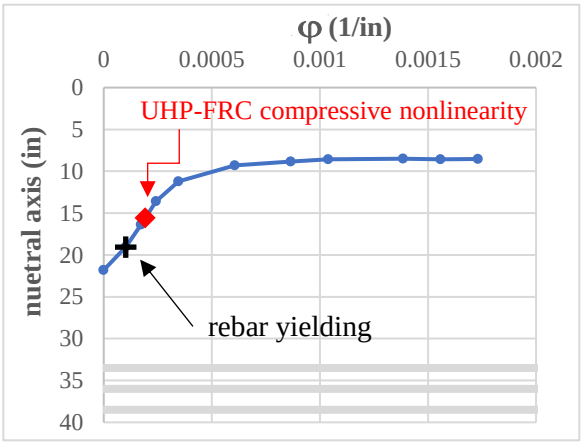

(a)

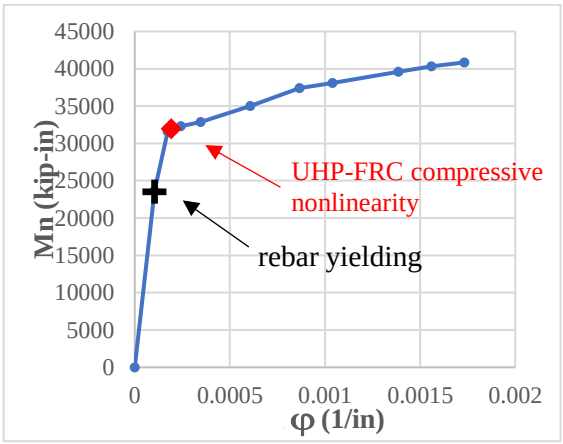

(b)

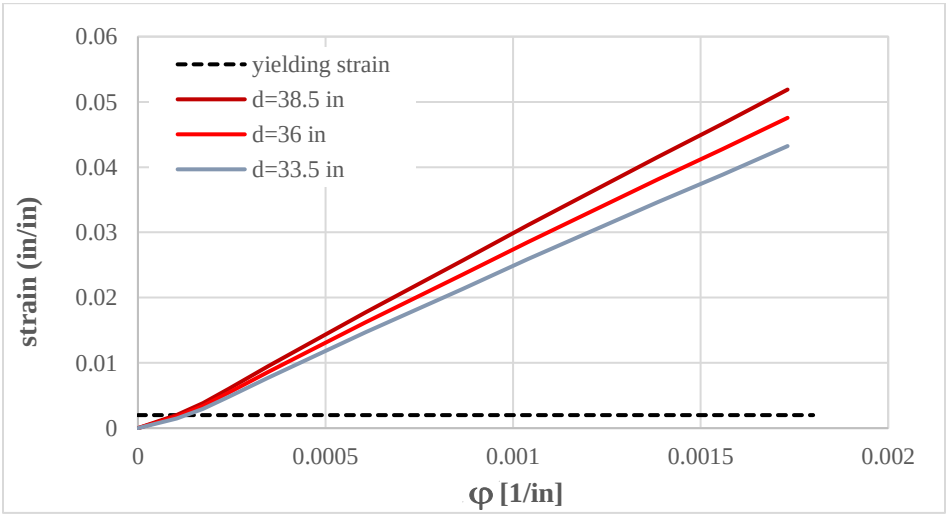

(c)

Figure 4-35 The changes of a) neutral axis, b) moment capacity and c) strain in rebars in section UHP/St60 40R-2

UHP/St60 40R-3

Figure 4-36 shows the section dimension and arrangement of longitudinal reinforcement steel rebars for section UHP/St60 40R-3. Table 4-9 summarizes the design and section parameters for section UHP/St60 40R-3. In this section, the total amount of reinforcement is deliberately selected such that the strain of the top layer in the compressive part of the section reaches 0.015 at the same time when the strain in the bottom layer of the tensile reinforcement reaches the rupture strain (0.1). Same as UHP-FRC sections with 16 in height, the compressive depth of the section reduces when the amount of tensile reinforcement reduces.

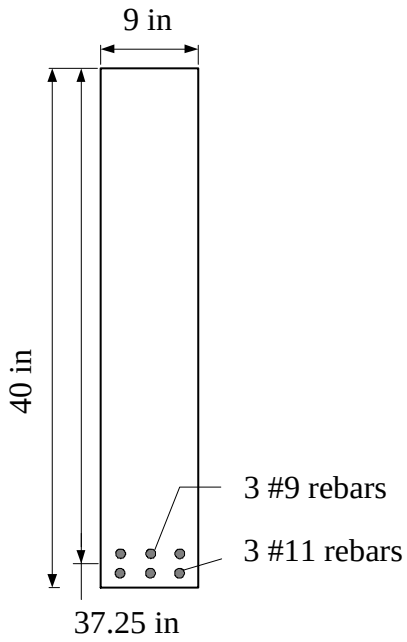

Figure 4-36 Section dimension and arrangement of longitudinal reinforcement steel rebars for section UHP/St60 40R-3

Table 4-9 design and section parameters for section UHP/St60 40R-3

f 'c =	22 ksi	reinf. Type=	Grade 60	ρ =	2.22%
e_{cu}=	0.015	max strain=	0.100	ρ_{TA}=	17.33%

Beam Width, b = 9 in

Total Beam Depth, h= 40 in

β1= 0.65

H.M.bars?	bar size	A_{st}	d
	#	[in^2]	[in]
3	11	4.68	38.5
3	9	3	36

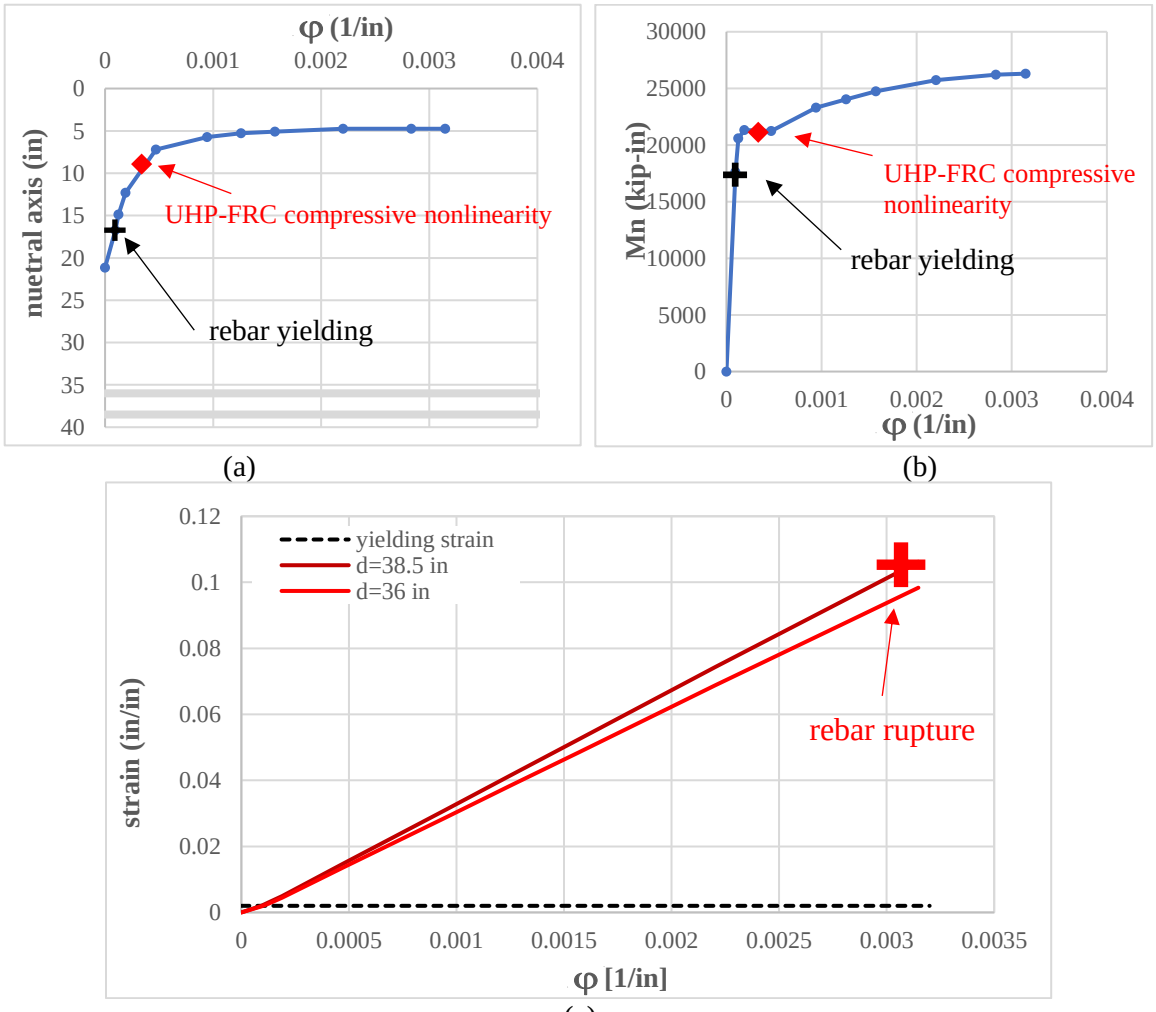

Figure 4-37 The changes of a) neutral axis, b) moment capacity and c) strain in rebars in section UHP/St60 40R-3

UHP/St60 40R-4

Figure 4-38 shows the section dimension and arrangement of longitudinal reinforcement steel rebars for section UHP/St60 40R-4. Table 4-10 summarizes the design and section parameters for section UHP/St60 40R-4. Since the amount of reinforcement in this section is less than UHP/St60 40R-3, the strain in the reinforcement reaches the usable rupture strain (0.1) prior to crushing in the concrete at the top layer in the compression part of the section.

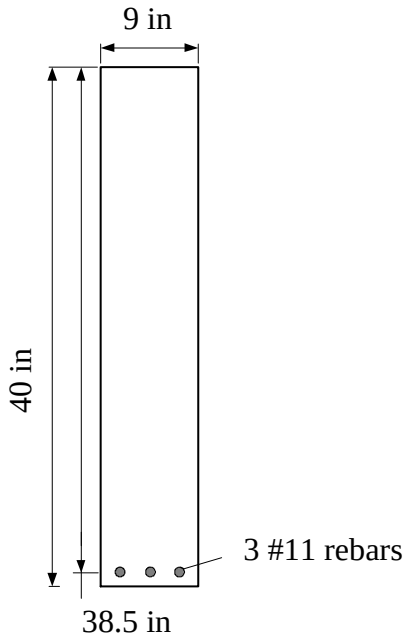

Figure 4-38 Section dimension and arrangement of longitudinal reinforcement steel rebars for section UHP/St60 40R-4

Table 4-10 design and section parameters for section UHP/St60 40R-4

f 'c =	22 ksi	reinf. Type=	Grade 60	ρ =	1.35%
e_{cu}=	0.015	max strain=	0.10	ρ TA=	17.33%

Beam Width, b =	9 in
Total Beam Depth, h=	40 in
β1=	0.65

H.M.bars?	bar size #	A_{st} [in^2]	d [in]
3	11	4.68	38.5

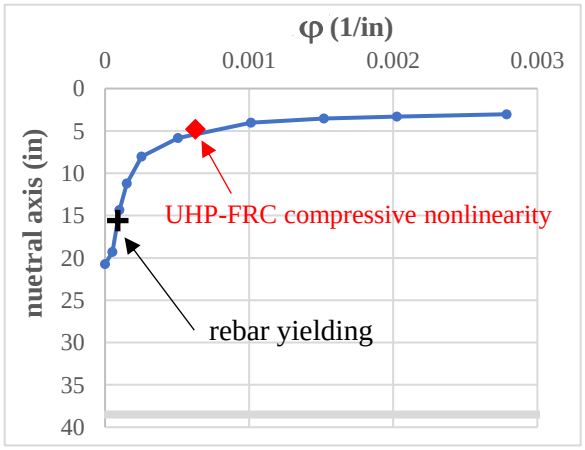

(a)

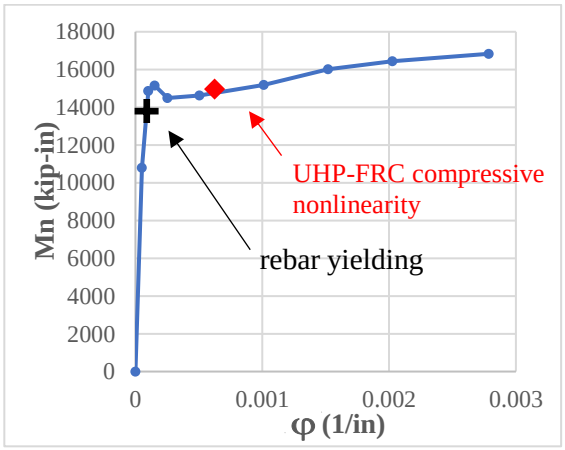

(b)

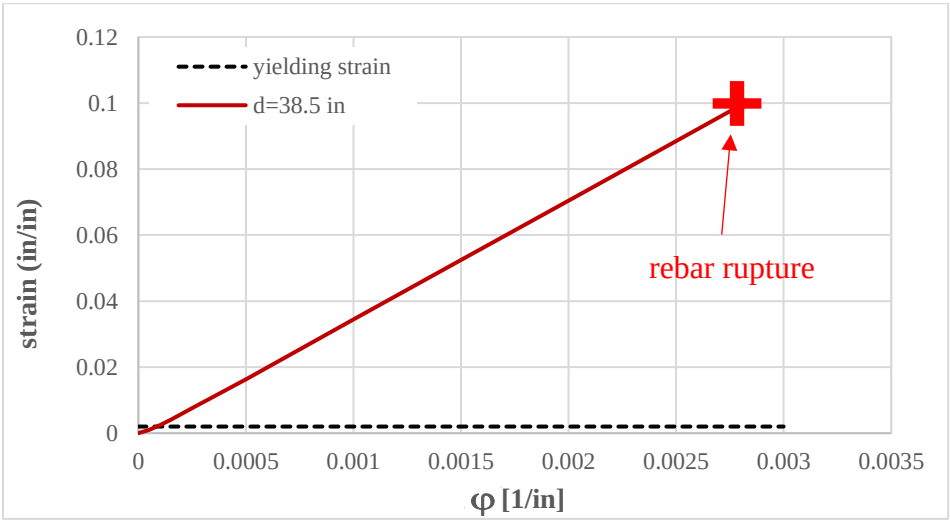

(c)

Figure 4-39 The changes of a) neutral axis, b) moment capacity and c) strain in rebars in section UHP/St60 40R-4

Figure 4-40 compares the moment curvature diagrams of UHP/St60 40R-1, UHP/St60 40R-2, UHP/St60 40R-3 and UHP/St60 40R-4. Same as the section with a height of 16 in, when the total amount of the tensile reinforcement is reduced, the ductility tends to increase. But this ductility increasing is ceased when the failure mode changes from concrete crushing to rupture in the tensile reinforcement. If the total amount of tensile reinforcement becomes below a certain threshold (UHP/St60 40R-3), not only the flexural capacity reduces, but also the ductility will reduce. Same as the previous set of sections, when higher amount of reinforcement is used, a better utilization of the ultra-high performance fiber reinforced concrete is achieved. It should be noted that, the tributary reinforcement ratio was the same in all the three sections.

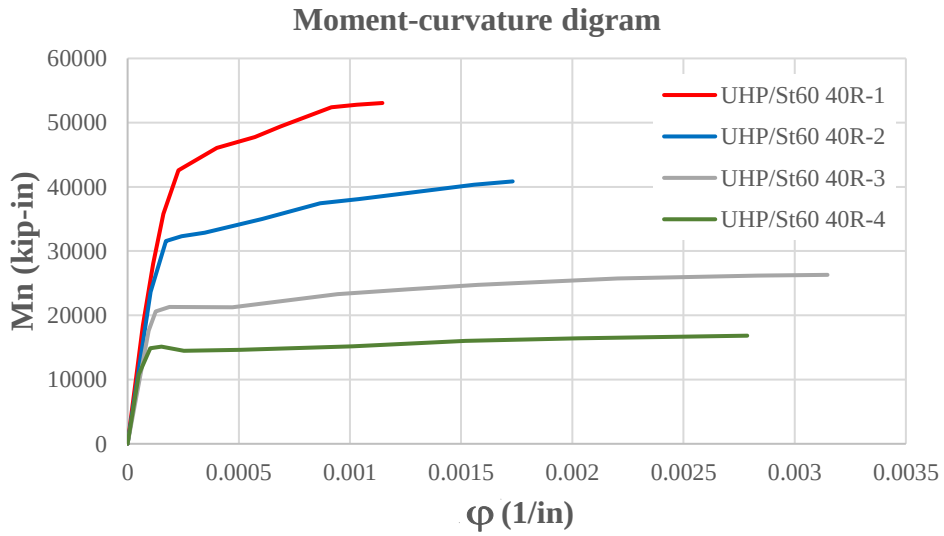

Figure 4-40 Comparison between moment curvature diagram of UHP/St60 40R-1, UHP/St60 40R-2, UHP/St60 40R-3 and UHP/St60 40R-4

4.6.3 Section property and reinforcement arrangement (I-shape section)

A common practice for designing large sections is to optimize the shape of the cross section to better utilize the materials. One way to implement this technique in concrete elements is to use a I- shape or a box section. When the thickness of the web is reduced, the loading from the weight of the removed part is reduced. However, since the flanges are located at the top and bottom of the section, the moment of inertia of the section is effectively kept high. Furthermore, when a section is designed with Ductile Concrete Strong Reinforcement (DCSR) design concept, since part of the ductility is coming from ductility of the ultra-high performance fiber reinforced concrete in compression, if the area of the concrete in compression zone is reduced, the section will show larger ductility. A similar concept is commonly used in traditional reinforced concrete design methods where the ductile failure is due to yielding of the steel reinforcement. But, in those methods same as a limited area for ductile concrete in compression, the amount of steel reinforcement is limited to ensure that the yielding in the reinforcements starts prior to concrete crushing.

In this section, the 40-in sections that were analyzed in the previous section is re-analyzed based on the new I-shaped sections. Also, another series of 120-in height section are presented and analyzed for use of ultra-high performance fiber reinforced concrete in long-span bridges with high loading demands. Since in these series of analyses, merely the section is analyzed, the dead load of the whole component will not show the effectiveness of this method, however, this I-shape/box shape is used for long-span bridge design later in this report.

UHP/St60 40I-1

Figure 4-41 shows the section dimension and arrangement of longitudinal reinforcement steel rebars for section UHP/St60 40I-1. Table 4-11 summarizes the design and section parameters for section UHP/St60 40I-1. In this section, the top layer in the compressive part of the section reaches 0.015 prior to the strain in the bottom layer of the tensile reinforcement reaches the rupture strain (0.1). Since the compression zone of the section is I-shaped and the web width is reduced, the total compressive force will reduce. As shown in Figure 4-42, the neutral axis is deeper in comparison with the UHP/St60 40R-2, which has the same amount of reinforcement but has a rectangular section. Also, due to this reduction in compression area, the nonlinearity of the section starts with UHP-FRC as it reaches the strain value of 0.003 earlier than yielding occurs in reinforcement.

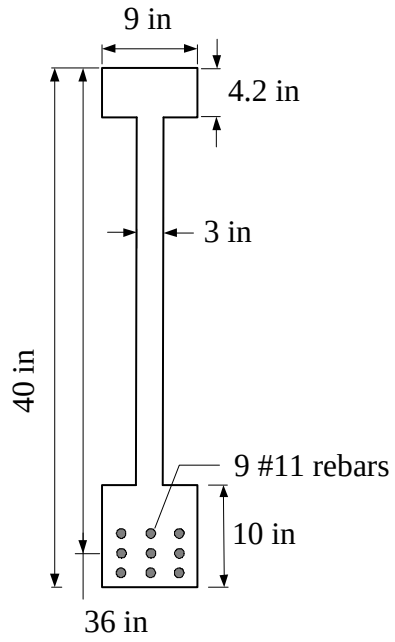

Figure 4-41 Section dimension and arrangement of longitudinal reinforcement steel rebars for section UHP/St60 40I-1

Table 4-11 design and section parameters for section UHP/St60 40I-1

f 'c =	22 ksi	reinf. Type=	Grade 60	ρ =	4.05%
e_{cu}=	0.015	max strain=	0.031	ρ_{TA}=	17.33%

Beam Width, b =	9 in
Total Beam Depth, h=	40 in
β1=	0.65
Flange thickness=	4.2 in
Web thickness=	3 in

H.M.bars?	bar size #	A_{st} [in^2]	d [in]
3	11	4.68	38.5
3	11	4.68	36
3	11	4.68	33.5

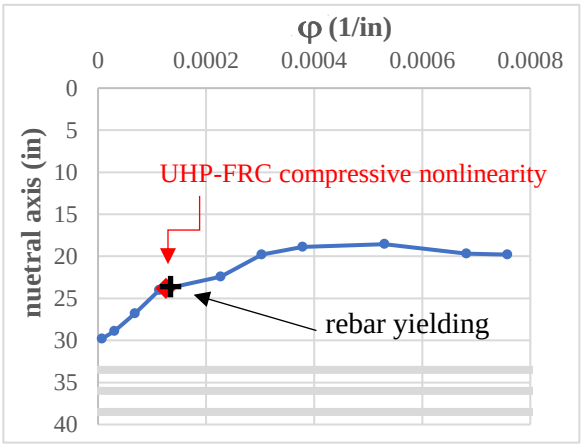

(a)

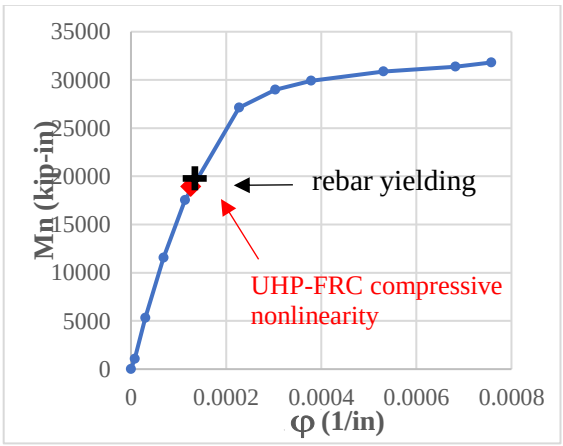

(b)

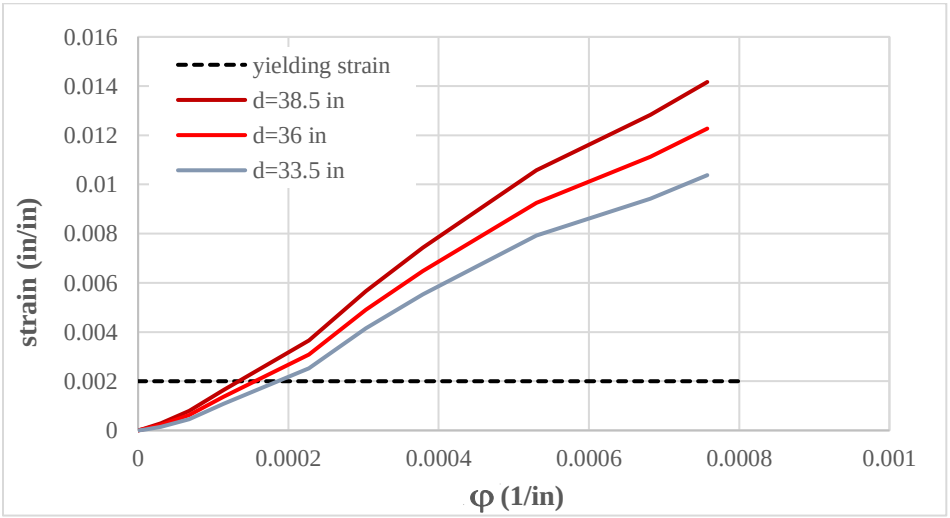

(c)

Figure 4-42 The changes of a) neutral axis, b) moment capacity and c) strain in rebars in section UHP/St60 40I-1

UHP/St60 40I-2

Figure 4-43 shows the section dimension and arrangement of longitudinal reinforcement steel rebars for section UHP/St60 40I-2. Table 4-12 summarizes the design and section parameters for section UHP/St60 40I-2. In this section, the total amount of reinforcement is deliberately selected such that the strain of the top layer in the compressive part of the section reaches 0.015 at the same time when the strain in the bottom layer of the tensile reinforcement reaches the rupture strain (0.1). Comparing to UHP/St60 40I-1, the neutral axis shifts upward, and the flexural capacity is reduced, where the reason is the reduction in the reinforcement amount used in this section. Also, since the compression zone is relatively stronger in this section, the yielding occurs prior to nonlinearity initiation in UHP-FRC.

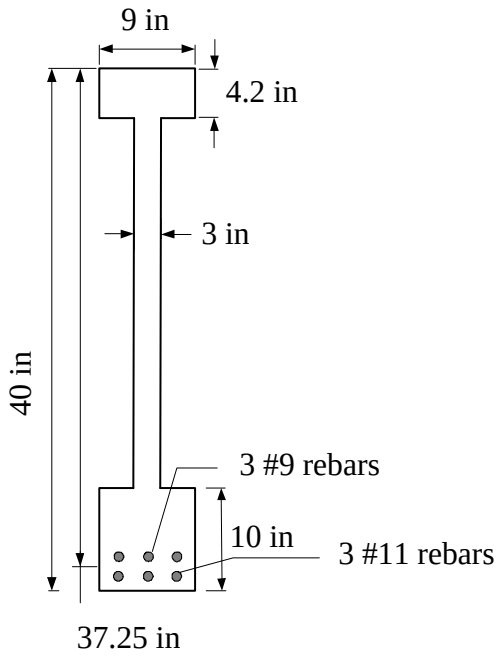

Figure 4-43 Section dimension and arrangement of longitudinal reinforcement steel rebars for section UHP/St60 40I-2

Table 4-12 design and section parameters for section UHP/St60 40I-2

f 'c =	22 ksi	reinf. Type=	Grade 60	ρ =	2.22%
e_{cu}=	0.015	max strain=	0.100	ρ_{TA}=	17.33%

Beam Width, b =	9 in
Total Beam Depth, h=	40 in
β1=	0.65
Flange thickness=	4.2 in
Web thickness=	3 in

H.M.bars?	bar size	A_{st}	d
	#	[in^2]	[in]
3	11	4.68	38.5
3	9	3	36

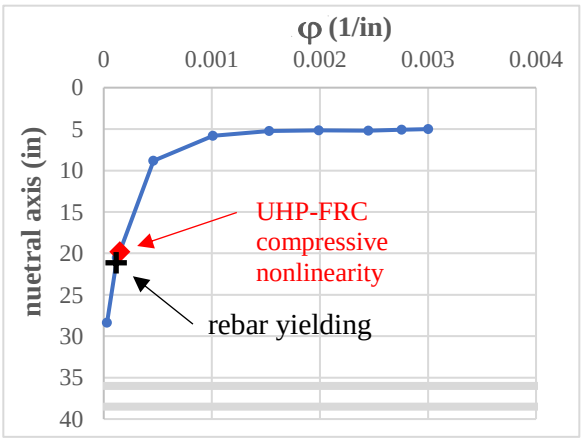

(a)

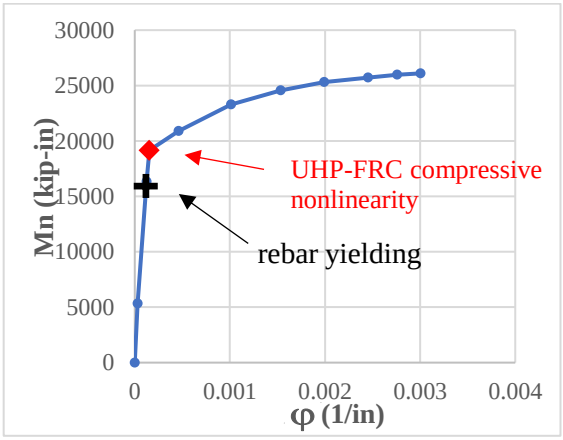

(b)

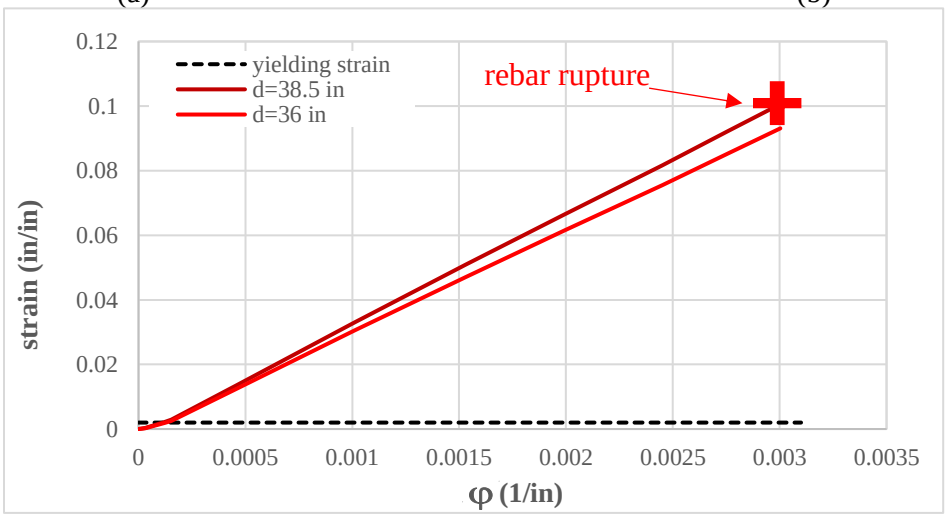

(c)

Figure 4-44 The changes of a) neutral axis, b) moment capacity and c) strain in rebars in section UHP/St60 40I-2

UHP/St60 40I-3

Figure 4-45 shows the section dimension and arrangement of longitudinal reinforcement steel rebars for section UHP/St60 40I-3. Table 4-13 summarizes the design and section parameters for section UHP/St60 40I-3. In this section, the total amount of reinforcement is even less than the previous one. Hence, the rupture strain is reached prior to concrete crushing.

The results of the numerical analysis for this section are presented in Figure 4-46. The curvature increment is stopped when the strain in the rebars reaches the rupture value (the last point in the plots). In this section the concrete does not crush. For this reason, comparing to the section UHP/St60 40I-2, both the maximum curvature and the maximum flexural strength drops.

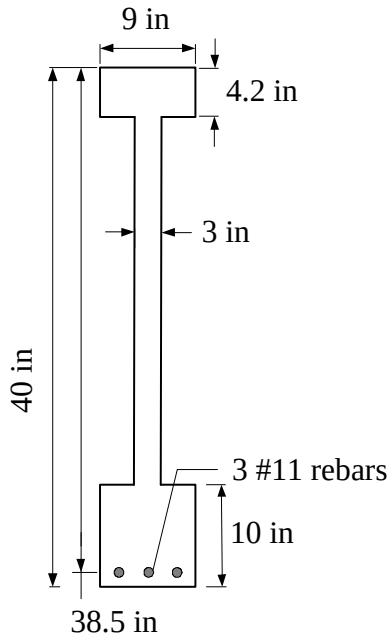

Figure 4-45 Section dimension and arrangement of longitudinal reinforcement steel rebars for section UHP/St60 40I-3

Table 4-13 design and section parameters for section UHP/St60 40I-3

f 'c =	22 ksi	reinf. Type=	Grade 60	ρ =	1.35%
e_{cu}=	0.015	max strain=	0.100	ρ_{TA}=	17.33%

Beam Width, b =	9 in
Total Beam Depth, h=	40 in
β1=	0.65
Flange thickness=	4.2 in
Web thickness=	3 in

H.M.bars?	bar size #	A_{st} [in^2]	d [in]
3	11	4.68	38.5

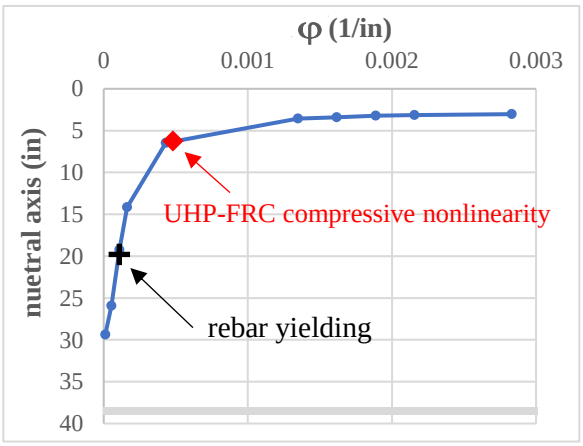

(a)

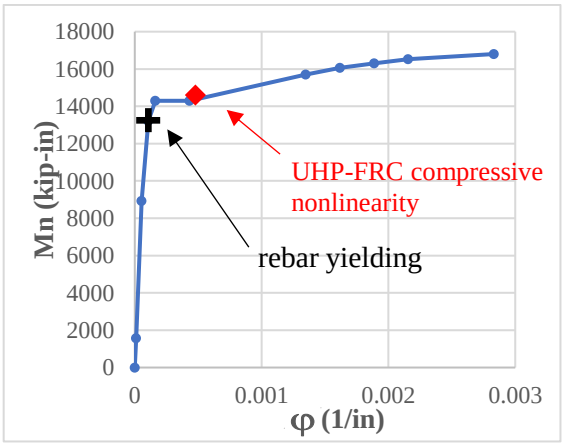

(b)

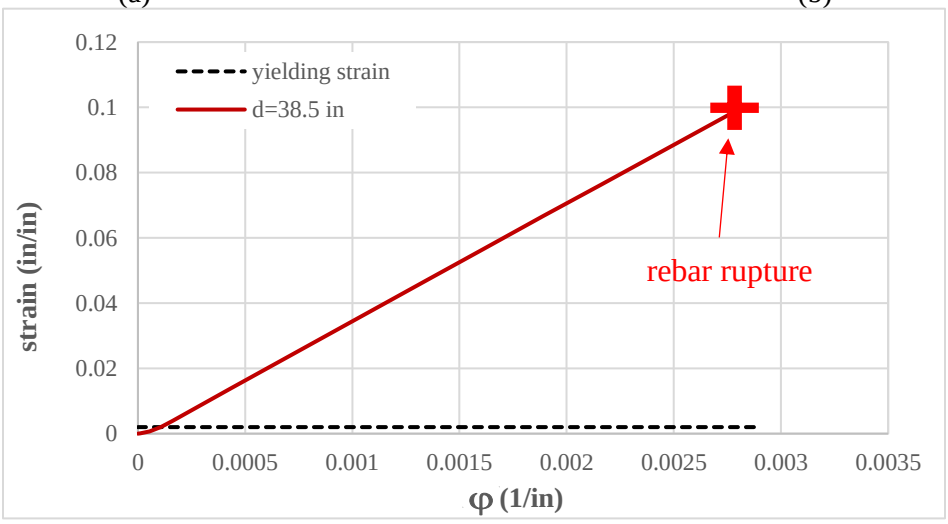

(c)

Figure 4-46 The changes of a) neutral axis, b) moment capacity and c) strain in rebars in section UHP/St60 40I-3

UHP/St60 120I-1

Figure 4-47 shows the section dimension and arrangement of longitudinal reinforcement steel rebars for section UHP/St60 120I-1. Table 4-14 summarizes the design and section parameters for section UHP/St60 120I-1. In this section, high amount of steel reinforcement is used. Figure 4-48 (a) shows that the is very deep which is due to high amount of reinforcement. Although the reinforcement is strong, the failure behavior of the section shows a great nonlinearity. This nonlinearity starts when the maximum compressive strain in UHP-FRC reaches 0.003 and further increases when the by yielding in rebar layers. Due to high amount of reinforcement and a low neutral axis even in larger curvatures, the strain levels in rebar layers are kept low. Even top layer of the rebars are still in linear zone (Figure 4-48 (c)).

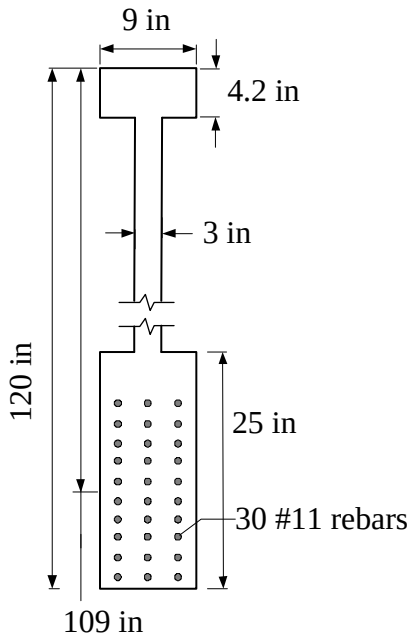

Figure 4-47 Section dimension and arrangement of longitudinal reinforcement steel rebars for section UHP/St60 120I-1

Table 4-14 design and section parameters for section UHP/St60 120I-1

f 'c =	22 ksi	reinf. Type=	Grade 60	ρ =	4.42%
e_{cu}=	0.015	max strain=	0.014	ρ_{TA}=	23.11%

Beam Width, b = 9 in
Total Beam Depth, h= 120 in
β1= 0.65
flange thickness tf= 4.2 in
web thickness= 2.5 in

Each row represents two layers of rebar

H.M.bars?	bar size #	A_{st} [in^2]	d [in]
6(2*3)	11	9.36	117.75
6(2*3)	11	9.36	112.75
6(2*3)	11	9.36	107.75
6(2*3)	11	9.36	102.75
6(2*3)	11	9.36	97.75

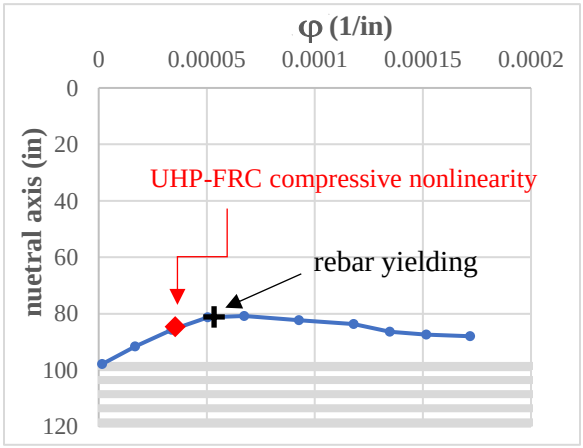

(a)

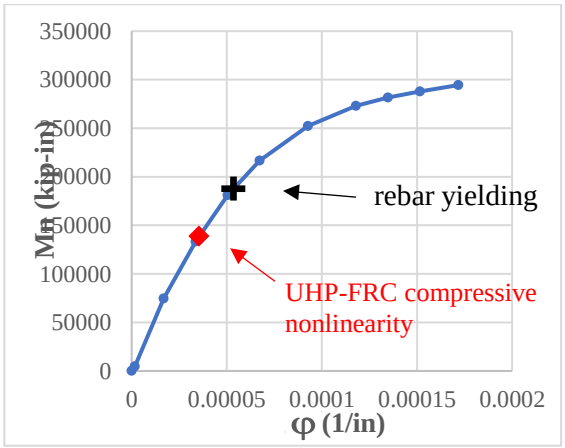

(b)

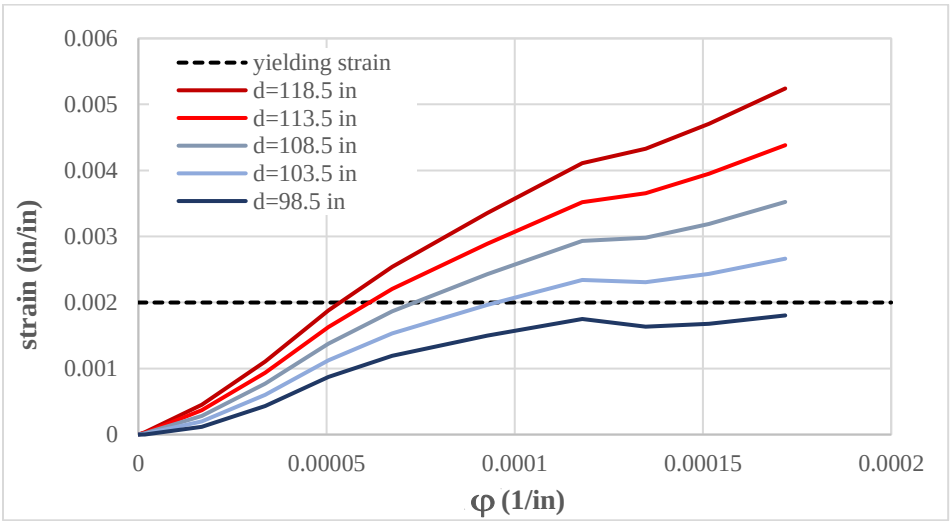

(c)

Figure 4-48 The changes of a) neutral axis, b) moment capacity and c) strain in rebars in section UHP/St60 120I-1

UHP/St60 120I-2

Figure 4-49 shows the section dimension and arrangement of longitudinal reinforcement steel rebars for section UHP/St60 120I-2. Table 4-15 summarizes the design and section parameters for section UHP/St60 120I-2. The total amount of reinforcement in this section is half of the UHP/St60 120I-1 section. However, even with the half ratio of reinforcement, the nonlinearity starts with the UHP-FRC reaching the 0.003 strain value prior to rebar yielding. In this section, the total reinforcement ratio (ρ = 2.19%) is slightly less than this ratio for UHP/St60 40I-2 (ρ = 2.22%); but the UHP-FRC compressive nonlinearity precedes the steel yielding.

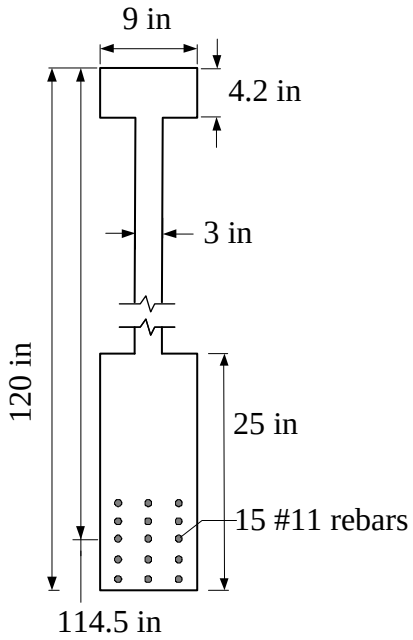

Figure 4-49 Section dimension and arrangement of longitudinal reinforcement steel rebars for section UHP/St60 120I-2

Table 4-15 design and section parameters for section UHP/St60 120I-2

f 'c =	22 ksi	reinf. Type=	Grade 60	ρ =	2.19%
e_{cu}=	0.015	max strain=	0.038	ρ_{TA}=	17.33%

Beam Width, b =	9 in
Total Beam Depth, h=	120 in
β1=	0.65
flange thickness tf=	4.2 in
web thickness=	2.5 in

H.M.bars?	bar size #	A_{st} [in^2]	d [in]
3	11	4.68	118.5
3	11	4.68	116
3	11	4.68	113.5
3	11	4.68	111
3	11	4.68	108.5

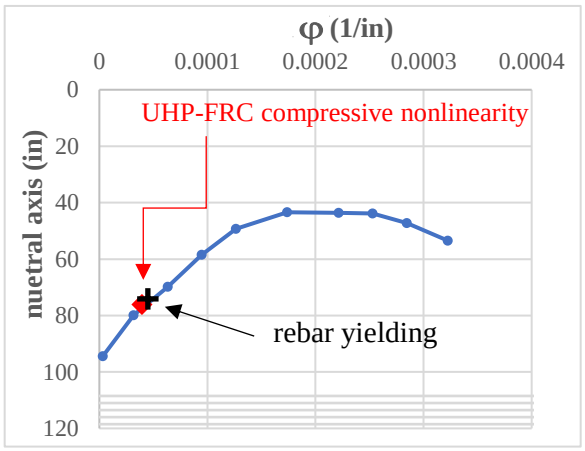

(a)

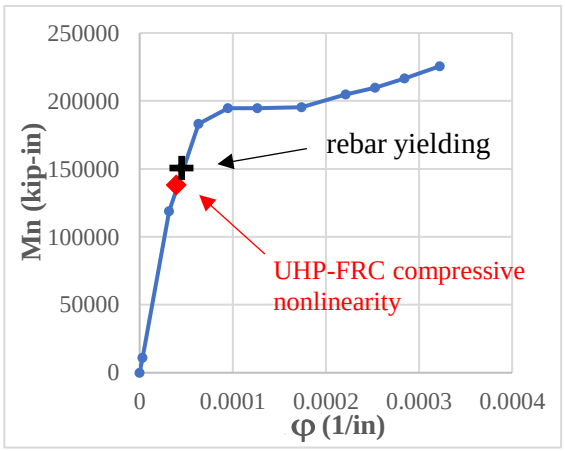

(b)

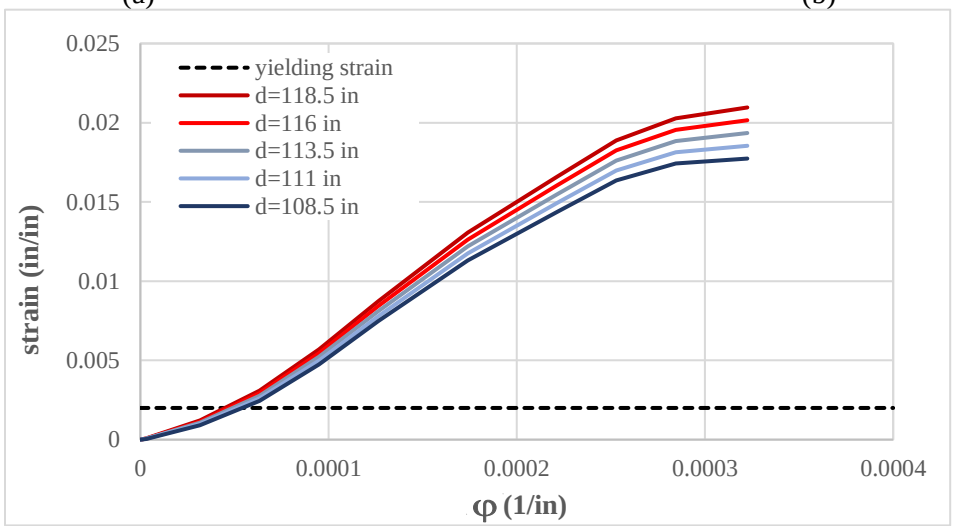

(c)

Figure 4-50 The changes of a) neutral axis, b) moment capacity and c) strain in rebars in section UHP/St60 40I-2

UHP/St60 120I-3

Figure 4-51 shows the section dimension and arrangement of longitudinal reinforcement steel rebars for section UHP/St60 120I-3. Table 4-16 summarizes the design and section parameters for section UHP/St60 120I-3. In this section, the total amount of reinforcement is even less than the previous one. Hence, the rupture strain is reached prior to concrete crushing.

The results of the numerical analysis for this section are presented in Figure 4-52. The curvature increment is stopped when the strain in the rebars reaches the rupture value (the last point in the plots). In this section the concrete does not crush. For this reason, comparing to the section UHP/St60 40I-2, both the maximum curvature and the maximum flexural strength drops.

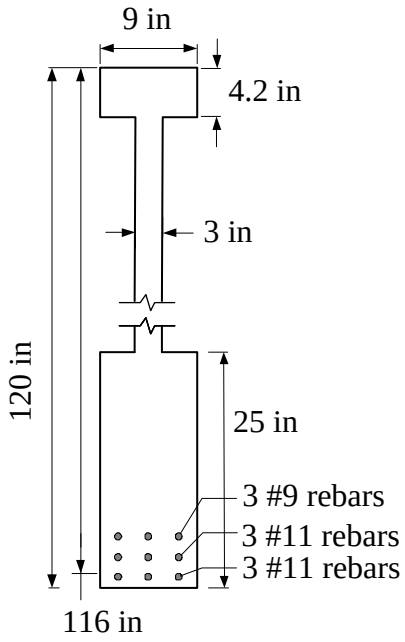

Figure 4-51 Section dimension and arrangement of longitudinal reinforcement steel rebars for section UHP/St60 120I-3

Table 4-16 design and section parameters for section UHP/St60 120I-3

f 'c =	22 ksi	reinf. Type=	Grade 60	ρ =	1.16%
e_{cu}=	0.015	max strain=	0.100	ρ_{TA}=	17.33%

Beam Width, b =	9 in
Total Beam Depth, h=	120 in
β1=	0.65
flange thickness tf=	4.2 in
web thickness=	2.5 in

H.M.bars?	bar size #	A_{st} [in^2]	d [in]
3	11	4.68	118.5
3	11	4.68	116
3	9	3	113.5

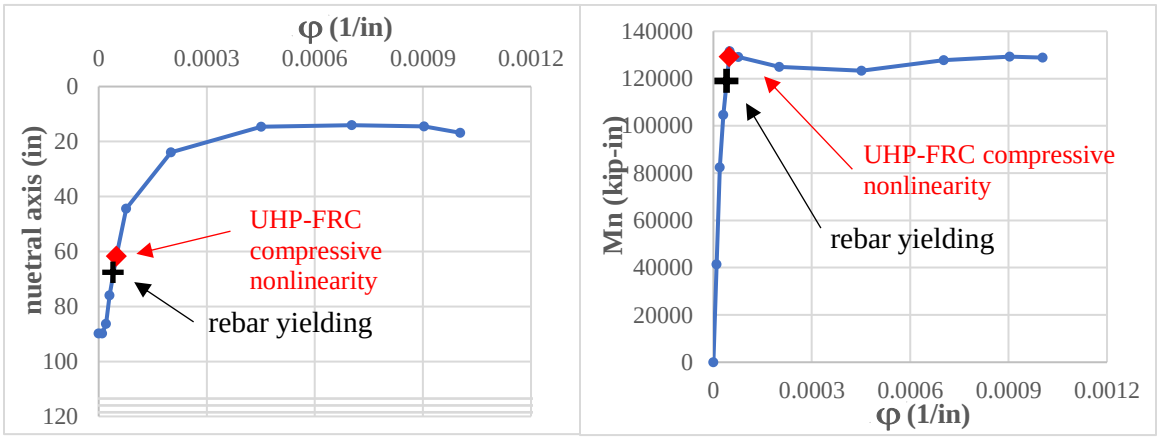

(a) (b)

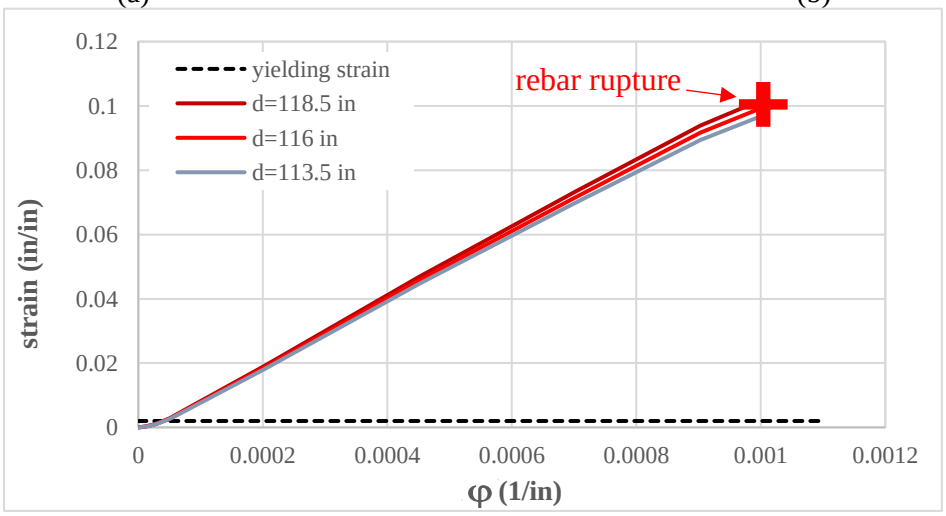

(c)

Figure 4-52 The changes of a) neutral axis, b) moment capacity and c) strain in rebars in section UHP/St60 120I-3

4.6.4 Summary

From the analyses it can be observe that:

- A comparison between UHP/St60 16R-2 and RC/St60 16R-1 demonstrates that if the appropriate amount of reinforcement is selected, not only the strength increases by a large amount, but the section would also be able to reach a curvature more in UHPFRC section.
- The nonlinear behavior of the section originates in both the yielding of the steel reinforcement rebars in tension and the compressive nonlinear behavior ultra-high performance fiber reinforced concrete. In order to reach the strain value of 0.003 in compression for UH-FRC, the reinforcement amount should be increased. The results show that, as the height of the beam increase the required reinforcement ratio that causes the compressive nonlinearity reduces.
- There is a trade-off between the post yielding strength hardening and the ductility in UHPFRC sections (applicable to concrete crushing failure types). When the steel amount is increases the overstrength and post yielding increases and, at the same time, the ductility decreases.
- For I-shape section beam or girder, the area of the compression zone is reduced. This will help the section to maintain a deep neutral axis. Consequently, the strain in the top layer of the UHP-FRC will increase with a greater rate. If UHP-FRC ,with a ductile compressive behavior and a large usable maximum compressive strain, is used, the nonlinearity starts due to higher strains in UHP-FRC. In this way, the use of material will reduce while at the same time a minimum required strength and ductility will be achieved.

Chapter 5
Part I

Application of DCSR Design Concepts in Bridges and Buildings

5.1 Bridge Girders Designed with DCSR Design Concept

In this section the practical use and design based on ductile-concrete strong-steel (DCSR) is presented. Different number of bridge sections with different span length are designed based on DCSR design concept.

5.1.1 Material

Ultra-High Performance Fiber Reinforced Concrete (UHP-FRC)

In this modeling, an Ultra-High Performance Fiber Reinforced Concrete (UHP-FRC) is used as the matrix of the section. In this series of analyses, a maximum compressive strength of 22 ksi is considered for the design purposes. The stress-strain behavior used for the design in from the experimental test results presented by Aghdasi et al. (2016). In this study, the same curve is scaled to a maximum compressive stress of 22 ksi. Figure 5-1 represents the compressive stress-strain curve used in this study. The initial module of elasticity of 6800 ksi is used for UHP-FRC in compression and the same value for it in tension up to the cracking point.

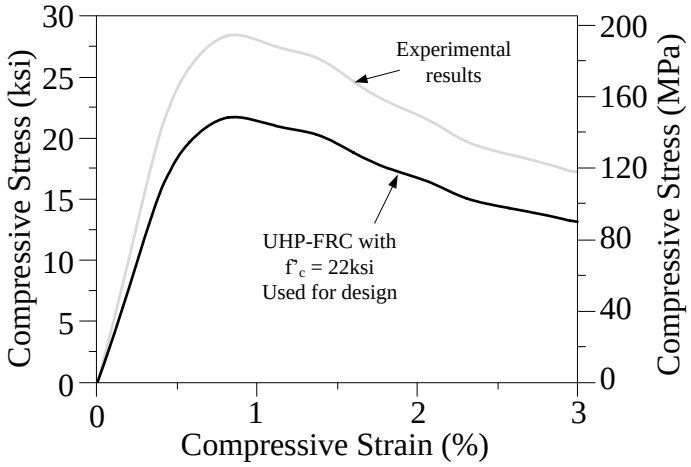

Figure 5-1 Compressive stress-strain curve for the UHP-FRC from experimental results (Aghdasi et al., 2016) and the scaled curve used in this study

Reinforcement

For reinforcement, ASTM A1035/A1035M bars are considered. These types of steel rebars are low in carbon and high in chromium that results in more resistance to corrosion and a higher tensile strength than conventional reinforcement (Rizkalla et al., 2005). ACI Design Guide for the Use of

ASTM A1035/A1035M Grade 100 (690) Steel Bars for Structural Concrete (ACI ITG-6R-10), provides an approximate lower bound behavior of Grade 100 bars by the following equations:

$$f_s = 29{,}000\varepsilon_s \quad ksi \quad for \quad 0 \le \varepsilon_s \le 0.0024 \quad Equation\ 5.1$$

$$f_s = 170 - \frac{0.43}{\varepsilon_s + 0.0019} \quad ksi \quad for \quad 0.0024 \le \varepsilon_s \le 0.02 \quad Equation\ 5.2$$

$$f = 150 \quad ksi \quad for \quad 0.02 \le \varepsilon_s \le 0.06 \quad Equation\ 5.3$$

The stress-strain curve is shown in Figure 5-2.

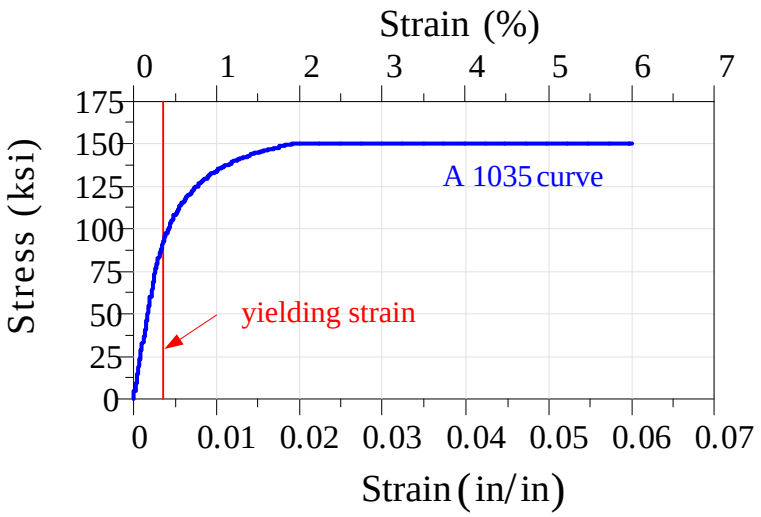

Figure 5-2 Stress-strain curve for A1035 reinforcing steel rebar

A simplified curve is provided in ACI design guide for design purposes. Figure 5-3 compares the idealized stress-strain curve with the idealized bilinear elastic-plastic stress-strain relationship for simplified design (ACI ITG-6R-10).

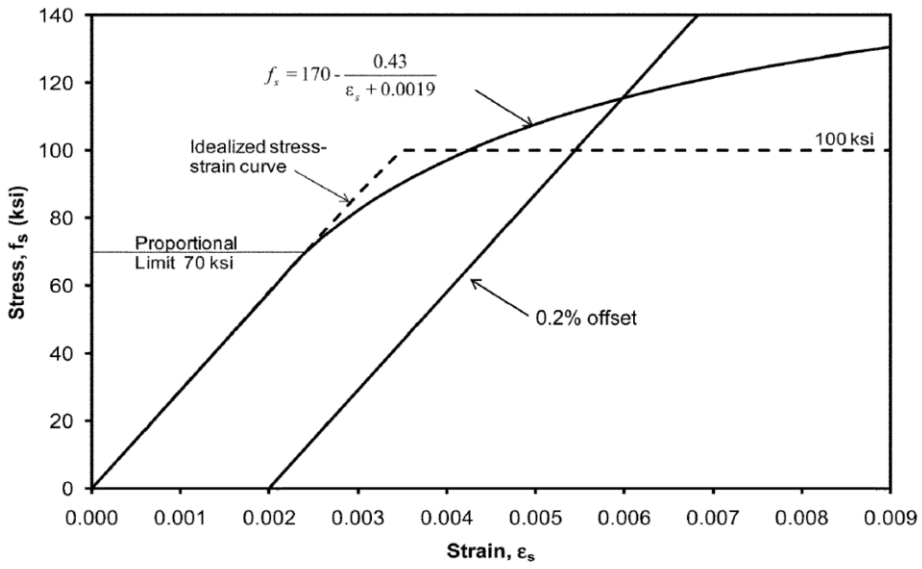

Figure 5-3 Approximated nonlinear stress-strain relationship of ASTM A1035/A1035M Grade 100 (690) steel and idealized bilinear elastic-plastic stress-strain relationship for simplified design (ACI ITG-6R-10)

5.1.2 Loadings

For design purposes in this section, AASHTO loading criteria are used (AASHTO, 2017).

For vehicular live loading for bridges, AASHTO requires a combination of:

- Design truck or design tandem
- Design lane load

The lanes are loading over a width of 10.0 ft transversely.

Design truck

Figure 5-4 shows the characteristics of the design truck. To produce the extreme force effects the spacing between the two 32 kips axles varies from 14 ft to 30 ft.

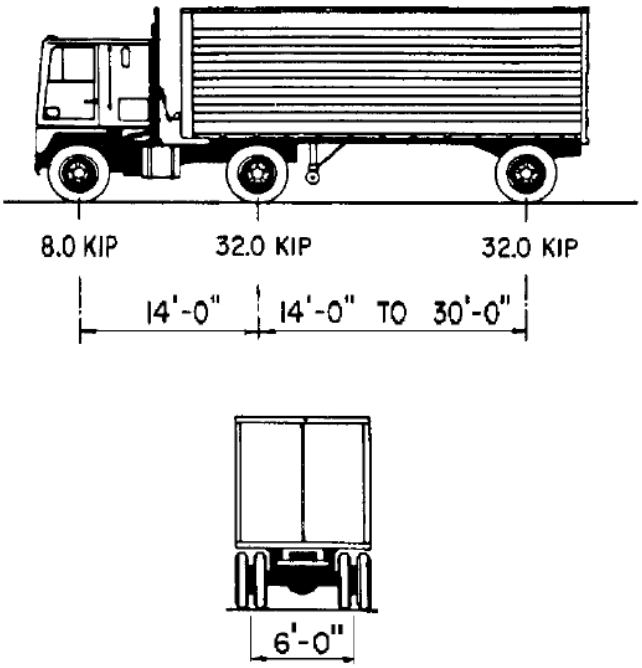

Figure 5-4 characteristics of the design truck (AASHTO)

Design lane load

As per AASHTO, a design lane load of 0.64 klf is applied. This loading is uniformly distributed in the longitudinal direction and for the transverse direction a lane with a width of 10.0 ft is considered.

Deflection

For deflection calculation, all the design lanes were loaded, and the supporting girders were designed to deflect equally as per AASHTO. The deflection was calculated based on the maximum of deflection values under three following loadings:

- The resulting from the design truck only applied to all lanes
- 25% of the design truck loading taken together with the design lane load
- And the live load for load combination of Service I (Table 5-1)

Table 5-1 load combinations and load factors (AASHTO, 2017)

Load Combination Limit State	*DC DD DW EH EV ES EL PS CR SH*	*LL IM CE BR PL LS*	*WA*	*WS*	*WL*	*FR*	*TU*	*TG*	*SE*	Use One of These at a Time				
										EQ	*BL*	*IC*	*CT*	*CV*
Strength I (unless noted)	γ_p	1.75	1.00	—	—	1.00	0.50/1.20	γ_{TG}	γ_{SE}	—	—	—	—	—
Strength II	γ_p	1.35	1.00	—	—	1.00	0.50/1.20	γ_{TG}	γ_{SE}	—	—	—	—	—
Strength III	γ_p	—	1.00	1.40	—	1.00	0.50/1.20	γ_{TG}	γ_{SE}	—	—	—	—	—
Strength IV	γ_p	—	1.00	—	—	1.00	0.50/1.20	—	—	—	—	—	—	—
Strength V	γ_p	1.35	1.00	0.40	1.0	1.00	0.50/1.20	γ_{TG}	γ_{SE}	—	—	—	—	—
Extreme Event I	γ_p	γEQ	1.00	—	—	1.00	—	—	—	1.00	—	—	—	—
Extreme Event II	γ_p	0.50	1.00	—	—	1.00	—	—	—	—	1.00	1.00	1.00	1.00
Service I	1.00	1.00	1.00	0.30	1.0	1.00	1.00/1.20	γ_{TG}	γ_{SE}	—	—	—	—	—
Service II	1.00	1.30	1.00	—	—	1.00	1.00/1.20	—	—	—	—	—	—	—
Service III	1.00	0.80	1.00	—	—	1.00	1.00/1.20	γ_{TG}	γ_{SE}	—	—	—	—	—
Service IV	1.00	—	1.00	0.70	—	1.00	1.00/1.20	—	1.0	—	—	—	—	—
Fatigue I— *LL, IM & CE* only	—	1.50	—	—	—	—	—	—	—	—	—	—	—	—
Fatigue II— *LL, IM & CE* only	—	0.75	—	—	—	—	—	—	—	—	—	—	—	—

5.1.3 Non-prestress girders with DCSR design concept

Deck Bulb-Tee (DBT) section

In a prior study, a modified non-prestressed UHP-FRC Deck Bulb-Tee (DBT) having a 95 ft long single span bridge was developed. In that research, two sections designed with Ductile-Concrete Strong-Reinforcement (DCSR) design concept were compared to a

conventional 95 ft long prestressed concrete Deck Bulb Tee (DBT) section with a 65 in depth (Kaka and Chao, 2018). The design is based on Strength I and Service III limit states per AASHTO LRFD specifications for HL-93 loading. Effective prestress is 160 ksi, and design concrete compressive strength used for the prestressed concrete beam is 8 ksi. The number of strands, Mn and Mcr of the DBT 65 prestressed girder are shown in Table 5-2. The two sections that are designed based on DCSR design concept, are designed with different Modulus of Rupture (MOR). For one of them a flexural cracking strength of f_r =2 ksi is considered in the design limitations, while for the other one a flexural cracking strength of f_r =3 ksi is used. These lower bound MORs are limitations are applied at the full-service load, so the girder does not experience a flexural cracking. Figure 5-5and Table 5-3 represents the section information for the two designed sections. The DBT Modified 65 with a flexural cracking strength of f_r =2 ksi, is 30% heavier than DBT 65 and uses seven No. 11 ASTM A1035 Grade 100 reinforcing bars (Figure 5-5 (a)). On the other hand, the DBT Modified 65 with a flexural cracking strength of f_r =3 ksi, provides a more optimal section that benefits a lighter section. This section also uses seven No. 11 ASTM A1035 Grade 100 reinforcing bars.

Table 5-2 Cracking and nominal moment capacities of a conventional prestressed DBT girder compared to a non-prestressed UHP-FRC DBT girder (UT Arlington research) (Kaka and Chao, 2018)

Deck bulb Tee design		**Pre-stressed (Grade 270 low-relaxation strands)**			**UHP-FRC (12-No.11 A1035 Grade 100 steel)**		
Height of the girder (in)	**Length of girder (ft)**	**Number of strands**	**Mn (kip-in)**	**Mcr (kip-in)**	**Section**	**Mn (kip-in)**	**Mcr (kip-in)**
65	95	18-0.6″ strands	59,385	47,306	DBT Modified 64	112,891	54,964 (f_r = 3 *ksi*)
					DBT Modified 65	116,635	49,468 (f_r = 2 *ksi*)

*Contribution of UHP-FRC in tension is ignored
Note: all the stress calculations are based on transformed section properties;

Table 5-3 Section information of a conventional prestressed DBT girder
Compared to a non-prestressed UHP-FRC DBT girder (UT Arlington research) (Kaka and Chao, 2018)

Section properties	**Height (in.)**	**Height of web (in.)**	**Width of flange (in.)**	**Area (in.^{2})**	**Inertia (in.^{4})**	**y_{bottom} (in.)**	**Weight (kip/ft)**
DBT 65	65	45	72	1003	559,367	41.95	1.05
DBT Modified 64	64	41	72	1007	657,902*	35.91	1.05
DBT Modified 65	65	39	72	1237	841,853*	34.04	1.30

*Transformed

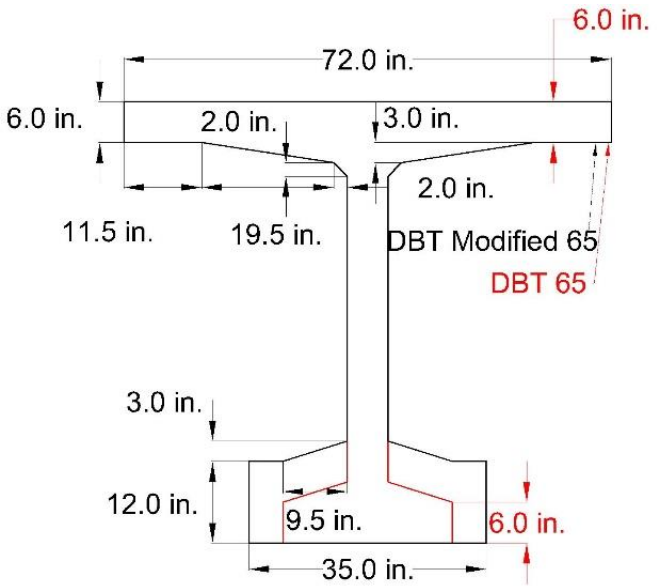

(a)

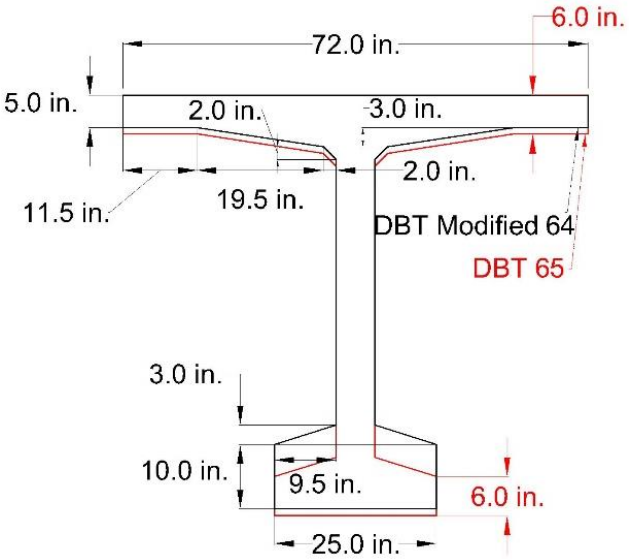

(b)

Figure 5-5 UHP-FRC DBT girder section: (a) DBT Modified 65: fr = 2 ksi and (b) DBT Modified 64: fr = 3 ksi (Kaka and Chao, 2018)

A 250 ft long bridge with UHP-FRC DBT girders

From the large-scale testing of UHP-FRC flexural members, it was observed that UHP-FRC has a very high flexural cracking strength. The f_r for each specimen was calculated using its transformed section properties. The results are summarized and listed in Table 5-4. These f_r values are similar to that obtained from the small specimen discussed in Chapter 3. The high f_r of UHP-FRC in highly reinforced flexural members allows eliminating prestress in bridge girders. While the cracking in prestressed concrete girders is controlled by prestress, reinforced UHP-FRC girders' crack control is based on high cracking strength and section modulus of the beam. In fact, the cracks are well controlled even after the first cracking due to the bridging effect provide by the fibers and high amount of reinforcing bars. This type of new non-prestressed girders is achieved by utilizing the unique mechanical characteristics of UHP-FRC and Ductile-Concrete Strong-Reinforcement (DCSR) design concept. The synergistic interaction of UHP-FRC and a high amount of reinforcement allows the member to remain uncracked under the service load. The uncracked section keeps the deflection small. Additionally, the high compressive ductility of UHP-FRC guarantees a ductile failure of the member at ultimate loading. Using UHP-FRC with high-strength corrosion-resistant reinforcing bars can create a non-prestressed girder that not only provides all the advantages of a conventional precast prestressed concrete girder but also possesses other merits, which can eliminate issues that prestressed concrete girders encounter.

Table 5-4 Cracking moments and corresponding f_r of RC and UHP-FRC specimens

Specimen	Cracking load, kips (kN)	Cracking Moment, kip-in (kN-m)	ρ_{TA} (only bottom layer rebars are used for the calculation)	First cracking strength, f_r, ksi (MPa)
RC	12 (53)	342 (39)	---	0.76 (5.24)
UHP-FRC #1	60 (267)	1,710 (193)	17%	3.18 (21.92)
UHP-FRC #2	60 (267)	1,710 (193)	17%	3.2 (19.17)
UHP-FRC #3	50 (222)	1,425 (161)	11%	3.0 (18.41)

To further emphasize the DCSR design concept, a 250 ft long bridge with a modified DBT section was analyzed using finite element analysis (FEA) with AASHTO dead and live loads. Girders designed with the DCSR concept typically have a large overstrength for ultimate strength. Hence, the design is controlled at the full-service load level to have the tensile stress at the bottom fiber of the girder less than its cracking strength. To satisfy the design requirements at the service loads (AASHTO Service-I and Service-III Limit States), eight optimized non-prestressed UHP-FRC DBT girders were used for the 50 ft wide bridge (Figure 5-6). Because the limiting criterion in the design is the tensile stress of the girder at the bottom layer, the section dimensions were optimized based on FEA to lower the neutral axis. A cracking strength of 3 ksi was used because experimental test results indicated that it can be reached as long as the cracking-control longitudinal reinforcement (the bottom layer of the rebars) ratio, ρ_{TA}, is at least approximately 15%. To provide the minimum ρ_{TA}, 22 No. 11 Grade 100 rebars were used (ρ_{TA} =15.25%). These bars can be easily placed at the bottom of the girder (Figure 5-6 (a)). The girders meet the service load

requirements. In addition, the nominal moment capacity of the section is 898,812 kip-in., which is more than twice the factored moment demand of 404,222 kip-in. Using the shear capacity of UHP-FRC from the large-scale test results, these girders do not require any shear reinforcement. However, a minimum shear reinforcement as per ACI and AASHTO provisions should be used.

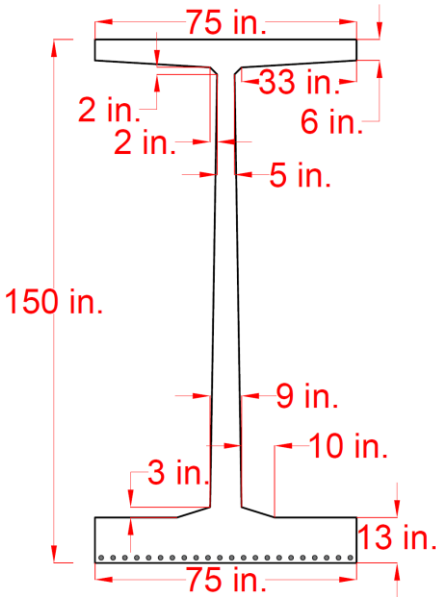

(a)

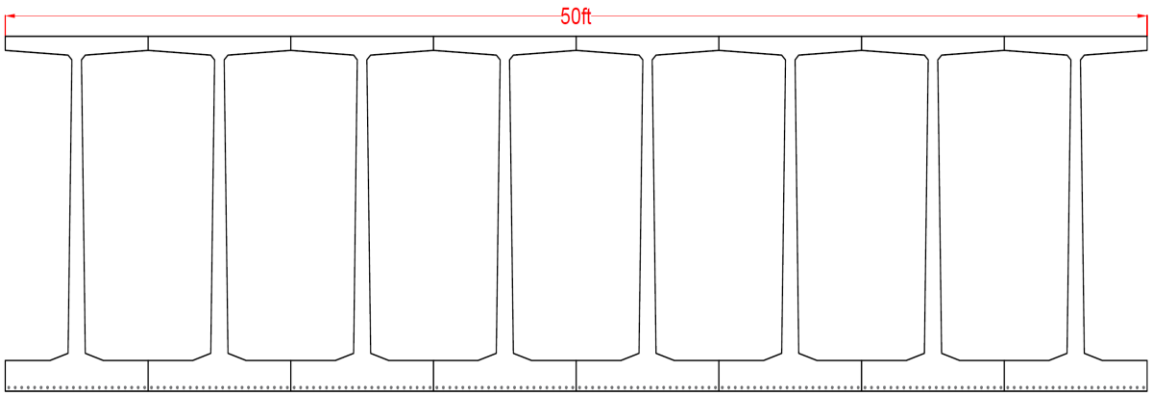

(b)

Figure 5-6 Prototype 250-ft long non-prestressed UHP-FRC DBT girders a) section dimensions and b) placement of eight girders providing a 50 ft width

Table 5-5 Section information of 250-ft long non-prestressed UHP-FRC DBT girder

Section properties	Height (in.)	Height of web (in.)	Flange width (in.)	Area (in^2)	Inertia (in^4)	y_{bottom} (in.)	Weight (kip/ft)
DBTM-150	150	126	75	2446.5	8,207,556	61.25	2.55

Optimized non-prismatic non-prestressed girders design with DCSR concepts for medium to long span bridges

One of the advantages of using Ductile-Concrete Strong-Reinforcement (DCSR) design concept is that construction of a non-prismatic section element is easily achievable because of eliminating the prestress. In this section, this feature of the DCSR is used to further optimize the section area and the total volume of Ultra-High Performance Fiber Reinforced Concrete (UHP-FRC).

Herein, three single span bridge girders with lengths of 95 ft (G95), 180 ft (G180) and 250 ft (G250) were designed and analyzed using finite element analysis (FEA) with AASHTO dead and live loads according to DCSR design concept. Since the ultimate capacity of a section designed by DCSR concept is naturally high, the girders were first designed by service load and then checked under ultimate loading, similar to the procedure for a conventional prestressed concrete girder.

In this study, box sections are developed to minimize the total area/weight of the girder. Using a box section with interior webs allows the designer to reduce the thickness of the top flange of the girder. The top flange thickness of all the UHP-FRC box girders, t_t (4.125 in., Figure 5-7), is the same as that of the second generation UHPC Pi-girders (Keierleber

et al., 2007). This thickness has proven sufficient to support AASHTO loads and local punching shears. Table 5-6 provides the section parameters of the UHP-FRC box sections.

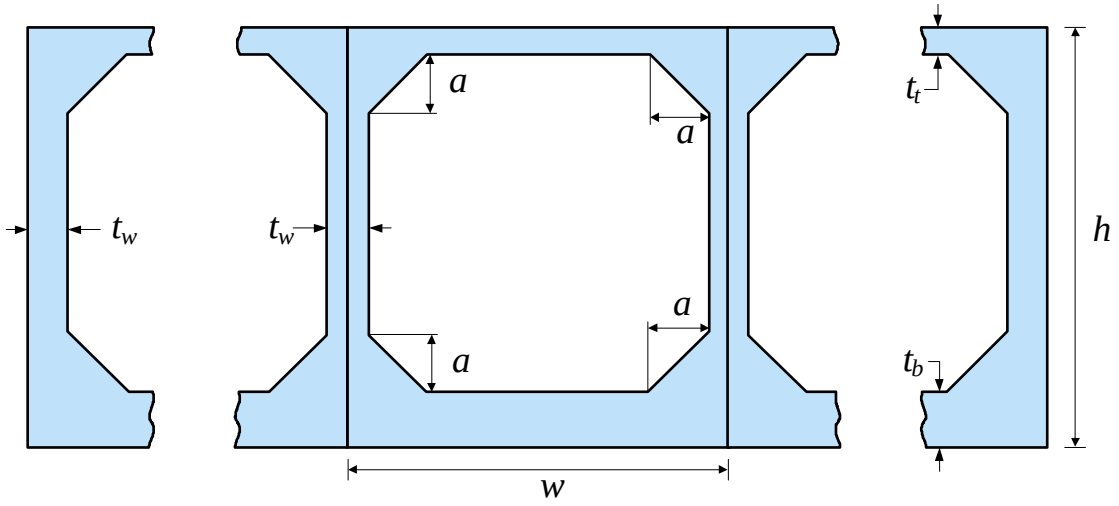

Figure 5-7 Box section unit with symmetrical dimensions

Table 5-6 Section parameters for all box girder sections

w (in.)	a (in.)	t_t (in.)
50	8	4.125

In each bridge, 12 box units shown in Figure 5-7 are used to create a bridge section having a total width of 50 ft. The box units can be connected through transverse post-tensioning. The shear strength of UHP-FRC is considered as 600 psi. ASTM A1035 high-strength reinforcing rebars (Gr. 100) are used in each unit. To provide the minimum longitudinal reinforcement, ρ_{TA}, 20 of #9 size rebars are used at the bottom layer of each unit and a ρ_{TA} of 13.33% is provided. Therefore, a design f_r of 3 ksi was used for service load. To minimize the weight of the girders, benefitting not using a prestress section, a non-prismatic section is used for the two longer spans. In these girders the middle 10% of the

length has a prismatic section, while from those points toward the supports the web thickness, height of the beam and the bottom flange thickness may vary to provide required stiffness and strength. Figure 5-8 schematically shows the section height variation along a girder. Table 5-7 summarizes the reinforcement arrangement and the dimensions of the sections for all the girders, both at the support and the midspan section.

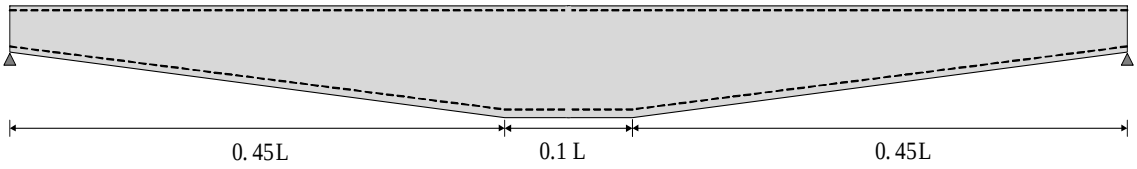

Figure 5-8 Non-prismatic section changes along the length of the girders

Table 5-7 Section dimensions for the girders

	Support			**Midspan**				
	h in.	**t_b** in.	**t_{web}** in.	**h** in.	**t_b** in.	**t_{web}** in.	**$A_{one\ unit}$** in.^{2}	**Reinforcement**
G95	40	5	4.75	40	5	4.75	743	20 #9 @ 38.5 + 12 #9 @ 36
G180	66	4.5	4.75	84	8	3.5	938 *	20 #9 @ 82.5
G250	120	4.5	4.5	120	16	3.0	1298 *	20 #9 @ 118.5

* Weighted average of the non-prismatic member

The tensile stresses obtained from analysis due to total service load at the bottom fiber of concrete in all the three bridges are shown in Table 5-8. The analyses indicate that UHP-FRC girders have sufficient shear strength at ultimate loading. Conservatively, a minimum shear reinforcement required by AASHTO LRFD is used. The sections are designed such that a service live load deflection limit of L/180 is met (Table 5-8). Also, the sections are checked against all the deflection loadings combinations discussed in the loading section. In these analyses the effect of reinforcing rebars are neglected, conservatively.

Table 5-8 FEA results of the girders

	Total tensile stress*	**Live Load Deflection**	**Shear stress**	
			Service	**Ultimate**
	ksi	in.	psi	psi
G95	**2.92** < 3.00	**1.42** < 1.43	337	548
G180	**2.99** < 3.00	**2.29** < 2.70	430	597
G250	**2.91** < 3.00	**2.47** < 3.75	424	572

Note: Calculations are for service load unless specified otherwise

***** Tensile stress at bottom fiber of the concrete section

After designing the sections based on service loading requirements, the flexural strength of the section against the ultimate flexural loading needs to be examined. Due to weak tensile strength of conventional concrete, the only element contributing in tensile part of the flexural strength of the section is the reinforcement rebars. However, if UHP-FRC is used, the tensile contribution of the matrix is considerable. Moreover, since the tension force coming from the UHP-FRC is considerable, the neutral axis will be kept in deeper

levels which is translated to relatively smaller lever arm in UHP-FRC section and make the conventional design concept unconservative for use in UHP-FRC members with considerable tensile strength. To study this issue, another FEA is performed in which the tensile strength of UHP-FRC is maintained to strains larger than the f_r strain. Regarding the DIC the maximum strain observed in the experimental specimens is 0.025 (Kaka and Chao, 2018). Also, even in direct tensile test result, the cracking strength (f_r) is maintained up to 0.015 strain (Kaka, 2017). Conservatively, the smaller amount is used for maximum tensile strain in FEA. In this modeling, an approximate lower bound behavior of Grade 100 bars is used (ACI ITG-6R-10). The FEA results are compared with the experimental test results for the specimen which satisfies the minimum ρ_{TA} (UHP-FRC #2). The results are represented in Figure 5-9. The results fit the behavior recorded by DIC.

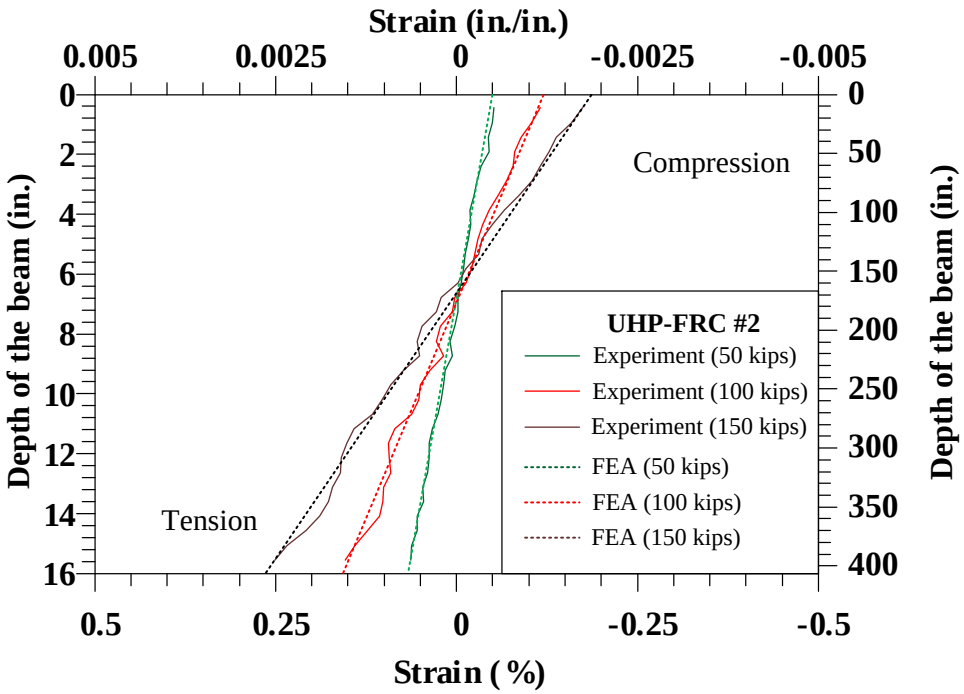

Figure 5-9 comparison between FEA and experimental result for specimen UHP-FRC #2

The same model verified with the test result was used to find the flexural strength of the girders for bridges. The flexural behavior of the sections is shown in Figure 5-10. In these analyses, the maximum curvature is the point at which the top layer in UHP-FRC reaches strain of 0.015.

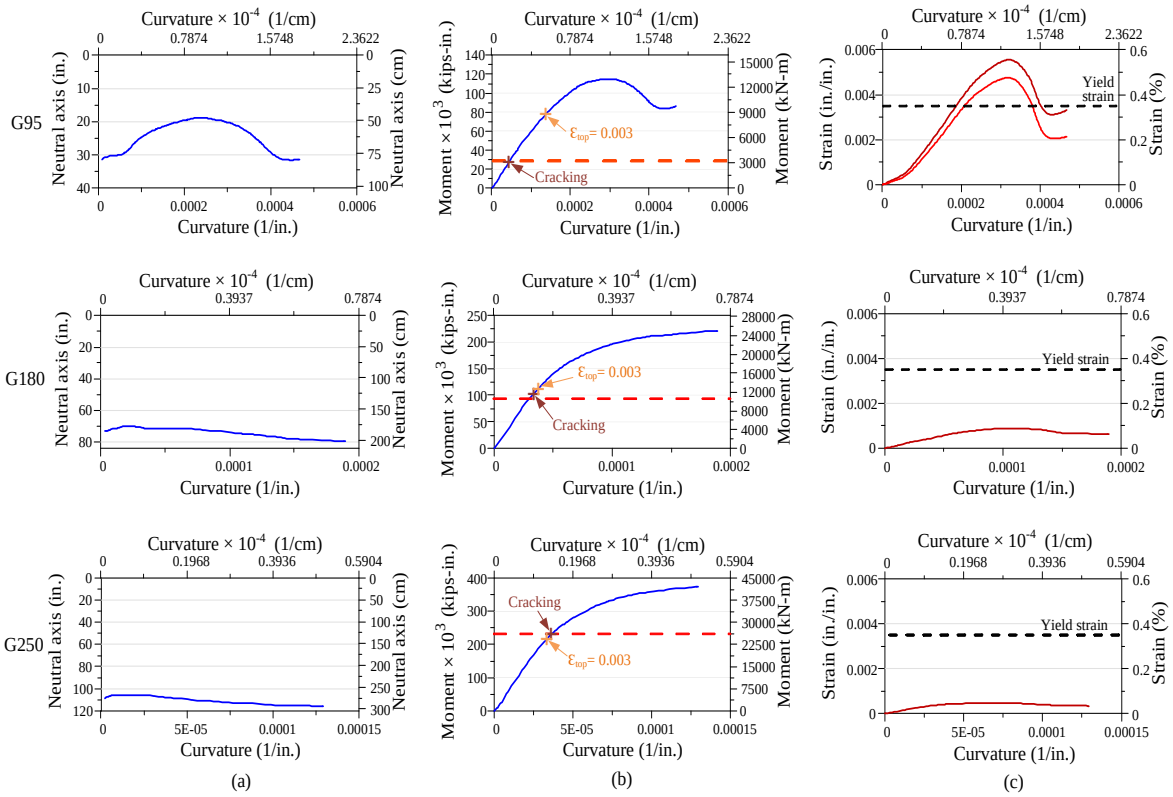

Figure 5-10 flexural behavior of the section due to increasing curvature: a) neutral axis, b) moment and c) strain in the rebars

Results show that the flexural strength of the girders are very larger than the demand at ultimate loading and this ratio increases as the section height reduces. In all the girders, the section remains uncracked at the bottom layer up to loadings close to or even higher than ultimate loading. This is because of the deep neutral axis in the girder due to UHP-FRC contribution in tension. Figure 5-10 (c) shows the maximum strain experienced in the

girders up to ultimate loading. The maximum strain is less than 0.006 in G95 and very smaller (even linear) for G180 and G250. This provides a great resilience for these girders.

5.2 Application of DCSR Design Concept in Columns

In this section the results of two small column specimens tested in Civil Engineering Lab Building of the University of Texas at Arlington are used (Karmacharya, 2019). Two small scale columns were designed and tested under large displacement reversals to investigate the new UHP-FRC/FRP column and the proposed new DCSR design concept. The first specimen was designed with a fiber dosage of 0.75% by volume of ultra-high molecular weight polyethylene (UHMW PE) fibers. The second specimen used 3% by volume of micro high-strength steel fibers. Both specimens were reinforced with BFRP bars. Note that, since the axial load ratio ($P_u/A_g f'_c$) is smaller for UHP-FRC columns due to its high compressive strength, no axial load was applied in the test specimens. Figure 5-11 shows the cross-section dimension and reinforcement arrangement in the column specimens.

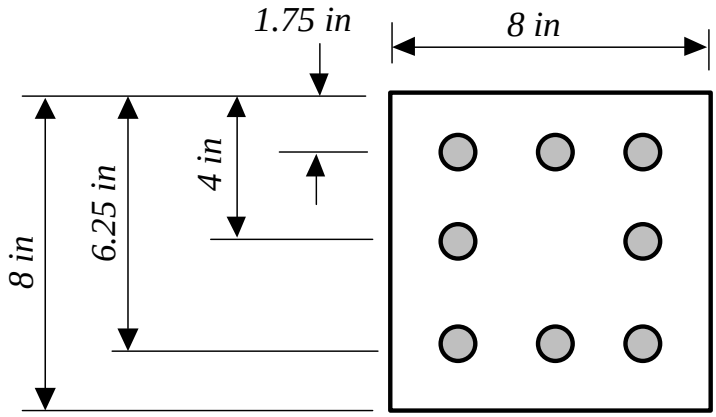

Figure 5-11 cross-section dimension and reinforcement arrangement in the column specimens

Based on the Ductile-Concrete Strong-Reinforcement (DCSR) design concept, the reinforcement in the section is to be designed strong enough to make the maximum strain in the compression zone of the matrix (here UHP-FRC) that occurs in the top layer of it reaches its maximum usable compressive strain prior to yielding or rupture occur in the reinforcements. In the following, the calculations that guarantee this happens in the design section is provided. for this purpose, the minimum amount of reinforcement that is required is calculated based on the geometry of the section and the characteristics of the materials.

To make sure that concrete failure occurs first:

$$T > C \qquad \textit{Equation 5.4}$$

Assuming that the neutral axis falls between the top and middle layers:

$$\Rightarrow T_1 + T_2 > C_1 + C_2 \qquad \textit{Equation 5.5}$$

$$\Rightarrow T_1 + T_2 - C_2 > C_1 \qquad \textit{Equation 5.6}$$

$$A^1_{FRP} E_{FRP}\, \varepsilon^1_{FRP} + A^2_{FRP} E_{FRP}\, \varepsilon^2_{FRP} - A^3_{FRP} E_{FRP}\, \varepsilon^3_{FRP} > (0.85)(0.65c) b f'_c \qquad \textit{Equation 5.7}$$

Based on assumption $A^1_{FRP} = A^3_{FRP} = 3A_{bar}$ and $A^2_{FRP} = 2A_{bar}$ and relying upon the plain sections remain plain principle, strain at each layer at the failure can be found as:

$$\varepsilon_{FRP}^{1} = (\frac{d_1}{c} - 1) \times \varepsilon_{cu} \; ; \; \varepsilon_{FRP}^{2} = (\frac{d_2}{c} - 1) \times \varepsilon_{cu} \; ; \; \varepsilon_{FRP}^{3} = (1 - \frac{d_3}{c}) \times \varepsilon_{cu} \quad \textit{Equation 5.8}$$

By substituting the given values to the equation:

$$A_{bar}\, E_{FRP}\, \varepsilon_{cu} \left[3 \times \left(\frac{d_1}{c} - 1\right) + 2 \times \left(\frac{d_2}{c} - 1\right) - 3 \times \left(1 - \frac{d_3}{c}\right)\right]$$

$$> \; (0.85)(0.65)\; c\; b\; f_c' \qquad \textit{Equation 5.9}$$

$$\Rightarrow A_{bar}\, E_{FRP}\, \varepsilon_{cu} \left(\frac{3d_1 + 2d_2 + 3d_3 - 8c}{c}\right) > \; (0.85)(0.65)\; c\; b\; f_c' \qquad \textit{Equation 5.10}$$

From the similar triangles at ultimate:

$$c = \frac{\varepsilon_{cu}}{\varepsilon_{cu} + \varepsilon_r} d_1 \; ; for\; simplicity\; \alpha = \frac{\varepsilon_{cu}}{\varepsilon_{cu} + \varepsilon_r} \Rightarrow c = \alpha\, d_1 \qquad \textit{Equation 5.11}$$

$$\Rightarrow A_{bar} \; > \; (0.85)(0.65)\; b \left(\frac{(\alpha\, d_1)^2}{3d_1 + 2d_2 + 3d_3 - 8(\alpha\, d_1)}\right) \left(\frac{f_c'}{E_{FRP}\, \varepsilon_{cu}}\right) \qquad \textit{Equation 5.12}$$

By multiplying both sides to the total number of rebars and dividing them by bd_1, minimum ratio of reinforcement can be calculated as:

$$\Rightarrow \rho_{min} = \frac{8 \times A_{bar,min}}{b d_1} = \; (0.85)(0.65) \; \left(\frac{8 \times \alpha^{\,2} d_1}{3d_1 + 2d_2 + 3d_3 - 8(\alpha\, d_1)}\right) \left(\frac{f_c'}{E_{FRP}\, \varepsilon_{cu}}\right) \qquad \textit{Equation 5.13}$$

By substituting the numbers in the given specimen:

$$c = \frac{\varepsilon_{cu}}{\varepsilon_{cu}+\varepsilon_r} d_1 = \frac{0.015}{0.015+0.020} 6.25 = 2.68\ in$$

From the similar triangles the absolute strain value at the top layers which works in compression is $\varepsilon_{FRP}^3 = 0.0019$ and in the middle layer that is in tension is $\varepsilon_{FRP}^2 = 0.0074$. Substituting the numbers in the equations:

$$(3\ \times A_{bar})(6141)\ (0.020) + (2\ \times A_{bar})(6141)\ (0.0074)$$

$$-\ (3\ \times A_{bar})(6141)\ (0.0019)\ > (0.85)(0.65 \times 2.68)(9)(20)$$

$$A_{bar}\ > 0.628\ in^2$$

To make sure that the concrete reaches the ultimate 0.015 strain before rupture occurs in the bottom layers of rebars ($\varepsilon_{FRP} < \varepsilon_r = 0.020$), rebars with area more than $0.628\ in^2$ are required. To satisfy this minimum, rebars of #8 are used.

Both specimens were reinforced with #8 BFRP bars of (25 mm diameter) with a tensile strength of 147 ksi (1014 MPa). The total reinforcement ratio was 14.8% for both specimens.

Figure 5-12 shows the details of the cross-section and dimensions as well as the loading protocol. Loading was applied at a distance of 34 in (864 mm) from the base.

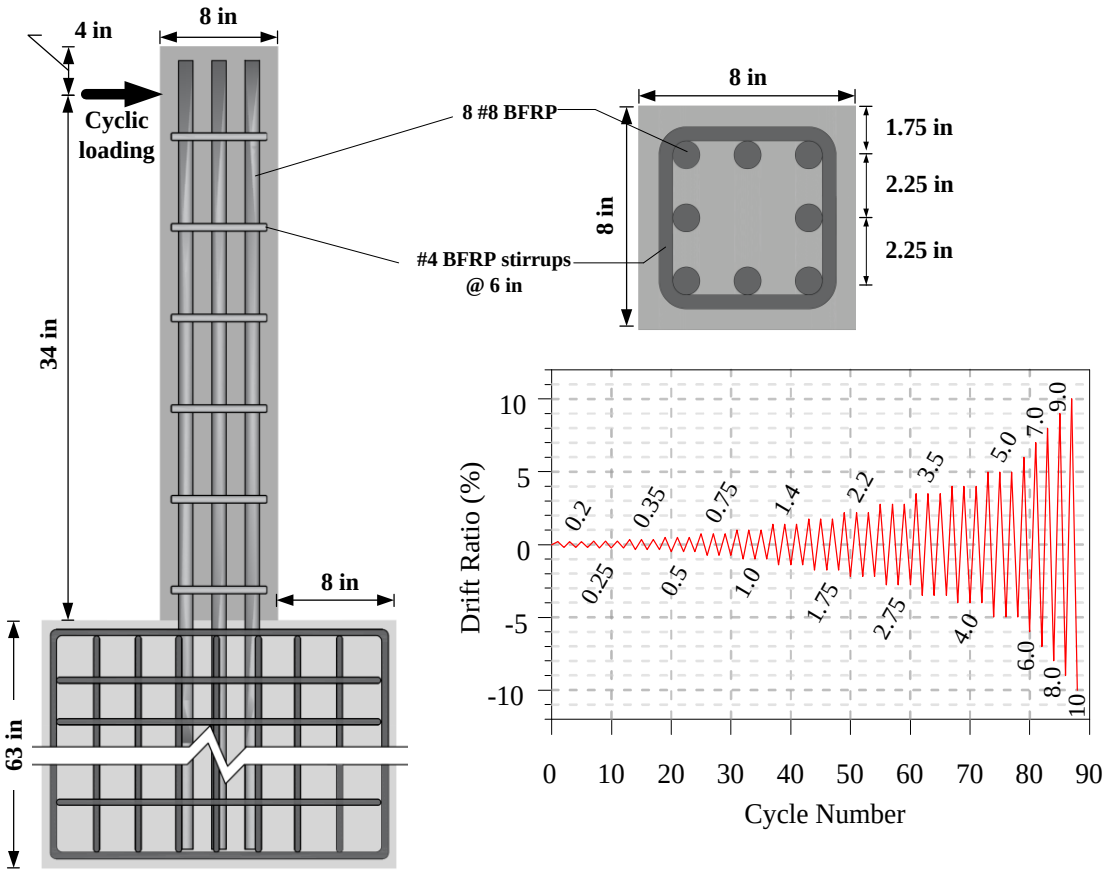

Figure 5-12 Cross-section and dimensions details of the UHP-FRC column specimens and loading protocol (1 in = 25.4 mm)

5.2.1 Experimental test results

The obtained comprehensive strengths on the testing day for first and second specimens were 15.2 ksi (105 MPa) and 19.9 ksi (137 MPa), respectively. For the first specimen, a maximum moment of 122 kip-ft (166 kN-m) was recorded at a drift ratio of 10%. The testing was terminated at 10% drift ratio due to the actuator's limited stroke distance. Moment versus drift ratio relationship showed large cyclic displacements without significant damage in the UHP-FRC material. As shown in Figure 5-13 (c), UHP-FRC

reinforced with UHMW PE fibers exhibits multiple cracks but has no severe concrete spalling and crushing like that which appears in conventional concrete or fiber-reinforced concrete at large drift ratios. A stable cyclic behavior was observed up to 9% drift ratio after which the moment started to decrease in the negative direction (Figure 5-13 (a)). The maximum moment recorded for the second specimen was 119 kip-ft (162 kN-m) at the drift ratio of 8%. Figure 5-13 (b) shows the second column specimen with a stable behavior and no strength degradation up to approximately 9% drift ratio. Similar to the first specimen, no significant damage was observed under large cyclic loading in the UHP-FRC material. Figure 5-13 (c) shows that UHP-FRC reinforced with micro high-strength steel fibers with much less cracking than UHP-FRC with UHMW PE fibers. Both cases indicate a significant reduction in repair costs after a moderate or design basis earthquake.

During the experiments, minor residual deformation was recorded for both specimens. Since the FRP bars remain elastic up to large drifts, they serve as the restoring force to pull back the columns to the initial position and enhance the resilience of the columns. The results show that even after experiencing large drift ratios (DR=10%), the columns could still maintain 80% of their maximum peak strengths.

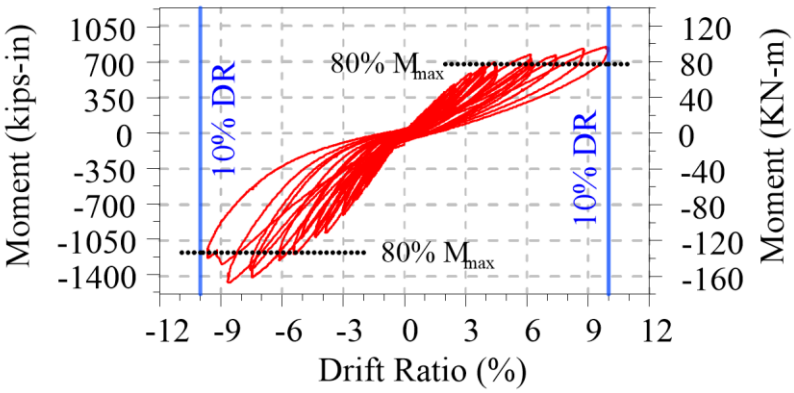

(a)

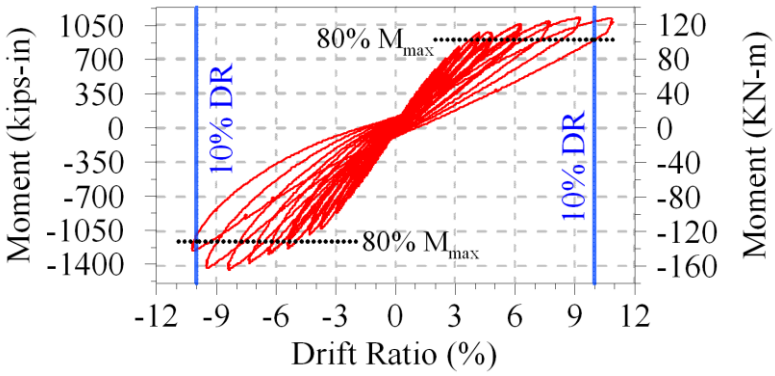

(b)

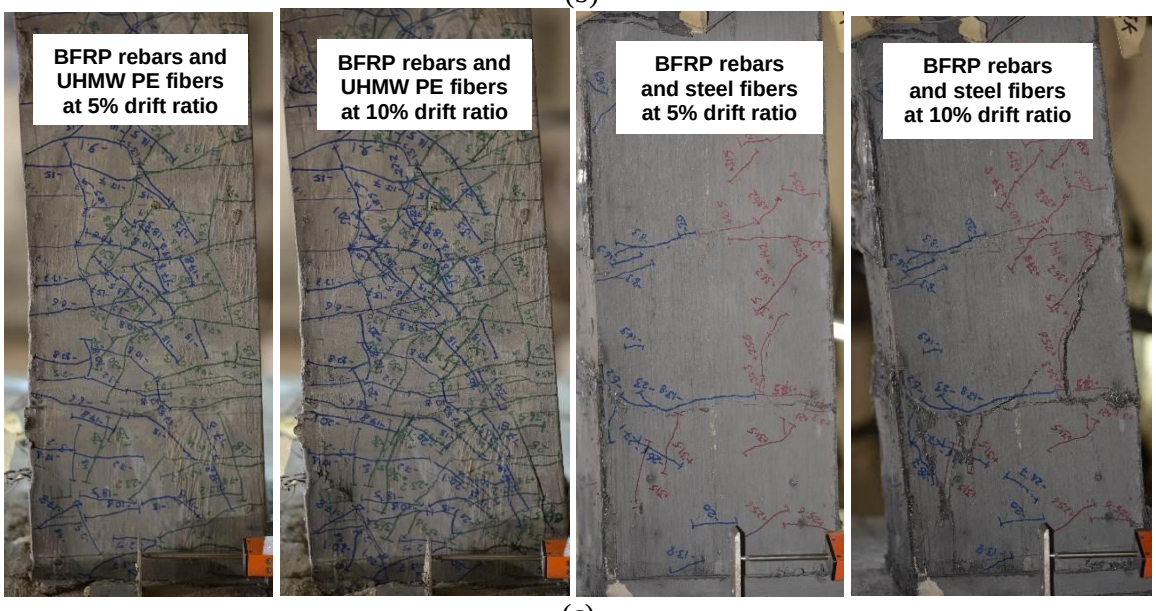

(c)

Figure 5-13 Moment versus drift ratio for specimen with UHP-FRC compressive strength of (a) 105 MPa and (b) 137 MPa, and (c) cracking patterns in UHP-FRC columns with different types of high-performance fibers

5.2.2 Digital Image Correlation (DIC) system result

During each test, a Digital Imaging Correlation (DIC) non-contact deformation measurement system was used to view the full field of strains and displacements as they developed on the surface. The DIC system has a 0.0001 (in./in.) measurement accuracy. Figure 5-14 depicts the maximum principal strain at third cycle of 2.75% drift ratio. Up to this stage, there was no cracking observed in the tension zone of the specimen. As illustrated, maximum principal strain value of 0.016 is recorded in this drift ratio. It shows that the UHP-FRC can undergo strain value of 1.6% in tension prior to cracking.

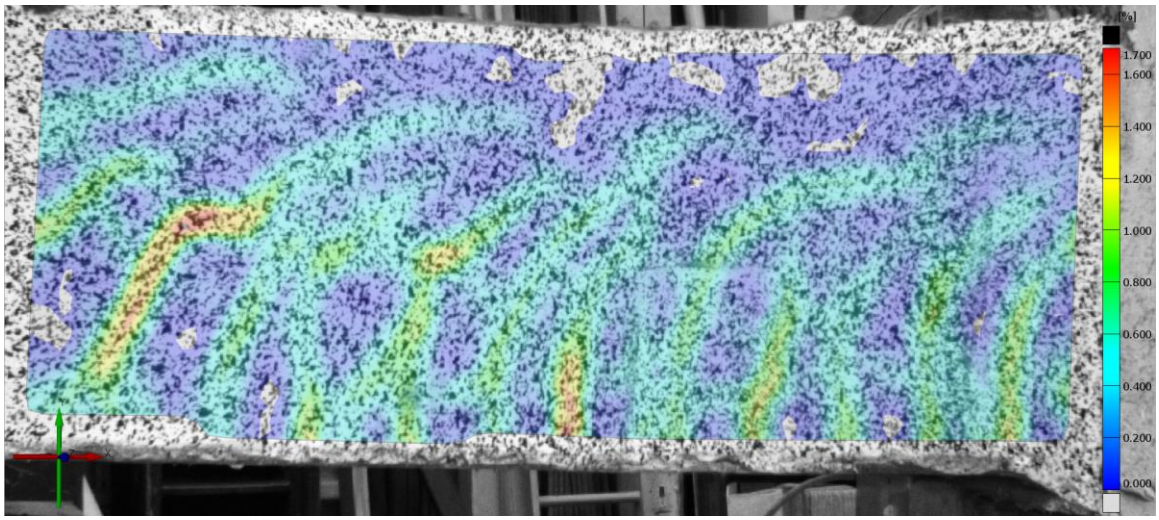

Figure 5-14 DIC results for the maximum principal strain at third cycle of 2.75% drift ratio for first specimen

Figure 5-15 represents the DIC reading for the minimum principal strain in the selected area of the beam. This plot which corresponds the cycle with 7% drift ratio, shows that the maximum compression strain in the concrete reaches strain value of 1.3% without sudden crushing. However, this does not mean that the maximum strain capacity of UHPFRC in

compression is limited to this number, since the strength of the whole system was limited due to rocking action of the foundation. The DIC results for the two specimens are provided in Appendix A of this report.

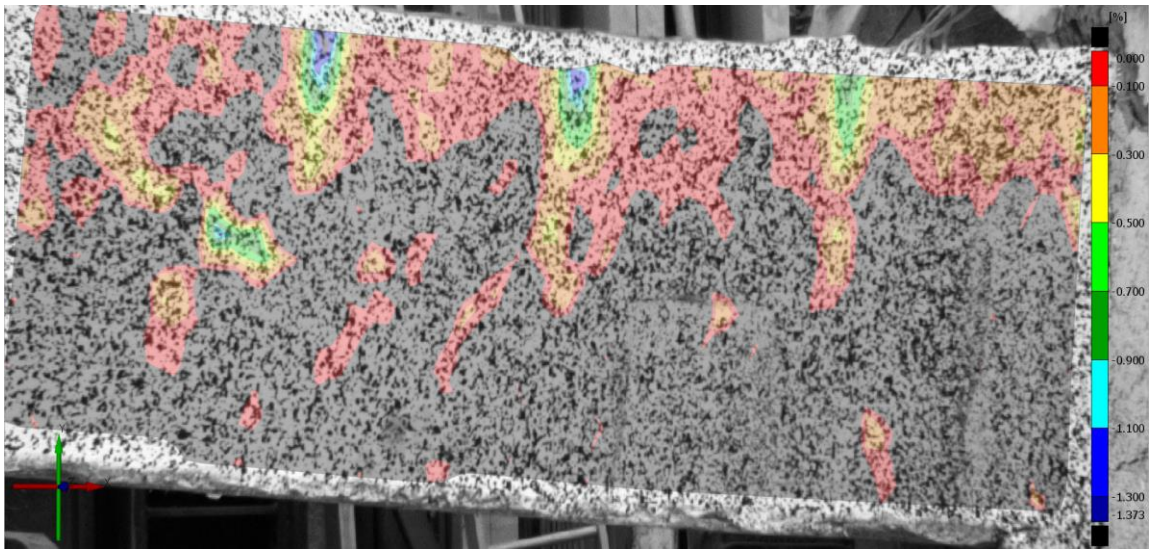

Figure 5-15 DIC results for the minimum principal strain at 7% drift ratio for first specimen

5.2.3 Collapse resistance of UHP-FRC columns designed by DCSR design concept

Plastic hinge model for collapse simulation

A plastic hinge in a member is usually simulated by a lumped spring model that has a zero length. Although the nonlinearity of the member occurs along a certain length, the zero-length plastic hinge model can typically be formulated to well simulate the overall behavior of entire plastic hinging region including flexural, shear, and slip deformation. The model used to simulate the plastic hinge of the conventional RC column is a peak-oriented model proposed by Ibarra (Ibarra et al., 2005). Figure 5-16 (a) shows the monotonic backbone

and hysteretic behavior of this model. The first slope in the monotonic backbone represents the elastic behavior of the section. After reaching the yielding moment, the section enters the strength hardening branch and continues up to the capping (peak) point. The post-peak stiffness becomes negative to indirectly simulate the in-cycle degradation of the section. In each cycle, the monotonic backbone shrinks to capture the cyclic degradation. Also, the reloading and unloading stiffness can be reduced to match the model with the experimental results. The monotonic backbone curve of this model can be defined through yield strength (M_y), elastic stiffness ($k_{elastic}$), strain hardening ratio (M_c/M_y), pre-capping rotation ($\theta_{pre\text{-}capping}$), post-capping rotation ($\theta_{post\text{-}capping}$), and residual strength (M_r) (Figure 5-16 (a)). With its energy-based deterioration parameters, this model captures the loading stiffness and strength deterioration, as well as the accelerated reloading and unloading stiffness deterioration. The hysteretic rules of Ibarra's model are used for the RC column as shown in Figure 5-16 (b). This model has been implemented in OpenSees (McKenna et al., 2000), which was used to carry out the nonlinear time-history analyses in this study.

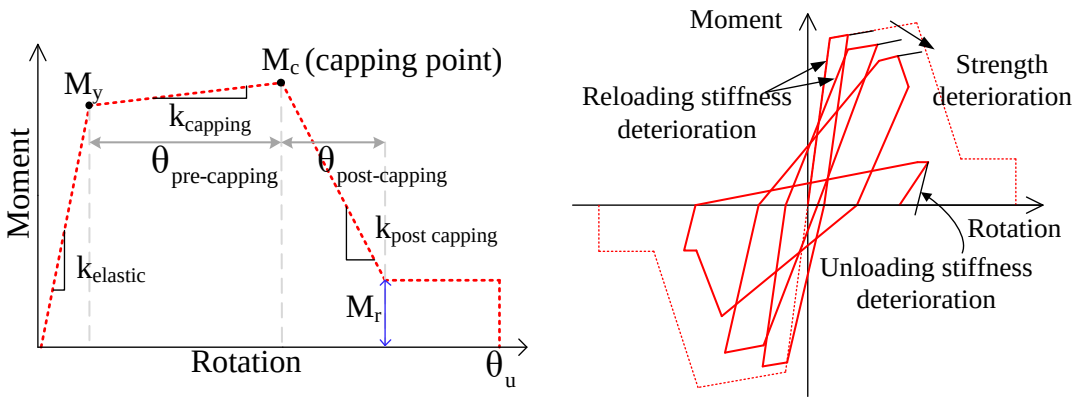

(a) (b)

Figure 5-16 (a) Monotonic backbone and (b) cyclic model recommended by Ibarra (Ibarra et al., 2005)

The model was also calibrated based on the test results of the two small-scale UHP-FRC/FRP columns, such that it can simulate the overall behavior of the member including all sources of deformation, as well as the self-centering behavior observed in the experimental tests. Although the strengths of the tested UHP-FRC columns maintained more than 80% the peak strengths up to 10% drift ratio (Figure 5-13), a maximum deformation limit of 9% drift ratio was conservatively assigned in the model. To simultaneously achieve the appropriate self-centering nonlinear cyclic behavior of a UHP-FRC column reinforced with FRP bars, three models were combined parallel to each other: 1) the Ibarra's model was used to simulate the degradation behavior, 2) a self-centering model (Christopoulos et al., 2008) was used to simulate the self-centering behavior, and 3) a MinMax model was defined to conservatively limit the deformation capacity of the model (Figure 6-5). When the MinMax material is applied to a model, it is assumed that the strength (or moment) of the model failed from that point on if the strain (or rotation) exceeds the minimum and maximum thresholds.

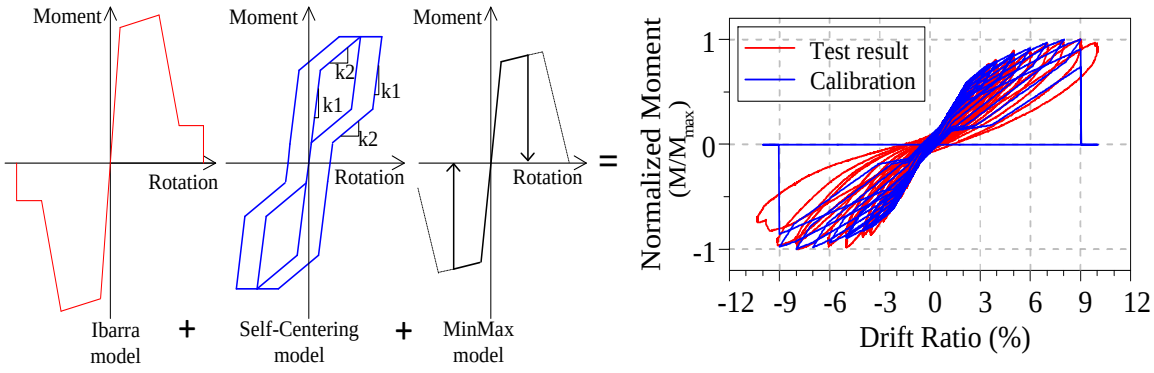

Figure 5-17 Ibarra, self-centering, and MinMax models were used parallel to each other to simulate column behavior

Incremental dynamic analysis (IDA) for special moment frame: RC and UHP-FRC

To investigate the collapse resistance of the UHP-FRC columns reinforced with FRP rebars, which are designed by the ductile-concrete strong-reinforcement (DCSR) design concept, two pairs of two-dimensional four-story and 20-story special moment frame (SMF) building were designed and analyzed. One of each pair was designed using conventional RC columns, and the other was designed using new UHP-FRC columns with FRP bars. The OpenSees software platform (McKenna et al., 2000) was used for the numerical simulations through incremental dynamic analysis (IDA) (Vamvatsikos and Cornell, 2002). To perform the IDA, a suit of 22 far-field records were selected. Since the structures were designed for stiff soil, the related records (site class C and D) were adopted from FEMA-P695 (2009), which were collected from the PEER-NGA database (2014). Conventional plastic hinge models were used for the beams in both structures. Lumped plastic hinges (PHs) were placed at both ends of the elements. To connect the PHs at the joints, beams and columns were connected through a two-dimensional beam-column-joint element object (Altoontash, 2004). Since the joints were designed by a strong-joint weak-column approach, the joints were modeled as an elastic element and their contribution to the drift ratio was negligible. A leaning column was modeled to account for the P-Delta effects of the gravity loads. This leaning column is pin-connected to the SMF and the base; hence, it does not contribute to the strength and stiffness of the frame. The built model is schematically shown in Figure 5-18.

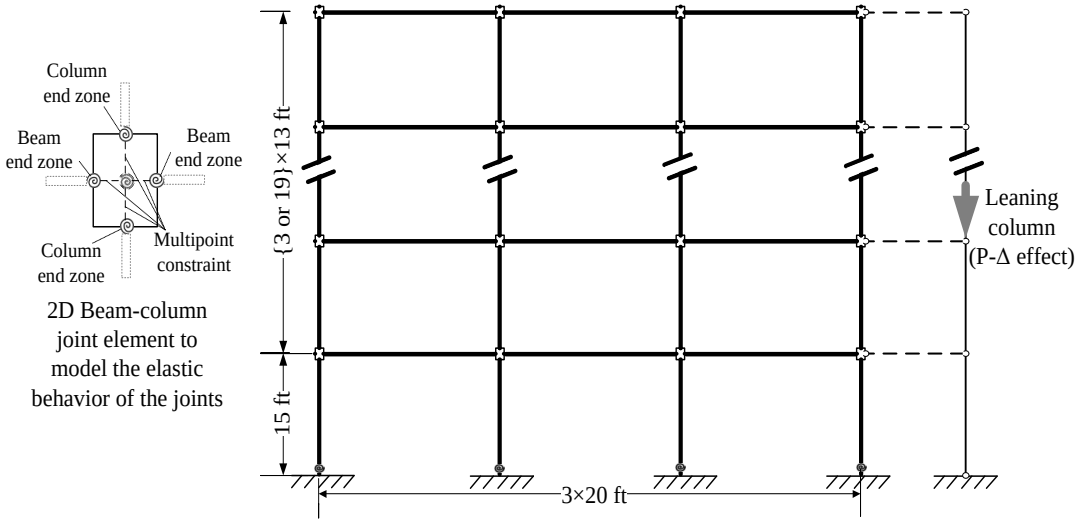

Figure 5-18 Schematic of the numerically modeled special moment frame (SMF)

Collapse resistance for the RC and UHP-FRC frames

The intensity measure (IM) is the spectral acceleration at the fundamental mode period of the building, while the damage measure (DM) is the maximum interstory drift ratio. A collapse IM is the point where a minor increment in the IM results in a significant increase in the DM. Figure 5-19 (a) and (b) illustrate the incremental dynamic analysis (IDA) results for four-story and 20-story buildings, respectively.

The gray lines represent a single IDA curve for each record. The solid line in each figure represents the IDA response of a UHP-FRC frame and each dashed line represents the IDA response for an RC frame. For the four-story building, the median IM for the frame with UHP-FRC columns that causes collapse is 17% (1.297g/1.111g) greater than the corresponding value for the RC frame. This shows the building that uses the new UHP-FRC/FRP columns and is designed by the DCSR concept has a larger collapse resistance

than the conventional RC one. The median collapse IM for the 20-story building with UHP-FRC/FRP columns is 7% (0.340g/0.318g) higher than the RC frame. The smaller difference in the collapse resistance for taller buildings is primarily because high-rise buildings experience less inelastic deformations. Studies on single-degree-of-freedom (SDOF) systems have shown that, the peak deformation ratios between inelastic and elastic analyses increases as the fundamental period of the system decreases (Ruiz-García and Miranda, 2003; Chopra and Chintanapakdee, 2004). This implies that the nonlinear behavior has a less dominating effect in long-period structures. Also, due to self-centering behavior of the UHP-FRC/FRP columns the residual deformations were very small, which indicates a fast recovery of the structures after a major earthquake.

Figure 5-20 (a) and (b) compare the first story residual drift ratios for the four-story and 20-story buildings with RC or UHP-FRC/FRP columns subjected to a design-basis earthquake (DBE) using Hector Mine earthquake ground motion.

When comparing both the four-story and 20-story building pairs, the self-centering behavior led to a much smaller residual drift ratios in the building with UHP-FRC/FRP columns, which contributes to the superior benefits of using UHP-FRC/FRP columns designed with the DCSR design concept.

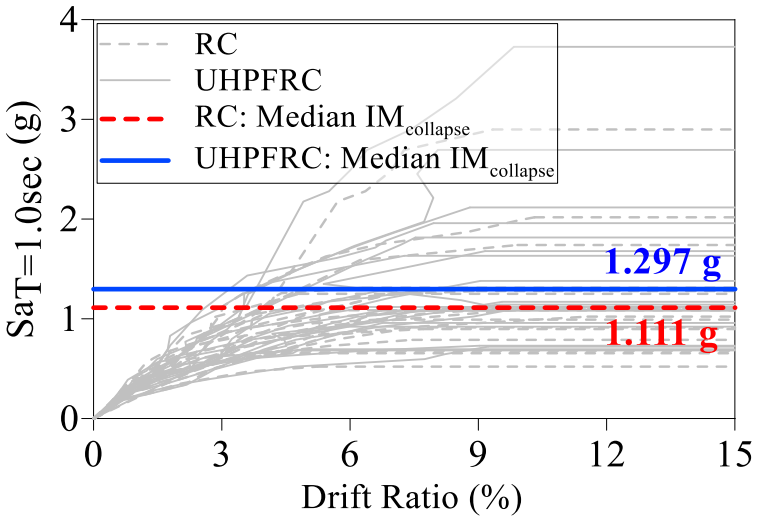

(a)

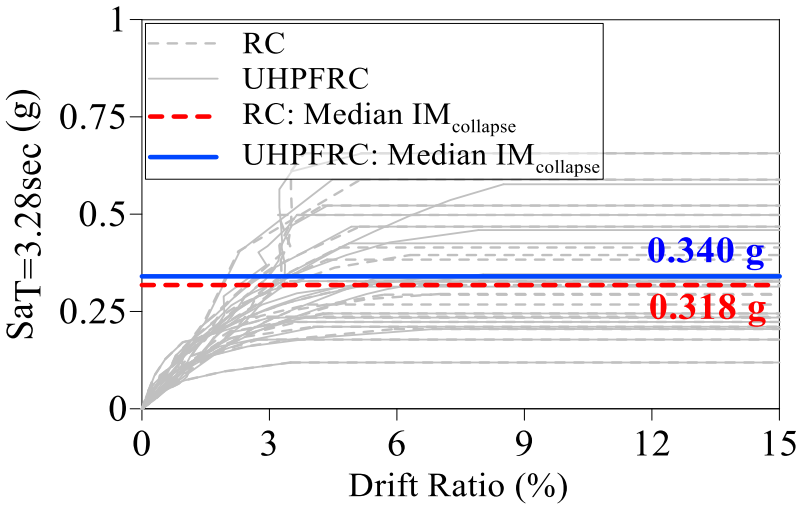

(b)

Figure 5-19 IDA results for RC and UHP-FRC (a) a 4-story SMF and (b) a 20-story SMF

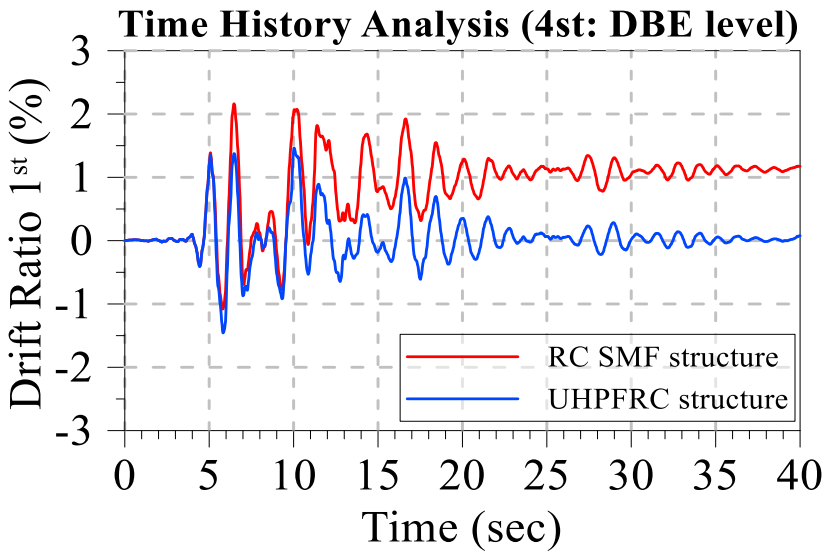

(a)

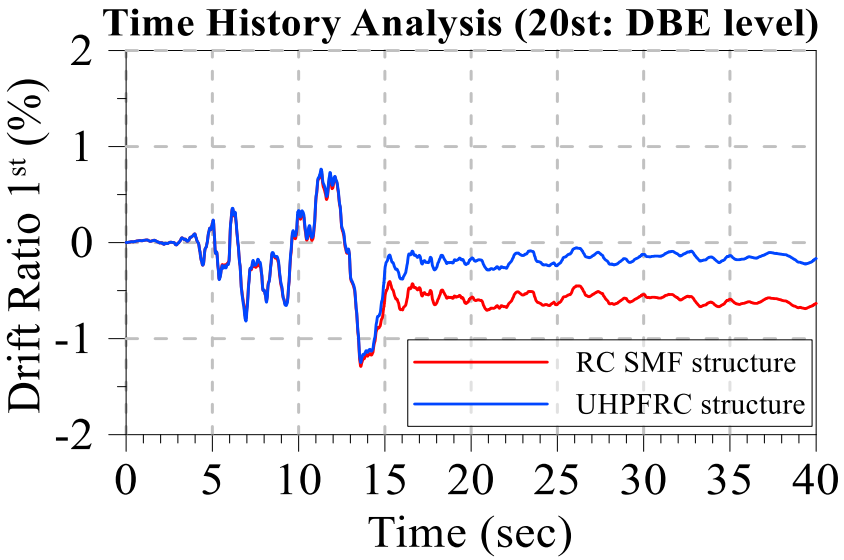

(b)

Figure 5-20 Drift Ratio of the first story from time-history analysis for RC and UHPC/FRP columns:
(a) 4-story SMF, and (b) 20-story SMF

Chapter 6
Part II

Introduction to

Collapse Assessment of RC and UHP-FRC

Columns Based on Experimental Results

6.1 Introduction

The purpose of design of a building against earthquake, is to provide life safety of the occupants. But meeting this problem has two significant issues. First, the applied load that is used for designing the building, is calculated based on probabilities. Therefore, we never know the exact earthquakes that the building will experience in its life. Instead of that based on probability studies maximum considered earthquake (MCE) is used for designing the building. Secondly, quantifying the number of occupants in a building at all moments is impossible. For those reasons, FEMA_P695 achieves Life Safety performance by requiring an acceptably low probability of collapse of the system subjected to MCE ground motions. Finding this probability needs conducting incremental dynamic analysis (IDA) approach, in which the collapse assessment of the system is required. In the extreme loading that causes collapse, most of the elements in a structure becomes nonlinear. Therefore, the parts of the system which are representative of the nonlinear behavior of members have dominating role in prediction of the response of the structure. The importance of the nonlinear behavior of the elements in near collapse drifts, necessitates the accurate modeling of columns, as columns are the most critical elements in providing collapse prevention and assuring the post-earthquake functionality and limited repair costs of buildings in earthquake. Nonlinear simulation of reinforced concrete columns has been studied by many researchers. However, numerical calibrations of these studies were conducted based on the results of small-scale columns. On the other hand, for many of these studies, regardless of the applied excitation the calibration was performed based on one type of artificial loading with many cycles. In this study, collapse assessment of the special moment reinforced concrete frames are investigated based on results from full-scale

concrete columns. In a prior study, full-scale columns, with same geometry and material, have been tested under different loading protocols. Results of the full-scale columns is used in this study to calibrate the real-size buildings. The results show that calibration only based on small-scale columns and one certain loading protocol could underestimate the response of the structure.

6.2 Literature review

6.2.1 Collapse assessment methodology

In the process of designing a building and assessing the performance of the building under a certain level of loading there are considerable number of uncertainties. FEMA-P695 categorizes sources of uncertainty explicitly as following: (1) record-to-record uncertainty; (2) design requirements-related uncertainty; (3) test data-related uncertainty; and (4) modeling uncertainty. In order to better predict the behavior of a structure, these uncertainties are needed to be addressed. One common way to quantify uncertainties is to utilize probability. FEMA-P695 proposes a procedure in which performance acceptability of a structure is calculated based on probability. This methodology uses incremental dynamic analysis (IDA) approach to assess the probability of collapse (Vamvatsikos and Cornell, 2002). In IDA procedure, the structure will be subjected to a set of records that the intensity of each of them will be scaled up until a certain defined damage index such as maximum interstory drift ratio of the structure, under each record, exceeds the maximum allowed value. At this point it is assumed that the structure has reached collapse.

To reduce the effect of record-to-record uncertainty, 22 pairs of far-field records are selected. This includes 44 ground motion components of these records. The events that are selected for the IDA is listed in Table 6-1. These ground motions are downloaded from PEER NGA database.

The selection of the records is such that the events can produce a greater risk of collapse of a building. Some of the criteria that are described in FEMA-P695 is briefed as follows:

Source Magnitude: to more likely to collapse the structure, the records are selected to have a magnitude of 6.5 or more ($M > 6.5$).

Source Type: strike-slip or reverse (thrust) sources

Site Conditions: either soft rock (Site Class C) or stiff soil (Site Class D)

Site-Source: located greater than or equal to 10 km from the fault rupture

After running the IDA for the given ground motions, the incremental dynamic analysis response plot will be provided (Figure 6-1 (a)). In this plot the vertical axis represents the intense measure (IM) and the horizontal axis represents the damage measure (DM). For example. Intense measure which will be increasing for each record to derive the single incremental dynamic analysis, could be Peak Ground Acceleration (PGA) or the Spectral acceleration of the fundamental period of the structure ($S_T(T_1)$). Also, the damage measure could be considered as the maximum inter-story Drift Ratio (DR) for all the stories in the building. From the IDA plot, the collapse fragility curve will be obtained. This is defined as cumulative distribution function (CDF) given from the collapse data points from the IDA curve (Figure 6-1 (b)). Having the IM for the fundamental period of the structure the probability of the collapse for it at MCE level, can be found from the fragility curve.

Table 6-1 Summary of Earthquake Event and Recording Station Data for the Far-Field Record Set (table A-4A of FEMA-P695)

ID No.	Earthquake			Recording Station	
	M	Year	Name	Name	Owner
1	6.7	1994	Northridge	Beverly Hills - Mulhol	USC
2	6.7	1994	Northridge	Canyon Country-WLC	USC
3	7.1	1999	Duzce, Turkey	Bolu	ERD
4	7.1	1999	Hector Mine	Hector	SCSN
5	6.5	1979	Imperial Valley	Delta	UNAMUCSD
6	6.5	1979	Imperial Valley	El Centro Array #11	USGS
7	6.9	1995	Kobe, Japan	Nishi-Akashi	CUE
8	6.9	1995	Kobe, Japan	Shin-Osaka	CUE
9	7.5	1999	Kocaeli, Turkey	Duzce	ERD
10	7.5	1999	Kocaeli, Turkey	Arcelik	KOERI
11	7.3	1992	Landers	Yermo Fire Station	CDMG
12	7.3	1992	Landers	Coolwater	SCE
13	6.9	1989	Loma Prieta	Capitola	CDMG
14	6.9	1989	Loma Prieta	Gilroy Array #3	CDMG
15	7.4	1990	Manjil, Iran	Abbar	BHRC
16	6.5	1987	Superstition Hills	El Centro Imp. Co.	CDMG
17	6.5	1987	Superstition Hills	Poe Road (temp)	USGS
18	7.0	1992	Cape Mendocino	Rio Dell Overpass	CDMG
19	7.6	1999	Chi-Chi, Taiwan	CHY101	CWB
20	7.6	1999	Chi-Chi, Taiwan	TCU045	CWB
21	6.6	1971	San Fernando	LA - Hollywood Stor	CDMG
22	6.5	1976	Friuli, Italy	Tolmezzo	--

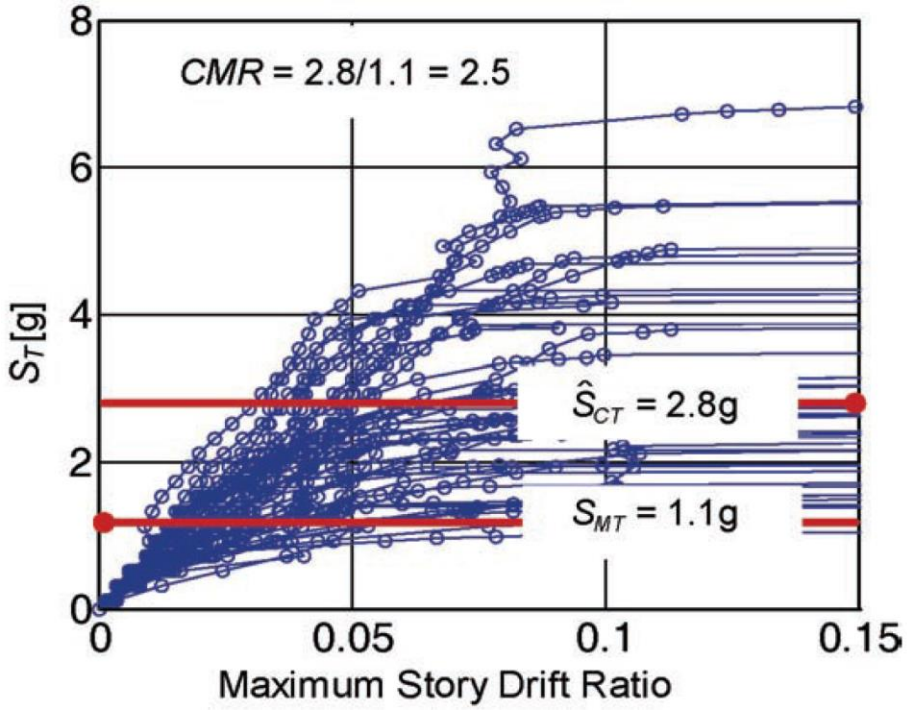

(a)

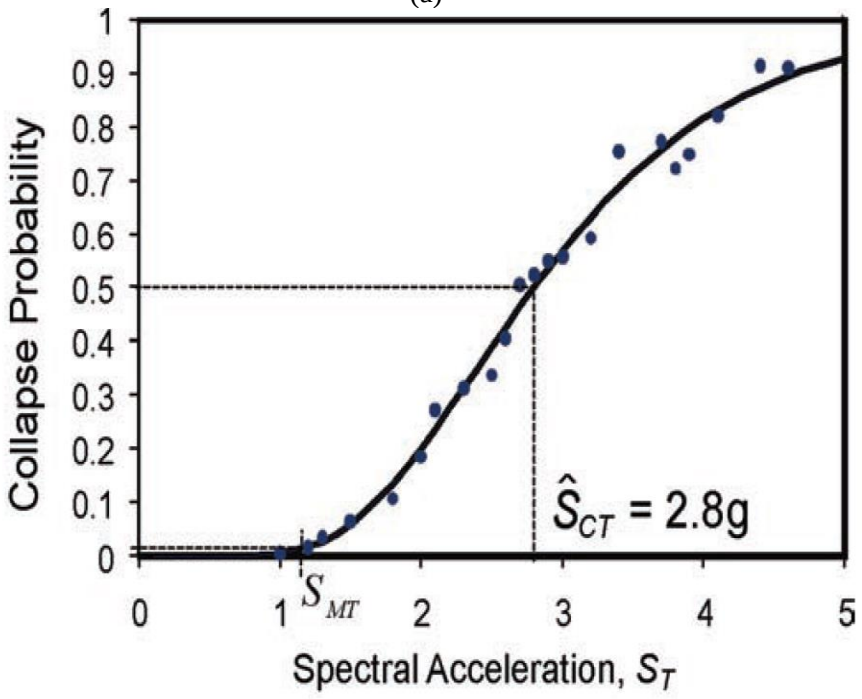

(b)

Figure 6-1 a) incremental dynamic analysis response plot, b) cumulative distribution function

The purpose of design of a building against earthquake, is to provide life safety of the occupants. However, meeting this problem has two significant issues. First, the applied load that is used for designing the building, is calculated based on probabilities. Therefore, predicting the exact earthquakes that the building will experience in its life is not possible. Instead, based on probability studies maximum considered earthquake (MCE) is used for designing the building. Secondly, quantifying the number of occupants in a building at all moments is impossible. Therefore, FEMA_P695 achieves “life safety performance“ by requiring an acceptably low probability of collapse of the system subjected to MCE ground motions. Finding this probability needs running incremental dynamic (IDA) approach, in which the collapse assessment of the system is required. In other word, the less probability of the collapse at MCE level, the safer of the building.

6.2.2 Different type of Beam-Column Models

Modeling a beam-column element can range from spring model to fundamental Finite element model as illustrated in Figure 6-2 from (a) to (e). All these models are phenomenological, and they rely on the way that they are calibrated. Concentrated models need to be calibrated based on the overall behavior of the component and on the other hand, toward the right side of the range to finite element models, calibration would be at material level. Regardless of the model selected, the behavior should be verified with the empirical test data. There are cons and pros for each of these models. Since the concentrated models imply less degree of freedom to the structure, it would be computationally cost-effective and more desirable for immense analyses, however, if more directly kinematics of the material is required a finite element model may be chosen. In this project, in order to

capture the critical type of deformation as well as meeting the huge number of analyses, the nonlinear spring hinge model is used to simulate the nonlinear rotational behavior of the beams and columns.

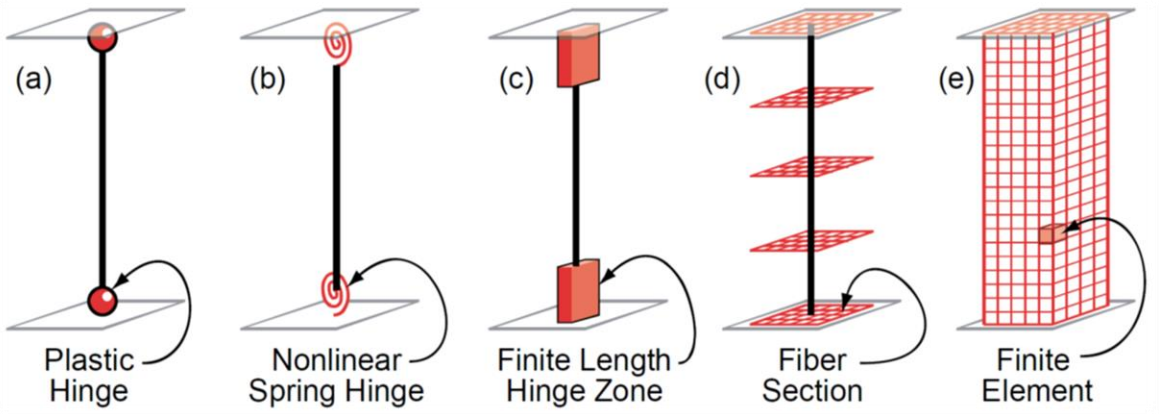

Figure 6-2 different type of beam column model (NIST GCR 17-917-46v1)

6.2.3 Plastic hinge model of reinforced concrete element

For simulating a more accurate model of a structural system, the nonlinear behavior of the members should be addressed. One way to predict the nonlinear behavior of a member in a structure, is defining plastic hinge at the nonlinear zone of the member. The plastic hinge in the member usually is defined as a lumped spring that has a zero length. Although, the nonlinearity of the member occurs along a certain length, the zero-length plastic hinge model is defined such that it can see the overall behavior of the member. For example, a column modeled by this method, consists of two plastic hinges at the ends and a linear element. The length of the line element is equal to the length of the member. Since the intermediate element is defined linearly, in loadings that cause higher deflections which yield in moments larger than the yielding moment capacity of the section, the plastic hinges are responsible to simulate the nonlinear behavior of the member. The moment capacity of

the member is limited to the capacity of the plastic hinge in the column. From this point, any increase in the loading will end in increase in the deflection or the drift of the story.

6.2.4 Seismic response of Plastic Hinge models

To predict the nonlinear behavior of a structure or an element, many numbers of models have been proposed. These models were produced to mimic the overall nonlinear behavior of the structure or its components such as elements or connections by being placed at the base of the model. These models range a vast variety of models from a simple elastic-plastic model to a complicated model that includes different types of degradations. Some of them are briefly described as the following:

1) elastic-plastic model

This model consists of a linear-elastic behavior until the point that yielding is reached. After this point, the stiffness of the model switches to zero and the strength would be maintained the same (Figure 6-3). This model does not see any degradation in stiffness or strength during hysteretic loading. Also, the unloading stiffness of this model is the same as the loading stiffness until it twice of the yielding value met during unloading.

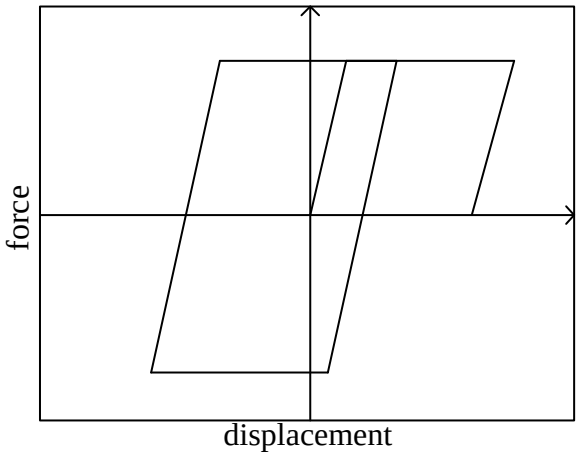

Figure 6-3 elastic-plastic model

Studies done by researches on a single-degree of freedom (SDOF) structures with this model showed that the effect of adding an elastic-plastic model to the structure would have more effects to the response of structures in short range of periods with periods less than 1.0s (Veletsos and Newmark, 1960). Generally, in these structures the peak lateral displacement of the SDOF system was larger than the linear-elastic systems with similar periods.

2) Strength-hardening

This model which is also a non-degrading model is similar to the elastic-plastic model, but the stiffness after the yielding will not drops to zero and the post-yielding stiffness is positive (Figure 6-4). The strength of the model would be increasing by deformation increases. This behavior that is also called the "strain-hardening" can be seen in different elements with different material. For example, for reinforced concrete frames this could be caused from the strain hardening that is coming from the reinforcement steel in one section or from the sequential yielding of other members if SDOF system is being considered. Similar to the previous model, the unloading stiffness is equal to the loading one.

Studies showed that the positive post-yield stiffness have minor effect in reduction of peak displacement for moderate and long-period structures (Ruiz-García and Miranda, 2003); Chopra and Chintanapakdee (2004). However, this positive post-yield stiffness can considerably reduce the residual drift of the structures after excitation (Kawashima et al., 1998; Ruiz-García and Miranda, 2006).

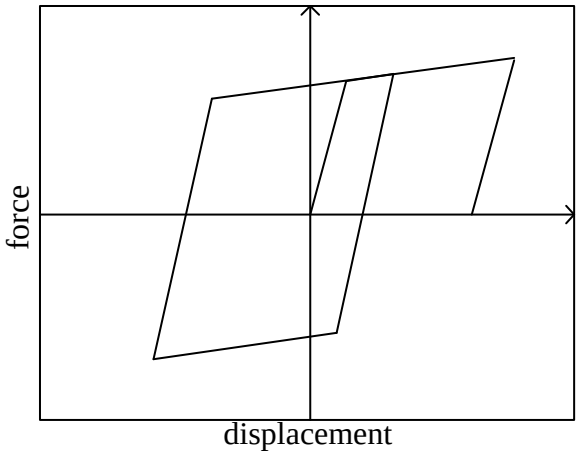

Figure 6-4 strength-hardening model

3) Stiffness-degrading

Stiffness degradation is a common behavior in different materials. For a reinforced concrete section this occurs because of cracking due to loading and unloading, debonding in rebars, concrete crushing due to reversal loading and interaction of shear and axial forces. It should be noted that the loading history will affect the amount of this degradation in term such as: the peak deformation experienced, the number of cycles and the sequence of the loading. Stiffness degradation can be modeled as types of loading and/or unloading. On the other hand, this degradation can be either a function of the maximum deformation experienced in the loading history or the hysteretic dissipated energy. Figure 6-5 represents a model with stiffness-degrading.

Studies demonstrated that applying this model to moderate and long-period structures, on average, will not increase the peak displacements in comparison with structures modeled with elastic-plastic model or bilinear strength-hardening models (Rahnama and Krawinkler, 1993; Shi and Foutch, 1997; Medina and Krawinkler, 2004). However, for short-period structures this model could leads to larger amount of peak displacement.

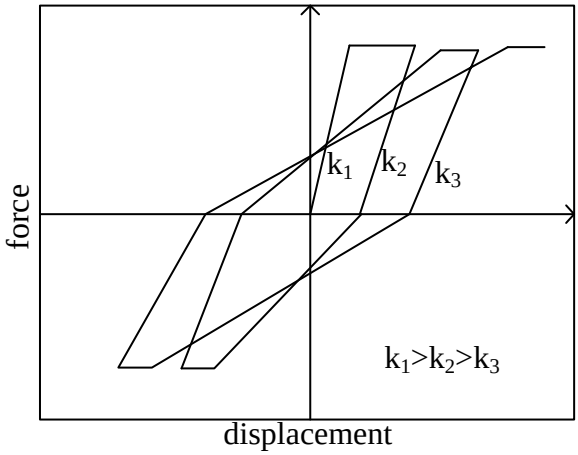

Figure 6-5 stiffness-degrading model

4) pinching

In reinforced concrete, pinching is typically produced by opening of cracks when displacement is imposed in one direction. Figure 6-6 represents the model schematically. However, short-period structures with pinching behavior experience peak displacements that tend to be larger than those experienced by systems with elastic-plastic or bilinear strength-hardening hysteretic behavior.

In the literature the structures with pinching model has been studied (Rahnama and Krawinkler, 1993; Shi and Foutch, 1997; Medina and Krawinkler, 2004; Ruiz-Garcia and Miranda, 2004). The comparison of using the pinching model in moderate and long-period structures with elastic-plastic model or bilinear strength-hardening model shows that the pinching model, despite the less dissipated energy in loading history, does not necessitate increase in peak displacement.

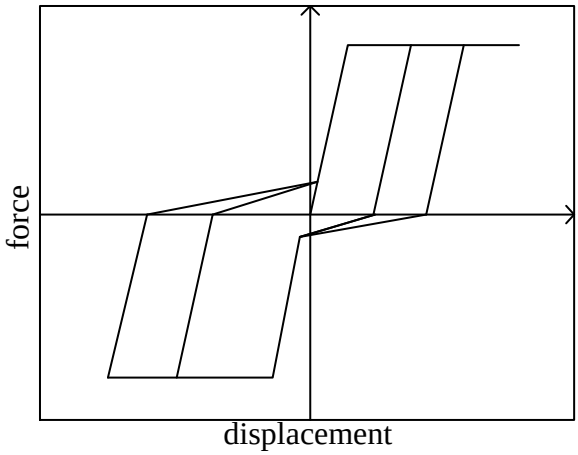

Figure 6-6 pinching model

5) Cyclic degradation

Cyclic degradation is referred to a behavior in which on the strength of the model reduces from one cycle to another (Figure 6-7). This degradation could be defined as a function of the maximum displacement or the hysteretic dissipated energy or combination of both. Like most of the previous models, the effect of cyclic degradation is less in structures with moderate and long-period models and more in structures with short periods.

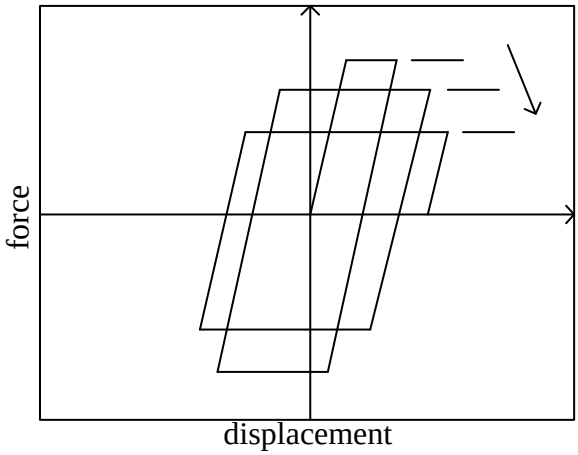

Figure 6-7 cyclic degradation model

6) In-cycle degradation

Unlike cyclic degradation, in-cycle degradation happens in one certain excursion when the deformation of the model exceeds a certain value (Figure 6-8). This results in a negative post-yield stiffness within a given cycle. In RC sections, this can occur due to concrete crushing, shear failure,

buckling or fracture of longitudinal reinforcement, and splice failures.

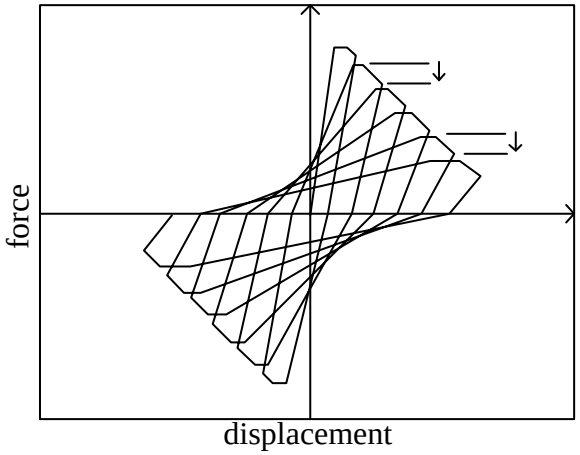

Figure 6-8 In-cycle degradation model

6.2.5 Capacity boundary of the Plastic Hinge

Modeling the plastic hinge of a reinforced concrete could be challenging. Lots of parameters should be considered in modeling a plastic hinge in reinforced concrete elements. Parameters such as: initial stiffness, yielding moment, cyclic degradation or in-cycle degradation, etc. There have been many models used previously by researchers. Most of these models have been calibrated with one type of loading. A frequent problem in this kind of calibration is that, although the model is working well in that kind of loading, it cannot work well in other types of loading. For example, if the model is calibrated by a loading in which there are lots of cycles, it might not work well in the loading that has

small number of cycles preceding a large deformation. However, loading is always an unknown parameter and would be different from one earthquake to another, as well as one story to another. Therefore, finding a model that can predict the cyclic behavior of a section accurately in all different kind of loadings would be beneficial.

In literature, five identical columns have been loaded under different type of loading protocols (Nojavan et al., 2015). The results show that some parameters of concrete column response would be changed depending on the applied loading protocol. To address this issue, some models have been developed. On way to model the behavior of the column is that to assign a monotonic backbone for the plastic hinge and use a degradation parameter to shrink the monotonic backbone in order to obtain the cyclic backbone (Figure 6-9 (a)). One major issue with this approach is that, since many of the tested elements are subjected to cyclic loadings, the monotonic backbone is being estimated from the cyclic response which would be affected by the formulation used in calibration method and parameters (Haselton and Deierlein, 2008). Another more conservative method is to define the monotonic and cyclic backbone from the envelope of the first cycle response of the cyclic loading (Figure 6-9 (b)). In this case, the monotonic backbone will be highly dependent on the defined cyclic loading protocol as well as the degradation rate of the tested column. lastly, an even more conservative method which is also adopted by ASCE-41 is to define both the monotonic and cyclic backbone the same as what mentioned in the second method, however this time when the strength degradation starts in cyclic loading, a sudden drop must be considered in the backbone and no cyclic or in-cycle degradation is allowed from that point on (Figure 6-9 (c)). Figure 6-9 (d) compares the monotonic backbones in the three described methods.

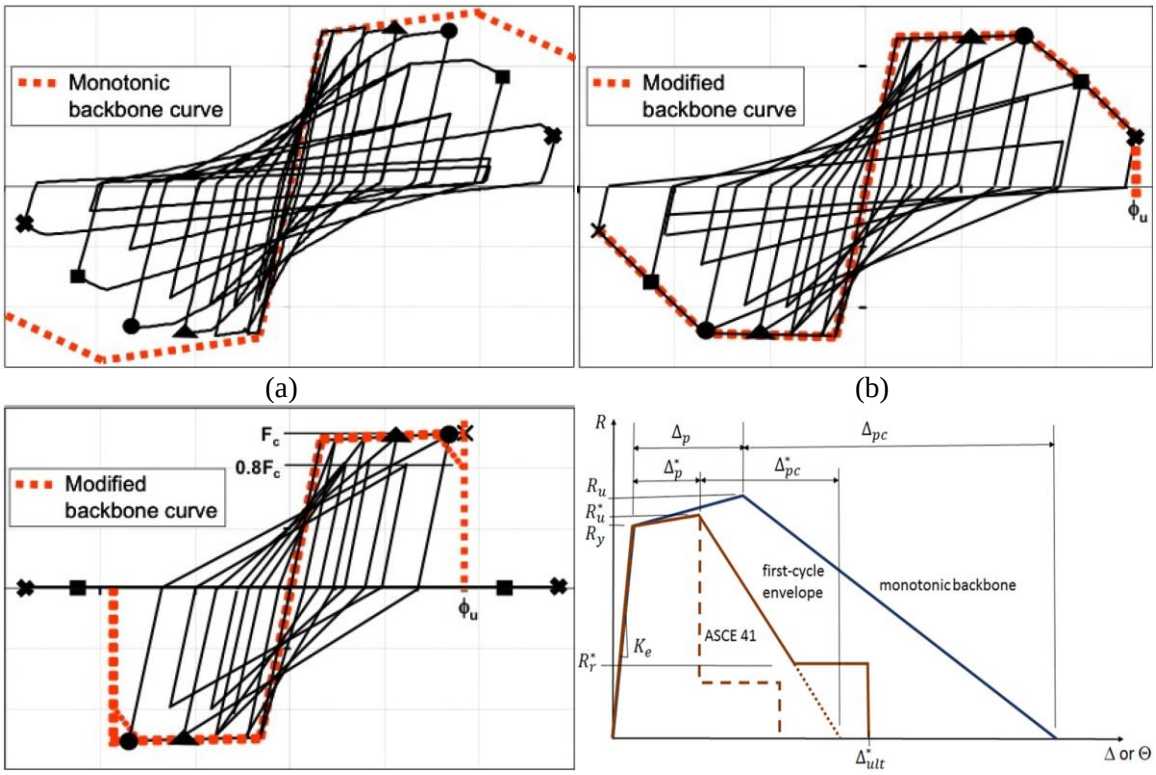

Figure 6-9. (a) Option 1 – Stiffness and Strength Degradation Model (b) Option 2 – Degraded Backbone Model (c) Option 3 – Limit Point Cutoff Model (d) Idealized component response curves and parameters (figure 4-3 & 4-5 of (PEER, 2017)

One drawback with the third method occurs when the IDA approach is being used. Generally, when a backbone like the one called "capacity boundary" in Figure 6-10 is defined, it will respond linearly up to yielding point (F_c). By increasing the intensity of the applied dynamic loading, the structure will respond pseudo linearly prior to softening initiates. This phase has the capacity to avoid dynamic instability up to the ultimate point in which the strength of the column/structure drops to zero. However, if the third model is used, the dynamic instability will occur right after the capping point associated with the deformation Δ_C, which is less than the ultimate deformation Δ_U. This can lead to a very underestimated result.

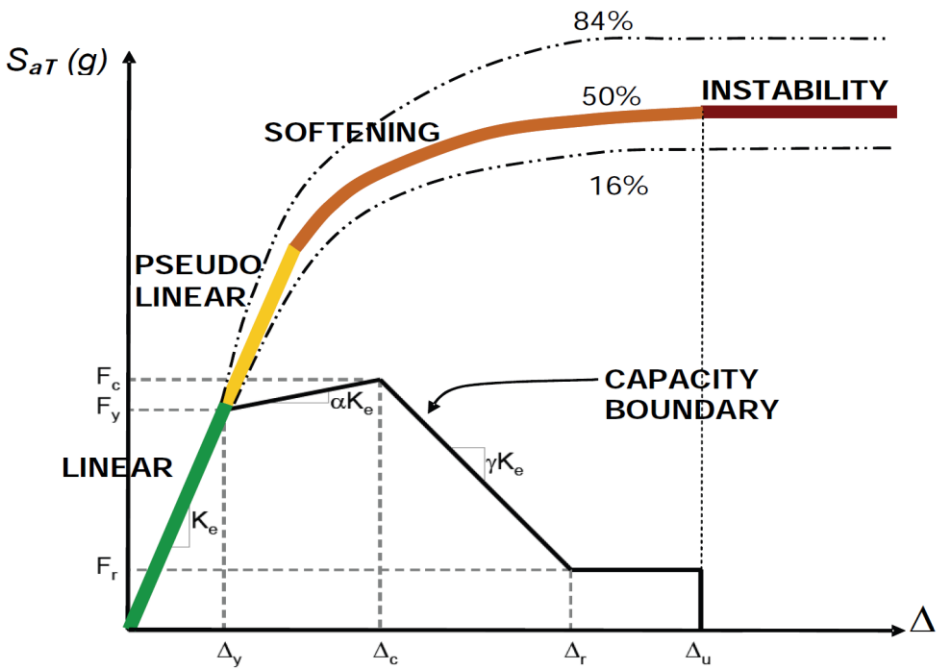

Figure 6-10. Relationship between IDA curves and the features of a typical force-displacement capacity boundary (FEMA_P440A)

6.2.6 Hysteresis model used in this study

For modeling the plastic hinge, the trilinear model proposed by Ibarra is used (Ibarra et al., 2005). Figure 6-11 (a) and (b) show the monotonic backbone and hysteretic behavior of this model, respectively. The first slope in the monotonic backbone, represent the elastic behavior of the section. After reaching the yielding moment, the section goes to the hardening part up to the capping (peak) point. The post-peak stiffness is negative to observe the in-cycle degradation of the section. To see the cyclic degradation, in each cycle the monotonic backbone shrinks by scaling down the strength of the strain hardening branch and strength of the peak point. Also, the reloading and unloading stiffness can be reduced to match the model with the experimental results. The monotonic backbone curve of this model can be defined through yield strength (M_y), elastic stiffness ($k_{elastic}$), strain hardening ratio (M_c/M_y), pre-capping rotation ($\theta_{pre\text{-}capping}$), post-capping rotation ($\theta_{post\text{-}capping}$) and residual strength (M_r) (Figure 6-11 (a)). Based on an energy-based deterioration parameter, this model captures the hardening behavior and strength deterioration, as well as the accelerated reloading and unloading stiffness deterioration. The hysteretic rules of Ibarra's

model are used for the RC column as shown in Figure 6-11 (b). This model that has been used for modeling is developed by Altoontash in OpenSees (Altoontash, 2004).

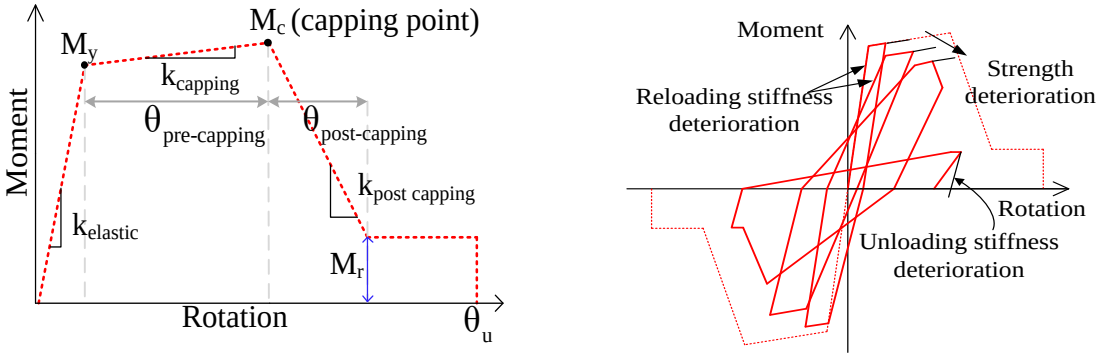

Figure 6-11 a) Monotonic backbone and b) cyclic behavior of model proposed by Ibarra.

The cyclic deterioration in each excursion of this model is defined by parameter β_i where:

$$\beta_i = \left(\frac{E_i}{E_t - \sum_{j=1}^{i} E_j} \right)^c$$

Equation 6.1

E_i is the hysteretic energy dissipated in excursion *i*, E_t is the reference hysteretic energy dissipation capacity, $E_t=\gamma F_y \delta_y$. The parameter γ which is related to section properties, expresses the hysteretic energy dissipation capacity which is calibrated from experimental results, and c is the parameter that determine the rate of deterioration (Rahnama and Krawinkler, 1993). For calculating M_y, the equation proposed by Panagiotakos and Fardis have been used (Panagiotakos and Fardis, 2001). Regarding this equation:

$$\frac{M_y}{bd^3} = \phi_y \left\{ E_c \frac{k_y^{\,2}}{2} \left(0.5(1+\delta') - \frac{k_y}{3} \right) + \frac{E_s}{2} \left[(1-k_y)\rho + (k_y - \delta')\rho' + \frac{\rho_v}{6}(1-\delta') \right] (1-\delta') \right\}$$

Equation 6.2

Where:

$$k_y = (n^2A^2 + 2nA + 2nB)^{1/2} - nA$$ Equation 6.3

$$A = \rho + \rho' + \rho_v + \frac{N}{bdf_y}$$ Equation 6.4

$$B = \rho + \rho'\delta' + 0.5\rho_v(1+\delta') + \frac{N}{bdf_y}$$ Equation 6.5

Where $\delta' = d'/d$, $n = E_s/E_c$, *b* is width of compression zone, d is effective depth of cross section, d′ distance of center of compression reinforcement from extreme compression fiber ρ, ρ', ρ_v, are tension reinforcement ratio determined as ratio of tension reinforcement area to *bd*, compression reinforcement ratio determined as ratio of compression reinforcement area to *bd,* web vertical reinforcement ratio of shear wall determined as ratio of total web area of longitudinal reinforcement between tension and compression steel to *bd,* respectively.

6.2.7 Importance of loading protocol

All the components that participate in resisting the applied seismic forces, have permanent memory of the past deformations and damages that they have experienced. This loading history affects the present health of the element and deteriorates its capacity in different ways. For an SFRS, this loading history effect results from all earthquakes it experiences from the first day of service. The main purpose of finding an appropriate loading protocol is to simulate the loading history for a given component to an acceptable level of confidence. However, one single loading protocol cannot mimic the loading history for a

member as it depends on many parameters. The response of the component varies considerably depending on the history of the loading protocol. This is illustrated in Figure 6-12 where the differences are evident between envelopes of cyclic test results (that is, backbone curve) from six identical reinforced concrete bridge piers subjected to various loading protocols (FEMA-P440A, 2009). It shows that, although the backbone curves are similar in small drift ratios (< 2.5%), the backbone curves differ for larger drift ratios depending on the loading protocol.

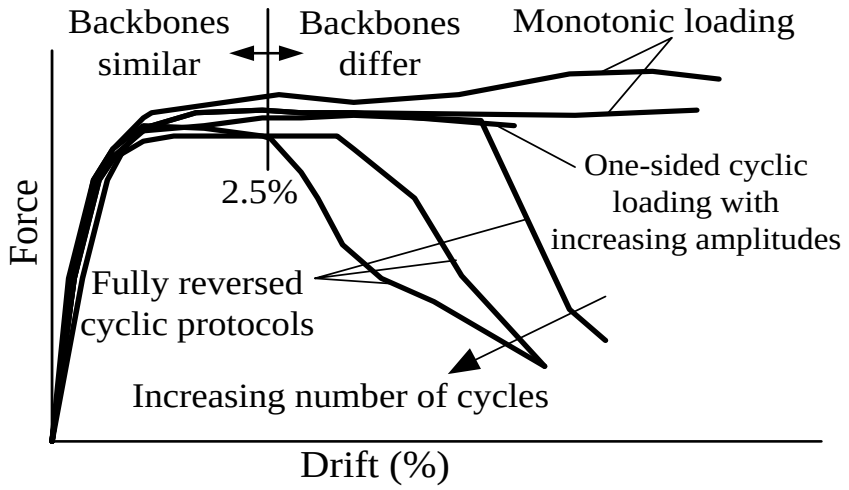

Figure 6-12 Envelopes of cyclic test results (backbones) from six identical reinforced concrete bridge piers subjected to various loading protocols (adapted from FEMA P-440A, Figure 2–20)

The force demands in a component subject to an earthquake force are affected by several parameters such as the intensity and frequency content of the ground motion, as well as modal properties, strength, stiffness, and the configuration of the structure (Krawinkler, 2009). When the applied loading changes, the response of the component changes accordingly. Consequently, the generated backbone curve differs from one loading to another. ASCE/SEI 41-17 (ASCE, 2017) provides an idealized force-deformation curve to incorporate the nonlinear characteristics of components of a building analyzed by nonlinear

static procedure (NSP) (Figure 6-13). Also, it uses the same backbone curve for the nonlinear dynamic procedure (NDP).

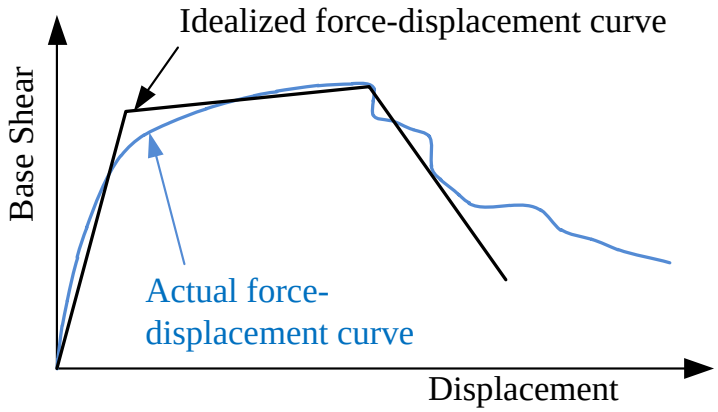

Figure 6-13 Idealized force-deformation curve

Beside using the backbone curve provided, ASCE/SEI 41-17 also allows one to develop the modeling parameters and the acceptance criteria based on available experimental data. This can be achieved by averaging the envelope curves of the cyclic tests data (ASCE, 2017). Figure 6-14 (c) illustrates the backbone curve construction using cyclic test envelopes. In the vast majority of cyclic tests, the loading protocol consisted of fully reversed incremental symmetric cyclic loading. While the effects of cyclic strength and stiffness degradation are considered in these cyclic protocols, it has a major shortcoming of defining the backbone curve solely based on fully reversed incremental symmetric cyclic loading (Krawinkler, 2009; Maison and Speicher, 2016; ASCE, 2017). This is because fully reversed cyclic loading differs significantly from the deformation histories at near-collapse response. To partially address this issue, ASCE/SEI 41-17 (ASCE, 2017) permits to modify the backbone parameters with the use of the monotonic response of the component. It allows the ultimate displacement of the backbone curve to be extended

(Figure 6-14 (c) and Figure 6-14 (d)) to the maximum displacement of the monotonic test result. However, it cannot be greater than 1.5 times of the capping point (where the tangent stiffness becomes negative) of the monotonic test. If multiple monotonic curves are available, the average of the ultimate displacement in the monotonic tests is recommended. Figure 6-14 (d) illustrates how a backbone curve is constructed by the combination of monotonically and cyclically tested components. Although this method permits a backbone curve that is constructed by both monotonic and cyclic backbones, the issue regarding the dependency of the backbone to the loading protocol is yet to be solved.

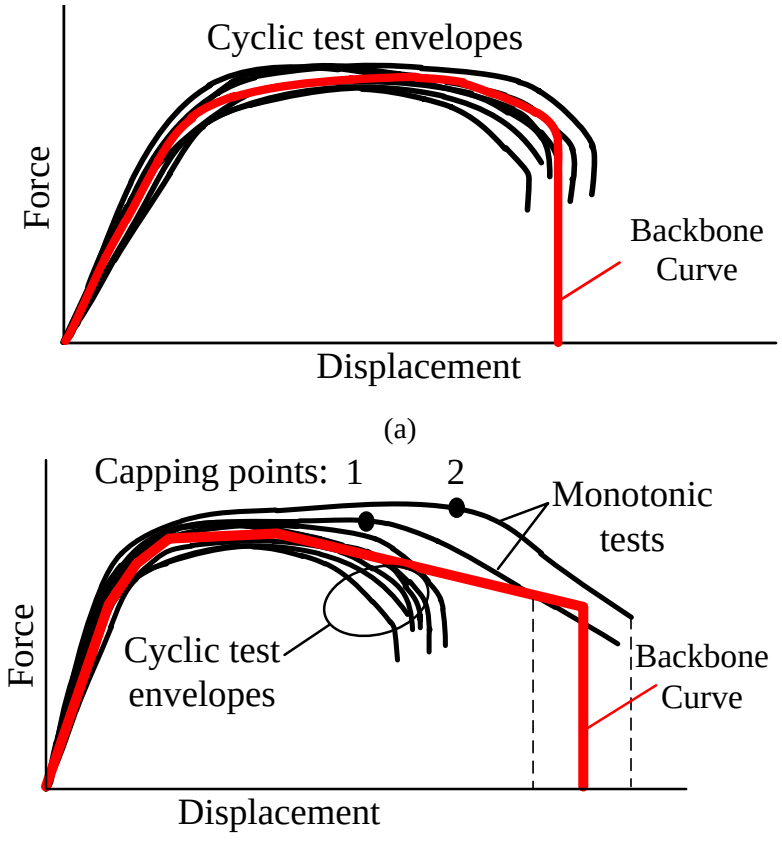

Figure 6-14 a) Backbone curve construction using cyclic test envelopes, and b) Backbone curve construction using cyclic test envelopes supplemented with monotonic tests (ASCE 41-17)

6.3 Full-scale reinforced concrete columns experimental data

In a prior study, five number of identical full-scale reinforced concrete columns has been subjected to different loading protocols (Nojavan et al., 2015). The columns were tested at the Multi-Axial Subassemblage Testing (MAST) facility at the University of Minnesota. The results of these experiments are used for verification purposes. The section of all the columns is a rectangular cross-section of 36 x 28 in. with sixteen #9 longitudinal bars as shown in Figure 6-15. Specimens are designed as a column for the ground-floor of a perimeter frame for a 20-story building (Nojavan et al., 2015). All the specimens were designed according to ACI 318-14 (ACI, 2014). Figure 6-16 represents the column details and dimensions.

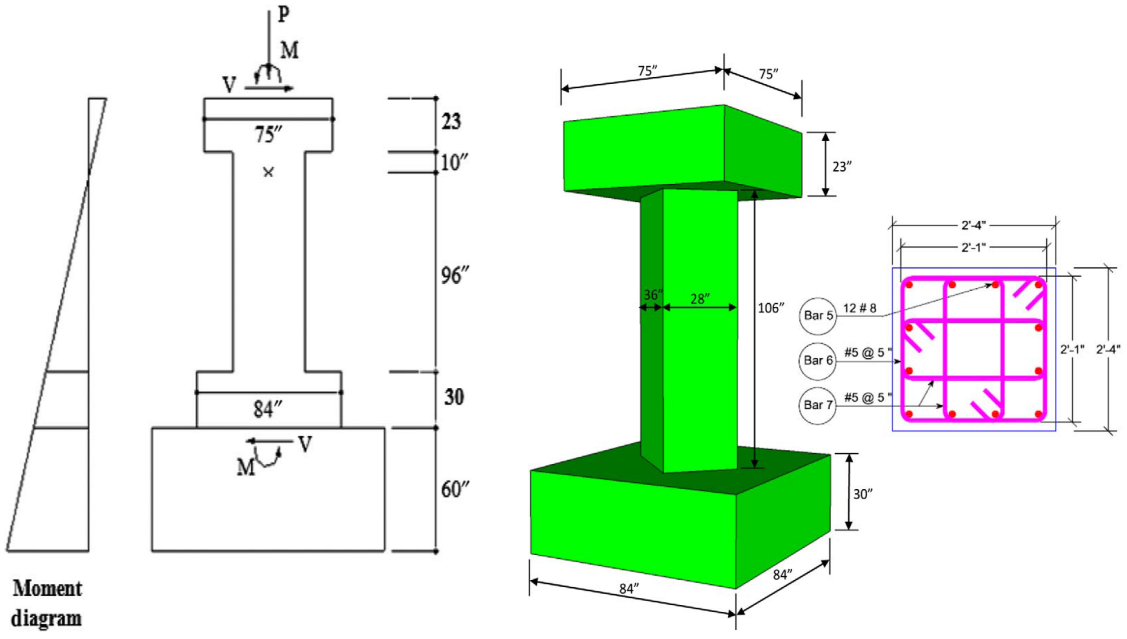

(a) (b)

Figure 6-15 a) locating inflection point and geometry of the specimens, b) dimension and cross section of the specimen (Nojavan et al., 2015)

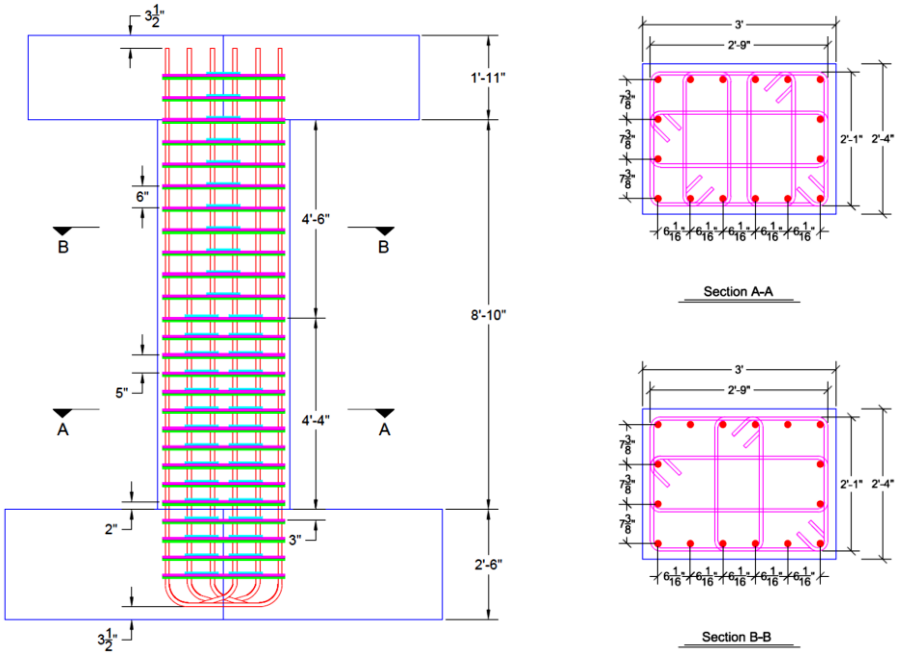

Figure 6-16 Column details and dimensions (Nojavan et al., 2015)

During the test, each specimen was subjected to a constant axial loading of 756 kips which is equal to an axial loading ratio of $p/p_0 = 0.15$, where p_0 is the production of gross cross-sectional area by the compressive strength of the concrete ($A_g f_c'$). However, the lateral load was different from one specimen to another. Figure 6-17 shows the loading protocols applied to the specimens and Figure 6-18 shows the column response under these loading protocols. In all the experiments the test was stopped either when the strength drop was more than 80% of the peak strength exhibited during the test or the drift could not be further increased due to capacity limitation of the actuator.

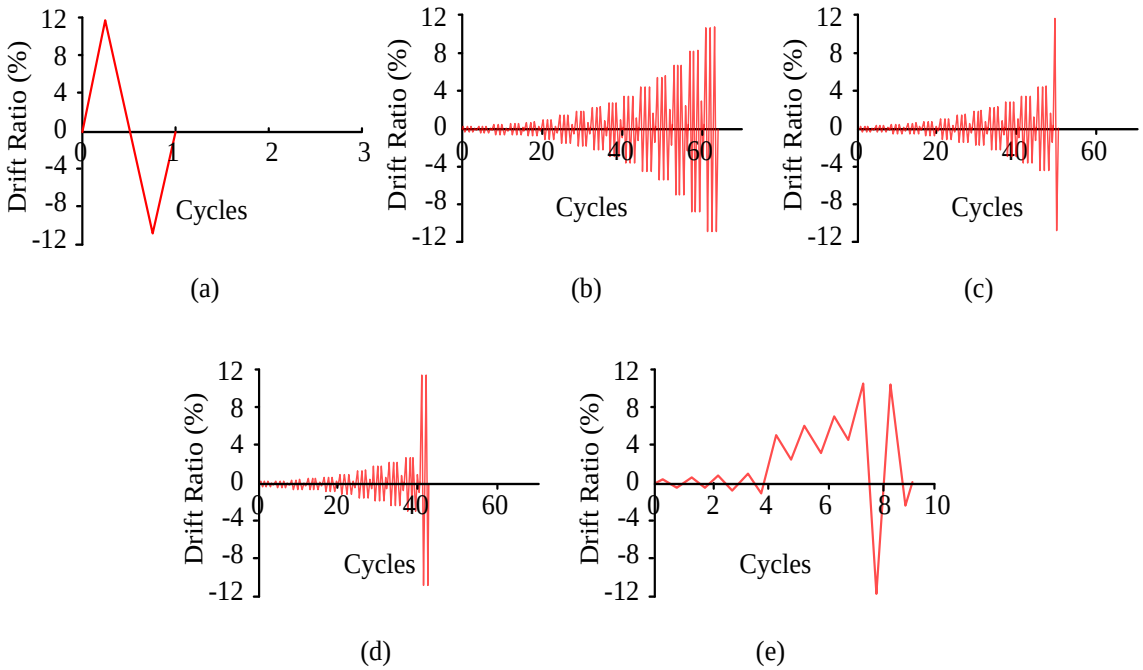

Figure 6-17 (a) single-cycle; (b) ACI 374 symmetric cyclic; (c) ACI 374 symmetric cyclic followed by final monotonic push #1;(d) ACI 374 symmetric cyclic followed by final monotonic push #2; (e) near-collapse (Nojavan et al., 2015)

The first loading includes a single symmetric loading (monotonic loading) with a maximum drift exceeding 10%, while the rest of loadings were selected to increase progressively during the test. The second loading protocol (Figure 6-17 (b)) follows a symmetric cyclic loading (ACI 374). Three cycles are performed for each peak drift ratio. Table 6-2 presents the loading sequence for the second loading protocol. The specimen experienced a significant strength loss after 4.375% DR which suggests that the column cannot exceeds this DR without substantial strength loss (Figure 6-18 (b)). Hence, the third loading protocol (Figure 6-17 (c)) followed the second loading protocol up to peak DR of 4.375%.

Table 6-2 loading sequence of the symmetric cyclic (ACI 374)

Cycle Group	Peak Drift (%)	Number of Cycles
1	0.2	3
2	0.25	3
3	0.35	3
4	0.5	3
5	0.75	3
6	1	3
7	1.4	3
8	1.75	3
9	2.2	3
10	2.75	3
11	3.5	3
12	4.375	3
13	5.75	3
14	6.85	3
15	8.25	3
16	10	3
17	11.75	3
18	13.5	3
19	15	3

The third loading protocol (Figure 6-17 (c)) follows the second loading protocol up to peak drift ratio of 4.375%. After three cycles performed for peak drift ratio of 4.375%, the specimen was loaded by a monotonic push exceeding 10% drift ratio. Figure 6-17 presents the loading sequence for the third loading protocol. As illustrated in Figure 6-18 (c), the column experienced a strength drop in the monotonic displacements. This is an appropriate loading protocol to reflect design level demands as it includes a series of incremental cyclic loadings and a large monotonic push to proceed to the failure state of the subassembly. However, this loading includes many numbers of cyclic loading prior to the monotonic push which is more similar to a cyclic loading rather than a near collapse loading protocol

that typically is biased toward one direction (ASCE 41-17). To further examine the column behavior under monotonic push preceded by cyclic loading, the next loading protocol was modified from the third loading protocol results. The fourth loading protocol (Figure 6-17 (d)) is similar to the third one with the large drift push induced after three cycles of 2.75% drift ratio. The peak drift ratio and their according number of cycles per each drift ratio are listed in Table 6-4. Loading protocols in Figure 6-17 (c) and Figure 6-17 (d) include many fully reversed cyclic displacements prior to the monotonic push. This type of loading protocol has many cycles and 2-3 cycles per deformation level, which is not representative of the ratcheting effect that leads to structural collapse. In other words, a near collapse loading protocol is typically biased toward one direction (ASCE, 2017). In this regard, the fifth loading protocol (Figure 6-17 (e)) was developed to simulate the near collapse loading applied to a column during a far-field earthquake record. In this loading protocol, a non-symmetrical push is following a few small cyclic (symmetrical) loading with drifts with less than 1% drift ratio.

Table 6-3 loading sequence of the third loading protocol

Cycle Group	Peak Drift (%)	Number of Cycles
1	0.2	3
2	0.25	3
3	0.35	3
4	0.5	3
5	0.75	3
6	1	3
7	1.5	3
8	2	3
9	2.75	3
10	3.25	3
11	4.375	3
12	>10	1

Table 6-4 loading sequence of the fourth loading protocol

Cycle Group	Peak Drift (%)	Number of Cycles
1	0.2	3
2	0.25	3
3	0.35	3
4	0.5	3
5	0.75	3
6	1	3
7	1.5	3
8	2	3
9	2.75	3
10	>10	2

6.3.1 Tests results

Figure 6-18 illustrates the response of the five identical columns under the five different loading protocols. Figure 6-18 (a) shows the column is pushed to 11% in both direction and its strength degradation became significant only after it experienced a fully reversed 11% DR cycle. This indicates that under monotonic displacement, the column was capable of undergoing even a large drift ratio (>10%) with no sudden drop in its strength.

Figure 6-18 (b) represents the response of the column under the loading protocol with many fully reversed cycles. Under this loading, the column maintained its peak strength up to 4% drift ratio and did not show a significant strength degradation. The column experienced sudden degradation at the 5.75% drift ratio due to rebar rupture in the longitudinal reinforcement. At the end of the third cycle the strength of the column was significantly dropped more than 80% of its peak strength (less than 20% of the peak strength).

Comparison between the responses of the column under 3rd and 4th loading protocol illustrates the effect of cyclic degradation. In the loading protocol with fewer number of cyclic loading prior to a monotonic push (Figure 6-18 (d)), no strength drop was noticed in the last cycle with large drift ratios (2.75% DR). On the other hand, the column shows a notable cyclic strength degradation after 4% drift ratio cycle under the third loading protocol (Figure 6-18 (c)). Also, in the last monotonic push cycle, the column exhibited a more significant strength drop in the reverse direction. While in there loading with fewer number of cyclic loading prior to a monotonic push the column is still capable to maintain its strength for a full cycle with a large drift ratio.

The response of the column under the near collapse loading protocol is shown in Figure 6-18 (c). A comparison between the loading protocol with one single large drift is similar to the near collapse loading protocol. This shows that the behavior of a column under a loading protocol with few numbers of cycles with small drift ratios (no larger than 2.75% DR) remain unchanged and the cyclic and in cycle strength degradation remains insignificant.

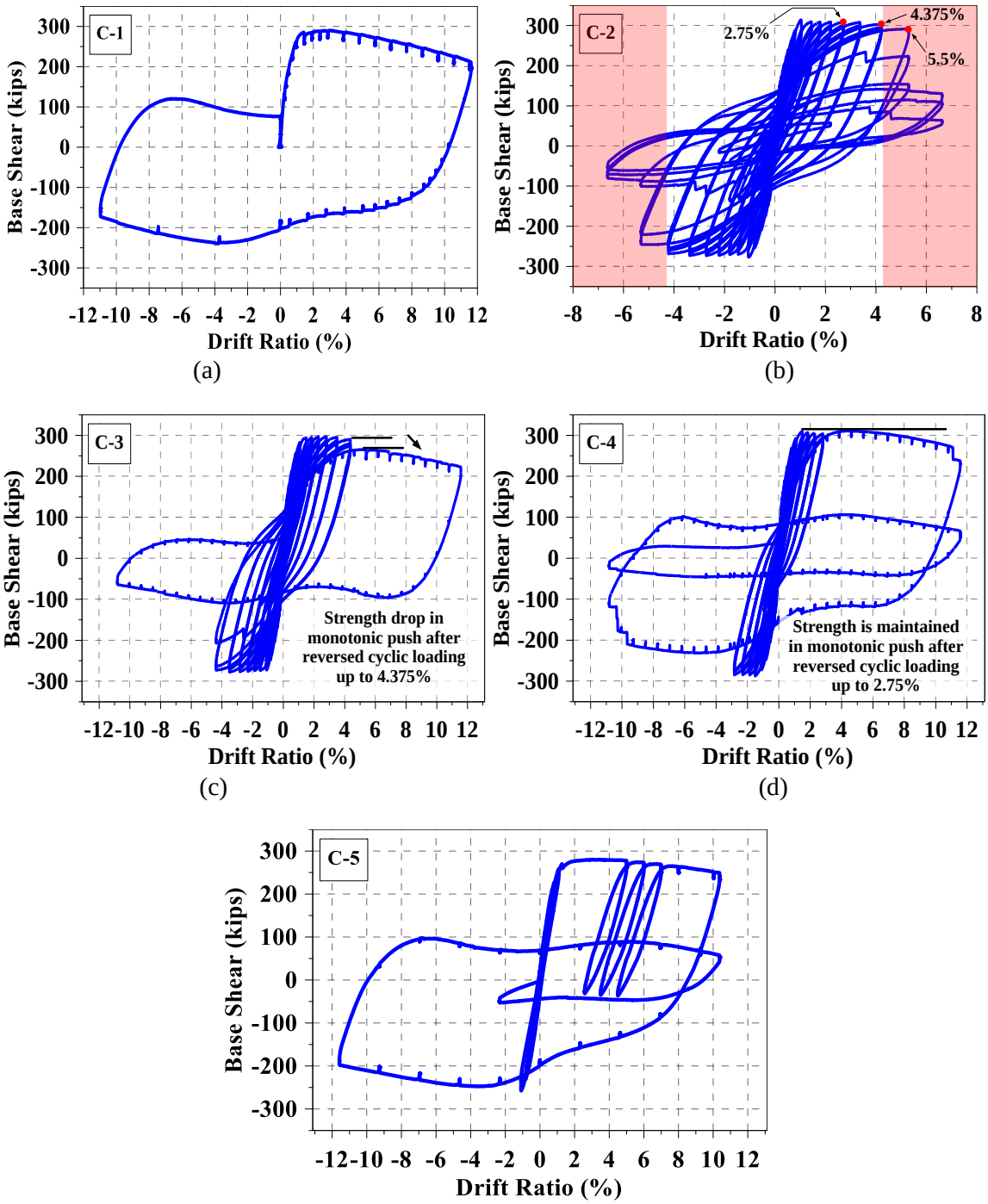

Figure 6-18 response of the identical columns to loading protocols (a) single-cycle; (b) ACI 374 symmetric cyclic; (c) ACI 374 symmetric cyclic followed by final monotonic push #1; (d) ACI 374 symmetric cyclic followed by final monotonic push #2; (e) near-collapse

Chapter 7
Part II

Dual-Degradation Model (DDM)

7.1 Introduction

When a column is subjected to vertical loading in combination with a relative lateral displacement between the two ends of the column, the vertical loading creates a horizontal couple (v) to satisfy equilibrium (Figure 7-1 (a)). This horizontal force is proportional to drift ratio (Δ/L) and the vertical force (P). Therefore, it will be increasing as the drift ratio increases. If the drift is produced due to static lateral loading applied at top of the column (V), the resulting base shear at the bottom of the column will be the difference of the applied lateral load and the magnitude of the couple force ($V_r = V - v$) (Figure 7-1 (b)). where v can be taken as the reduction of the lateral strength due to the P-Delta effect.

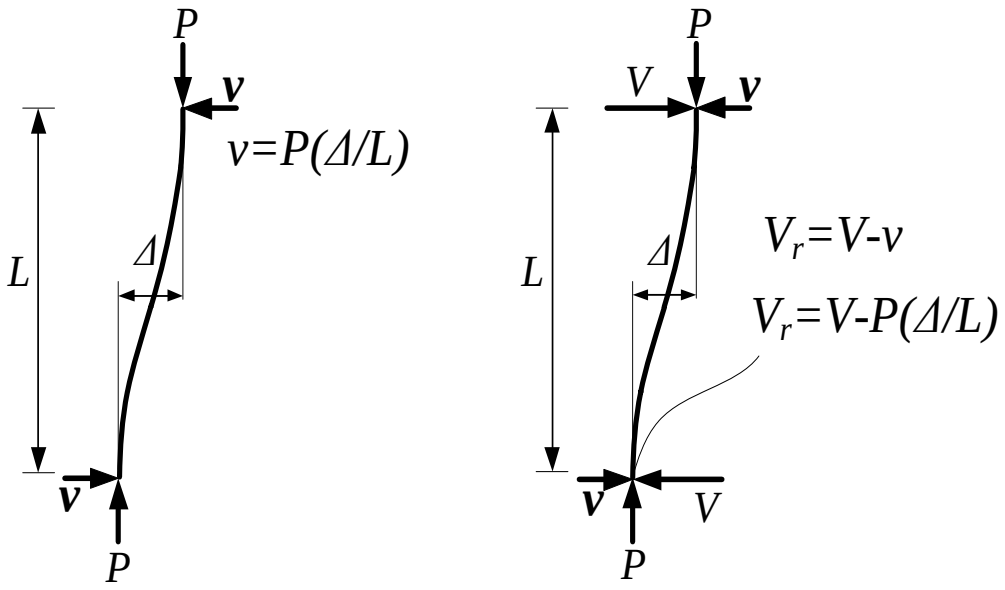

Figure 7-1 a) vertical couple force to satisfy equilibrium and b) the resulting base shear

The reduction in the lateral load resistance (or resultant base shear) is smaller where the drift ratio is small. However, the reduction becomes significant when the drift ratio reaches larger levels. Therefore, if the post-yielding stiffness of the response has a small positive

value, a negative stiffness can be recorded during the test due to the large reduction in the lateral load resistance. The post-yield stiffness is affected not only by the P-Delta effect but can also be affected by strength and stiffness degradation due to damage of the column under cyclic forces. Two types of degradation have been identified which include cyclic degradation and in-cycle degradation (FEMA-P440, 2009). Cyclic degradation is defined as a strength and stiffness degradation occurring in subsequent cycles and a system with cyclic degradation has stable dynamic response. On the other hand, in-cycle degradation is defined as a strength and stiffness degradation occurring within the same cycle which yielding occurs and a system with in-cycle degradation is prone to dynamic instability or collapse. FEMA 440A (2009) states that in-cycle strength degradation can occur due to P-Delta effect, material nonlinearities, or combination of both. FEMA 440A further explains that material nonlinearities leading to in-cycle strength degradation include concrete crushing, concrete shear failure, buckling or fracture of longitudinal rebars, and splice failures.

If the reduction in the lateral load resistance is misinterpreted as completely resulting from material nonlinearities and is implemented as a negative post-capping stiffness in the plastic hinge model, the model would not be able to represent the real column behavior. This becomes more critical in perimeter moment frames commonly used in modern buildings. These perimeter moment frames typically have a smaller axial force ratios in columns due to smaller tributary gravity loads and large column cross-section because moment frames are only located around the perimeter of a building. Since smaller axial force ratio results in less strength degradation (FEMA- P695, 2009), a larger portion of the lateral resistance reduction will be originating from the P-Delta effect. To illustrate the

contributions of in-cycle strength degradation, Figure 7-2 compares measured base shear with and without P-Delta (removing P-Delta force computed according to Figure 6-18).

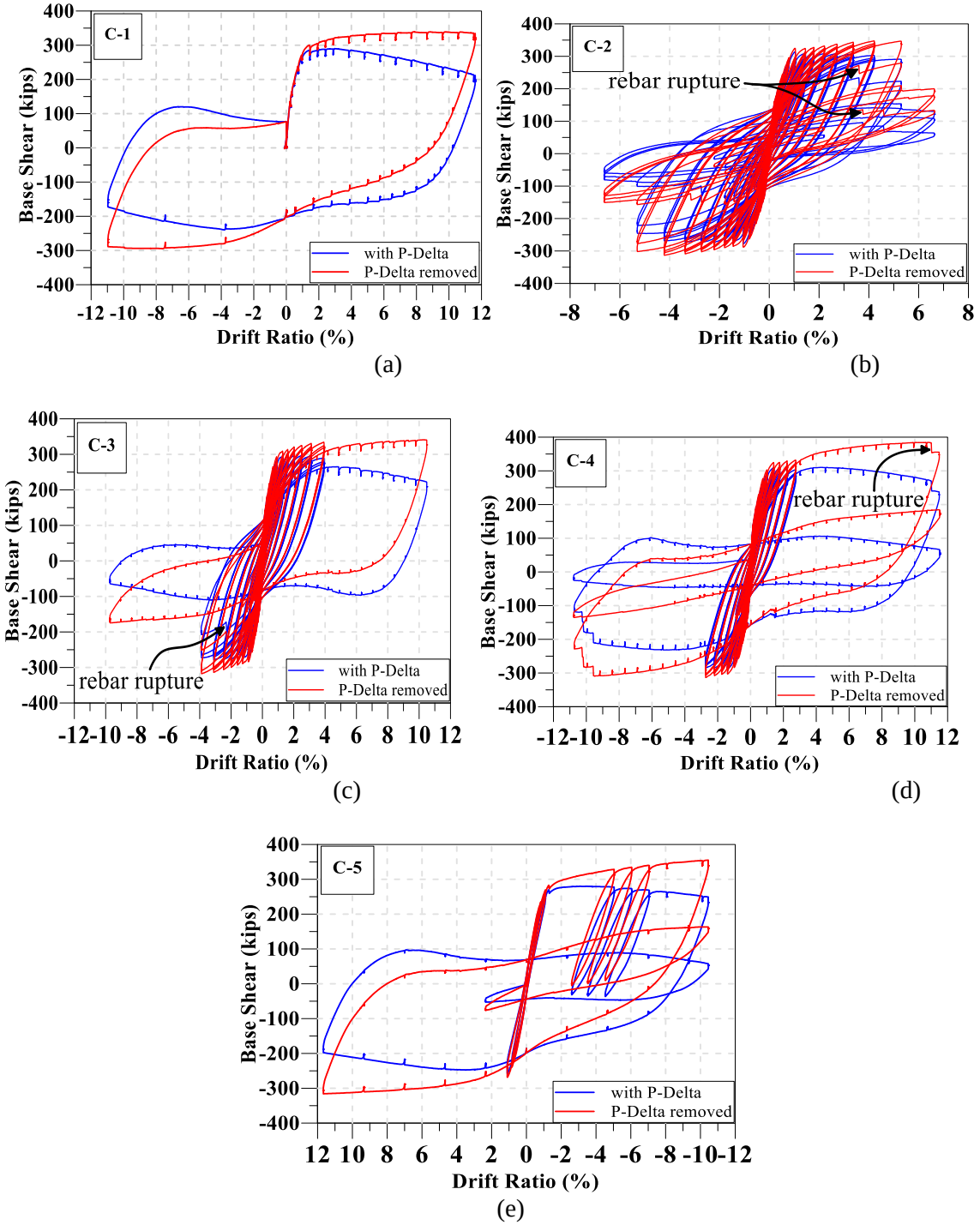

Figure 7-2 Base shear results with the P-Delta effect removed for various loading protocols

It is observed that when the P-Delta effect is removed, no evidence shows gradual negative stiffness or in-cycle strength degradation exists due to any of the loading protocols used even up to very large drift ratios (DR >10%). In the loading protocols that include many fully reversed displacement cycles, sudden drops are observed due to rupture of the rebars. However, in the same cycle, the strength picked up again after the drop. This pattern is observed even in the second and third cycles of the maximum drift level for the cyclic loading protocol (Figure 7-2 (b)). This observation from these full-scale and ACI-318 compliant columns indicates that some of the material nonlinearities (concrete crushing, buckling or fracture of longitudinal rebars) play a negligible role in the dynamic instability of a structure. Most importantly, this means that the post-yielding stiffness of this column remains positive and a backbone curve that includes negative stiffness is not an appropriate representative for the plastic hinge model.

7.2 Backbone Curve

The cyclic backbone curve is generated by means of a series of secants that connect the peak strength of the specimen in the first cycle of i^{th} drift level to the $(i+1)^{th}$ one (GCR.17-917-45, 2017). Generally, after reaching the nonlinear part of the curve, the peak strength of a reinforced concrete column increases in a range of small drifts. However, when the drift demand increases, the peak strength for the first cycle at each drift starts to degrade from one level to the next larger drift level. Figure 7-3 shows the derivation of the first and second cycle backbone curves.

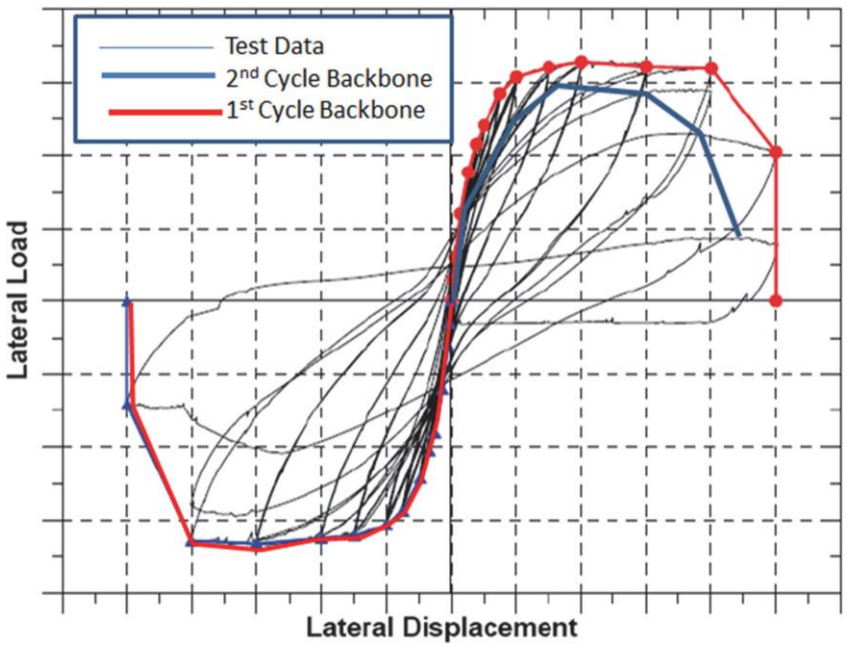

Figure 7-3 Derivation of first and second cycle backbones from cyclic test data (figure 2-4 of GCR 17-917-45, NIST, 2017)

There are limitations and drawbacks in generating the backbone curve with this method. Since the backbone is derived from enveloping the peak strength from one smaller drift step to the next larger one, it mistakenly reads cycle-to-cycle strength degradation in lieu of in-cycle degradation. Further, should a fully reversed cyclic incremental loading protocol with three full cycles at each drift level (such as symmetric cyclic loading- ACI 374) used, the cycle-to-cycle degradation rate will increase. Hence, plastic hinge models using this capacity boundary will exhibit an abrupt in-cycle degradation that originates from cyclic degradation. For this reason, ASCE/SEI 41 permits to modify the cyclic backbone by combining it with a monotonic one (ASCE, 2017). However, the resulting backbone still will be affected by the cyclic backbone and contains the abrupt post-yielding negative slope. Although this method has merits when it is used for nonlinear static

analysis, it cannot accurately predict the actual cyclic responses in nonlinear dynamic analysis (*GCR.17-917-45*, 2017).

To further elaborate the drawback of using the cyclic backbone curve, Figure 7-4 compares the cyclic backbone curves (solid red lines) plotted versus a new type of strength envelope curve (dashed black lines) for two loading protocols with large number of cycles. In this strength envelope curve, instead of using secants connecting the peak strength for different drift levels, the maximum base shear for any drift level is used. The P-Delta effect is also removed for better presentation of the in-cycle strength degradation in each loading protocol. The sudden drops in the dashed black curves, shows the cycle-to-cycle (cyclic) strength degradation. For both loading protocols, the cyclic backbone curve shows an increasing negative stiffness for drifts larger than 4%. However, the corresponding strength envelope curves, which lay out the maximum base shear at each drift level, show positive stiffness in all the range of experienced drifts for each specimen.

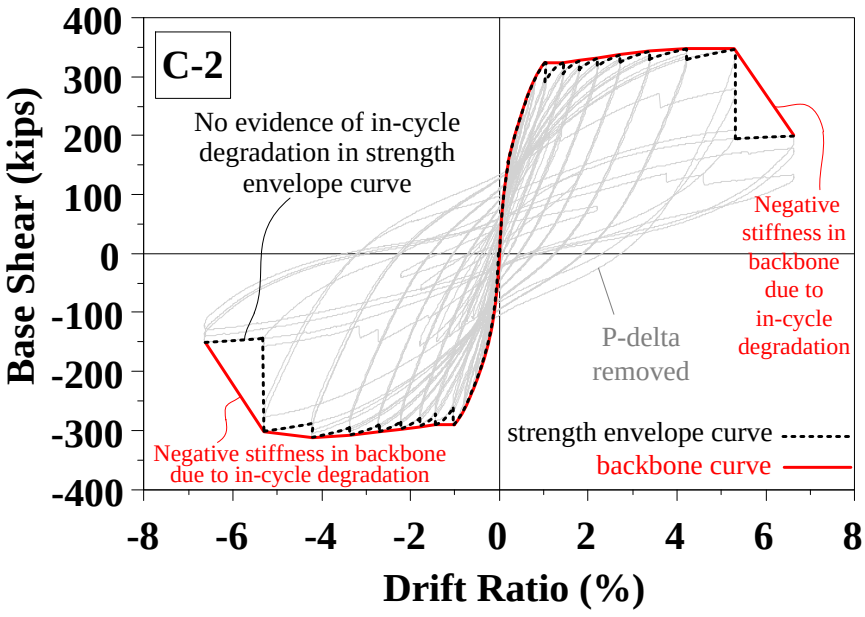

(a)

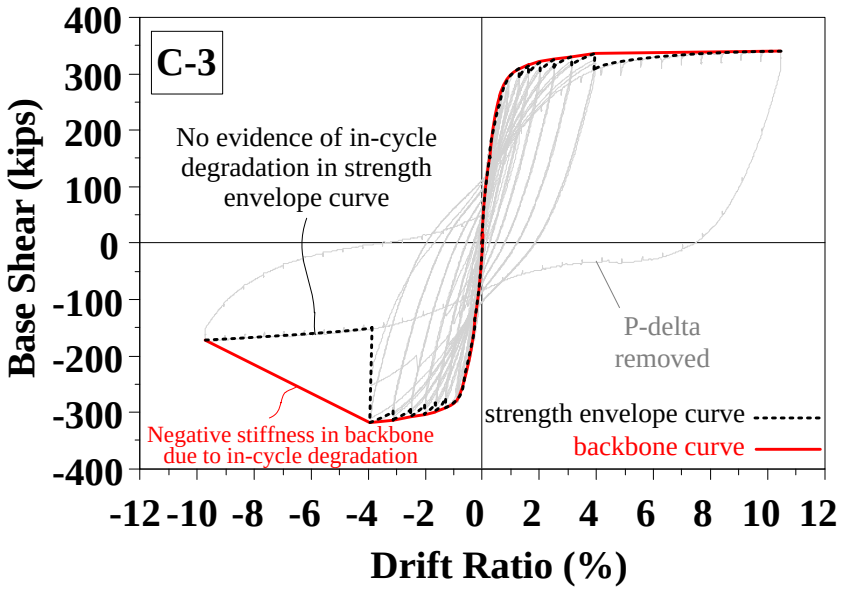

(b)

Figure 7-4 Comparison between the backbone curves of test column specimens in typical method and the real strength envelope for a) symmetric cyclic loading and b) many numbers of symmetric cyclic followed by a monotonic push #1

Figure 7-5 also compares the cyclic backbone curves (dotted lines) plotted versus the strength envelope curve (solid lines) for different loading protocols. To emphasize the positive stiffness of the column response when the drift ratio is increasing (even after a sudden drop), the P-Delta effect is removed for the strength envelope curve. The sudden drops in the plot for column C2 (black-solid line in Figure 7-5Figure 7-5 (a)) and column C4 (black-solid line in Figure 7-5 (b)), shows the cycle-to-cycle (cyclic) degradation. The cyclic backbone and the envelope curve are the same for the column C1 and C5 if the P-delta is removed. However, for C2 and C3, with considerable number of fully reversed cycles, the differences become noticeable. For both loading protocols, the cyclic backbone curve shows an increasing negative stiffness for drifts larger than 3%. However, the

corresponding envelope curves, which lay out the maximum base shear at each drift, show positive stiffness in all the range of experienced drift for each specimen.

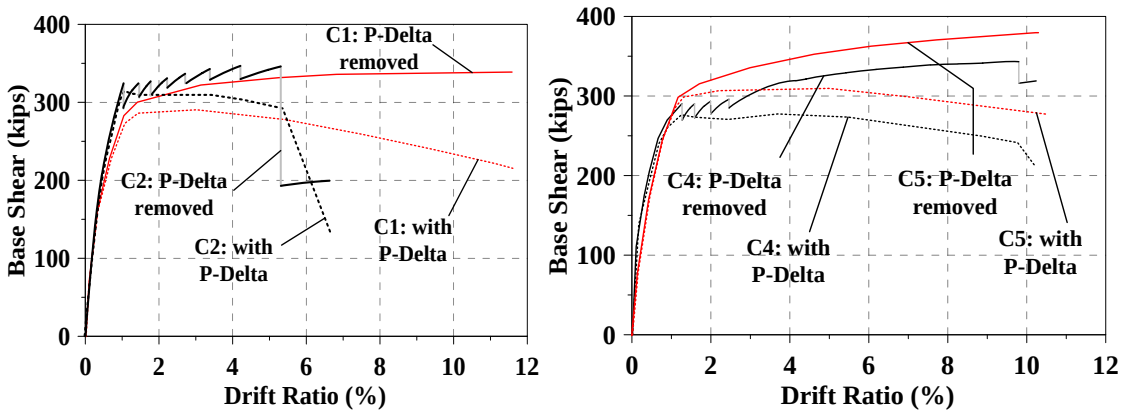

(a) (b)

Figure 7-5 Comparison of the cyclic backbone curves plotted versus the strength envelope curve for a) C1 and C2, and b) C4 and C5

Another issue with overestimated negative stiffness in many current plastic hinge models is that the underestimated peak strength that limits transferring the earthquake force from the base to upper stories (PEER, 2017). Figure 7-6 compares three different post-capping stiffnesses and the corresponding flexural strengths in a plastic hinge model. The three backbone curves follow the same path up to capping point where the rotation is θ_c and the flexural strength is M_c. If the rotation increases to $\theta_1$the flexural strength would behave differently in the three curves. As illustrated in Figure 7-6, the model with larger negative stiffness would exhibit smaller remaining strength at rotation equal to θ_1. Due to complexity of the nonlinear dynamic analysis, this may result in different scenarios. If the first story columns of a building are modeled with an overestimated negative stiffness, the shear transferred to upper stories will be limited to the boundary capacity of the columns

in the lower stories. If the dynamic stability of the building is maintained, this may lead to underestimated drift for upper stories.

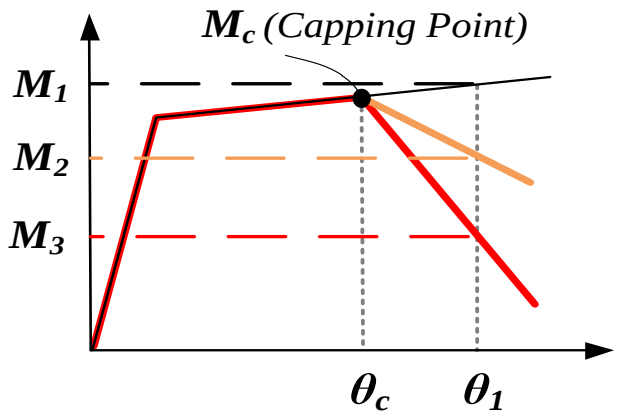

Figure 7-6 different post-capping stiffness in a plastic hinge model

Figure 7-7 shows the prediction of the backbone curve for the full-scale columns mentioned above using equations proposed in the literature (PEER, 2008). The equations predict a steep post-capping negative stiffness for the column which is not observed in the experimental test.

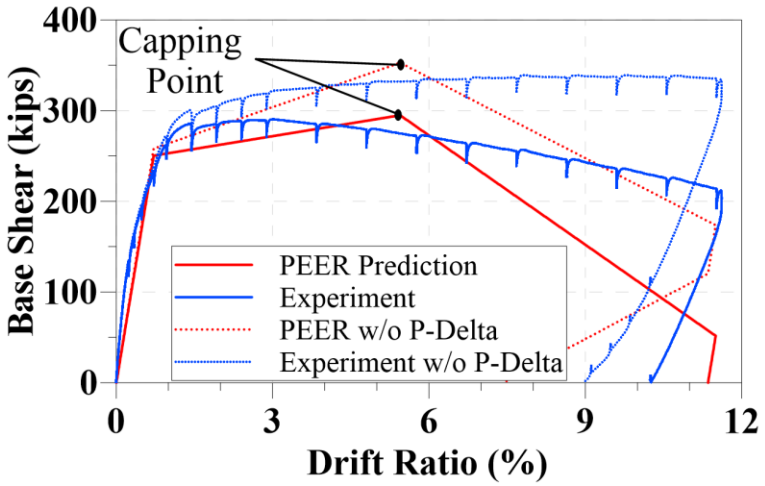

Figure 7-7 PEER backbone prediction for the full-scale column test results (P-Delta included in the structural model)

7.3 Dual Degrading Model (DDM)

One way to model structural component response by means of a zero-length plastic hinge element is to define a monotonic backbone for the plastic hinge and apply deteriorating parameters to produce the cyclic response (PEER, 2017). In this procedure, the degradation parameters are obtained through calibration according to experimental results database. In prior studies, a set of equations are proposed to predict the strength and initial stiffness, as well as these parameters for RC columns (PEER, 2008; Haselton et al., 2016). A simplified equation to calculate the degradation parameter is as follows:

$$\lambda = (170.7)(0.27)^{v}(0.10)^{s/d} \qquad \textit{Equation 7.1}$$

Where v is axial load ratio ($P/A_g f_c'$) and s/d is the ratio of tie spacing to the depth of the column. Based on the same procedure, NIST (GCR 17-917-45, 2017) presents simulated responses for the five columns tested by Nojavan et al. (2015) as shown in Figure 6-18. However, it states that they are individually calibrated to provide the best possible fit. Figure 7-8 represents the comparison between the numerical and experimental results; where the numerical models was individually calibrated to match the experimental results. That is, each set of parameters needs to be recalibrated to predict the behavior if the column is subjected to another loading protocol. However, it is imperative to develop a model that can predict the cyclic behavior of a column section under different loading histories This is because the actual loading history from a future earthquake-loading history is essentially unknown and is different from one part of a building to another. Consequently, it is

challenging to calibrate a plastic hinge model in advance to have an accurate model to predict the structure's behavior.

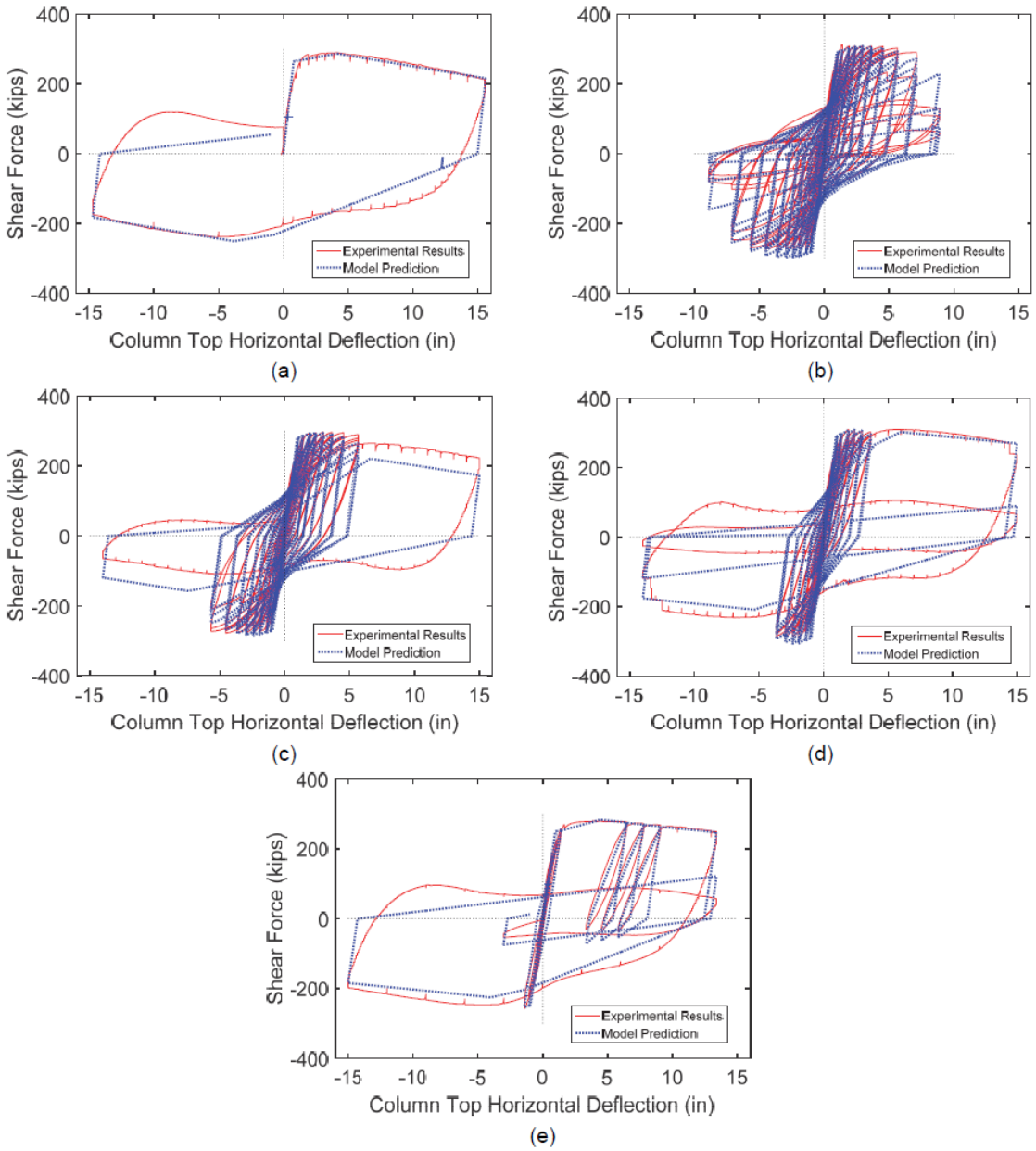

Figure 7-8 Experimental test data and calibrated model predictions for five different loading protocols: (a) monotonic in each direction; (b) ACI 374 (ACI, 2005) symmetric cyclic; (c) ACI 374 symmetric cyclic followed by monotonic push # 1; (d) ACI 374 symmetric cyclic followed by monotonic push # 2; (e) and a near–collapse loading protocol (after Nojavan et al. 2014; 2016). (GCR 17-917-45, 2017)

Figure 7-9 gives an example where the response, based on the model proposed by Ibarra et al. (2005), was first calibrated based on a near-collapse history (Figure 7-9 (a) and Figure 6-17 (e)), but it does not capture well the response when the loading history had multiple symmetrical cycles (Figure 7-9 (b) and Figure 6-17 (c)). This illustrates the limitations of using current hysteretic models in predicting the cyclic response of a component under different types of loading protocols.

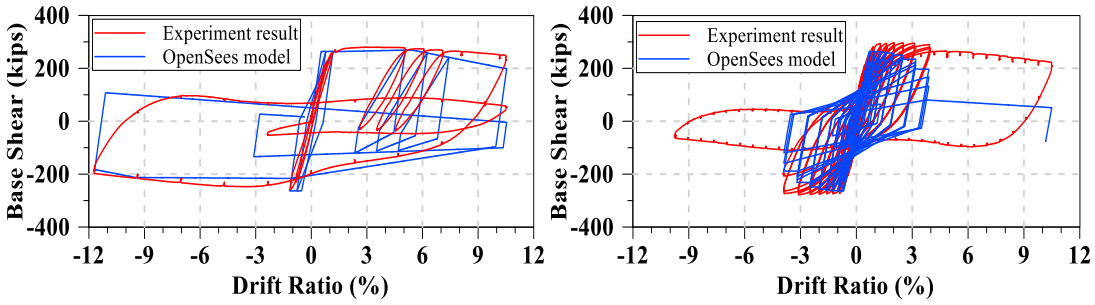

Figure 7-9 Simulation results using Ibarra's model versus experimental results (Nojavan et al., 2015)

The need for recalibrating the columns for each loading protocol, illustrates the limitations of using current hysteretic models in predicting the cyclic response of a component under different types of loading protocols.

To better predict the inelastic behavior of an RC column under different loading protocols, as well as to consider the fact that the material nonlinearities are not a major factor leading to in-cycle deterioration as observed from full-scale column tests, two major differences were applied in the modified model:

1) Allowing the post-capping behavior (negative stiffness) to be shifted to a large displacement for the cases without in-cycle degradation due to material nonlinearities:

The rationale supporting this modification is based on the observation in the full-scale column testing results. As discussed above, the comparison between the responses of the full-scale columns with and without the P-Delta effect, indicates that assuming capping point occurring at a small rotation in the backbone curve results in an incorrect behavior of the column. In all the test results, the major source of negative post-peak stiffness was the P-Delta effect (Figure 7-2). Hence, to predict a realistic column behavior, the plastic hinge model needs to fit the test results after the P-Delta effect is removed. Figure 7-10 (a) illustrates this modification schematically. For the cases which have obvious in-cycle degradation due to material nonlinearities, the capping point can be defined at smaller rotation according to the experimental results or simulations obtained from fiber models.

2) Dual-degradation behavior:

In the typical plastic hinge model such as Ibarra's model (Ibarra et al., 2005), all deterioration related parameters are incorporated in one single "spring" associated with the plastic hinge. Our studies indicate that it is practically very challenging to calibrate the single-spring model using multiple loading protocols simultaneously. That is, the single-spring model can only be calibrated by one loading protocol at a time, and it needs to be recalibrated if the member is subjected to loading histories that are significantly different from the one used for calibration. This is a main drawback because if one set of parameters can fit multiple distinct loading histories, it can provide higher accuracy for a structure subjected to different loading histories resulted from earthquakes. Our studies show that this issue can be significantly minimized by using two or more parallel springs which expand the number of deterioration parameters. In this study, a two-spring model was adopted, and each spring is assigned a different set of values to the deterioration parameters

hence the two springs exhibit different rates of deteriorations (Figure 7-10). This approach shows promising results in calibrating the plastic hinge model by multiple loading protocols simultaneously with only one set of parameters. While additional parallel springs could be used to further optimize the plastic hinge model, the two-spring model has been shown to provide sufficient accuracy and significantly minimize the effort in calibration.

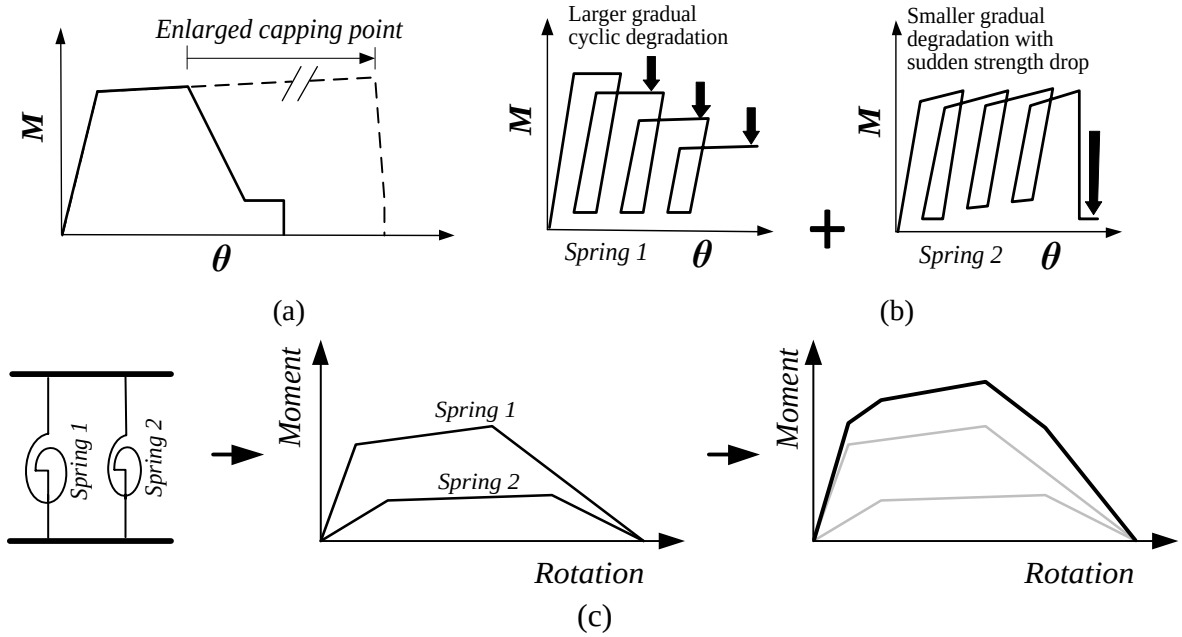

Figure 7-10 a) enlarged capping point, b) combined gradual and sudden degradation of the sub-models and c) parallel springs mechanism

In the proposed two-spring model, one of the springs has a gradual cyclic strength degradation with larger deterioration from one cycle to the next cycle while the other spring has a smaller cyclic strength degradation but a large sudden drop in strength beyond certain cumulative rotations (Figure 7-10 (b)). The gradual degradation simulates factors contributing to strength degradation such as concrete cracking and crushing while the

sudden degradation represents loss in strength such as rebar rupture after large amount of cumulative inelastic strains. The two springs are implemented by means of defining two zero-length elements that work parallelly at the plastic hinge (Figure 7-10 (c)). The post-peak stiffness of the model can be positive or negative for each of the paralleled sub-models depending on the severity of the material damage. In this model, if needed, the positive post-yield stiffness which represents the strain-hardening of steel reinforcement can be assigned to either spring. An example is given in Spring 2 in Figure 7-10 (b).

To numerically generate this dual degrading model, a column is built in OpenSees platform (McKenna et al., 2000), and then the two springs are implemented in the plastic hinge. Both springs use a peak-oriented hysteretic model such as the Ibarra in Opensees (Figure 6-11). Based on an energy-based deterioration parameter, this model captures the hardening behavior and strength deterioration, as well as the accelerated reloading and unloading stiffness deterioration. The cyclic deterioration in each excursion of this model is defined by parameter β_i where:

$$\beta_i = [E_i / (E_t - \sum_{j=1}^{i} E_i)]^c \qquad \text{Equation 7.2}$$

where E_i is the hysteretic energy dissipated in excursion i, E_t is the reference hysteretic energy dissipation capacity, $E_t = \gamma F_y \delta_y$. The parameter γ which is related to section properties, expresses the hysteretic energy dissipation capacity which is calibrated from experimental results or fiber model analysis, and c is the parameter that determine the rate of deterioration. (Rahnama and Krawinkler, 1993).

When experimental results with identical columns subjected to different loading protocols are not available, the calibration can be done by using fiber models. It has been shown the

fiber model can accurately generate the hysteresis response of a RC section (details are given in the next section), including strength degradation. While a fiber model is a useful tool to generate the hysteresis response of a RC section, it is still not a practical tool for nonlinear time-history analyses of structures due to the convergency problems, especially the incremental dynamic analysis (IDA).

To establish and calibrate the Dual Degrading Model, the authors recommend first use a monotonic curve obtained from an experimental result or fiber model analysis to define the parameters in the monotonic backbone of the model. Then, calibrate the model using at least three loading protocols with many numbers of cycles with and without a monotonic push. The multiple cycles and the monotonic push can help calibrate the behavior of the cyclic deterioration and the effect of a large unidirectional displacement after cyclic deterioration. These loading protocols can be similar to those shown in Figure 6-17 (b), (c), and (d). Figure 7-11 illustrates the application of the proposed Dual Degrading Model using the full-scale column test results shown in Figure 6-18.

As discussed above, only set of parameters are required to simulate the behavior resulted from all five loading protocols. The optimized values for the cyclic strength deterioration parameters for Spring 1 are: deterioration rate, c = 1.6 and hysteretic energy dissipation capacity, γ = 11,000. For Spring 2: deterioration rate, c = 2.2 and hysteretic energy dissipation capacity, γ = 240. Note that in the Ibarra model there are other three sets of c and γ for the post-capping strength deterioration, reloading stiffness deterioration, and unloading stiffness deterioration. However, these three sets of parameters have minimum effect on the hysteresis loops and can be generally deactivated to reduce the convergency issues for nonlinear time-history analysis.

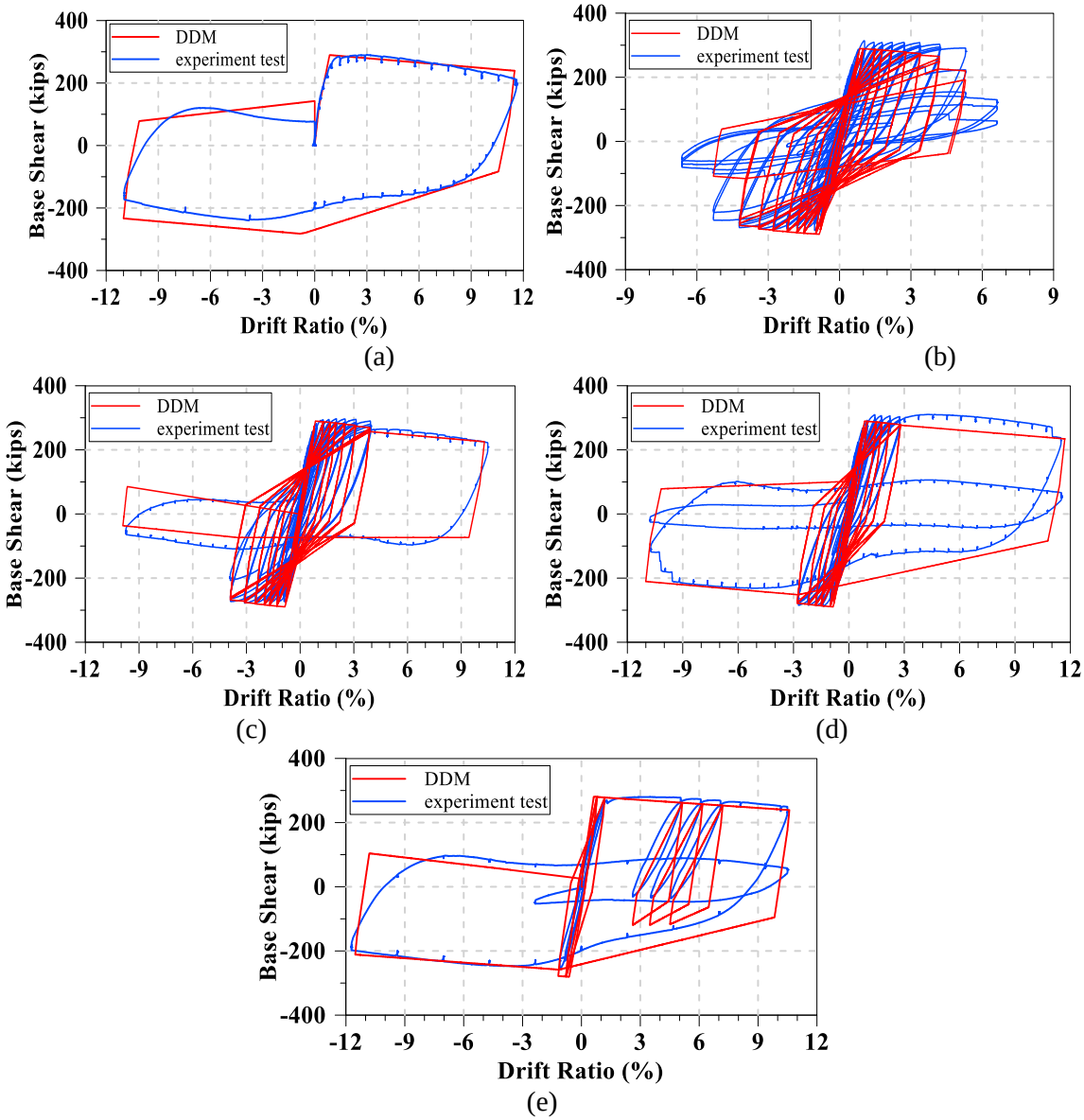

Figure 7-11 One set of calibration for dual degrading model (DDM) used to predict the column response under different types of loading protocol

7.4 Fiber model

A fiber model can be developed to provide the database for calibration purposes for the plastic hinges simulated with DDM. To show the validity of the fiber model, the analysis results of the fiber model are compared with the experimental results of the full-scale

columns (Nojavan et al., 2015). The fiber model uses constitutive models and elements implemented in OpenSees (McKenna et al., 2000). Typically, a fiber model consists of two parts: 1) a zero-length element at the base (Figure 7-12Figure 7-12 (c)), and 2) a nonlinear beam-column element (Figure 7-12 (b)). The nonlinear beam-column element uses a fiber-section to implement the stress-strain law (Neuenhofer and Filippou, 1998). The section is discretized into smaller fibers, each of which is assigned with appropriate uniaxial concrete or steel general stress-strain law. The fibers have different material properties for cover concrete (unconfined) and core concrete (confined). The concrete's stress-strain curve is determined by equations according to Mander et al. (1988). For the reinforcing steel fibers, a linear strain accumulation model is used to account for the low-cycle fatigue effect; that is, beyond certain accumulated inelastic strains, the reinforcing steel will rupture. The zero-length element is added in the model to account for the shear deformation and bar-slip of the fiber model. As recommended in NIST (*GCR.17-917-45*, 2017), a shear stiffness of $0.4E_cA_g$ and a rotational stiffness with a linear stiffness are included in the zero-length element which is located at the bottom of the column. The rotational stiffness can be calculated as:

$$K_{SE} = \frac{2M_y}{\phi_y l_{sp}} \qquad \textit{Equation 7.3}$$

Where the yield penetration length:

$$l_{sp} = \frac{l}{38.4(3.2)} \frac{f_y}{\sqrt{f_c'}} d_b \qquad \textit{Equation 7.4}$$

This elastic bar-slip spring cause bar-slip softening occurs in the shape of softening the steel fiber hardening slope (*GCR.17-917-46v3*, 2017).

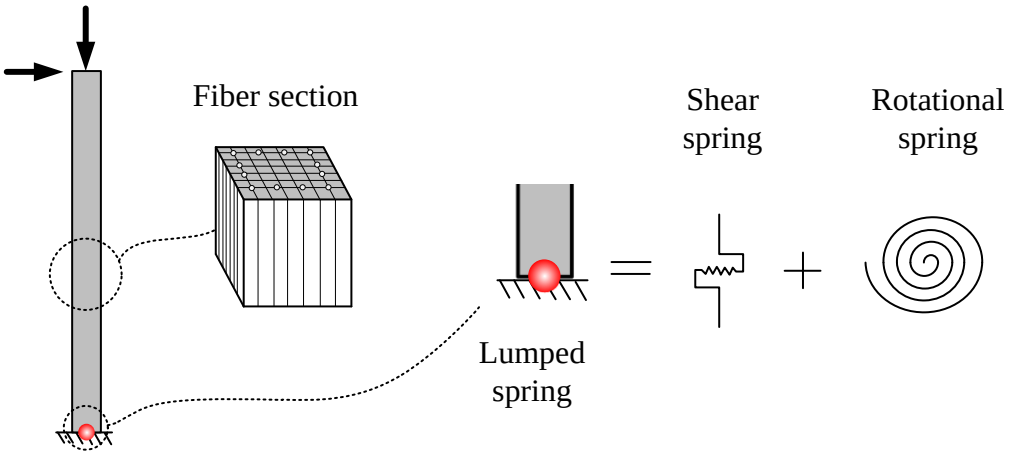

Figure 7-12 a) column model, b) fiber section and c) zero-length element

Figure 7-13 compares fiber model results and the full-scale column test results under different loading protocols. The P-Delta effect is also considered. It can be observed that the hysteresis responses of the RC column predicted by the fiber model match well the test results, including the cyclic degradations. Notably, the fiber model is conservative in terms of predicting low-cycle fatigue life of the steel reinforcement (for instance, Figure 7-13 (c)); however, it has marginal impact to the overall response. Therefore, fiber models are an appropriate alternative to produce hysteresis responses for RC columns under different loading histories and can be used to establish the database for calibration of column plastic hinges.

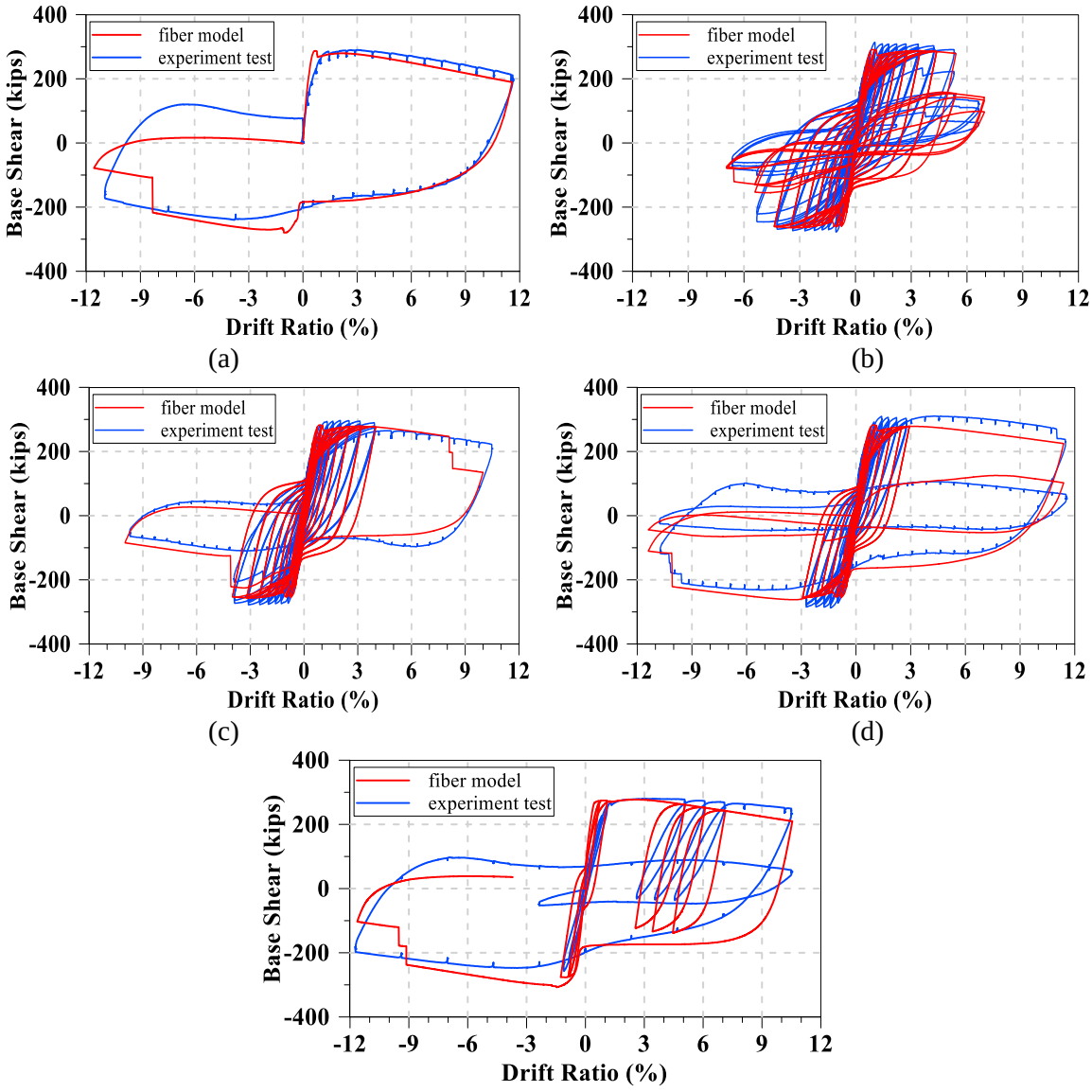

Figure 7-13 Fiber model results and full-scale column test results (Nojavan et al., 2015) under different types of loading protocols (including P-Delta effect)

7.5 Time history analysis

7.5.1 Four story building

To investigate the effect of DDM, two 2D four-story three-bay special moment frames (SMFs) were analyzed using OpenSees software (Figure 7-14). The section and reinforcement details of all members can be found elsewhere (Haselton, 2006; FEMA, 2009b). The plastic hinge models in the first SMF's columns were created by using the procedure documented in prior studies as discussed previously (PEER, 2008; Haselton et al., 2016). Their strength, stiffness, and degradation parameters were obtained from a set of equations given in the PEER report (PEER, 2008). On the other hand, for the second SMF, its RC column sections were first modeled by fiber models in OpenSees. These fiber models were subjected loading protocols shown in Figure 6-17 (b), (c), and (d). In addition, the backbone curves of the sections were generated by the fiber model using a monotonic loading protocol. However, to have a fair comparison, M_y and $k_{elastic}$ were kept the same as those in the models for the first SMF. Next, a DDM was built for each column. Each DDM has the same backbone curve as the corresponding fiber model. Each DDM was then calibrated for the degradation parameters using the loading protocols shown in Figure 6-17 (b), (c), and (d). Note to have a fair comparison, the plastic hinge models in both SMFs use the Ibarra model. The cyclic strength deterioration parameters, c and γ, for each DDM were found through a trial-and-error process.

P-Delta effect of the gravity loads is considered in the model by a leaning column as shown in Figure 7-14. Typical floor plan of the models is shown in Figure 7-15. This leaning column is connected through hinges to the SMFs to avoids its contribution in the lateral

stiffness of the frames. Beams and columns were connected through a two-dimensional beam-column-joint element object (Altoontash, 2004) that connect the plastic hinges to the beam-column elements. Joint shear strength was determined based on a strong-joint weak-beam criterion according to ACI code Section 18.8.4.1 (ACI, 2019).

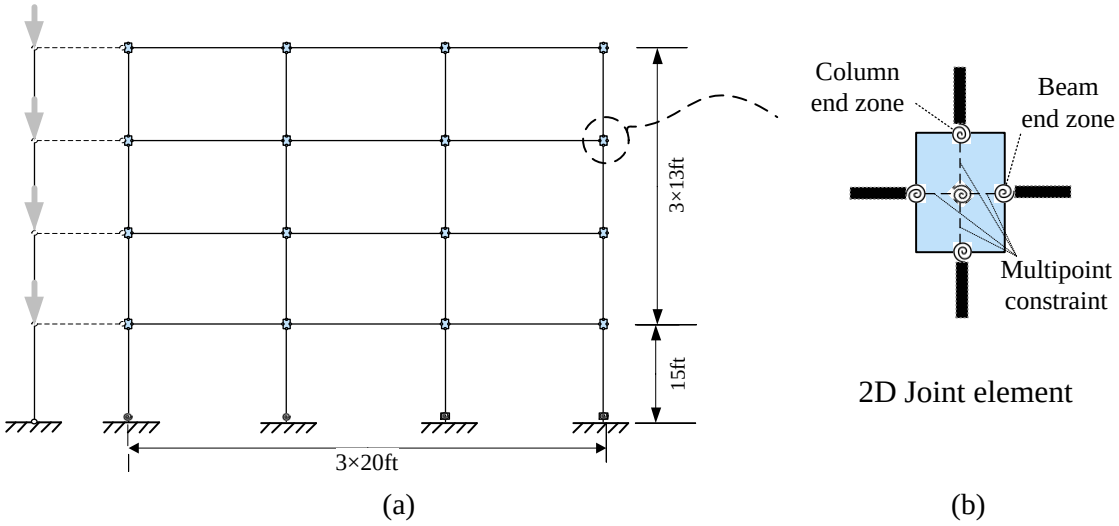

Figure 7-14 a) schematic of the 4-st SMF models and b) 2D joint element

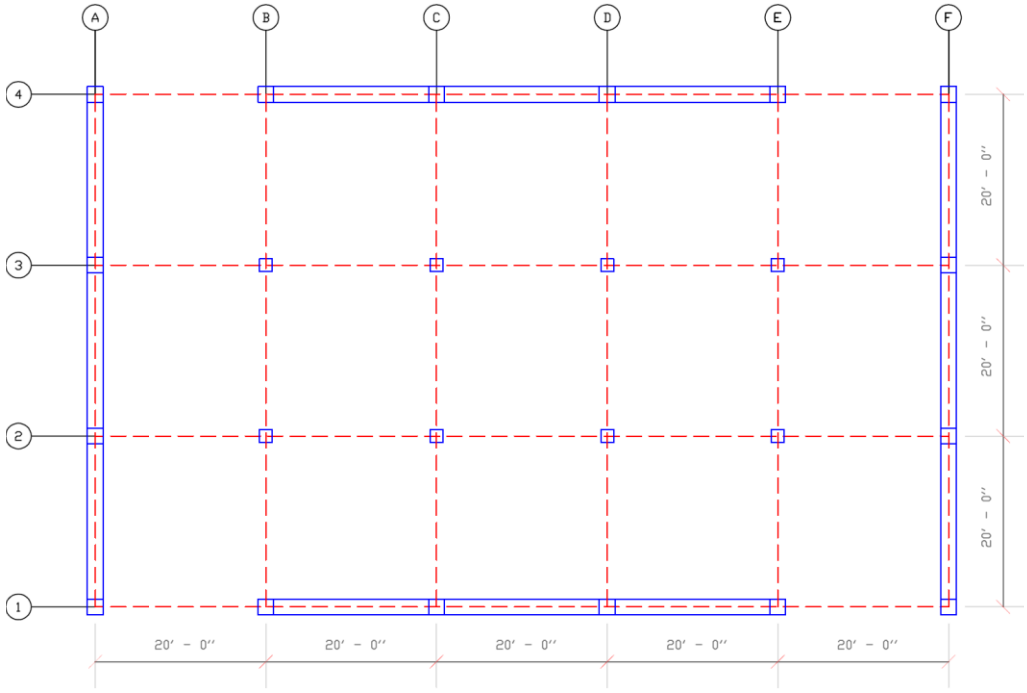

Figure 7-15 Typical floor plan of the models

7.5.2 Time history results

Both frames were subjected to an earthquake record with two different scales. The larger scaling factor was for the purpose of pushing the frames to large drift ratios to observe the effect of strength deteriorations. In these analyses, horizontal component in the maximum direction of the Imperial Valley ground motion is used (PEER Ground Motion Database). Figure 7-16 shows the response spectrum with 5% damping ratio of the Maximum Considered Earthquake (MCE_R), design level, and two scaled ground motions.

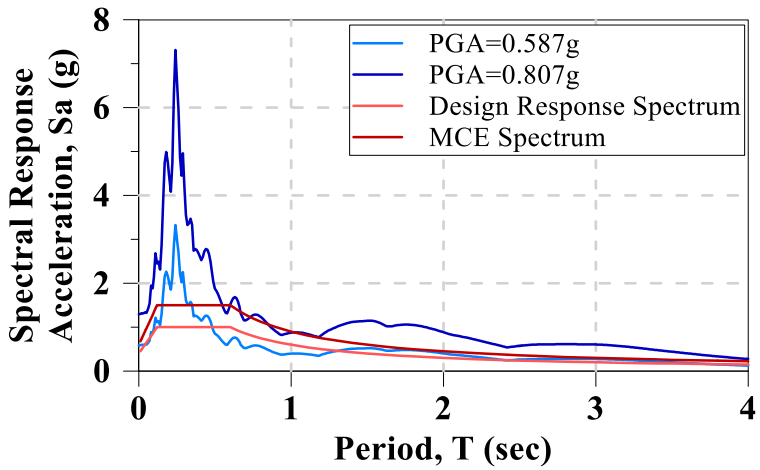

Figure 7-16 Response Spectrum

The results of the analyses show that the two models' behavior similarly when the two buildings are subjected to the ground motion with the smaller scaling factor. Figure 7-17 compares the time history drift ratio results for the two models. It represents that the time history drift ratio plots for the first and the second story have similar response in the building that the columns are modeled with DDM (labeled as "DDM") and the building with columns modeled with the equations proposed in the literature (labeled as "PEER") (PEER, 2008). Also, the results show that the residual drift ratio in models are the same under the ground motion with the peak ground acceleration of 0.587g and the differences

are marginal. However, when the ground motion with the larger scaling factor is applied the results differ significantly. The time history response of the drift ratio for both of the models under the ground motion record with peak ground acceleration of 0.807g are presented in Figure 7-18. It shows that the scaling of the record is increased largely, it will affect the response of the building to a great extent. For example, the time history drift ratio response for the dual degrading model building increases in larger amounts. Also, the permanent residual drifter ratio in DDM building increases significantly. The residual drift ratio for the second floor in DDM building is more than twice up there other one (Figure 7-18 (b)).

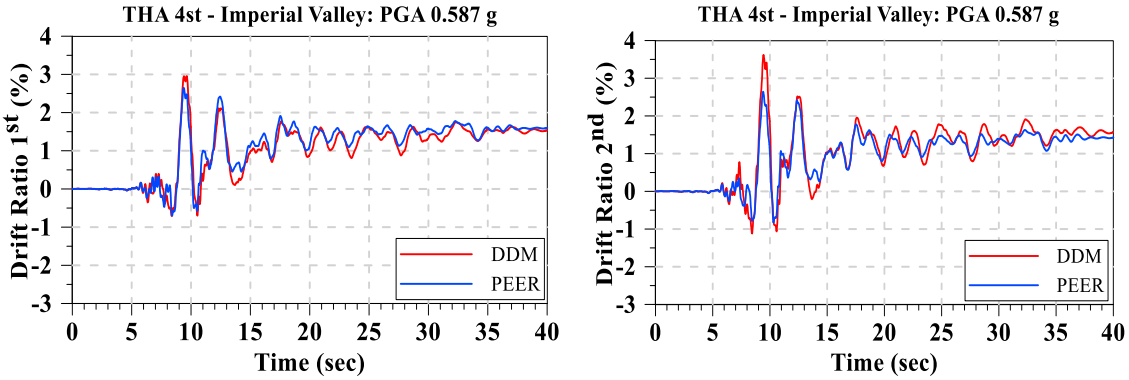

(a) (b)

Figure 7-17 Time history drift ratio response of the scaled ground motion with a peak ground acceleration of 0.587g for a) first and b) second column

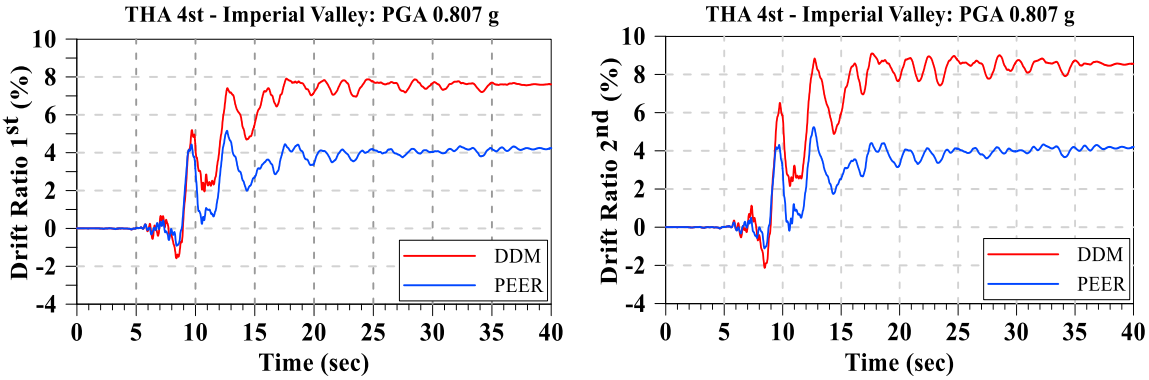

(a) (b)

Figure 7-18 Time history drift ratio response of the scaled ground motion with a peak ground acceleration of 0.807g for a) first and b) second column

The differences between the response of the two models are also exhibited in their time history base shear. Figure 7-19 illustrates that the base shear responses for the record with the smaller peak ground acceleration in the two models are similar. However, under the larger excitation the response plots diverge. For the dual degrading model building, the base shear reduction rate is significantly slower. The negative stiffness of the conventional model limits the strength capacity of the first-floor columns. This is more effective when the drift ratios become larger where the negative stiffness dominates the behavior of the columns and reduces their strength and stiffness. As shown here, the dynamic response of the building could be significantly affected when the scaling of the record is increased.

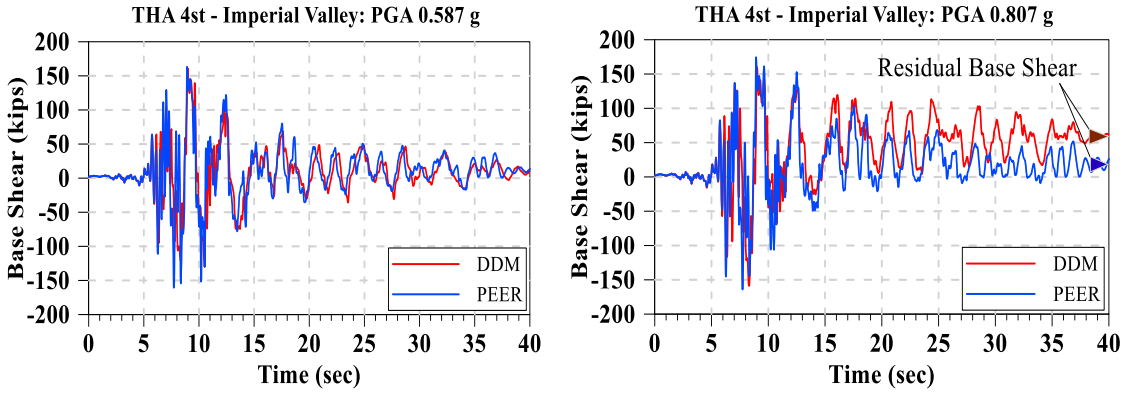

(a) (b)

Figure 7-19 Time history base shear response of a ground floor column for the scaled ground motions with a peak ground acceleration of a) 0.587g and b) 0.807g

The base shear versus drift ratio response plot for the two models under two scaled ground motions are presented in Figure 7-20. Overall, the behavior of the two models is similar under a moderate ground excitation (Figure 7-20 (a)). However, the magnified record reveals the effect of defining early negative stiffness in the plastic hinge zero-length element model. Figure 7-20 (b) shows that if the model's capacity boundary misrepresents

the columns' strength capacity, it turns in to a false maximum drift ratio prediction as well as the incorrect base shear in larger drifts.

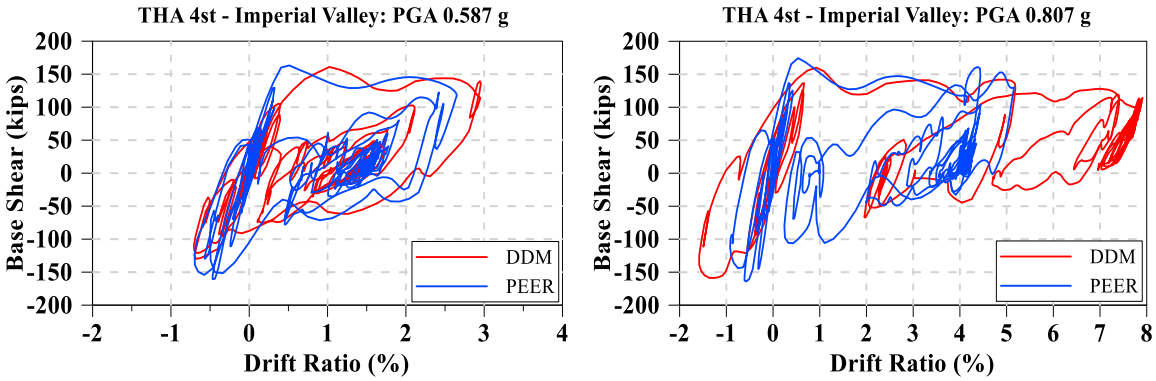

(a) (b)

Figure 7-20 base shear versus drift ratio TH plot for the internal column of the first story for a) PGA= 0.587 g and b) PGA= 0.807

7.6 Summary and conclusion

In this study a new model for RC plastic hinge columns is proposed. This model uses a dual degrading method to eliminate the dependency of modeling calibration to the loading protocol. Since, the parameters of the model are not formulized, this method is applicable to any hysteretic model. Although, the model is verified by the results of five identical column with different types of loading protocol, further experimental full-scale test results with different variables can improve the model.

The results for time history analysis for a four-story building shows that accurate modeling of the column behavior up to large drift ratios is essential to the response of the building. The comparison between dual degrading model and the formulized model available in the literature, reveals that the drift ratio and the base shear response in nonlinear time history analysis is highly affected by the post-yielding stiffness. The difference becomes larger if

a larger ground motion is subjected. The results show that early negative post-capping stiffness in the model, could misrepresent a lesser experienced drift ratio and forces in highly nonlinear demanding excitations.

Chapter 8
Part II

Incremental Dynamic Analysis (IDA)

8.1 Introduction

In this chapter, the time history (TH) and incremental dynamic analysis (IDA) results are presented. To investigate the collapse resistance of columns modeled with the new Dual Degrading Model (DDM), two pairs of perimeter frames of two-dimensional four-story and 20-story special moment frame (SMF) building were designed and analyzed. All the buildings were designed as special moment frames, however, for the nonlinear dynamic analysis each model was constructed once with the modeling parameters proposed in the literature (Haselton et al., 2016; PEER 2008) and the corresponding pair model was constructed with the DDM. The OpenSees software platform (McKenna et. al, 2000) was used for the numerical simulations through time history incremental dynamic analysis (IDA) (Vamvatsikos and Cornell, 2002). To perform the IDA, a suit of far-field records was selected (Table 6-1). Since the structures were designed for stiff soil, the related records (site class C and D) were adopted from FEMA-P695 (2009). The records were collected from the PEER-NGA database (PEER Ground Motion Database). The description of the records is provided in the chapter 6 of this report.

To investigate the effect of columns' plastic hinge constructed with dual degrading model (DDM), the plastic hinges in the beam elements are modeled similarly in each pair of buildings. Lumped plastic hinges (PHs) were placed at both ends of the elements and a nonlinear elastic beam-column element is used in between. To connect the PHs at the joints, beams and columns were connected through a two-dimensional beam-column-joint element object (Altoontash, 2004). Since the joints were designed by a strong-joint weak-column approach, the joints were modeled as an elastic element and their contribution to the drift ratio was negligible. A leaning column was modeled to account for the P-Delta

effects of the gravity loads. This leaning column is pin-connected to the SMF and the base; hence, it does not contribute to the strength and stiffness of the frame. The built model is schematically shown in Figure 8-1. The overall characteristics of the model are obtained from Haselton and Deierlein (2007).

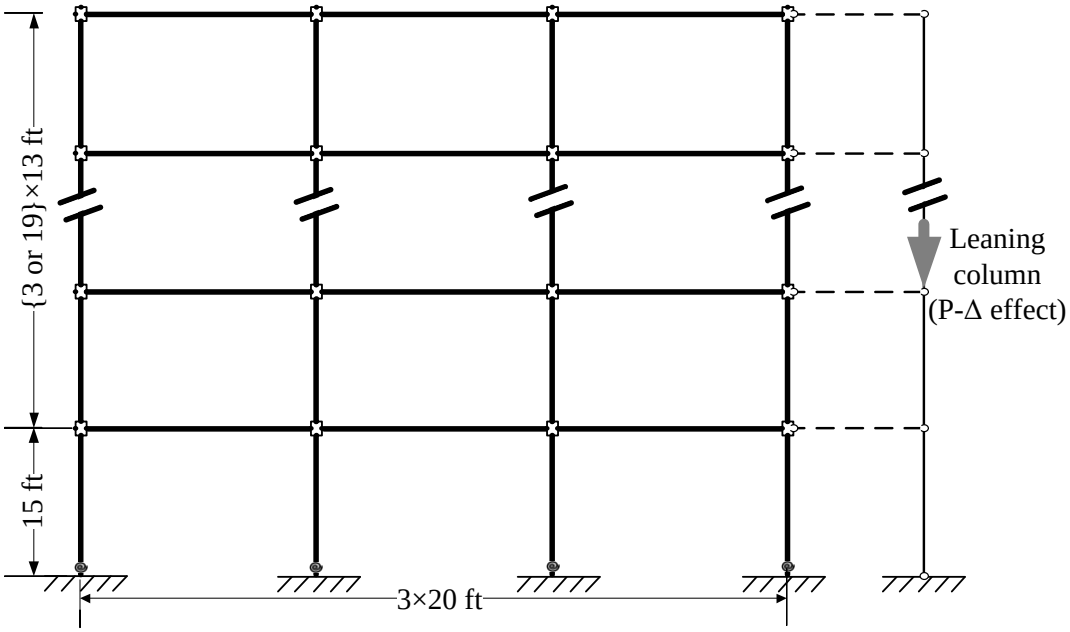

(a)

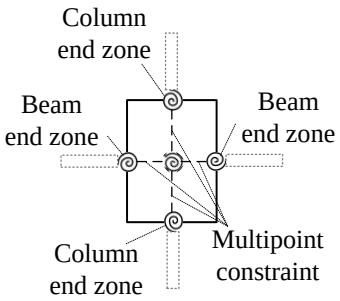

2D Beam-column joint element to model the elastic behavior of the joints

(b)

Figure 8-1 (a) Schematic of special moment frame with dimensions and (b) the two-dimensional beam-column-joint element object

8.2 Fiber model

One feature of the Dual degrading model is that it is calibrated based on different loading protocols. Therefore, for a certain column, it is required to have experimental test results for the column under different type of loading protocols or using a numerical model to predict the behavior of the given column under different loading protocols. Since, it is impossible to produce the data for all columns under different types of loading, using a numerical model is inevitable. In this study, this method is used to produce the data base needed to calibrate the plastic hinge models for the column elements in the buildings. For this purpose, the fiber element model described in the previous section is used. For each of the columns, a numerical fiber model is constructed. Then. They are loaded under different types of loading protocols. The loading protocols are similar to the series of loading protocols that are used for the large-scale experimental column study. However, the maximum drift ratio for the loadings that include a monotonic push is limited to 10%. For the nest step, the plastic hinge models are constructed with DDM, are calibrated based on the results from fiber models. Figure 8-2 represents the results of a column at the first floor of the 4-story building for the fiber model and the calibrated plastic hinge constructed with the dual degrading model (DDM). For all the columns, the results are individually compared to have the best matching result under different types of loading that were used. The parameters of the DDM plastic hinges are calibrated such that the significant strength loss of the model occurs at the same drift ratio that the strength loss occurs for the fiber element model, under different types of loading protocol. If the DDM column cannot mimic the behavior of the fiber model under one certain loading, the parameters are calibrated to generate a conservative behavior for the column. For example, as shown in

Figure 8-2, the response of DDM follows the fiber model for all the loadings expect for the third loading protocol (Figure 8-2 (c)), in which the strength drops faster in the reverse direction of the last drift step.

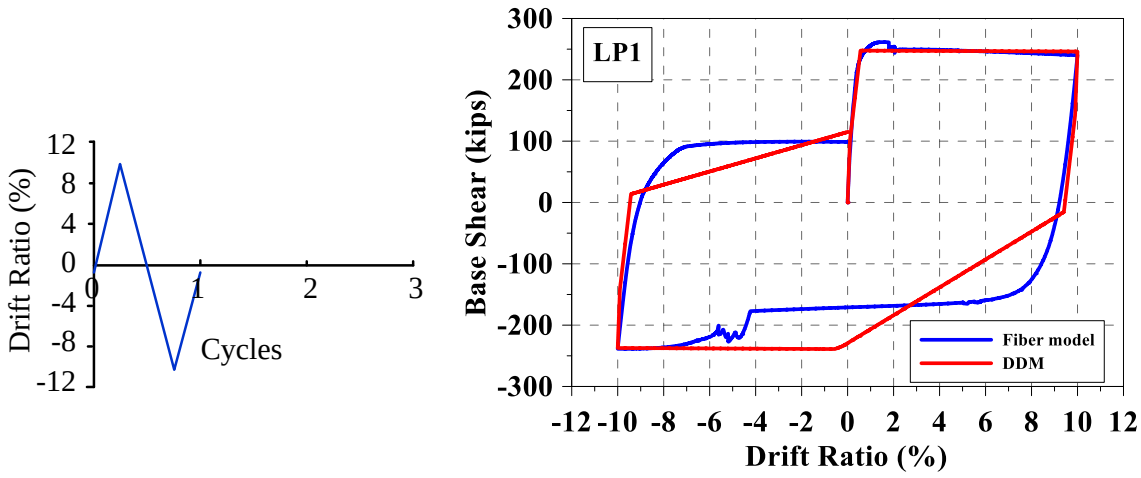

(a)

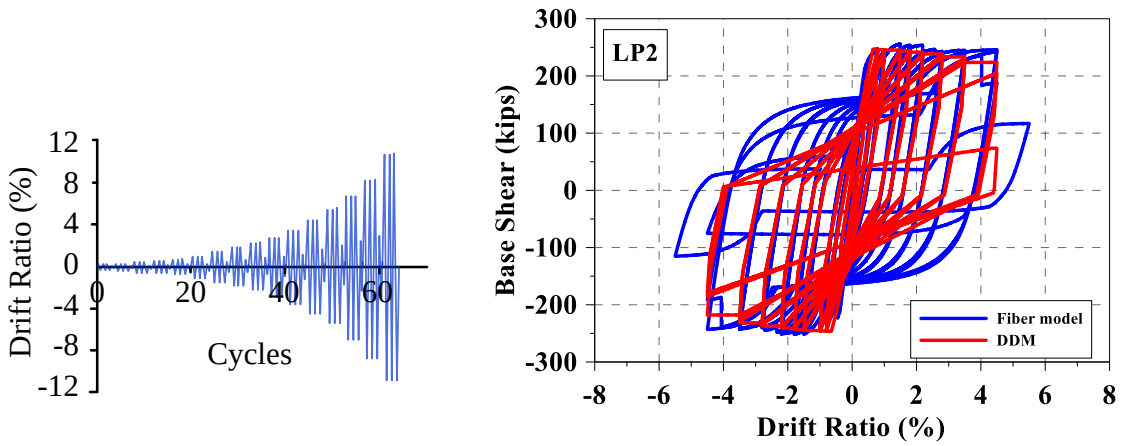

(b)

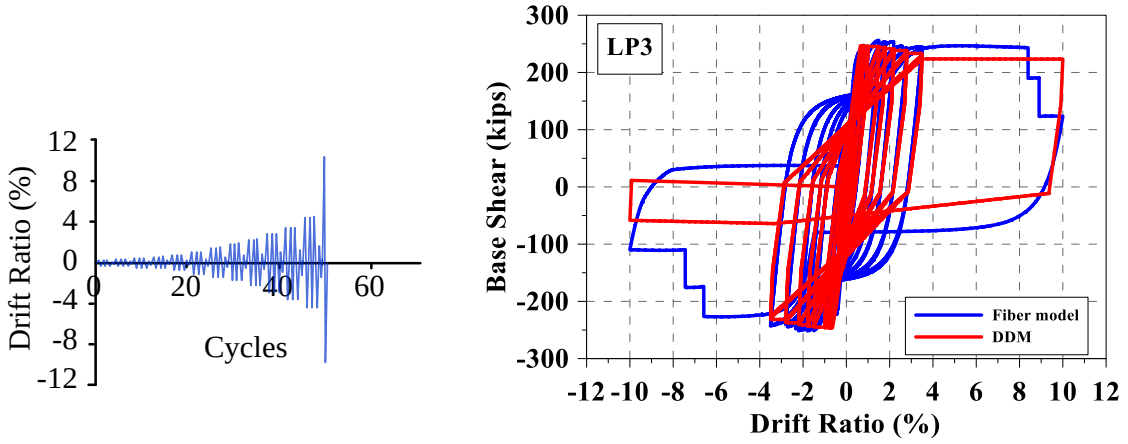

(c)

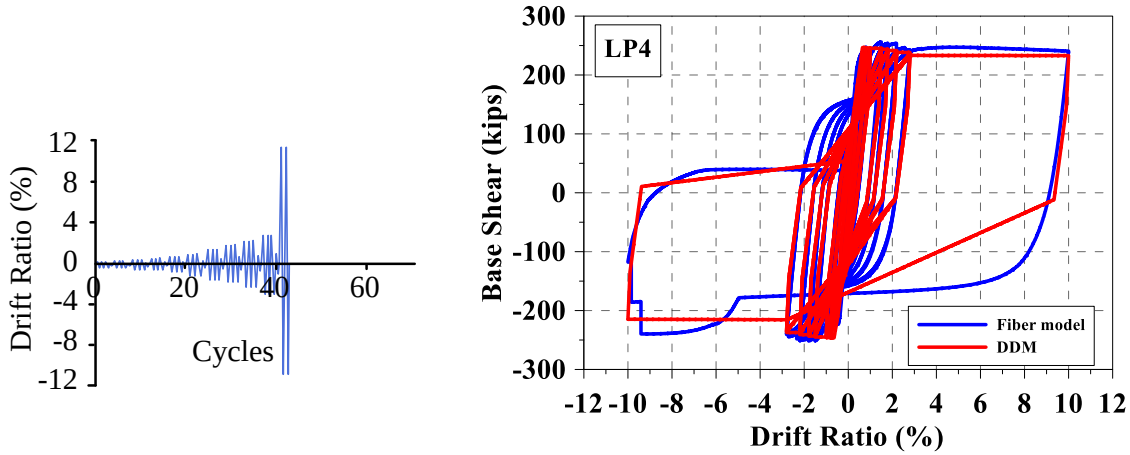

(d)

Figure 8-2 loading protocol and the response comparison for the fiber model with DDM for (a) single-cycle; (b) ACI 374 symmetric cyclic; (c) ACI 374 symmetric cyclic followed by final monotonic push #1;(d) ACI 374 symmetric cyclic followed by final monotonic push #2

8.3 Record to record time history analysis

In this section, the time history analysis results under different earthquake events are provided, for the 4-story buildings. Figure 8-3 represents the drift ratio histogram for the first floor of each of the two 4-story buildings, for the Kocaeli event with a Peak Ground Acceleration of PGA=0.312 g for different scales of the record. Generally, the results are following the same trend. However, when the scale of the applied record increases, the differences become more noticeable. For the record with the peak ground acceleration of 0.593 g, which is the scaling prior to collapse for both models, the model constructed with dual degrading model (DDM), exhibits a maximum drift ratio of 6% at the first floor, while this value is recorded as 4% for the model constructed with Ibarra's model that uses parameters given in PEER report (2007). This model is called PEER model in this chapter. Also, the comparison between the maximum drift ratio recorded for all the stories (Figure 8-4), shows that the collapse pattern also changes when the record is scaled up to collapse level. The maximum drift occurs at the second floor for the building with PEER model, while the DDM building collapses due to excessive lateral drift at the first floor. Also, for the record with the largest scaling, the total displacement of the top floor is more in the DDM building (Figure 8-5). Although, typically the DDM undergoes a larger drift ratio with less strength loss, the overall experienced drift ratio could be even more. This means that the overestimation of the strength loss for the columns, could results in an underestimation in the response of the building, especially for the record with near collapse characteristics.

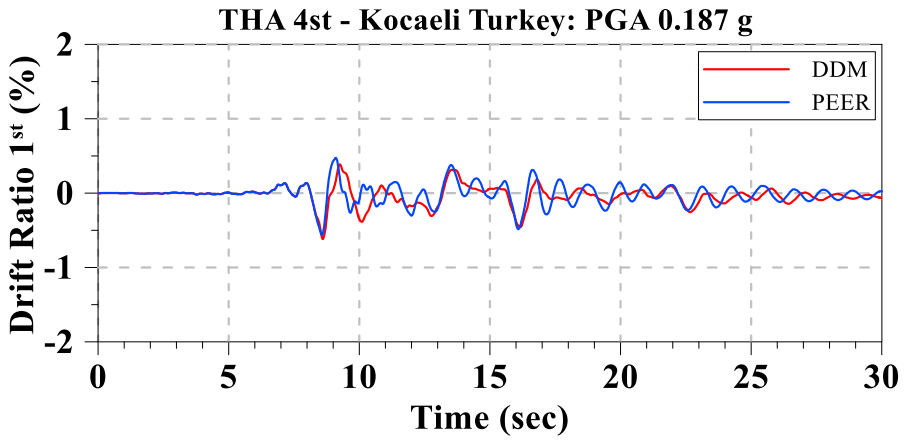
THA 4st - Kocaeli Turkey: PGA 0.187 g
DDM
PEER
Drift Ratio 1st (%)
Time (sec)
2
1
0
-1
-2
0
5
10
15
20
25
30

(a)

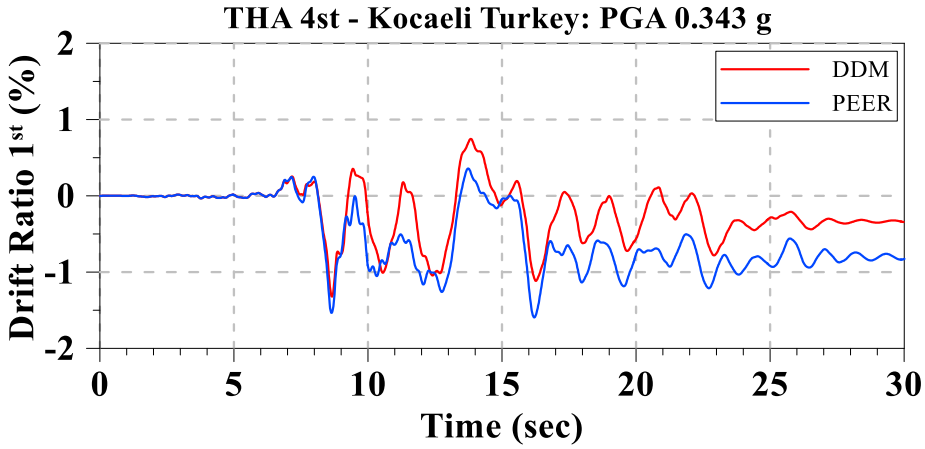
THA 4st - Kocaeli Turkey: PGA 0.343 g
DDM
PEER
Drift Ratio 1st (%)
Time (sec)
2
1
0
-1
-2
0
5
10
15
20
25
30

(b)

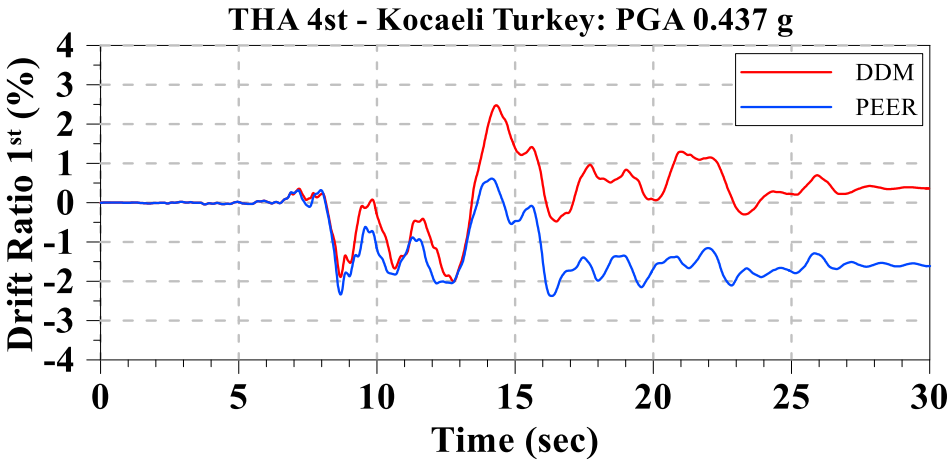
THA 4st - Kocaeli Turkey: PGA 0.437 g
DDM
PEER
Drift Ratio 1st (%)
Time (sec)
4
3
2
1
0
-1
-2
-3
-4
0
5
10
15
20
25
30

(c)

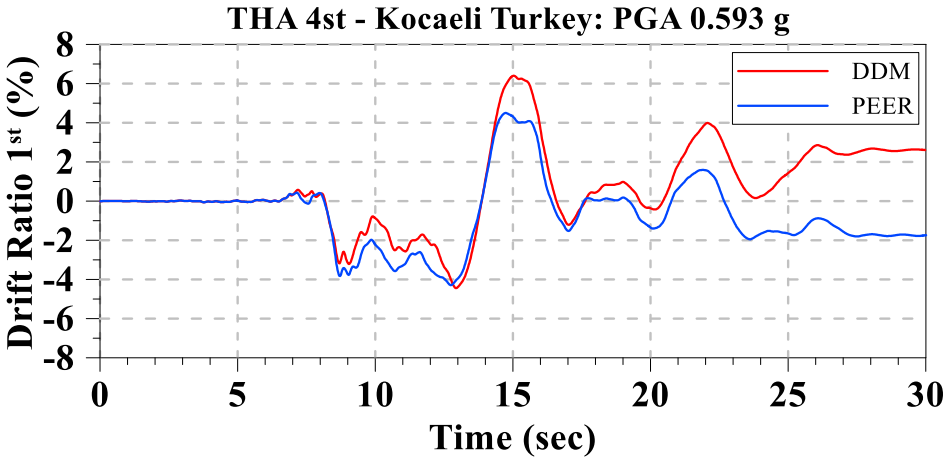

(d)

Figure 8-3 TH results of the 4-story frames for the Kocaeli event with
a) PGA= 0.187 g, b) PGA= 0.343 g, c) PGA= 0.437 g and d) PGA= 0.593 g

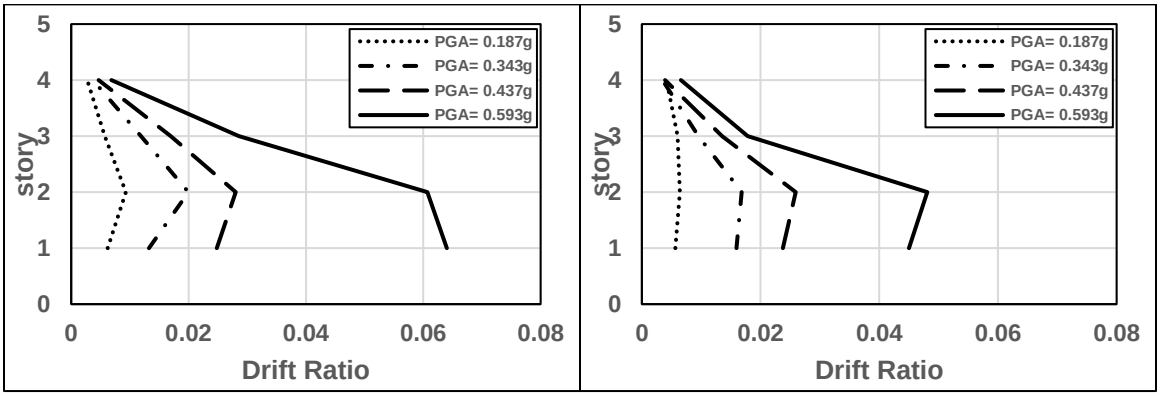

(a) (b)

Figure 8-4 Drift ratio for all stories of the 4-story frames for different scaled record (Kocaeli):
a) DDM and b) PEER model

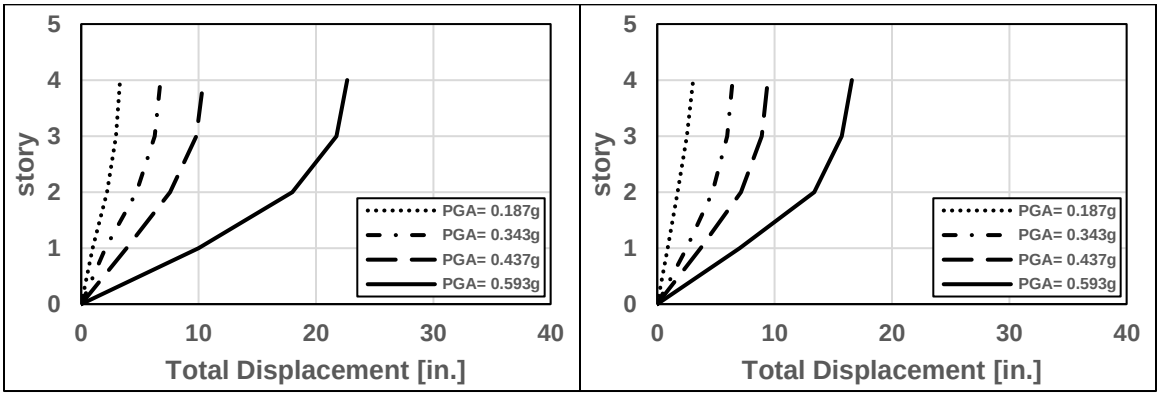

(a) (b)

Figure 8-5 Displacement for all stories of the 4-story frames for different scaled record (Kocaeli):
a) DDM and b) PEER model

Figure 8-6 represents the drift ratio histogram for the first floor of each of the two 4-story buildings, for the Hector Mine event with a Peak Ground Acceleration of PGA=0.265 g for different scales of the record. For this record, the differences between the response of the two models are noticeable from the smaller scales (Figure 8-6 (a)). Unlike the previous record, the maximum drift recorded for the model with PEER model are having greater values for different scales. Also, this model collapses under a record with smaller scale with a peak ground acceleration of PGA= 0.954 g where the DDM building reaches a scaled record with PGA= 1.458 g with a maximum drift ratio of 7%. Figure 8-7 shows the maximum DR recorded for each floor of both buildings. For all the scaled records the maximum DR occurs at the second floor. However, for the DDM building, the drift for the third and the fourth (top) floor does not drop significantly due to strength maintaining and absence of a post-capping steep negative stiffness in the dual degrading model. Figure 8-8 represents the total displacement for each floor for the TH analysis for both models.

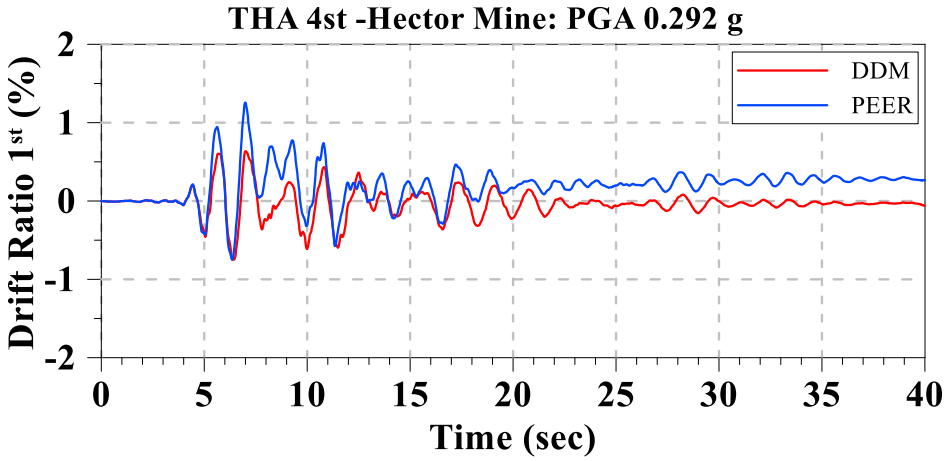

(a)

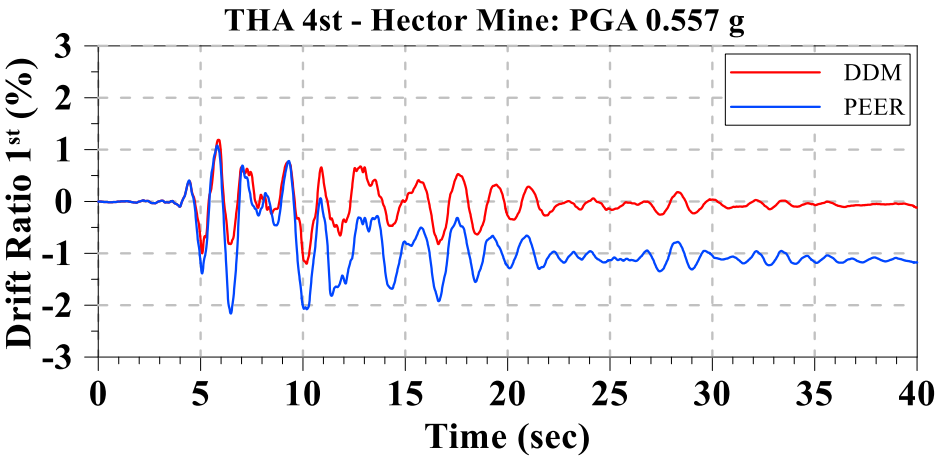

(b)

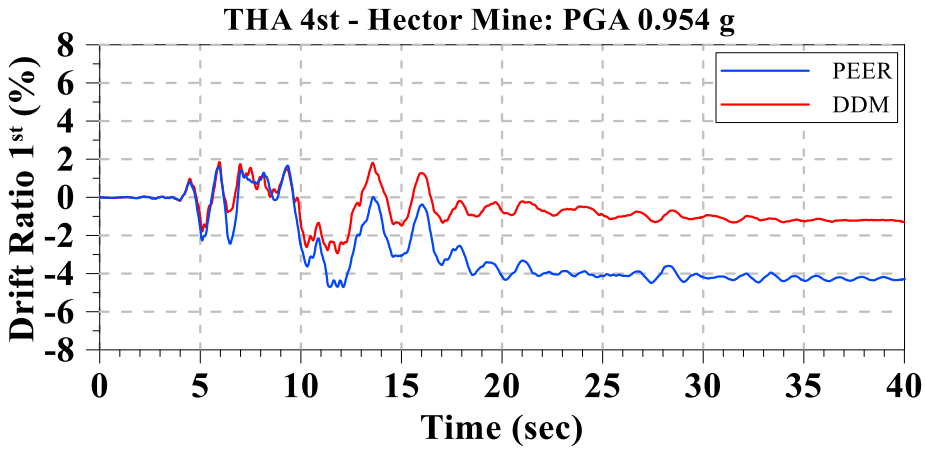

(c)

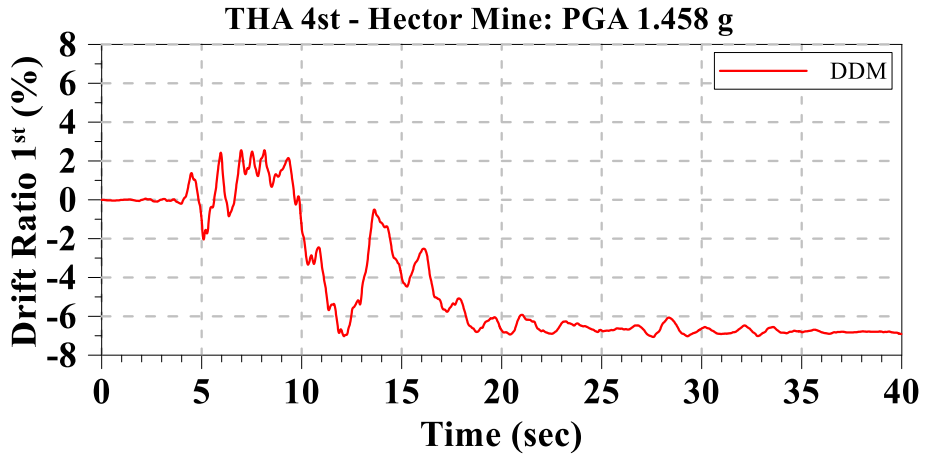

(d)

Figure 8-6 TH results of the 4-story frames for the Hector Mine event with a) PGA= 0.292 g, b) PGA= 0.557 g, c) PGA= 0.954 g and d) PGA= 1.458 g

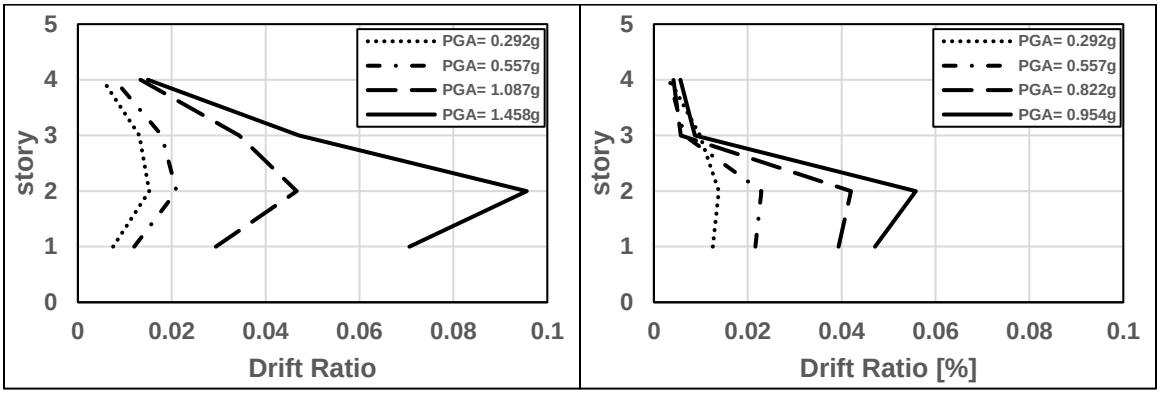

(a) (b)

Figure 8-7 Drift ratio for all stories of the 4-story frames for different scaled record (Hector Mine): a) DDM and b) PEER model

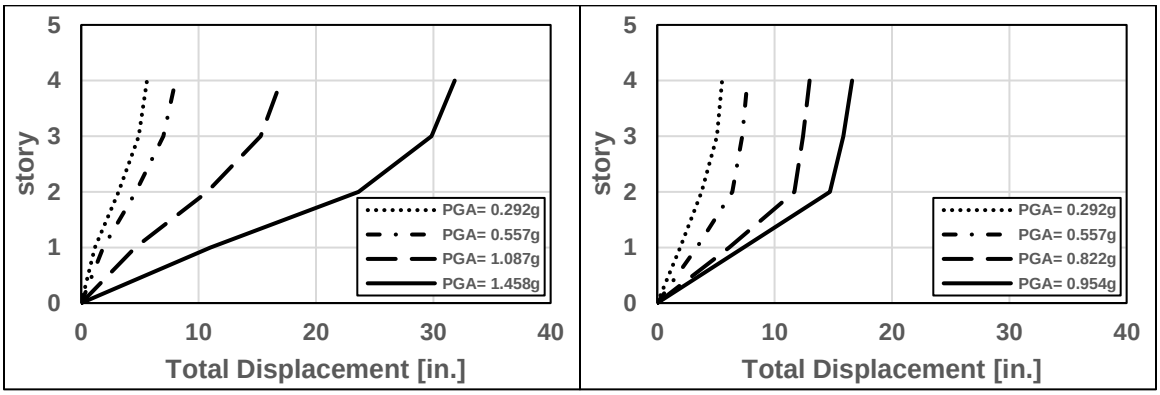

(a) (b)

Figure 8-8 Displacement of the 4-story frames for all stories for different scaled record (Hector Mine): a) DDM and b) PEER model

The drift ratio histogram of the time history results for the Manjil record with PGA of the un-scaled record of 0.515 g is presented in Figure 8-9. When the DDM is used for the plastic hinges, the maximum drift in the first story exhibits larger values. Figure 8-10 shows that, the pattern for the maximum drift recorded for each floor of the DDM building remains the same even up to collapse levels. This shows that a plastic hinge model without a premature capping point can even change the failure mode of the building.

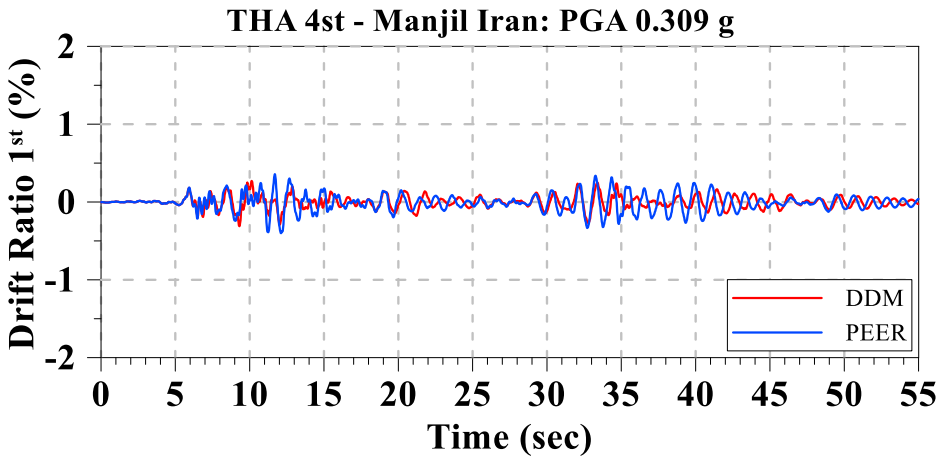
THA 4st - Manjil Iran: PGA 0.309 g
Drift Ratio 1st (%)
Time (sec)
DDM
PEER

(a)

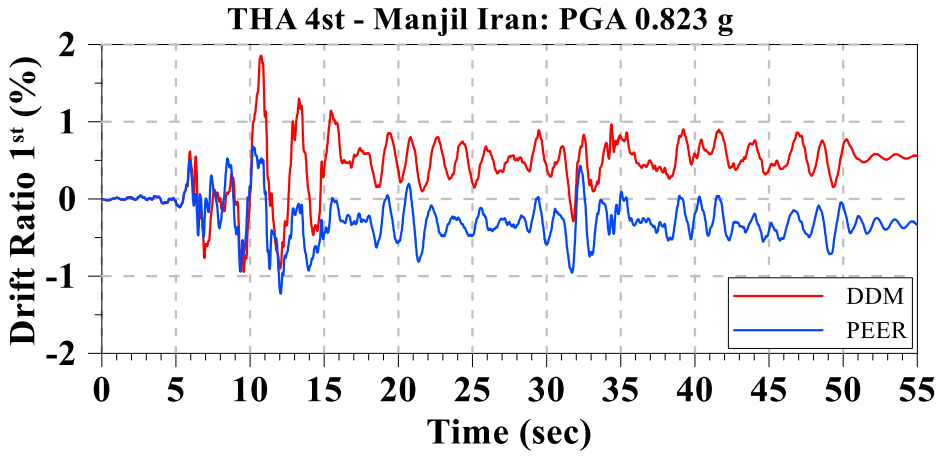
THA 4st - Manjil Iran: PGA 0.823 g
Drift Ratio 1st (%)
Time (sec)
DDM
PEER

(b)

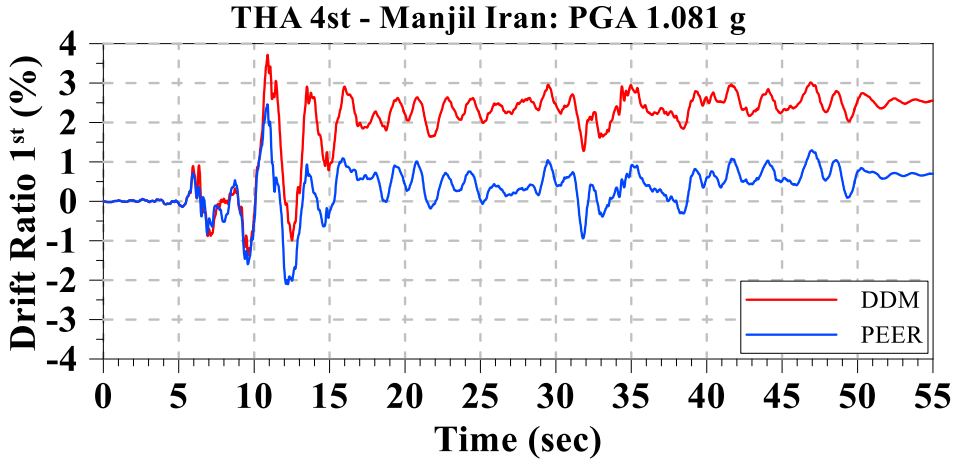
THA 4st - Manjil Iran: PGA 1.081 g
Drift Ratio 1st (%)
Time (sec)
DDM
PEER

(c)

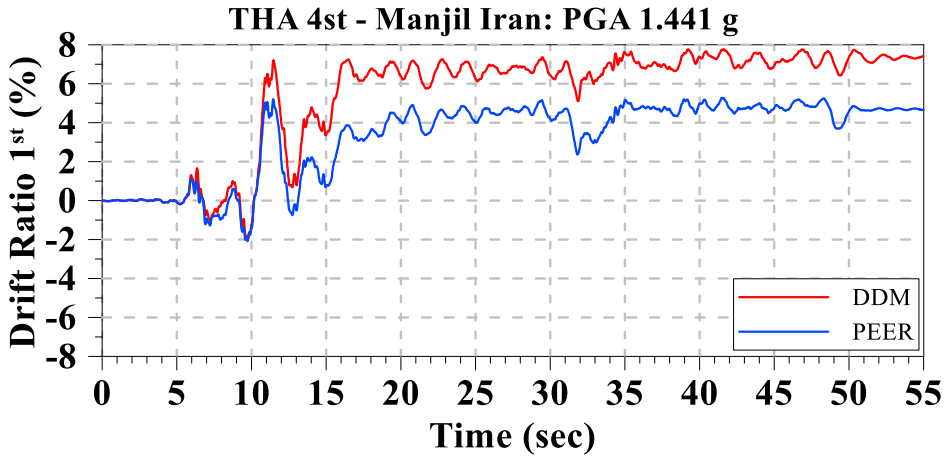

(d)

Figure 8-9 TH results of the 4-story frames for the Manjil Iran event with a) PGA= 0.309 g, b) PGA= 0.823 g, c) PGA= 1.081 g and d) PGA= 1.441 g

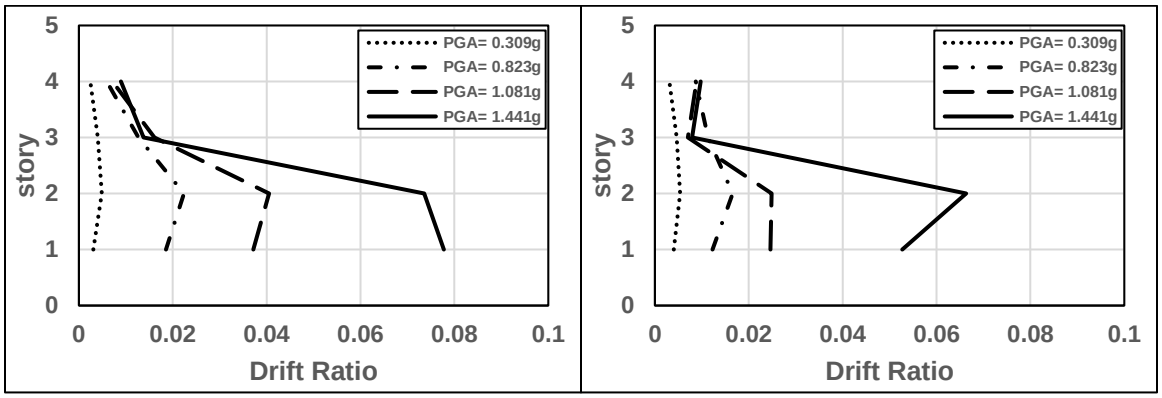

(a) (b)

Figure 8-10 Drift ratio of the 4-story frames for all stories for different scaled record (Manjil): a) DDM and b) PEER model

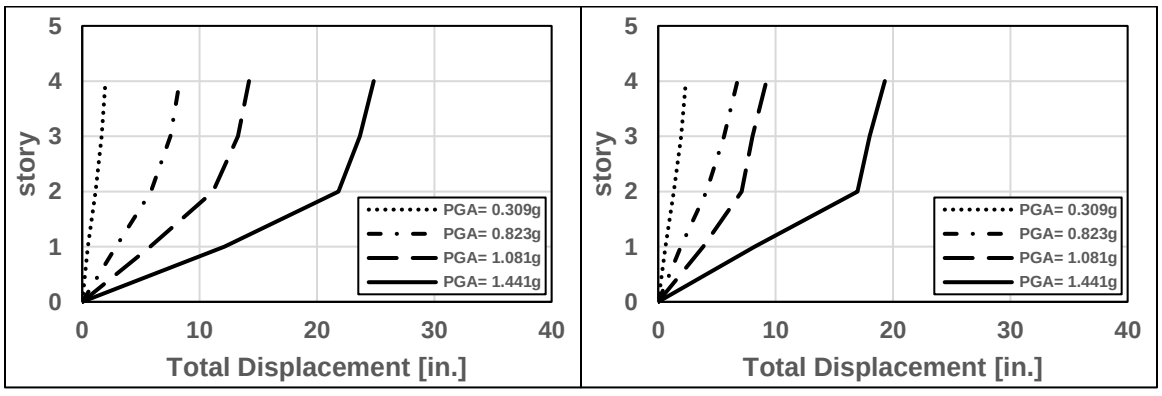

(a) (b)

Figure 8-11 Displacement of the 4-story frames for all stories for different scaled record (Manjil): a) DDM and b) PEER model

The responses of the 20-story building frames are similar and show an insignificant different in both record-to-record analysis and different scales of a given record. Figure 8-12 to Figure 8-17 compares the drift ratio and displacement for all the floors for the 20-story pair models. The DDM building drift ratio exhibits slightly higher drift in lower stories. This difference becomes larger as the scaling of the ground motion increases. However, the overall responses of the models are the same. In the 4-story buildings, when the plastic hinges that were modeled with Ibarra's spring model were replaced by the DDM plastic hinges, this could result in a change in the failure mode of the structure. Generally, the DDM 4-story buildings experience a larger lateral displacement at the first floor. Also, when the a scale of the ground motion increases up to collapse levels, it shows that the collapse of the building will be due to excessive lateral displacement at the first floor. However, for the 20-story building replacement of Ibarra plastic hinges by DDM plastic hinges does not change the failure mode of the building. This occurs because lateral collapse occurs in smaller drifts for the high-rise buildings with larger natural period. At smaller drifts, the behavior of the Ibarra's model and dual degrading model are similar. Hence, the overall behavior of the models will be similar and consequently, the collapse resistant of the models would be the similar. More information on the IDA result are provided in Appendix B of this report.

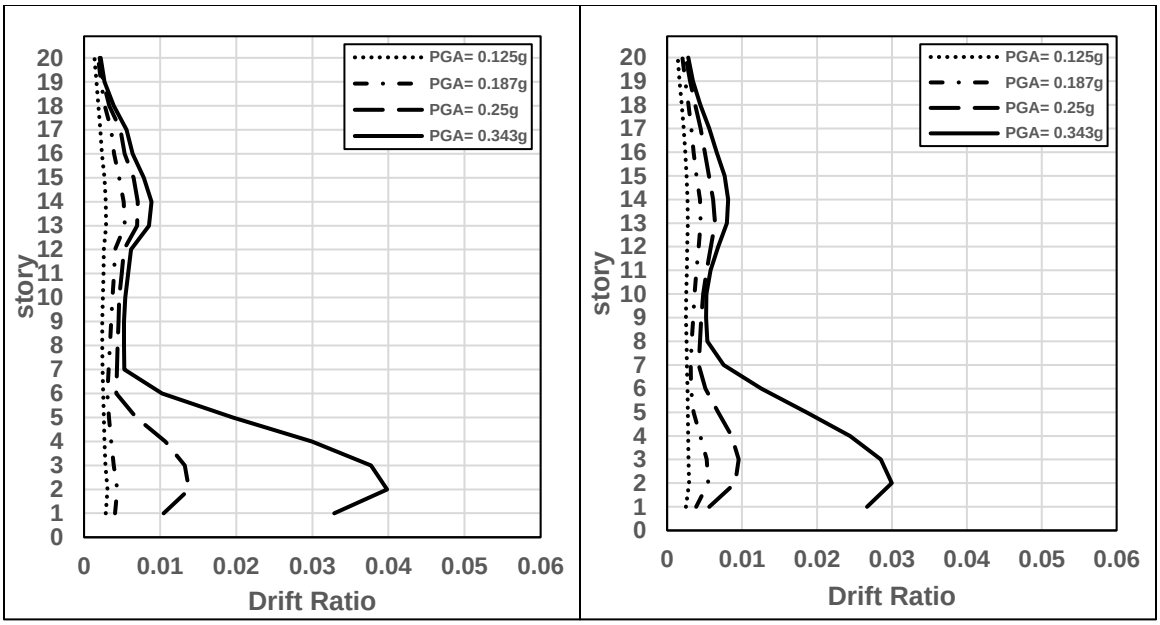

(a) (b)

Figure 8-12 Drift ratio for all stories of the 20-story frames for different scaled record (Kocaeli): a) DDM and b) PEER model

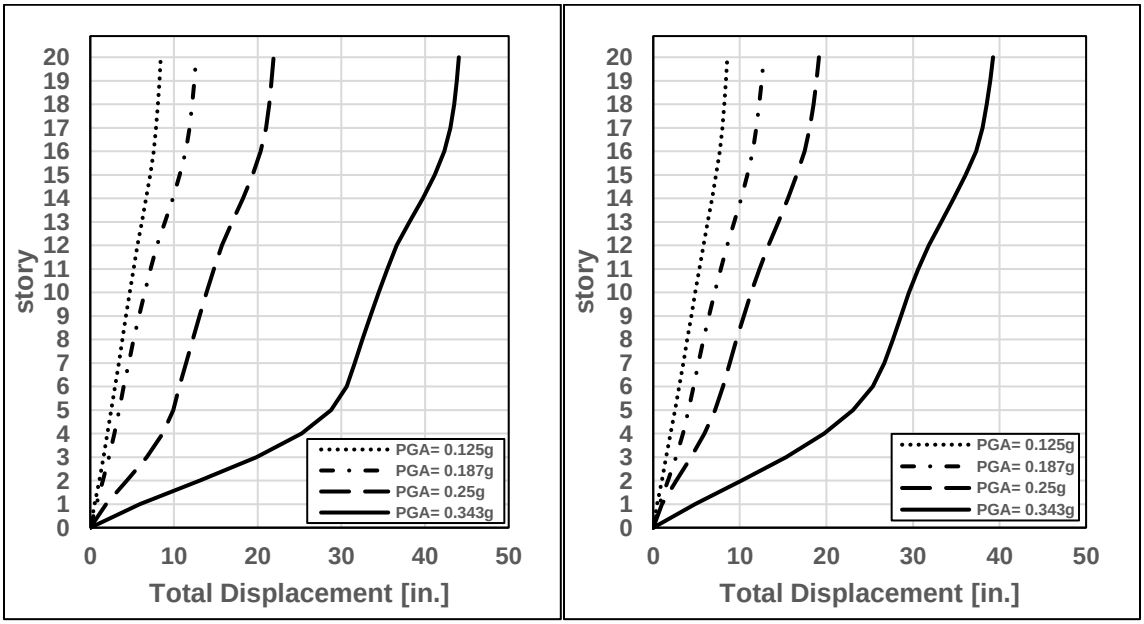

(a) (b)

Figure 8-13 Displacement for all stories of the 4-story frames for different scaled record (Kocaeli): a) DDM and b) PEER model

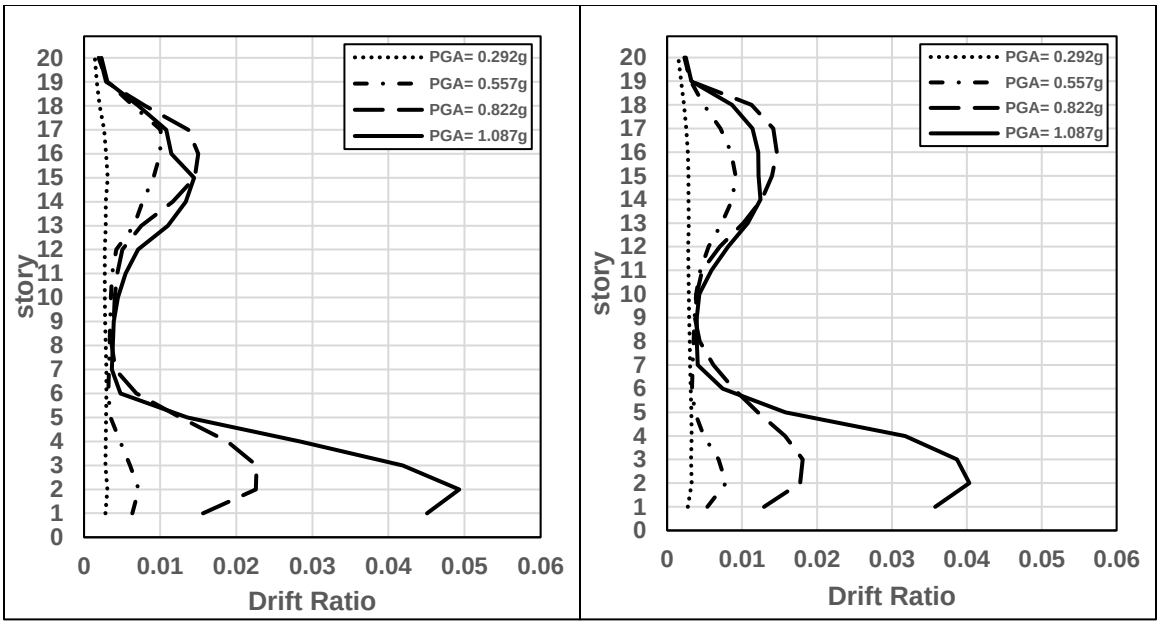

(a) (b)

Figure 8-14 Drift ratio for all stories of the 20-story frames for different scaled record (Hector Mine): a) DDM and b) PEER model

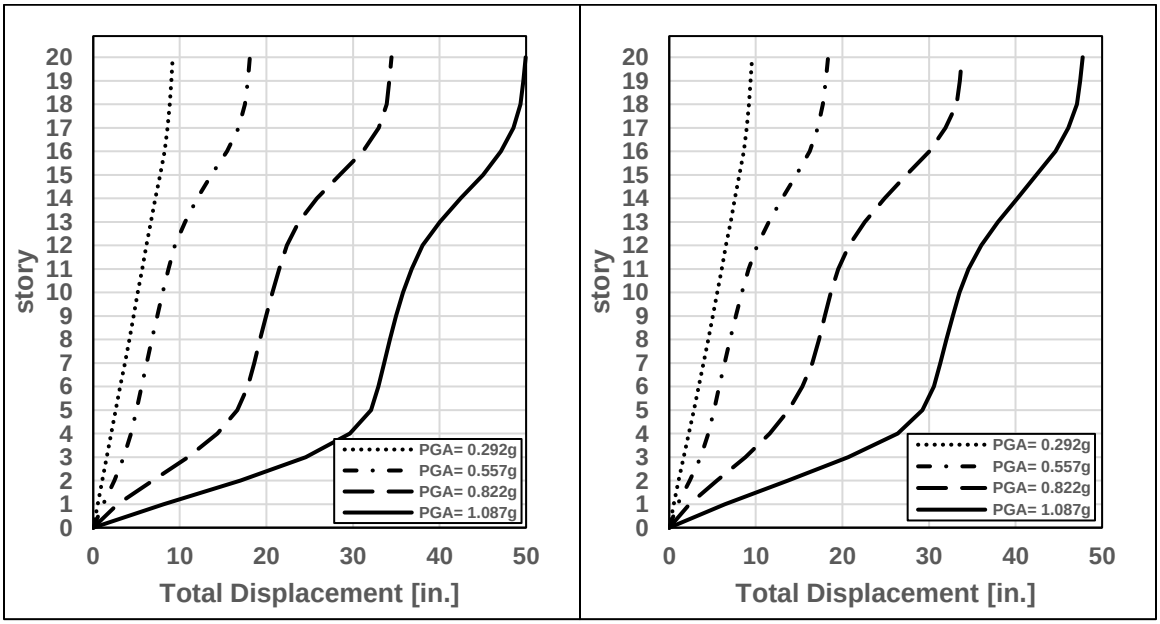

(a) (b)

Figure 8-15 Displacement for all stories of the 4-story frames for different scaled record (Hector Mine): a) DDM and b) PEER model

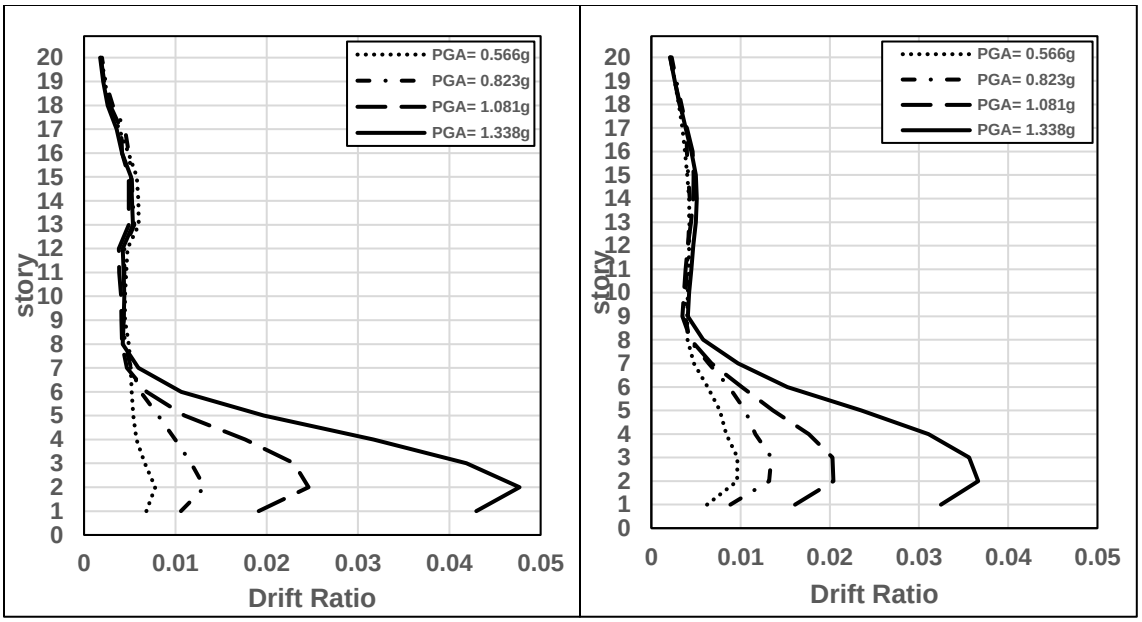

(a) (b)

Figure 8-16 Drift ratio for all stories of the 20-story frames for different scaled record (Manjil): a) DDM and b) PEER model

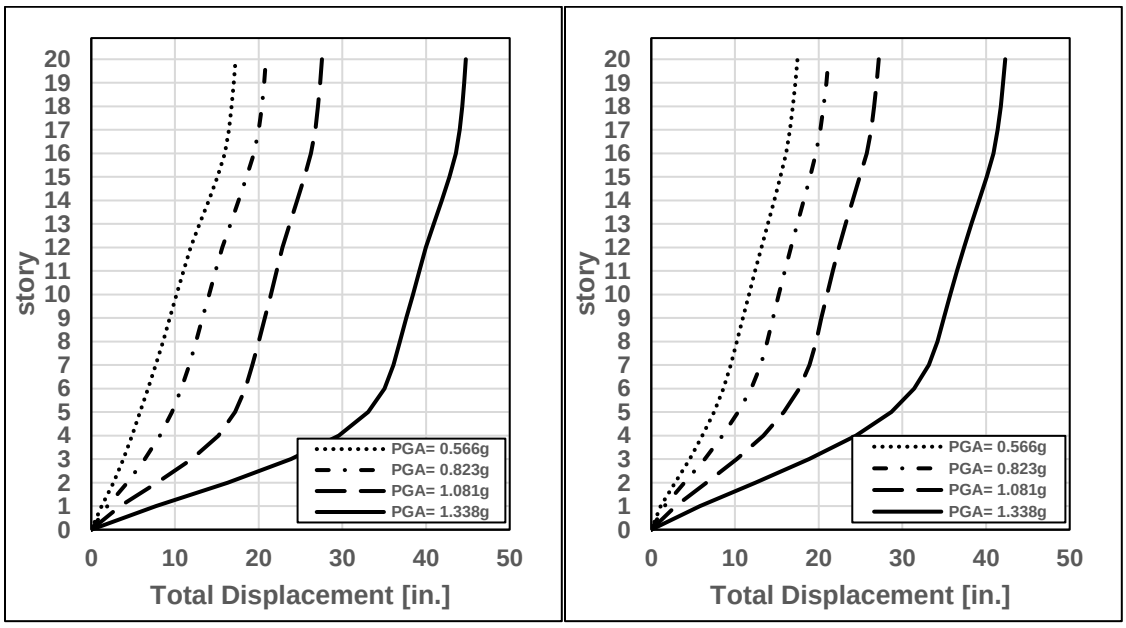

(a) (b)

Figure 8-17 Displacement for all stories of the 4-story frames for different scaled record (Manjil): a) DDM and b) PEER model

8.4 Incremental dynamic analysis

To compare the collapse resistance of the dual degrading model and the PEER model with parameters given in PEER report (PEER, 2007), two series of Incremental Dynamic Analyses (IDA) (Vamvatsikos, 2002) are performed. Using many numbers of records in this approach, the dependency of the results to each record will be reduced. In this study, the suite of ground motions tabulated in Table 6-1 are used to perform the incremental dynamic analysis. For each of the 4-story and the 20-story buildings, two pair of frames are modeled. One of the models in each pair is constructed with column plastic hinges modeled with DDM and the other one with Ibarra model. Then, all the building frames are subjected to incremental dynamic analysis. To investigate the effect of the DDM plastic hinge in columns, only the columns' plastic hinges are different in the models and all other characteristics of the buildings are the same in each pair of buildings. The models are described in the chapter 7 of this report.

For the incremental dynamic analyses, the collapse of the building is achieved by the excessive lateral displacement in a story. For this reason, the drift ratio is considered as the damage measure for incremental dynamic analysis. Also, the peak ground acceleration of the ground motions is used for the intense measure. Hence, ground motions are scaled, and the drift ratios are recorded during the analyses. Figure 8-18 represents the incremental dynamic analysis results for four story buildings. The IDA curves in this plot are showing the maximum story drift ratio for each ground motion with increasing peak ground acceleration. Also, for each model, the average of collapse intense measures for all the ground motions is provided. The results showed that, on average, the collapse resistance of the model with DDM plastic hinges is increased by 12% (1.336/1.186).

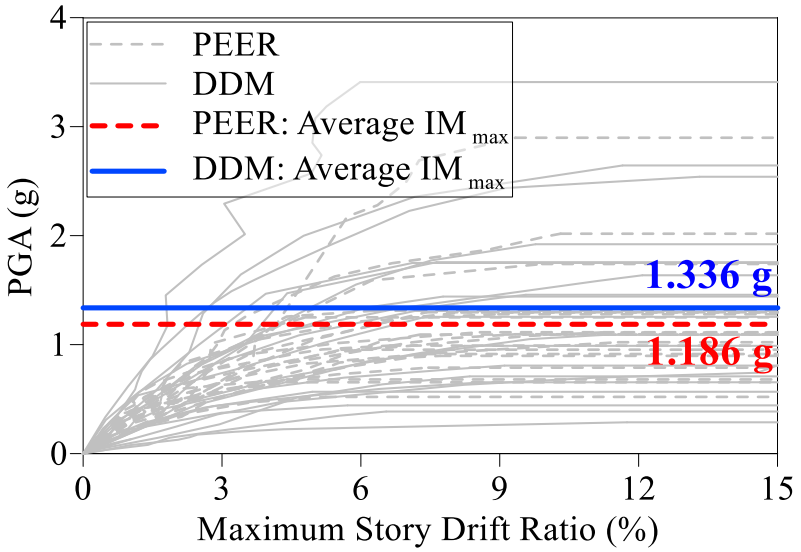

Figure 8-18 Incremental dynamic analysis response plot of peak ground acceleration versus maximum story drift ratio for 4-story buildings

FEMA-P695 (2009) defines collapse level intensity as the intense measure which result in median collapse of the seismic-force-resisting system. In another word, if the ground motions are scaled to this level, half of them would cause the structure to collapse. Also, Figure 8-19 represents the incremental dynamic analysis response plot of spectral acceleration versus maximum story drift ratio for 4-story buildings. Based on the collapse data from the IDA results, a collapse fragility curve is derived through cumulative distribution function (CDF), which relates the ground motion intensity to the probability of collapse (Ibarra et al., 2002). Figure 8-20 represents the cumulative distribution plot obtained from the IDA results for the 4-story buildings by fitting a lognormal distribution to the collapse data. The results show 9% improvement in the collapse intensity when the DDM plastic hinges are used (1.26/1.13). Also, for spectral accelerations larger than 0.5 g, the fragility curve for the DDM building shows an enhanced performance with less probability of collapse at the given spectral acceleration.

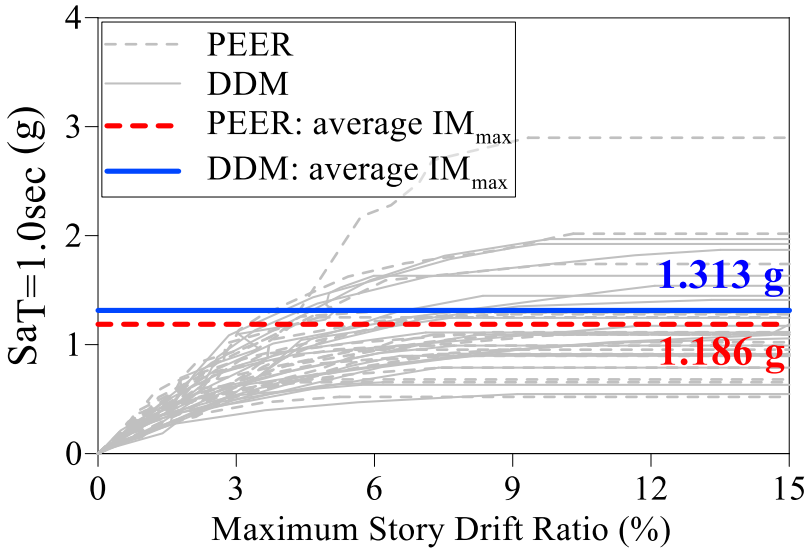

Figure 8-19 Incremental dynamic analysis response plot of spectral acceleration versus maximum story drift ratio for 4-story buildings

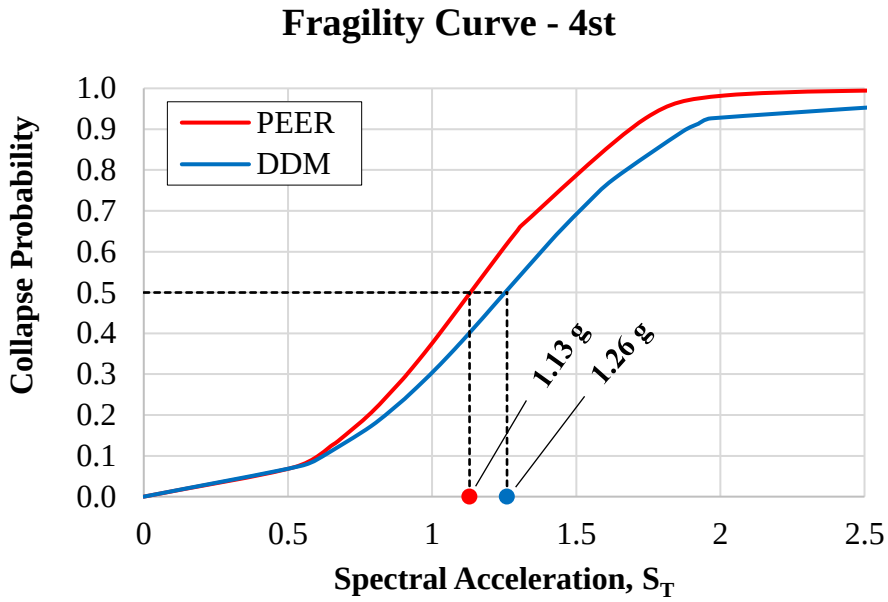

Figure 8-20 Collapse fragility curve, or cumulative distribution function for 4-story buildings

Figure 8-21shows the IDA response plot of peak ground acceleration versus maximum story drift ratio for the 20-story buildings. Same as the similar behavior of the two models when subjected to each record, the responses of the models are similar in IDA results. The DDM and PEER models are showing close average intense measure. Also, for the IDA results with spectral acceleration intense measure (Figure 8-22), the models are showing similar behavior under all ground motions.

Figure 8-23 shows cumulative distribution function for 20-story buildings. Unlike the 4-story models, the PEER building is exhibiting slightly better collapse performance. However, the difference is marginal and the collapse probability for both models follow the same path at different spectral accelerations.

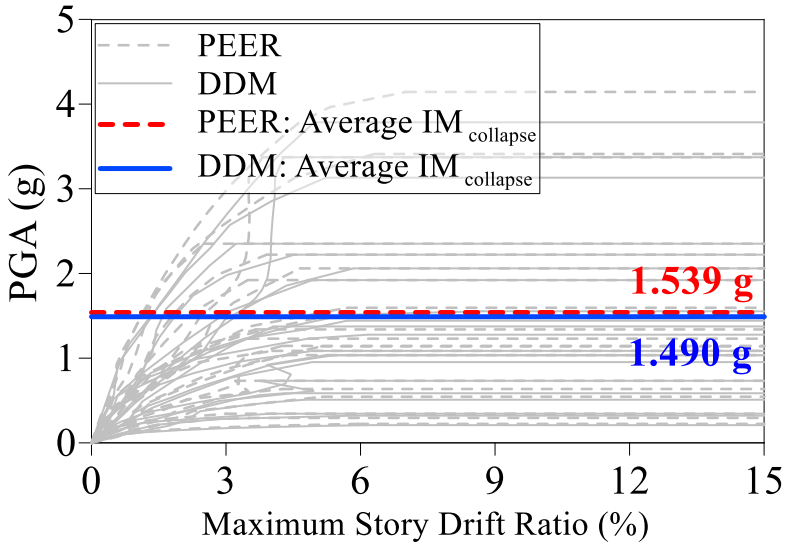

Figure 8-21 Incremental dynamic analysis response plot of peak ground acceleration versus maximum story drift ratio for 20-story buildings

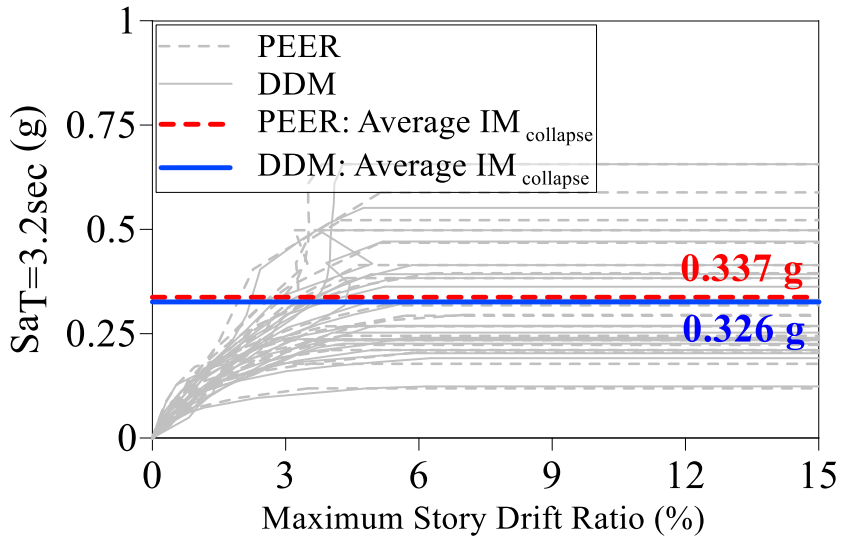

Figure 8-22 Incremental dynamic analysis response plot of spectral acceleration versus maximum story drift ratio for 20-story buildings

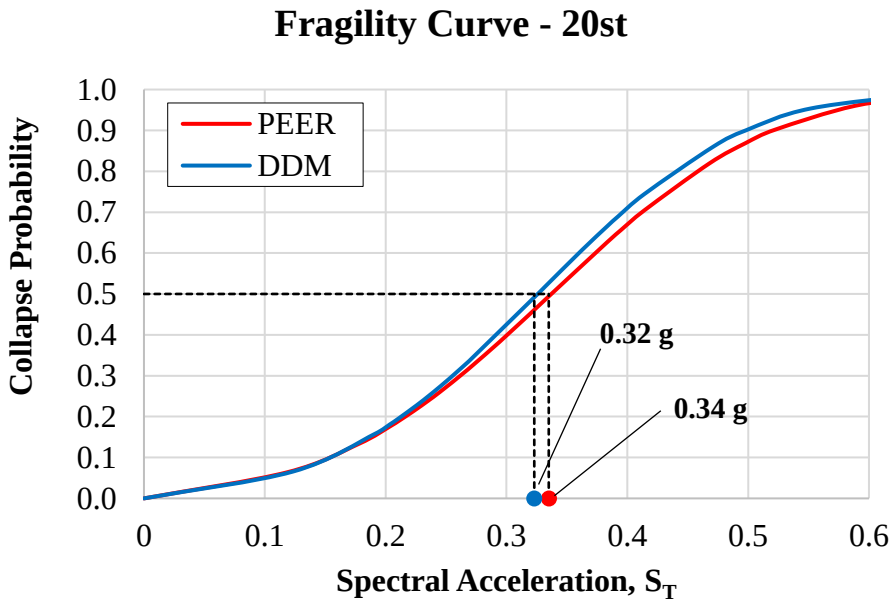

Figure 8-23 Collapse fragility curve, or cumulative distribution function for 20-story buildings

Incremental dynamic analysis response plot of spectral acceleration versus maximum story drift ratio for four-story and 20-story buildings are compared in Figure 8-24. The results

show that the collapse maximum story drift ratio range for the four-story buildings occurs in larger drift ratios. This explains the similar behavior of the two models for the 20-story building. The differences of the models become significant in larger drift ratios and are similar in small drift ratio levels (Figure 8-25). Hence, when the plastic hinges are experiencing larger rotations, the differences become larger.

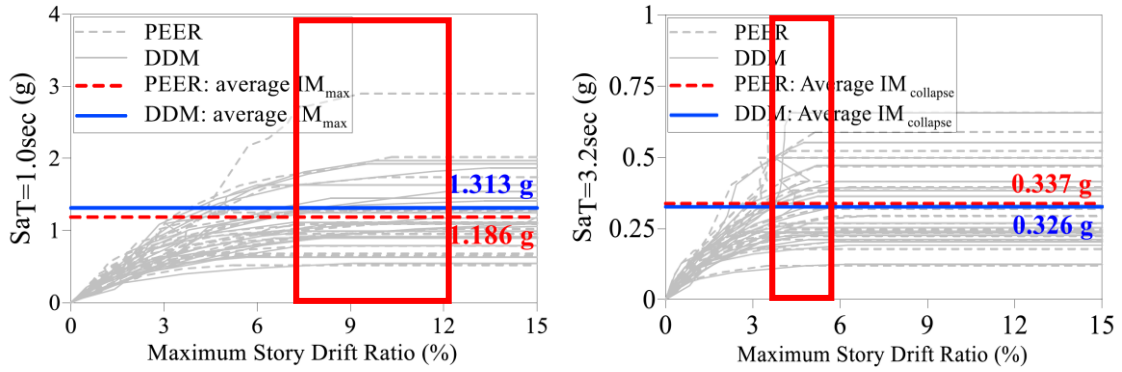

(a) (b)

Figure 8-24 IDA response plot of spectral acceleration versus maximum story drift ratio for a) four-story, and b) 20-story buildings

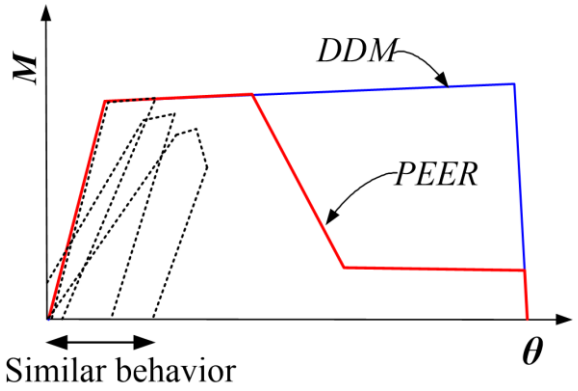

Figure 8-25 similar behavior of DDM plastic hinge and PEER proposed equations for Ibarra's model parameters in small rotations

8.5 Summary and conclusion

In this study, a new dual degrading model was used to assess the collapse resistance of buildings. For this purpose, two pairs of four-story and 20-story RC SMFs where used. One of each pair were modeled with PEER proposed parameters for Ibarra model. For the other one, the new DDM were used for the plastic hinges of the columns. This new model was calibrated based on the results of a series of fiber models for each column subjected to four different loading protocol.

All the models were subjected to incremental dynamic analysis. The results show that using the DDM plastic hinges, that are capable to mimic the behavior of a column under different type of loading protocols, will improve the collapse resistance of the model. However, for the 20-story buildings, this pattern is not applicable. As the period of the structure increases, the effect of nonlinear behavior of the plastic hinges decreases. The maximum drifts in which collapse occurs reduces for high rise buildings. Hence, the effect of DDM plastic hinges, that majorly differ from previous models at larger drift ratios, becomes insignificant for high rise buildings.

Chapter 9
Part II

Improved PH with UHP-FRC

Major part of this chapter is presented in the ACI paper titled “Seismically robust ultra-high-performance fiber-reinforced concrete columns” (Chao et al., 2021).

9.1 Introduction

Reinforced concrete (RC) special moment frame (SMF) columns in the lower stories of high-rise buildings in areas of high seismicity are usually subjected to high axial loads and large shear force and bending moments resulting from earthquake forces. The strength demand is further increased due to the P-Delta effect. Columns are the most critical structural member in SMFs, providing collapse prevention of buildings in earthquake-prone areas. Damaged concrete columns can be difficult to repair, which reduces the resilience of structures after major earthquakes and their aftershocks. Furthermore, damage in columns can lead to catastrophic structural collapse, which is a major concern in any area recovering from a recent earthquake. To provide safety protection to the buildings, these RC columns must possess adequate deformation capacity which is usually achieved by providing confinement to the core concrete through extensive transverse reinforcement as required by ACI code Section 18.7.5 (ACI, 2019).

This study uses the testing results of two full-scale columns, identical in geometry and reinforcement, except one is made of normal strength concrete and the other is a column with a plastic hinge region fully cast in UHP-FRC (Nojavan, 2007). This chapter presents an investigation of the effect of UHP-FRC in potentially improving drift capacity and providing greater collapse prevention capacity.

9.2 Experimental program

In this experiment, two identical columns were tested under large axial loads and displacement reversals up to failure. Figure 9-1 (a) shows the Dimensions and

reinforcement details of the test columns. In one of the two columns (the UHP-FRC column), the conventional concrete is replaced by the UHP-FRC material at the 40 of the bottom of the component (Figure 9-1 (b)).

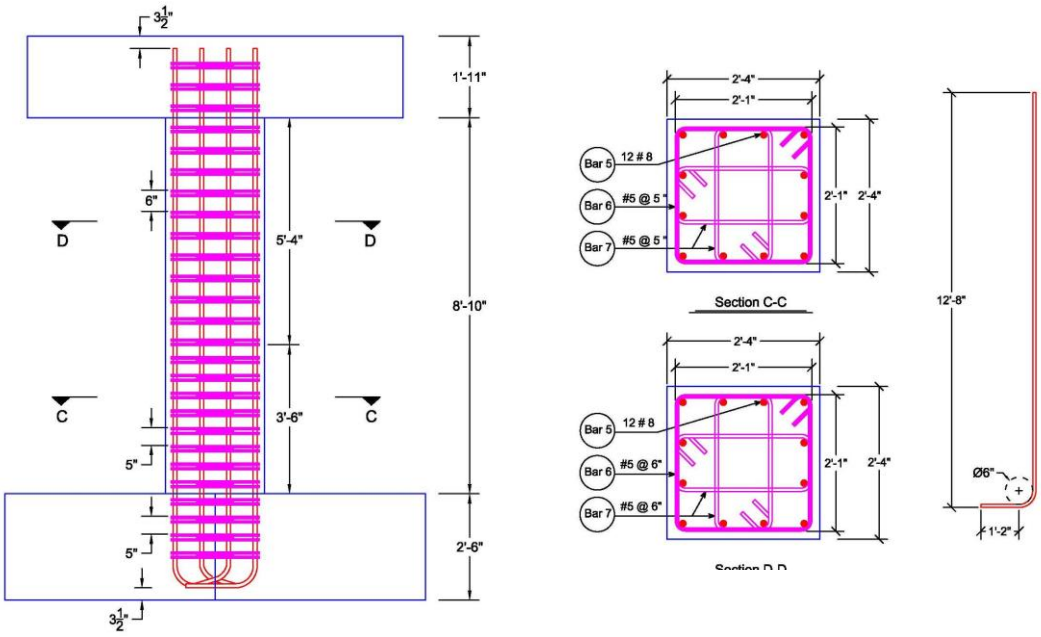

(a)

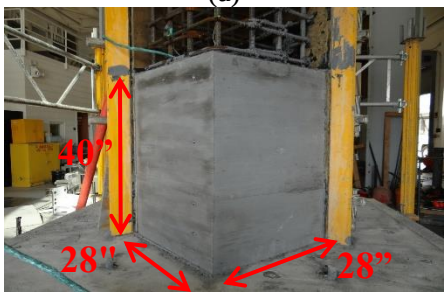

(b)

Figure 9-1 a) Dimensions and reinforcement details of the test columns and b) UHP-FRC at the bottom 40 in of the UHP-FRC column (Chao et al., 2021)

The material property used for the columns tested can be found elsewhere (Nojavan, 2007; Chao et al., 2021). The lateral displacements along the principal axis were applied according to the loading protocol as per ACI-374 (2005). Figure 9-2 represents the loading

protocol adopted for both columns. It was in an incrementally increasing fully reversed cyclic pattern until the specimen's strength degraded to 20 percent or less of its peak lateral strength exhibited during the test. Three fully reversed cycles were applied at each major drift ratio level. In between two different drift ratio levels, intermediate cycles were applied at a magnitude of 1/3 of the preceding major drift ratio level. As shown in Figure 9-2, an extensive number of cycles were applied to the specimens, which represented an extreme loading condition.

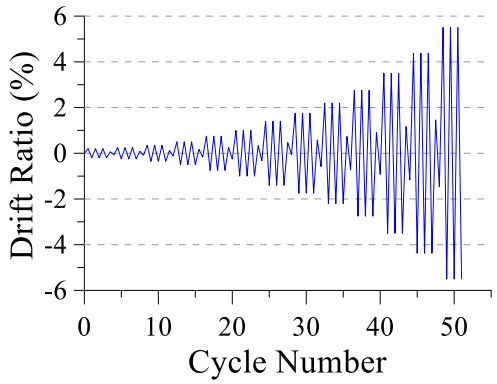

Figure 9-2 Reversed cyclic drift ratio protocol for column specimens in accordance with ACI 374 (2005)

9.3 Experimental results

Figure 9-3 represents the hysteresis curves for both specimens up to 5.5% drift ratio. The response of the RC column shows that the strength degradation starts from early stages with lower drift ratios (Figure 9-3 (a)). However, for the UHP-FRC column, the strength is maintained to larger drift levels followed by a sudden drop in the strength after 4% DR (Figure 9-3 (b)). Also, when the displacement increases, the UHP-FRC column has a lesser amount of residual displacement after unloading. This self-centering behavior is shown even up to 5.5% drift ratio (Figure 9-3 (b)).

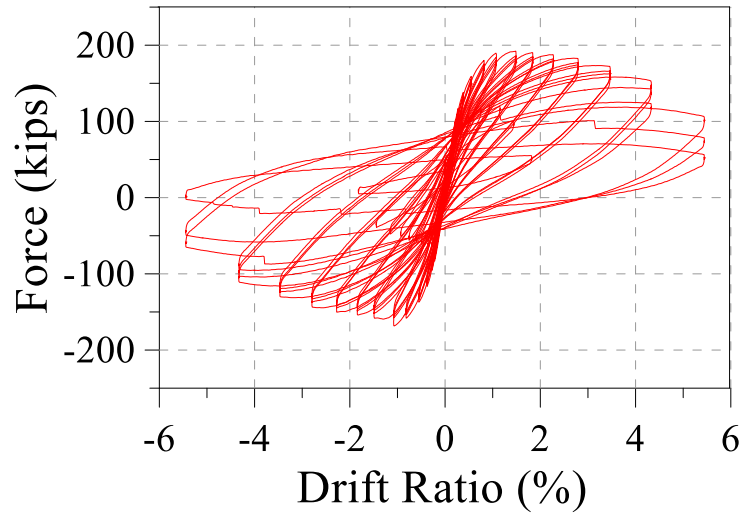

(a)

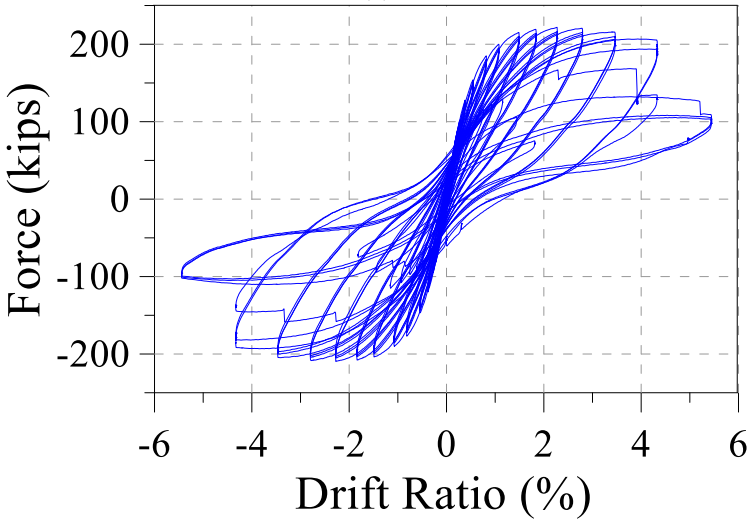

(b)

Figure 9-3 Force versus drift ratio responses of (a) RC column, (b) UHP-FRC column (Nojavan, 2007)

The RC column experienced it maximum strength at 1.0% drift ratio (Figure 9-4 (c)). The initiation of this strength drop accompanied by crushing of the concrete at the corners of the columns (Figure 9-4 (a)). At this drift ratio, flexural cracks are present in the RC column while the UHP-FRC column does not show any cracking or crushing in the concrete (Figure 9-4 (b)). The maximum strength of the UHP-FRC is slightly higher at this DR.

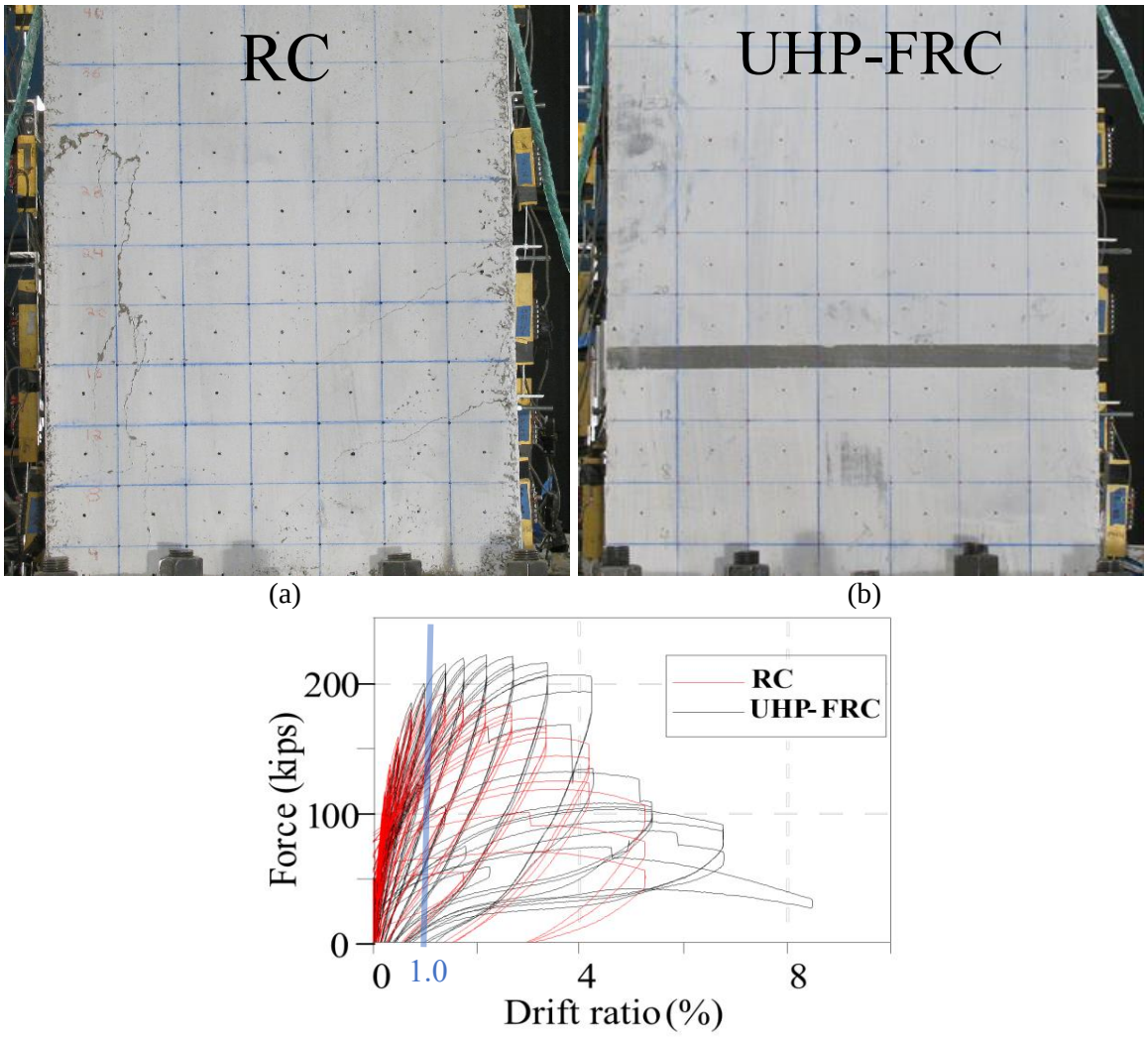

Figure 9-4 Damage of a) RC column and b) UHP-FRC column at 1% drift ratio, and c) the response comparison at 1% DR

The strength degradation of the UHP-FRC column did not occur up to 2.75% DR (Figure 9-5 (c)). Unlike the RC column, the UHP-FRC column exhibited a low rate of strength degradation maintained 90% of its peak strength at 4% DR. at this stage the RC column showed a higher damage level with more concrete crushing and flexural cracking at the bottom of the column; while the UHP-FRC column still did not exhibit any significant damage at the plastic hinge zone (Figure 9-5 (a) and (b)).

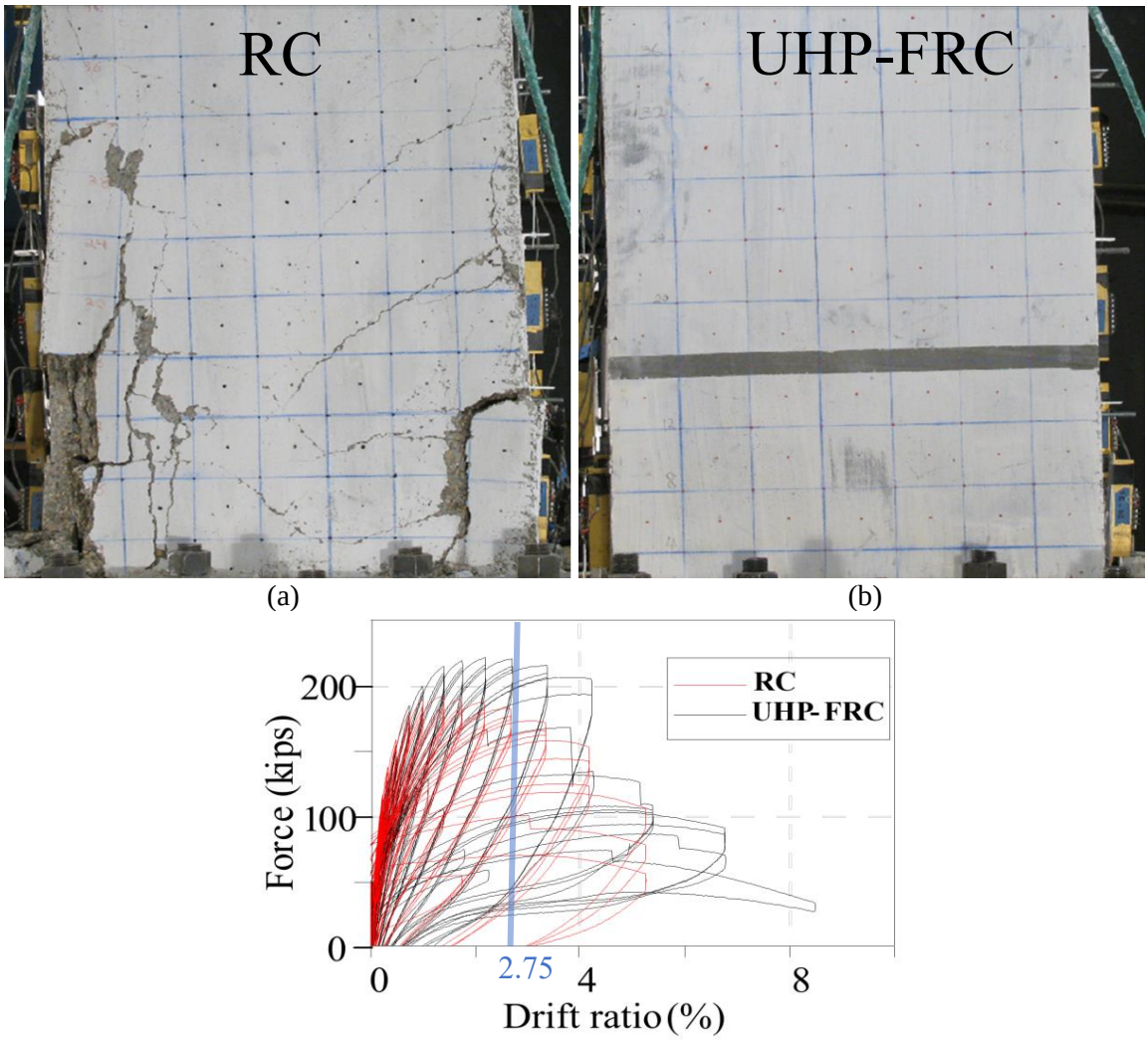

Figure 9-5 Damage of a) RC column and b) UHP-FRC column at 2.75% drift ratio, and c) the response comparison at 2.75% DR

The strength of the UHP-FRC column occurs reduces more than 50% at the 5.25% drift ratio (Figure 9-6 (c)). Although the strength is significantly dropped, the UHP-FRC column does not show major damage in the column (Figure 9-6 (b)). However, the RC column has been severely damaged at this stage (Figure 9-6 (a)). The gradual degradation of the RC column is due to flexural cracking, crushing, and spalling of the concrete as well as yielding in the rebars, while this is not applicable to the UHP-FRC column.

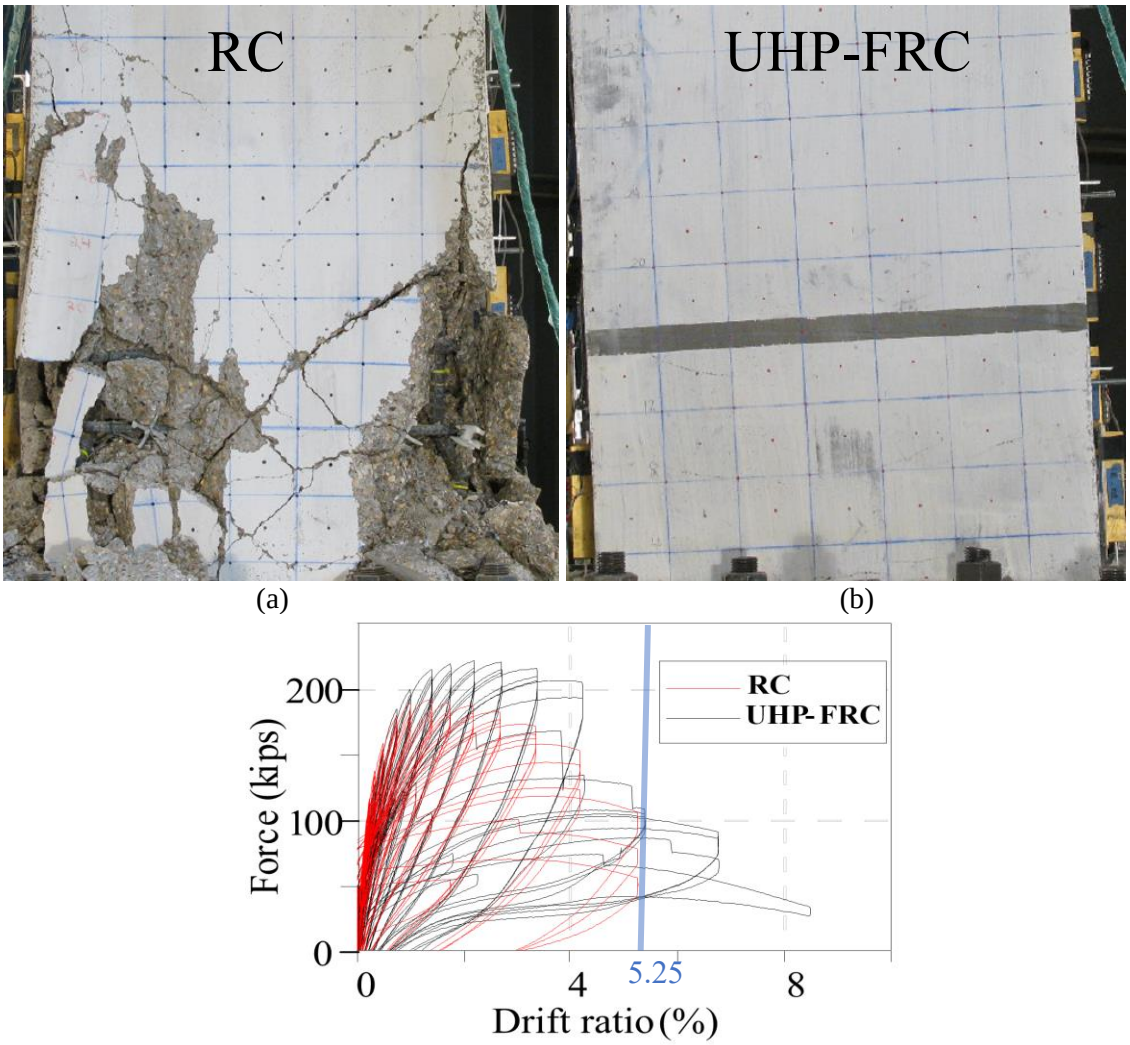

Figure 9-6 Damage of a) RC column and b) UHP-FRC column at 5.25% drift ratio, and c) the response comparison at 5.25% DR

Figure 9-7 shows the rebar fracture of the RC and the UHP-FRC column. For the RC column, the fracture of the rebar is in the column and at the plastic hinge zone of the component. However, for the UHP-FRC column, the fracture occurs at the interface of the column and the footing. A closer study of the rebar strain record during the experiment explains it. Figure 9-8 strain distributions of longitudinal reinforcement along the column height of the column and in the footing as well as the location of the strain gauges attached

to the rebars. The comparison shows that the rebar strain enlarges in the RC column in lower drift levels in the plastic hinge zone. But for the UHP-FRC column it is kept even under the yielding strain at larger DR. This explains the self-centering behavior of the UHP-FRC column. Since the strain in the rebars are kept low and near the yielding strain, the residual displacement of the column will be small. This explains the strength maintaining in the UHP-FRC column followed by a sudden drop. For the RC column, the spalling and crushing of the concrete causes the buckling of the concrete. While the strong bond between the UHP-FRC and the rebar does not let the rebar to be de-bonded and the strain, and consequently the tensile stress, concentrates at the bottom of the column where it interfaces the footing. The red ribbons in Figure 9-8 represents the approximate location of rebar fracture in each of the columns along its height.

(a) RC (b) UHP-FRC

Figure 9-7 (a) fracture of longitudinal rebars (b) fracture of rebar at the footing and column interface (Chao et al., 2021)

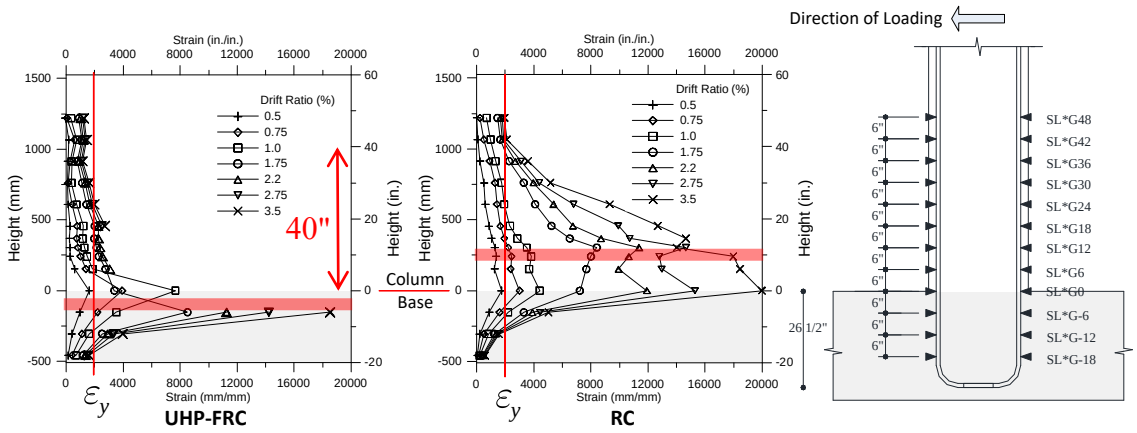

Figure 9-8 Strain (×106) distributions of longitudinal reinforcement along the column height (Chao et al., 2021)

9.4 Effective lateral stiffness

Figure 9-9 compares the average lateral force versus the drift ratio backbone curves for both columns. The lateral stiffness of both columns is approximately the same before 0.5% DR. From this point on, the concrete cracking sustained by the RC column subjected to cyclic reversals becomes significant, and the lateral stiffness drops corresponding to the increased cracking along the height of the RC column, which lowers the stiffness of the RC column. Notably, while the conventional concrete above 40 in. (1016 mm) cracked, the UHP-FRC column had greater lateral stiffness beyond 0.5% DR. A column's effective lateral stiffness is commonly evaluated by a linearized secant stiffness, based on the first point where the longitudinal reinforcement yields (Mehanny et al., 2001; Elwood and Eberhard, 2009). As discussed earlier, the first longitudinal bar yielding was observed at 0.57% DR and 0.51% for the RC and UHP-FRC columns, respectively. The secant stiffness of both columns was determined based on the yield DRs and plotted in Figure 9-9. Note

that the P-Delta force, although small at this drift ratio level, has been subtracted from Figure 9-9. Clearly, while the stiffness of the UHP-FRC column is slightly higher, the difference is marginal at this drift level. In addition, Figure 9-9 also shows the secant stiffness for both columns according to the equation proposed by Elwood and Eberhard (2009), which considers the axial load ratio $P/f_c'A_g$, dimensions of the columns and longitudinal rebars, and the equivalent cantilever length. The stiffness in Figure 9-9 was calculated assuming the column is a cantilever (Elwood and Eberhard, 2009) with a length of 8 ft (2438 mm). Clearly, the estimated secant stiffness is smaller than the measured one. The estimated UHP-FRC column's stiffness is lower than the RC's because of the low compressive axial load ratio used in the equation. It should be noted that Elwood and Eberhard's equation was never intended to apply to a column with UHP-FRC.

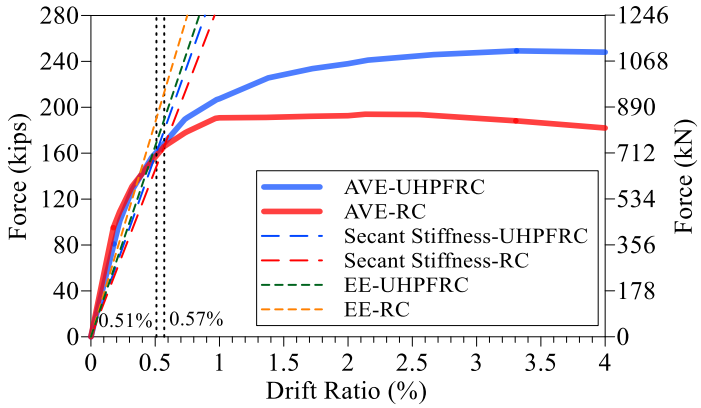

Figure 9-9 Comparison of lateral stiffness between RC and UHP-FRC columns

9.5 Collapse resistance of SMFs with UHP-FRC columns

As shown in Figure 9-3, the UHP-FRC column has greater displacement ductility capacity and strength than the RC column. The impact of these two factors on the collapse resistance performance of SMF was investigated in this study. The OpenSees software platform

(McKenna et al., 2000) was used for the numerical simulations through incremental dynamic analysis (IDA) (Vamvatsikos, 2002). To model the strength and stiffness cyclic deterioration, a peak-oriented hysteretic model developed by Ibarra et al. (2005) is used (Figure 6-11). Based on an energy-based deterioration parameter, this model captures the hardening behavior and strength deterioration, as well as the accelerated reloading and unloading stiffness deterioration. The hysteretic rules of Ibarra's model are used for the RC column as shown in Figure 9-10 (a). Unlike the RC column, it is observed that the UHP-FRC column shows a self-centering behavior beyond 4% DR. This feature is added to the model by combining Ibarra's model as illustrated in Figure 9-10 (a) with a self-centering material model as shown in Figure 9-10 (b). The UHP-FRC model is calibrated to capture the effect of the self-centering behavior with a reduction in strength for drift ratios larger than 4% DR. Figure 9-11 shows the agreement between the calibrated numerical and experimental results of RC and UHP-FRC columns. The P-Delta effect is included in the simulated response.

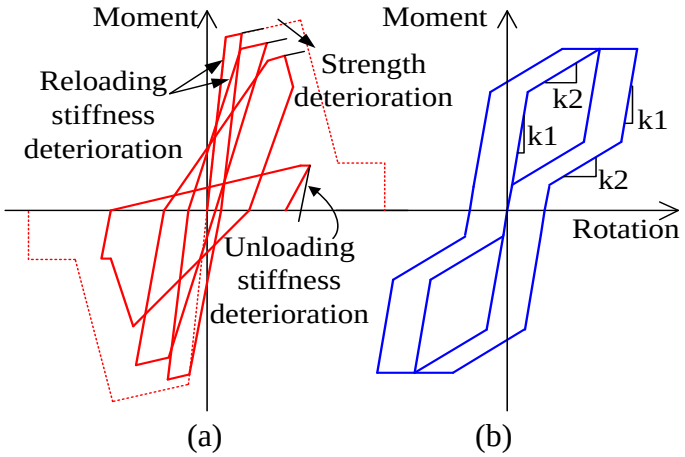

Figure 9-10 Hysteresis behavior of (a) the Ibarra model and (b) the self-centering model

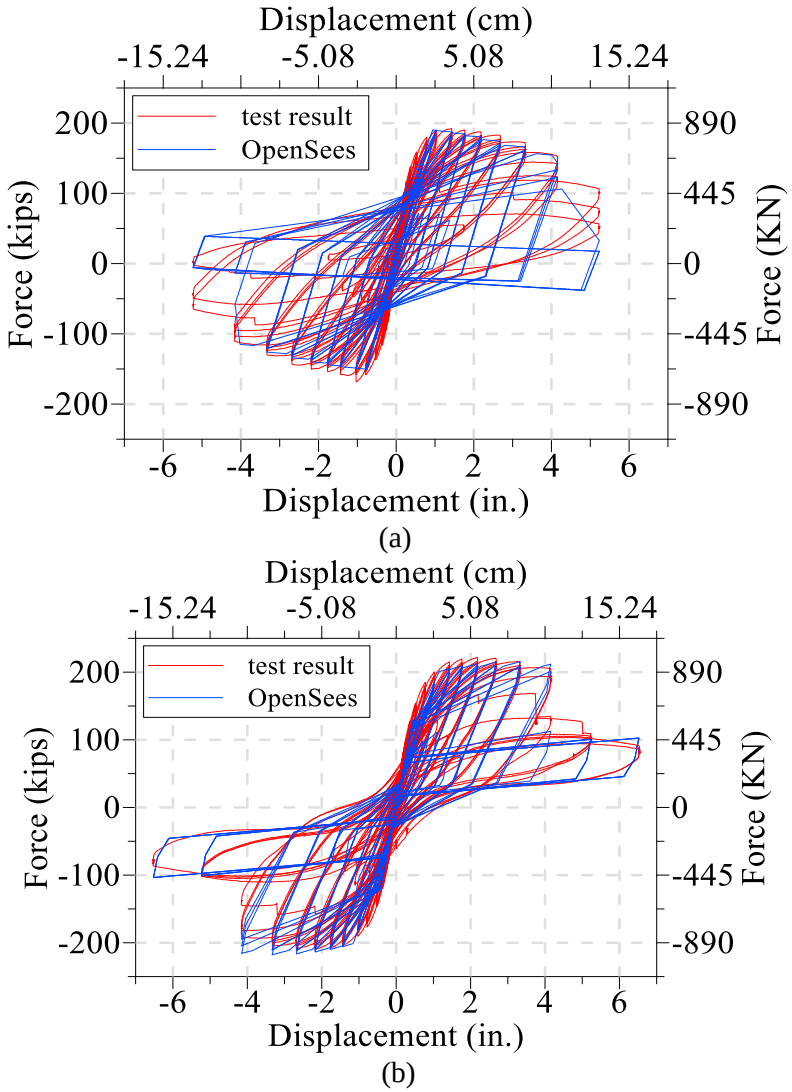

Figure 9-11 Comparison between the simulated and test response of (a) the RC column and (b) the UHP-FRC column

To avoid weak-column strong-beam strength and to satisfy the minimum flexural strength of the column, the sections were designed according to ACI code Section 18.7.3.2 such that the sum of nominal flexural strength of the columns at the face of the joints is greater than 1.2 times this value for the connected beams (ACI, 2019). To improve the collapse capacity, the column-to-beam flexural strength ratios were selected to be close to or more than 2.0 (Haselton and Deierlein, 2007). This minimum value of all SCWB ratios for the

first floor is 1.9 for both the RC and UHP-FRC frames. Table 9-1 lists the SCWB ratios for all the stories.

Table 9-1 SCWB ratios for all the stories

	col 1 (ext)	col 2 (int)	col 3 (int)	col 4 (ext)
story 4	3.48	1.74	1.74	3.48
story 3	4.24	2.12	2.12	4.24
story 2	4.00	2.00	2.00	4.00
story 1	3.77	1.90	1.90	3.77

9.6 IDA results for UHP-FRC and RC columns with equal strength

To investigate the collapse resistant performance of the UHP-FRC column under seismic loading, two 2D four-story three-bay SMFs were analyzed using OpenSees software: one with RC columns and the other with UHP-FRC columns. Two features of the UHP-FRC columns are: 1) improved deformation capacity and 2) the self-centering behavior. Although it is well-known that an improved deformation capacity of columns increases the collapse capacity of the system (FEMA-P440, 2009), the collapse assessment of the self-centering behavior of reinforced concrete moment frames needs further investigations.

For the SMF with UHP-FRC columns, it is assumed that UHP-FRC is used only in the plastic hinging regions of all columns. Regular RC beams are used for both SMF models. The peak strengths of both columns were kept the same to investigate the effect of the greater pre-capping deformation capacity in the UHP-FRC column (Figure 9-3). That is, the peak strength of UHP-FRC was reduced 15.6% to duplicate the RC column peak strength. Lumped plastic hinges (PHs) were placed at both ends of the elements. To connect

the PHs at the joints, beams and columns were connected through a two-dimensional beam-column-joint element object (Altoontash, 2004). Since joint shear strength was determined based on a strong-joint weak-beam criterion (ACI, 2019) the joints are modeled elastically and their contribution to the drift ratio is negligible. In addition, results from RC and UHP-FRC frames analyses subjected to a scaled record up to a near collapse PGA indicate that the contribution of joint deformation to the drift ratio is less than 0.7%. A leaning column is modeled to account for the P-Delta effects of the gravity loads. The leaning column does not contribute to the strength and stiffness of the frame. The built model is shown in Figure 9-12 (a). A suite of 10 ground motion records from the PEER-NGA database were used for the IDA. The selected records have relatively large magnitudes ranging from 6.5 to 7.1. All the records are from stations located in areas with a soil type C or D rather than soft soils or near field records. Table 9-2 lists the records used in this study, which are from prior studies (Vamvatsikos et al, 2003; Haselton and Deierlein, 2007).

The intensity measure (IM) for the IDA curve in this study is the peak ground acceleration (PGA) of the scaled records. Since the sides-way collapse is targeted in this study, the damage measure (DM) is considered as the absolute value of the maximum drift ratio of the stories. Reaching the flatline of the IDA curve for each record is achieved by increasing the IM in small intervals. This increment amount is reduced when the scaling is close to collapse. Finally, the collapse IM is defined as the point at which a small increase of its magnitude results in a very large DM. The solid and dashed gray lines in Fig. 18a are for individual IDA curves for UHP-FRC and RC columns, respectively. All the individual IDA curves demonstrate that the SMF with UHP-FRC columns has a larger collapse IM than the SMF with conventional RC columns. The average IDA curves for the UHP-FRC and

RC SMFs are shown as the solid blue and dashed red lines, respectively. The average collapse IMs for the UHP-FRC frame is 1.87g, while this value for the RC frame is 1.55g. The comparison between these values indicates that SMF with UHP-FRC columns can resist a near collapse ground motion with a 20% higher PGA than the SMF with conventional RC columns. The vertical blue and red arrows in Figure 9-12 (b) point to the average of maximum drift ratios in UHP-FRC and RC buildings, respectively. From an RC to a UHP-FRC column, this value increases from 6.5% to 10.1% with a 55% increase. This shows that greater deformation capacity in a column leads to a higher maximum drift ratio accompanied by a larger collapse IM.

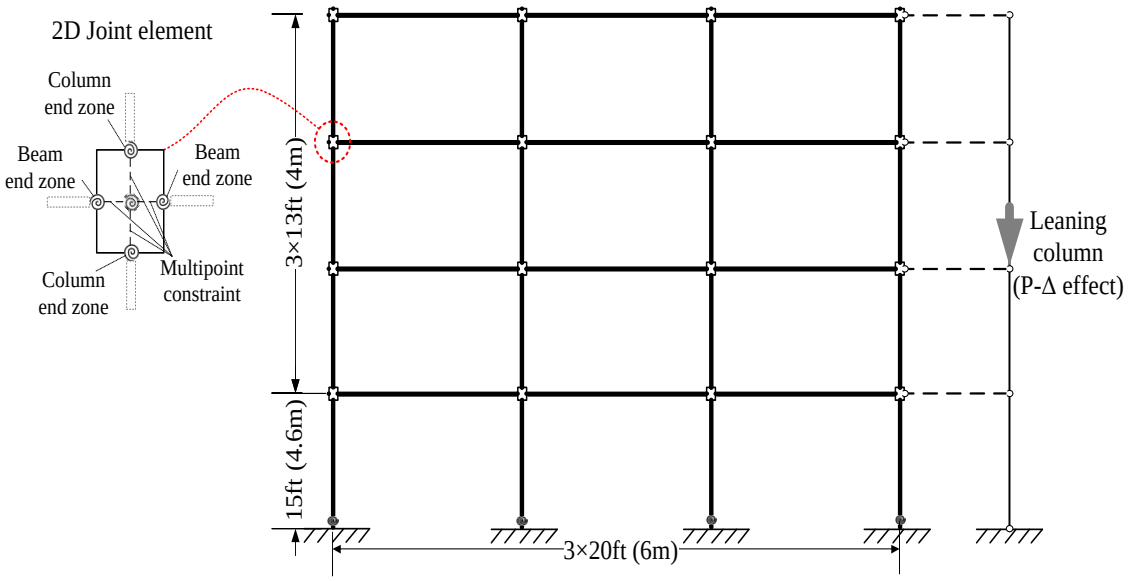

(a)

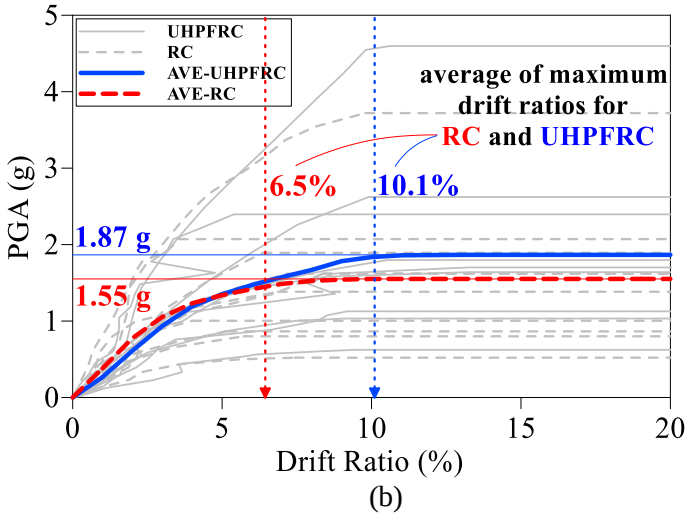

(b)

Figure 9-12 (a) Schematic of the numerically modeled four-story SMF and (b) the individual and average IDA curves of SMFs with RC and UHP-FRC columns having equal strength

Table 9-2 Ground motion records used for incremental data analysis (IDA)

No.	Event	Year	Station	Component	Magnitude	PGA
1	Loma Prieta	1989	Hollister Diff. Array	255	6.9	0.279g
2	San Fernando	1971	LA, Hollywood Stor. Lot	180	6.6	0.195g
3	Imperial Valley	1979	Chihuahua	282	6.5	0.245g
4	Superstition Hill	1987	Wildlife Liquefaction Array	360	6.7	0.208g
5	Duzce, Turkey	1999	Bolu	000	7.1	0.728g
6	Friuli, Italy	1976	Tolmezzo	000	6.5	0.351g
7	Hector mine	1999	Hector	000	7.1	0.266g
8	Kobe, Japan	1995	Kakogawa	000	6.9	0.251g
9	Imperial Valley	1979	Compuertas	285	6.5	0.147g
10	Imperial Valley	1979	El Centro Array	140	6.5	0.143g

Note: records are from PEER-NGA database

9.7 Summary and conclusions

This chapter investigated the application of UHP-FRC in enhancing the seismic performance of concrete columns. Data for two full-scale columns specimens were used they were identical in geometry and reinforcement details. One was a 100% RC column, and the other was made with UHP-FRC at the plastic hinge region. Both were tested under the same boundary conditions and loading protocol. The performance of the test specimens was evaluated in terms of load-displacement responses, lateral stiffness, rotation of the plastic hinge regions, ultimate strength, and collapse resistant capability. This study suggests that UHP-FRC columns have advantageous characteristics compared to that of RC and HSC columns and are a viable alternative for seismic resistant structures. Incremental dynamic analyses of a four-story prototype SMF indicated that using UHP-FRC columns increases the collapse peak ground acceleration by 20% due to their greater deformation capacity.

The UHP-FRC column failure occurred due to fracture of the rebar at the interface of the column and footing. The strain concentration caused the rebar rupture and sudden drop of the column capacity. This behavior can be improved if the ductile-concrete strong-reinforcement (DCSR) design concept is used. If based on DCSR design method, the amount of the rebars is enlarged, the stress and consequently the strain in the rebars will be controlled and the self-centering behavior of the column will be maintained as well.

Chapter 10

Summary and Conclusion

10.1 Summary and conclusion for part 1

The revolutionary features of UHP-FRC material permits the development of new design methods. The ductile-concrete strong-steel (DCSR) design concept utilizes the high strength and enlarged compressive ductility of the UHP-FRC to enhance the ductility of the component. The nonlinear behavior of the section originates in both the yielding of the steel reinforcement rebars in tension and the compressive nonlinear behavior ultra-high performance fiber reinforced concrete. To reach the strain value of 0.003 in compression for UH-FRC, the reinforcement amount is increased.

The analyses results show a greater strength and ductility for beam sections design with DCSR design concept. In a more optimized section, such as I-shape (or box) section beam or girder, the area of the compression zone is reduced. This will help the section to maintain a deep neutral axis. Consequently, the strain in the top layer of the UHP-FRC will increase with a greater rate. If UHP-FRC, with a ductile compressive behavior and a large usable maximum compressive strain, is used, the nonlinearity starts due to higher strains in UHP-FRC. In this way, the use of material will reduce while at the same time a minimum required strength and ductility will be achieved.

The experimental results are used to assess the DCSR designed column sections. The ductility of the columns under large displacement reversals was maintained up to a drift ratio of 9% without strength degradation. Also, the column exhibits a self-centering behavior with minor residual deformation and enhanced resilience of the column. The comparison of the incremental dynamic analysis results for a SMF with conventionally designed column, and a SMF constructed with DCSR columns reveals that using DCSR designed columns can improve the collapse resistance of the building.

10.2 Future study suggestion for part 1

One of the topics that can help to further develop the DCSR design concept, is to study the effect of more reinforcement on the bonding strength between the fibers and the matrix subjected to cyclic loadings with many numbers of cycle.

In this study, the flexural cracking strength of the UHP-FRC was studied through small-scale beams. To further investigate this feature of UHP-FRC, the results of large-scale specimens will be useful. Also, a combination of tests with varying fiber volume and reinforcement are required to evaluate the effect of each fiber volume and reinforcement ratio on the flexural cracking strength of the UHP-FRC.

Another study could be focused on the long-term cost efficiency of the DCSR design concept. High-performance materials have higher initial construction cost but provide more durable structures. Hence, the cost efficiency of these type of methods should be studied for the whole service life of the structures.

10.3 Summary and conclusion for part 2

In this study a new model for RC plastic hinge columns is proposed. This model uses a dual degrading method and is constructed with two non-linear zero-element springs that are working in parallel. To eliminate the dependency of modeling calibration to the loading protocol, this model uses the results of a column (either from experimental tests or fiber model) subjected to different types of loading protocols. Since, the parameters of the model are found numerically, this method is applicable to any hysteretic model. To find the efficacy of the model, the results of five nominally identical columns are used. It is shown

that the model is able to fit the results with one set of parameters for all the loading protocols.

The results of the time history analysis for a four-story building show that accurate modeling of the column behavior up to large drift ratios affects the response of the building. The comparison between dual degrading model and the formulized model available in the literature, reveals that the drift ratio and the base shear response in nonlinear time history analysis is affected by the post-yielding stiffness. The difference becomes larger if a larger ground motion is subjected. The results show that early negative post-capping stiffness in the model, could misrepresent a lesser experienced drift ratio and forces in highly nonlinear demanding excitations.

Also, the new DDM plastic hinge was used to assess the collapse resistance of buildings. For this purpose, two pairs of 4-story and 20-story RC SMFs where used. One of each pair were modeled with PEER proposed parameters for Ibarra model. For the other one, the new DDM were used for the plastic hinges of the columns. This new model was calibrated based on the results of a series of fiber models for each column subjected to four different loading protocol. All the models were subjected to incremental dynamic analysis. The results show that using the DDM plastic hinges, that are capable to mimic the behavior of a column under different type of loading protocols, will improve the collapse resistance of the model. However, for the 20-story buildings, as the period of the structure increases, the effect of nonlinear behavior of the plastic hinges decreases. The results show that, the collapse drift reduces for high rise buildings. Hence, the effect of DDM plastic hinges, that majorly differ from previous models at larger drift ratios, becomes insignificant for high rise buildings.

10.4 Future study suggestion for part 2

The real behavior of columns is affected by the size of the column. For a future study, the author suggests a series of full-scale columns under different type of loading protocols with varying important parameters such as axial loading ratio.

In this study, the effect of dual-degradation model was investigated for four-story and 20-story buildings with no irregularities. To find the effect of the DDM columns on collapse resistance, a wide range of buildings with different number of stories and different irregularities are helpful.

Reference

AASHTO (2017). *LRFD Bridge Design Specifications, 7th edition*. American Association of State Highway and Transportation Officials (AASHTO). Washington, D.C.

ACI Committee 318 (2011). *Building Code Requirements for Structural Concrete (ACI 318-11) and Commentary (ACI 318R-11)*. American Concrete Institute, Farmington Hills, MI.

ACI Committee 318 (2019). *Building Code Requirements for Structural Concrete (ACI 318-19) and Commentary (ACI 318R-19)*. American Concrete Institute, Farmington Hills, MI.

ACI Committee 374 (2005). *Acceptance Criteria for Moment Frames Based on Structural Testing and Commentary*, ACI 374.1-05. American Concrete Institute, Farmington Hills, MI.

ACI Committee 440 (2015). *Guide for the Design and Construction of structural concrete reinforced with Fiber Reinforced Polymer (FRP) bars (ACI 440.1 R-15)*. American Concrete Institute Farmington Hills, USA.

ACI Innovation Task Group 6 (2010). *Design Guide for the Use of ASTM A1035/A1035M Grade 100 (690) Steel Bars for Structural Concrete (ACI ITG-6R-10).* American Concrete Institute, Farmington Hills, MI.

Aghdasi P, Heid AE, Chao SH. (2016). Developing Ultra-High-Performance Fiber-Reinforced Concrete for Large-Scale Structural Applications. *ACI Materials Journal*, 113(5), 559–570.

Ahlborn TM, Harris DK, Misson DL, Peuse EJ (2011). Characterization of strength and durability of ultra-high-performance concrete under variable curing conditions. *Transportation Research Record*, 2251(1), 68–75.

Altoontash A (2004). *Simulation and damage models for performance assessment of reinforced concrete beam-column joints*. Stanford university Stanford, California.

Arias, A. (1970). A measure of earthquake intensity. Seismic Design for Nuclear Power Plants. *Massachusetts Institute of Technology*.

American Society of Civil Engineers (ASCE) (2017). *Seismic evaluation and retrofit of existing buildings, ASCE/SEI 41-17,* Reston, VA.

Aviram A, Stojadinovic B, Parra-Montesinos GJ, Mackie K (2010). Structural response and cost characterization of bridge construction using seismic performance enhancement strategies. *Technical Report PEER 2010/01*, Pacific Earthquake Engineering Research, Berkeley, USA.

Balaguru, P. N., Shah, S. P. (1992). Fiber-reinforced Cement Composites. McGraw-Hill, 530 pages.

Chao S-H, Liao W-C, Wongtanakitcharoen T, et al. (2007). Large scale tensile tests of high performance fiber reinforced cement composites. *Fifth International RILEM Workshop on High Performance Fiber Reinforced Cement Composites (HPFRCC5).*

Chao. S.-H., Shamshiri, M., Liu, X., Palacios, G., Schultz, A. Nojavan, A. (2021). *Seismically robust ultra-high-performance fiber-reinforced concrete columns*. ACI Structural Journal. 118, No. 2, 17-32.

Chopra AK, Chintanapakdee C (2004). Inelastic deformation ratios for design and evaluation of structures: single-degree-of-freedom bilinear systems. *Journal of Structural Engineering*, 130(9), 1309–1319.

Christopoulos C, Tremblay R, Kim HJ, Lacerte M (2008). Self-centering energy dissipative bracing system for the seismic resistance of structures: development and validation. *Journal of Structural Engineering*, 134(1), 96–107.

DeJong, S.J., and MacDougall, C. (2006). Fatigue Behaviour of MMFX Corrosion-Resistant Reinforcing Steel. Proceedings of the 7th International Conference on Short and Medium Span Bridges, Montreal, Canada.

Fantilli, A.P., Mihashi H., Vallini, P. (2009). Multiple cracking and strain hardening in fiber-reinforced concrete under uniaxial tension. *Cement and Concrete Research*, 39(12), 1217-1229

Federal Highway Administration (FHWA) (2011). Ultra-High Performance Concrete. *TechNote, FHWA-HRT-11-038,* Federal Highway Administration, Washington DC, USA.

FEMA-P440A (2009). Effects of Strength and Stiffness Degradation on Seismic Response. *Report No FEMA_P440A*. Federal Emergency Management Agency, Washington DC, USA.

FEMA-P695 (2009). Quantification of Building Seismic Performance Factors. *Report No FEMA P695*. Federal Emergency Management Agency, Washington DC, USA.

Freyssinet, E. (1936). A Revolution in the Technique of the Utilization of Concrete. *The Structural Engineer*. 14(5), May 1936, pp. 242-259.

Elwood, K. J. and Eberhard, M. O. (2009). *Effective Stiffness of Reinforced Concrete Columns*. ACI Structural Journal, V. 106, No. 4, July-August 2009, pp. 476-484.

Haselton CB and Deierlein GG. (2008). Assessing Seismic Collapse Safety of Modern Reinforced Concrete Moment-Frame Buildings. *PEER report, 1547-058X ; 2007/08*. Berkeley: University of California.

Haselton, C. B., Liel, A. B., Taylar-Lange, S. C., and Deierlein, G. G. (2016). Calibration of model to simulate response of reinforced concrete beam-columns to collapse, *ACI Structural Journal* 113, No. 6, 1141-1152.

Horii H, Nemat-Nasser S (1985). Compression-induced microcrack growth in brittle solids: Axial splitting and shear failure. *Journal of Geophysical Research: Solid Earth*, 90(B4), 3105–3125.

Ibarra, L., Medina R., and Krawinkler H. (2002). *Collapse assessment of deteriorating SDOF systems*. Proceedings, 12th European Conference on Earthquake Engineering, London, Elsevier Science. Ltd, paper #665.

Ibarra L., Medina R., Krawinkler H. (2005). Hysteretic models that incorporate strength and stiffness deterioration. *Earthquake Engineering & Structural Dynamics*, 34(12), 1489–1511.

Jones, S., Martys, N., Lu, Y., and Dale Bentz, D. (2015). Simulation studies of methods to delay corrosion and increase service life for cracked concrete exposed to chlorides. *Cement and Concrete Composites*, 58, pp. 59-69.

Kaka VB. (2017). Applications of Ultra-High Performance Fiber-Reinforced Concrete on Flexural Structural and Architectural Members. Master of science in civil engineering. The university of texas at arlington

Kaka VB and Chao S-H (2018). Investigation of Eliminating Prestress in Bridge Girders with the Use of Non-Prestressed Ultra-High-Performance Fiber-Reinforced Concrete Girders. *Structures Congress 2018: Bridges, Transportation Structures, and Nonbuilding Structures.* American Society of Civil Engineers Reston, VA, 65-80.

Karmacharya A. (2019). Use of Ultra-High-Performance Fiber-Reinforced Concrete (UHP-FRC) for Fast and Sustainable Repair of Pavement and a New Sustainable Structural Member with Ultra-High-Performance Fiber-Reinforced Concrete (UHP-FRC) and Fiber-Reinforced Polymer (FRP) Reinforcement. Master of science in civil engineering. The university of texas at arlington

Kawashima K, MacRae GA, Hoshikuma J-i, et al. (1998). Residual displacement response spectrum. *Journal of Structural Engineering* 124: 523-530.

Keierleber B, Phares B, Bierwagen D, et al. (2007). Design of Buchanan County, Iowa, bridge using ultra high performance concrete and PI girders. *Proceedings of the 2007 Mid-Continent Transportation Research Symposium.* Citeseer.

Khaja, M. N., and Sherwood, E. G. (2013). Does the shear strength of reinforced concrete beams and slabs depend upon the flexural reinforcement ratio or the reinforcement strain? *Canadian journal of civil engineering*, 40(11), 1068-1081.

Krawinkler H. (2009). Loading histories for cyclic tests in support of performance assessment of structural components. *The 3rd international conference on advances in experimental structural engineering, San Francisco.*

Lignos DG, Krawinkler H and Whittaker A. (2009). Contributions to collapse prediction of steel moment frames through recent earthquake simulator collapse tests.

Proceedings 3rd International Conference on Advances in Experimental Structural Engineering, San Francisco, CA.

Leonhardt, F. (1964). Prestressed Concrete—Design and Construction. Second Edition. Wilhelm Ernst & Sohn. 677 pages.

Lin, T.Y., and Burns, N.H. (1981). Design of Prestressed Concrete Structures. Third Edition. John Wiley & Sons. 646 pages.

Maison BF and Speicher MS. (2016). Loading protocols for ASCE 41 backbone curves. *Earthquake Spectra* 32: 2513-2532.

Mander JB, Priestley MJ and Park R. (1988). Theoretical stress-strain model for confined concrete. *Journal of Structural Engineering* 114: 1804-1826.

McKenna, F., Fenves, G. L. , and Scott, M. H. (2000). *Open system for earthquake engineering simulation*. University of California, Berkeley, CA.

Medina RA and Krawinkler H. (2004). Influence of hysteretic behavior on the nonlinear response of frame structures. *Proceedings of the 13th World Conference on Earthquake Engineering.* 1-6.

Mehanny, S. S. F, Kuramoto, H, and Deierlein, G. G. (2001). *Stiffness Modeling of Reinforced Concrete Beam-Columns for Frame Analysis*. ACI Structural Journal, V. 98, No. 2, March-April 2001, pp. 215-225.

Mehta, P. K. and Monteiro, P. J. M. (2014). Concrete—Microstructure, Properties, and Materials, Fourth edition, McGraw-Hill.

Naaman, A.E. (2012). Prestressed Concrete Analysis and Design—Fundamentals. Third Edition, Techno Press 3000. 1176 pages.

Nanni A. (1993). Flexural behavior and design of RC members using FRP reinforcement. *Journal of Structural Engineering*, 119(11), 3344–3359.

Nanni A, De Luca A, Zadeh HJ (2014). *Reinforced concrete with FRP bars: Mechanics and design.* CRC Press, 1st edition.

National Cooperative Highway Research Program (NCHRP) (2017). *Use of Fiber-Reinforced Polymers in Highway Infrastructure*. NCHRP Synthesis 512, Washington DC, USA.

National Institute of Standards and Technology (NIST) (2017). *Guidelines for Nonlinear Structural Analysis for Design of Buildings Part IIb – Reinforced Concrete Moment Frames, GCR.17-917-46v3,* Gaithersburg, MD.

National Institute of Standards and Technology (NIST) (2017). *Recommended Modeling Parameters and Acceptance Criteria for Nonlinear Analysis in Support of Seismic Evaluation, Retrofit, and Design, GCR.17-917-45* Gaithersburg, MD.

Neuenhofer A and Filippou FC. (1998). Geometrically nonlinear flexibility-based frame finite element. *Journal of Structural Engineering* 124: 704-711.

Nilson, A.H. (1987). Design of Prestressed Concrete. Second Edition. John Wiley & Sons. 592 pages.

Nojavan A, Schultz AE, Haselton C, et al. (2015). A new data set for full-scale reinforced concrete columns under collapse-consistent loading protocols. *Earthquake Spectra* 31: 1211-1231.

Nojavan S. (2007). Damage Imaging Algorithms For Structural Health Monitoring Using Electromagnetic Waves.

Ovitigala T, Ibrahim MA and Majasj I. (2016). Serviceability and Ultimate Load Behavior of Concrete Beams Reinforced with Basalt Fiber-Reinforced Polymer Bars. 113.

Panagiotakos TB and Fardis MN (2001). Deformations of reinforced concrete members at yielding and ultimate. *Structural Journal* 98: 135-148.

Pacific Earthquake Engineering Research Center (PEER). *Ground Motion Data Base* [Online]. University of California, Berkeley Available: https://ngawest2.berkeley.edu/ [Accessed 03 March 2021]

Pacific Earthquake Engineering Research (PEER) (2008). *Beam-Column Element Model Calibrated* for *Predicting Flexural Response Leading to Global Collapse of RC Frame Buildings, PEER Report 2007/03,* University of California, Berkeley.

Pacific Earthquake Engineering Research (PEER) (2017). Guidelines for Performance Based Seismic Design of Tall Buildings. *PEER Report 2017/06,* University of California, Berkeley.

Pacific Earthquake Engineering Research (PEER) (2014). *Pacific Earthquake Engineering Research Center: PEER Ground Motion Database*. https://ngawest2.berkeley.edu/

Precast/Prestressed Concrete Institute (PCI) (2011). Bridge Design Manual. Third Edition

Rahnama M and Krawinkler H. (1993). *Effects of soft soil and hysteresis model on seismic demands*: John A. Blume Earthquake Engineering Center Standford.

Rizkalla S, Zia P, Seliem H, et al. (2005) Evaluation of MMFX Steel for NCDOT concrete bridges.

Ruiz-García J, Miranda E (2003). Inelastic displacement ratios for evaluation of existing structures. *Earthquake Engineering & Structural Dynamics*, 32(8), 1237–1258.

Ruiz-García J, Miranda E. (2006). Residual displacement ratios for assessment of existing structures. *Earthquake engineering & structural dynamics* 35: 315-336.

Scrivener, K. L., Vanderley M. J., and Gartner, E. M. (2018). "Eco-efficient cements: Potential economically viable solutions for a low-CO2 cement-based materials industry," Cement and Concrete Research, Vol. 114, 2-26.

Shah, Surendra P. (1992). Do fibers increase the tensile strength of cement-based matrix?. *Materials Journal* 88.6: 595-602.

Shi, S. and Foutch, D.A. (1997). Evaluation of connection fracture and hysteresis type on the seismic response of steel buildings. University of Illinois Engineering Experiment Station.

Stratford, T. and Burgoyne, C. (2003). Shear Analysis of Concrete with Brittle Reinforcement. ASCE *Journal of Composites for Construction*, 7(4), 323-330.

Vamvatsikos D, Cornell C.A. (2002). Incremental dynamic analysis. *Earthquake Engineering & Structural Dynamics*, 31(3), 491–514.

Vamvatsikos, D., Jalayer, F., Cornell, C. A. (2003). *Application of incremental dynamic analysis to an RC-structure.* Proceedings of the FIB Symposium on Concrete Structures in Seismic Regions, pp. 75-86.

Veletsos A and Newmark NM. (1960). Effect of inelastic behavior on the response of simple systems to earthquake motions. Department of Civil Engineering, University of Illinois.

Wang H and Belarbi AJASJ, SP230. (2005). Flexural behavior of fiber-reinforced-concrete beams reinforced with FRP rebars. 51: 895-914.

Wight, J. K. (2016). Reinforced Concrete – Mechanics and Design. 7th Ed., Pearson Education, Hoboken, NJ, 1144 pp.

Appendix A

In this appendix, the digital imaging correlation (DIC) system processed data are provided for the two specimens described in chapter 5, in the application of DCSR design concept in columns section. The details on the specimens tested are provided in Fig.App.A- 1. Afterward, the longitudinal strain (ε_x) value at each step is calculated for the two specimens.

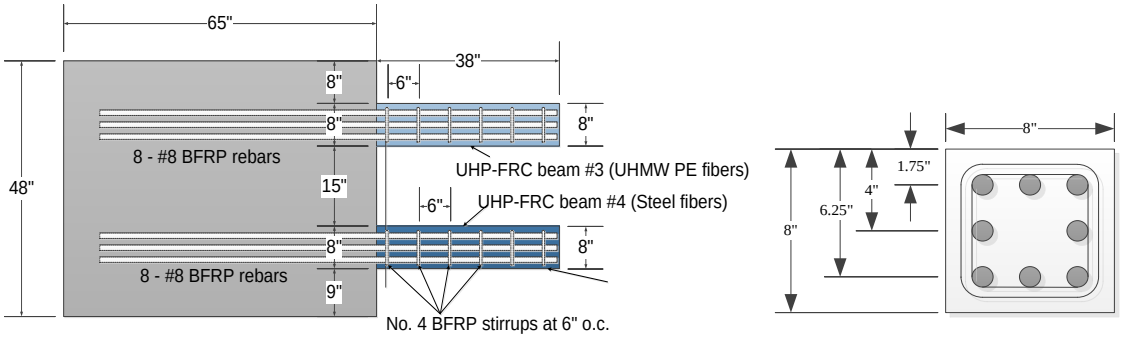

Fig.App.A- 1 Experimental test details (Karmacharya, 2019)

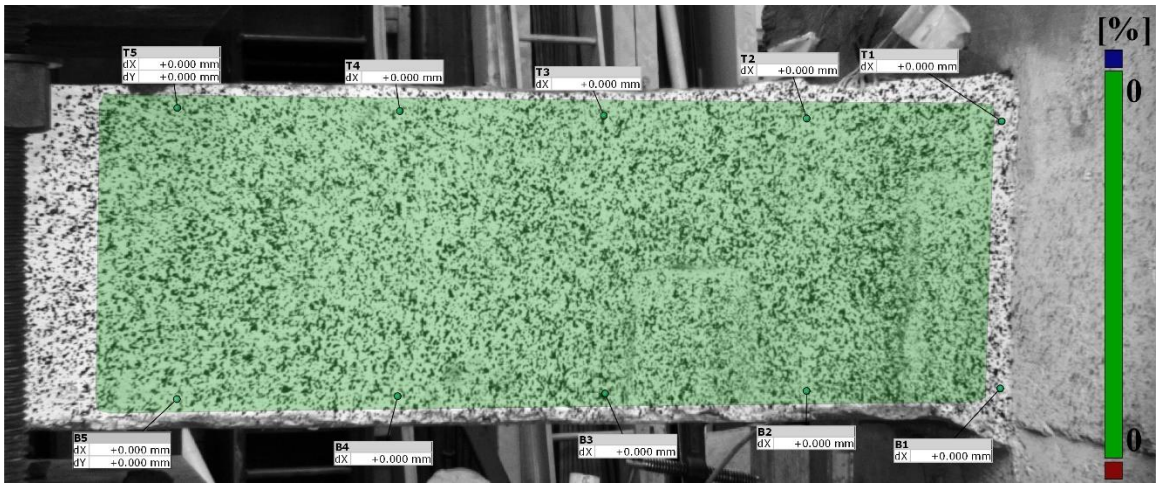

Fig.App.A- 2 The surface along which the longitudinal strain (ε x) value for the first specimen is calculated

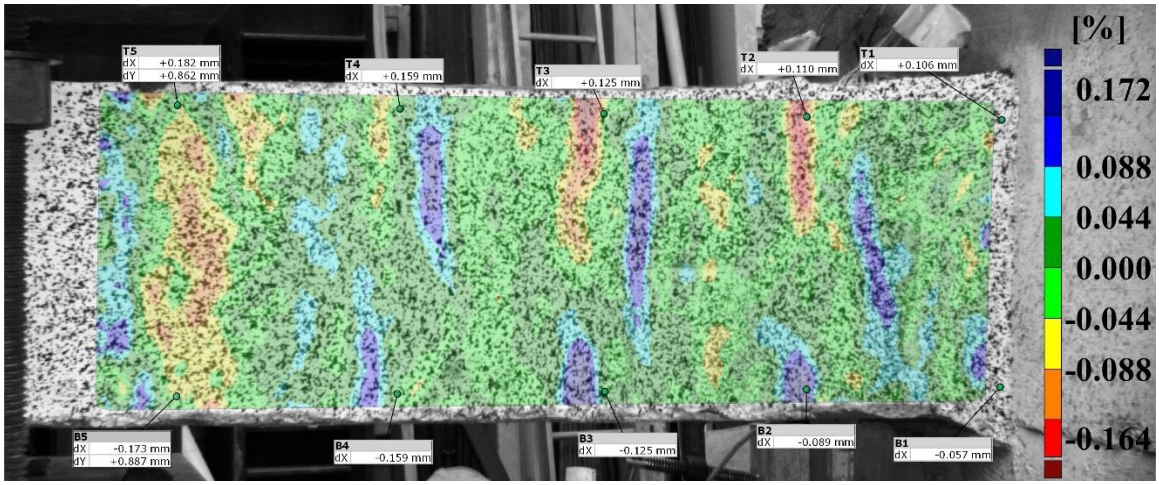

Fig.App.A- 3 longitudinal strain (ε_x) value for the first specimen at 0.2% drift ratio

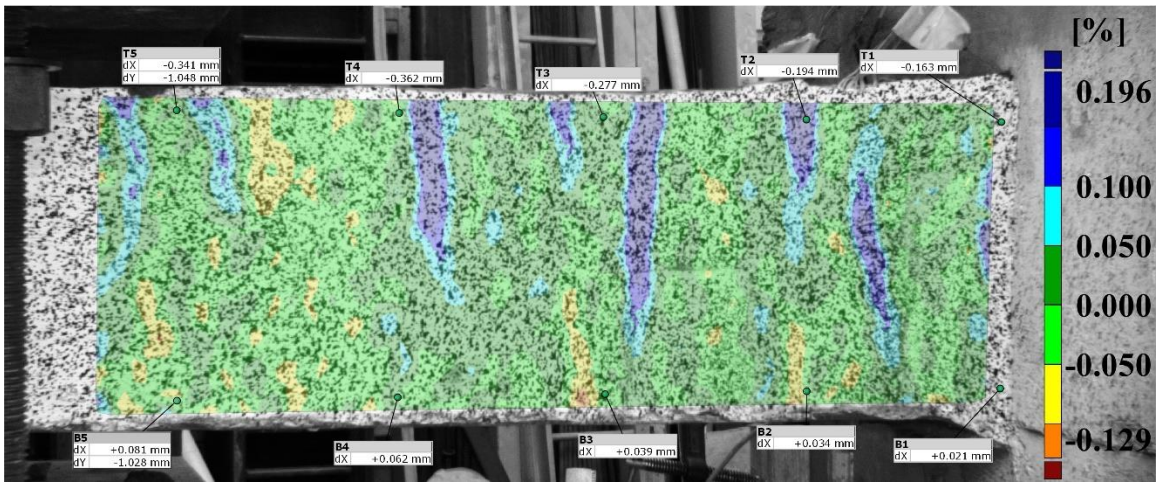

Fig.App.A- 4 longitudinal strain (ε_x) value for the first specimen at -0.2% drift ratio

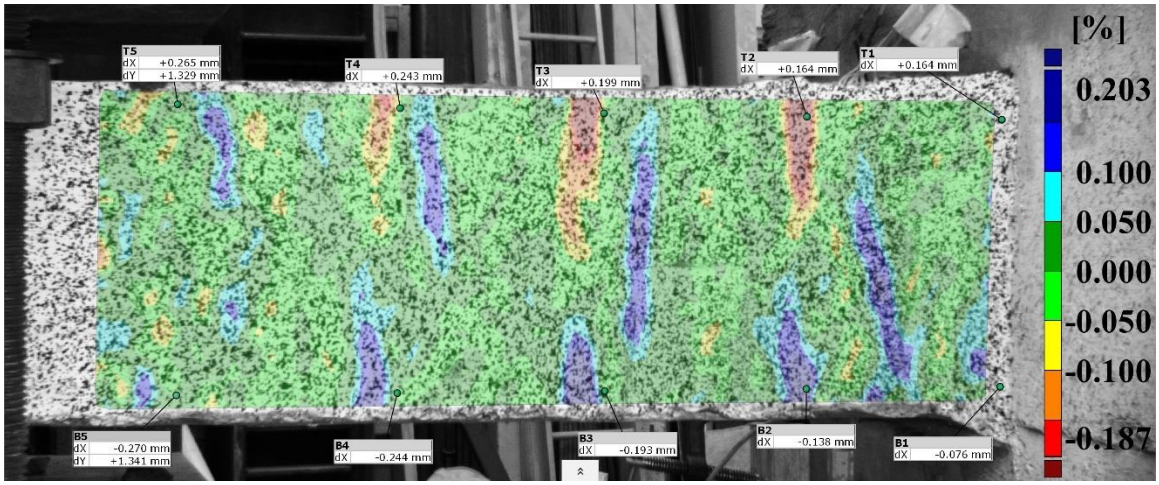

Fig.App.A- 5 longitudinal strain (ε_x) value for the first specimen at 0.25% drift ratio

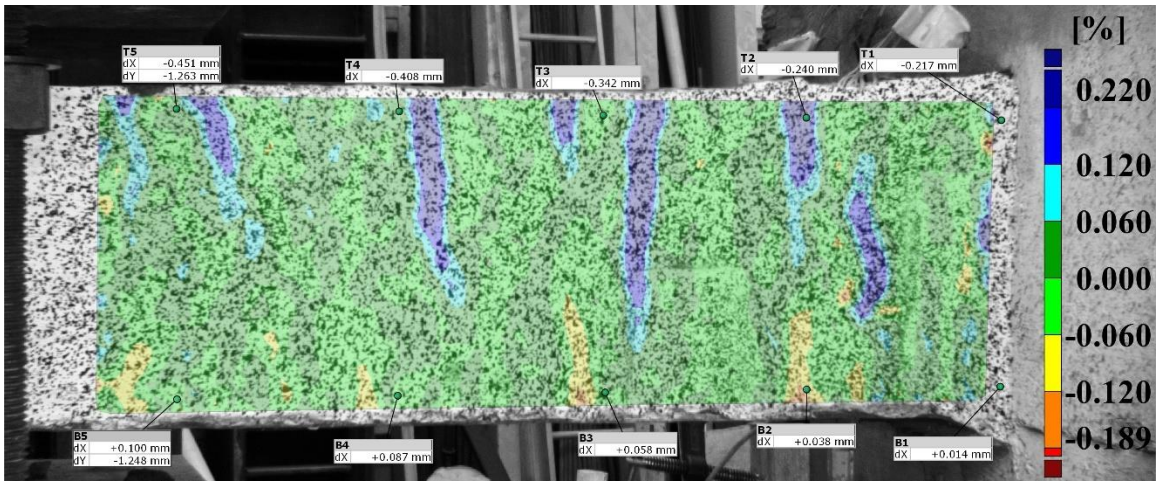

Fig.App.A- 6 longitudinal strain (ε_x) value for the first specimen at 0.25% drift ratio

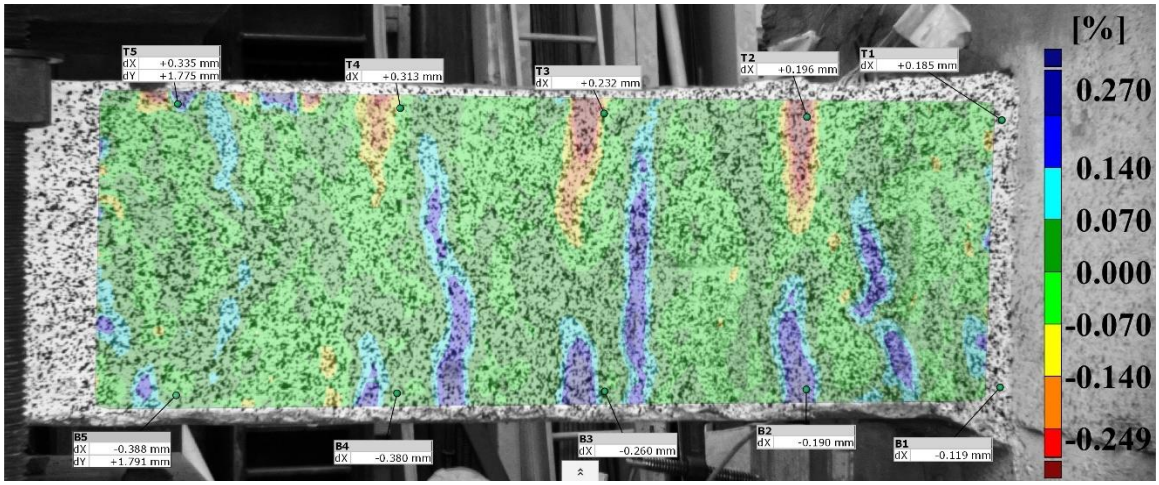

Fig.App.A- 7 longitudinal strain (ε_x) value for the first specimen at 0.35% drift ratio

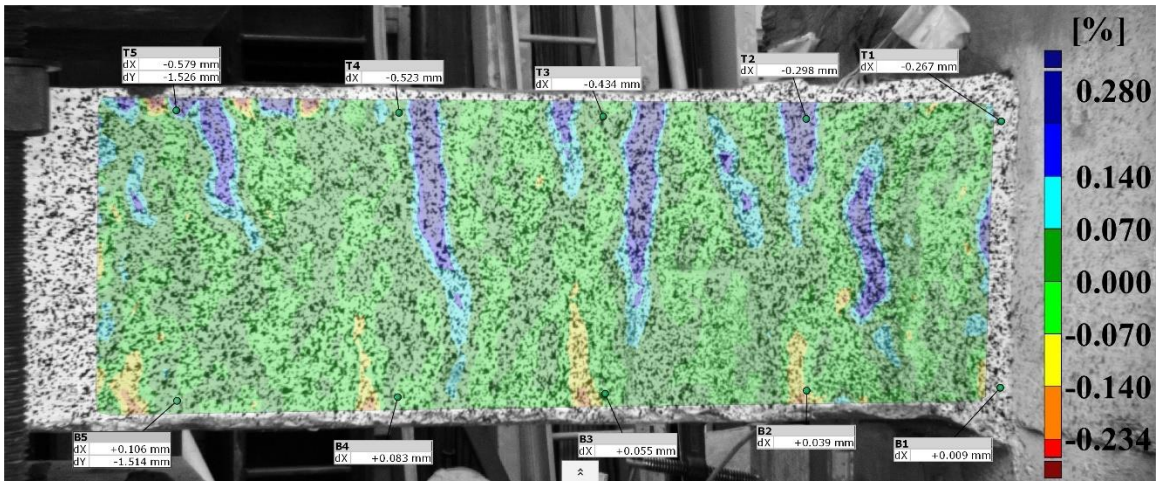

Fig.App.A- 8 longitudinal strain (ε_x) value for the first specimen at -0.35% drift ratio

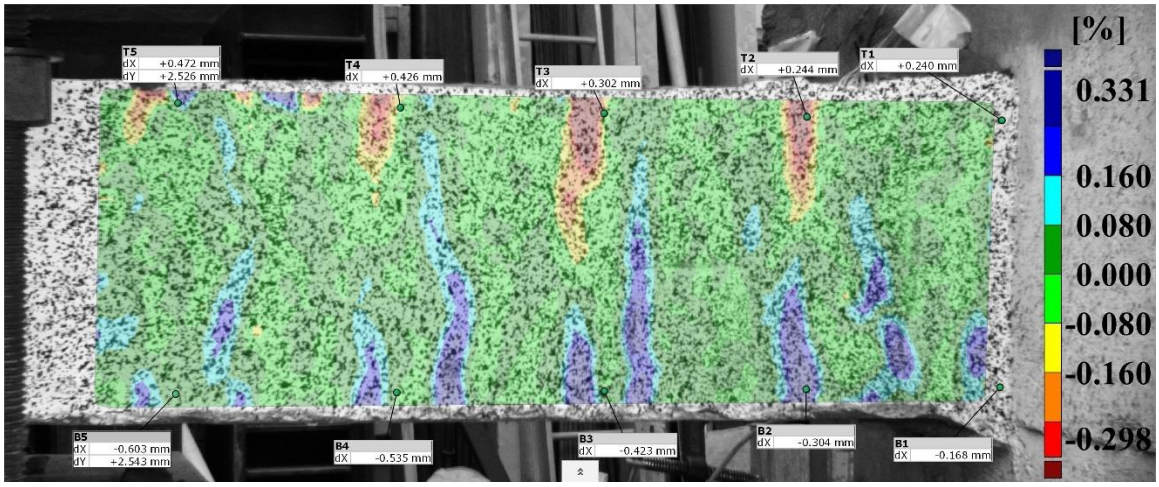

Fig.App.A- 9 longitudinal strain (ε_x) value for the first specimen at 0.5% drift ratio

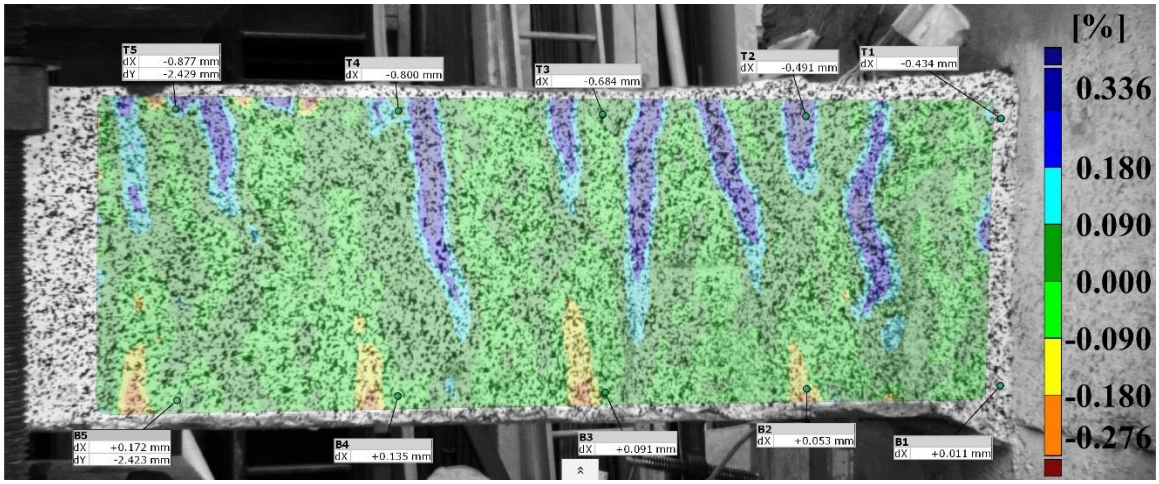

Fig.App.A- 10 longitudinal strain (ε_x) value for the first specimen at -0.5% drift ratio

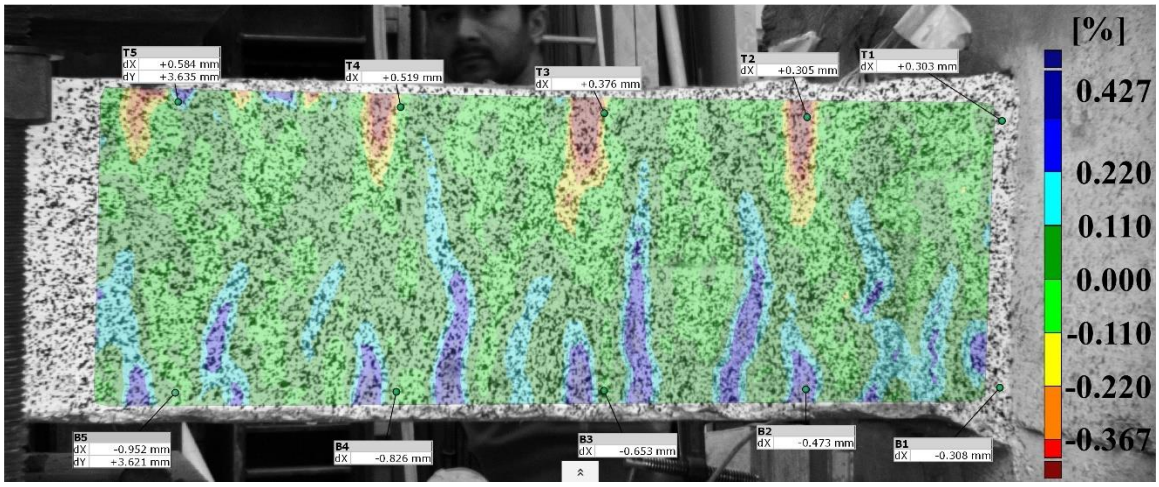

Fig.App.A- 11 longitudinal strain (ε_x) value for the first specimen at 0.75% drift ratio

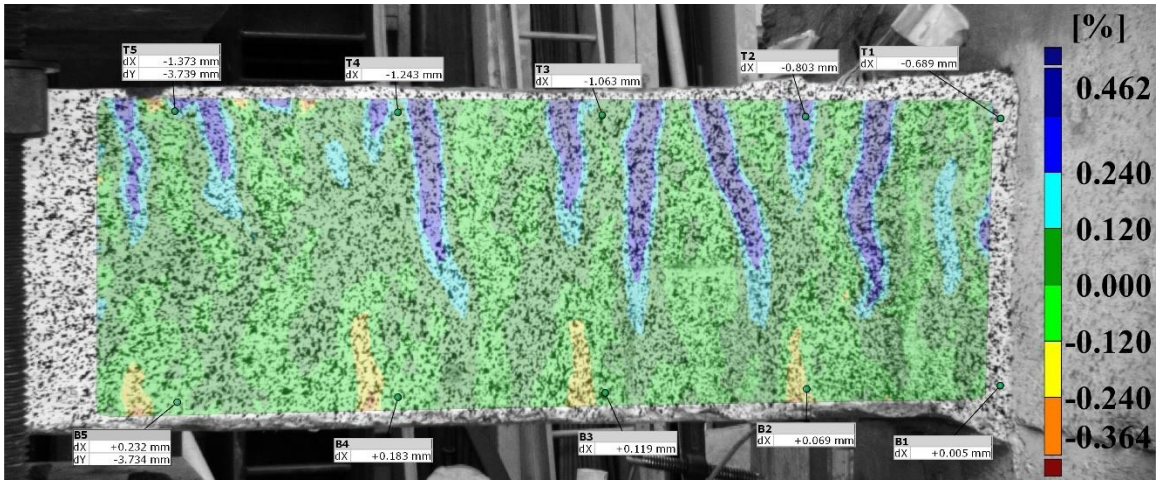

Fig.App.A- 12 longitudinal strain (ε_x) value for the first specimen at -0.75% drift ratio

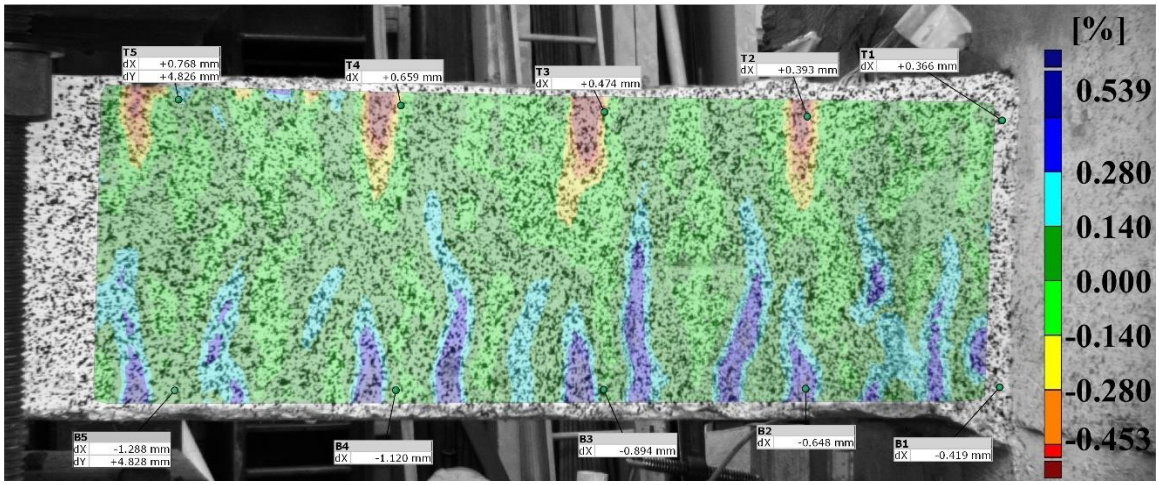

Fig.App.A- 13 longitudinal strain (ε_x) value for the first specimen at 1.0% drift ratio

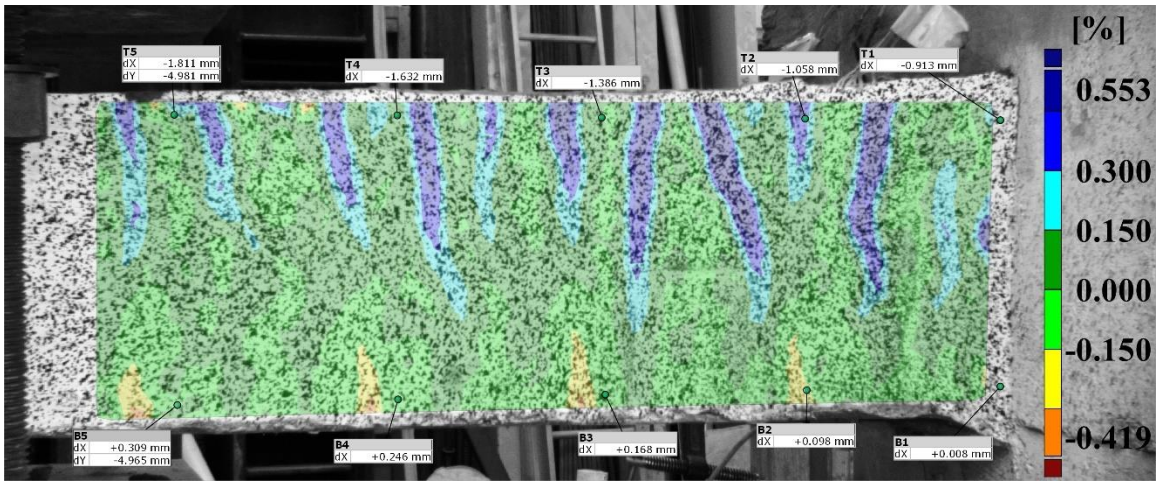

Fig.App.A- 14 longitudinal strain (ε_x) value for the first specimen at -1.0% drift ratio

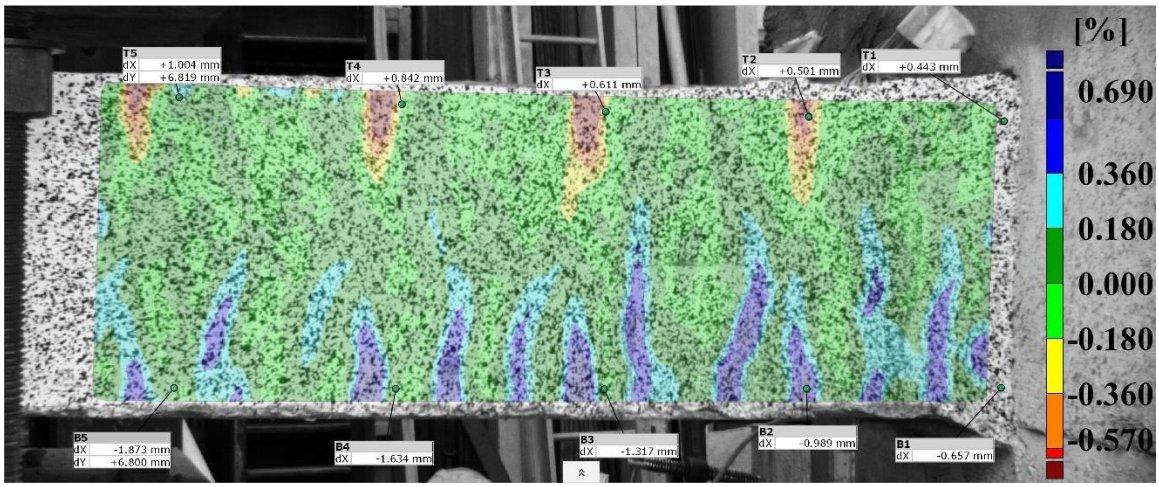

Fig.App.A- 15 longitudinal strain (ε_x) value for the first specimen at 1.4% drift ratio

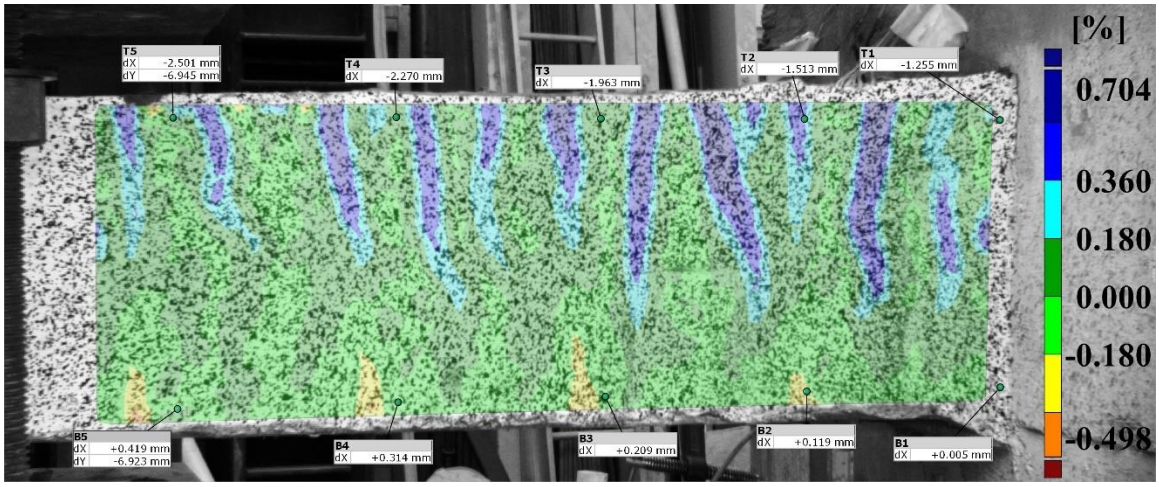

Fig.App.A- 16 longitudinal strain (ε_x) value for the first specimen at -1.4% drift ratio

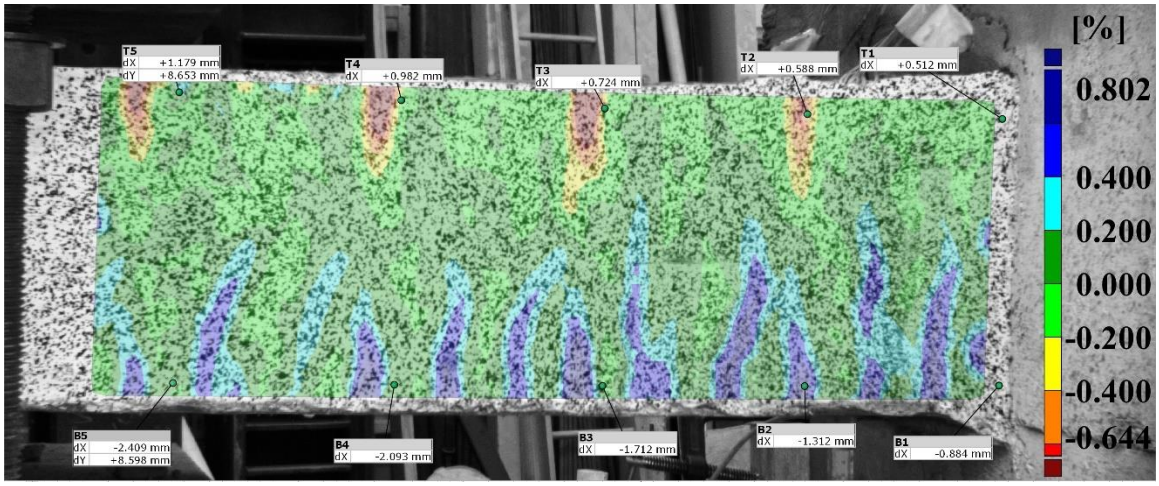

Fig.App.A- 17 longitudinal strain (ε_x) value for the first specimen at 1.75% drift ratio

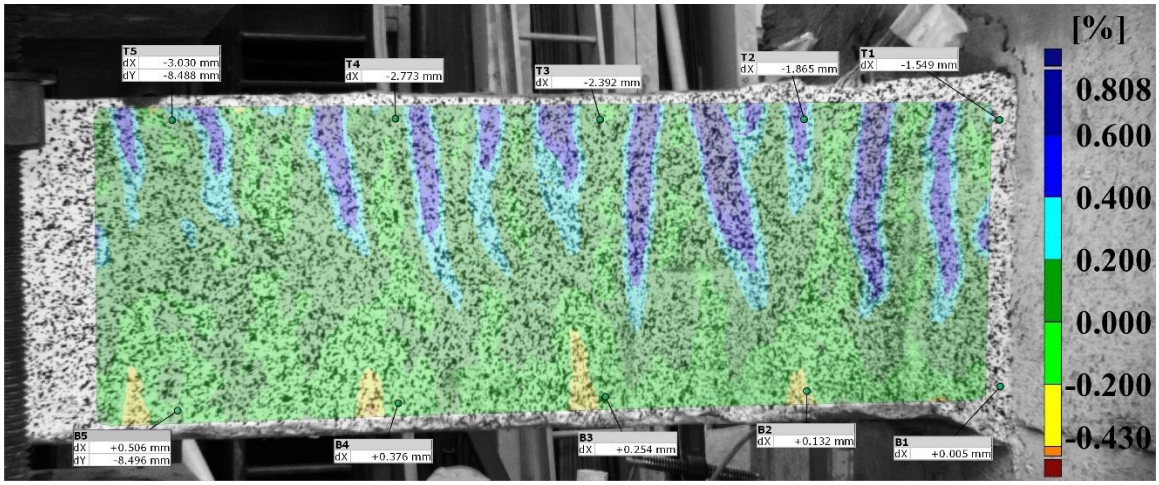

Fig.App.A- 18 longitudinal strain (ε_x) value for the first specimen at -1.75% drift ratio

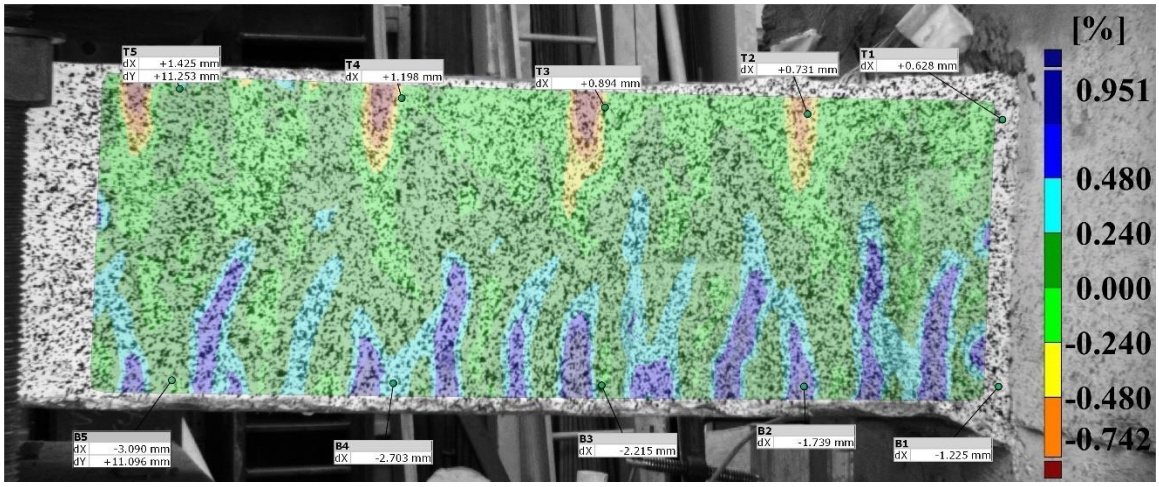

Fig.App.A- 19 longitudinal strain (ε_x) value for the first specimen at 2.2% drift ratio

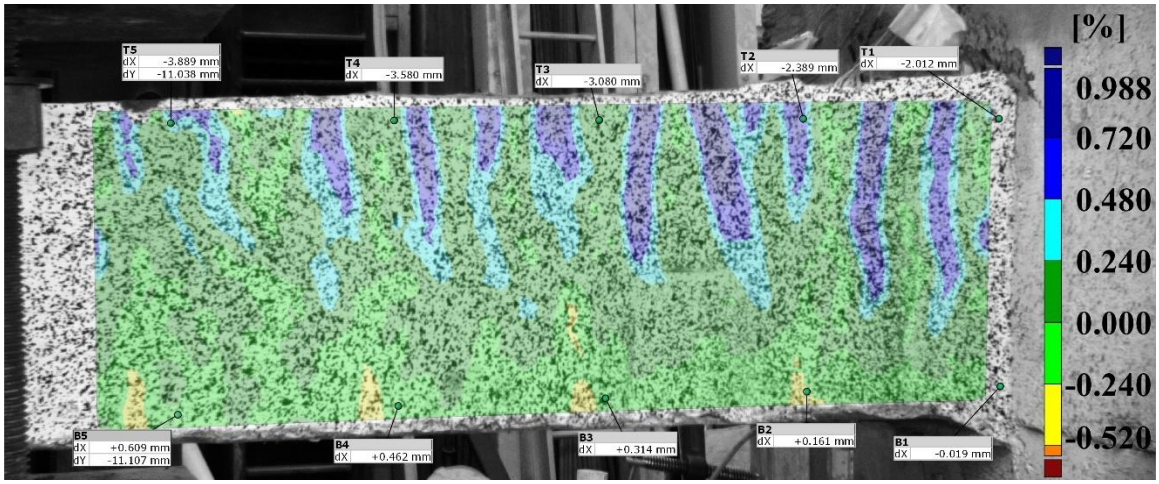

Fig.App.A- 20 longitudinal strain (ε_x) value for the first specimen at -2.2% drift ratio

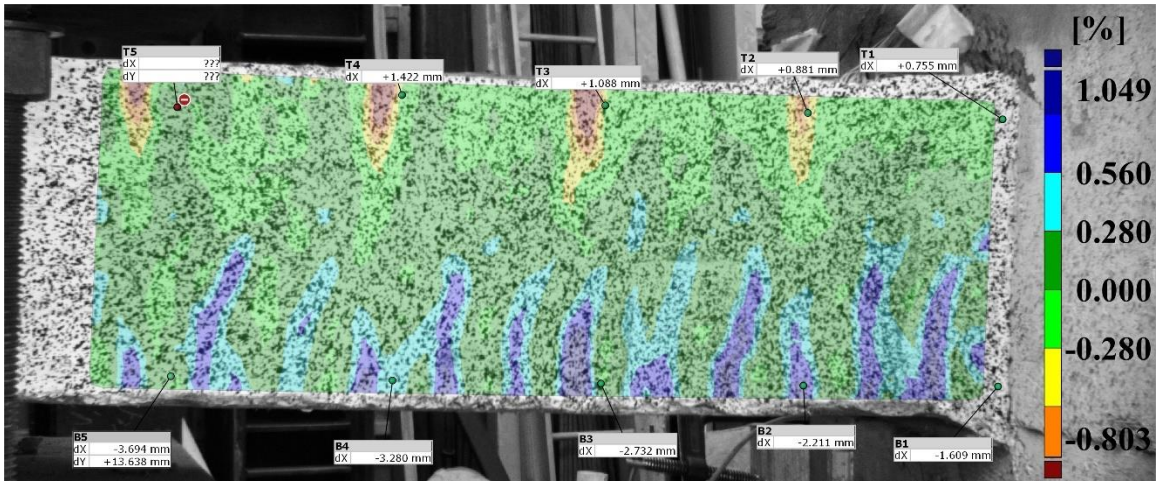

Fig.App.A- 21 longitudinal strain (ε_x) value for the first specimen at 2.75% drift ratio

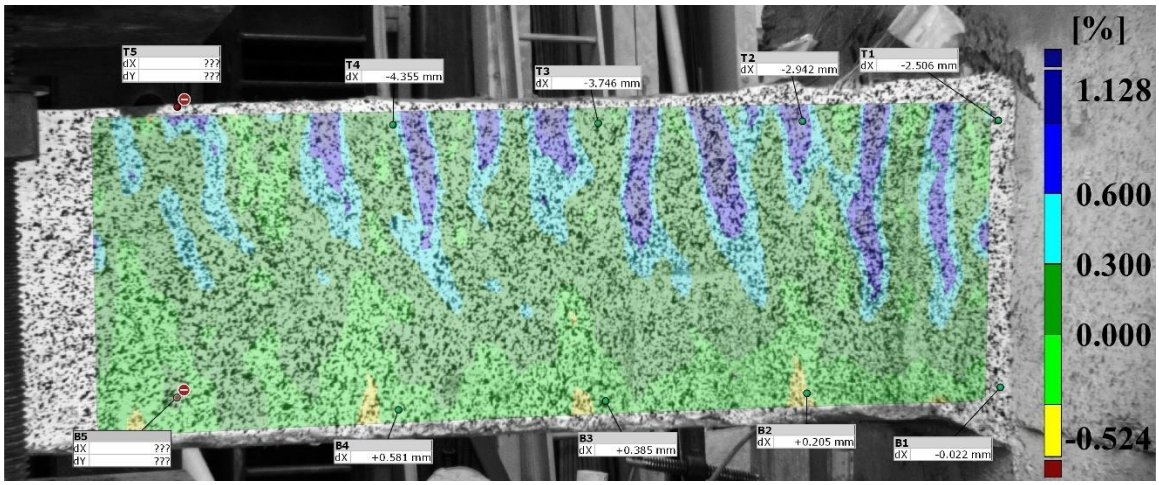

Fig.App.A- 22 longitudinal strain (ε_x) value for the first specimen at -2.75% drift ratio

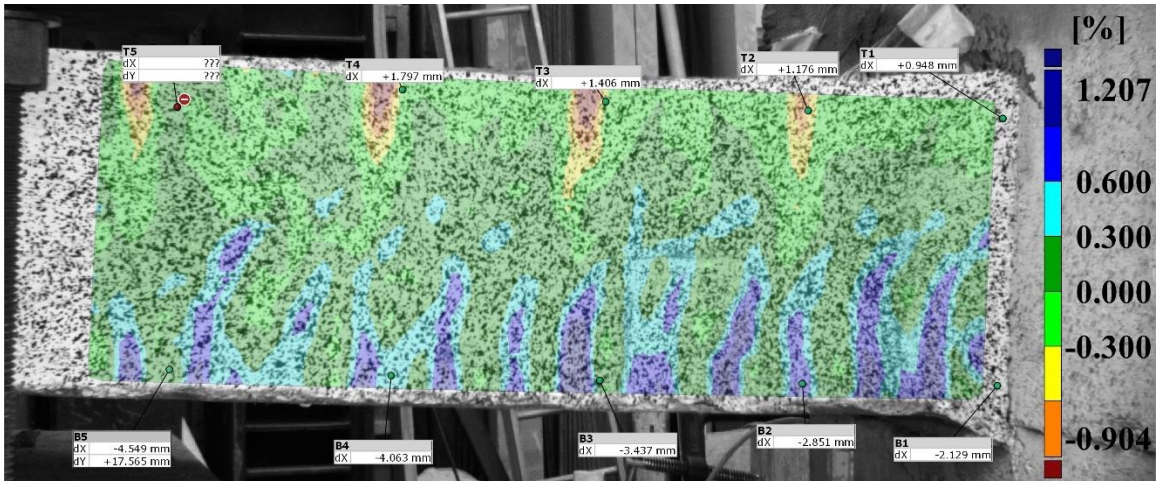

Fig.App.A- 23 longitudinal strain (ε_x) value for the first specimen at 3.5% drift ratio

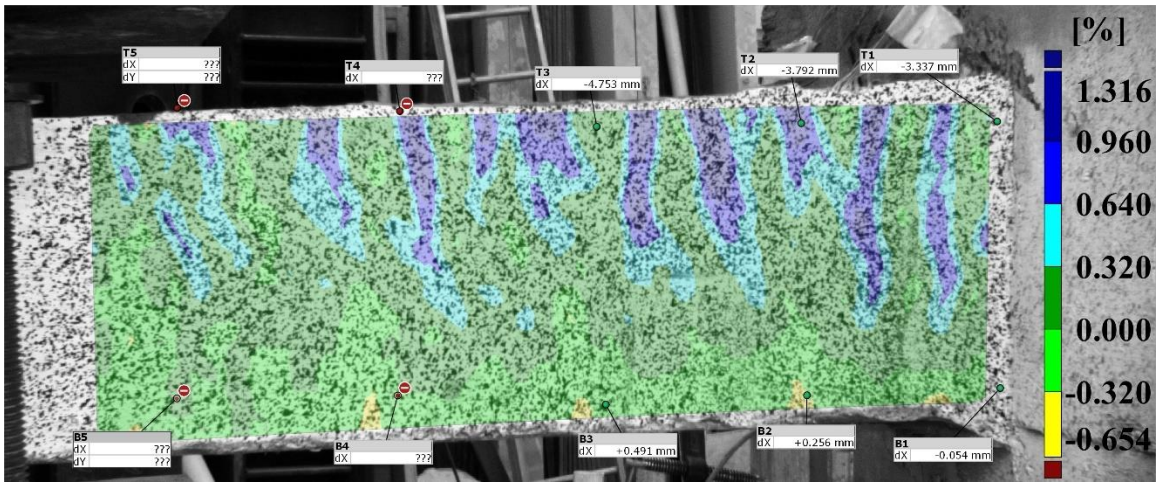

Fig.App.A- 24 longitudinal strain (ε_x) value for the first specimen at -3.5% drift ratio

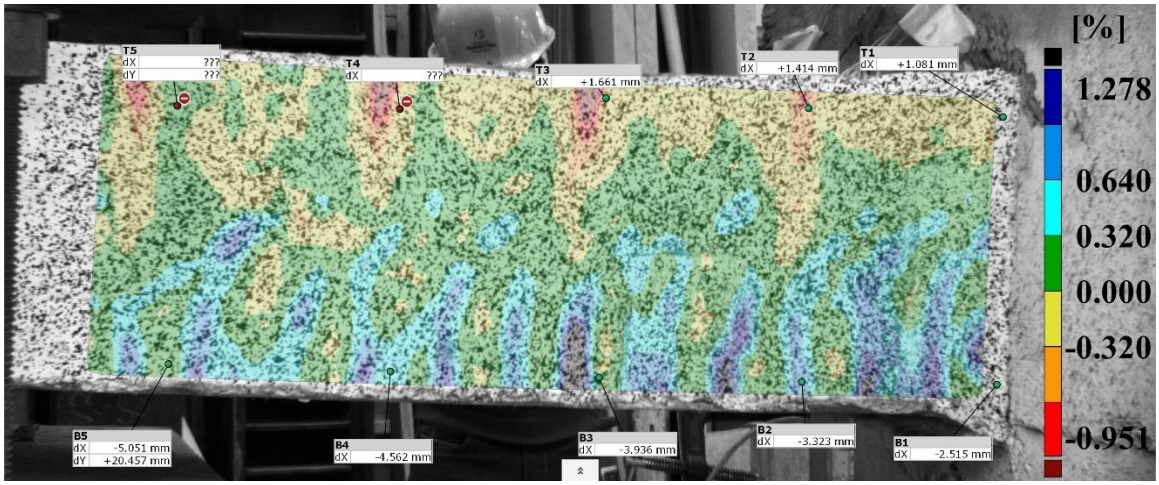

Fig.App.A- 25 longitudinal strain (ε_x) value for the first specimen at 4.0% drift ratio

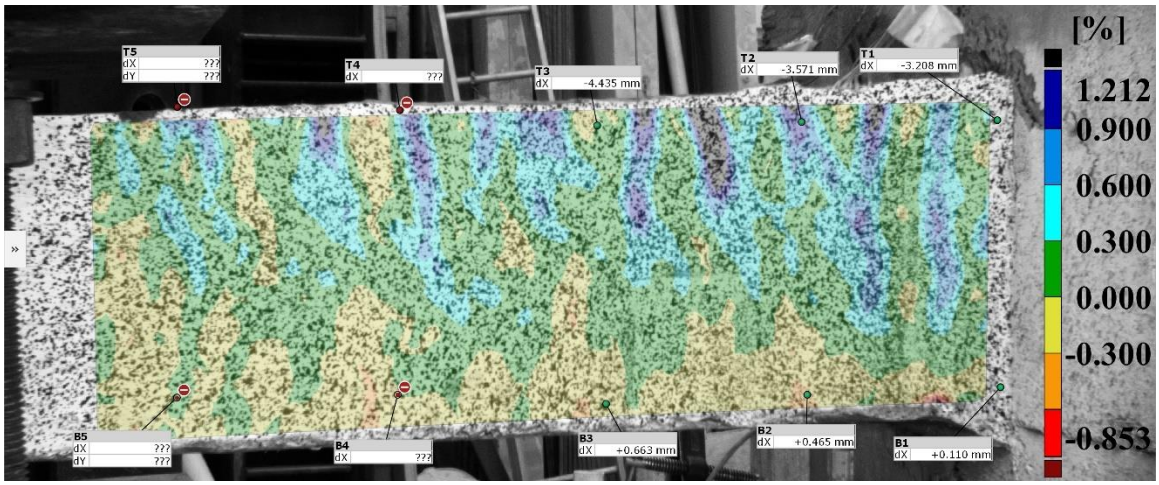

Fig.App.A- 26 longitudinal strain (ε_x) value for the first specimen at -4.0% drift ratio

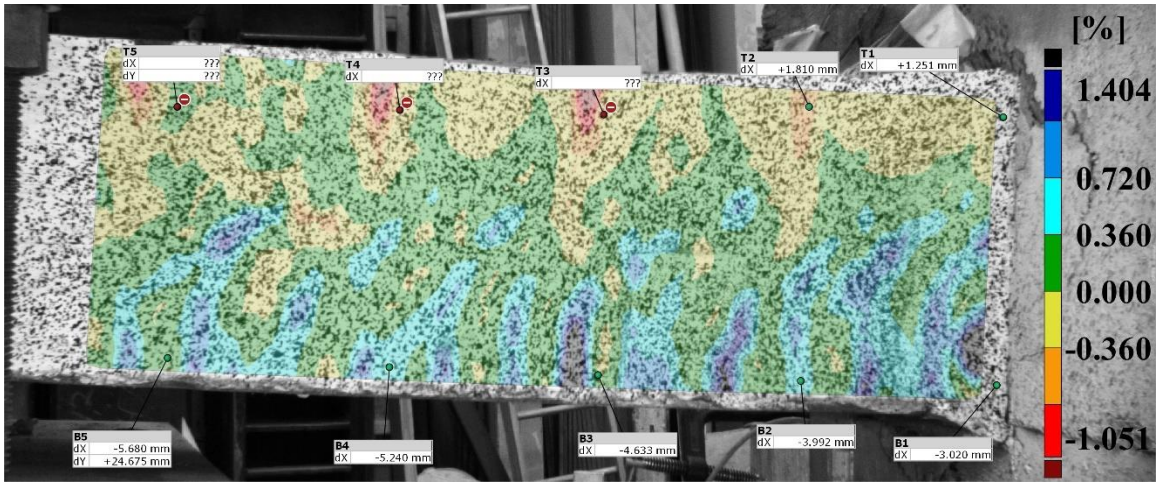

Fig.App.A- 27 longitudinal strain (ε_x) value for the first specimen at 5.0% drift ratio

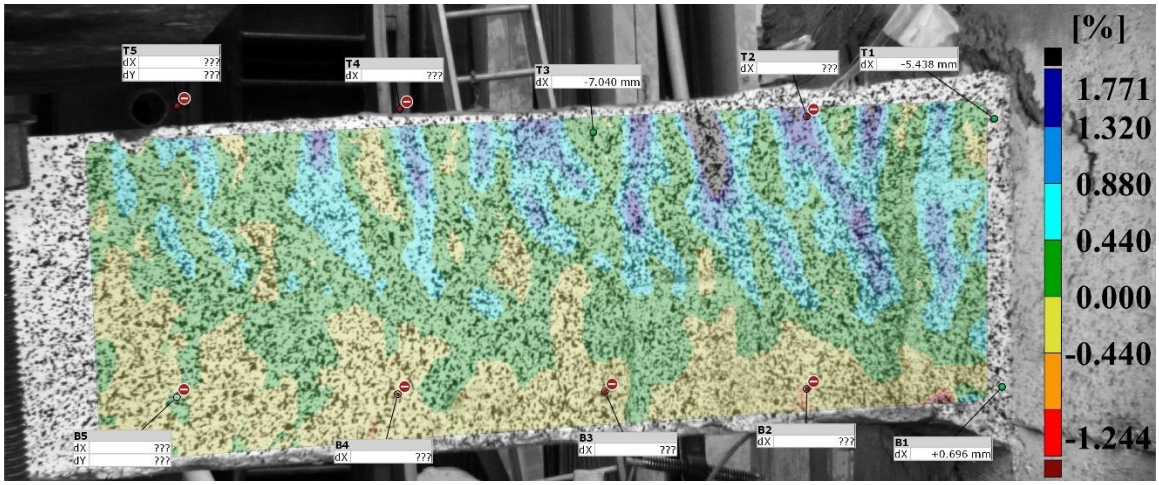

Fig.App.A- 28 longitudinal strain (ε_x) value for the first specimen at -5.0% drift ratio

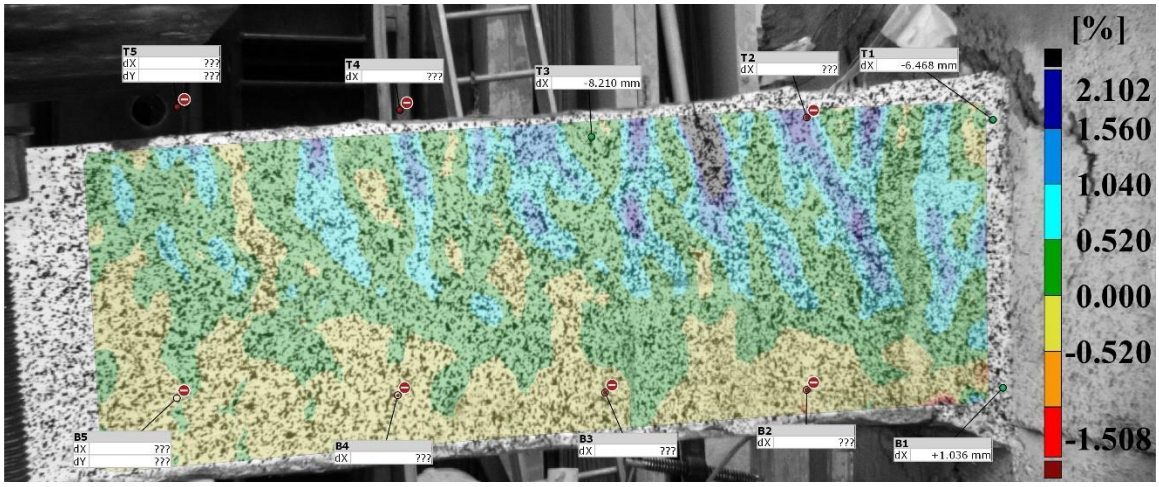

Fig.App.A- 29 longitudinal strain (ε_x) value for the first specimen at -6.0% drift ratio

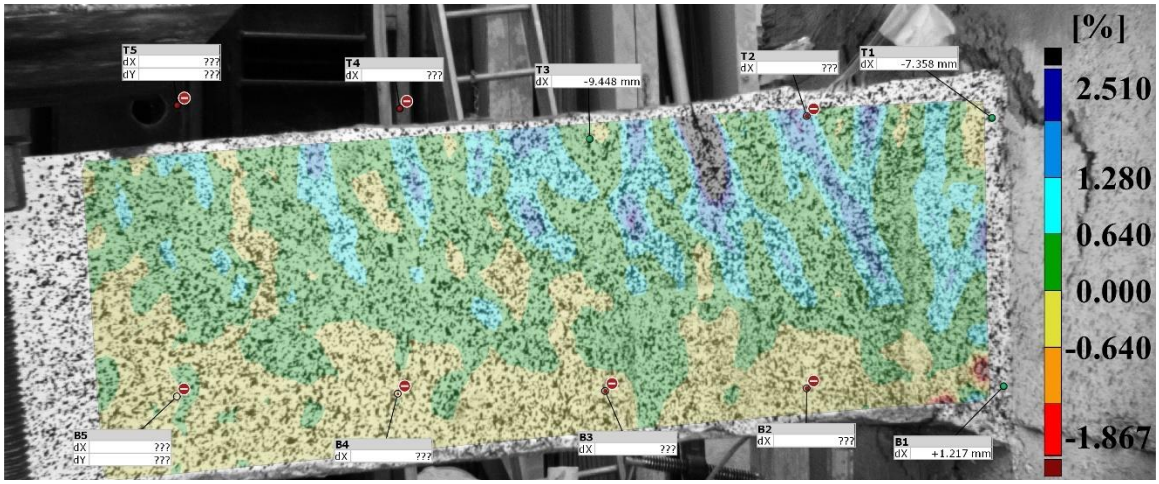

Fig.App.A- 30 longitudinal strain (ε_x) value for the first specimen at -7.0% drift ratio

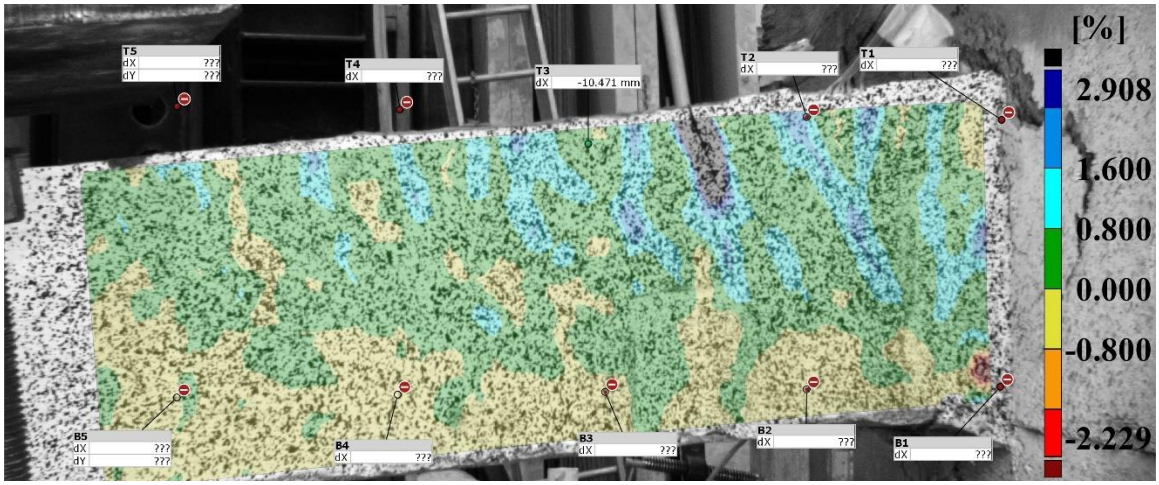

Fig.App.A- 31 longitudinal strain (ε_x) value for the first specimen at -8.0% drift ratio

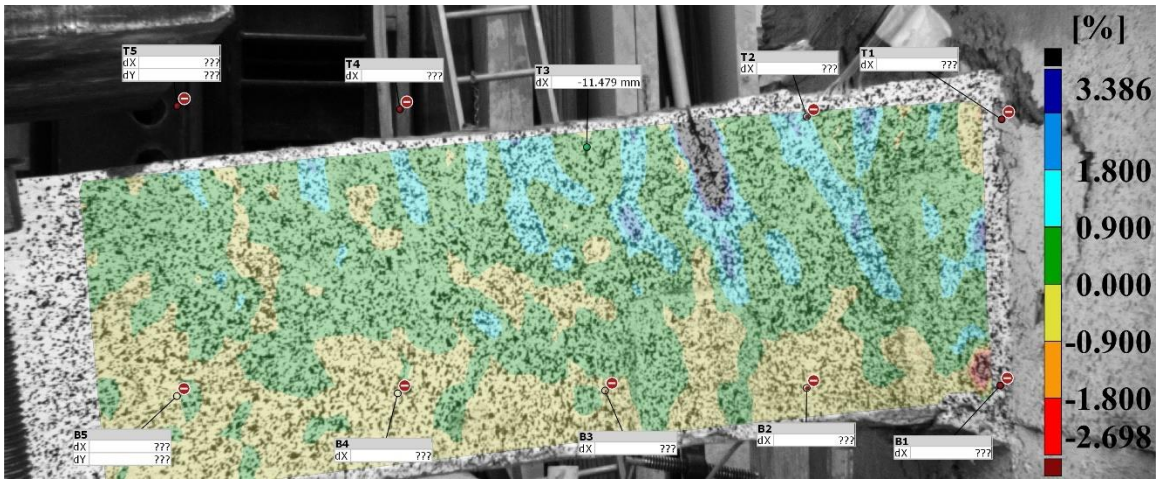

Fig.App.A- 32 longitudinal strain (ε_x) value for the first specimen at -9.0% drift ratio

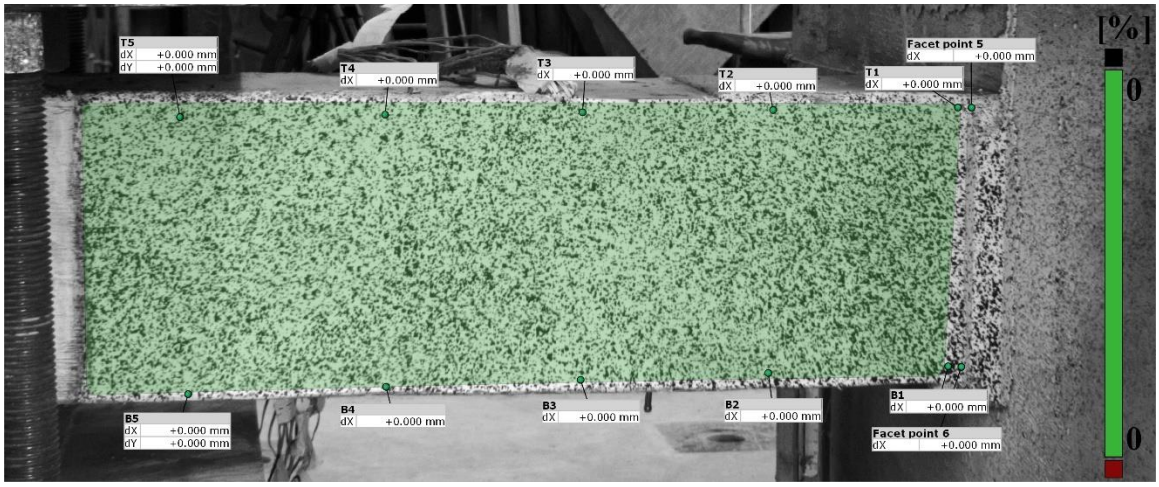

Fig.App.A- 33 The surface along which the longitudinal strain (ε x) value for the first specimen is calculated

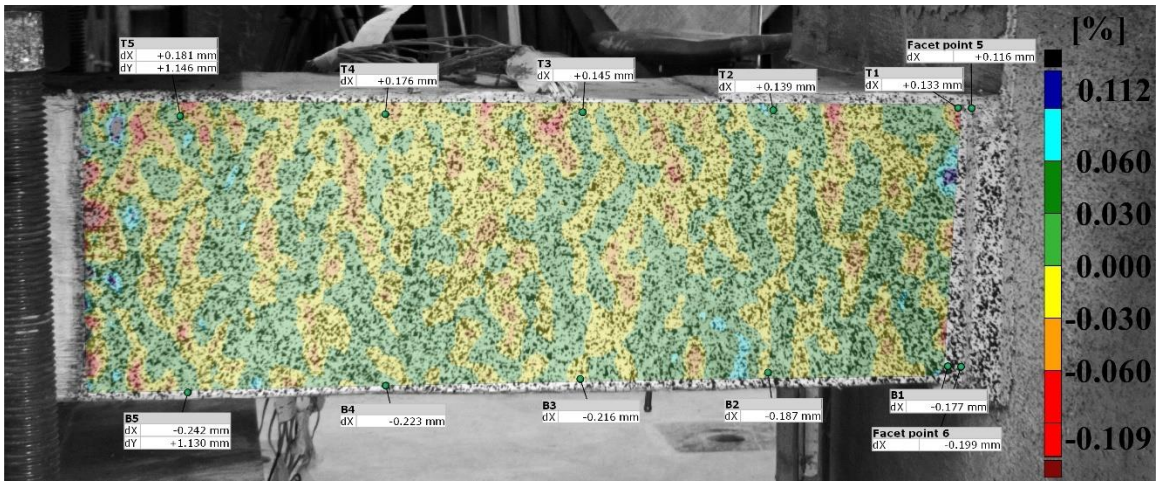

Fig.App.A- 34 longitudinal strain (ε_x) value for the second specimen at 0.2% drift ratio

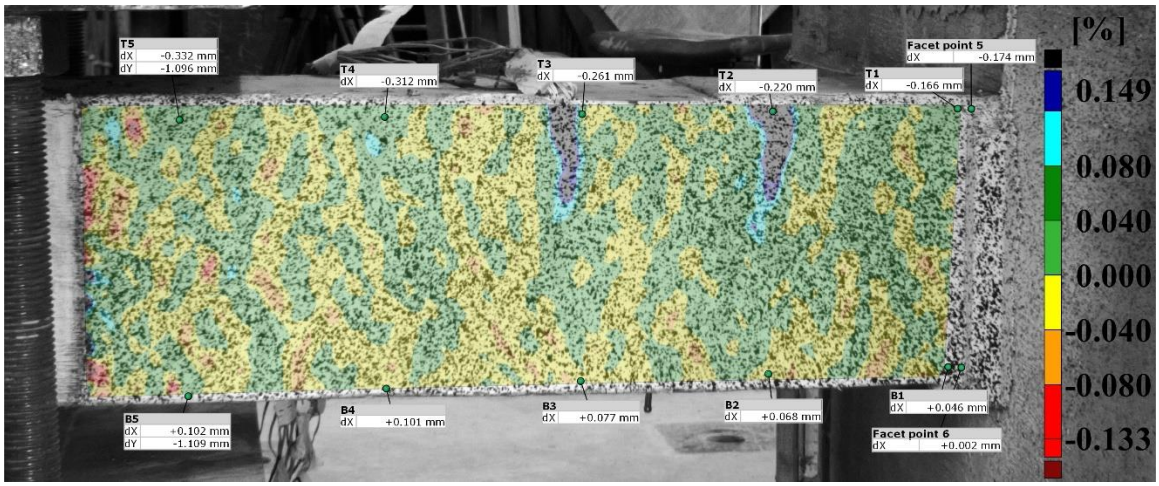

Fig.App.A- 35 longitudinal strain (ε_x) value for the second specimen at -0.2% drift ratio

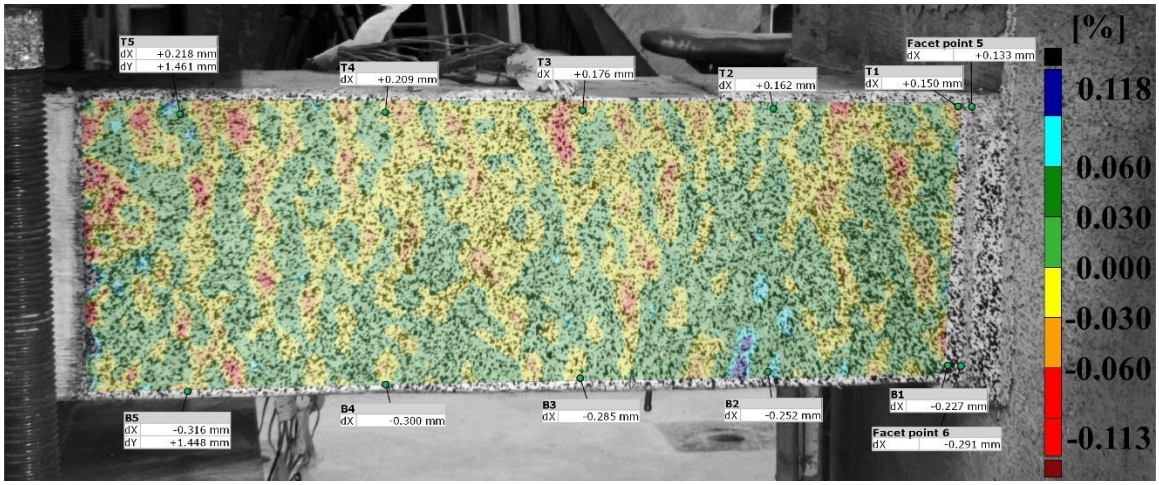

Fig.App.A- 36 longitudinal strain (ε_x) value for the second specimen at 0.25% drift ratio

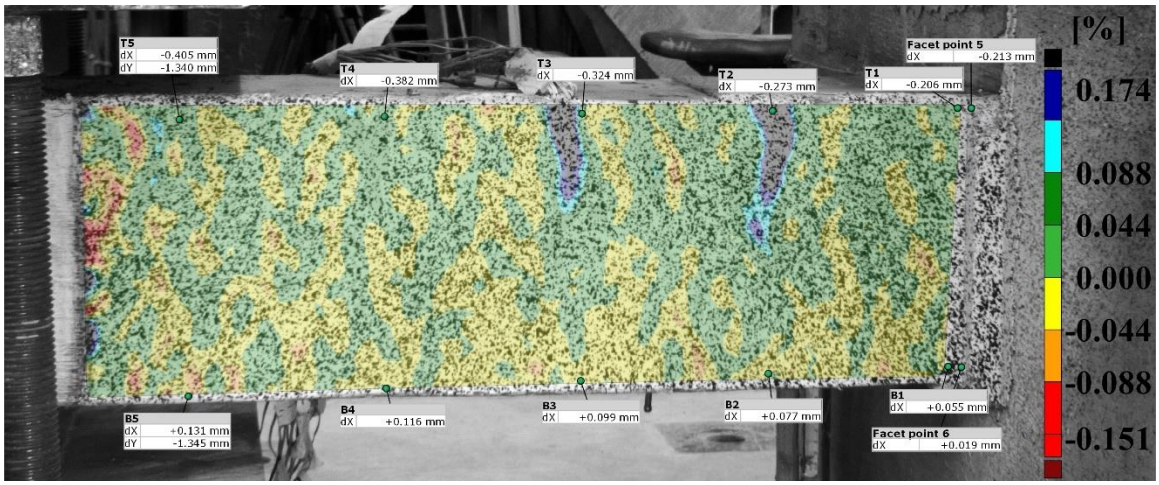

Fig.App.A- 37 longitudinal strain (ε_x) value for the second specimen at 0.25% drift ratio

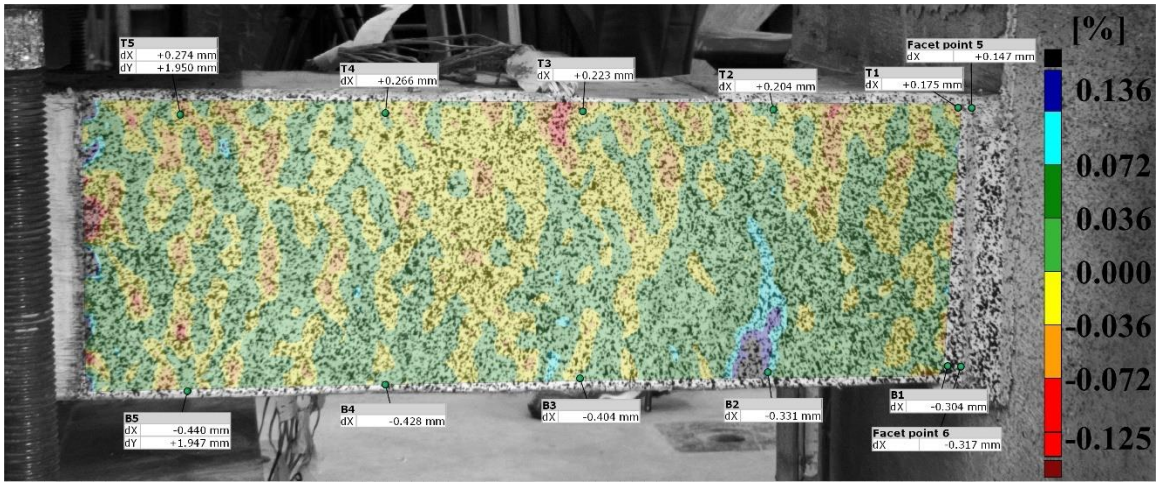

Fig.App.A- 38 longitudinal strain (ε_x) value for the second specimen at 0.35% drift ratio

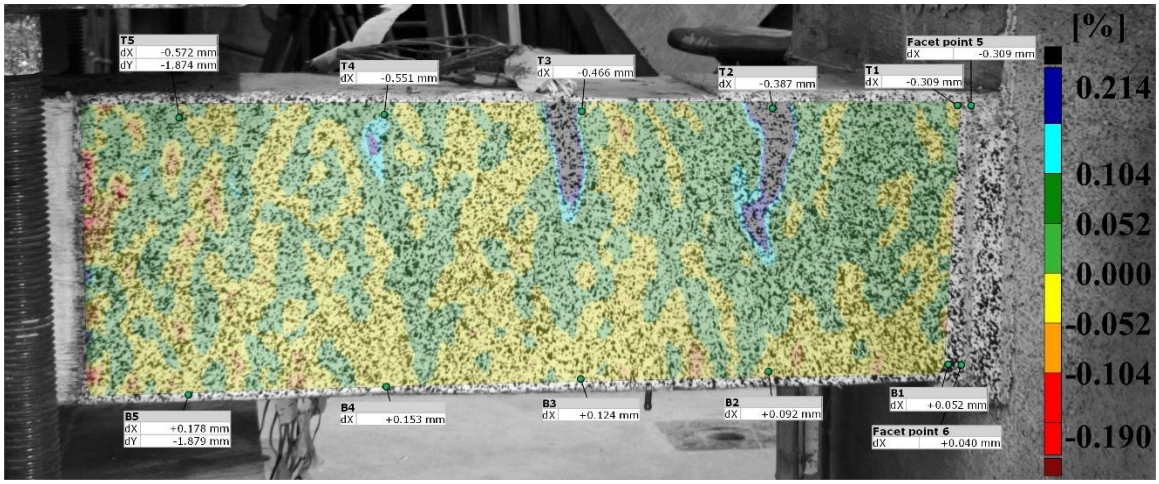

Fig.App.A- 39 longitudinal strain (ε_x) value for the second specimen at -0.35% drift ratio

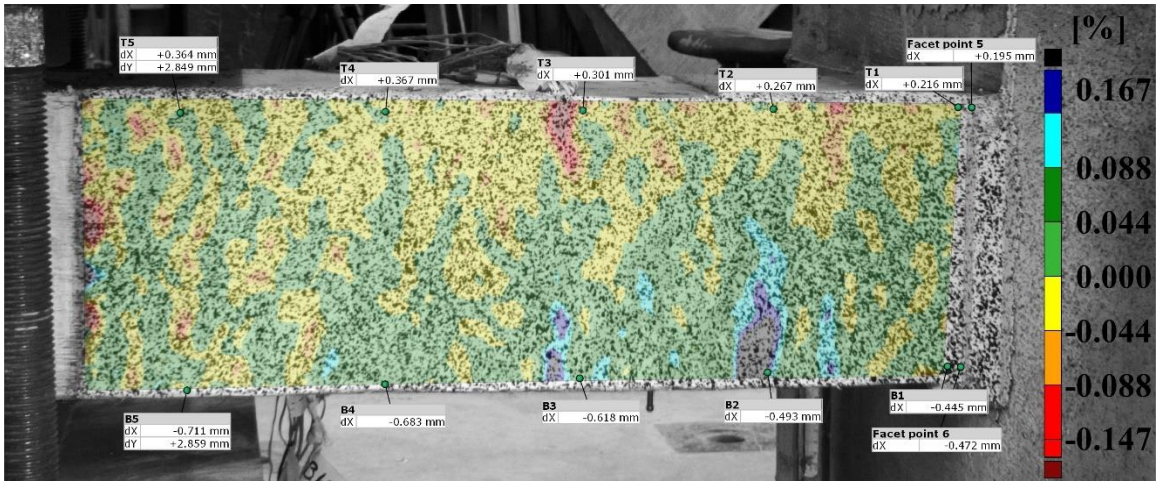

Fig.App.A- 40 longitudinal strain (ε_x) value for the second specimen at 0.5% drift ratio

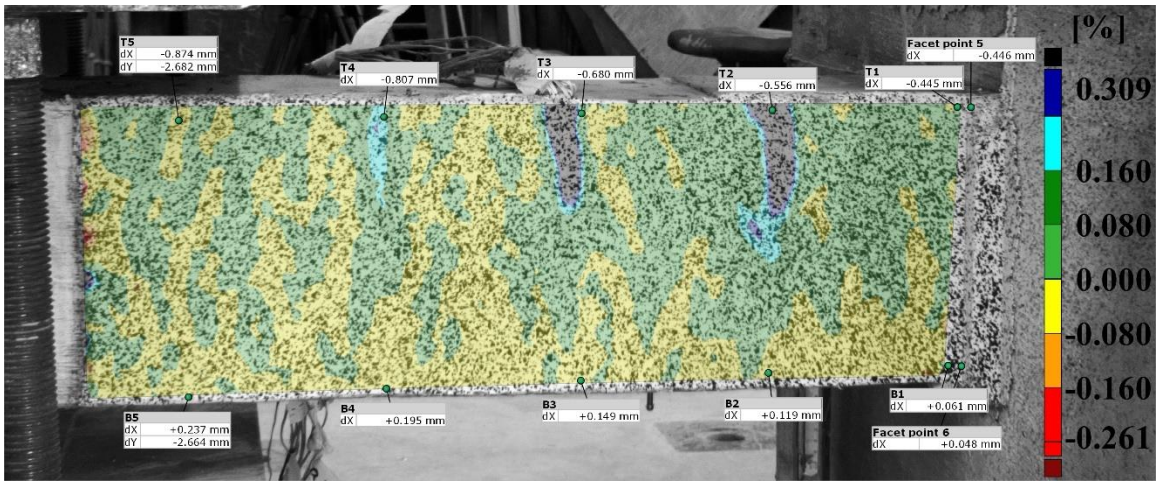

Fig.App.A- 41 longitudinal strain (ε_x) value for the second specimen at -0.5% drift ratio

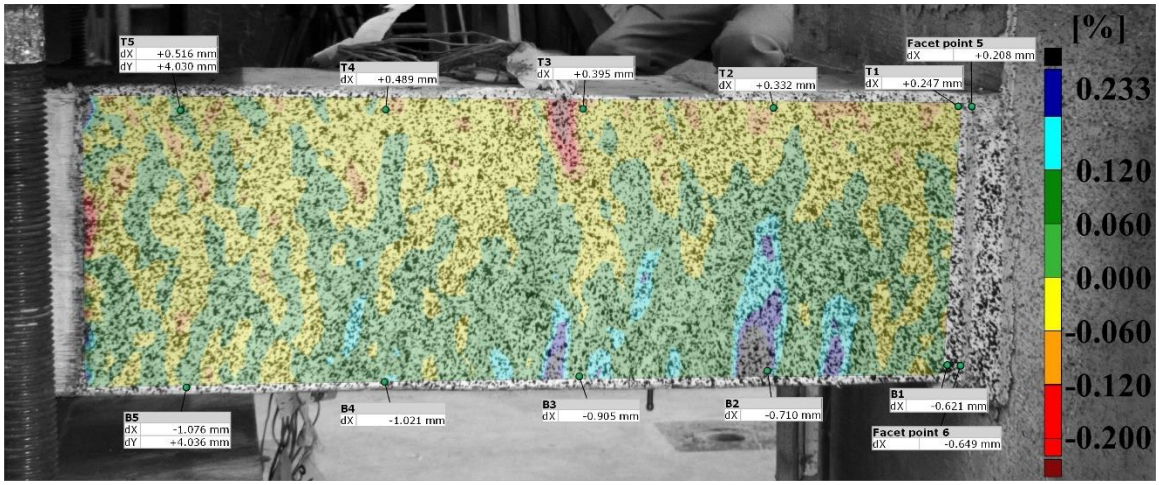

Fig.App.A- 42 longitudinal strain (ε_x) value for the second specimen at 0.75% drift ratio

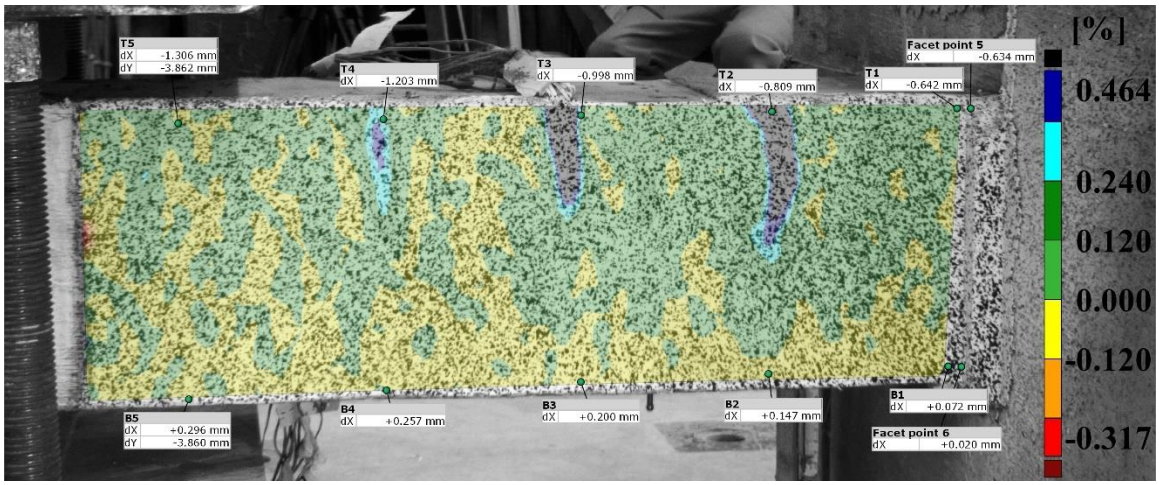

Fig.App.A- 43 longitudinal strain (ε_x) value for the second specimen at -0.75% drift ratio

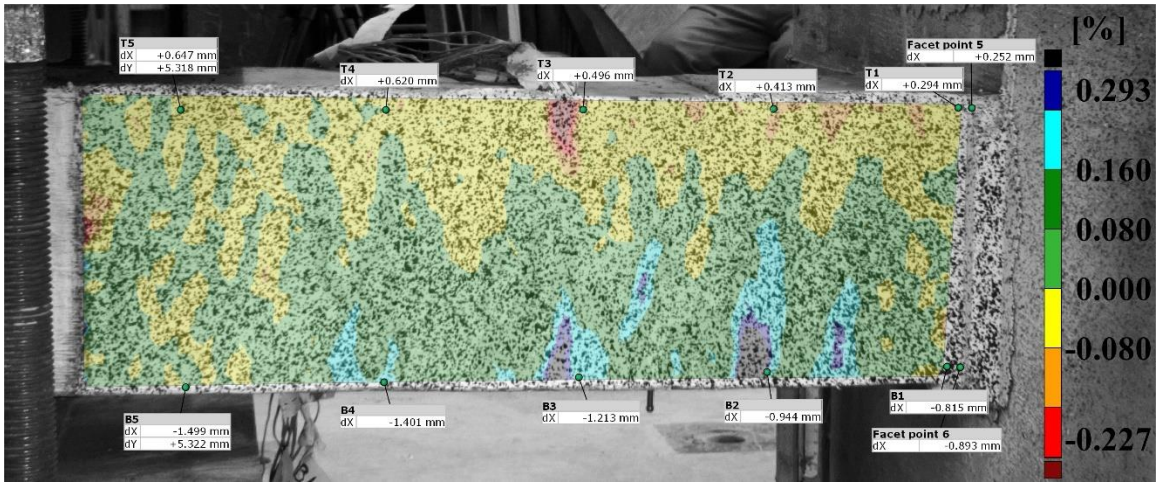

Fig.App.A- 44 longitudinal strain (ε_x) value for the second specimen at 1.0% drift ratio

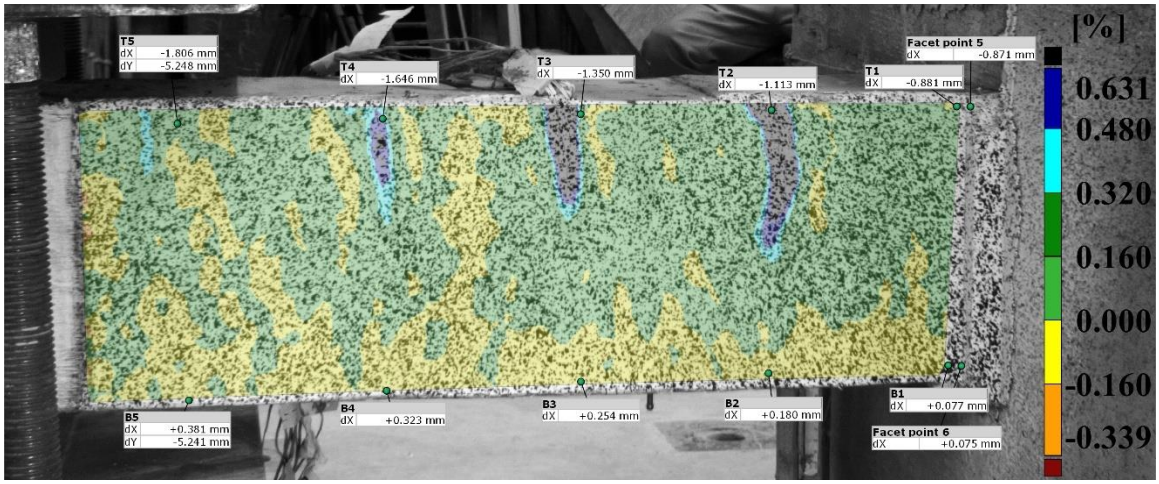

Fig.App.A- 45 longitudinal strain (ε_x) value for the second specimen at -1.0% drift ratio

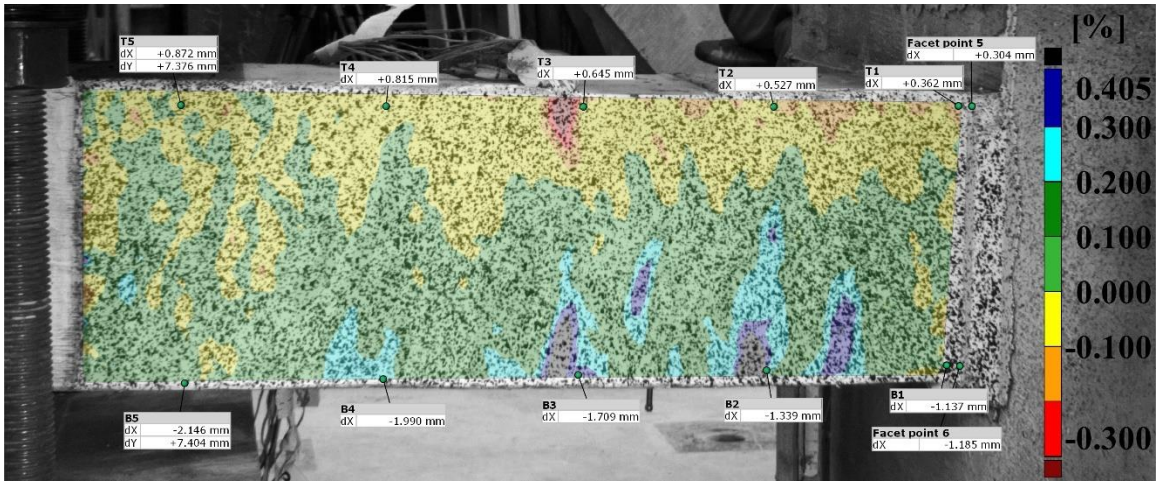

Fig.App.A- 46 longitudinal strain (ε_x) value for the second specimen at 1.4% drift ratio

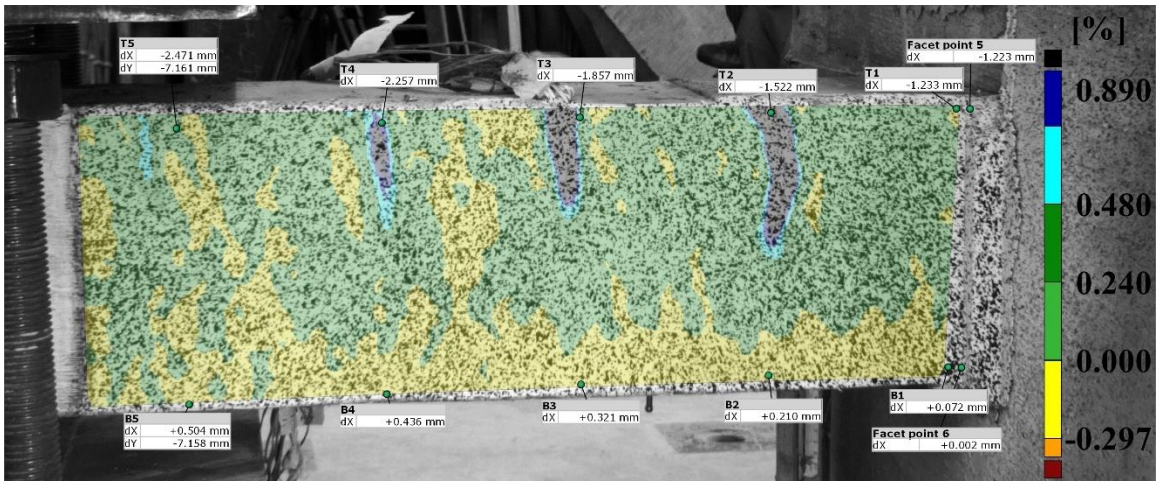

Fig.App.A- 47 longitudinal strain (ε_x) value for the second specimen at -1.4% drift ratio

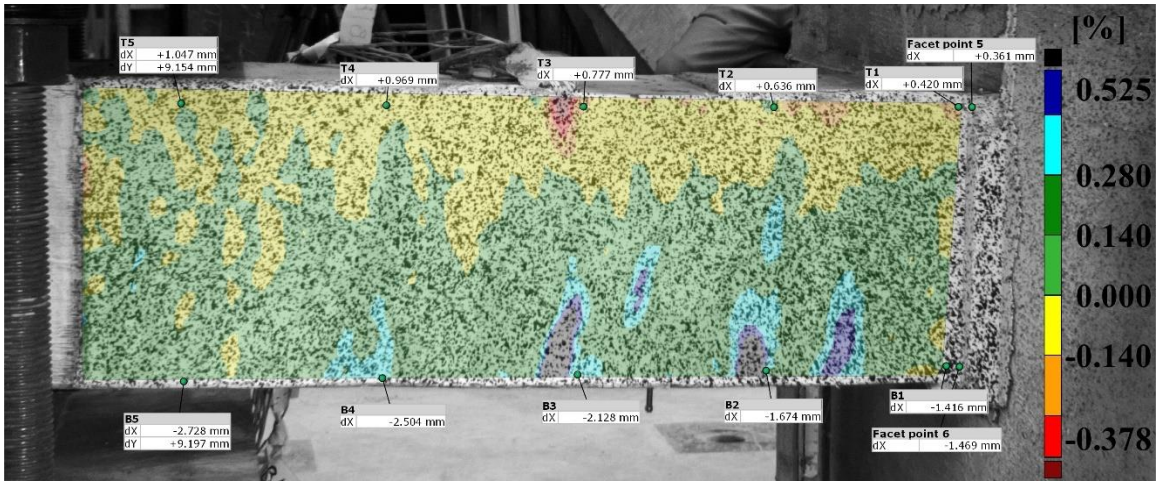

Fig.App.A- 48 longitudinal strain (ε_x) value for the second specimen at 1.75% drift ratio

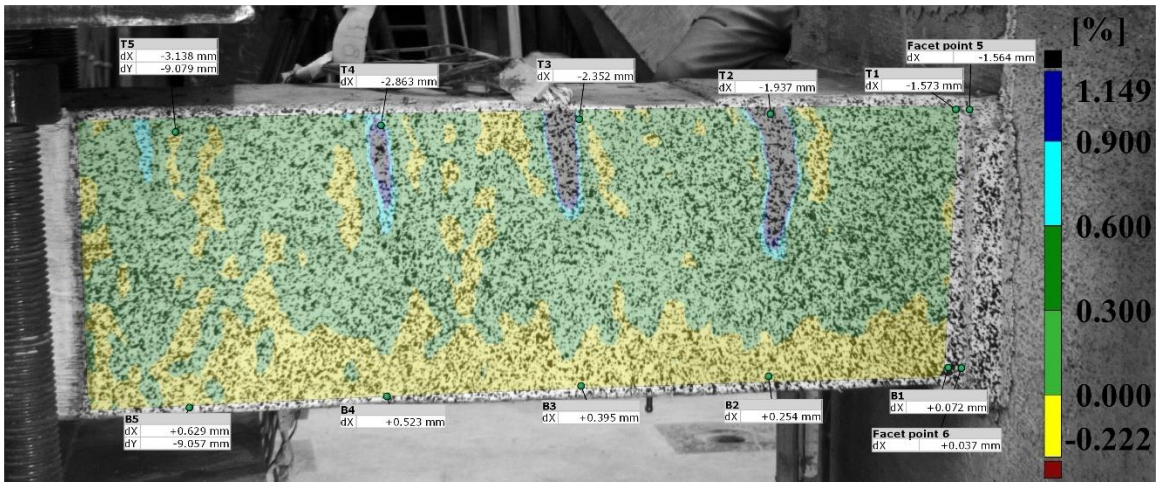

Fig.App.A- 49 longitudinal strain (ε_x) value for the second specimen at -1.75% drift ratio

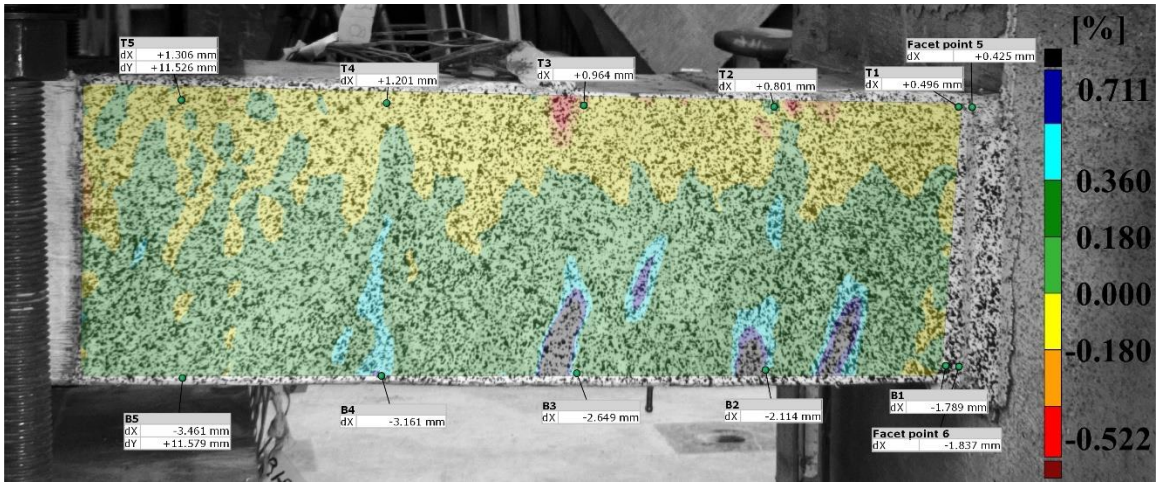

Fig.App.A- 50 longitudinal strain (ε_x) value for the second specimen at 2.2% drift ratio

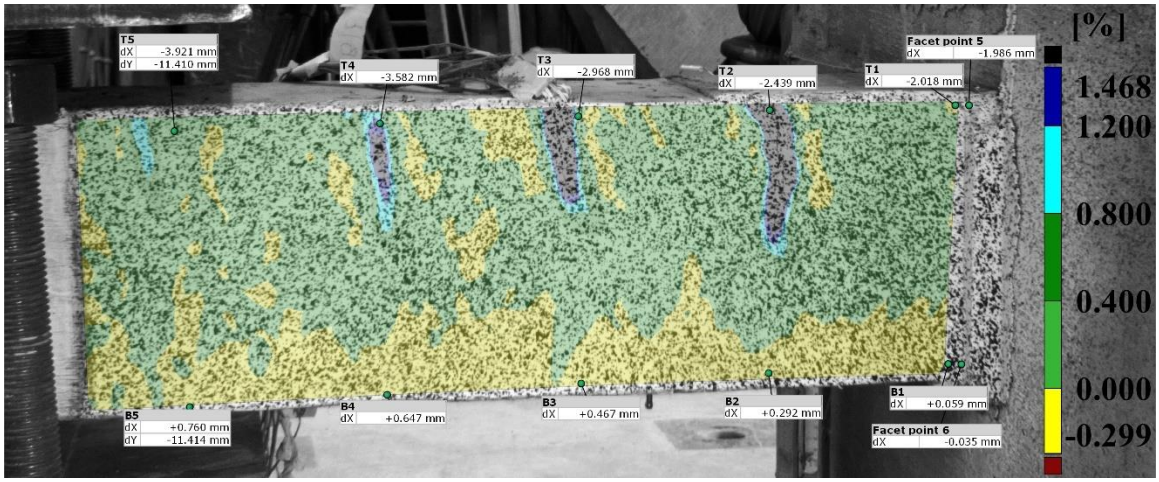

Fig.App.A- 51 longitudinal strain (ε_x) value for the second specimen at -2.2% drift ratio

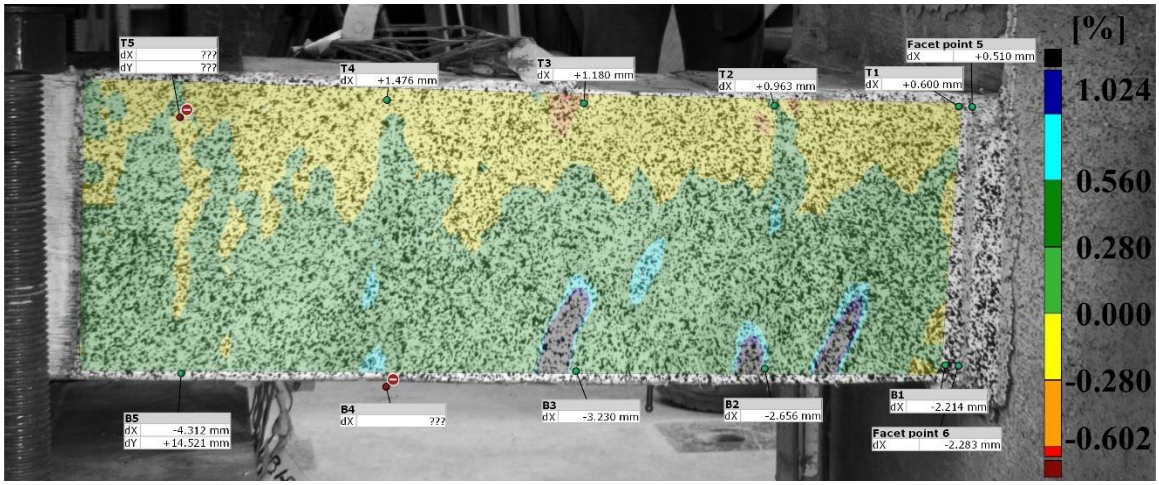

Fig.App.A- 52 longitudinal strain (ε_x) value for the second specimen at 2.75% drift ratio

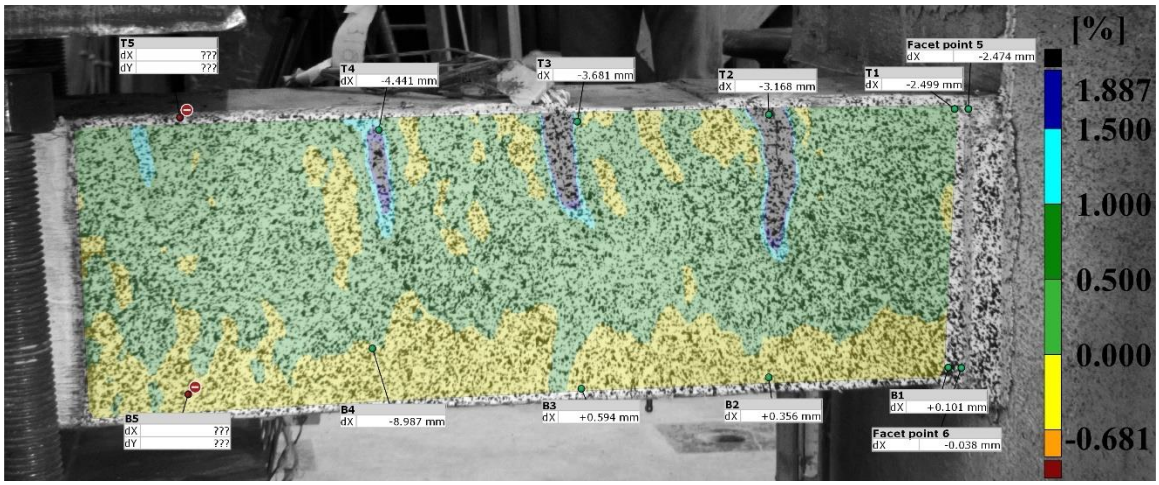

Fig.App.A- 53 longitudinal strain (ε_x) value for the second specimen at -2.75% drift ratio

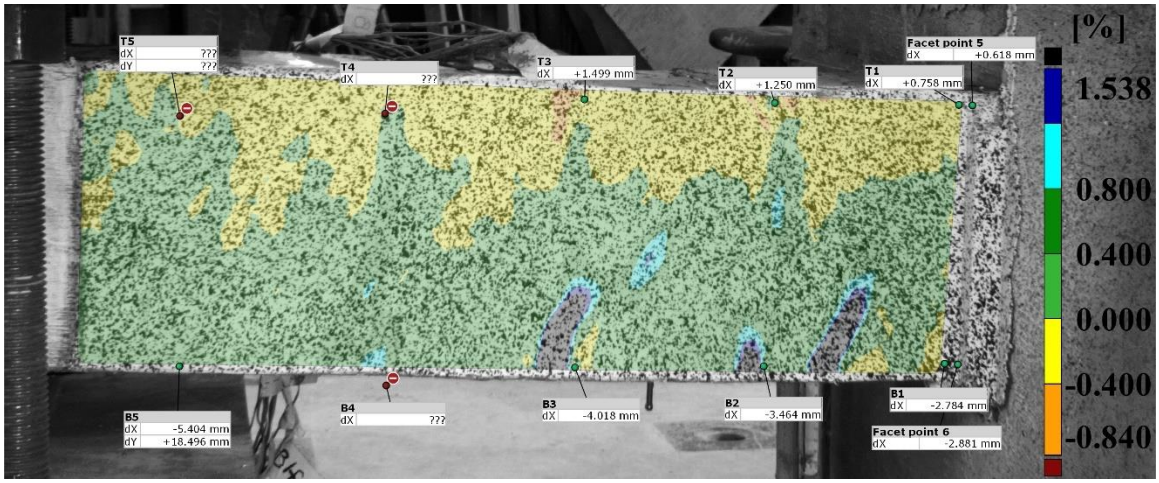

Fig.App.A- 54 longitudinal strain (ε_x) value for the second specimen at 3.5% drift ratio

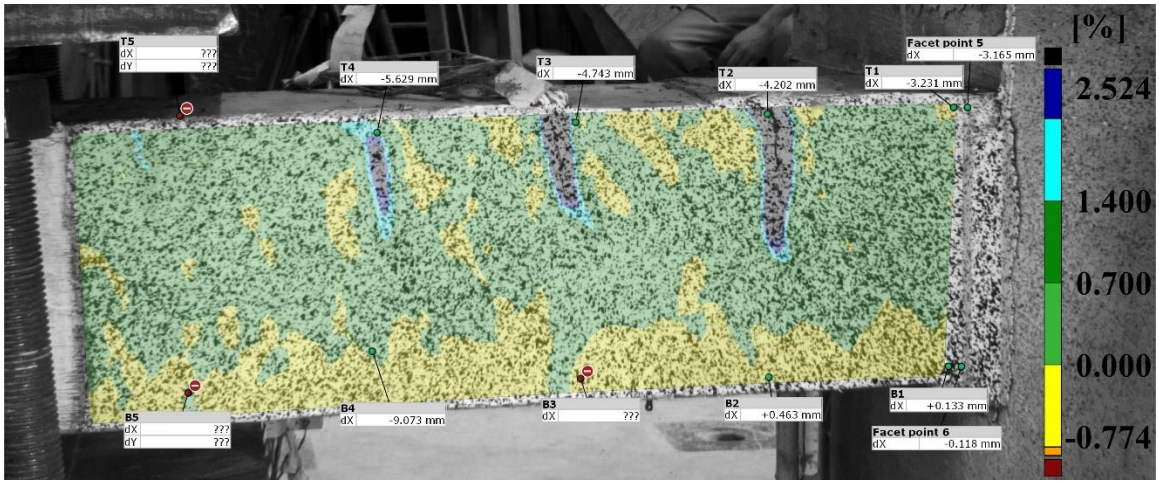

Fig.App.A- 55 longitudinal strain (ε_x) value for the second specimen at -3.5% drift ratio

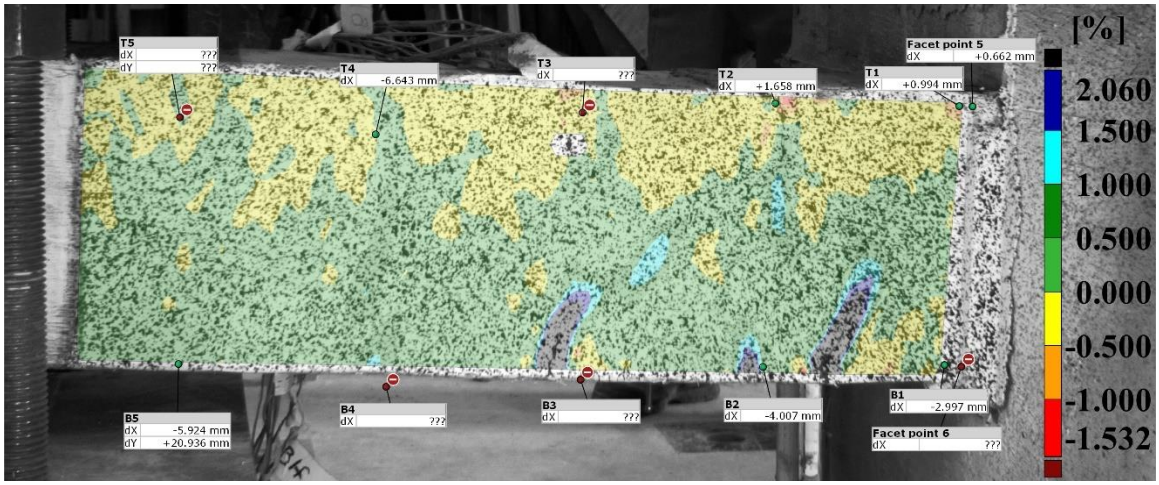

Fig.App.A- 56 longitudinal strain (ε_x) value for the second specimen at 4.0% drift ratio

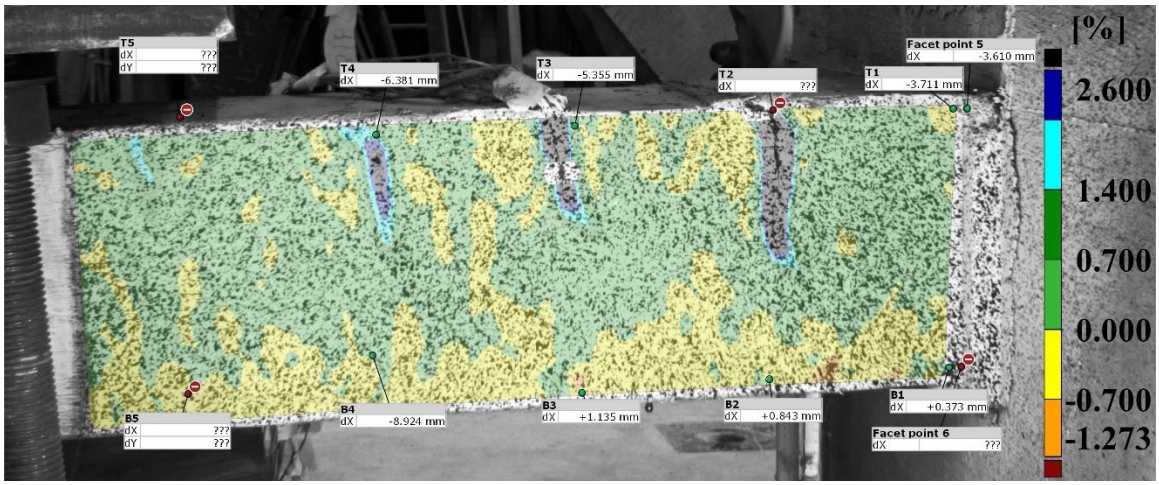

Fig.App.A- 57 longitudinal strain (ε_x) value for the second specimen at -4.0% drift ratio

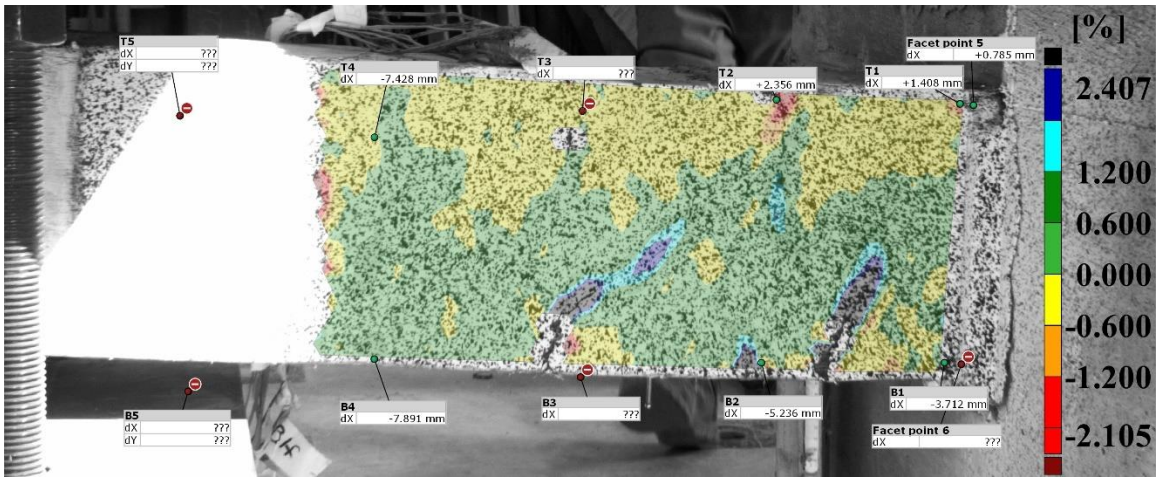

Fig.App.A- 58 longitudinal strain (ε_x) value for the second specimen at 6.0% drift ratio

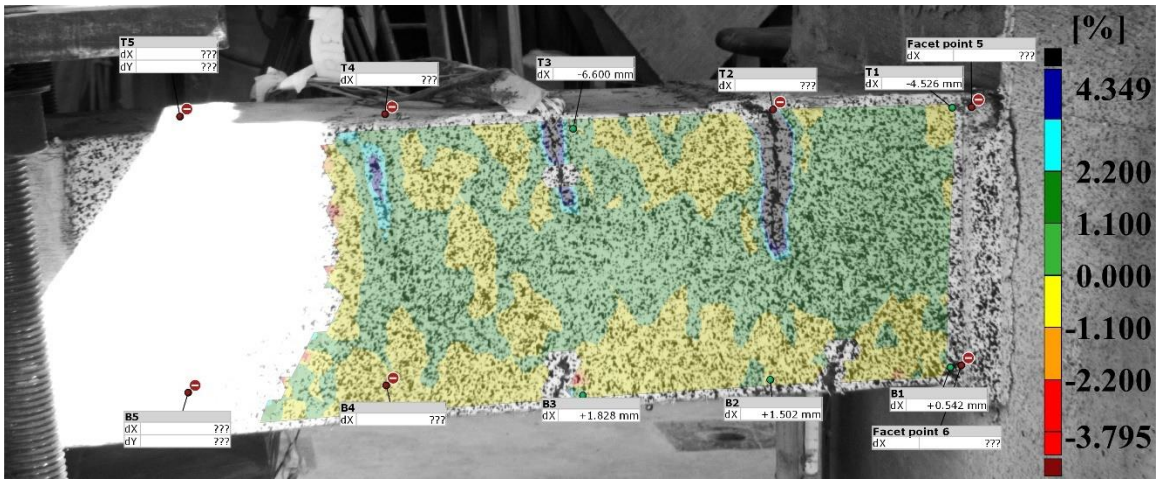

Fig.App.A- 59 longitudinal strain (ε_x) value for the second specimen at -6.0% drift ratio

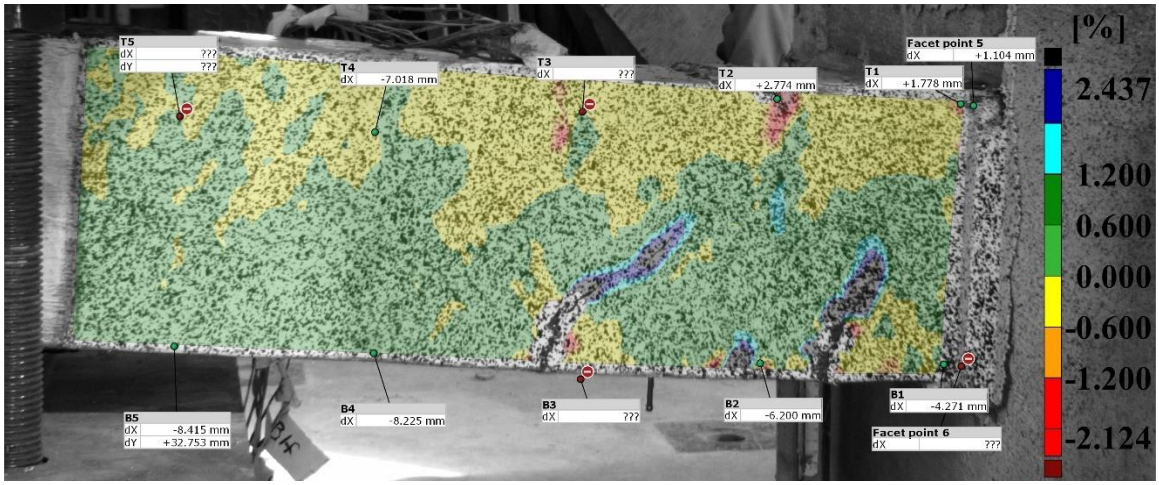

Fig.App.A- 60 longitudinal strain (ε_x) value for the second specimen at 7.0% drift ratio

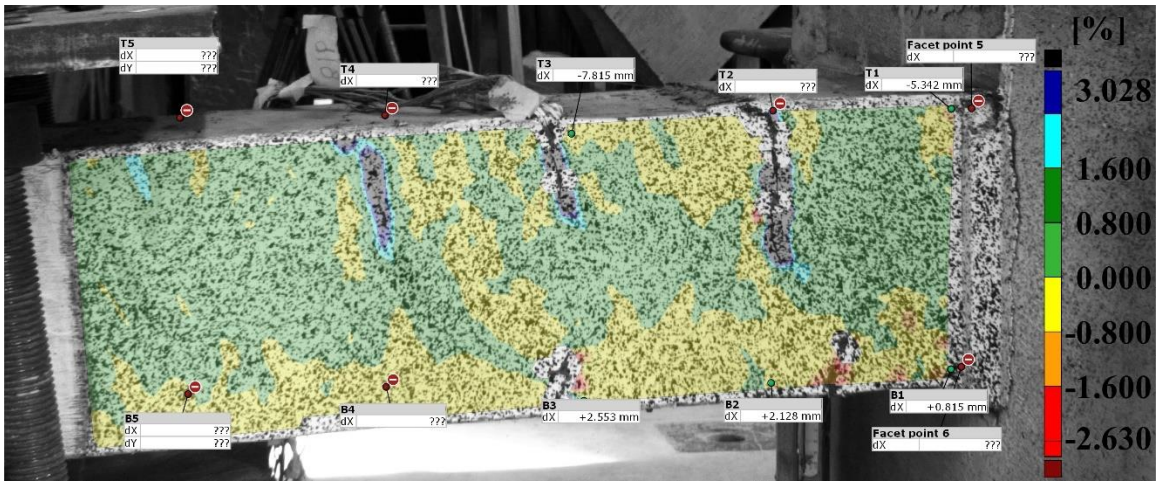

Fig.App.A- 61 longitudinal strain (ε_x) value for the second specimen at -7.0% drift ratio

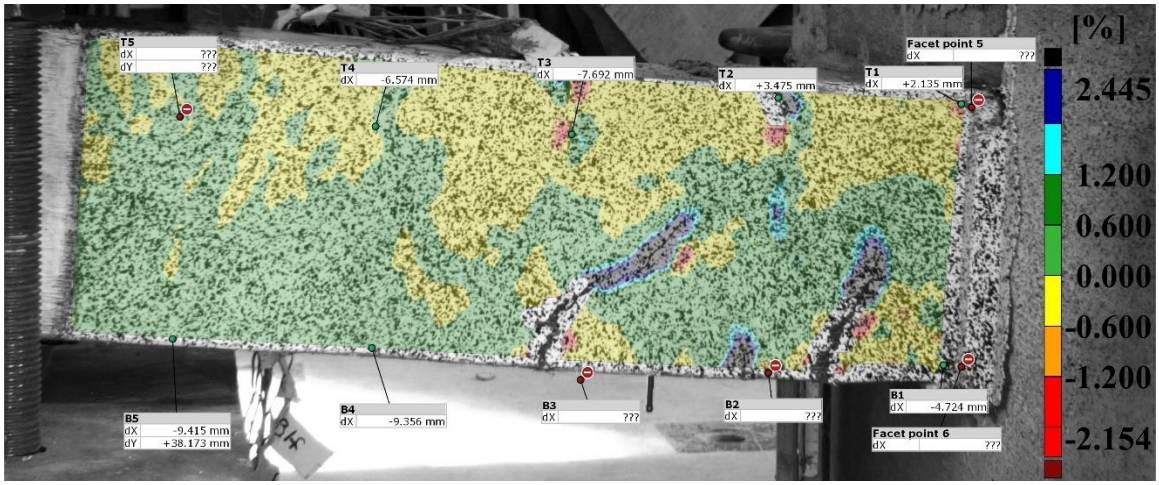

Fig.App.A- 62 longitudinal strain (ε_x) value for the second specimen at 8.0% drift ratio

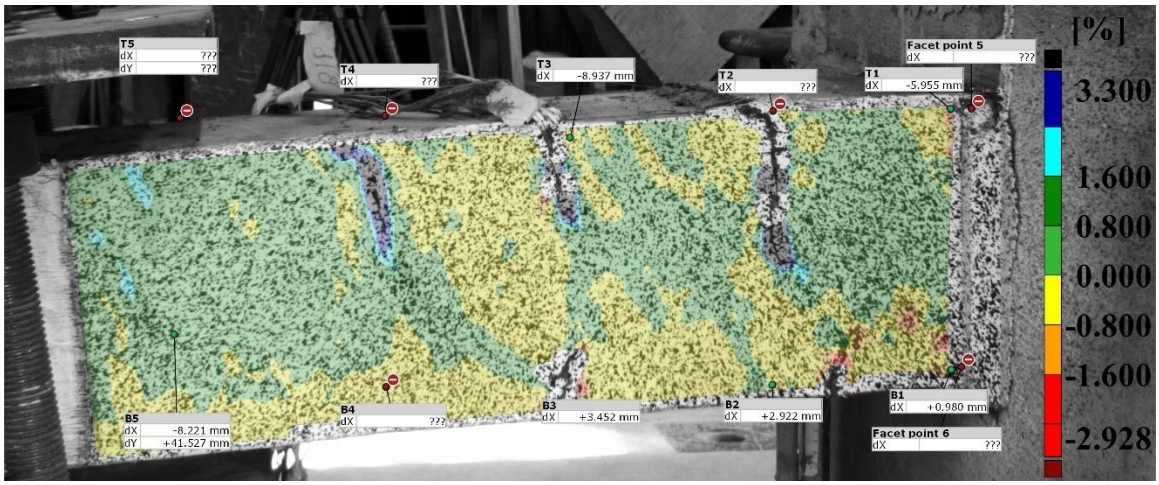

Fig.App.A- 63 longitudinal strain (ε_x) value for the second specimen at -8.0% drift ratio

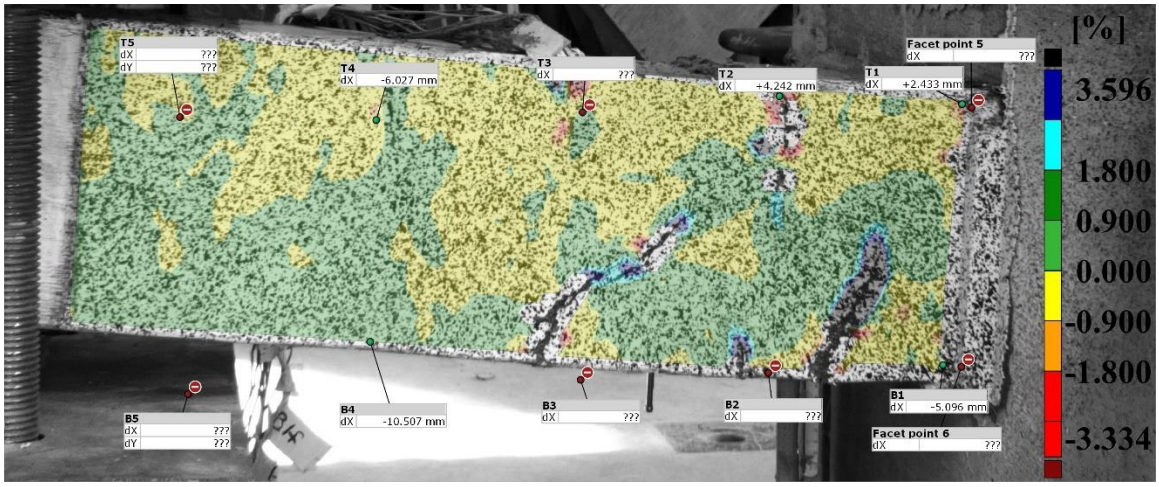

Fig.App.A- 64 longitudinal strain (ε_x) value for the second specimen at 9.0% drift ratio

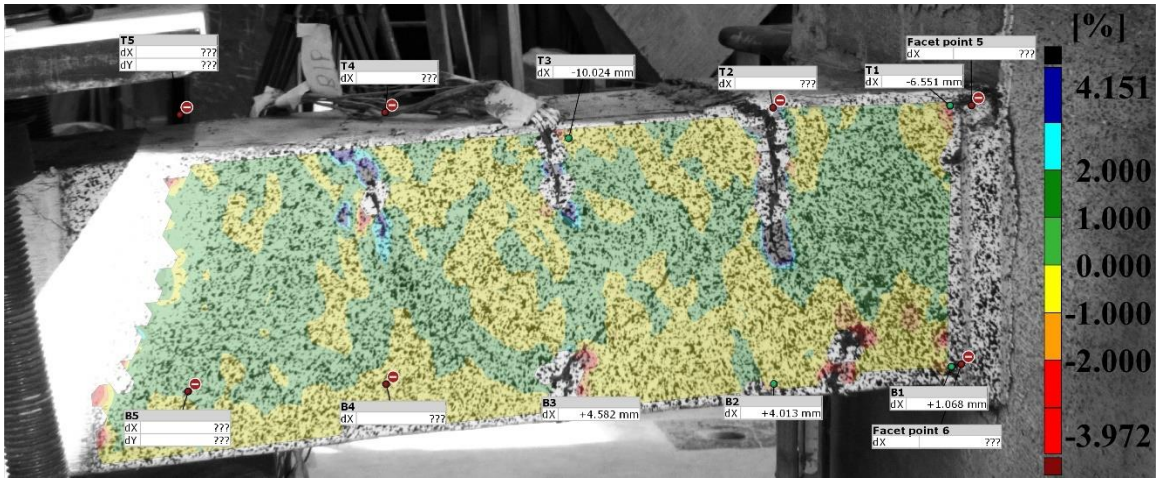

Fig.App.A- 65 longitudinal strain (ε_x) value for the second specimen at -9.0% drift ratio

Appendix B

In this appendix, the analyses result for the 4-story and 20-story SMFs for both DDM, and PEER frames are provided. The maximum story drift ratio and the maximum story displacement for each pair of frames are compared. The results are presented for each ground motion with varying scale. The results are presented for the four-story frames first and the ground motion characteristics are presented in that section.

4-Story Buildings

Event/Record: Northridge-01, 1/17/1994, Beverly Hills - 14145 Mulhol, 9

PGA of the un-scaled record: 0.443g

Record duration: 30 sec

Significant duration of the Arias Intensity:

$D_{5\text{-}95}$= 9.260

$D_{5\text{-}75}$= 5.960

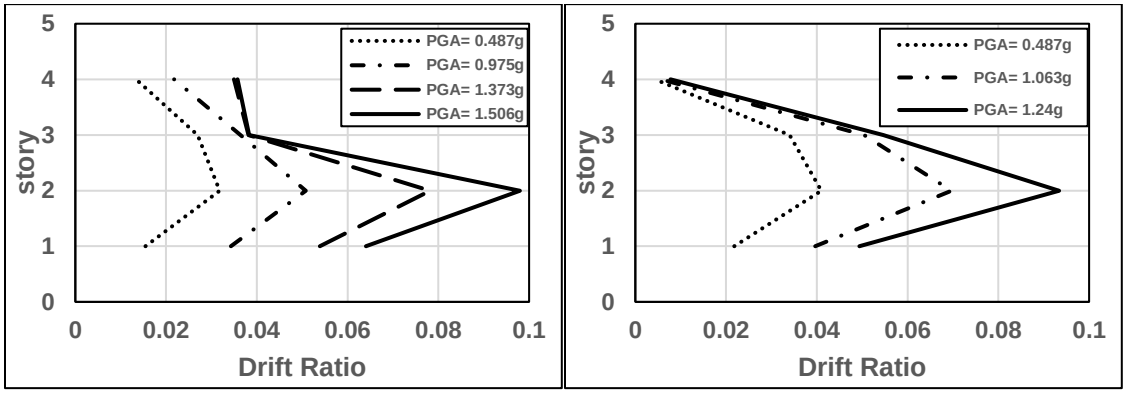

(a) (b)

Fig.App.B- 1 Maximum story drift ratio for varying scaled ground motion for a) DDM and b) PEER frame

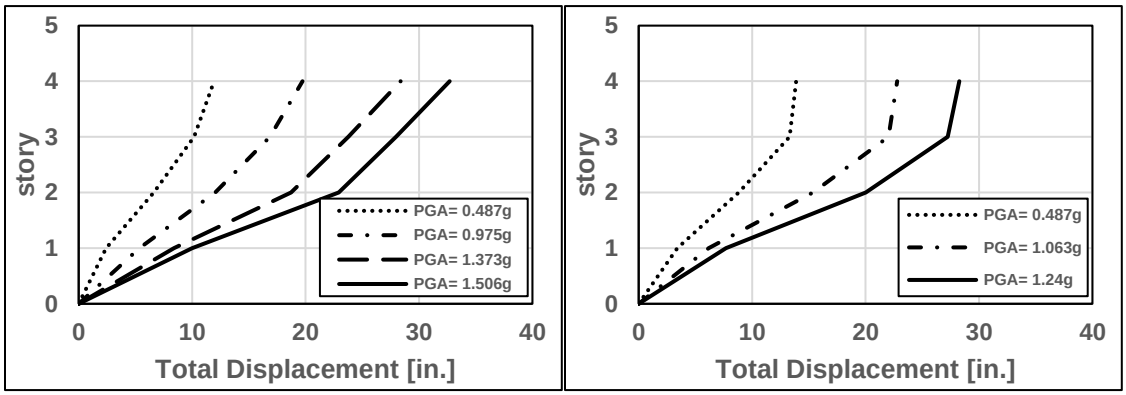

(a) (b)

Fig.App.B- 2 Maximum story displacement for varying scaled ground motion for a) DDM and b) PEER frame

4-Story Buildings

Event/Record: Northridge-01, 1/17/1994, Canyon Country - W Lost Cany, 0

PGA of the un-scaled record: 0.404g

Record duration: 20 sec

Significant duration of the Arias Intensity:

$D_{5\text{-}95}$= 6.27 sec

$D_{5\text{-}75}$= 3.16 sec

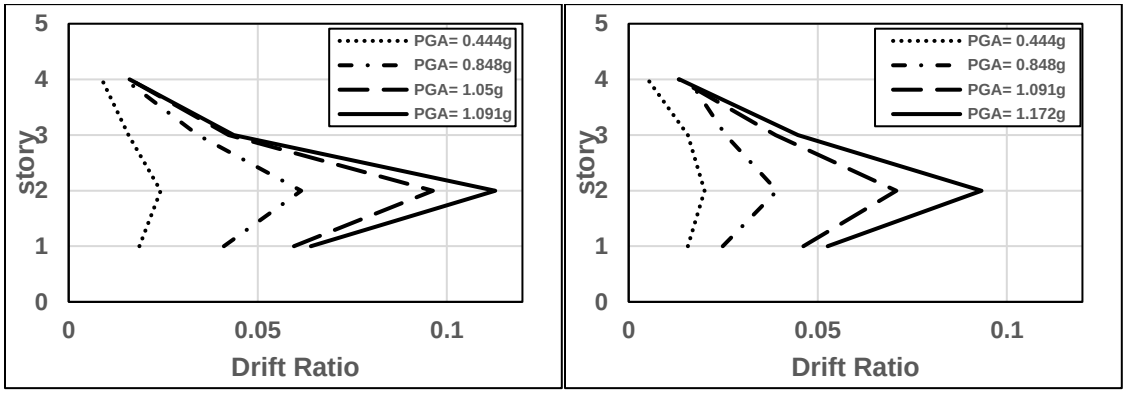

(a) (b)

Fig.App.B- 3 Maximum story drift ratio for varying scaled ground motion for a) DDM and b) PEER frame

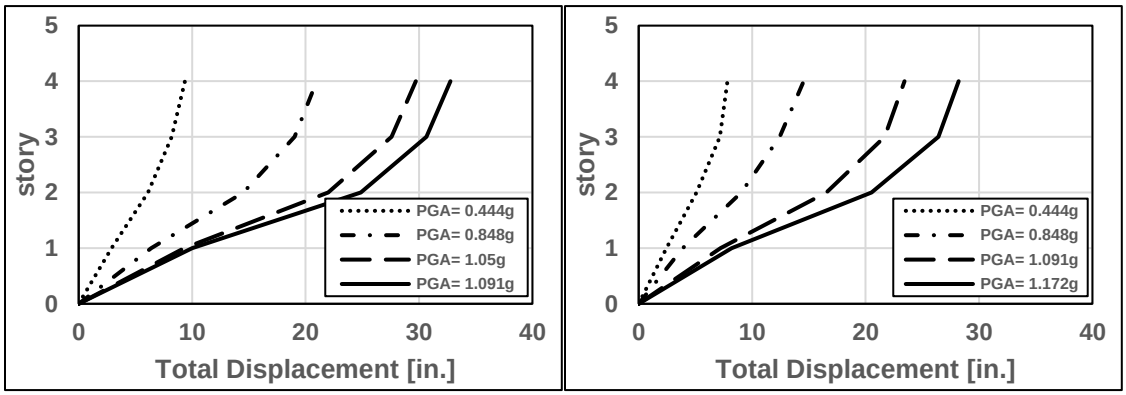

(a) (b)

Fig.App.B- 4 Maximum story displacement for varying scaled ground motion for a) DDM and b) PEER frame

4-Story Buildings

Event/Record: Duzce Turkey, 11/12/1999, Bolu, 0

PGA of the un-scaled record: 0.735g

Record duration: 56 sec

Significant duration of the Arias Intensity:

$D_{5\text{-}95}$= 8.55 sec

$D_{5\text{-}75}$= 2.65 sec

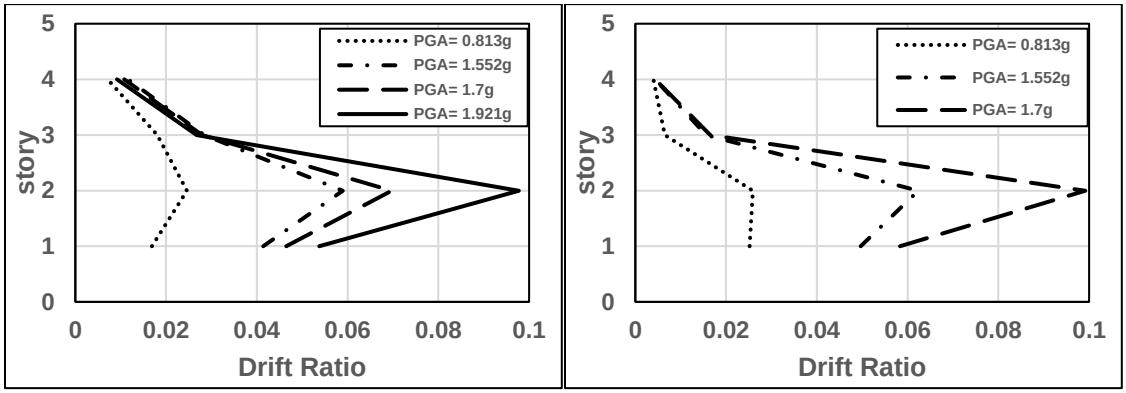

(a) (b)

Fig.App.B- 5 Maximum story drift ratio for varying scaled ground motion for a) DDM and b) PEER frame

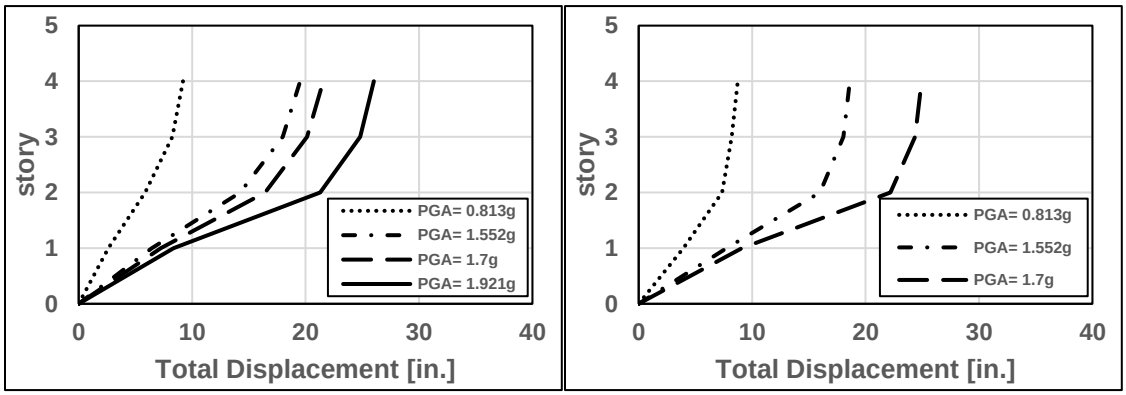

(a) (b)

Fig.App.B- 6 Maximum story displacement for varying scaled ground motion for a) DDM and b) PEER frame

4-Story Buildings

Event/Record: Hector Mine, 10/16/1999, Hector, 0

PGA of the un-scaled record: 0.265g

Record duration: 45 sec

Significant duration of the Arias Intensity:

$D_{5\text{-}95}$= 11.67 sec

$D_{5\text{-}75}$= 6.36 sec

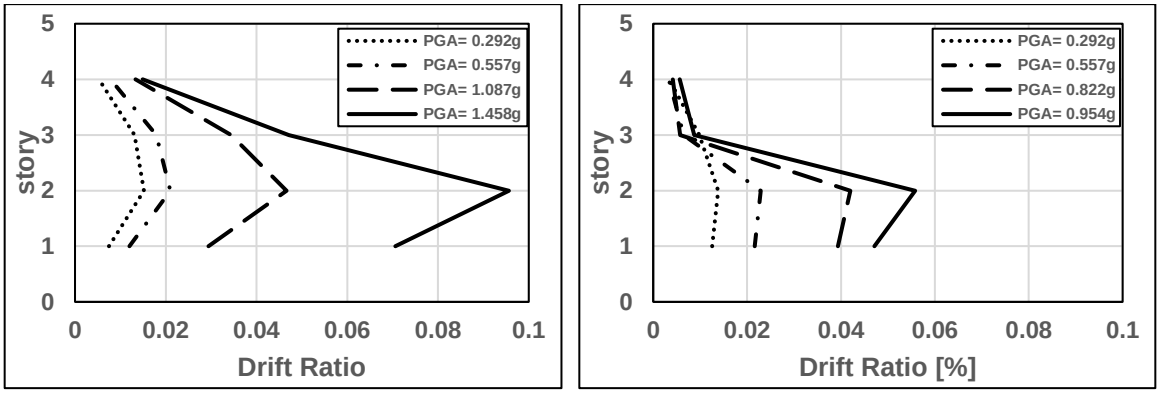

(a) (b)

Fig.App.B- 7 Maximum story drift ratio for varying scaled ground motion for a) DDM and b) PEER frame

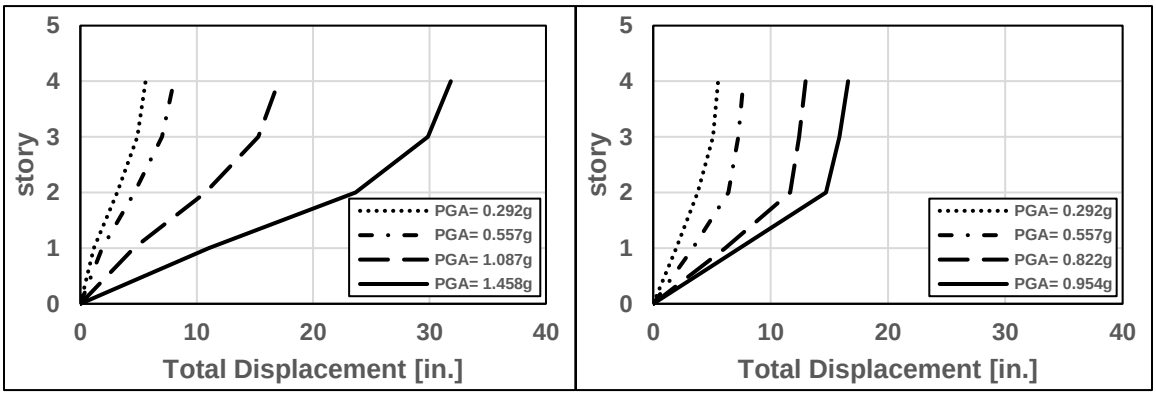

(a) (b)

Fig.App.B- 8 Maximum story displacement for varying scaled ground motion for a) DDM and b) PEER frame

4-Story Buildings

Event/Record: Imperial Valley-06, 10/15/1979, Delta, 262

PGA of the un-scaled record: 0.236 g

Record duration: 100 sec

Significant duration of the Arias Intensity:

$D_{5\text{-}95}$= 51.41 sec

$D_{5\text{-}75}$= 24.36 sec

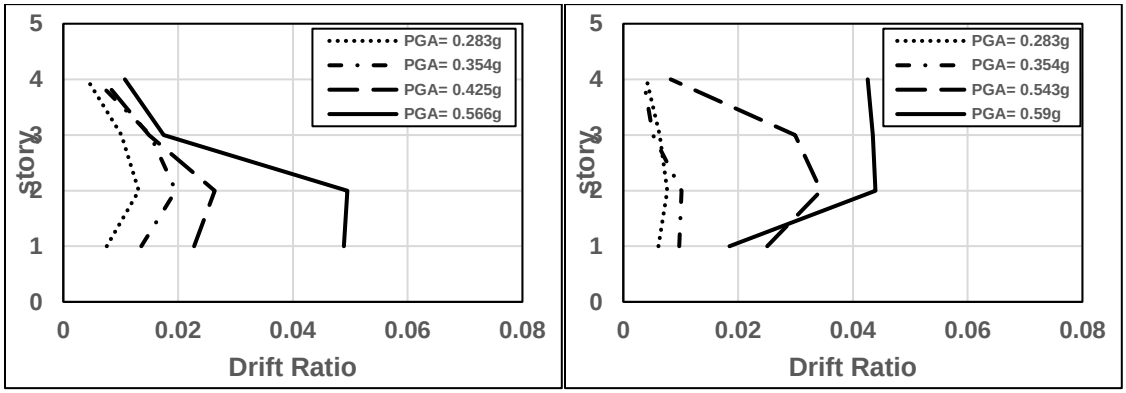

(a) (b)

Fig.App.B- 9 Maximum story drift ratio for varying scaled ground motion for a) DDM and b) PEER frame

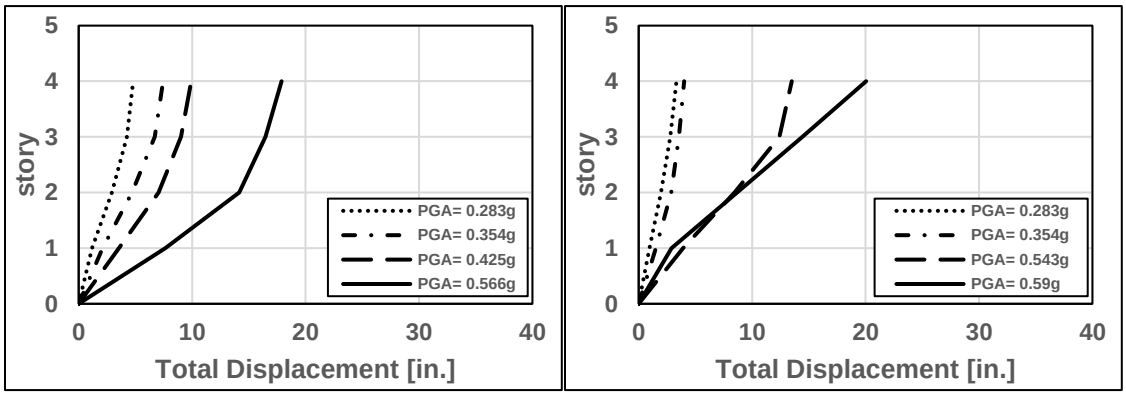

(a) (b)

Fig.App.B- 10 Maximum story displacement for varying scaled ground motion for a) DDM and b) PEER frame

4-Story Buildings

Event/Record: Imperial Valley-06, 10/15/1979, El Centro Array #11, 140

PGA of the un-scaled record: 0.367 g

Record duration: 39 sec

Significant duration of the Arias Intensity:

$D_{5\text{-}95}$= 9.00 sec

$D_{5\text{-}75}$= 4.49 sec

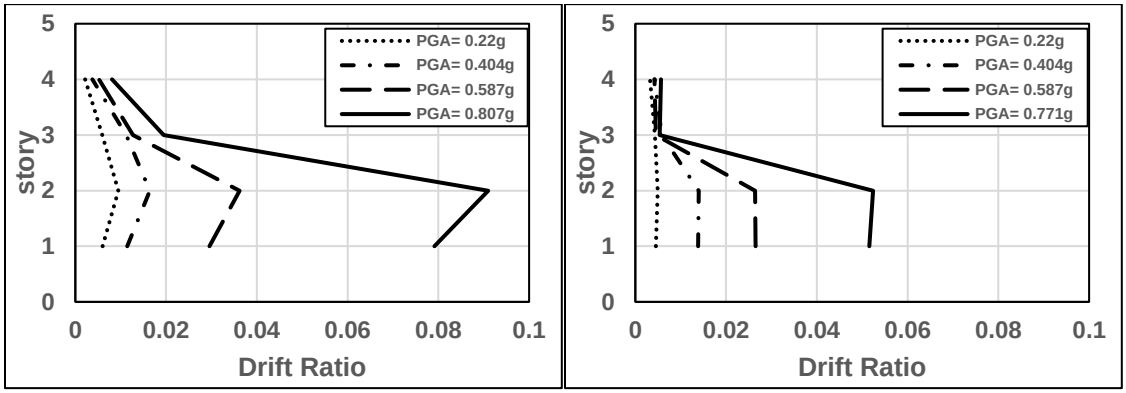

(a) (b)

Fig.App.B- 11 Maximum story drift ratio for varying scaled ground motion for a) DDM and b) PEER frame

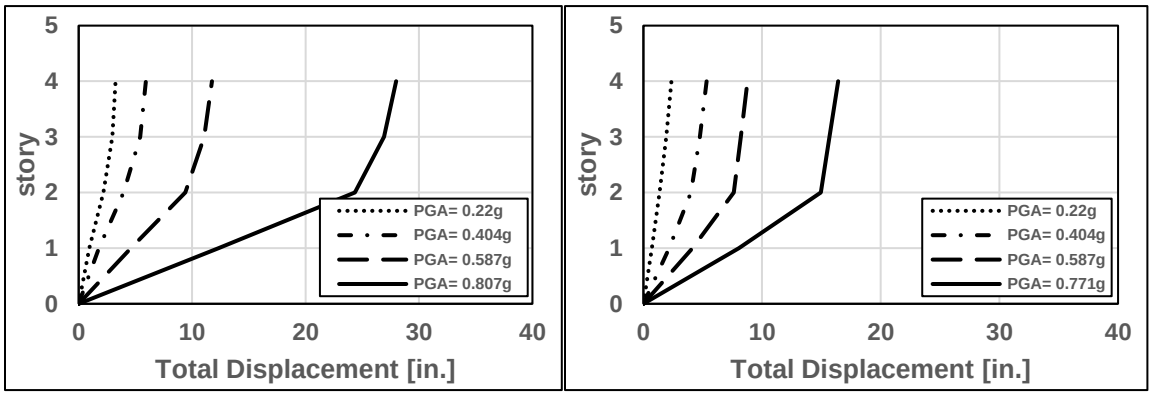

(a) (b)

Fig.App.B- 12 Maximum story displacement for varying scaled ground motion for a) DDM and b) PEER frame

4-Story Buildings

Event/Record: Kobe Japan, 1/16/1995, Nishi-Akashi, 0

PGA of the un-scaled record: 0.483g

Record duration: 41 sec

Significant duration of the Arias Intensity:

$D_{5\text{-}95}$= 9.60 sec

$D_{5\text{-}75}$= 3.96 sec

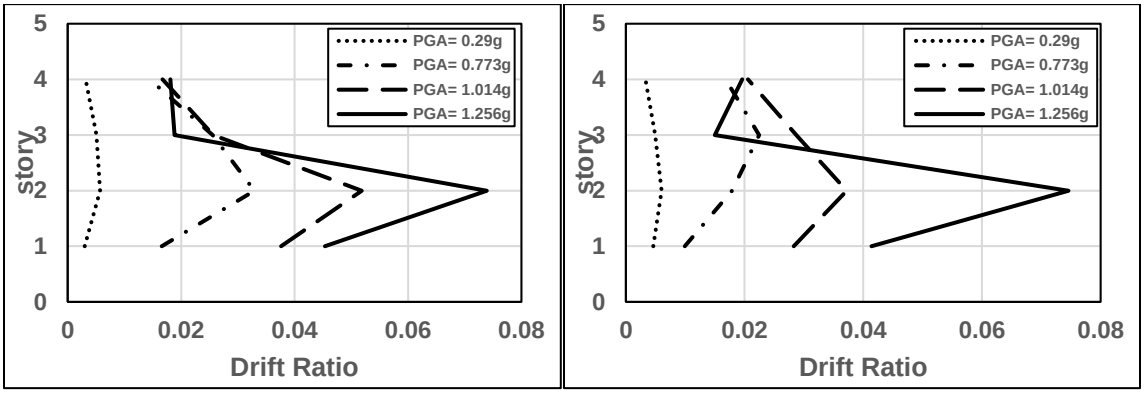

(a) (b)

Fig.App.B- 13 Maximum story drift ratio for varying scaled ground motion for a) DDM and b) PEER frame

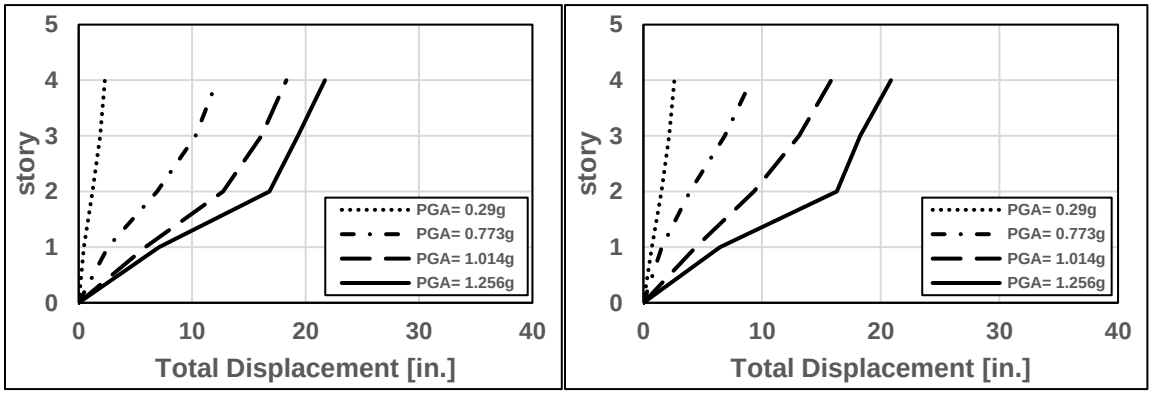

(a) (b)

Fig.App.B- 14 Maximum story displacement for varying scaled ground motion for a) DDM and b) PEER frame

4-Story Buildings

Event/Record: Kobe Japan, 1/16/1995, Shin-Osaka, 0

PGA of the un-scaled record: 0.225 g

Record duration: 41 sec

Significant duration of the Arias Intensity:

$D_{5\text{-}95}$= 10.35 sec

$D_{5\text{-}75}$= 3.77 sec

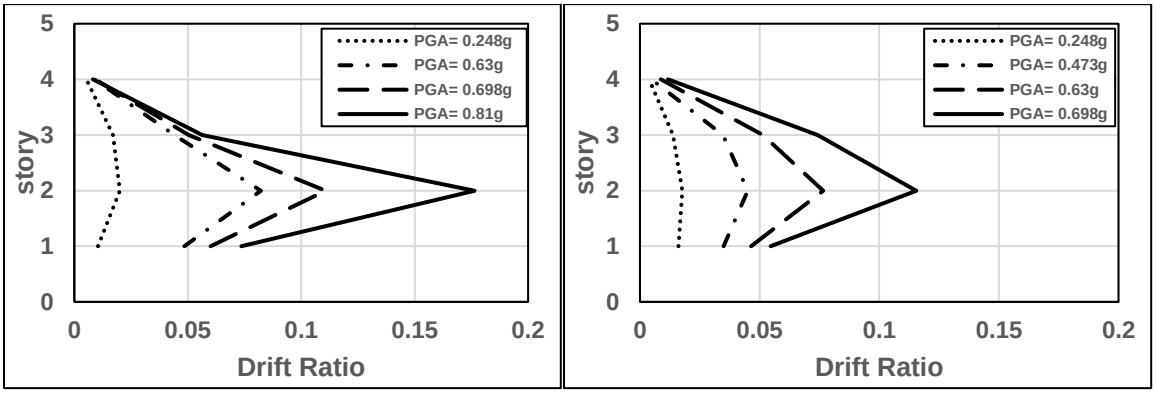

(a) (b)

Fig.App.B- 15 Maximum story drift ratio for varying scaled ground motion for a) DDM and b) PEER frame

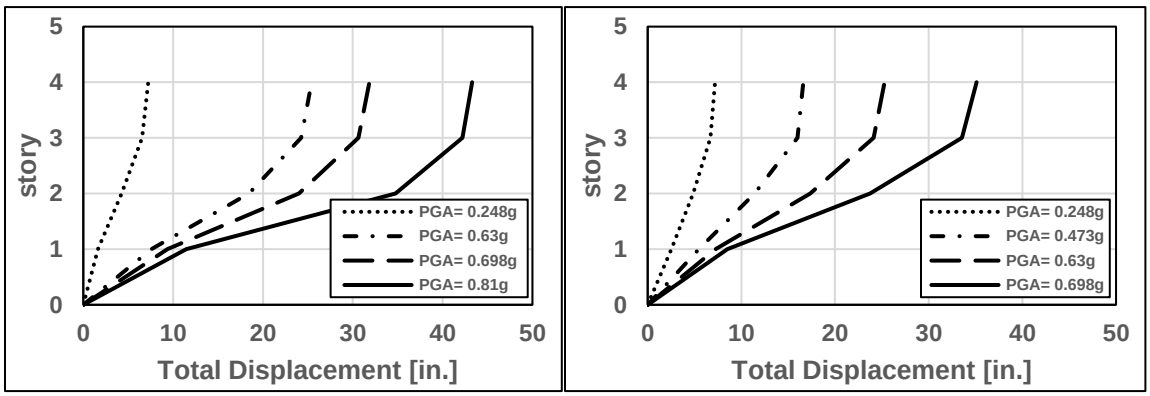

(a) (b)

Fig.App.B- 16 Maximum story displacement for varying scaled ground motion for a) DDM and b) PEER frame

4-Story Buildings

Event/Record: Kocaeli Turkey, 8/17/1999, Duzce, 180

PGA of the un-scaled record: 0.312 g

Record duration: 27 sec

Significant duration of the Arias Intensity:

$D_{5\text{-}95}$= 11.76 sec

$D_{5\text{-}75}$= 6.12 sec

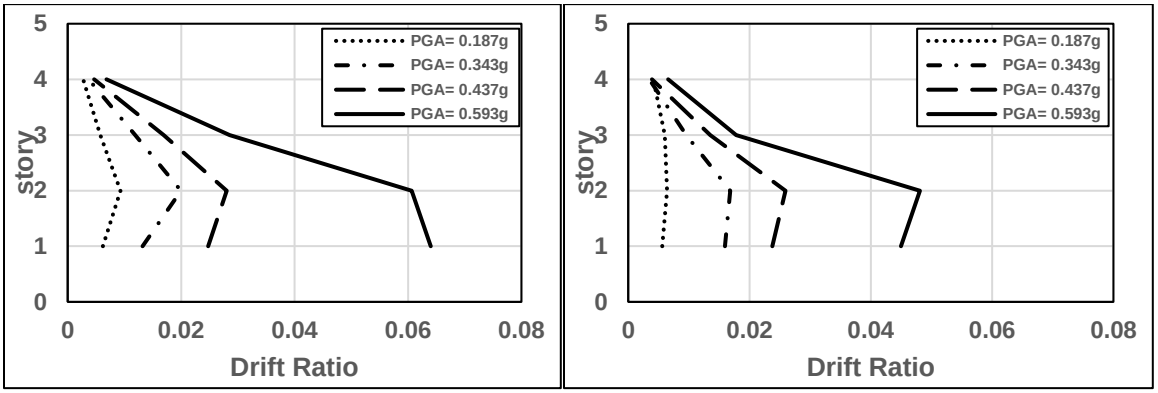

(a) (b)

Fig.App.B- 17 Maximum story drift ratio for varying scaled ground motion for a) DDM and b) PEER frame

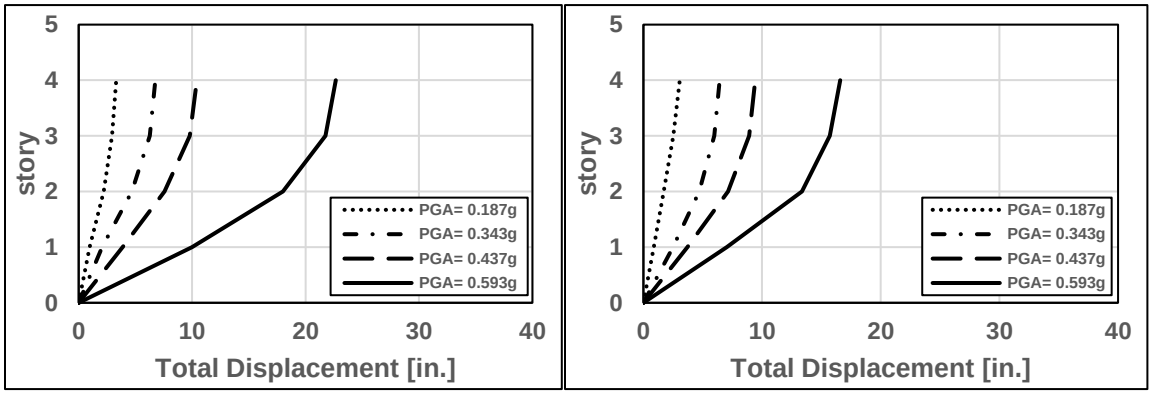

(a) (b)

Fig.App.B- 18 Maximum story displacement for varying scaled ground motion for a) DDM and b) PEER frame

4-Story Buildings

Event/Record: Kocaeli Turkey, 8/17/1999, Arcelik, 0

PGA of the un-scaled record: 0.210 g

Record duration: 30 sec

Significant duration of the Arias Intensity:

$D_{5\text{-}95}$= 11.05 sec

$D_{5\text{-}75}$= 7.68 sec

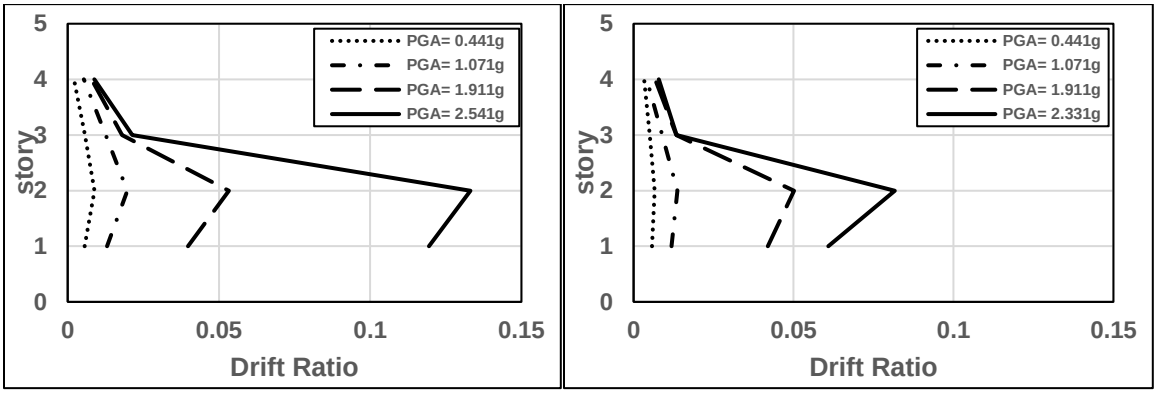

(a) (b)

Fig.App.B- 19 Maximum story drift ratio for varying scaled ground motion for a) DDM and b) PEER frame

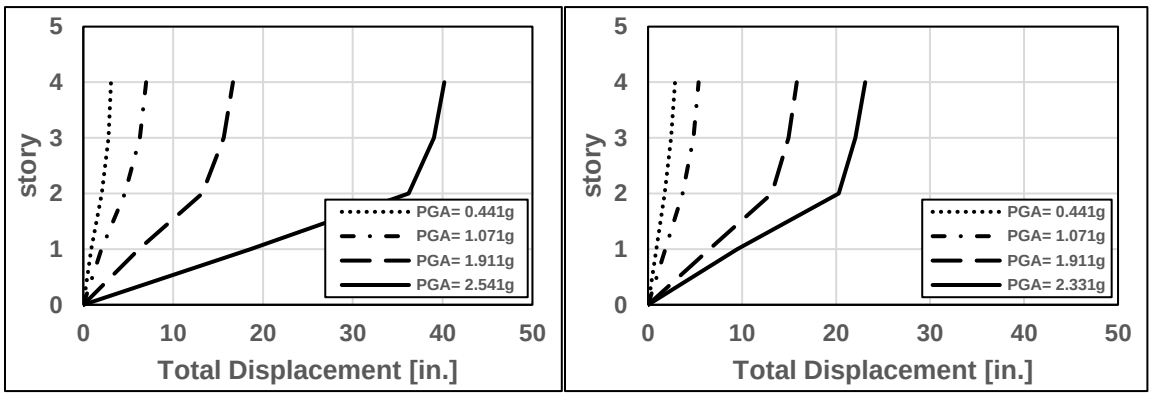

(a) (b)

Fig.App.B- 20 Maximum story displacement for varying scaled ground motion for a) DDM and b) PEER frame

4-Story Buildings

Event/Record: Landers, 6/28/1992, Yermo Fire Station, 270

PGA of the un-scaled record: 0.245 g

Record duration: 44 sec

Significant duration of the Arias Intensity:

$D_{5\text{-}95}$= 17.58 sec

$D_{5\text{-}75}$= 7.08 sec

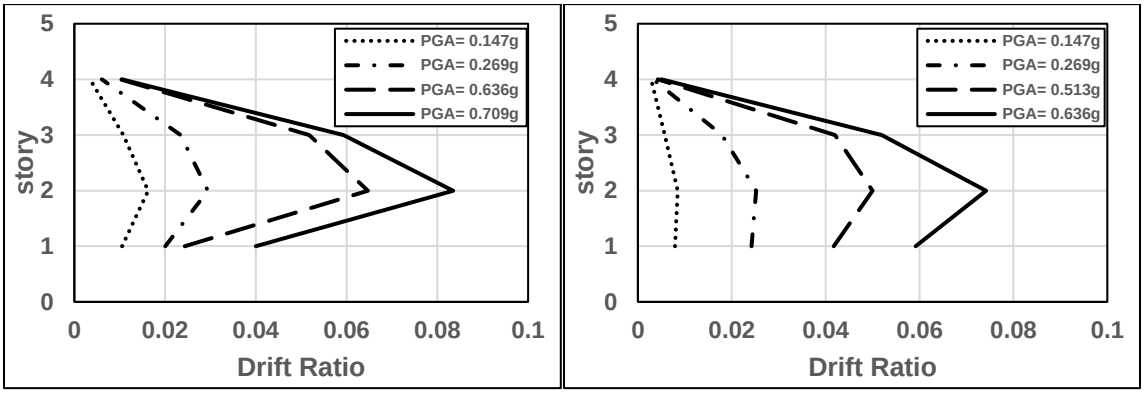

(a) (b)

Fig.App.B- 21 Maximum story drift ratio for varying scaled ground motion for a) DDM and b) PEER frame

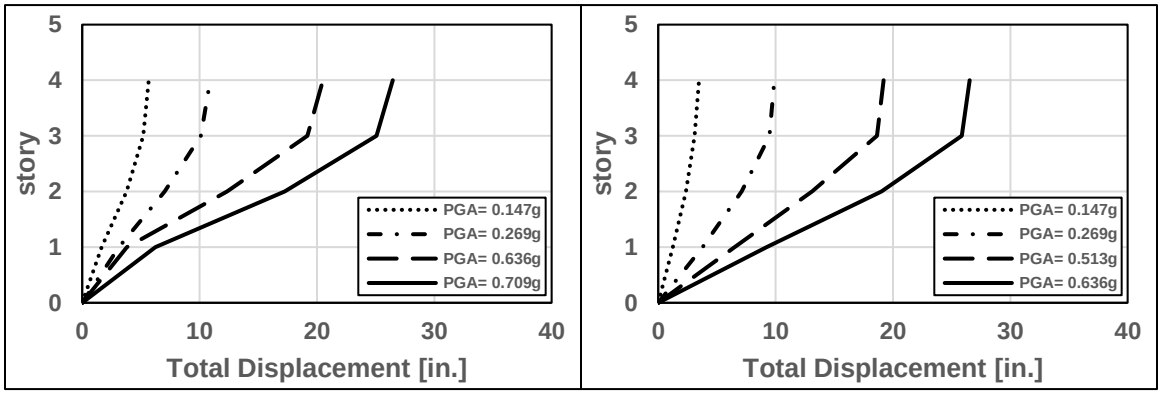

(a) (b)

Fig.App.B- 22 Maximum story displacement for varying scaled ground motion for a) DDM and b) PEER frame

4-Story Buildings

Event/Record: Landers, 6/28/1992, Coolwater, LN

PGA of the un-scaled record: 0.284 g

Record duration: 28 sec

Significant duration of the Arias Intensity:

$D_{5\text{-}95}$= 10.58 sec

$D_{5\text{-}75}$= 6.07 sec

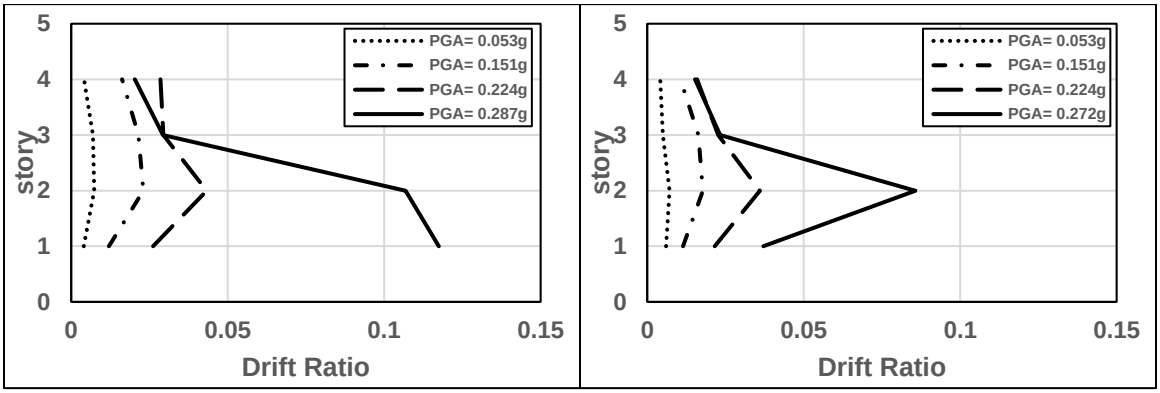

(a) (b)

Fig.App.B- 23 Maximum story drift ratio for varying scaled ground motion for a) DDM and b) PEER frame

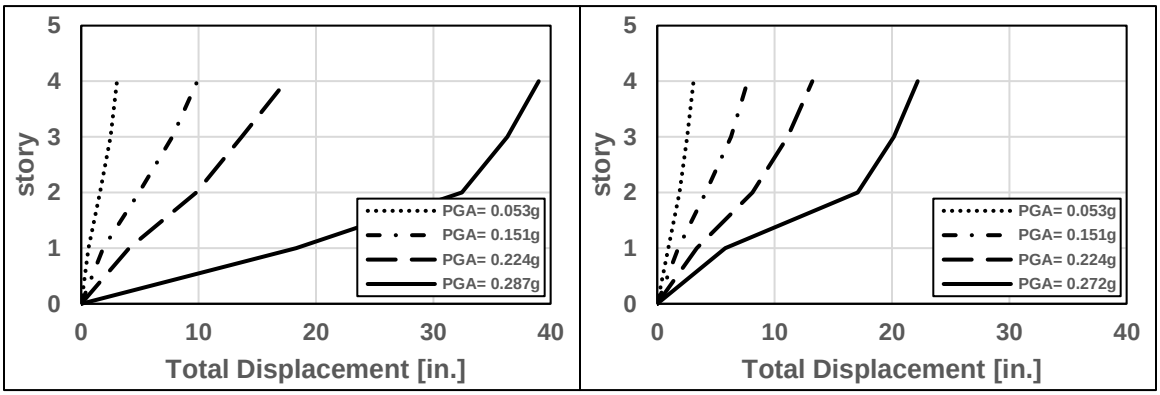

(a) (b)

Fig.App.B- 24 Maximum story displacement for varying scaled ground motion for a) DDM and b) PEER frame

4-Story Buildings

Event/Record: Loma Prieta, 10/18/1989, Capitola, 0

PGA of the un-scaled record: 0.511 g

Record duration: 40 sec

Significant duration of the Arias Intensity:

$D_{5\text{-}95}$= 12.15 sec

$D_{5\text{-}75}$= 5.62 sec

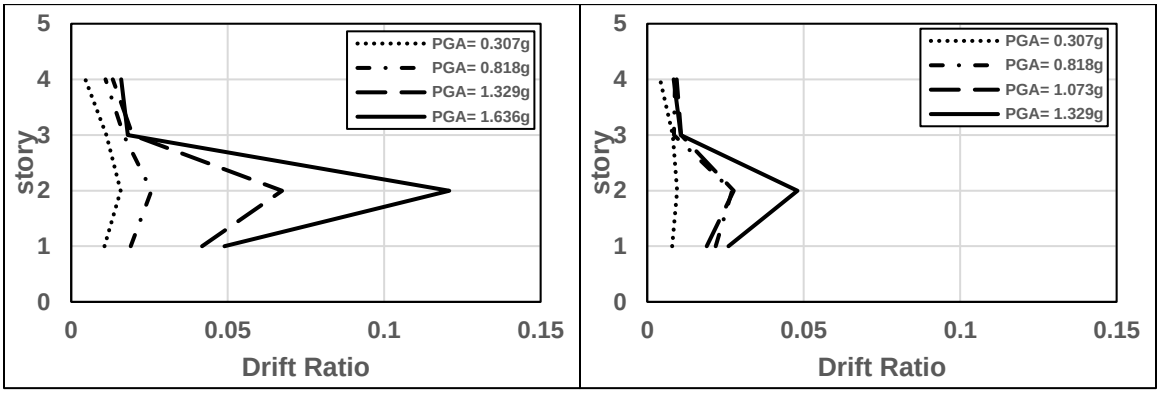

(a) (b)

Fig.App.B- 25 Maximum story drift ratio for varying scaled ground motion for a) DDM and b) PEER frame

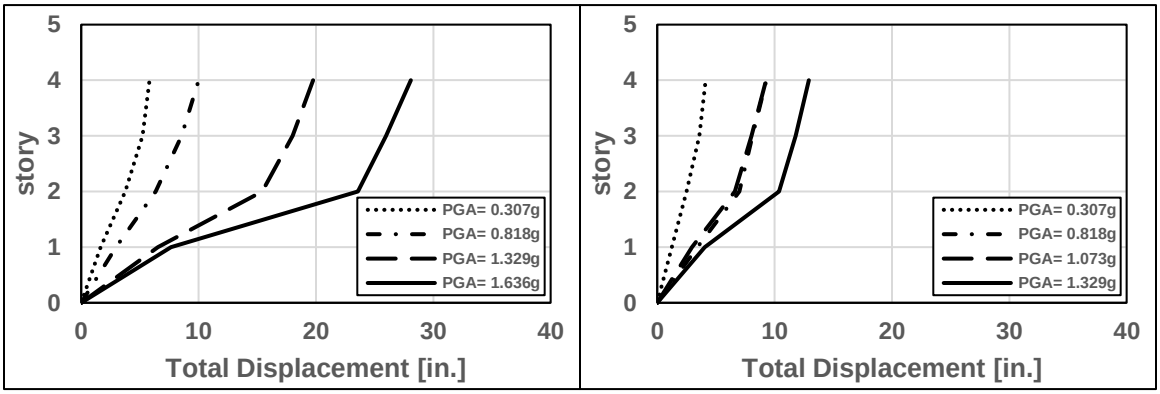

(a) (b)

Fig.App.B- 26 Maximum story displacement for varying scaled ground motion for a) DDM and b) PEER frame

4-Story Buildings

Event/Record: Loma Prieta, 10/18/1989, Gilroy Array #3, 0

PGA of the un-scaled record: 0.559 g

Record duration: 40 sec

Significant duration of the Arias Intensity:

$D_{5\text{-}95}$= 6.38 sec

$D_{5\text{-}75}$= 1.74 sec

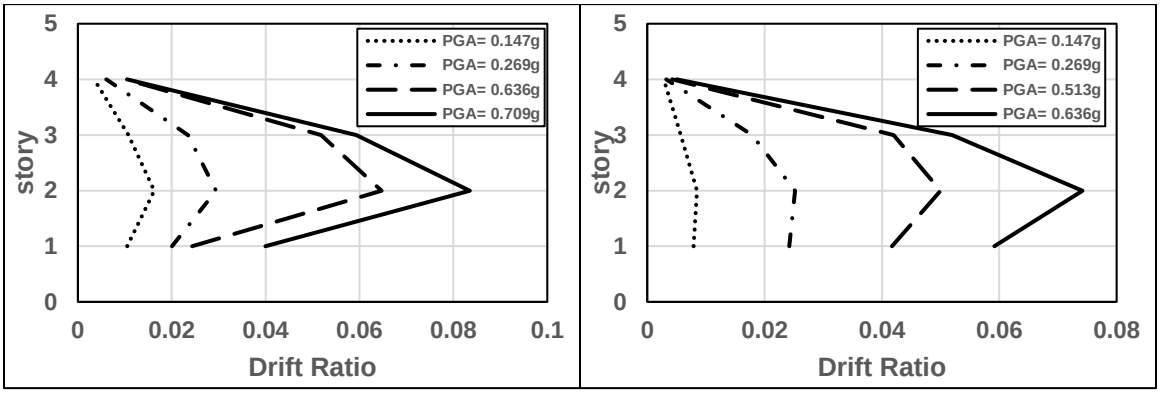

(a) (b)

Fig.App.B- 27 Maximum story drift ratio for varying scaled ground motion for a) DDM and b) PEER frame

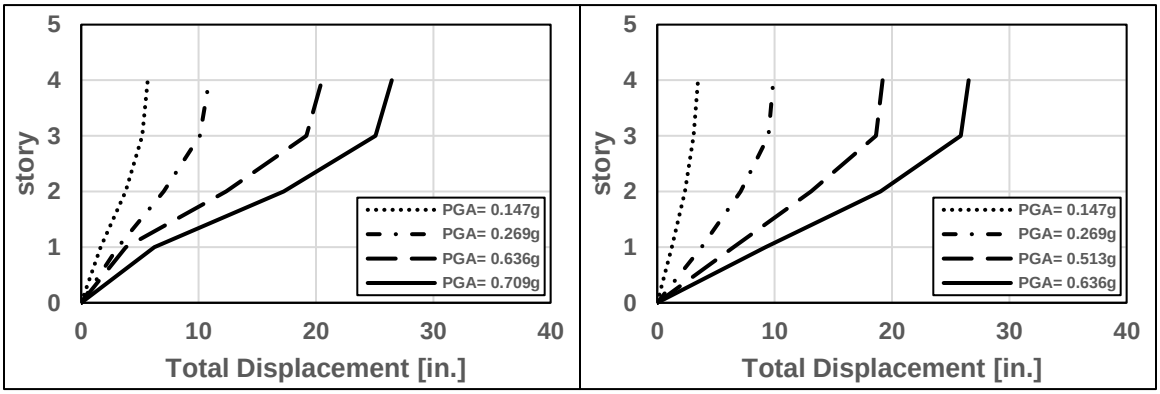

(a) (b)

Fig.App.B- 28 Maximum story displacement for varying scaled ground motion for a) DDM and b) PEER frame

4-Story Buildings

Event/Record: Manjil Iran, 6/20/1990, Abbar, L

PGA of the un-scaled record: 0.515 g

Record duration: 53 sec

Significant duration of the Arias Intensity:

$D_{5\text{-}95}$= 28.66 sec

$D_{5\text{-}75}$= 7.40 sec

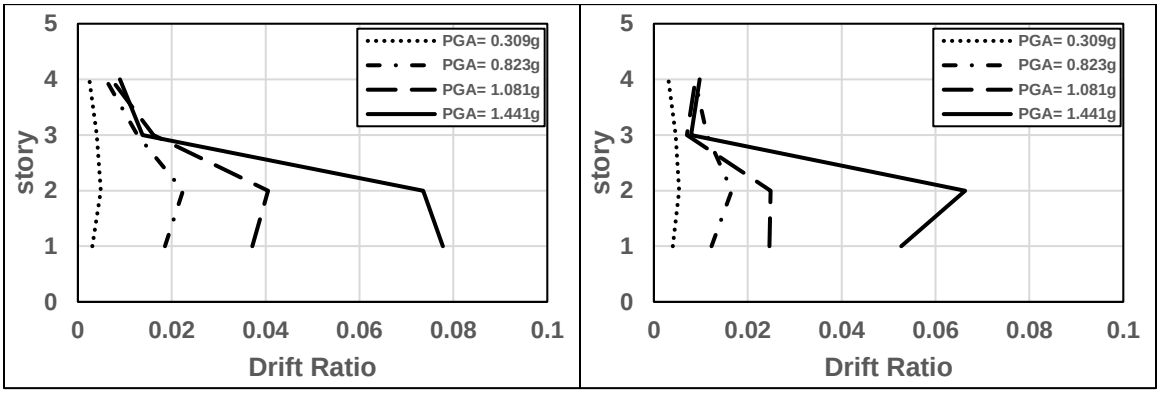

(a) (b)

Fig.App.B- 29 Maximum story drift ratio for varying scaled ground motion for a) DDM and b) PEER frame

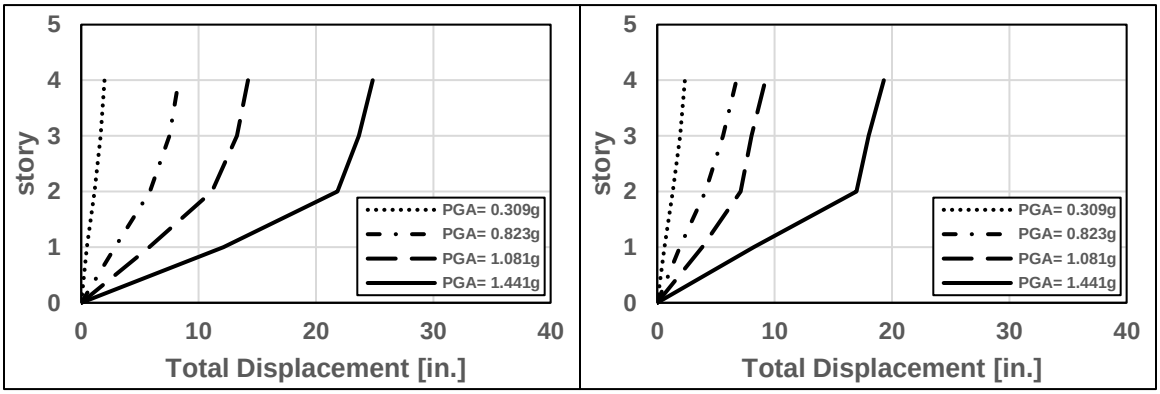

(a) (b)

Fig.App.B- 30 Maximum story displacement for varying scaled ground motion for a) DDM and b) PEER frame

4-Story Buildings

Event/Record: Superstition Hills-02, 11/24/1987, El Centro Imp. Co. Cent, 0

PGA of the un-scaled record: 0.357 g

Record duration: 60 sec

Significant duration of the Arias Intensity:

$D_{5\text{-}95}$= 27.99 sec

$D_{5\text{-}75}$= 7.05 sec

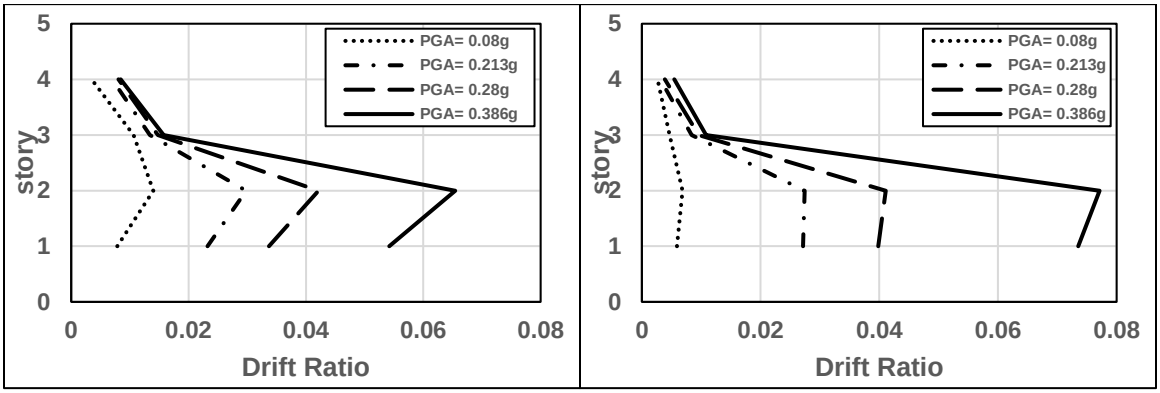

(a) (b)

Fig.App.B- 31 Maximum story drift ratio for varying scaled ground motion for a) DDM and b) PEER frame

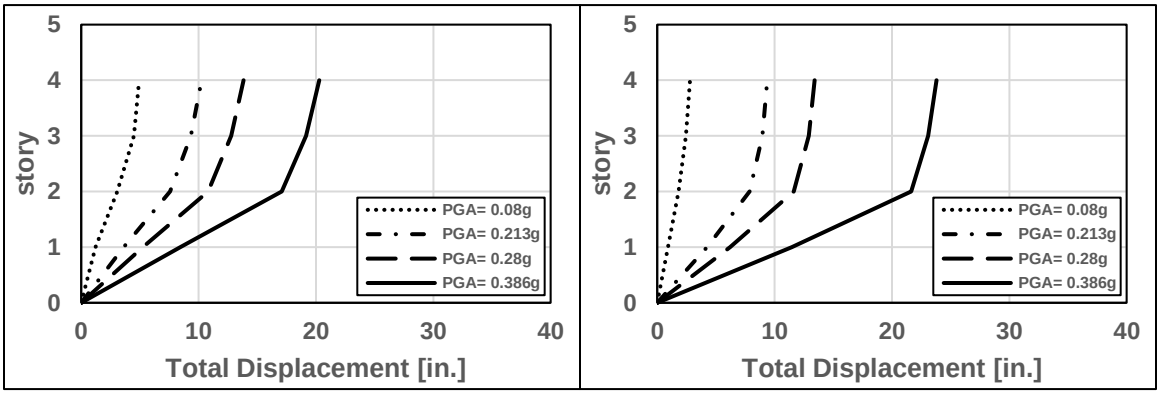

(a) (b)

Fig.App.B- 32 Maximum story displacement for varying scaled ground motion for a) DDM and b) PEER frame

4-Story Buildings

Event/Record: Superstition Hills-02, 11/24/1987, Poe Road (temp), 270

PGA of the un-scaled record: 0.475 g

Record duration: 22 sec

Significant duration of the Arias Intensity:

$D_{5\text{-}95}$= 13.69 sec

$D_{5\text{-}75}$= 9.77 sec

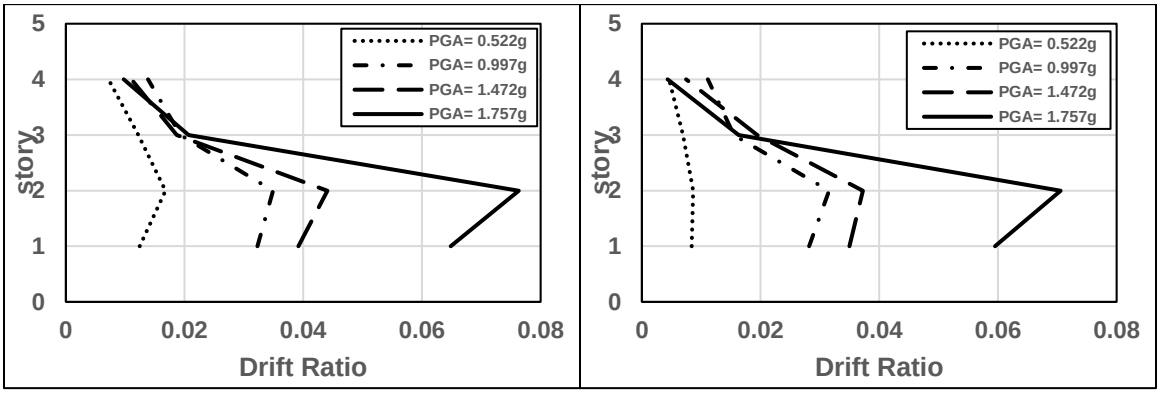

(a) (b)

Fig.App.B- 33 Maximum story drift ratio for varying scaled ground motion for a) DDM and b) PEER frame

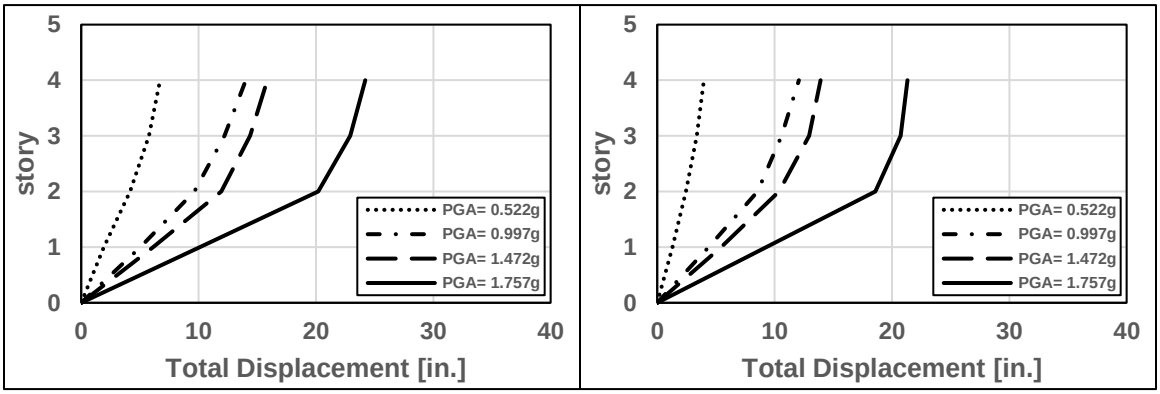

(a) (b)

Fig.App.B- 34 Maximum story displacement for varying scaled ground motion for a) DDM and b) PEER frame

4-Story Buildings

Event/Record: Chi-Chi Taiwan, 9/20/1999, CHY101, E

PGA of the un-scaled record: 0.340 g

Record duration: 90 sec

Significant duration of the Arias Intensity:

$D_{5\text{-}95}$= 30.38 sec

$D_{5\text{-}75}$= 13.46 sec

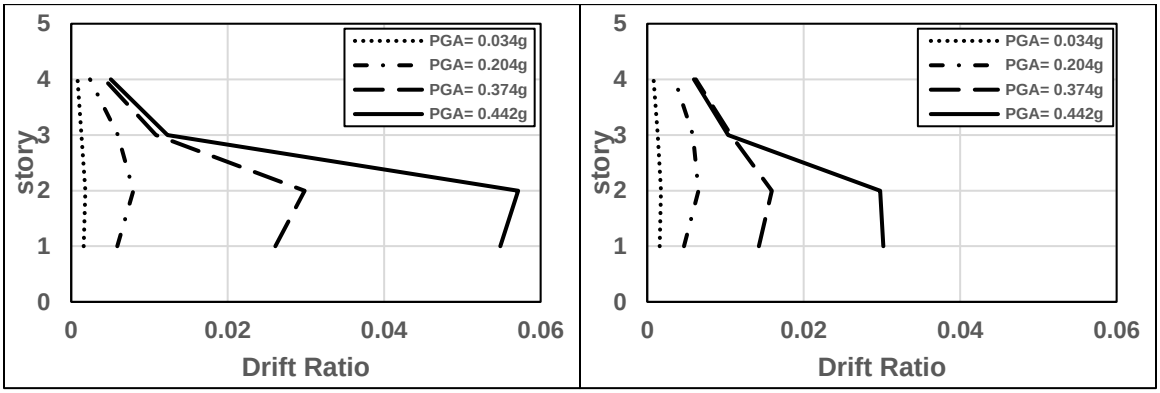

(a) (b)

Fig.App.B- 35 Maximum story drift ratio for varying scaled ground motion for a) DDM and b) PEER frame

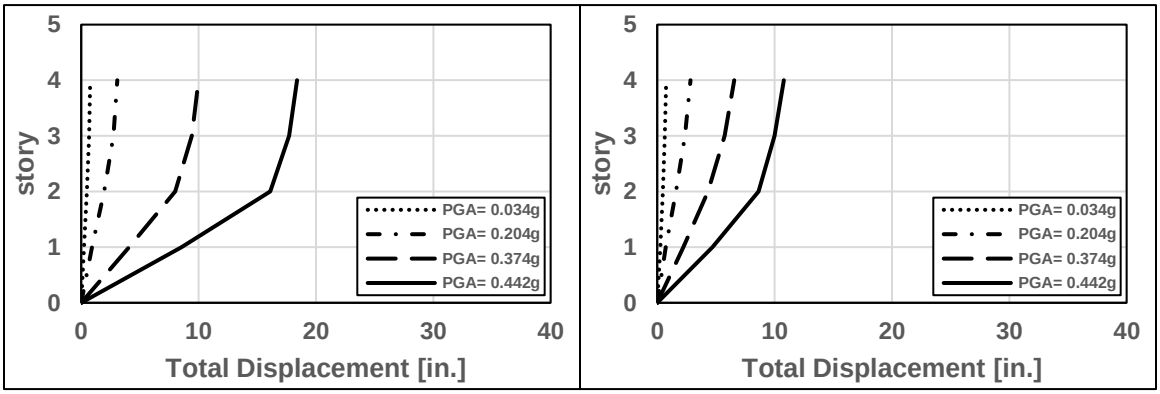

(a) (b)

Fig.App.B- 36 Maximum story displacement for varying scaled ground motion for a) DDM and b) PEER frame

4-Story Buildings

Event/Record: Chi-Chi Taiwan, 9/20/1999, TCU045, E

PGA of the un-scaled record: 0.473 g

Record duration: 90 sec

Significant duration of the Arias Intensity:

$D_{5\text{-}95}$= 11.34 sec

$D_{5\text{-}75}$= 7.49 sec

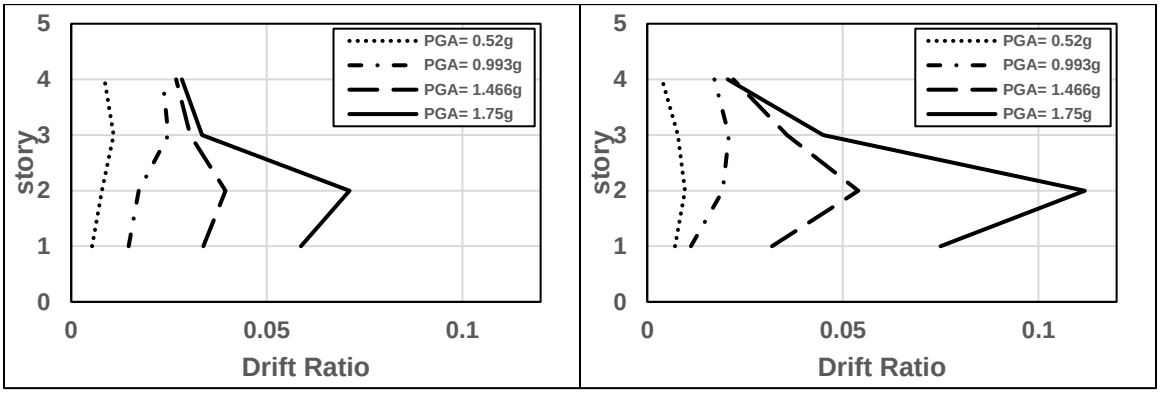

(a) (b)

Fig.App.B- 37 Maximum story drift ratio for varying scaled ground motion for a) DDM and b) PEER frame

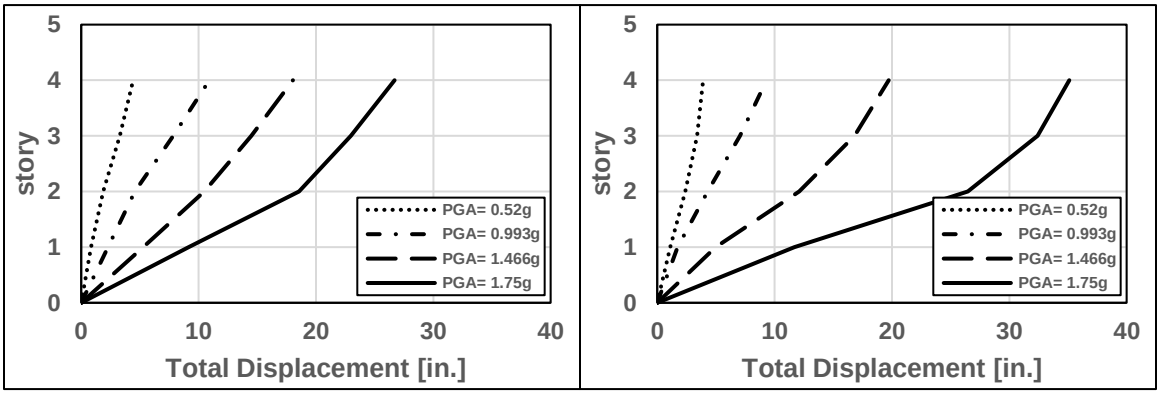

(a) (b)

Fig.App.B- 38 Maximum story displacement for varying scaled ground motion for a) DDM and b) PEER frame

4-Story Buildings

Event/Record: San Fernando, 2/9/1971, LA - Hollywood Stor FF, 90

PGA of the un-scaled record: 0.225 g

Record duration: 79 sec

Significant duration of the Arias Intensity:

$D_{5\text{-}95}$= 13.15 sec

$D_{5\text{-}75}$= 5.24 sec

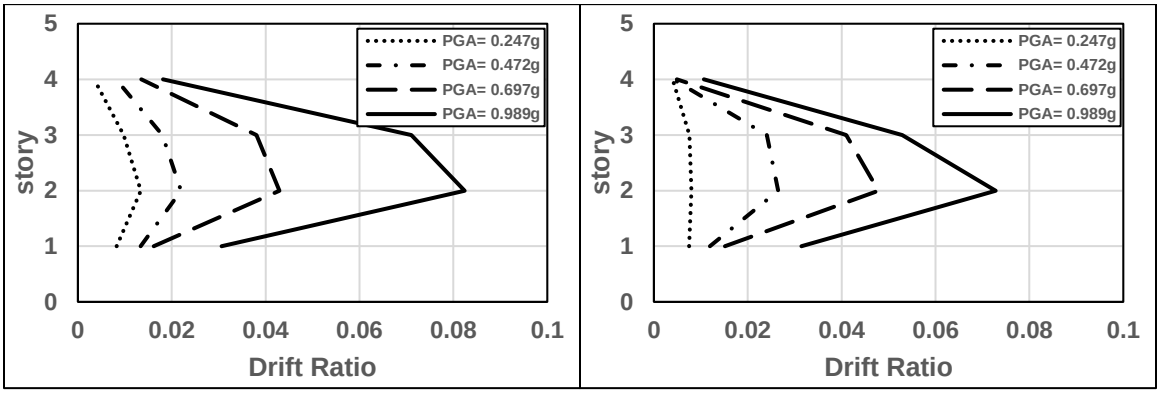

(a) (b)

Fig.App.B- 39 Maximum story drift ratio for varying scaled ground motion for a) DDM and b) PEER frame

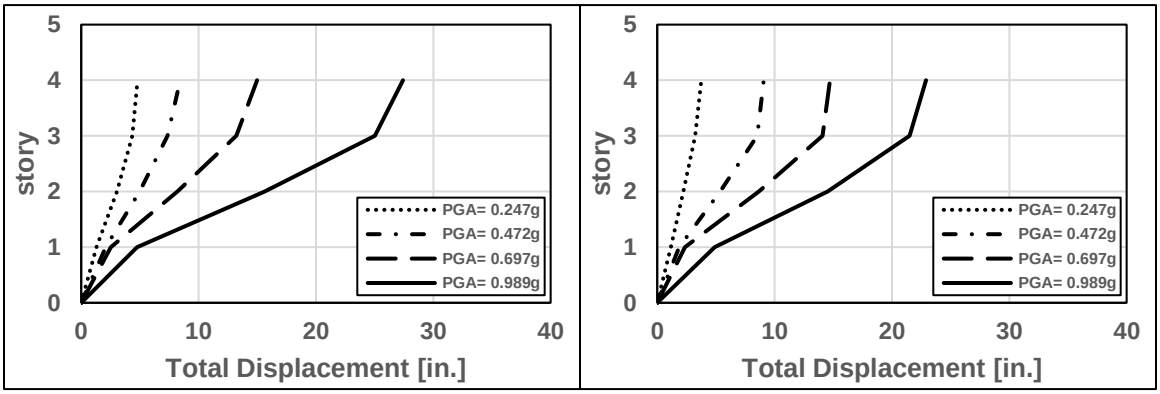

(a) (b)

Fig.App.B- 40 Maximum story displacement for varying scaled ground motion for a) DDM and b) PEER frame

4-Story Buildings

Event/Record: Friuli Italy-01, 5/6/1976, Tolmezzo, 0

PGA of the un-scaled record: 0.357 g

Record duration: 36 sec

Significant duration of the Arias Intensity:

$D_{5\text{-}95}$= 4.24 sec

$D_{5\text{-}75}$= 2.55 sec

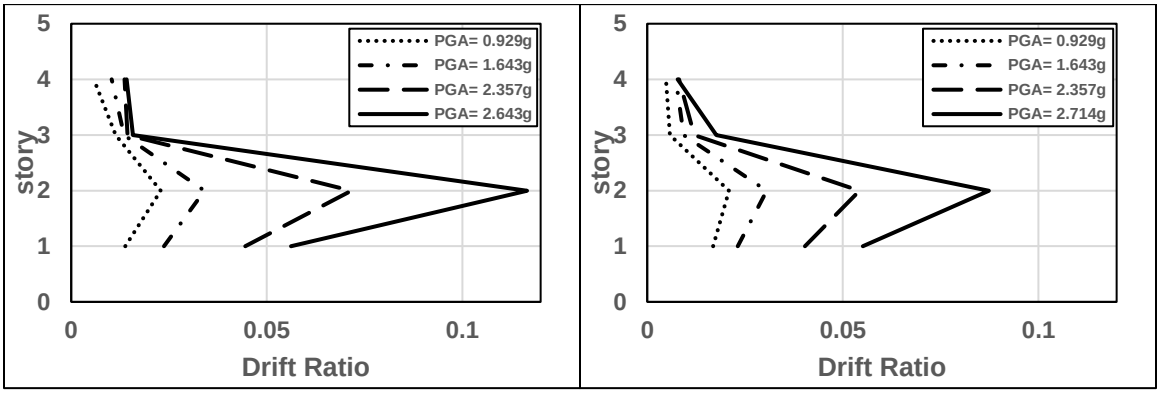

(a) (b)

Fig.App.B- 41 Maximum story drift ratio for varying scaled ground motion for a) DDM and b) PEER frame

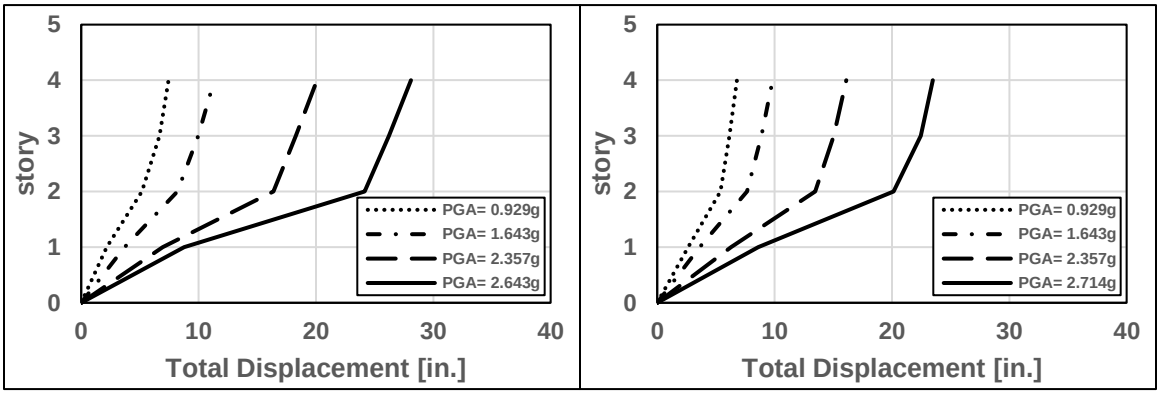

(a) (b)

Fig.App.B- 42 Maximum story displacement for varying scaled ground motion for a) DDM and b) PEER frame

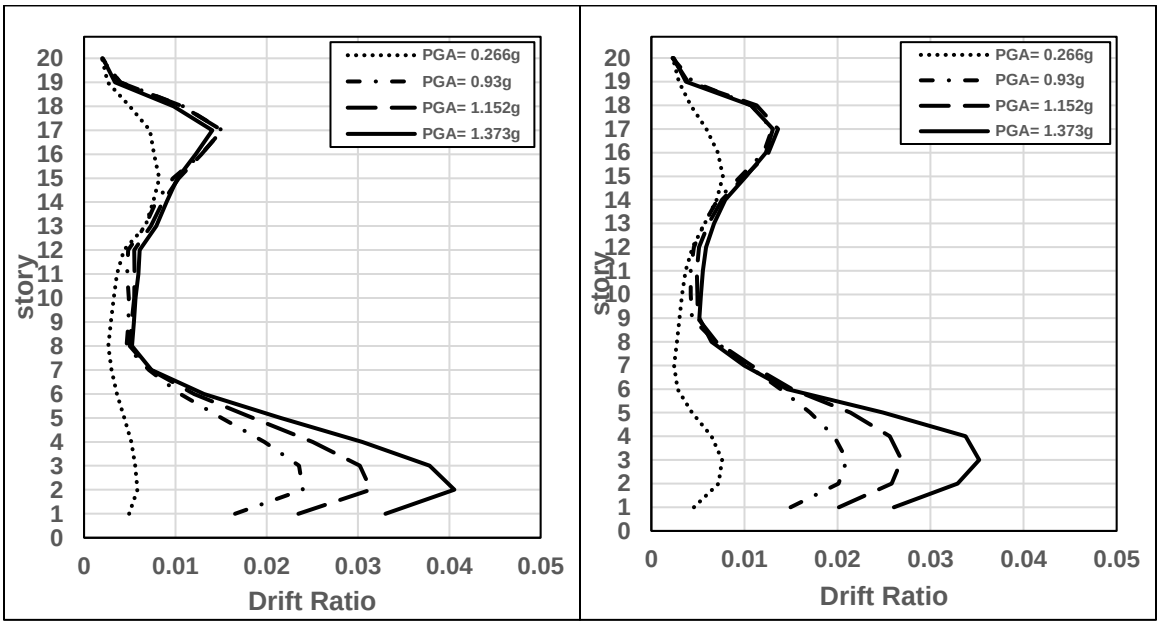

(a) (b)

Fig.App.B- 43 Maximum story drift ratio for varying scaled ground motion for a) DDM and b) PEER frame

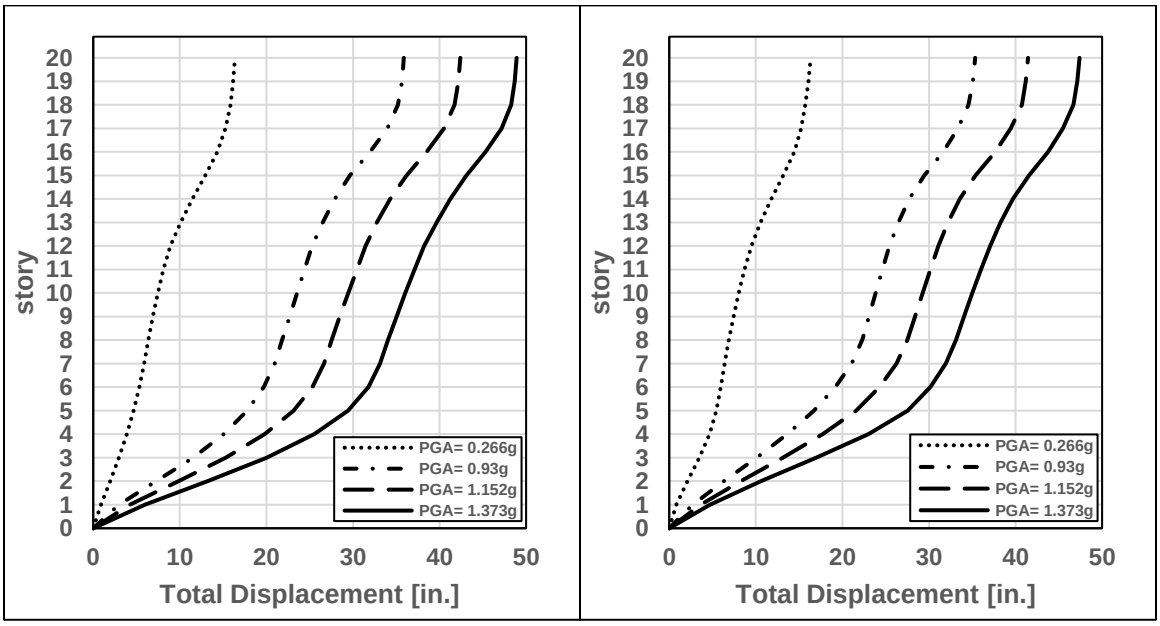

(a) (b)

Fig.App.B- 44 Maximum story displacement for varying scaled ground motion for a) DDM and b) PEER frame

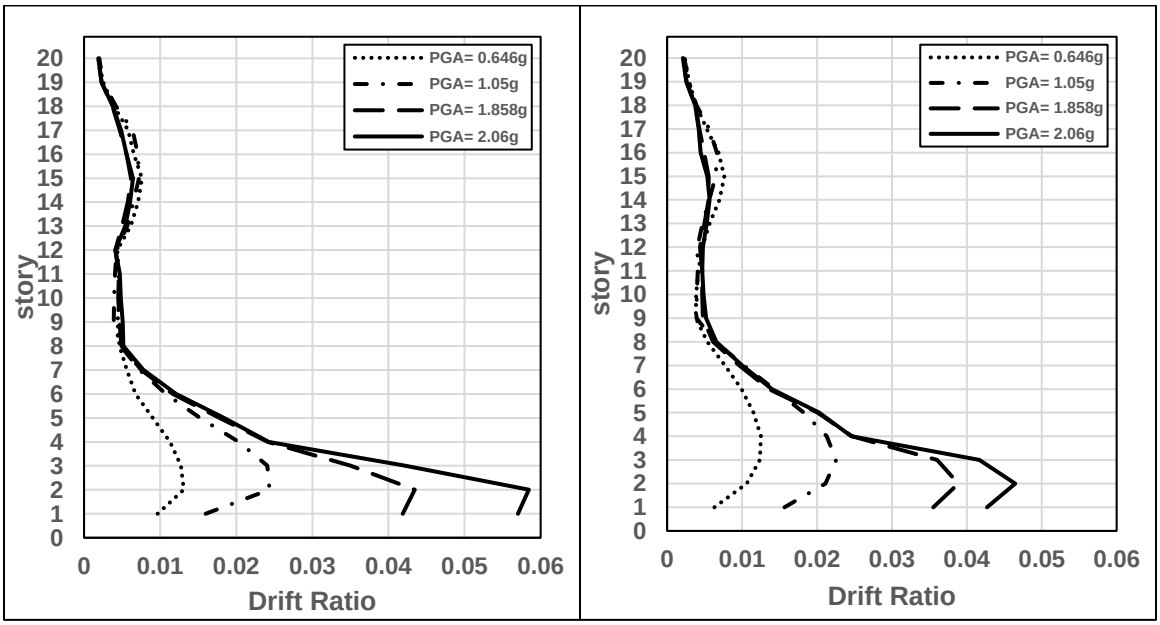

(a) (b)

Fig.App.B- 45 Maximum story drift ratio for varying scaled ground motion for a) DDM and b) PEER frame

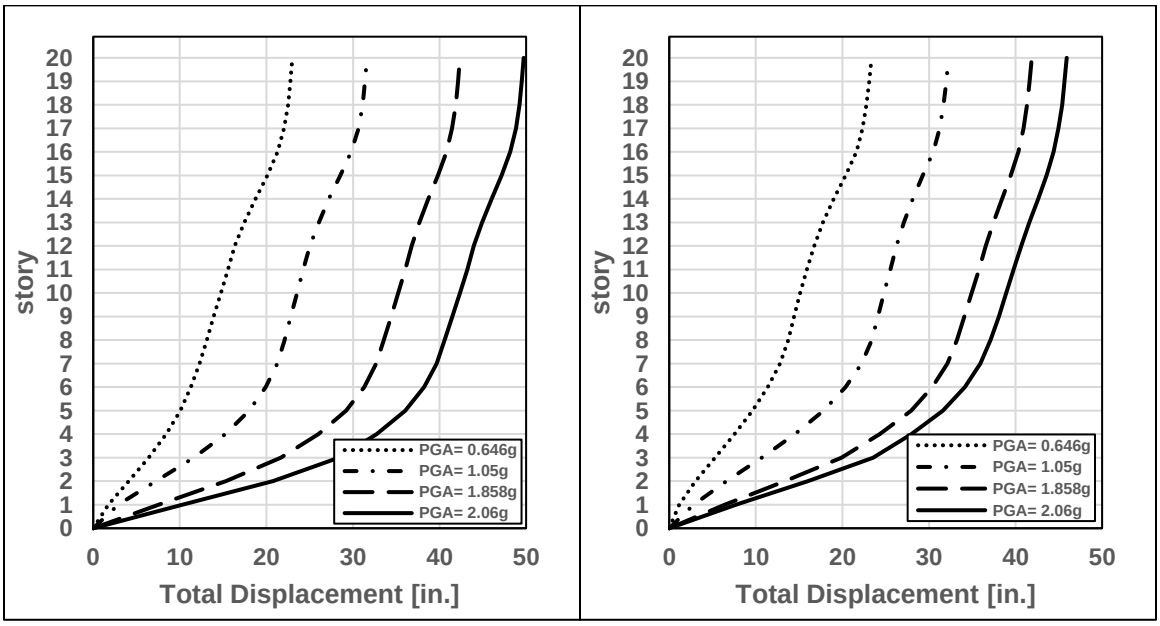

(a) (b)

Fig.App.B- 46 Maximum story displacement for varying scaled ground motion for a) DDM and b) PEER frame

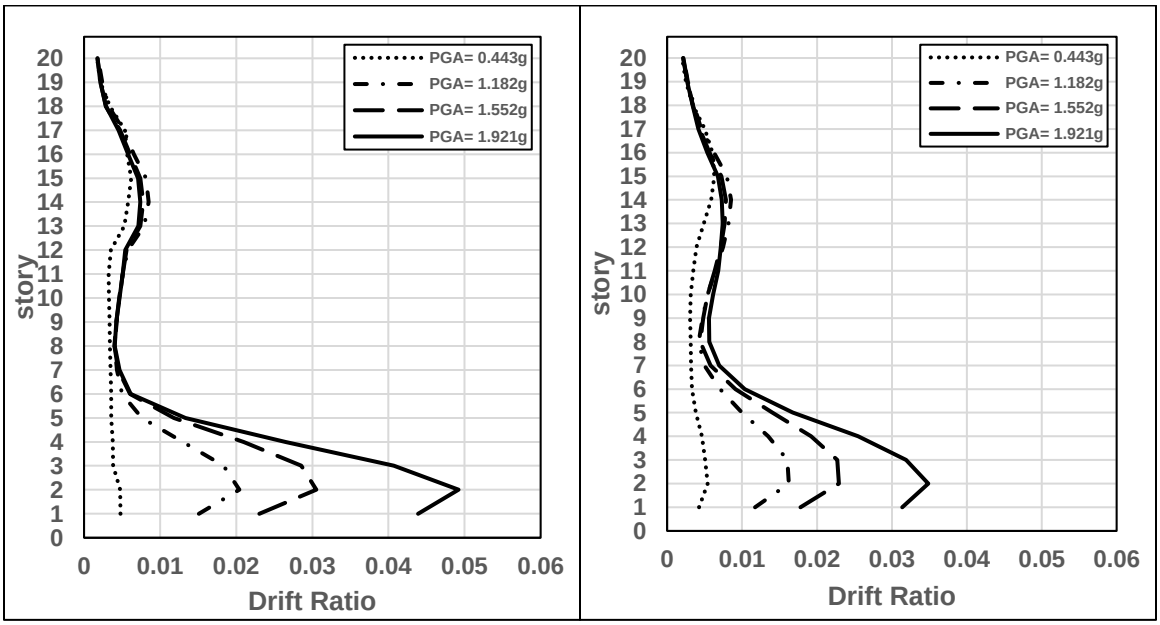

(a) (b)

Fig.App.B- 47 Maximum story drift ratio for varying scaled ground motion for a) DDM and b) PEER frame

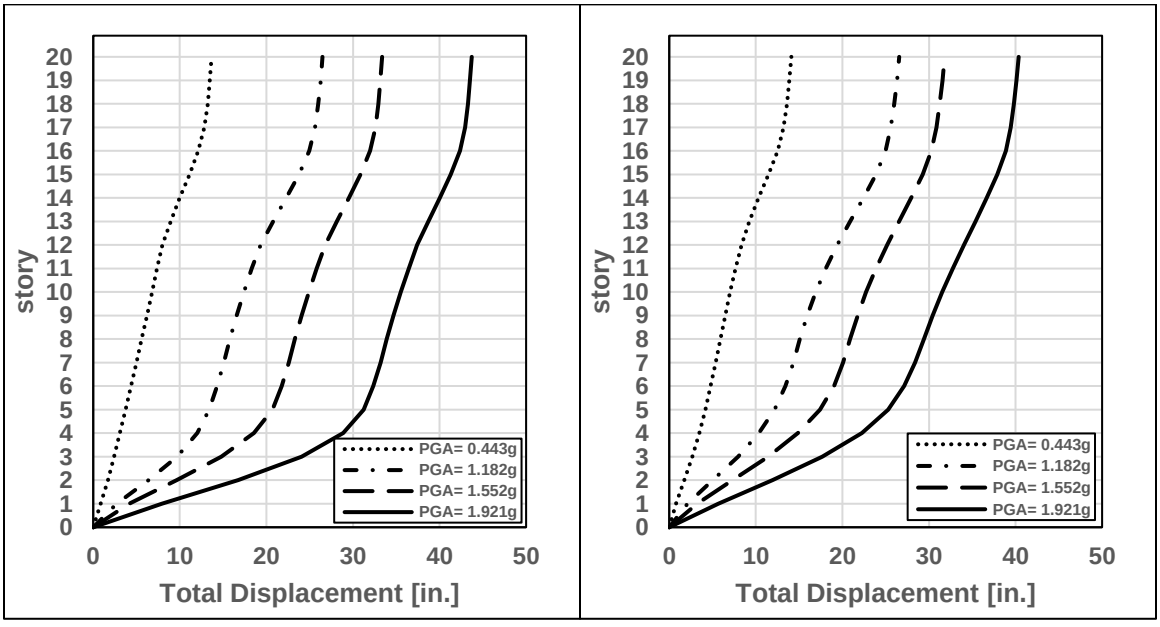

(a) (b)

Fig.App.B- 48 Maximum story displacement for varying scaled ground motion for a) DDM and b) PEER frame

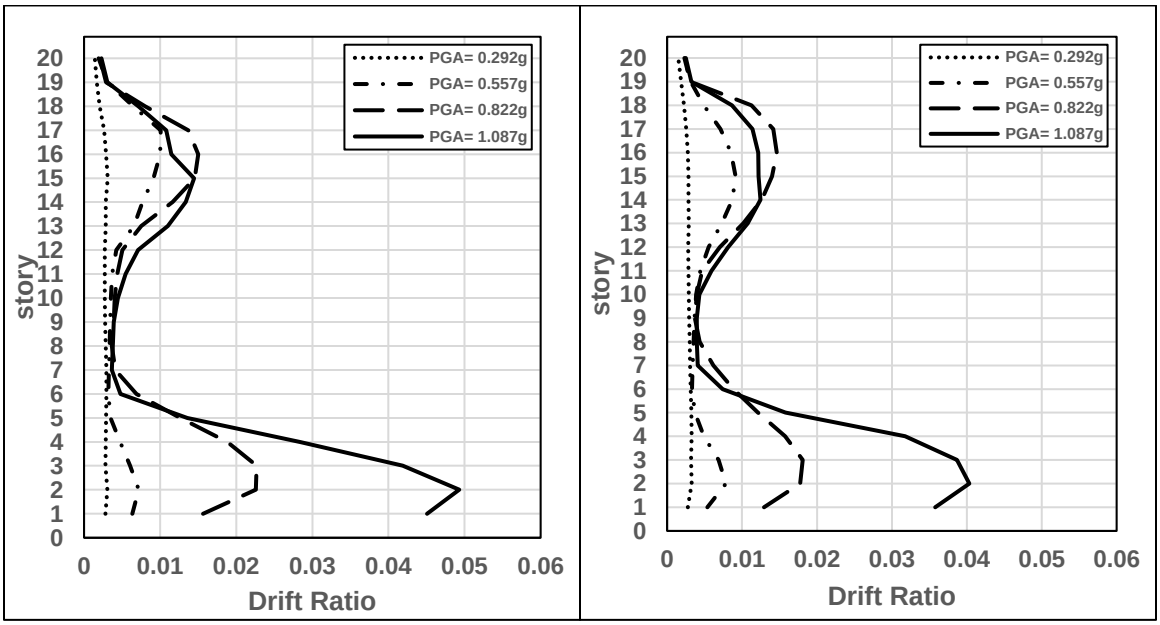

(a) (b)

Fig.App.B- 49 Maximum story drift ratio for varying scaled ground motion for a) DDM and b) PEER frame

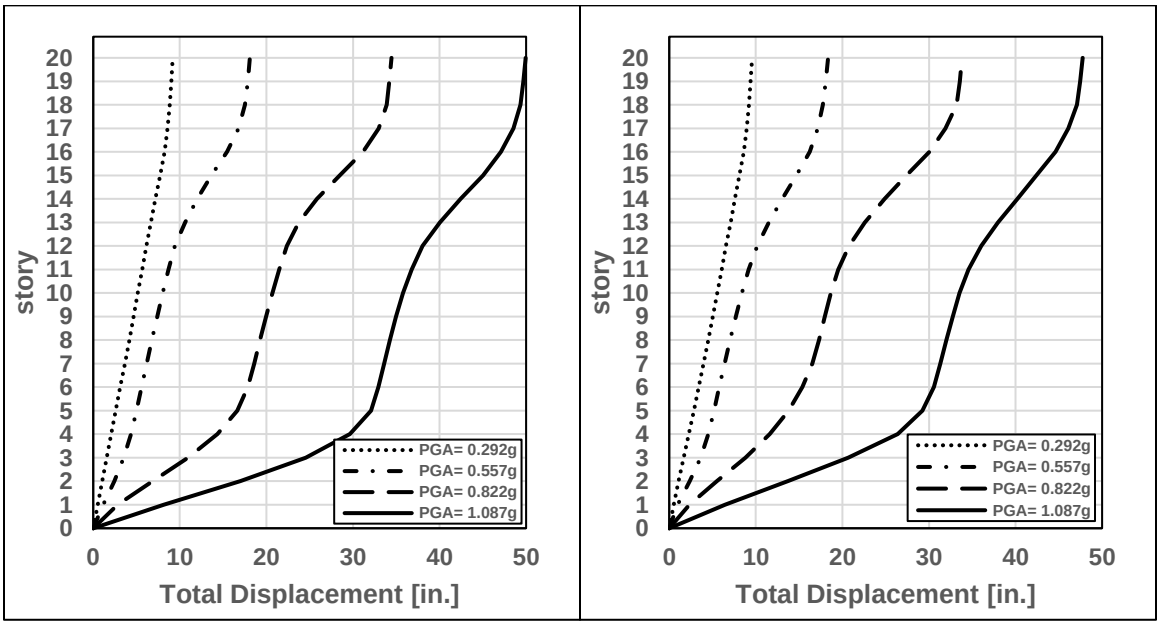

(a) (b)

Fig.App.B- 50 Maximum story displacement for varying scaled ground motion for a) DDM and b) PEER frame

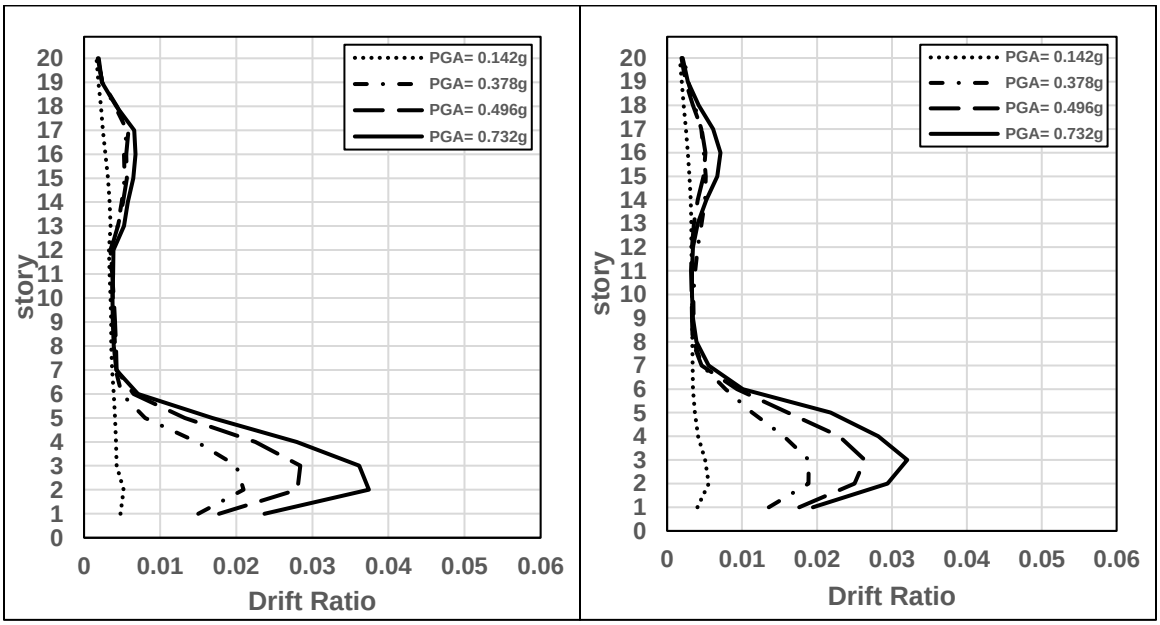

(a) (b)

Fig.App.B- 51 Maximum story drift ratio for varying scaled ground motion for a) DDM and b) PEER frame

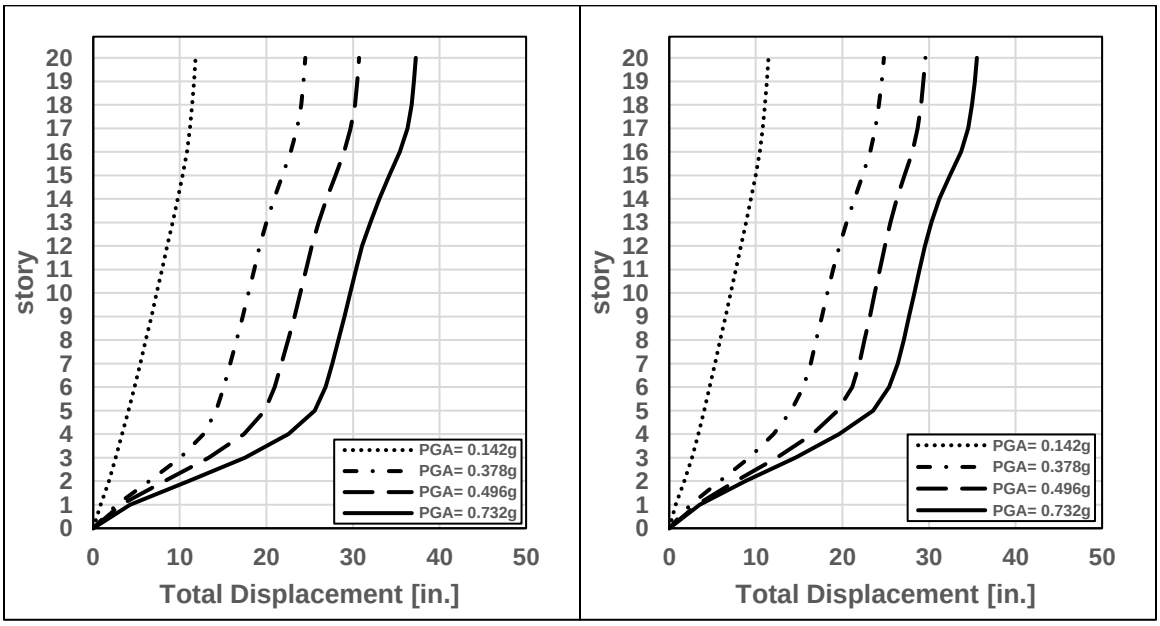

(a) (b)

Fig.App.B- 52 Maximum story displacement for varying scaled ground motion for a) DDM and b) PEER frame

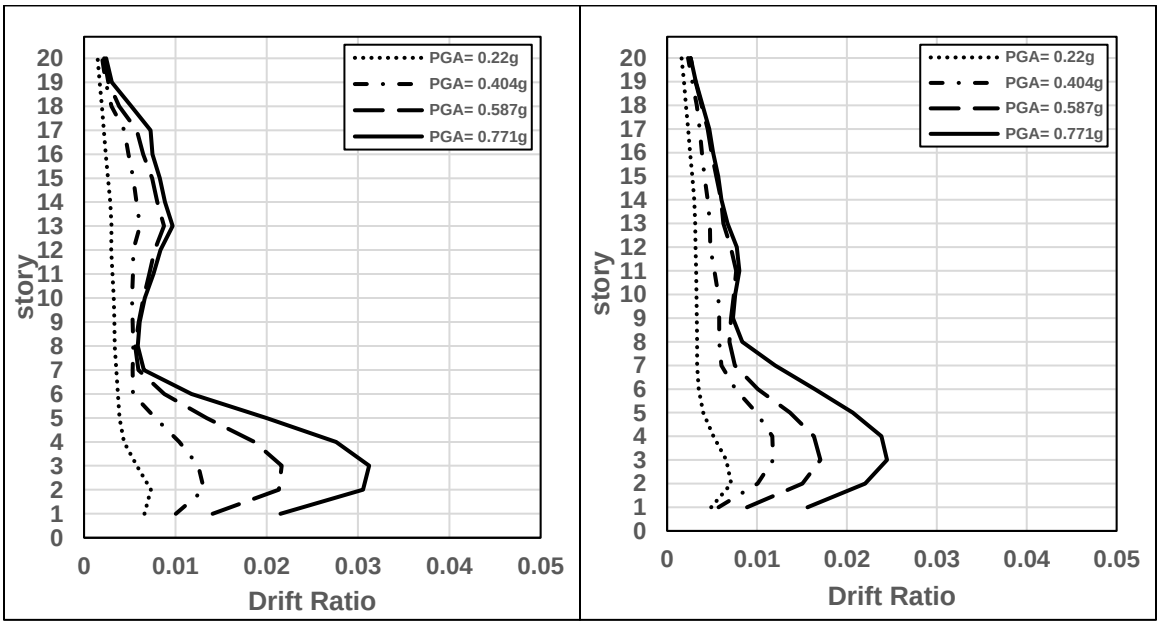

(a) (b)

Fig.App.B- 53 Maximum story drift ratio for varying scaled ground motion for a) DDM and b) PEER frame

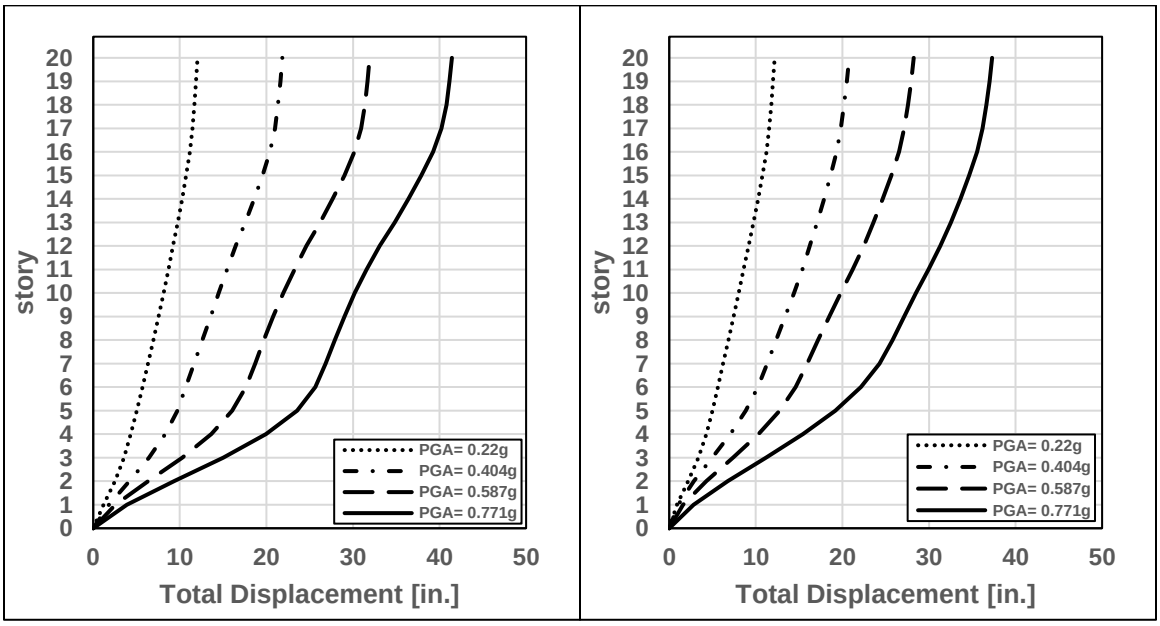

(a) (b)

Fig.App.B- 54 Maximum story displacement for varying scaled ground motion for a) DDM and b) PEER frame

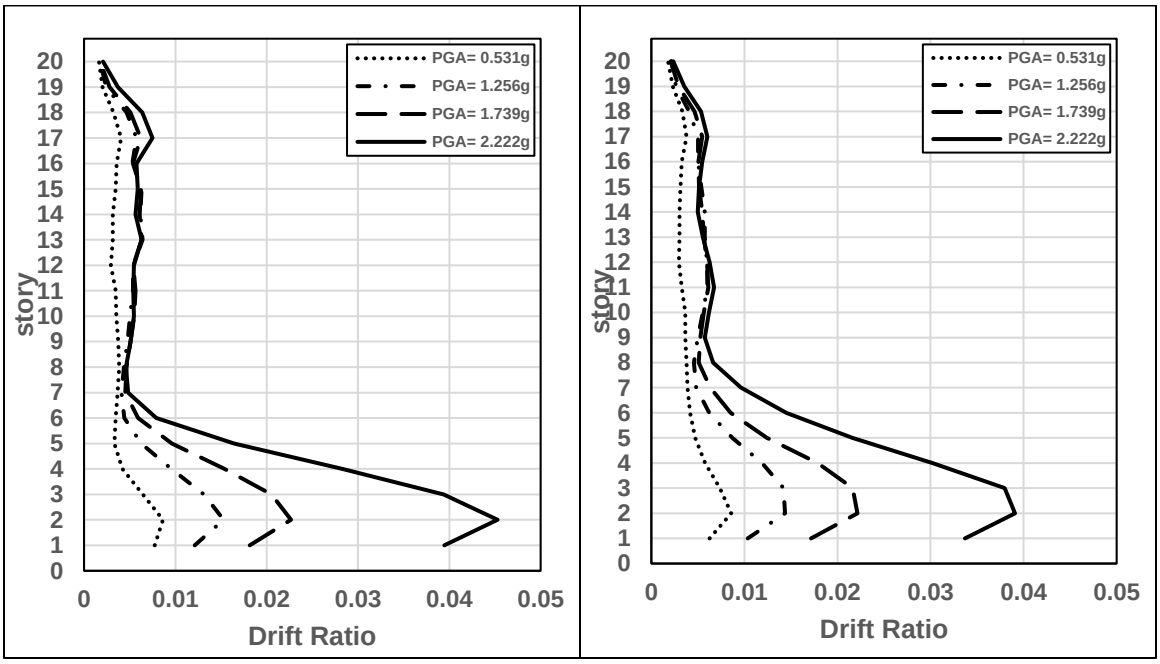

(a) (b)

Fig.App.B- 55 Maximum story drift ratio for varying scaled ground motion for a) DDM and b) PEER frame

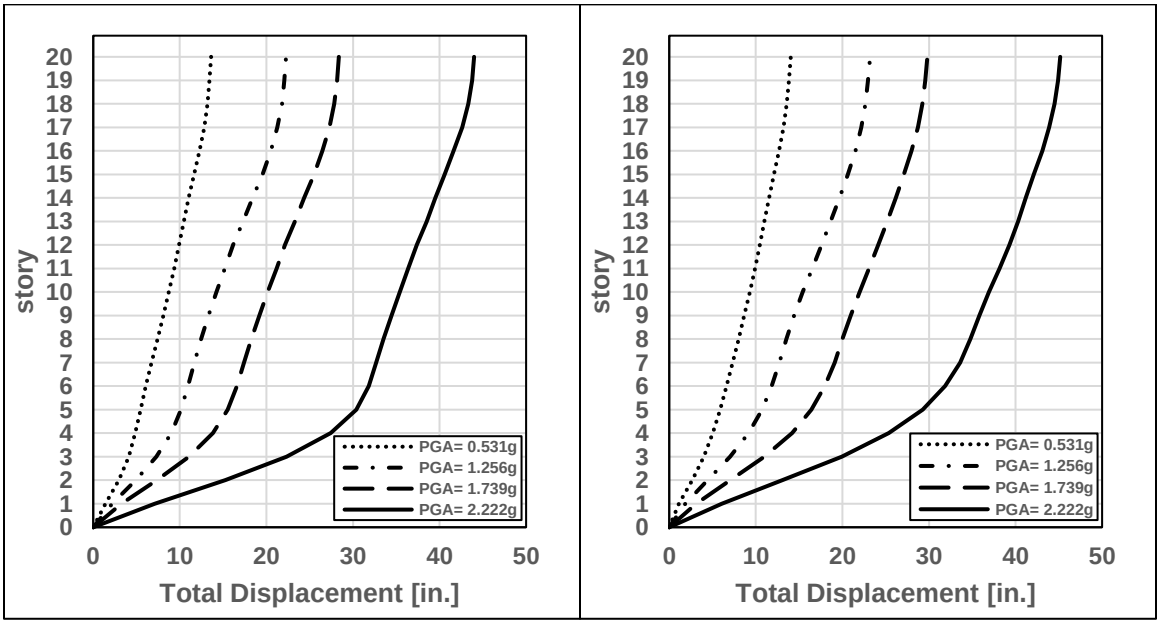

(a) (b)

Fig.App.B- 56 Maximum story displacement for varying scaled ground motion for a) DDM and b) PEER frame

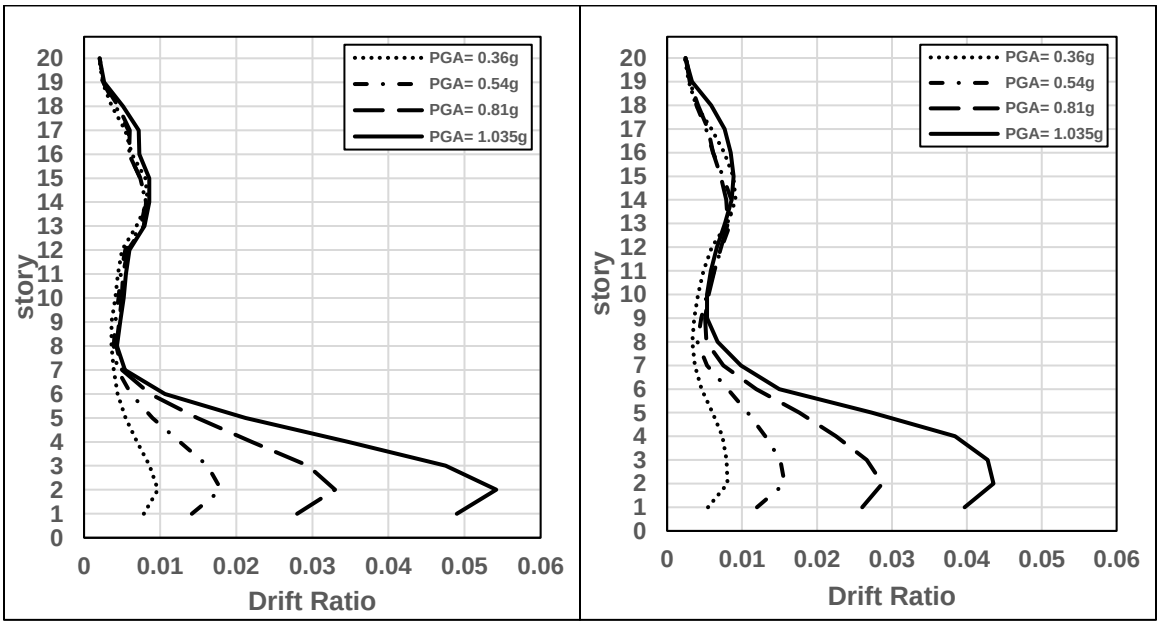

(a) (b)

Fig.App.B- 57 Maximum story drift ratio for varying scaled ground motion for a) DDM and b) PEER frame

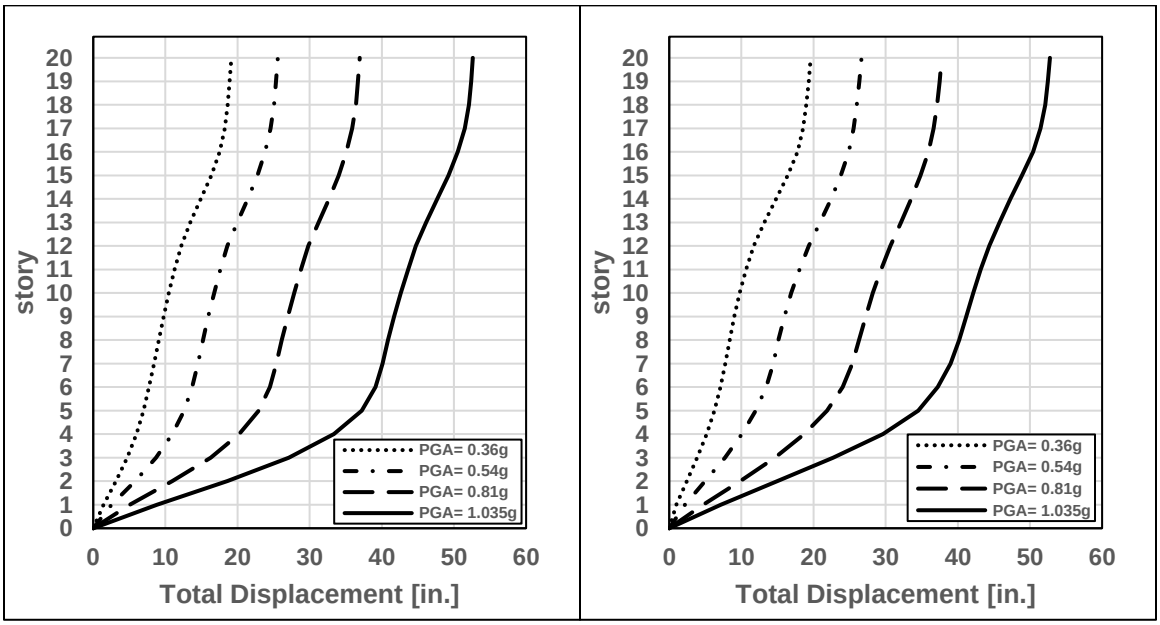

(a) (b)

Fig.App.B- 58 Maximum story displacement for varying scaled ground motion for a) DDM and b) PEER frame

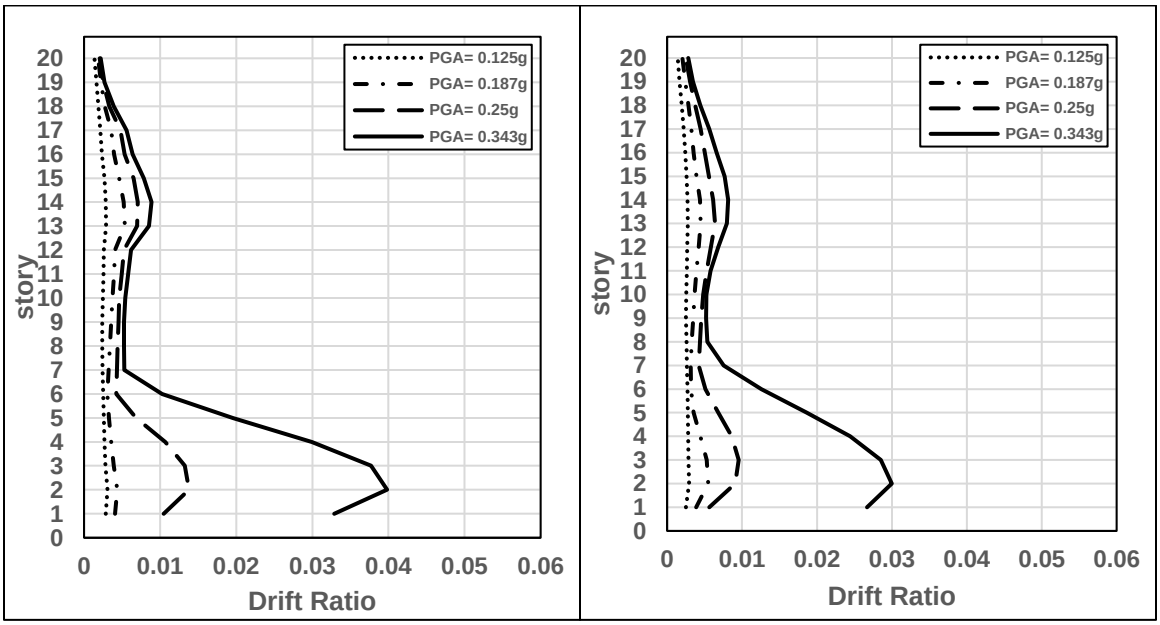

(a) (b)

Fig.App.B- 59 Maximum story drift ratio for varying scaled ground motion for a) DDM and b) PEER frame

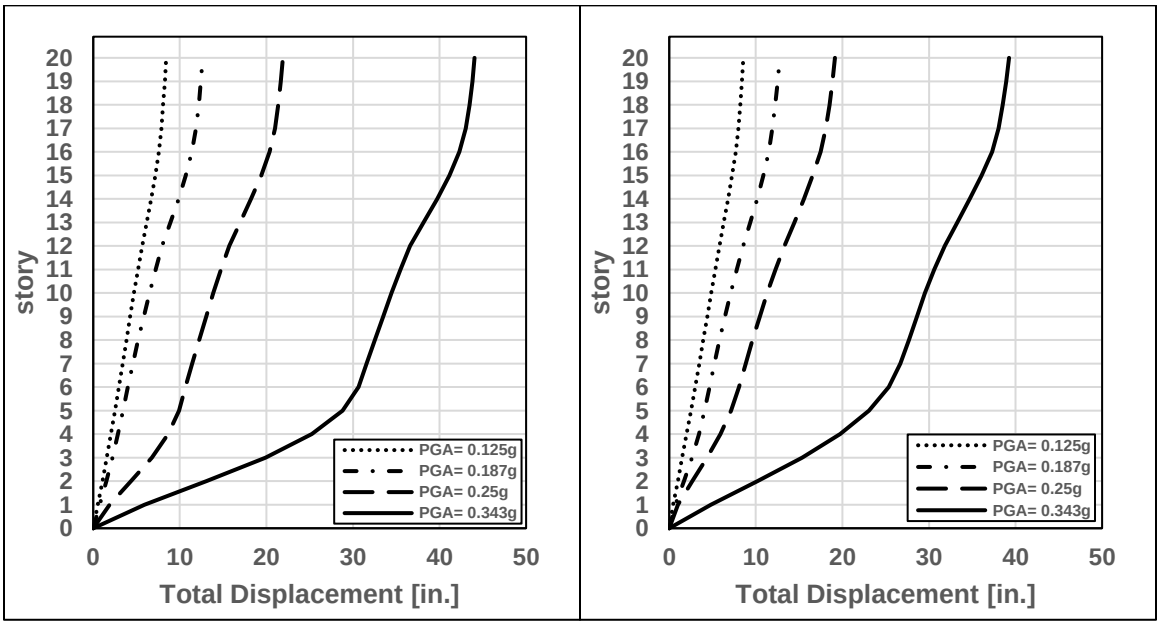

(a) (b)

Fig.App.B- 60 Maximum story displacement for varying scaled ground motion for a) DDM and b) PEER frame

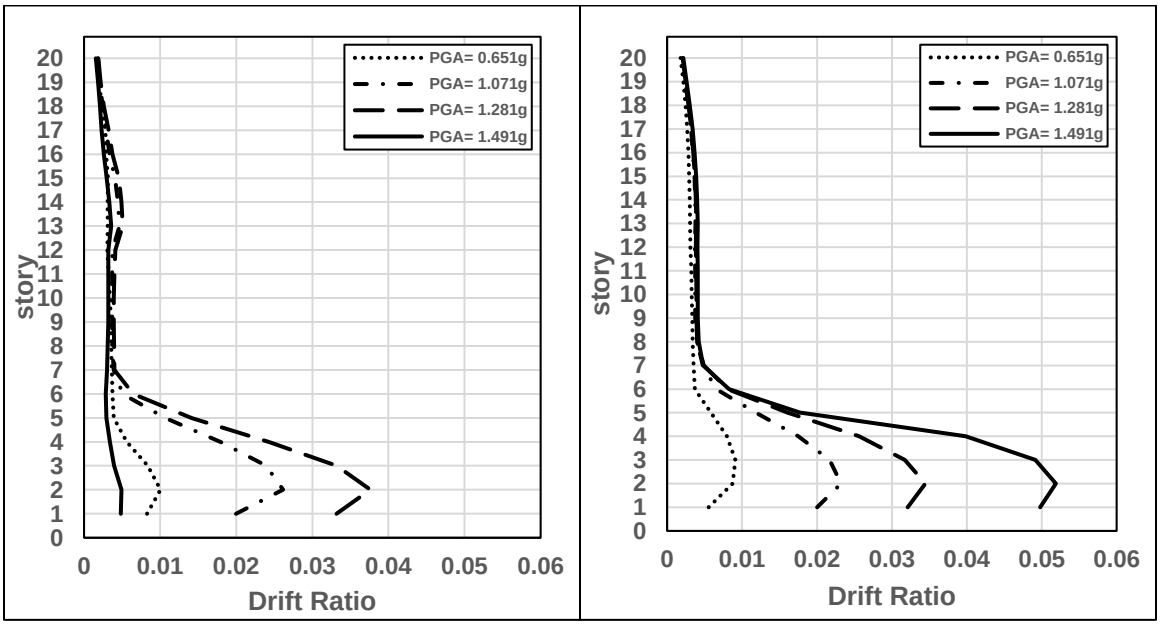

(a) (b)

Fig.App.B- 61 Maximum story drift ratio for varying scaled ground motion for a) DDM and b) PEER frame

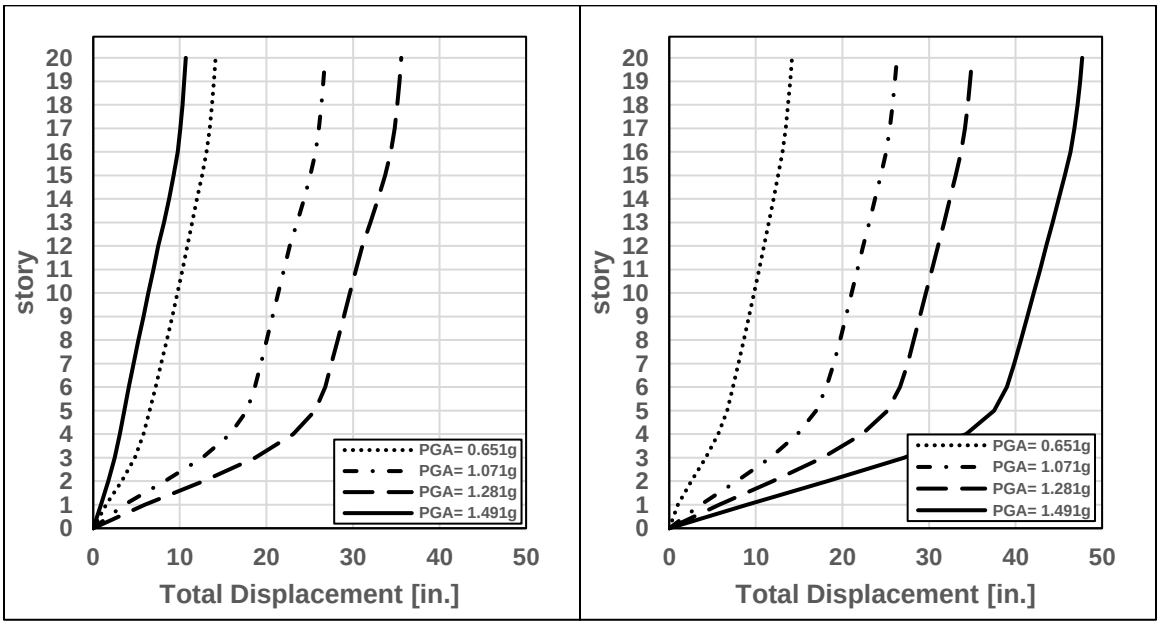

(a) (b)

Fig.App.B- 62 Maximum story displacement for varying scaled ground motion for a) DDM and b) PEER frame

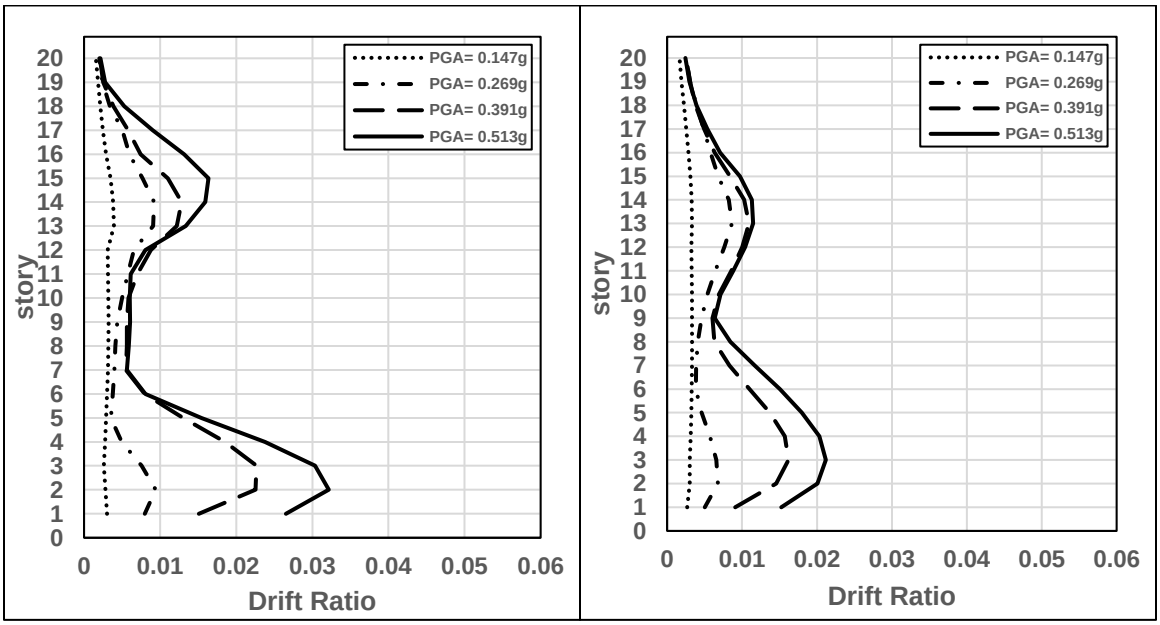

(a) (b)

Fig.App.B- 63 Maximum story drift ratio for varying scaled ground motion for a) DDM and b) PEER frame

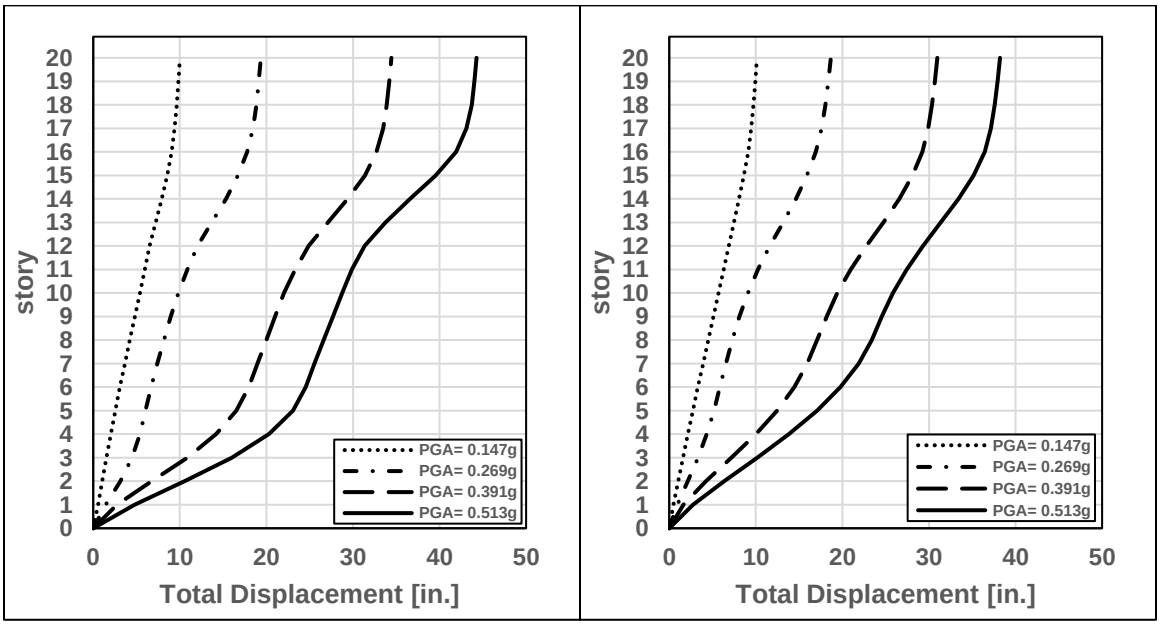

(a) (b)

Fig.App.B- 64 Maximum story displacement for varying scaled ground motion for a) DDM and b) PEER frame

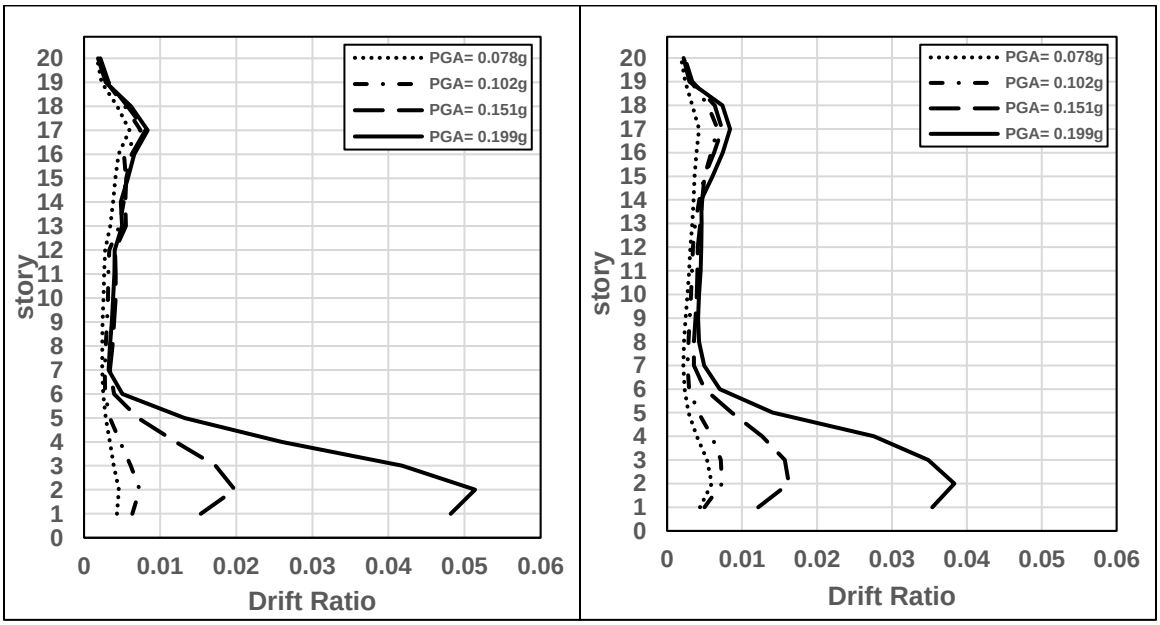

(a) (b)

Fig.App.B- 65 Maximum story drift ratio for varying scaled ground motion for a) DDM and b) PEER frame

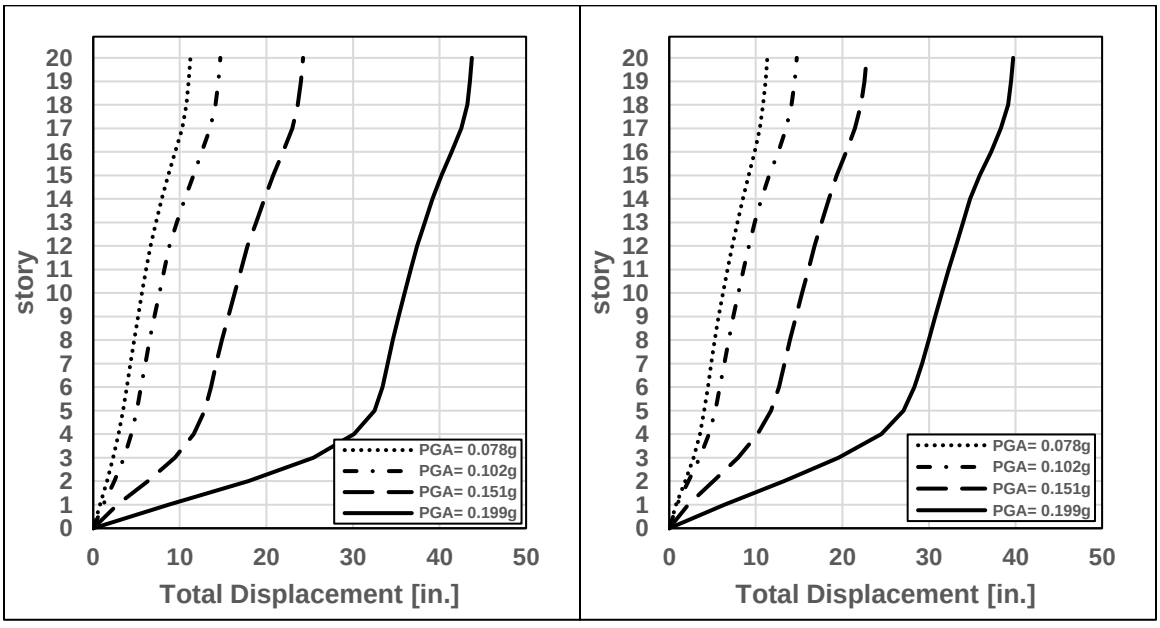

(a) (b)

Fig.App.B- 66 Maximum story displacement for varying scaled ground motion for a) DDM and b) PEER frame

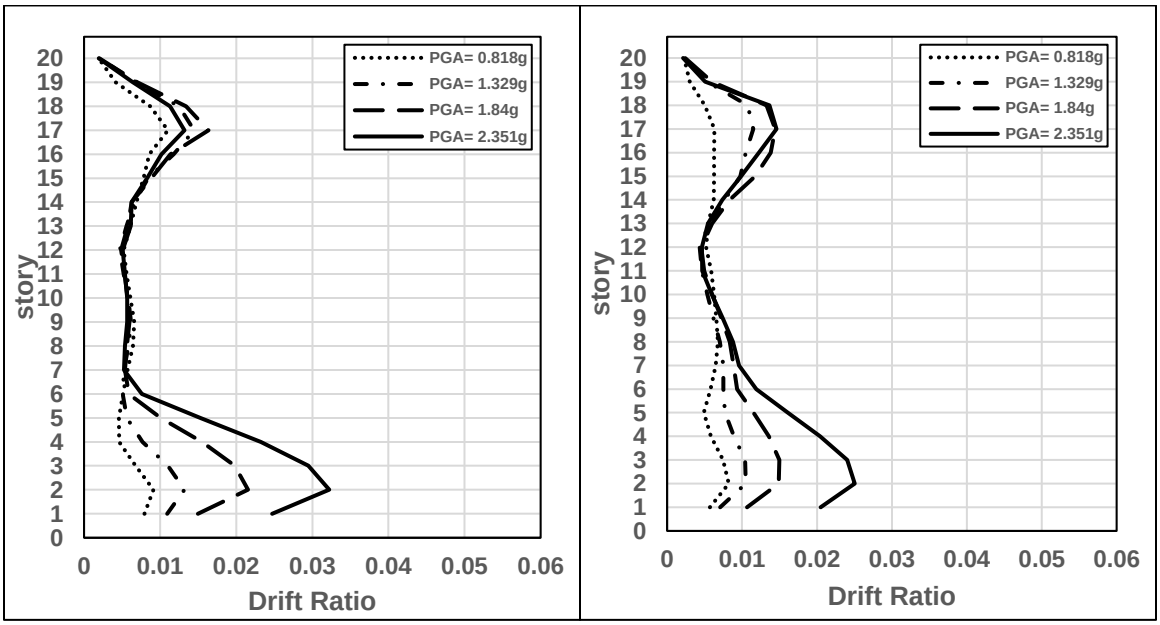

(a) (b)

Fig.App.B- 67 Maximum story drift ratio for varying scaled ground motion for a) DDM and b) PEER frame

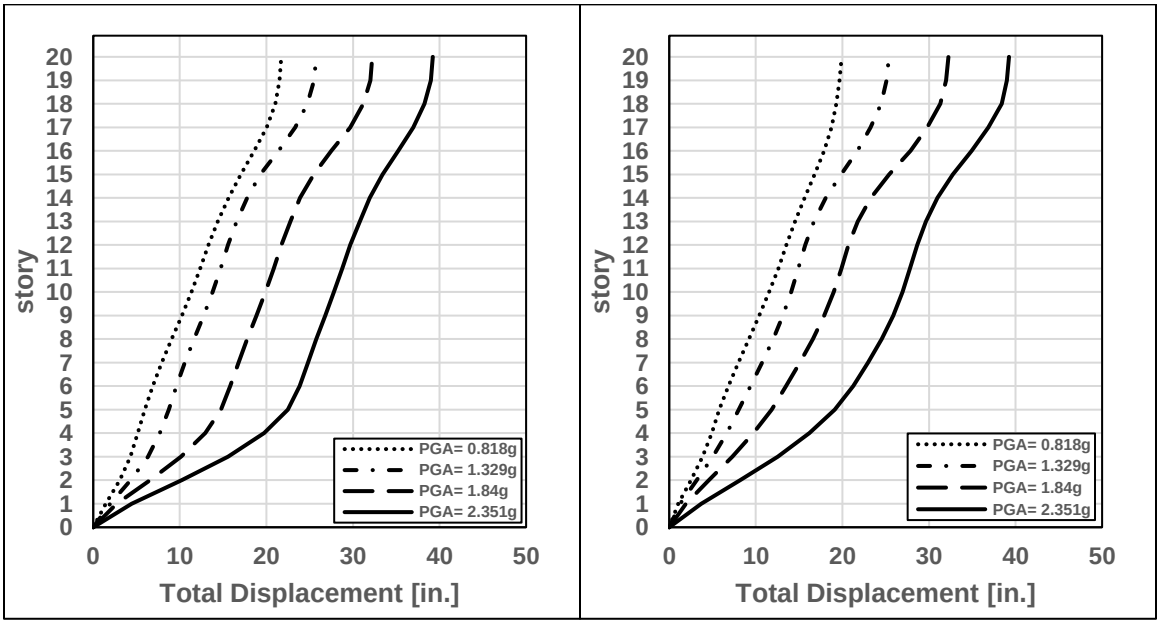

(a) (b)

Fig.App.B- 68 Maximum story displacement for varying scaled ground motion for a) DDM and b) PEER frame

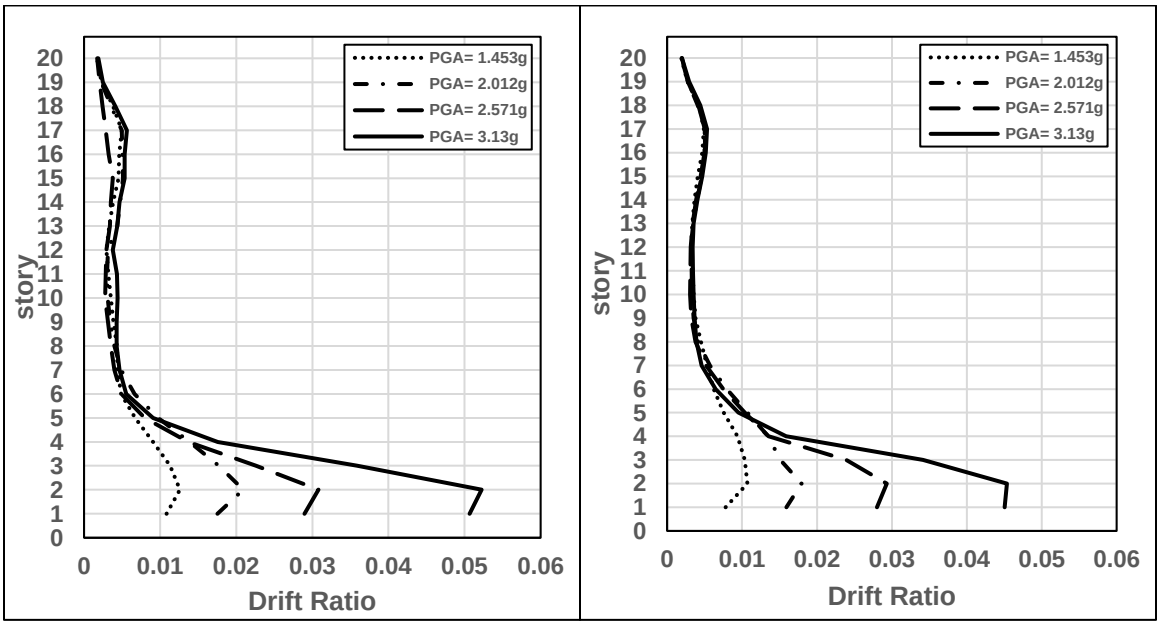

(a) (b)

Fig.App.B- 69 Maximum story drift ratio for varying scaled ground motion for a) DDM and b) PEER frame

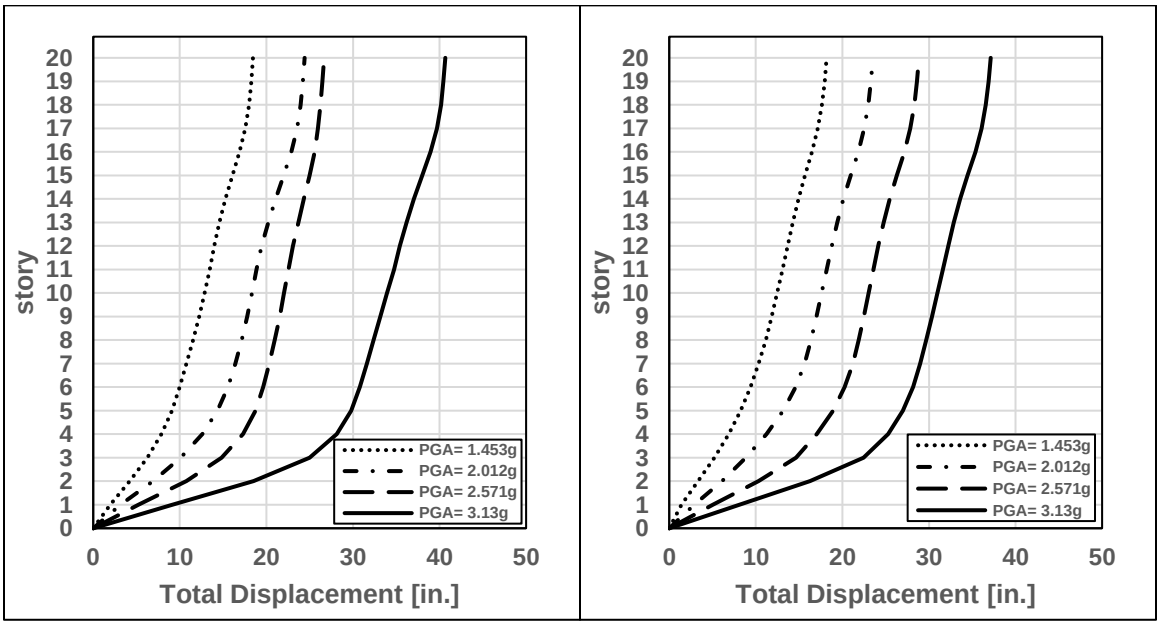

(a) (b)

Fig.App.B- 70 Maximum story displacement for varying scaled ground motion for a) DDM and b) PEER frame

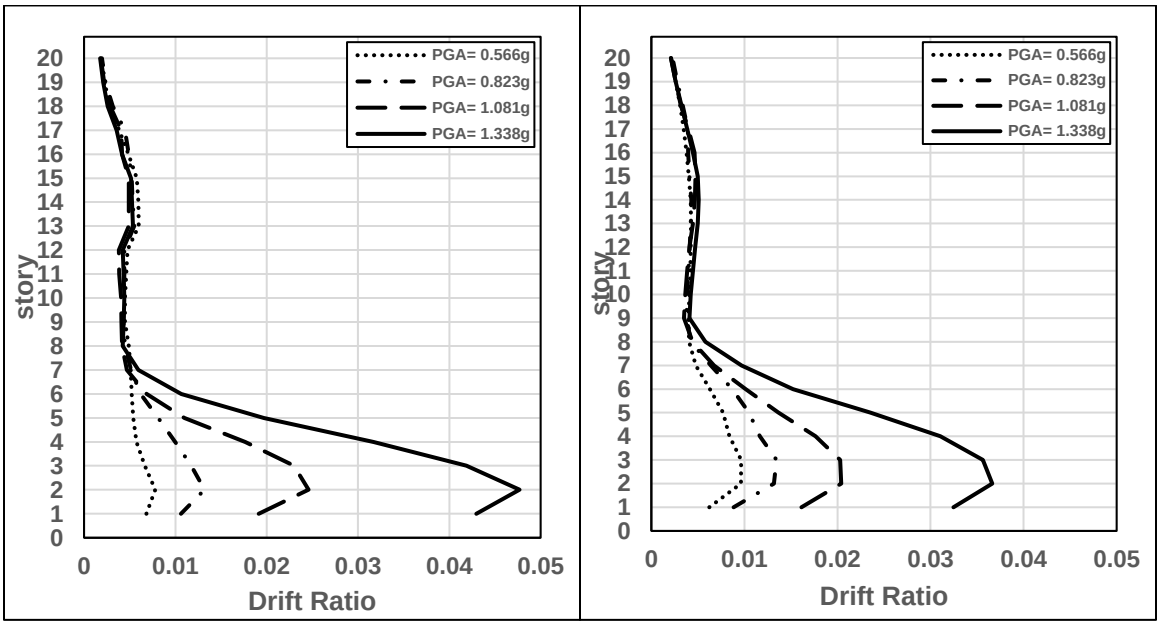

(a) (b)

Fig.App.B- 71 Maximum story drift ratio for varying scaled ground motion for a) DDM and b) PEER frame

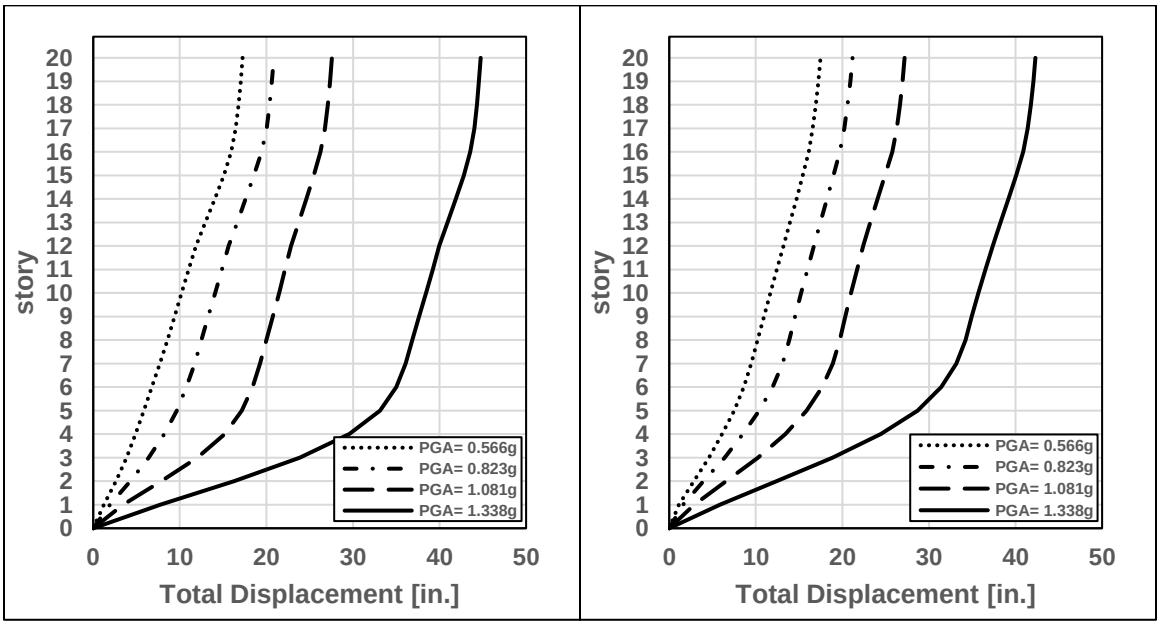

(a) (b)

Fig.App.B- 72 Maximum story displacement for varying scaled ground motion for a) DDM and b) PEER frame

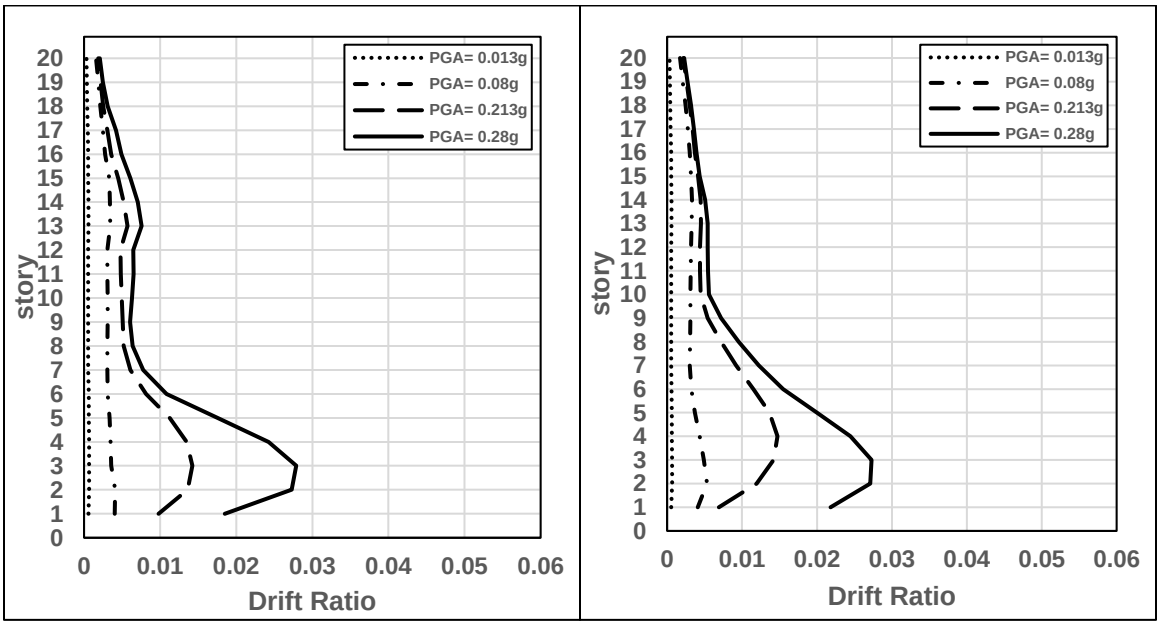

(a) (b)

Fig.App.B- 73 Maximum story drift ratio for varying scaled ground motion for a) DDM and b) PEER frame

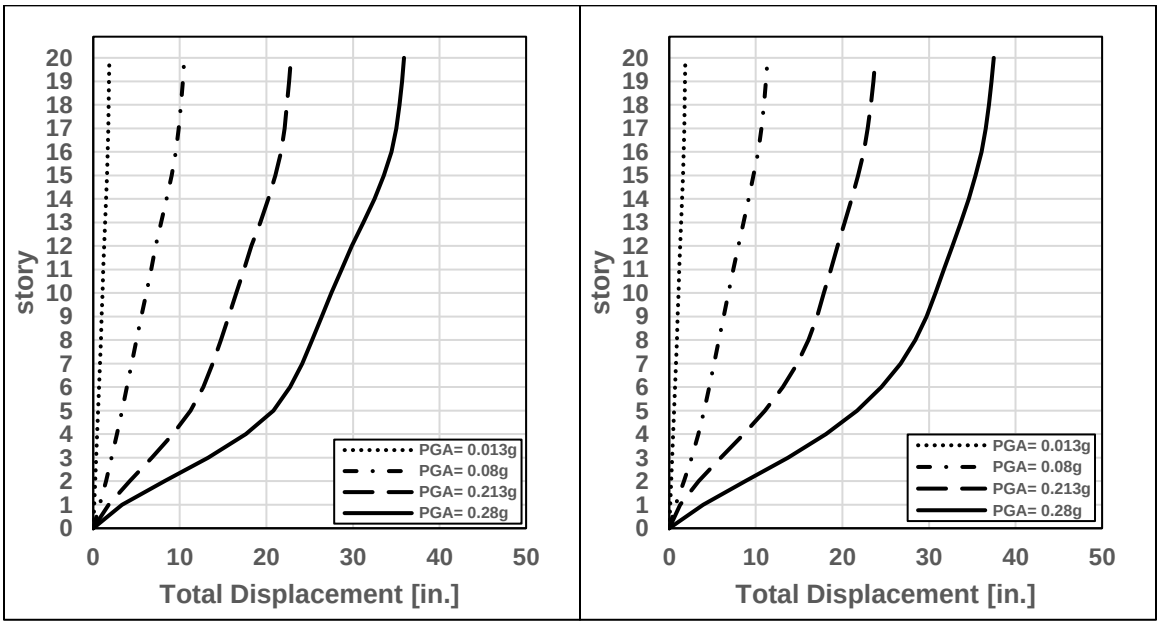

(a) (b)

Fig.App.B- 74 Maximum story displacement for varying scaled ground motion for a) DDM and b) PEER frame

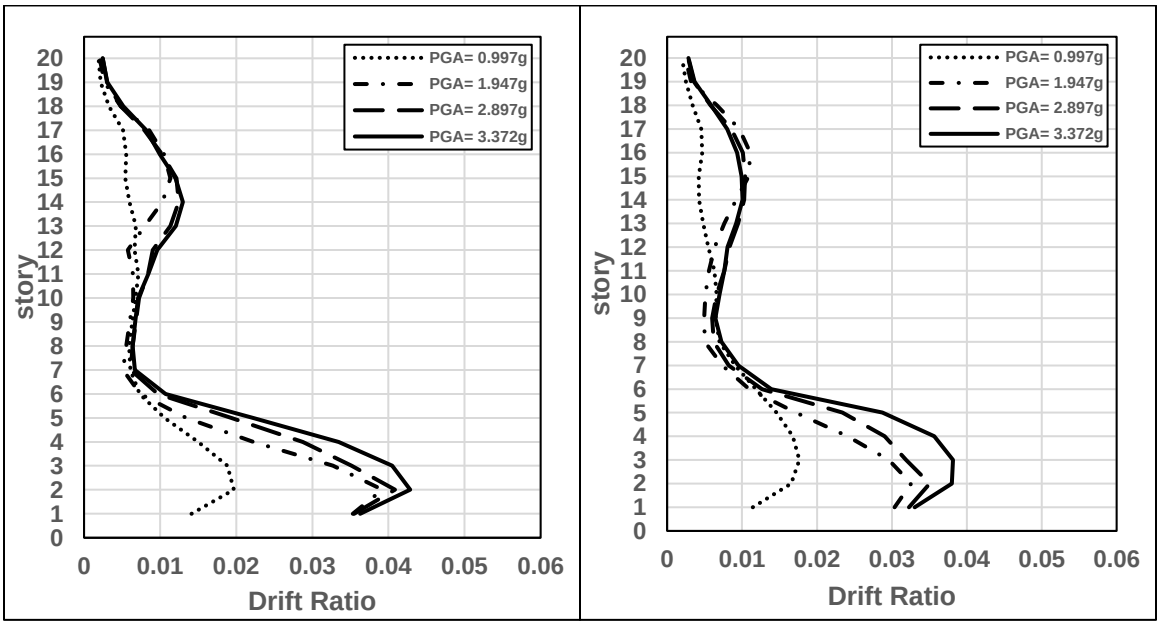

(a) (b)

Fig.App.B- 75 Maximum story drift ratio for varying scaled ground motion for a) DDM and b) PEER frame

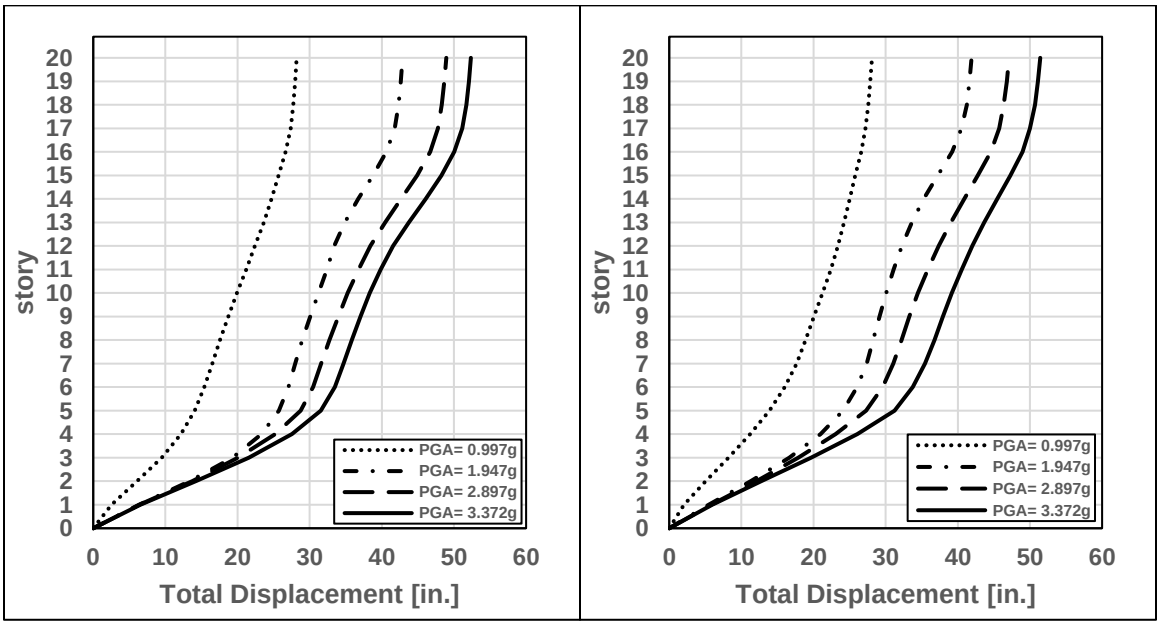

(a) (b)

Fig.App.B- 76 Maximum story displacement for varying scaled ground motion for a) DDM and b) PEER frame

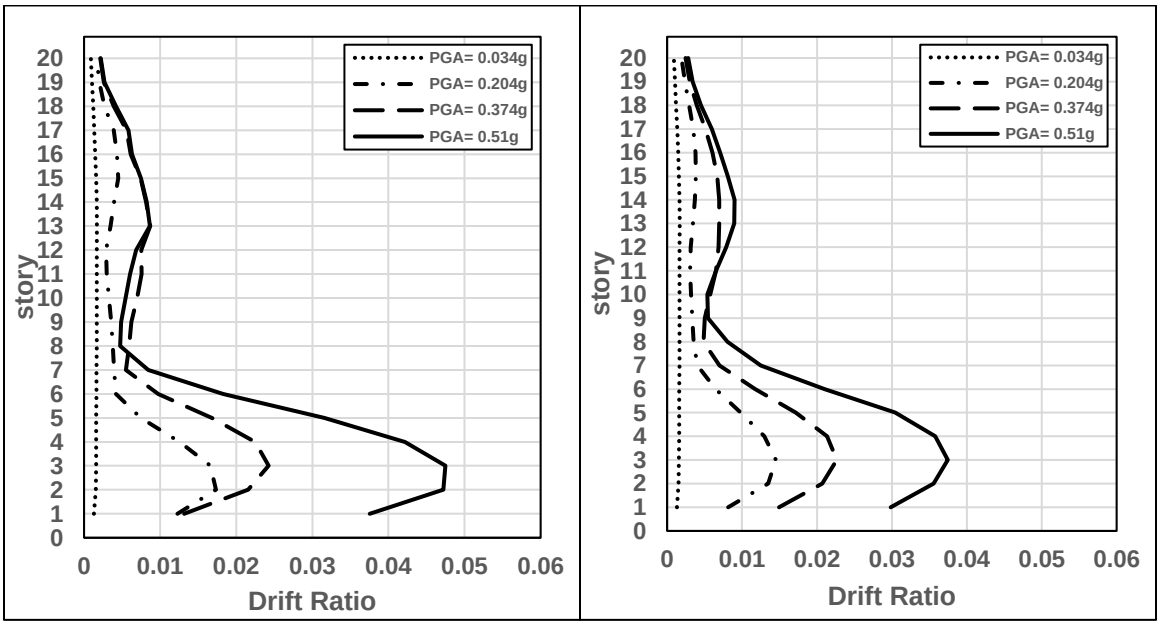

(a) (b)

Fig.App.B- 77 Maximum story drift ratio for varying scaled ground motion for a) DDM and b) PEER frame

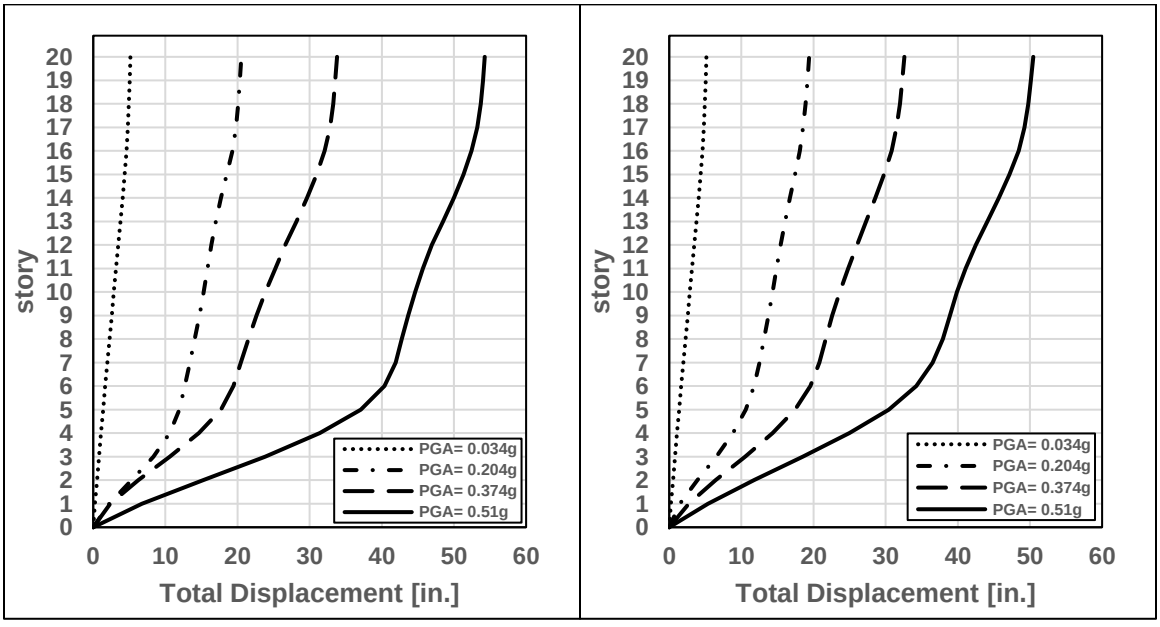

(a) (b)

Fig.App.B- 78 Maximum story displacement for varying scaled ground motion for a) DDM and b) PEER frame

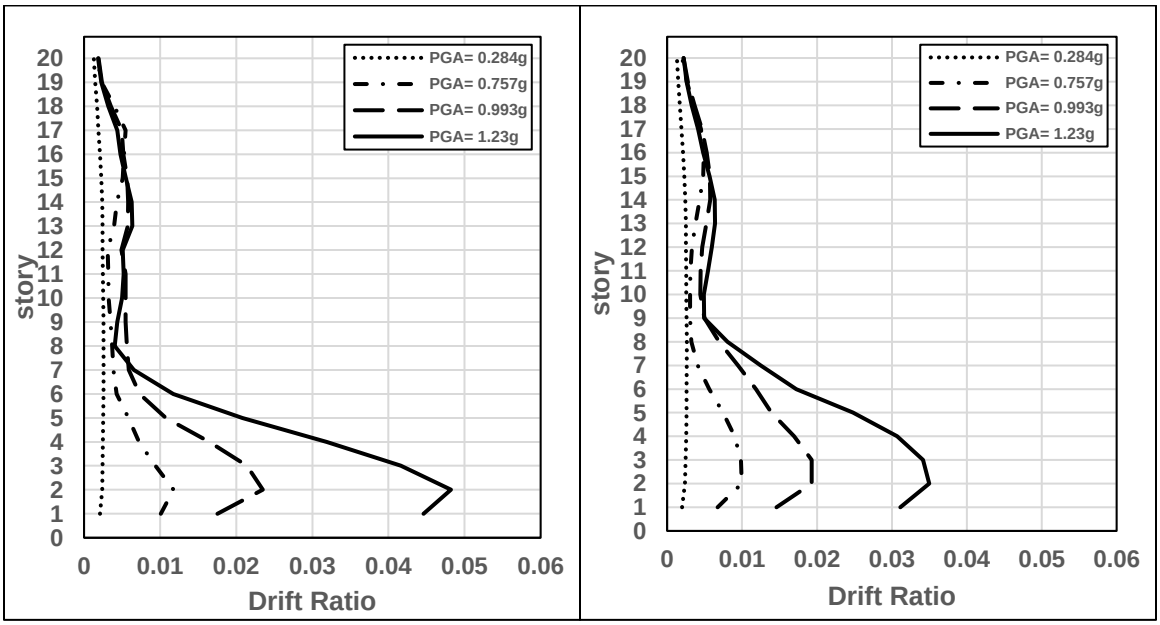

(a) (b)

Fig.App.B- 79 Maximum story drift ratio for varying scaled ground motion for a) DDM and b) PEER frame

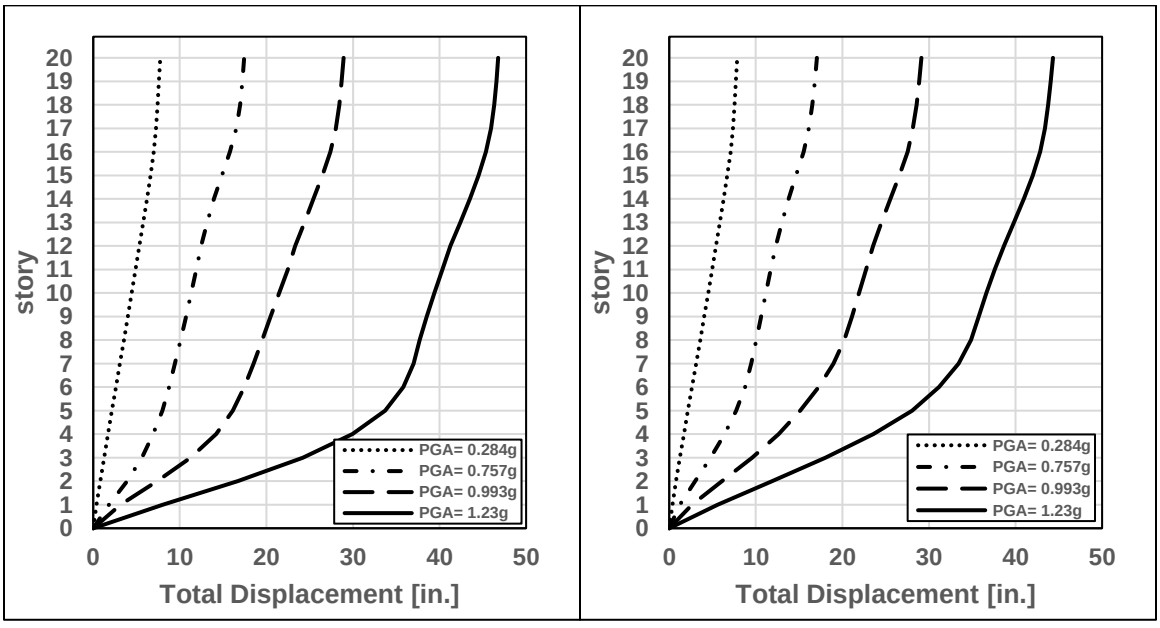

(a) (b)

Fig.App.B- 80 Maximum story displacement for varying scaled ground motion for a) DDM and b) PEER frame

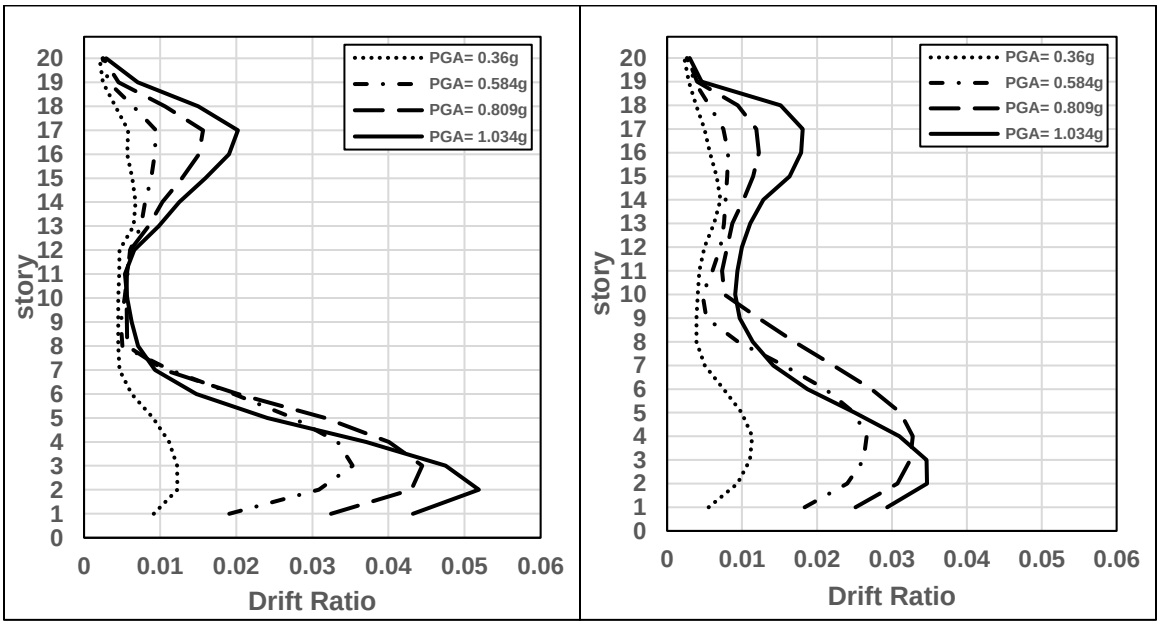

(a) (b)

Fig.App.B- 81 Maximum story drift ratio for varying scaled ground motion for a) DDM and b) PEER frame

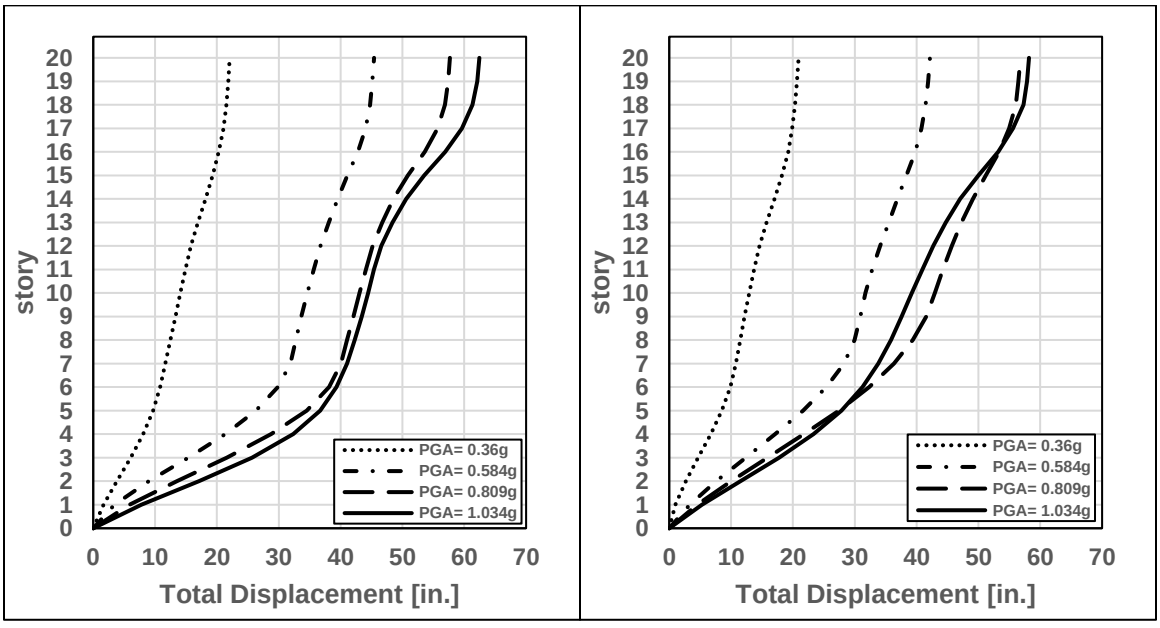

(a) (b)

Fig.App.B- 82 Maximum story displacement for varying scaled ground motion for a) DDM and b) PEER frame

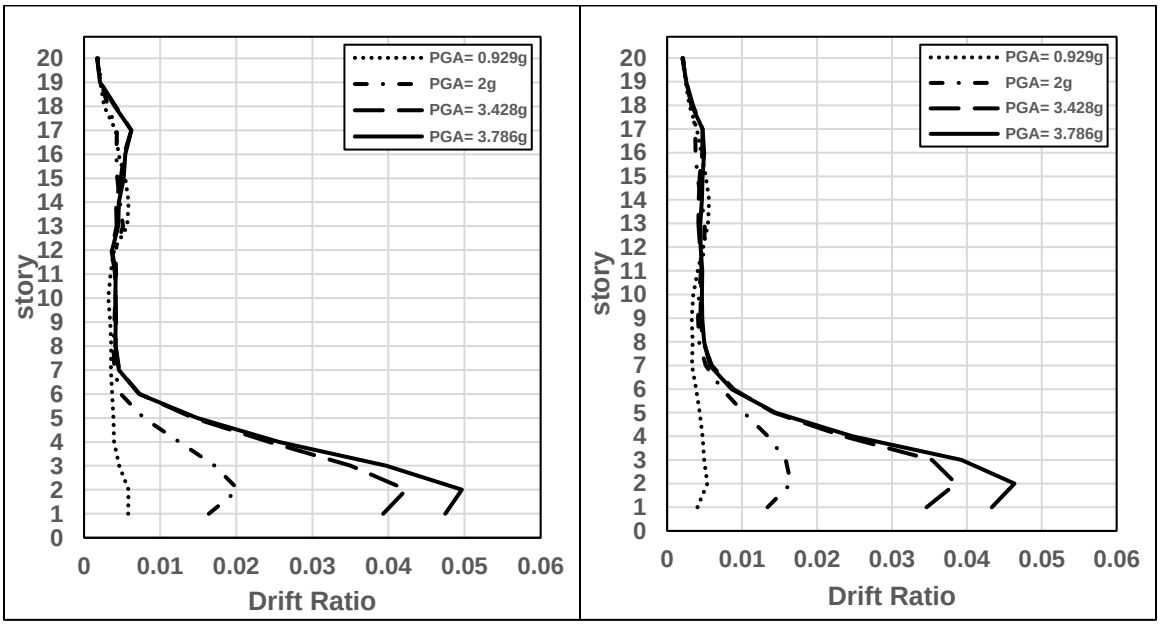

(a) (b)

Fig.App.B- 83 Maximum story drift ratio for varying scaled ground motion for a) DDM and b) PEER frame

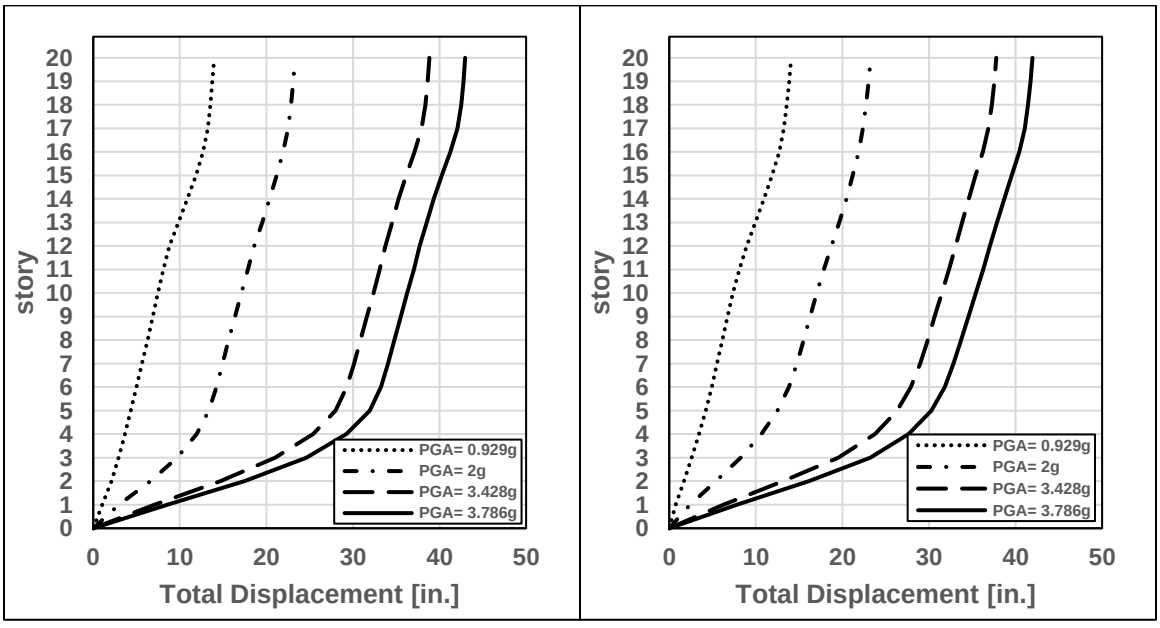

(a) (b)

Fig.App.B- 84 Maximum story displacement for varying scaled ground motion for a) DDM and b) PEER frame

Biographical Information

Seyed Missagh Shamshiri Guilvayi obtained his Bachelor of Science in the field of Civil Engineering in 2011 from the K. N. Toosi (KNT) University of Technology, Tehran, Iran. Same year, he was admitted to Sharif University of Technology (SUT), Tehran, Iran. Missagh pursued his master's degree in that university in the field of structural engineering. After two years of the compulsory military service, he travelled abroad to continue his education at the University of Texas at Arlington, USA. In Fall 2016, he started his PhD in the field of structural engineering in various research topics including Ultra High-Performance Fiber-Reinforced Concrete, non-prestressed long-span bridges, reinforced concrete buildings, structural dynamics and collapse assessment of RC buildings subjected to extreme loadings. Missagh also participated in extracurricular activities such as student engineering organizations during his PhD. He graduated in Summer 2021 with a PhD in Civil Engineering.

Missagh secured a postdoctoral position and will be continuing his academic career as a research assistant at the University of Texas at Arlington. Also, he will be serving as an instructor in that university.